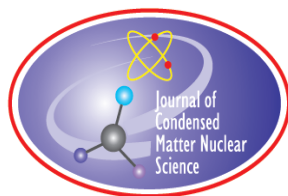


JOURNAL OF CONDENSED MATTER NUCLEAR SCIENCE

Experiments and Methods in Cold Fusion

**Proceedings of the ICCF 22 Conference,
September 8–13, 2019, Assisi, Italy**

VOLUME 33, August 2020



JOURNAL OF CONDENSED MATTER NUCLEAR SCIENCE

Experiments and Methods in Cold Fusion

Editor-in-Chief

Jean-Paul Biberian
Marseille, France

Editorial Board

Peter Hagelstein
MIT, USA

George Miley
*Fusion Studies Laboratory,
University of Illinois, USA*

Xing Zhong Li
Tsinghua University, China

Michael McKubre
SRI International, USA

Edmund Storms
KivaLabs, LLC, USA

JOURNAL OF CONDENSED MATTER NUCLEAR SCIENCE

Volume 33, August 2020

© 2020 ISCMNS. All rights reserved. ISSN 2227-3123

This journal and the individual contributions contained in it are protected under copyright by ISCMNS and the following terms and conditions apply.

Electronic usage or storage of data

JCMNS is an open-access scientific journal and no special permissions or fees are required to download for personal non-commercial use or for teaching purposes in an educational institution.

All other uses including printing, copying, distribution require the written consent of ISCMNS.

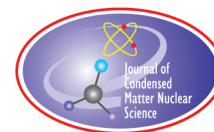
Permission of the ISCMNS and payment of a fee are required for photocopying, including multiple or systematic copying, copying for advertising or promotional purposes, resale, and all forms of document delivery.

Permissions may be sought directly from ISCMNS, E-mail: CMNSEditor@iscmns.org. For further details you may also visit our web site: <http://www.iscmns.org/CMNS/>

Members of ISCMNS may reproduce the table of contents or prepare lists of articles for internal circulation within their institutions.

Orders, claims, author inquiries and journal inquiries

Please contact the Editor in Chief, CMNSEditor@iscmns.org or webmaster@iscmns.org



JOURNAL OF CONDENSED MATTER NUCLEAR SCIENCE

Volume 33

2020

CONTENTS

RESEARCH ARTICLES

- Excess Energy Generation using a Nano-sized Multilayer Metal Composite and Hydrogen Gas 1
Yasuhiro Iwamura, Takehiko Itoh, Jirohta Kasagi, Shoichi Murakami and Mari Saito
- Latest Progress in Research on AHE and Circumstantial Nuclear Evidence by Interaction of Nano-Metal and H(D)-Gas 14
Akito Takahashi, Hiroyuki Ido, Atsushi Hattori, Reiko Seto, Atsushi Kamei, Joji Hachisuka, Toyoshi Yokose, Yutaka Mori, Akira Taniike and Yuichi Furuyama
- Mass and Heat Flow Calorimetry in Brillouin's Reactor 33
Francis Tanzella, Robert Godes, Jin Liu and Robert George
- Progress Toward an Understanding of LENR–AHE Effects in Coated Constantan Wires in D₂ Atmosphere: DC/AC Voltage Stimulation 46
Francesco Celani, C. Lorenzetti, G. Vassallo, E. Purchi, S. Fiorilla, S. Cupellini, M. Nakamura, R. Burri, P. Boccanera, P. Cerreoni and A. Spallone
- The Thermoneutral Potential in Electrochemical Calorimetry for the Pd/D₂O System 74
Melvin H. Miles
- Active LANR Systems Emit a 327.37 MHz Maser Line 81
Mitchell R. Swartz
- Pulsatile Superhyperfine Lines at 327.37 MHz Herald LANR Activity and Possible Mass–Energy Transfer 111
Mitchell R. Swartz
- FCC Vacancies in ZrO₂PdD are the Active LANR Site 126
Mitchell R. Swartz

Elliptic Tracks: Evidence For Superluminal Electrons? <i>Keith A. Fredericks</i>	145
Condensed Plasmoids (CPs) – A Quantum-Mechanical Model of the Nuclear Active Environment of LENR <i>Lutz Jaitner</i>	168
The Electromagnetic Considerations of the Nuclear Force <i>N.L. Bowen</i>	194
An Examination of the Updated Empirical Data in Support of the Shell Model <i>N.L. Bowen</i>	224
Review of Seebeck Calorimeters Used in LENR Experiments <i>Bengisu Sisik and David J. Nagel</i>	234
Basics of Air-Flow Calorimetry <i>Jacques Ruer</i>	252
Buoyant Heat Transport in Flow Calorimetry <i>Mitchell R. Swartz</i>	268
Highly Relativistic Deep Electrons and the Dirac Equation <i>Jean-Luc Paillet and Andrew Meulenberg</i>	278
Distant Behind-screen Action of Undamped Temperature Waves(Long-distance Propagation, X-ray Generation, LENR Stimulation <i>V.I. Vysotskii, M.V.Vysotskyy, A.A. Kornilova, T.B. Krit, S.N. Gaydamaka and P.L. Hagelstein</i>	296
Application of Correlated wave Packets for Stimulation of LENR in Remote Targets) <i>V.I. Vysotskii and M.V.Vysotskyy</i>	305
Could LENR Change the World? <i>Jacques Ruer</i>	314
Creation of Fe Isotopes in Natural Geology Crusts as the Result of Self-controlled Global Biostimulated LENR in Oceans and Seas <i>V.I. Vysotskii, M.V. Vysotskyy, A.A. Kornilova, S.N. Gaydamaka, A.A. Novakova, D.S. Novikov and V.V. Avdonin</i>	323
The Possible Role of LENR in Dentistry (Reasons, Effects and Prevention) <i>A.A. Kornilova, S.N. Gaydamaka, A.I. Panchishin, V.I. Vysotskii, M.V.Vysotskyy and A.A. Bolotokov</i>	333

Preface

The 22nd International Conference on Condensed Matter Nuclear Science, ICCF-22, was held on September 8–13, 2019, in Santa Margherita degli Angeli near Assisi, Italy, at the Hotel and Conference Centre, Domus Pacis, organized by William Collis with Co-chair Claudio Pace. There were 152 participants and 57 oral presentations were made with a further 27 poster papers.

The philosophy of the conference followed the successful ICCF-21 held in June 2018 in Colorado, USA. Emphasis was on a good value for money and creating a convivial atmosphere. We were very lucky to find the right balance in a down town hotel and conference centre with costs even pilgrims could afford! The banquet was held in the hotel gardens with a medieval entertainment and music. <http://www.claudiopace.it/iccf22-renaissance-banquet-and/> Several participants dressed up in costume and recited their lines. During the banquet the Giuliano Preparata Medal was awarded to Dr. Vladimir Vysotskii. We also organized an open bar pioneered at ICCF-21 and on three evenings drinks were available after dinner in the foyer to allow participants to continue scientific discussions.

The format of the conference followed that of previous years starting with a reception on Sunday evening with the usual plenary sessions starting on Monday morning and continuing until Friday mid-day. There was an excursion by coach to Assisi on the Tuesday. More details of the conference can be found online at <https://iscmns.org/iccf22/>.

The International Advisory Committee received the presentation by Dr Chongen Huang and appointed Professor Tian ZhongQun to organize ICCF-23 in China. We wish our Chinese colleagues every success in organizing the next conference during these uncertain times of Covid-19.

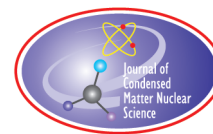
I would like to end by thanking all those who made ICCF-22 such a success starting with my co-chairman Claudio Pace. He organized most of the local arrangements. A big thank you is due to Assia, Misa, Elettra, Ursula, Emanuele, Ruby, Alan and to our patrons ISCMNS, LENRIA, NICHENERGY, ASSISI NEL VENTO, not forgetting our anonymous financial sponsors. And of course we are grateful to the Domus Pacis staff, particularly, Giuseppe, Chiara and Sabrina.

Sincerely,

Dr. Bill Collis

(Chairman, Organizing Committee for ICCF-22)

August 2020



Research Article

Excess Energy Generation using a Nano-sized Multilayer Metal Composite and Hydrogen Gas

Yasuhiro Iwamura*, Takehiko Itoh[†] and Jirohta Kasagi

Research Center for Electron Photon Science, Tohoku University, Sendai, Miyagi 982-0826, Japan

Shoichi Murakami and Mari Saito

CLEAN PLANET Inc., Tokyo 105-0022, Japan

Abstract

New type of excess heat experiments using a nano-sized metal multilayer composite and hydrogen gas have been performed based on the permeation-induced transmutation experiments with multilayer thin film and excess heat experiments with nano-particles. Two nano-sized metal multilayer composite samples, which were composed of Ni, Cu, CaO, Y₂O₃ thin films on bulk Ni (25 mm × 25 mm × 0.1 mm), were placed in a vacuum chamber. These samples were fabricated by Ar ion beam sputtering method. After baking of the samples, H₂ gas was introduced into the chamber up to about 230 Pa at 250°C. Then, the Ni based multilayer thin films started to absorb H₂ gas. Amount of absorbed H₂ gas can be evaluated by the pressure measurement of the chamber. Typically, after about 50,000 s, H₂ gas was evacuated and simultaneously the samples were heated up by the ceramic heater up to 500–900°C. The evacuation and heating process seem to trigger heat generation reactions. Heat burst phenomena were simultaneously detected by a radiation thermometer looking at the surface of the multilayer thin film and a thermocouple located near the metal composite. It shows that heat measurement by the thermocouple embedded in the ceramic heater correctly reflects surface temperature detected by the radiation thermometer. Excess energy generation using nano-sized multilayer Cu/Ni metal composite and Cu/Ni metal with third material (CaO, Y₂O₃) composite were presented. Maximum released excess energy reached 1.1 MJ and average released energy per absorbed total hydrogen was 16 keV/H or 1.5 GJ/H-mol. It cannot be explained by any known chemical process and suggests that the observed heat generation must be of nuclear origin. Various analysis methods, such as SEM-EDX or TOF-SIMS, had been applied to obtain information about what kind of reactions occur by the interaction of the nano-sized multilayer metal composite with hydrogen gas.

© 2020 ISCMNS. All rights reserved. ISSN 2227-3123

Keywords: Anomalous heat, Excess heat, Gas loading, Heat burst, Hydrogen gas, Multilayer thin film, Nano material, Nano-sized metal composite

*E-mail: iwamura@lms.tohoku.ac.jp.

[†]Also at: CLEAN PLANET Inc., Tokyo 105-0022, Japan.

1. Introduction

Permeation-induced transmutation phenomenon, which is completely different from conventional transmutation by nuclear reactors or accelerators, was first reported in 2002 [1]. D₂ gas permeation through a nano-structured multilayer thin film composed of Pd and CaO thin film and Pd substrate with a target element induces nuclear transmutation reactions [2–4]. The temperature of the Pd complex is typically 70°C and the pressure of D₂ gas is 1 atm. Permeation-induced nuclear transmutation reactions were firstly observed at Mitsubishi Heavy Industries and were successfully replicated by other institutes such as Toyota R&D center [5]. Typical target element is Cs and produced element is Pr. Transmutation reactions of Sr, Ba, W into Mo, Sm, Pt were also observed by this method. It seemed that 2, 4 or 6 deuterons make fusion with the target materials. In this research, deuterium diffusion through nano-sized multilayer thin film was a key factor and the elemental analysis was important technique.

The Collaborative Research Project between six Japanese organizations funded by New Energy and Industrial Technology Development Organization (NEDO) on anomalous heat effects was done from Oct. 2015 to Oct. 2017 using Ni, Pd, Cu, and Zr nano-particles. Anomalous heat generation, which is too much to be explained by any known chemical process, was observed. Qualitative reproducibility was confirmed between the Kobe University and Tohoku University [6–9]. The authors replicated the experiments using nano-Pd/Ni fabricated by glow discharge with D₂ gas developed by Mizuno [10]. In these experiments, nano-sized particles and diffusion of hydrogen and deuterium were one of key factors to observe the heat effects and precise heat estimation was crucial.

Combining above factors and methods, we developed a new type of excess heat experiments using a nano-sized metal multilayer composite and hydrogen gas. Larger excess energy per H was obtained using the present method.

2. Experimental

A schematic of the experimental set-up is shown in Fig. 1(a). Two nano-sized metal multilayer composites were placed in the center of the chamber. The chamber, made of stainless steel (type 304), had two ports for introducing and evacuating gas, respectively. H₂ gas and its pressure were monitored by a Pirani gauge. The chamber could be evacuated by a turbo molecular pump. The multilayer samples could be heated up by a ceramic heater (MS-1000R; Sakaguchi E. H Voc Corp.) in which a thermocouple (Pt-PtRh13%) was embedded. Heater temperature was measured by the thermocouple. The surface temperature of a sample was evaluated by an infrared radiation thermometer (IR-CAQ3CS; Chino Corp.). The detector was made of InGaAs and two wavelengths, 1.55 and 1.35 μm , were used in this work. Gamma-rays were monitored by a NaI (TI) scintillation counter (TCS-1172; Hitachi, Ltd.) during all experiments, for safety. Heater input power was supplied by a DC power source with constant voltage mode. The input voltage and current were measured both by voltage and current monitors provided by the power supply and an independent voltmeter and amperemeter, respectively.

A detailed drawing of the Ni based nano-sized metal multilayer composite is shown in Fig.1(b). It was composed of a Ni Plate (25 mm square and 0.1 mm thickness) and Cu–Ni multilayer thin film (25 mm diameter circle and few 10 nm thickness). Two nano-sized metal multilayer composite samples were heated by the ceramic heater (25 mm square and 2.2 mm thickness) through SiO₂ plates (0.1 mm thickness). If certain energy generation reactions would happen on the surface of samples, the temperature of the embedded thermocouple (heater temperature) would rise. Simultaneously, infrared emission detected by the radiation thermometer, which corresponds to surface temperature of the sample, would increase. Photos of the experimental set-ups and STEM image of Cu-Ni multilayer thin film are shown in Fig. 2.

A Ni plate (25 mm square and 0.1 mm thickness, purity up to 99.9%, Furuuchi Chemical Co.) was washed with acetone and annealed in vacuum ($<10^{-4}\text{Pa}$) at 900°C for 72 h. It was then cooled to room temperature in a furnace and washed with HNO₃/H₂O to remove impurities on the surface of the Ni plate. The surface of the plate was covered by layers of Cu (2 nm) and Ni (14 nm) which were obtained by alternately sputtering 2 nm thick Cu and 14 nm

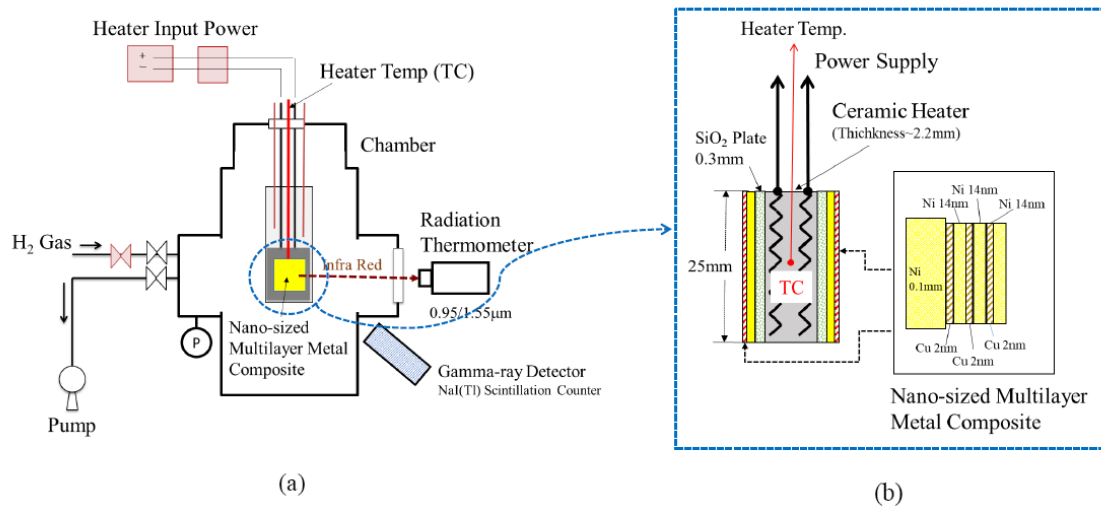


Figure 1. Experimental set-up. (a) Schematic of experimental apparatus, (b) detail drawing around nano-sized multilayer metal composite.

thick Ni layers. 2 nm thick CaO or Y₂O₃ thin films were inserted into the Ni layers in some cases. The thicknesses of the layers were measured by a crystal thickness monitor. Fabrication process is performed by Ar ion beam sputtering.

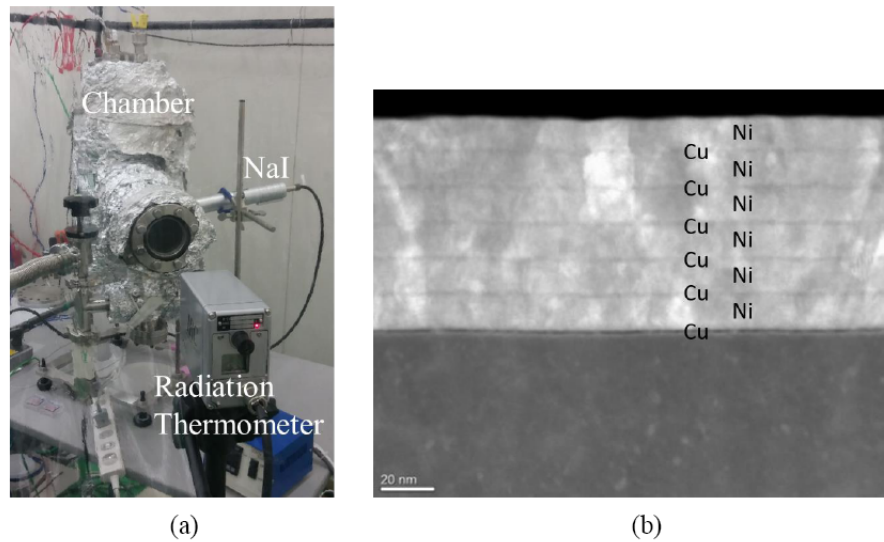


Figure 2. Photos of experimental apparatus and cross-sectional view of nano-sized metal multilayer composites; (a) outer view of the present experimental set-ups, (b) STEM (scanning transmission electron microscope) image of Cu–Ni multilayer thin film.

The samples are sputtered at room temperature and the voltage and current of the Ar beam are 1 kV and 10 mA, respectively.

The experimental procedure is as follows. Two nano-sized metal multilayer composites were placed in the chamber and baked for 1–2 days at temperature more than 200°C to remove H₂O on the surface *under vacuum condition*. After baking, H₂ gas was introduced into the chamber up to about 230 Pa at 250°C. Usually H₂ gas was loaded for about 16 h. Then, H₂ gas was evacuate by the turbo molecular pump and simultaneously the samples were heated up by the ceramic heater up to 500–900°C. These process triggers heat generation reactions and observed excess heat. Typically, after 8 h, the heater input was turned down and the samples were made cool down to 250°C. These processes (H₂ loading, heating up and cooling down samples) were repeated several times changing heating temperature.

During the above experimental procedure, hydrogen atoms are supposed to diffuse from the Ni plate through the nano-sized metal multilayer to the surface. The diffusion mechanism of hydrogen atoms is well known as “quantum diffusion” [11]. Hydrogen atoms are hopping from a site to another site in metal. We assume that hydrogen flux is one of the key factors to induce condensed matter nuclear reactions and the hydrogen flux is intentionally arranged by the present experimental method. Hydrogen flux **J** from the nano-sized metal multilayer composite to the chamber is caused by gradient of hydrogen concentration and gradient of temperature as shown in Eq. 1 [12].

$$\mathbf{J} = -nD \left(\nabla c + \frac{cQ^* \nabla T}{k_B T^2} \right), \quad (1)$$

where n is the number of lattice atoms per unit volume, c is hydrogen concentration defined as the hydrogen/host-metal atom ratio, D is diffusion coefficient and Q^* is the heat of transport.

3. Results and Discussion

3.1. Excess heat estimation

Heat analysis of this system is based Eq. (2) as explained in Fig. 3(a).

$$k \frac{T_H - T_w}{L} A_H + 2A_S \varepsilon \sigma (T_S^4 - T_w^4) = P_{in} + H_{ex}, \quad (2)$$

where k is thermal conductivity, T_H the heater temperature, T_S the surface temperature, T_W wall temperature of the chamber, L the length between the heater and wall, A_S surface area of the sample, ε the emissivity of the sample, σ the Stefan–Boltzmann constant, P_{in} the electrical heater input and H_{ex} is excess power that is generated heat power by the condensed matter nuclear reactions. This equation is obtained under the following assumptions.

- (1) Thermal conduction via H₂ gas is negligible as H₂ pressure is low enough.
- (2) Radiation from chamber wall is negligible because T_W is room temperature.
- (3) The electrical input power is constant. blank run, in which same sized Ni bulk.

A blank run, in which same sized Ni bulk samples without multilayer thin films were used, was performed with the same procedure described above. Figure 3(b) shows the relationship between input power given to the ceramic heater and heater temperature detected by the thermocouple. Generated excess heat power can be evaluated based on the blank run result. Generated heat can be evaluated by Eq. (1).

The radiation thermometer was introduced recently, so we now have many experimental results with the heater temperature only. As a first step of data analysis, experimental data analysis was done based on the assumption that ε is constant for Ni based nano-sized metal multilayer composite and Ni bulk. In the next step, excess heat will be evaluated more preciously by measuring ε for each sample.

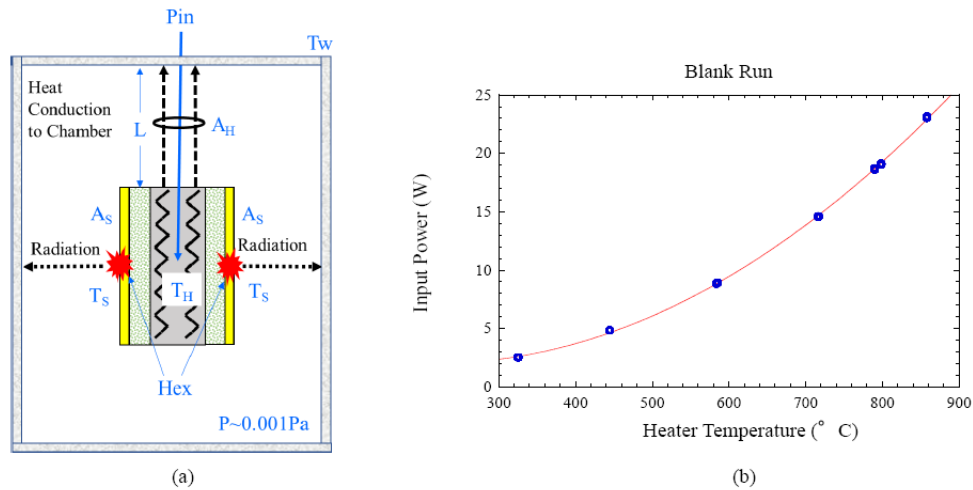


Figure 3. Excess heat evaluation; (a) Model of excess heat evaluation, (b) Relationship between input power (W) and heater temperature for blank run.

3.2. Excess heat generation and its evaluation

Examples of experimental results are shown in Figs.4 and 5. The structures for the samples were shown in Fig. 4. The ratio of Ni and Cu was the same for the four samples; Cu/Ni=1/7 in these examples. It was selected based on the past NEDO project results [7–9]. Also CaO and Y₂O₃ were selected based on the permeation-induced transmutation results [1–4].

Figure 5 shows pressure of the chamber and excess heat for each sample. Red and blue lines mean excess heat

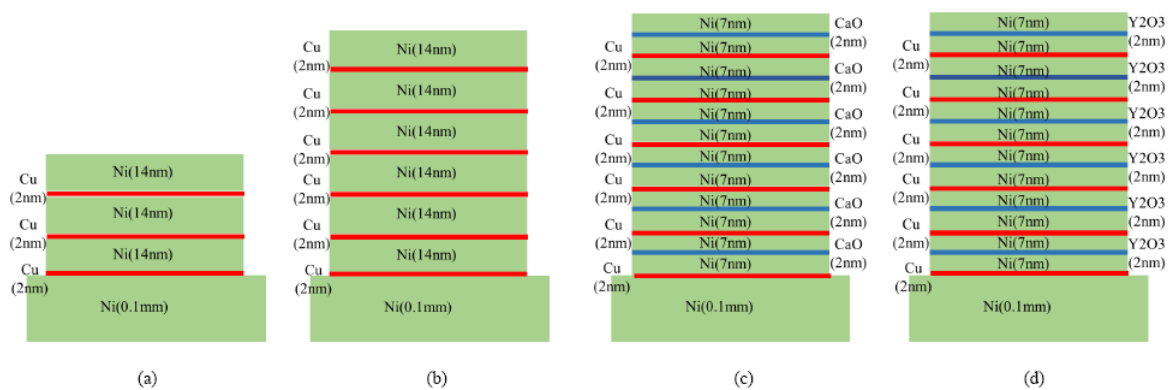


Figure 4. Structures of nano-sized multilayer metal composite samples; (a) example #1: 3 layers of Cu 2 nm and Ni 14 nm, (b) Example #2: 6 layers of Cu 2 nm and Ni 14 nm, (c) Example #3: 6 layers of CaO 2 nm, Cu 2 nm and Ni 14 nm, (d) Example #4: 6 layers of Y_2O_3 2 nm, Cu 2 nm and Ni 14 nm.

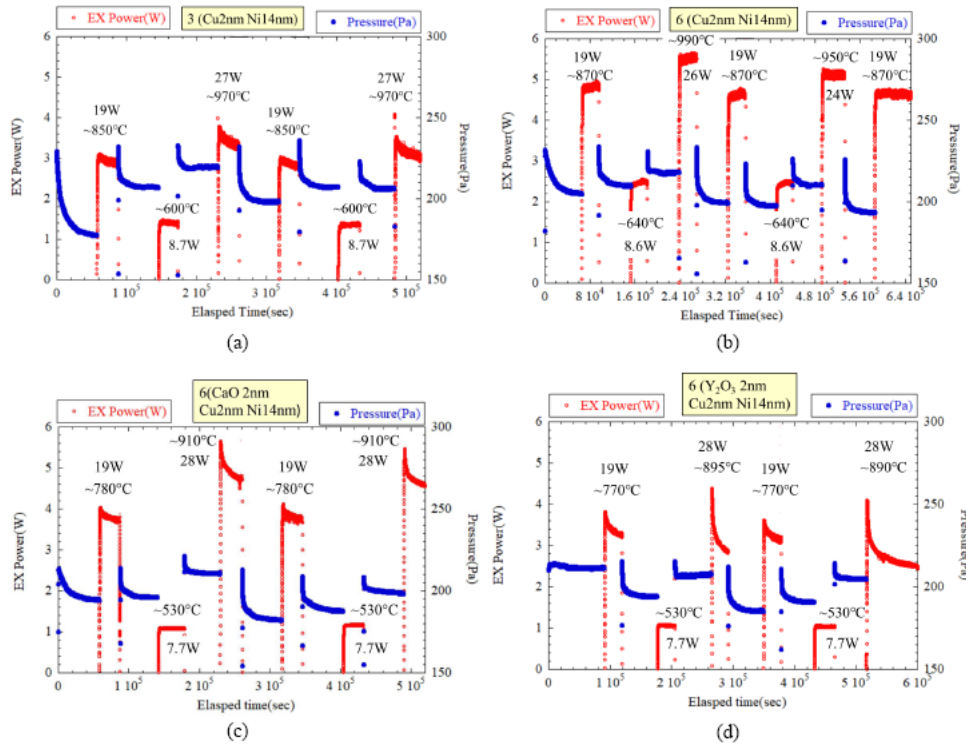


Figure 5. Examples on excess heat generation; (a) example #1: 3 layers of Cu 2 nm and Ni 14 nm, (b) example #2: 6 layers of Cu 2 nm and Ni 14 nm, (c) example #3: 6 layers of CaO 2 nm, Cu 2 nm and Ni 14 nm, (d) example #4: 6 layers of Y_2O_3 2 nm, Cu 2 nm and Ni 14 nm.

and pressure of the chamber, respectively. At the beginning of each experiment, hydrogen gas was introduced to the chamber and absorbed into the Ni based nano-sized multilayer metal composite at 250°C. The pressure for each experiment gradually decreased as shown in the Fig. 5. The amount of hydrogen absorbed by each sample was estimated based on the pressure change and temperature of the chamber. After about 16 h, H_2 gas was evacuated and simultaneously each sample was heated up by the ceramic heater. After that, excess heat more than input power was observed for each experiment as shown in Fig. 5. The input power for each experiment was stable during a one cycle; for example, 19 W was applied to the ceramic heater from about 6×10^4 s to about 9×10^4 s in Fig. 5(a).

Comparing experiments (a)–(d), excess heat for experiment (b) was largest. Although input power for the first excess heat event (from 6×10^4 to 9×10^4 s) in Fig. 5(a) and (b) was the same (19 W), heater temperatures were about 850°C and 880°C, respectively. A significant temperature difference was observed between the two cases. For each experiment (c) and (d), which CaO and Y_2O_3 was inserted to each Ni film, excess heat was different. Although input power for the third excess heat event (CaO: from 2.3×10^6 to 2.6×10^6 s, Y_2O_3 : from 2.6×10^6 to 2.9×10^6 s) in Fig. 5(c) and (d) was the same (28 W), heater temperatures were about 910°C and 895°C, respectively. A significant temperature difference was also observed between the experiments (c) and (d). It should be noted that the properties of heat dissipation were different for experiments (a) and (b) and experiments (c) and (d) because experimental set-ups were different for the two cases.

Time dependence of excess heat for the four experiments was different; excess heat tended to increase for the 6 Cu

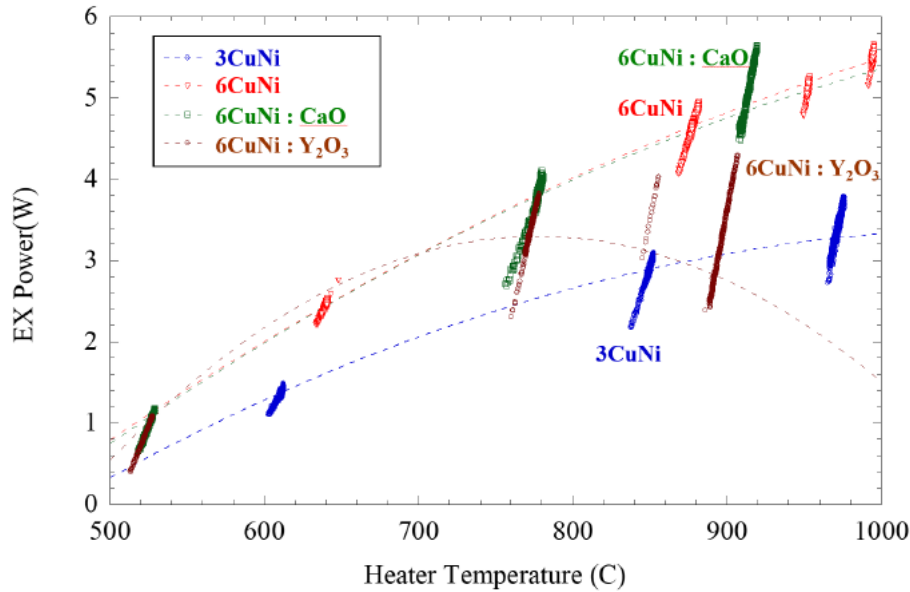
Table 1. Released excess energy per hydrogen for the four examples.

	#1 (three layers of Cu–Ni)	#2 (six layers of Cu–Ni)	#3 (six layers of CaO–Cu–Ni)	#4 (six layers of Y ₂ O ₃ –Cu–Ni)
Absorbed H (mol)	7.6×10^{-4}	7.3×10^4	5.1×10^4	3.7×10^4
Absorbed number of H	4.6×10^{20}	4.4×10^{20}	3.0×10^{20}	2.3×10^{20}
Total excess energy (J)	4.6×10^5	1.1×10^6	5.9×10^5	2.6×10^5
Excess energy per H (J/H-mol)	6.0×10^8	1.5×10^9	1.2×10^9	6.8×10^8
Excess energy per H (eV/H)	6.3×10^3	1.6×10^4	1.2×10^4	7.1×10^3

and Ni-layer experiment (b), however, excess heat decreased for the other experiments. We can see that excess heat power and its time dependence changed depending on the structure the multilayer thin film region.

Figure 6 illustrates the temperature dependence on the excess heat power for the four examples. Excess heat tended to increase as temperature increase, however, Y₂O₃ sample (Example #4) take a peak around 750°C. Temperature dependencies for the four samples looks like convex shapes. They did not depend on fourth power of temperature and it suggests that these observed excess heat powers were not attributed to the artifacts caused by thermal radiation.

Released excess energies per hydrogen for the four examples were evaluated based on the experimental results. Table 1 summarizes the amount of absorbed hydrogen, total excess energy and excess energy per absorbed hydrogen. The amount of excess energy was calculated by the time integration of excess powers for each experiment. They ranged from 0.26 to 1.1 MJ. Although it seems highly unlikely that all the absorbed hydrogen atoms reacted, we can still estimate that average released energies per absorbed total hydrogen for examples #1–#4 were 6.3 keV/H, 16 keV/H, 12 keV/H and 7.1 keV/H, respectively. Obviously, the released excess energy per hydrogen atom for all the experiments demonstrated here are too large to be explained by any known chemical reactions. This strongly suggests

**Figure 6.** Temperature dependence on excess power for four examples.

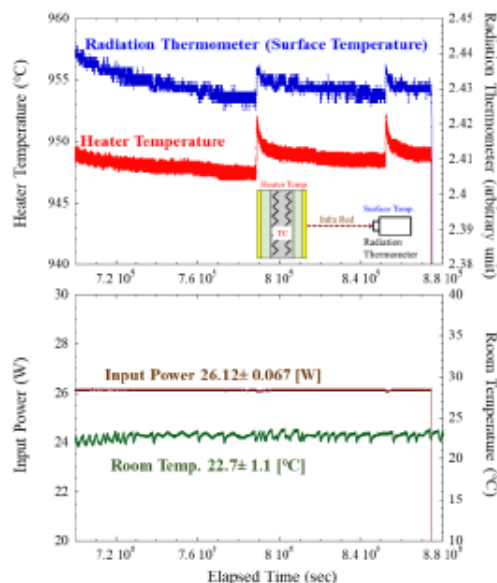


Figure 7. Simultaneously detected by a radiation thermometer looking at the surface of the multilayer thin film and a thermocouple located in the center of heater.

that some condensed matter nuclear reactions were induced in our experiments, although it is not clear at present what kind of reactions occurred. According to the results, about 10^{-3} of the absorbed hydrogen might react if the condensed matter nuclear reactions would release energy order from 1 to 10 MeV. Identification of reaction products is very important future work, in addition to more precisely excess heat evaluation.

Heat burst phenomena were observed by the radiation thermometer and the thermocouple in the heater simultaneously as shown in Fig.7. Output from the radiation thermometer, which corresponds to the surface temperature of samples, is plotted as the upper blue line, and heater temperature is plotted as the lower red line in the upper graph of Fig.7. Input electrical power and room temperature around the chamber are drawn in the lower graph. A significant simultaneous increase of surface and heater temperature were observed twice, while no significant changes for input electrical power and room temperature were detected during these burst events. This means that heat measurement by the thermocouple embedded in the ceramic heater correctly reflected surface temperature detected by the radiation thermometer.

3.3. Analysis of nano-sized multilayer metal composite

It is very important to identify what kind of reactions occur by the interaction of the nano-sized multilayer metal composite with hydrogen gas. Scanning Electron Microscope–Energy Dispersive X-ray Spectroscopy (SEM–EDX), Inductively Coupled Plasma–Mass Spectrometry (ICP–MS), Time-of-Flight Secondary Ion Mass Spectrometry (TOF–SIMS), Quadrupole Mass Spectrometer (Q–Mass), X-ray Photoelectron Spectroscopy (XPS), Transmission Electron Microscope (TEM), Scanning Transmission Electron Microscope (STEM) and the other analysis methods have been applied to the nano-sized multilayer metal composite before and after experiments and released hydrogen gas as shown in Table 2. We would like to search for reaction products and investigate what is happening in the nano-sized multilayer metal composite. It is considered that the material analysis leads to obtain key factors to control condensed matter

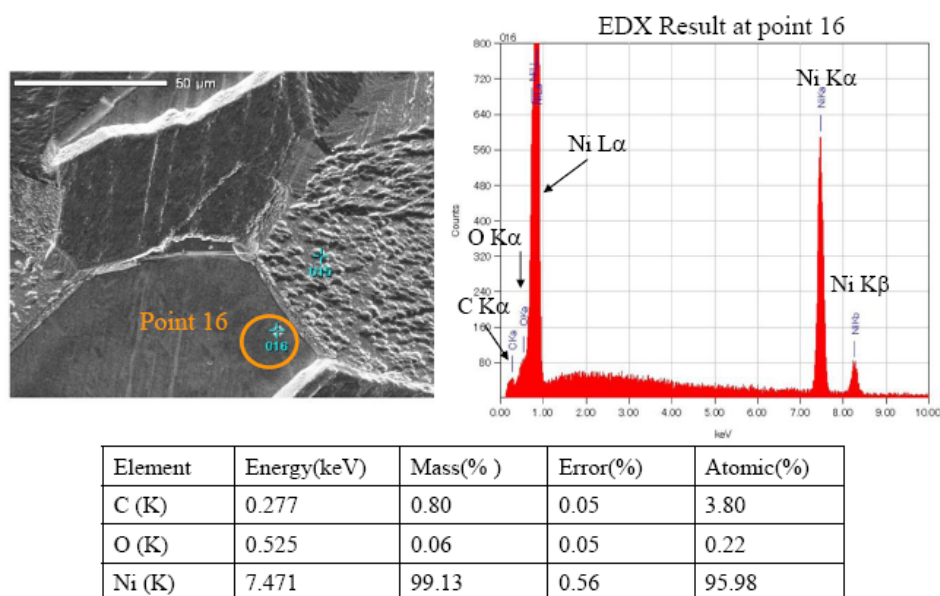
Table 2. Analysis methods for understanding reaction mechanism.

Method	Outline
SEM-EDX	Surface shape and atomic electron structure
ICP-MS	High sensitivity mass spectrometry
TOF-SIMS	High resolution mass spectrometry
Q-Mass	Mass spectrometry for released gas
XPS	Surface sensitive photo electron spectrometry
TEM, STEM	Cross sectional view of nano scale material

nuclear reactions.

The SEM and EDX results for a blank run Ni plate sample are shown in Fig. 8. Model JSM-6500F by JEOL was used for the analysis and acceleration voltage was 15 kV. The analysis result for the point 16 in the SEM image is shown. Ni, O and C peaks are detected by EDX and we understand Ni is the main element. As C is the common contamination element and the sample after blank run was exposed to the air, this is a reasonable result.

Figure 9 shows SEM and EDX results of the sample with six layers of Cu 2 nm and Ni 14 nm (Example #2) before and after the excess energy generation experiment. Before the experiment, Ni, Cu, O, C and W were observed as shown in Fig. 9(a). As W (tungsten) was used as a filament of ion beam sputtering device, it was possible to consider that W was detected by EDX. In contrast, many elements after heat generation experiment were detected by EDX. Ni, Cu, O, C, Si, Na, Mg, Al and K were detected, although each element should be confirmed by other method. Ni, Cu, O and C are reasonable to be detected, however, origins of Na, Mg, Al and K are difficult to identify. Although Si is one of common elements and often detected as a contaminant, amount of Si in this case seems too much. Ni, Cu, O and C were detected on almost all the analysis points for the sample with six layers of Cu 2 nm and Ni 14 nm, however, Na,

**Figure 8.** SEM and EDX results of blank run Ni plate.

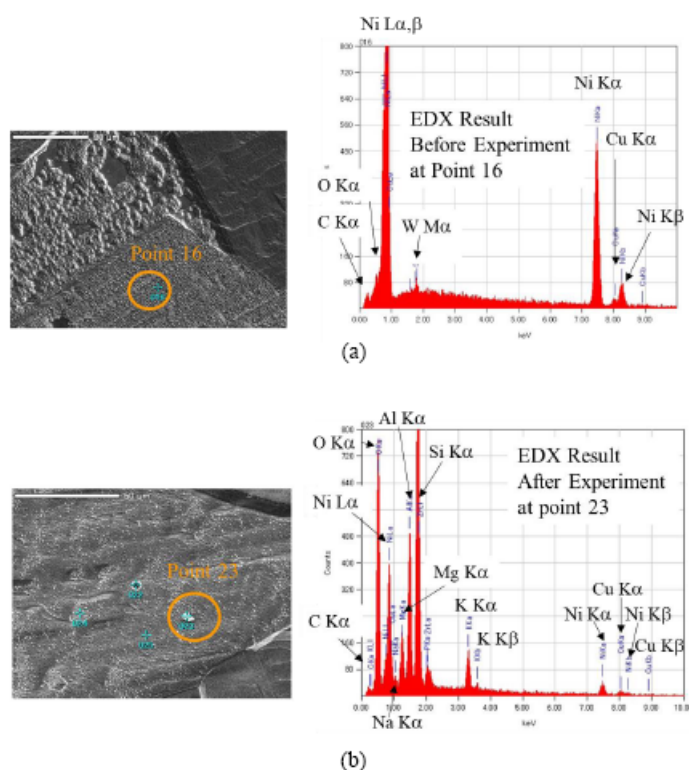


Figure 9. SEM and EDX results of the sample with six layers of Cu 2 nm and Ni 14 nm; (a) before experiment, (b) after experiment.

Mg, Al and K were detected at a few points. Of course, they are common elements and we should take consideration of many contamination chances and careful analysis is necessary.

TOF–SIM was applied for the sample with six layers of Cu 2 nm and Ni 14 nm (Example #2). Elemental surface distribution analyzed by TOF–SIMS is shown in Fig. 10. SIMS 5 by ION–TOF GmbH was used for the analysis and primary ion was Bi⁺. Ion energy was 25 kV, ion current was 1.0 pA and the field of view was 101.6 × 101.6 μm².

Non-uniform distribution for each element was observed. Lighter place means larger signal strength. Na and K were detected at similar places but not corresponded exactly. A hot spot for Ca overlapped with higher places for Na and K. A hot spot for Ti overlapped with K. At present, we do not have an explanation for the distributions for Na, Ca, K and Ti.

We can see that Mn TOF–SIMS signal is strong while Fe signal is weak at the same region. Fe is a common element and Fe can be contaminated easily, because Fe is main element of stainless steel. Mn is also contained in stainless steel. However, inverse surface distributions for Fe and Mn does not give us reasonable explanation if we would postulate that Mn and Fe were derived from stainless steel.

Example of depth profiles of the sample with six layers of Cu 2 nm and Ni 14 nm with Y₂O₃ is shown in Fig. 11. TOF–SIMS device is the same as described in Fig.10 and the sputter Ion was O²⁺, energy and current were 1 kV and 120 nA, respectively. According to the depth profile of Y (yttrium), we can see that multilayer structure remained partially. Fe, Cr and Mn, which could be supposed to be derived from stainless steel during sputtering processes,

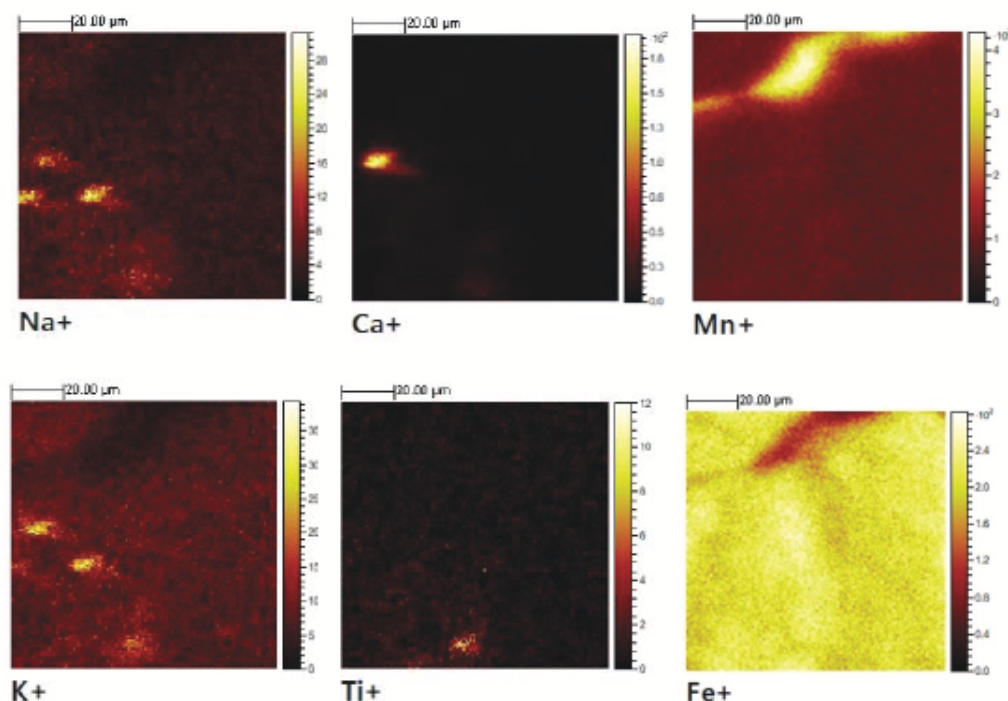


Figure 10. Elemental surface distributions the sample with six layers of Cu 2 nm and Ni 14 nm after excess heat generation analyzed by TOF-SIMS.

differently distributed. This fact might be in contradiction with stainless steel contamination process. Also we notice that the ratio of Cu/Ni got larger near the surface. The reason is unclear at present. Si, major surface impurity, seems to be reasonably distributed if it diffused from the surface.

It is important to continue to investigate further by these analysis methods paying attention to the discrimination of contamination, in order to identify what is happening in the nano-sized multilayer metal composite with hydrogen gas.

4. Concluding Remarks

New type of excess heat experiments using a nano-sized metal multilayer composite and hydrogen gas have been performed based on the permeation-induced transmutation experiments with multilayer thin film and excess heat experiments with nano-particles. Anomalous Excess energy generation using nano-sized multilayer Cu/Ni metal composite and Cu/Ni metal with third material (CaO, Y₂O₃) composite were observed. Maximum released excess energy reached 1.1 MJ and average released energy per absorbed total hydrogen was 16 keV/H or 1.5 GJ/H-mol. It cannot be explained by any known chemical process and suggests that the observed heat generation must be of nuclear origin. Many analysis methods have been applied to identify what kind of reactions occur by the interaction of the nano-sized multilayer metal composite with hydrogen gas.

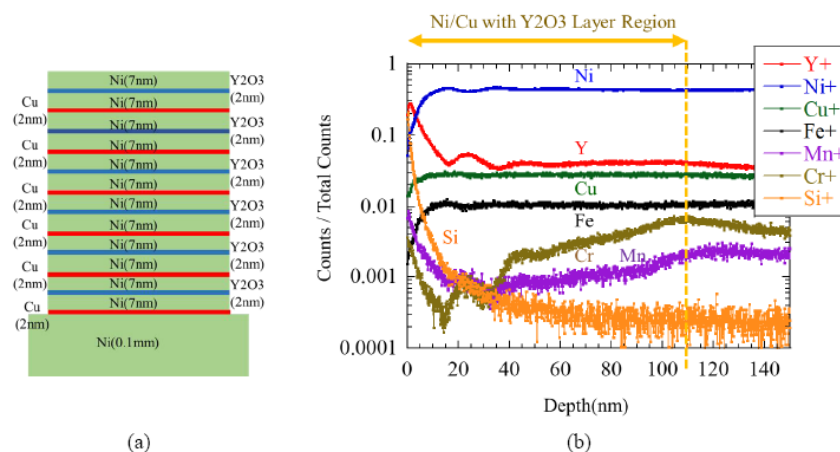


Figure 11. An example of TOF–SIMS analysis; (a) structure of the sample before experiment, (b) depth profiles of the after excess heat generation.

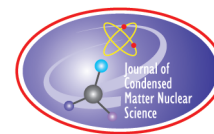
Acknowledgements

The authors acknowledge Mr. H. Yoshino, Mr. S. Hirano, Mr. M. Ise, Dr. T. Hioki and Mr. M. Hattori, who are the members of CLEAN PLANET Inc., for their significant assistance. The authors also thank Mr. M. Takeya, Prof. H. Kikunaga and Mr. Y. Shibasaki of Tohoku University for their support. This work is supported by CLEAN PLANET Inc., Research Center for Electron Photon Science of Tohoku University Electron Photon, Tanaka Kikinzoku Memorial Foundation and The Thermal and Electric Energy Technology Foundation.

References

- [1] Y. Iwamura, M. Sakano and T. Itoh, Elemental analysis of Pd complexes: effects of D₂ gas permeation, *Jpn. J. Appl. Phys.* **41** (2002) 4642–4650.
- [2] Y. Iwamura, T. Itoh, N. Gotoh and I. Toyoda, Detection of anomalous elements, X-ray and excess heat in a D₂–Pd system and its interpretation by the electron-induced nuclear reaction model, *Fusion Technol.* **33** (1998) 476–492.
- [3] Y. Iwamura, T. Itoh, M. Sakano, N. Yamazaki, S. Kuribayashi, Y. Terada, T. Ishikawa, D. Sekiba, H. Yonemura and K. Fukutani, Observation of low energy nuclear transmutation reactions induced by deuterium permeation through multilayer Pd and CaO thin film, *J. Condensed Matter Nucl. Sci.* **4** (2011) 132–144.
- [4] Y. Iwamura, T. Itoh and S. Tsuruga, Transmutation reactions induced by deuterium permeation through nano-structured Pd multilayer thin film, *Current Sci.* **108** (4) (2015) 628–632.
- [5] T. Hioki, N. Takahashi, S. Kosaka, T. Nishi, H. Azuma, S. Hibi, Y. Higuchi, A. Murase and T. Motohiro, Inductively coupled plasma mass spectrometry study on the increase in the amount of Pr atoms for Cs-ion-implanted Pd/CaO multilayer complex with deuterium permeation, *Jpn. J. Appl. Phys.* **52** (2013) 107301.
- [6] A. Kitamura, A. Takahashi, R. Seto, Y. Fujita, A. Taniike and Y. Furuyama, Effect of minority atoms of binary Ni-based nano-composites on anomalous heat evolution under hydrogen absorption, *J. Condensed Matter Nucl. Sci.* **19** (2016) 1–10.
- [7] A. Kitamura, A. Takahashi, K. Takahashi, R. Seto, T. Hatano, Y. Iwamura, T. Itoh, J. Kasagi, M. Nakamura, M. Uchimura, H. Takahashi, S. Sumitomo, T. Hioki, T. Motohiro, Y. Furuyama, M. Kishida and H. Matsune, Excess heat evolution from nanocomposite samples under exposure to hydrogen isotope gases, *Int. J. Hydrogen Energy* **43** (2018) 16187–16200.
- [8] Y. Iwamura, T. Itoh, J. Kasagi, A. Kitamura, A. Takahashi and K. Takahashi, Replication experiments at tohoku university on anomalous heat generation using nickel-based binary nanocomposites and hydrogen isotope gas, *J. Condensed Matter*

- Nucl. Sci.* **24** (2017) 191–201.
- [9] Y. Iwamura, T. Itoh, J. Kasagi, A. Kitamura, A. Takahashi, K. Takahashi, R. Seto, T. Hatano, T. Hioki, T. Motohiro, M. Nakamura, M. Uchimura, H. Takahashi, S. Sumitomo, Y. Furuyama, M. Kishida and H. Matsune, Anomalous heat effects induced by metal nano-composites and hydrogen gas, *J. Condensed Matter Nucl. Sci.* **29** (2019) 119–128.
 - [10] T. Itoh, Y. Iwamura, J. Kasagi and H. Shishido, Anomalous excess heat generated by the interaction between nano-structured Pd/Ni surface and D₂/H₂ gas, *J. Condensed Matter Nucl. Sci.* **24** (2017) 179–190.
 - [11] Y. Fukai, Evidence for quantum diffusion of hydrogen in Ta: quench-recovery experiments revisited, *Jpn. J. Appl. Phys.* **23**(8) (1984) 596–598.
 - [12] H. Wipf, Electro- and thermo-transport of hydrogen in metals, *Hydrogen in Metals II*, G. Alefeld and J. Völkl (Eds.), Springer, Berlin, 1978, pp. 273–304.



Research Article

Latest Progress in Research on AHE and Circumstantial Nuclear Evidence by Interaction of Nano-Metal and H(D)-Gas

Akito Takahashi^{*,†,‡}

Osaka University, Suita, Osaka 565-0871, Japan

Hiroyuki Ido, Atsushi Hattori, Reiko Seto, Atsushi Kamei and Joji Hachisuka

Technova Inc., Chiyoda-ku, Tokyo 1000011, Japan

Toyoshi Yokose, Yutaka Mori, Akira Taniike and Yuichi Furuyama

Kobe University, Kobe, Hyogo 657-8501, Japan

Abstract

Recent results on anomalous heat effect (AHE) by interaction of binary nano-composite metal powders and H (or D) gas, after the NEDO-MHE project (2015–2017) are the subject of this paper. The Pd–Ni₁₀/zirconia (PNZ10) and Cu–Ni₇/zirconia (CNZ7) powders by melt-spun and calcination method were for AHE active material samples, and were re-used by additional calcination. An amount of 80–400 W/kg level excess thermal power W_{ex} of sustainable continuity for several weeks has been reproducibly observed at elevated temperature around 300°C, by using re-calcined PNZ-type samples with D-gas, significantly in net D-gas desorption mode. Specific reaction energy (η -value) per D-transferred was very large as from 100 eV/D to 500 eV/D. Very weak (0.1–0.2 n/J level) neutron emission looked correlating with the rise-up heat burst of thermal power after joule heating started. These results can be of the circumstantial evidence of the AHE by the nano-metal D-gas interaction. Data of 50–140 W/kg level excess thermal power was repeatedly obtained by CNZ-type samples with H-gas at elevated temperatures after the saturation of H-gas absorption (endothermic) by sample. Excess thermal power of ca. 50–70 W continued for more than two weeks by 505 g CNZ7r (re-calcined) sample, with very strange evolution of the cooled-flat and oscillating TC4 RC upper flange temperatures. (continued in the next page)

© 2020 ISCMNS. All rights reserved. ISSN 2227-3123

Keywords: Anomalous heat, Circumstantial nuclear evidence, Enhancement, Elevated temperature, Excess thermal power, Gas turbulence, Hydrogen gas, 100 W/kg, Nano-composite-metals, Ni-based, Over 1 keV/H(D), Repeated calcination, Specific reaction energy

*Corresponding author. E-mail: akito@sutv.zaq.ne.jp.

[†]Also at: Technova Inc., Chiyoda-ku, Tokyo 1000011, Japan.

[‡]Emeritus Prof. of Osaka University.

(continued from the title page)

The effect has been investigated, and we concluded as a kind of turbulence gas-flow of up- and down-stream by strong local AHE. Big or small heat bursts were observed many times in the increasing data after the start of external heating from room temperature. The η -values were obtained to be very large as higher than 10,000 eV/H-transfer for CNZ7r sample runs, implying some nuclear effect. Observation of AHE can be repeated by the interaction of H (or D) gas and Ni-based nano-composites metal powders. Reproducibility is established. Condition to realize the apparent equilibrium pressure with maximum dynamic H (or D) gas flux in both directions of desorption and sorption on the surface of nano-composite metal particle, which is considered to be the key factor. Higher temperature more than 300°C for RC with homogeneous gas feed for eliminating the gas turbulence is to be tested.

1. Introduction

The anomalous heat effect (AHE) by the interaction of hydrogen-isotope-gas and nickel-based nano-composite samples as Pd–Ni/zirconia (PNZ) and Cu–Ni/zirconia (CNZ) powder samples at elevated temperatures around 300°C has been studied intensively [1,2] under the NEDO-MHE project in 2015–2017 [3], for verifying the existing of the phenomenon and finding conditions of excess power generation in controllable way. As reviewed in [4], the 8-year-long (2008–2015) series of study on AHE by the interaction of metal nano-particles and D(H)-gas under the collaboration of Technova Inc. and Kobe University has become the basis for the collaborative research of NEDO-MHE. The AHE phenomenon has been replicated by independent experiments at Tohoku University as well as at Kobe University under the collaboration study of the NEDO-MHE (Metal Hydrogen Energy) project [5–7]. Observed excess thermal power levels of AHE were on the level of 3–20 W, and more enhancement for industrial application was expected.

To scale up the AHE power level, study has been extended [8,9] independently at Kobe University as the collaboration project with Technova Inc., after the 2015–2017 NEDO-MHE project. Big heat burst of ca. 3 kW for about 100 s was observed by the 1 kg Cu1Ni7/zirconia sample (CNZ7) with hydrogen gas in the initial heating-up phase, but sustaining excess thermal power around 300°C temperature of reaction chamber (RC) was small as ca. 14 W/kg for many months [8]. The heat burst happened with gas-desorption to give 6.5 eV per desorbed H atom. We discussed big exothermic energy by the H-desorption is not by chemical origin. However, as reported in this paper, our succeeding experiments with the re-calcined sample (CNZ7r) has shown about eight times enhancement, which is excess thermal power (100–140 W/kg level). Our succeeding experiments with re-calcined PNZ10r (Pd1Ni10/zirconia/re-calcined) sample with D-gas have also given significant enhancement of excess thermal power (50–120 W/kg level), as shown in this paper. During the scale-up experiments, we had the new findings of H(D)-gas turbulence effect on the Kobe-Technova C-calorimetry system. Somewhat detail of the H-gas turbulence effect under the strong local AHE, which underestimated drastically excess thermal power by coolant-oil outlet temperatures and did not affect the calorimetry by the position-averaged RC temperatures, will be reported and discussed in this paper. Typical AHE data for heating rise-up phase of each run, and for several weeks sustaining excess thermal power runs, are shown in this paper for CNZ7, CNZ7r and PNZ10r runs.

We reported [1–9] repeatedly on the fact that specific reaction energy per H (or D) transferred (or spent) was too large to explain by the known chemical reaction energies. In this paper, we add newer results of anomalously high specific reaction energy over 1 keV/H(D)-transferred under the AHE phenomenon. In the case of runs by PNZ10r sample with D-gas, time evolution pattern of very weak neutron emission looked correlating with rapid local AHE temperature rise in RC. These observations must be circumstantial evidences of some nuclear reactions for underlying mechanisms of the AHE, as predicted by the condensed cluster fusion theory (CCF/TSC theory) by A. Takahashi (see many papers downloadable at Research Gate [10]). For an introduction of CCF/TSC theories, the review paper [11] is recommended.

2. Experimental Methods and Procedure

The fabrication procedures of Pd–Ni/zirconia and Cu–Ni/zirconia for nano-composite samples were described in our previous papers [1–9]. The outline is (1) making thin (ca. 10 μm) amorphous ribbons of $\text{Pd}_x\text{Ni}_y\text{Zr}_z$ or $\text{Cu}_x\text{Ni}_y\text{Zr}_z$ metal composite alloys by the melt-spun method, (2) calcination in electric oven at ca. 450°C for 120–180 h, and (3) making ca. 0.1 mm size powders by automatic mortaring machine. The atomic ratios of $x/y/z$ are approximately from 1/10/20 to 1/7/14. In the present work, we used Pd1/Ni10/Zr20 and Cu1/Ni7/Zr14 for PNZ10 and CNZ7 samples, respectively. After the first H(or D) gas charging and elevating temperature runs (#M-N, N=1,2,3), we took out the sample from RC to make re-calcination in electric oven in ambient air with ca. 450°C for ca. 180 h. Then we reused for the second H(D)-charging and temperature-elevation runs (#M-N, N = 1, 2, 3).

Between $M = 1$ and 2 or $M = 2$ and 3, we made the so-called baking treatment with 250–450°C RC average temperature under vacuum–evacuation to meet the final RC pressure < 1 Pa. The second and third re-calcined samples are renamed with suffix r, as PNZ10r and CNZ7r.

To realize the nano-core/incomplete shell structure with 2–10 nm nano-islands in ceramics (zirconia in the present case) supporter flake (several tens micron), atomic ratio of minor outer shell element (Pd or Cu in our case) and inner core (Ni in our case) may have optimum value around Pd (or Cu)/Ni = 1/7 to 1/10. The PNZ10 sample for the present work has Pd/Ni = 1/10. The CNZ 7 sample has Cu/Ni = 1/7. Confirmation of nano-islands has been made by the STEM/EDS analysis, for samples done in previous studies [3,4]. STEM/EDS analysis for used samples in the present work is under way, which is considered to be of key information why the AHE enhancement is caused by the repeated calcination treatment.

The C system schematics for AHE calorimetry at Kobe University has been many times shown [1,2,4–9]. We copied again in Fig. 1 for reader's convenience.

Calorimetry calibration data are given in [8] for TC1-TC6, TC2-TC6, and RTDav-TC6, by using blank sample of 1 mm diameter zirconia beads (ca. 1.4 kg) for oil flow rate 18.4 cm^3/min . In order not to make correction for oil-flow rate variation during runs, experimenters have adjusted flow rate for keeping around 18.4 cm^3/min in needed timing (several times per run). For heating up RC, we used constant power supply units by Keithley Co., so that we did not need any correction for input heater power variation for (W1,W2)= (120,80) W and (140,95) W ET (elevated temperature) runs.

H (or D) gas was initially filled in gas cylinder (Fig. 1) having volume of 4 l (for H-gas) and 2 l (for D-gas), and fed to RC through Super Needle Valve (valve with arrow in Fig. 1). Initial pressure of Gas Cylinder was 0.4–1.0 MPa. By adjusting the SNV path size, we set gas flow rate as it took about 60 min to reach the equilibrium pressures at Ps and Pr for the case of blank calorimetry runs. When we had the AHE of significant amount, evolution of Pr and Ps were changed significantly from the blank runs. From the variation of Ps and Pr, we could calculate rate of H (or D) gas molars (or number of atoms) transferred by the runs. For the present works, H-gas was used for CNZ7 and CNZ7r runs, and D-gas was used for PNZ10r runs. D-gas runs for CNZ-type samples and H-gas runs for PNZ-type samples are yet to be done.

Typical patterns of the AHE experiments are as follows,

- (1) baking the sample (#1-0, #2-0),
- (2) H (or D) gas charging to RC at room temperature (RT) (heaters: (0, 0), #1-1, #2-1),
- (3) elevate RC temperature (heaters: (120, 80), #1-2, #2-2),
- (4) cool RC to RT (heaters: (0, 0), #1-3, #2-3),
- (5) elevate RC temperature (heaters: (140, 95), #1-4, #2-4), and so on.

Actual run-tables are given in Tables 1–3, respectively, for CNZ7, CNZ7r, and PNZ10r.

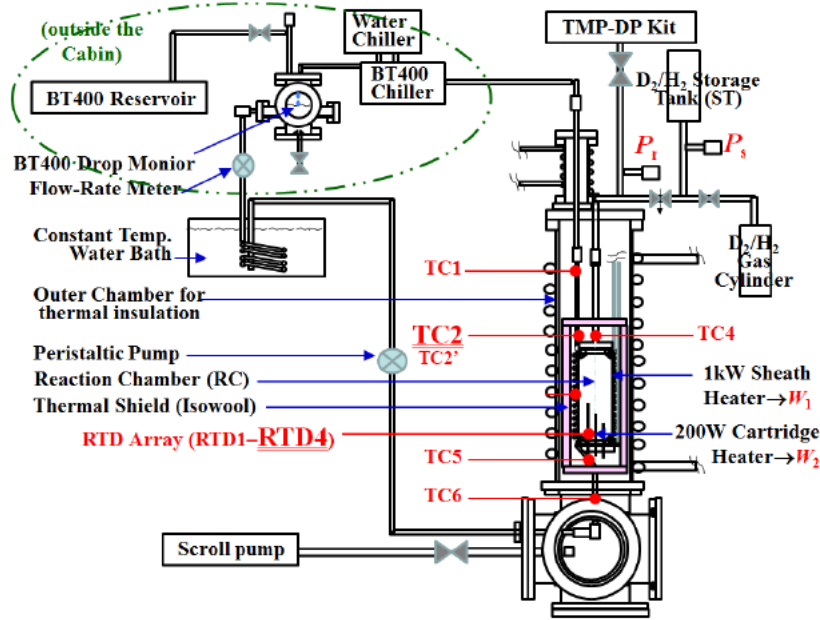


Figure 1. Schematic of the C system of Kobe University for AHE calorimetry, equipped with oil-flow-calorimeter system with flow-rate-monitors and dual heaters (W_1, W_2).

3. Results and Discussions

3.1. H(D)-gas turbulence effect by local large AHE

We first time observed a big heat burst of 152 W, estimated by flow calorimetry by the #1-2 run of CNZ7 (see Table 1). At the burst, temperature of coolant-oil out-let points (TC1 and TC2 in Fig. 1) reached peak in about 2 min. Consider-

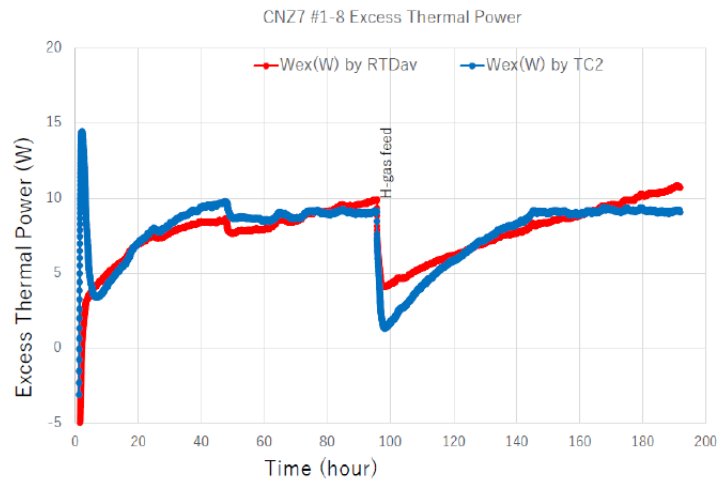


Figure 2. Typical time-evolution of sustaining excess thermal power by CNZ7 ET runs.

Table 1. Run table of CNZ7 (1137g CNZ7 sample + 439 g zirconia beads filler).

Run Number ID	W1, W2 (W)	Gas Fill Ps Pressure	Starting Time	RTD4 max(deg C)	Wex max (W)
1-1	0,0	H 0.93 MPa	2018/9/18	96	24
1-2	120,80		2018/9/19	470	152
1-3	95,60	H 0.46 MPa	2018/9/20	233	0
1-4	120,80	H 0.86 MPa	2018/9/21	272	-2
1-5	0,0	H 0.83 MPa	2018/9/25	25	0
1-6	120,80		2018/9/25	284	10
1-7	0,0		2018/9/28	25	0
1-8	120,80	H 0.49 MPa	2018/10/1	283	10
1-9	140,95	H 0.52 MPa	2018/10/9	320	11
1-10	120,80		2018/10/12	281	8.9
1-11	140,95		2018/10/15	331	19
1-12	0,0		2018/11/7	25	0
1-13	140,95		2018/11/12	321	14.6
2-0	140,40	baking/evacuation	2018/11/19	253	
2-1	0,0	H 0.2 MPa	2018/11/21	26	1
2-2	120,80		2018/11/26	281	8
2-3	140,95		2018/12/3	321	13.9
2-4	0,0		2018/12/21	24.6	0
2-5	140,95	H 0.29 MPa	2019/1/9	318	17.9
3-0	140,40	baking/evacuation	2019/1/18	256	
3-1	0,0	H 0.43 MPa	2019/1/21	26.5	1
3-2	120,80		2019/1/21	280	7
3-3	0,0		2019/1/28		0
3-4	140,95		2019/1/28	319	14
4-0	140,40	baking/evacuation	2019/2/4		
4-1	0,0	H 0.3 MPa	2019/2/6	25.5	0.7
4-2	140,95		2019/2/6	319	14.4

ing very slow time constant of flow calorimetry (about 60 min, measured by the blank run with dummy zirconia), it was estimated by impulse response function for the calorimetry system that the real exothermic reaction power happened at about 100 s with ca. 3 kW peak [8]. As written in [8], we charged H-gas at room temperature (#1-1 run), before the #1-2 run. In the #1-1 run, we observed 0.35 H/Ni loading ratio and 124 kJ heat, which corresponded 1.2 eV/H. We discussed there [8] that the burst was not by H₂O formation, but by some anomalous heat. We feared possible explosion accidents in further runs, and decided to decrease the amount of sample to be half (ca. 0.5 kg) from the next experiment CNZ7r.

We have tried many runs with CNZ7 sample (ca. 1 kg) by changing the heating conditions and H-gas initial pressure (see Table 1). We have not observed similar heat bursts in later runs than #1-2, and long sustaining excess thermal power level was rather small as 10–20 W levels. Typical data of sustaining excess thermal power by the CNZ7 ET (elevated temperature) runs are shown in Fig. 2.

We see good agreement in calorimetry between one by oil-mass flow method (TC2 in Fig. 2) and the other by average RC temperature method (RTDav), except for the initial rise-up responses. In this case, time evolution data of temperatures at interested points (TC4, TC2 and RTDav) behaved very similarly (see Fig.3). This kind of state in calorimetry can be regarded as normal. However, when there happens large local AHE, we have met observation of very strange behavior of TC4 (gas inlet/outlet point of RC upper flange) temperature evolution, which was significantly lower than oil-outlet temperatures (TC1 and TC2), as we explain in the following.

In Fig. 4, we show temperature evolution data for the #1-2 burst event. Obviously, the behavior of TC4 is very strange with many oscillatory down-spikes. In our previous paper [8], we made speculation that the TC4 flat-and

Table 2. Run table of CNZ7r (505g CNZ7r sample + 863 g zirconia beads filler).

Run Number ID	W1, W2 (W)	Gas Fill Ps Pressure	Starting Time	RTD4 max(deg C)	Wex max (W) by RTDav
CNZ7r 1-0	140,40	Baking under Evac	2019/5/10		
CNZ7r 1-1	0,0	Ps=0.468 Mpa H-gas	2019/5/13	29.6	0.7
CNZ7r 1-2	120,80		2019/5/13	280.5	52
CNZ7r 1-3	140,95		2019/5/15	319.7	56.5
CNZ7r 1-4	120,80		2019/6/3	282.6	48.6
CNZ7r 1-4	120,80	Ps=0.47 Mpa H-gas	2019/6/5	282.7	48.6
CNZ7r 1-5	0,0		2019/6/7	25.8	0
CNZ7r 1-6	140,95		2019/6/10	318.6	57.9
CNZ7r 1-7	[140,85][140,105]		2019/6/14	320	54.8
CNZ7r 1-8	0,0		2019/6/14	26	0
CNZ7r 1-9	140,95		2019/6/17	317	56
CNZ7r 1-10	0,0		2019/6/18		
CNZ7r 1-11	140,95		2019/6/19	319	57.3
CNZ7r 1-12	120,80		2019/6/20	282	50
CNZ7r 1-13	[140,80][100,80]		2019/6/21	292	49
CNZ7r 1-14	0,0		2019/6/21	27	0
CNZ7r 1-15	120,80		2019/6/24	281.5	52
CNZ7r 2-0	140,40	Baking under Evac	2019/6/26		
CNZ7r 2-1	0,0	H-gas feed Ps=0.46 MPa	2019/6/28		
CNZ7r 2-2	140,95		2019/7/1	323	70
CNZ7r 2-3	0,0		2019/7/5	27	0
CNZ7r 2-4	120,80		2019/7/8	283	61
CNZ7r 3-0	140,40	Baking under Evac	2019/7/10		
CNZ7r 3-1	0,0	H-gas 0.44 MPa	2019/7/17	26.5	0.1
CNZ7r 3-2	140,90		2019/7/17	321	69.2
CNZ7r 3-3	0,0		2019/7/19	27	0

oscillatory evolution was due to transient local balance in endothermic H-absorption and desorption. However, it was wrong. From our succeeding experiments with CNZ7r and PNZ10r of re-calcined samples, we have reached the confirmation of strong H(D)-gas turbulence effect under locally strong AHE occurrence, which made drastic underestimation of excess thermal power by using data at TC1 and TC2, due to causing strong distortion of temperature distribution of

Table 3. Run table of PNZ10r (505g PNZ10r sample + 863 g zirconia beads filler).

Run Number ID	W1, W2 (W)	Gas Fill Ps Pressure	Starting Time	RTD4 max(deg C)	Wex max (W) by RTDav
1-0	140,40	Baking	2019/2/27		
1-1	0,0	D gas Ps=0.96 MPa	2019/3/1	69	15
1-2	120,80		2019/3/4	293	35
1-3	0,0		2019/3/8	26	0
1-4	140,95		2019/3/13	318	33
1-4	140,95	D gas Ps=0.366 MPa	2019/3/20	323.8	14.4
2-0	140,40	Baking	2019/3/27		
2-1	0,0	D MPa gas Ps=0.363 MPa	2019/4/1	54	4.2
2-2	140,95		2019/4/3	318.8	33.5
2-3	0,0	D IW gas Ps=0.951 MPa	2019/4/10	31.7	3.3
2-4	140,95		2019/4/10	320.7	24
3-0	140,40	Baking	2019/4/15		
3-1	0,0	D gas Ps=0.373 MPa	2019/4/17	56.9	4.2
3-2	140,95		2019/4/19	318.9	31

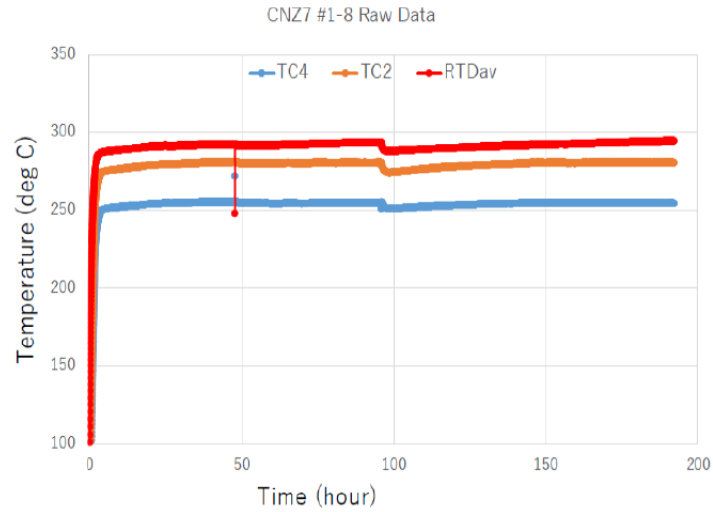


Figure 3. Temperature evolution data of CNZ7 #1-8 run for TC4, TC2 and RTDav, where data for a minute are missing before time 50 h.

the C-system. We have also confirmed that the calorimetry by average RC temperature with RTDav was most reliable in all cases, unless the gas pressure of RC is smaller than 0.1 MPa. Variation of data in RC gas pressure during each run is not shown in Table 1, which shows initial fed H-gas pressures only. For calorimetry calibration run by RTDav, the method-and-data was explained in ([8], Fig. 9). In Fig. 5, we show the excess thermal power data for the burst event.

At the burst peak, we did not see the H-gas turbulence effect though the peak data by RTDav is smaller than that by TC2. Sensors RTD1,2,3,4 are positioned at 3, 6, 9, and 12 cm from the bottom of RC (20 cm high in inner volume).

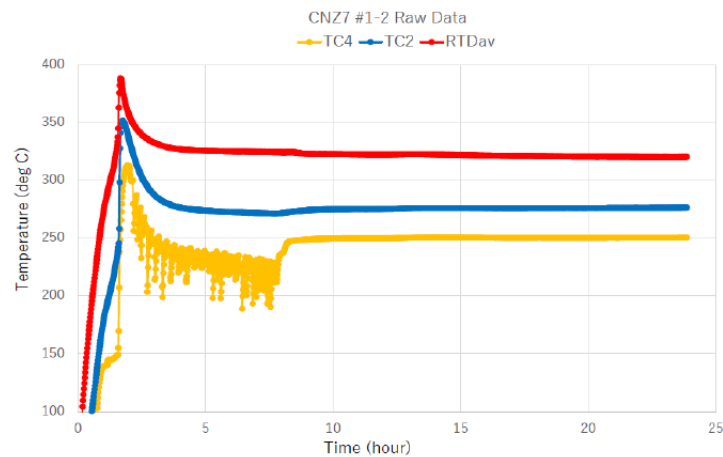


Figure 4. Temperature evolution data for the CNZ7 #1-2 burst event.

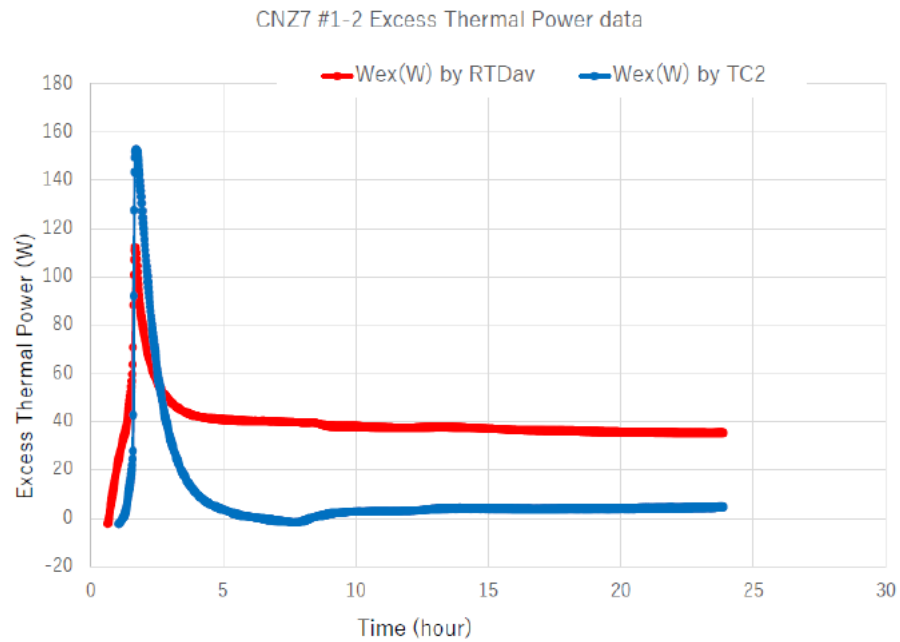


Figure 5. Data for excess thermal power for the CNZ7 #1-2 burst event.

The 1 kg CNZ7 sample with zirconia beads filler in this run filled fully RC volume. Therefore, Data by RTDav did not contain temperature information in RC upper region, and RTD4 data showed highest value 470°C to imply higher

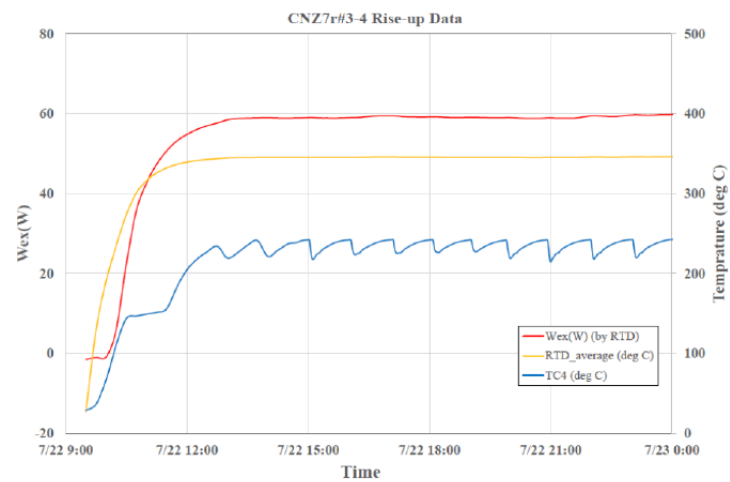


Figure 6. Typical rise-up data for 505g CNZ7r ET runs, example for CNZ7r #3-4.

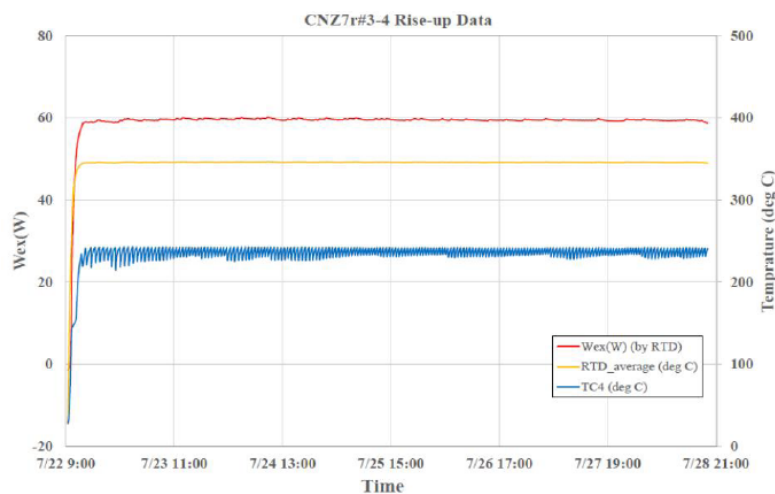


Figure 7. The whole data of one week run for CNZ7r #3-4 (120,80) with H-gas.

temperatures at higher points more than 12 cm.

The excess thermal power data by RTDav after the peak are reliable and the data by TC2 should be drastic underestimation due to the H-gas turbulence, which decreased the upper flange temperature as observed by TC4 and disturbed TC2 and TC1 temperatures to be downward. Consequently, we have confirmed that ca. 40 W excess thermal power remain the same after the burst for a day.

In Fig. 6, we show rise-up data by CNZ7r #3-4. (120,80), the last run of CNZ7r (not listed in Table 2).

The whole data for a week of CNZ7r #3-4 with (120,80) heater power input are shown in Fig. 7.

Obviously, quite similar behavior of TC4 temperature evolution as to that on CNZ7 #1-2 ET run is seen (TC4

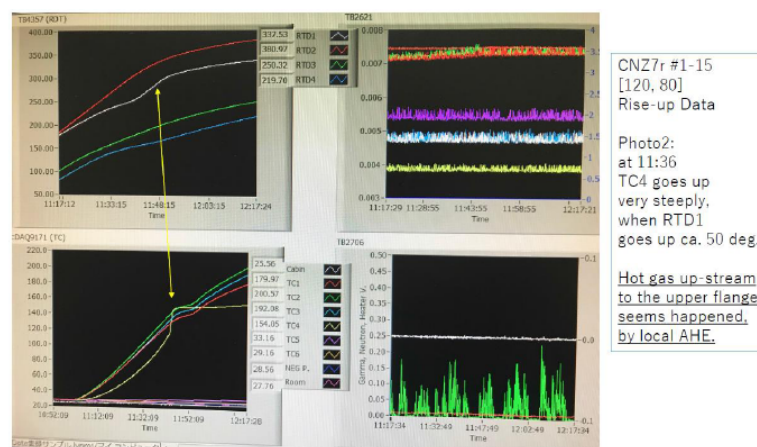


Figure 8. Typical view for the H-gas turbulence effect on rise-up data of CNZ7r ET run.

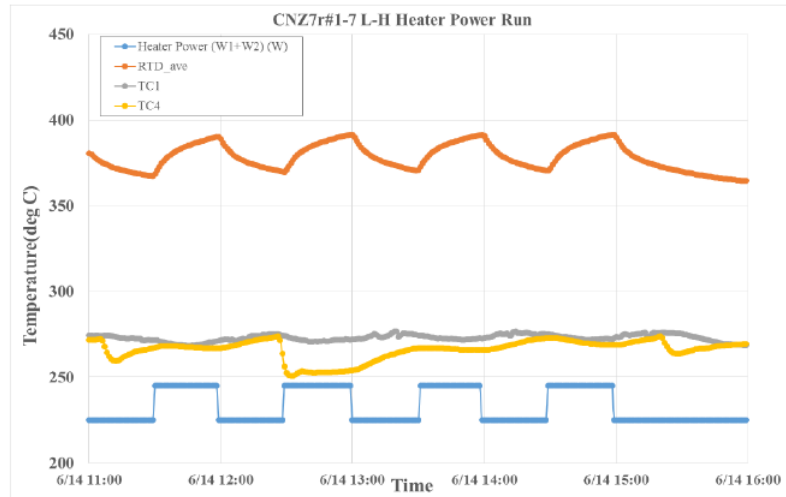


Figure 9. The low–high heating data under local AHE, from CNZ7r #1-7 run.

evolution in Fig. 7 is different from Fig. 4). The oscillatory TC4 fluctuation looks chaotic as you see in Fig. 7.

This is regarded as an indication of strong local AHE, which makes H-gas turbulence by generation of chaotic up- and down-stream-paths of convectional gas flow in RC.

We have seen many cases of such phenomena in CNZ7r and PNZ10r ET runs. Some details of on-going data on the NI (National Instruments)-Lab-View display are given in our slide presentation at ICCF22 [12]. We only show one example in Fig. 8.

We can see that the flat cooled temperature evolution at TC4 decreased temperatures at TC1, TC2 and TC3 (see

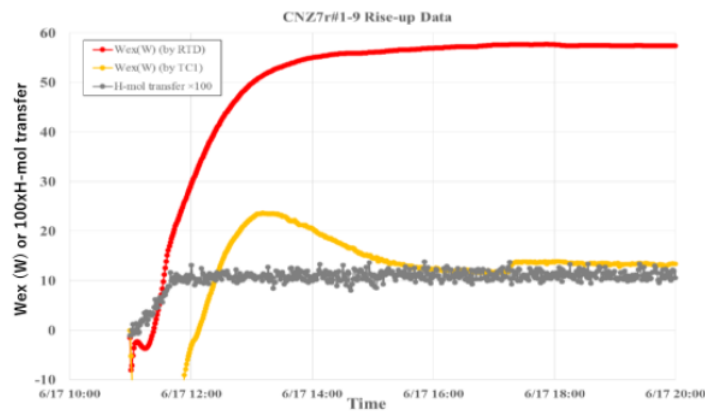


Figure 10. Excess thermal power data and H-gas transferred data for CNZ7r #1-9 run.

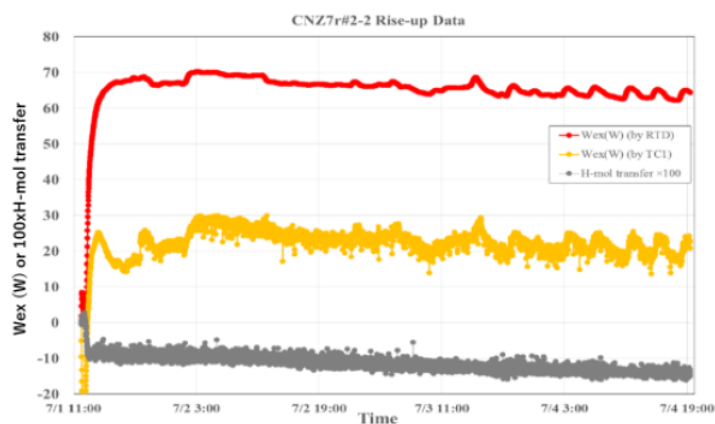


Figure 11. Excess thermal power data and H-gas absorption rate, for CNZ7r #2-2.

lower left photo). Many more data are available in [12].

To investigate the effect of H-gas turbulence on calorimetry, we have done the low–high heating operation as shown in Fig. 9. Clearly, the evolution of TC4 is too strange to regard normal, and accordingly the oil-outlet temperature TC1 is distorted negatively when heater power increased. Fortunately, evolution of average RC temperature estimated by RTD_{av} looks normal behavior. Consequently, we can employ the calorimetry by RTD_{av} to be a valid measure at all the times.

3.2. Typical AHE excess thermal power data

We now show typical excess thermal power data for CNZ7r and PNZ10r ET runs. Many data are given in [12]. We only show few typical data here.

In Figs. 10 and 11, we show excess thermal power data for CNZ7r ET runs.

As already discussed, heat power calorimetry by TC1 is in drastic underestimation in this case, due to the H-gas turbulence effect under AHE, and the excess power by RTD_{av} is reliable. Excess thermal power reached ca. 57 W and continued several days until when we changed the heating condition. The net sample weight of CNZ7r is 505 g, so that the relative power level is ca. 113 W/kg. The excess power level increased by the re-calcination (from CNZ7 to CNZ7r) to about 8–10 times. It is a drastic positive effect on the AHE enhancement purpose. An interesting point inferring the mechanism is the fact that AHE is taking place after the desorption of H-gas saturated and with small fluctuation of H-gas sorption/desorption balance (see gray plots).

In Fig. 11, we show another typical data for rise-up ET run just after the baking treatment for CNZ7r #2-2.

Evidently, excess thermal power was enhanced to about 20% (to ca. 70–65 W) by the baking treatment. Relative power level is ca. 130 W/kg. AHE happened after the initial rapid H-absorption (endothermic, we know) and during slow H-absorption mode in this case with small gas in/out fluctuation.

Succeeding ET run after cooling RC to room temperature showed repeatable generation of AHE as seen in Fig. 12. However, AHE in this case took place after the H-gas desorption rate saturated. From these results by Figs. 10–12, we can confirm that heat generation reaction consumed only very small amount of H-gas and happened in delicate balance of H-gas in and out on/through nano-composite islands surfaces of CNZ sample [11]. We have found that H-gas pressure in RC looked optimum for 0.1–0.5 MPa.

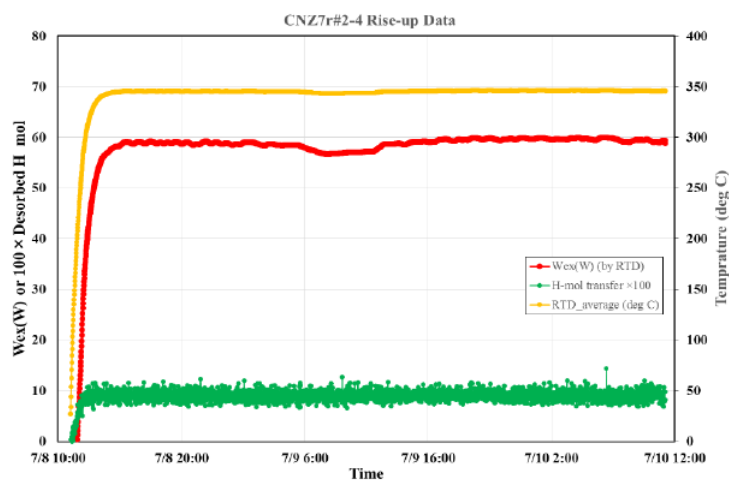


Figure 12. Rise-up data of excess thermal power, average RC temperature and H-gas transferred for CNZ7r #2-4 [120, 80] ET run.

In Figs.13–15, we show typical AHE data for PNZ10r with D (deuterium)-gas.

As seen in Fig. 13, the first ET run by PNZ10r #1-2 had heat hump at rise-up evolution. We omitted to show RT run #1-1 with initial D-gas charging, as it is not so important as we discussed much in [9] that O-reduction was small for re-calcined samples as the cases of PNZ6r and PNZ6rr runs showed [9]. We concluded that H₂O formation heat

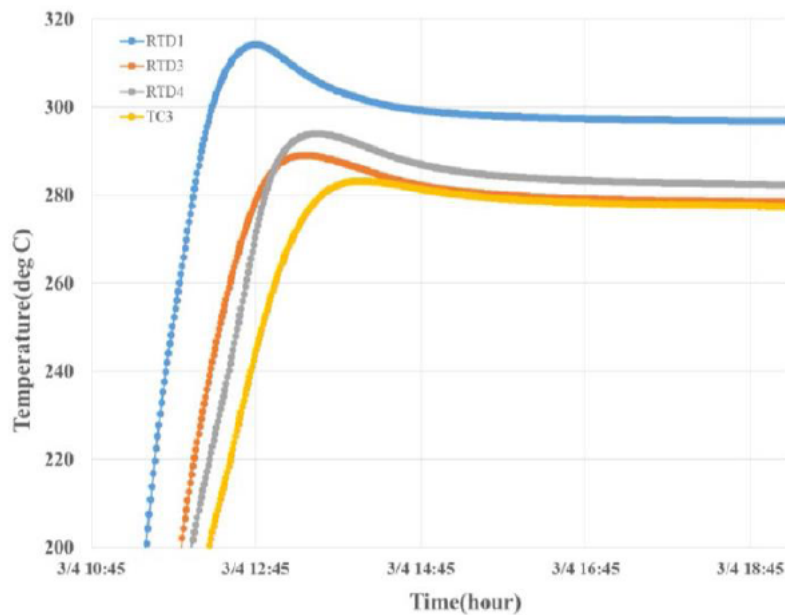


Figure 13. Temperature rise-up data for PNZ10r #1-2 (120, 80) ET run.

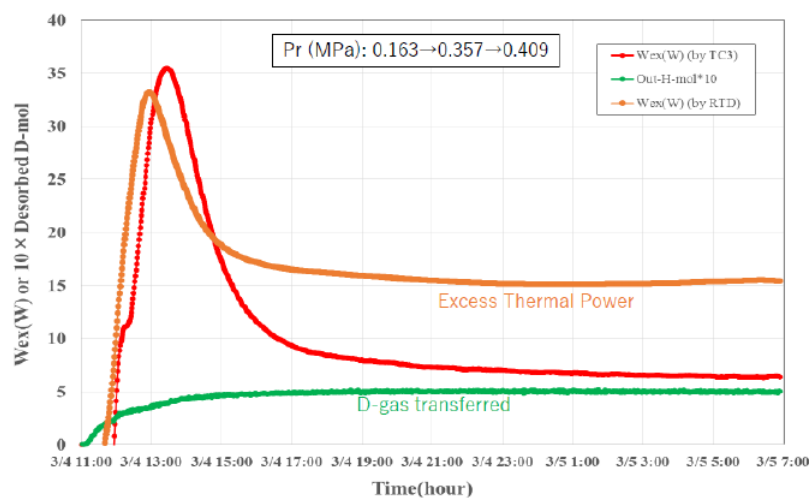


Figure 14. Excess thermal power and D-desorption rate for PNZ10r #1-2 ET run.

was not the cause of this heat burst.

Small amount ($\text{Pd/Ni} = 1/10$) of Pd on possible Ni nano-core of islands [11] may have strong catalytic effect [9] to absorb much deuterium (or hydrogen) at #1-1 RT run (1.5 D-mol absorbed). By heating up of #1-2 run, absorbed D-atoms looked desorbed partially first and reached at Ps and Pr pressure equilibrium. Under the slowly going desorption condition, AHE excess thermal power appeared as shown in Fig. 14. Corresponding to the heat bursts of RTD1,2,3,4 and TC3 temperatures, excess thermal power had small heat burst of ca. 35 W peak and decreased to ca. 15 W (by RTD_{av}) of sustaining level for several days. It happened during the D-desorption mode, and we do not have good reason to explain large exothermal energy generation under the D-gas desorption, in the chemistry sense. This fact may imply that heat source may be nuclear origin.

After the second baking of sample (PNZ10r #2-0 run), D-gas absorption was small (0.37 D mol absorbed) at RT run. In Fig. 15, we show excess thermal power and D-desorption rate for PNZ10r #2-2 ET run. The excess thermal power level of sustaining evolution increased to ca. 30 W, which is double score of those of PNZ10r #1-2. The baking treatment is confirmed again to be effective for PNZ10r sample also.

As reported in [9], excess thermal power by ET runs of PNZ10 was very small as ca. 5 W. We can say that the re-calcination treatment could enhance AHE by 3–6 times, as seen by data of PNZ10r.

To summarize the effect of re-calcination and baking, please see Tables 4 and 5.

Data of RC temperatures are of RTD_{av}, namely averaged value of four points by RTD1-4 in RC.

From these tables, we can say that the present sample treatments by re-calcination and baking are very useful to enhance the excess thermal power per sample weight. We are looking forward to seeing the results by the third re-calcination to make CNZ7rr and PNZ10rr (see our JCF20 presentation and paper in December 13–14, 2019, Fukuoka, Japan).

3.3. Circumstantial nuclear evidence by AHE

During all experimental runs, we monitored radiation levels of neutron (by He-3 counter dose meter) and gamma-spectrum (by NaI scintillator), comparing to those of natural backgrounds. No meaningful counting increase or un-

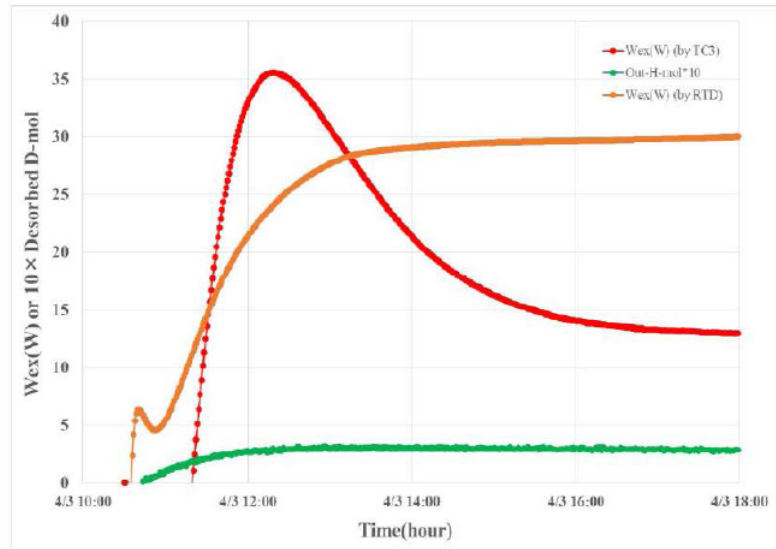


Figure 15. Excess thermal power and D-desorption rate for PNZ10r #2-2 (140, 95) ET run.

Table 4. Summary of enhancement effect of excess thermal power by re-calcination and baking for CNZ7 and CNZ7r.

Run ID, nominal	Heater Input (W1, W2) W	Wex (W/kg): CNZ7	Wex (W/kg): CNZ7r	RC Temp. (°C): CNZ7	RC Temp. (°C): CNZ7r
#1-2	120, 80	(152, burst)	96	(382)	336
#1-4	140, 95	12	110	366	384
#2-2	120, 80	7	118	295	346
#2-4	140, 95	14	126	358	392
#3-2	120, 80	9	115	298	345
#3-4	140, 95	13	137	349	393
Sample (g)		1,150	505		

Table 5. Summary of enhancement effect of excess thermal power by re-calcination and baking for PNZ10 and PNZ10r.

Run ID, nominal	Heater Input (W1, W2) W	Wex (W/kg): PNZ10	Wex (W/kg): PNZ10r	RC Temp. (°C): PNZ10	RC Temp. (°C): PNZ10r
#1-2	120, 80	5	47	280	301
#1-4	140, 95	4	95	310	366
#2-2	120, 80	10		306	
#2-4	140, 95	14	77	342	357
#3-2	120, 80	8		298	
#3-4	140, 95	18	124	348	379
Sample (g)		965	450		

known spectral peaks have ever been observed by the NaI spectroscopy. Natural background of gamma-rays is more than 100 times than neutrons. Therefore, to detect some increase of gamma-rays by AHE-origin nuclear events, which can be modelled as primary-radiation-free reactions and secondary very weak radiations [11], are very difficult unless

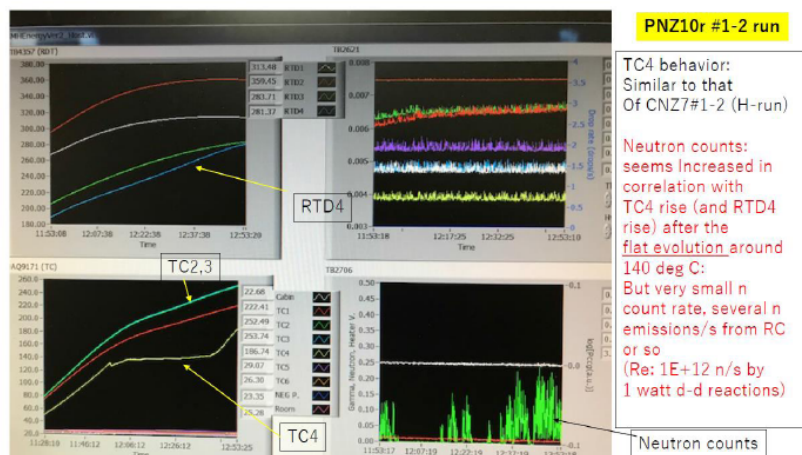


Figure 16. Case of heat-neutron correlation by PNZ10r #1-2 rise-up evolution-1.

the AHE power level would increase in MW level or so. Instead, weak neutron emission might be detected with lower AHE power conditions.

The AHE experiments with PNZ sample and deuterium (D) gas might provide visible neutron emission even with not very large excess power conditions. Examples of such cases are shown in Figs.16 and 17 for PNZ10r #1-2 run at rise-up heat hump.

When RC local temperature RTD4 increased, corresponding to the increase of TC4 temperature escaping from

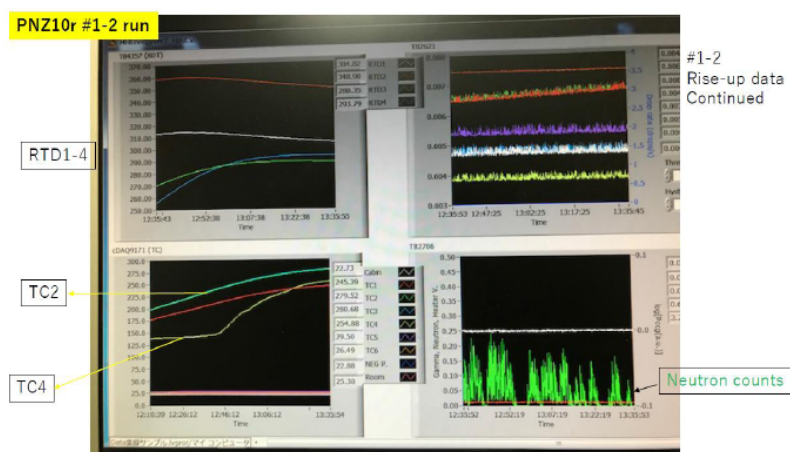


Figure 17. Case of heat-neutron correlation by PNZ10r #1-2 rise-up evolution-2.

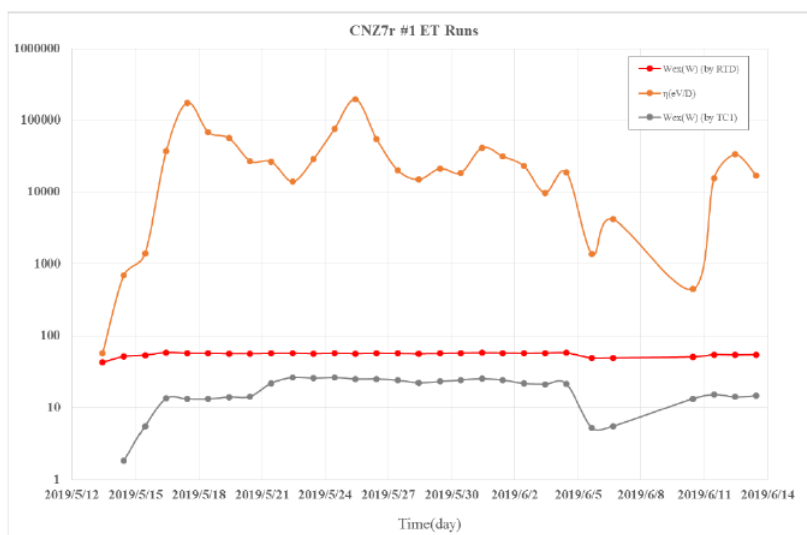


Figure 18. Evolution data of specific reaction energy (*brown*) by AHE for CNZ7r ET runs.

the flat evolution (by D-gas turbulence), neutron counts looks increasing (Fig. 16), and later RC temperatures are decreasing in correlation with the decrement of neutron counts (Fig. 17). Since the response of neutron detection is very fast (less than 1 ms), thermal power response by RTDs and TCs of RC are too slow (30–60 min time constant) to pick up possible nuclear reaction bursts. Namely, shapes of neutron count rates might show true timing of excess heat origin. During sustaining excess thermal power modes for weeks, weak increase of neutron counts looked sporadic events, which might tell us that AHE nuclear events do not taking place continuously, but do intermittently. Level of neutron yield was 0.1 n/J, which is on the order of 1.0×10^{-13} of that by supposed d–d reactions.

Another inferred evidence of nuclear like signature is coming from specific reaction energy data (η -value) per H(D)-transfer. In Fig. 18, we show observed evolution of specific reaction energy per H-transfer by CNZ7r sample for one month long series of runs.

Total heat observed is 128 MJ for 27 days with ca. 55 W excess thermal power level sustaining condition. Corresponding specific reaction energy per H-transfer is mostly more than 10 keV/H, and sometimes took over 0.1 MeV/H, which is very close to nuclear reaction energy level. Considering that not all transferred Hs were spent by AHE reactions, real reaction energy may be more than 0.1 MeV.

In the case of specific reaction energy observation for PNZ10r runs, we had very small gas leakage from RC, unfortunately. Probably, because of the leakage, obtained specific energy data may have been underestimated. We show the results in Fig. 19. Level of reaction energy per D-transfer is from ca. 100 to 500 eV/D. Of course, such data are still beyond explanation by some chemical reactions those are of level in 1 eV/D or less.

We can recall our previous data by PNZ6rr as shown in Fig. 20. Largest η -values are close to 1000 keV/D (namely 1 MeV/D) that is really of nuclear reaction signature. Significant high local excess power level as 55 W was observed in central zone of RC (see Fig. 20), though total heat recovery data by oil flow showed near 10 W level [9]. As we have explained already in this paper, the D-gas turbulence effect made drastic underestimation of excess thermal power by TC2 and we understand that it should have happened also in the PNZ6rr runs [9]. We can re-evaluate the data of

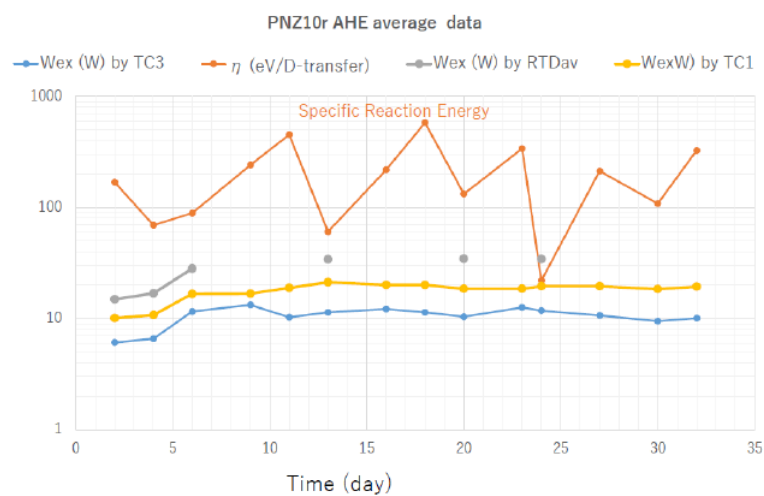


Figure 19. Specific reaction energy data by PNZ10r ET runs.

Fig. 20 now to conclude that ca. 55 W excess thermal power in Fig. 20 is reliable and real. We used ca. 120 g sample for PNZ6rr. Relative excess thermal power was ca. 460 W/kg.

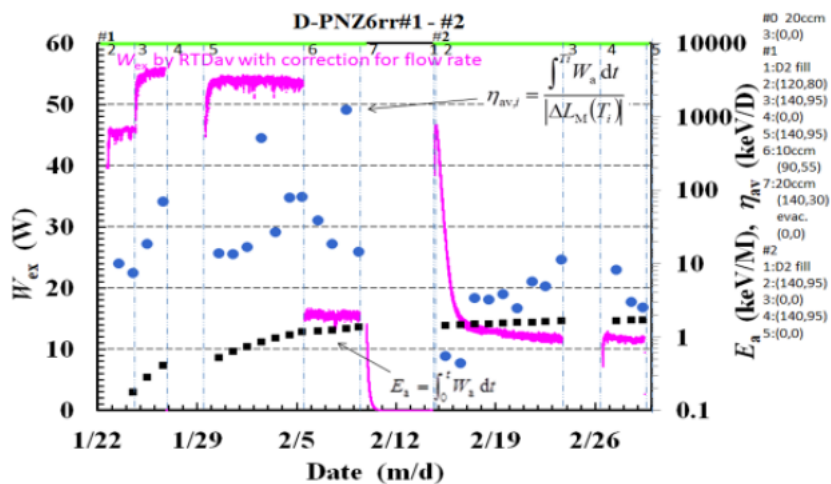


Figure 20. Processed data of excess thermal power (pink graph), integrated heat energy per M (black square) and eta-value (sky blue circle) for PNZ6rr ET runs around 300°C RC temperature, obtained by RTD-average data, after [9].

4. Summary and Concluding Remarks

As new findings, the H(D)-gas turbulence effect in RC under strong AHE power becomes strong in our C-calorimetry system, when we have met strong local AHE power evolution in RC. This gas turbulence effect cooled the RC upper flange and generated chaotic temperature evolution of TC4 upper flange temperature and mostly decreased oil-outlet temperatures monitored at TC1 and TC2. Fortunately, calorimetry by average RC temperature (RTDav) is not distorted visibly and we can rely it as measure of real excess thermal power for all the time.

The re-calcination treatment of CNZ7 and PNZ10 powders is effective to enhance excess thermal power by nearly one order of magnitude. And the baking treatment between ET runs is also effective to enhance AHE.

We got useful knowhow for fabricating sample powders as initial calcination conditions, mortaring process and re-calcination. We may expect more enhancement of AHE power by the second re-calcination to make CNZ7rr and PNZ10rr powders.

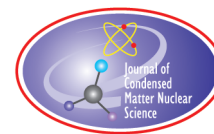
Now we can say that reproducibility of AHE generation with 100–400 W/kg excess thermal power level is established by the present nano-composite metal and H (or D)-gas interaction method. Simply, we call it Metal Hydrogen Energy (MHE) as the primary energy generation method.

Origin of AHE can be regarded as some nuclear origin as suggested modeled by [11]. We have obtained concrete results of circumstantial evidence of nuclear-like signatures in the present work.

References

- [1] A. Kitamura, A. Takahashi, K. Takahashi, R. Seto, T. Hatano, Y. Iwamura, T. Itoh, J. Kasagi, M. Nakamura, M. Uchimura, H. Takahashi, S. Sumitomo, T. Hioki, T. Motohiro, Y. Furuyama, M. Kishida and H. Matsune, Comparison of excess heat evolution from zirconia-supported Pd–Ni nanocomposite samples with different Pd/Ni ratio under exposure to hydrogen isotope gases, *Proc. JCF18*, 2018, pp. 14–31.
- [2] A. Kitamura, A. Takahashi, K. Takahashi, R. Seto, T. Hatano, Y. Iwamura, T. Itoh, J. Kasagi, M. Nakamura, M. Uchimura, H. Takahashi, S. Sumitomo, T. Hioki, T. Motohiro, Y. Furuyama, M. Kishida and H. Matsune, Excess heat evolution from nanocomposite samples under exposure to hydrogen isotope gases, *Int. J. Hydrogen Energy* **43** (2018) 16187–16200.
- [3] A. Takahashi, A. Kitamura, K. Takahashi, R. Seto, T. Hatano, Y. Iwamura, T. Itoh, J. Kasagi, M. Nakamura, M. Uchimura, H. Takahashi, S. Sumitomo, T. Hioki, T. Motohiro, Y. Furuyama, M. Kishida, H. Matsune, Phenomenology and controllability of new exothermic reaction between metal and hydrogen, technical report uploaded at research gate: https://www.researchgate.net/publication/322160963_Brief_Summary_Report_of_MHE_Project_Phenomenology_and_Controllability_of
- [4] A. Takahashi, A. Kitamura, K. Takahashi, R. Seto, T. Yokose, A. Taniike and Y. Furuyama, Anomalous heat effects by interaction of nano-metals and D(H)-gas, *Proc. ICCF20*, Tohoku University, 2016, downloadable at Research-Gate: https://www.researchgate.net/publication/313310565_Anomalous_Heat_Effects_by_Interaction_of_Nano-Metals_and_HD-Gas
- [5] A. Kitamura, A. Takahashi, K. Takahashi, R. Seto, Y. Matsuda, Y. Iwamura, T. Itoh, J. Kasagi, M. Nakamura, M. Uchimura, H. Takahashi, T. Hioki, T. Motohiro, Y. Furuyama, M. Kishida and H. Matsune, Collaborative examination on anomalous heat effect using nickel-based binary nanocomposites supported by zirconia, *J. Condensed Matter Nucl. Sci.* **24** (2017) 202–213.
- [6] Y. Iwamura, T. Itoh, J. Kasagi, A. Kitamura, A. Takahashi, K. Takahashi, R. Seto, Replication experiments at tohoku university on anomalous heat generation using nickel-based binary nanocomposites and hydrogen isotope gas, *J. Condensed Matter Nucl. Sci.* **24** (2017) 191–201.
- [7] Y. Iwamura, T. Itoh, J. Kasagi, A. Kitamura, A. Takahashi, K. Takahashi, R. Seto, M. Uchimura, H. Takahashi, T. Hioki, T. Motohiro, Y. Furuyama, M. Kishida and H. Matsune, Anomalous heat effects induced by metal nano-composites and hydrogen gas, *J. Condensed Matter Nucl. Sci.* **29** (2019) 119–128.
- [8] T. Yokose, A. Takahashi, K. Takahashi and Y. Furuyama, Anomalous # CNZ7 sample and H-Gas, *Proc JCF19*, 2019, pp. 18–35.
- [9] A. Takahashi, T. Yokose, K. Takahashi, R. Seto, A. Kitamura and Y. Furuyama, Repeated calcination and AHE by PNZ6

- sample, *Proc. JCF19*, 2019, pp. 1–17.
- [10] A. Takahashi, Many theoretical papers listed in Research Gate,
https://www.researchgate.net/project/Leading-the-Japanese-Gvt-NEDO-project-on-anomalous-heat-effect-of-nano-metal-and-hydrogen-gas-interaction?_sg=olKc4Ns5DMkZNQZBbB3g-QEiObIDjIy_1XpIY0pjj-KIYInbjzTZs1GlgZyGeKAbqRCFkvnT_QBdTLHTE1W4iFwsuuieleAZSz-.
- [11] A. Takahashi, Background for condensed cluster fusion, *Proc. JCF15*, 2015, pp. 63–90.
- [12] A. Takahashi, T. Yokose, Y. Mori, A. Taniike, Y. Furuyama, H. Ido, A. Hattori, R. Seto, A. Kamei and J. Hachisuka, Latest progress in research on ahe and circumstantial nuclear evidence by interaction of nano-metal and H(D)-gas, *ICCF22* presentation, 2019/9/8-13, Assisi, Italy,
https://www.researchgate.net/publication/335690203_Latest_Progress_in_Research_on_AHE_and_Circumstantial_Nuclear_Evidence_by_Metal_and_HD-Gas



Research Article

Mass and Heat Flow Calorimetry in Brillouin's Reactor

Francis Tanzella*

Energy Research Center LLC, San Carlos, CA 94070, USA

Robert Godes, Jin Liu and Robert George

Brillouin Energy Corporation, Berkeley, CA 94705, USA

Abstract

Brillouin Energy (BEC) has continued performing calorimetry measurements on the metal (e.g. Ni)/ceramic/Cu coated ceramic tube (catalyst) in a H₂ atmosphere with nanosecond pulses applied across the coatings. The Energy Research Center (ERC) has been examining and verifying BEC's calorimetry for over 18 months since 2 of the calorimeters have been moved from SRI International to BEC's laboratory. We have continued our testing of new materials, material fabrication techniques, and electrical stimulation methods to produce excess power and energy output. By applying fast pulses of several hundred volts and tens of nanoseconds long, the current follows the "skin-effect" principle and is concentrated at the outer metal–ceramic interface but returns through the bulk of the Cu. Two stimulation methods were used – steady-state and dynamic. In the steady-state method, the pulse power is measured directly using fast oscilloscopes that record the voltage across the catalyst and a shunt resistor in series with the catalyst. The resistance of the shunt resistor is measured accurately under DC and pulse conditions. The input pulse power is determined by multiplying the calculated root-mean-square voltage and current and recorded every 10 s. Using a version of the system identification (SI) heat-flow model designed specifically for the BEC calorimeter, the power reaching the five temperature sensors is determined during simultaneous continuous ramps of both heater and pulse powers. The power emanating from the catalyst is determined during sequences of less frequent, longer duration, low voltage pulses (LVP) and compared to that found using more frequent, shorter duration, high voltage pulses (HVP). The power determined during the less frequent LVP is set as the input power during that sequence. The power of the stimulation pulses during the more frequent HVP sequences is maintained equal to that during the less frequent LVP. Then the calculated power output from the tube is divided by that calculated during the reference sequences, giving a so-called coefficient of performance (COP). We have also used mass flow calorimetry to determine COP. Low voltage, long pulses are chosen to match the input power from high voltage, short pulses. The low voltage pulses are not thought to stimulate LENR, while the high voltage pulses are. This provides a method to compare matching input power under conditions that stimulate LENR with conditions that do not. Any excess heat detected from the high voltage pulse condition is considered to be generated by LENR rather than resistive heating.

© 2020 ISCMNS. All rights reserved. ISSN 2227-3123

Keywords: Excess energy, Hydrogen gas, Nickel, Pulse stimulation, System identification

*Corresponding author. E-mail: consulting@tanzella.name.

1. Introduction

Since 2012, first SRI International (SRI) and later Energy Research Center (ERC) have been performing tests on two different versions of Brillouin Energy Corp.'s low-energy nuclear reactors (LENR) [1]. We have operated these reactors independently in an attempt to verify results that Brillouin has found with these reactors and others like them. We have also monitored and advised Brillouin on the results from identical reactors operated by Brillouin in their own laboratory. This paper reports on the verification and validation of results [2] obtained in Brillouin's laboratory since the last report. Brillouin has indicated that it has designed the control systems in its reactors to drive the underlying physics of LENR, as described in its Controlled Electron Capture Reaction (CECR) hypothesis [3]. The CECR hypothesis explains how BEC believes that their reactors generate controlled LENR reaction heat. Our study did not attempt to prove or disprove Brillouin's CECR hypothesis.

The systems tested and described in this report consist of three parts: catalysts, reactors, and calorimeters. The catalysts are the reactive components of the system. The reactors provide the environment and stimulation that causes the catalysts to produce reaction heat. The calorimeter is used to measure the thermal efficiency and absolute heat produced by the catalyst-reactor system. The calorimeter was designed by both SRI and Brillouin personnel to be perfectly matched to the reactor. The results from four of these reactors are described in this report.

Brillouin's system design utilizes both SI and mass flow calorimetry, in which a heat spreader catalyst and reference temperatures are held constant by varying the input heater power while applying different types of stimulation that also input power to the reactor/calorimeter. This "dynamic" method of analysis allows us to analyse all power entering or affecting the catalyst as well as all power emanating from the catalyst based on differential equations describing temperature and power variations. While this requires several days of calibration and up to 40 h of excitation to verify that calibration, it allows for the testing of 12-parameter variations per hour versus one or two in the traditional mass flow, steady-state method.

2. Experiment

2.1. Reactor design

The catalyst consists of metal and ceramic coatings applied to a ceramic substrate, which in some configurations includes a heater and thermocouple. Generally, these coatings alternate between a hydrogen-absorbing metal and an insulating ceramic. The exact size, shape and composition of this catalyst is considered proprietary at this time.

Other designs have used more or fewer layers. All of the layers are porous, allowing the gas(es) in the reactor chamber access to all coatings. A heater, if present, and a thermocouple are located in the axial and radial center of the substrate. The power to the heater is measured directly from the voltage and current supplied by the direct current (DC) power supply. A schematic diagram of the reactor/calorimeter system is shown in Fig. 1. A photograph of the reactor internals is shown in Fig. 2.

2.2. Measurement

The catalyst is stimulated by sending pulses between the outer layer or layers and the inner copper layer. The nature of the pulses is such that its current travels primarily on the surface of the metal in contact with the ceramic (the "skin effect") [4]. This effect is caused by the very fast rise time of the pulses and is dependent on the magnetic permeability of the metal. Although the skin effect is present on both surfaces of a metal, in a multi-layer system the greatest current is passed at the interface with the greater dielectric [1], in this case the ceramic. An example of this pulse design, which Brillouin refers to as a "Q-Pulse", is shown in Fig. 3. The pulse width presently used is from ~ 30 to 10,000 ns with a duty cycle normally of less than 1%. More detail on the pulse trains are shown here [3]. All catalysts are measured

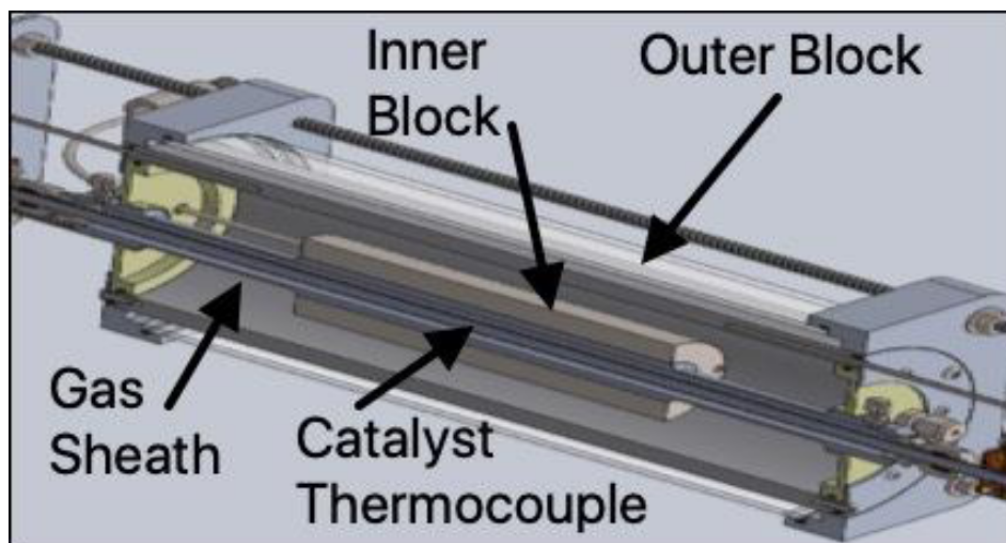


Figure 1. Cut-away schematic drawing of isoperibolic reactor.

using a “Hi-Pot” tester before use. Any one that shows measurable current when 500 V is passed between the two metal layers is rejected. Any voltage breakdown would reduce the possibility of the current pulse passing the complete length of the catalyst. As such, any capacitor discharge is avoided.

The stimulation power imparted to the catalyst is measured using a circuit shown in Fig. 4. The pulse is generated

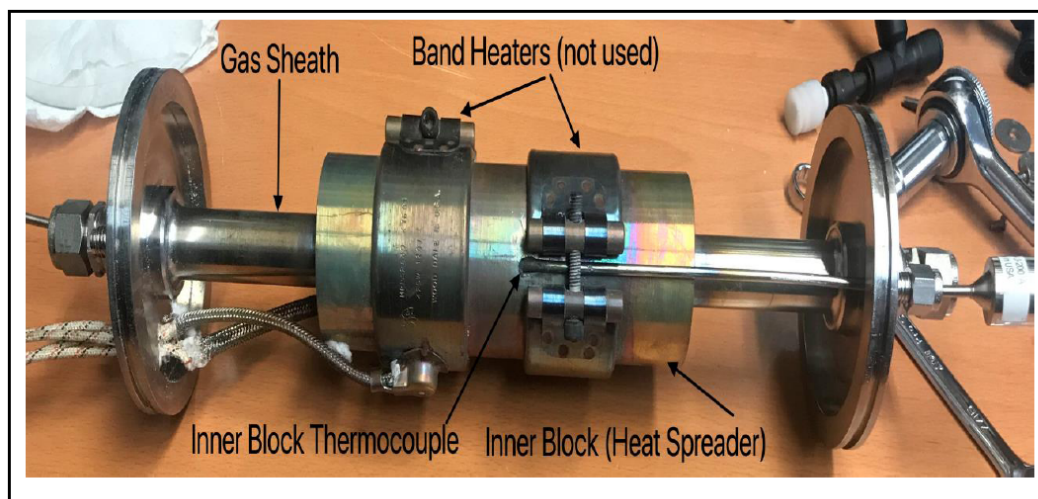


Figure 2. Photograph of reactor internals.

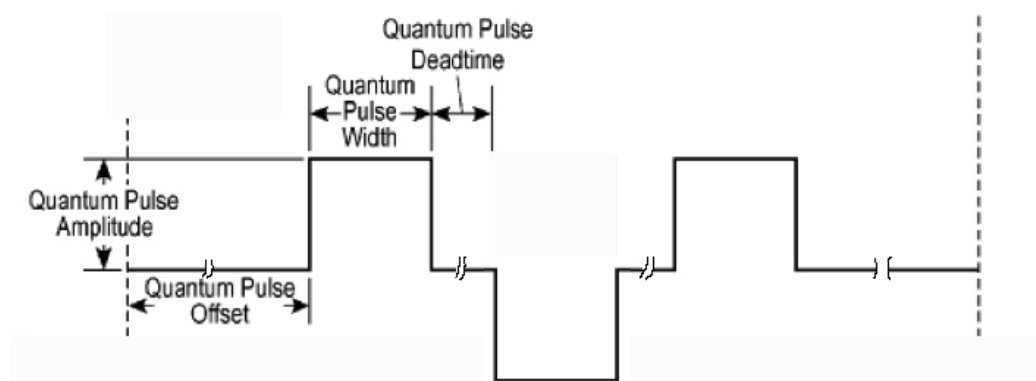


Figure 3. Example of Brillouin's "Q-Pulse".

by a proprietary *Q*-Pulse board and delivered to the catalyst using series and termination resistors that help match the load impedance to that of the pulse board output. Using a high-speed oscilloscope, the voltage across the end of the catalyst nearest the pulse board (V_1) is measured as well as the voltage across the opposite end of the catalyst (V_2) across the termination resistor (Z_{term}). The Z_{term} also acts as a current measuring resistor so the current is calculated as V_2/Z_{term} . The root mean square (rms) voltage across the Z is then converted to the rms current. The system is designed to be a "well matched" transmission line with a characteristic impedance near 2.0Ω and verified using a time-domain reflectometer.

The power imparted to the catalyst is determined using the red and blue voltage traces shown in Fig. 5. The difference between the two voltage traces is calculated after aligning them in a way that minimizes the time difference. (The time difference, which may be due to the RC time constant of the system or simply the propagation speed of the pulse, is approximately 5 ns or approximately $0.3 c$, where c is the speed of light.) This overestimates the power imparted to the catalyst by a small amount since any phase lag between voltage and current would impart less input power. The current calculated from V_2 is shown in black and the product of it with the voltage difference (power) is shown in green. It has been shown that the power calculation is essentially the same (within measurement error) whether it is calculated by multiplying the current and voltage plots point by point or by multiplying the calculated

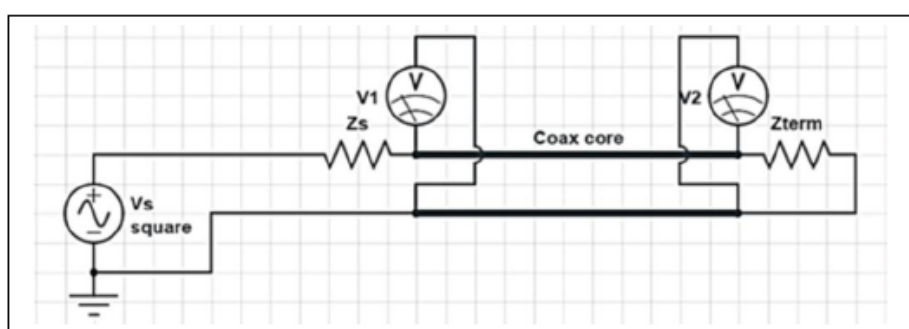


Figure 4. Pulse power measurement circuit.

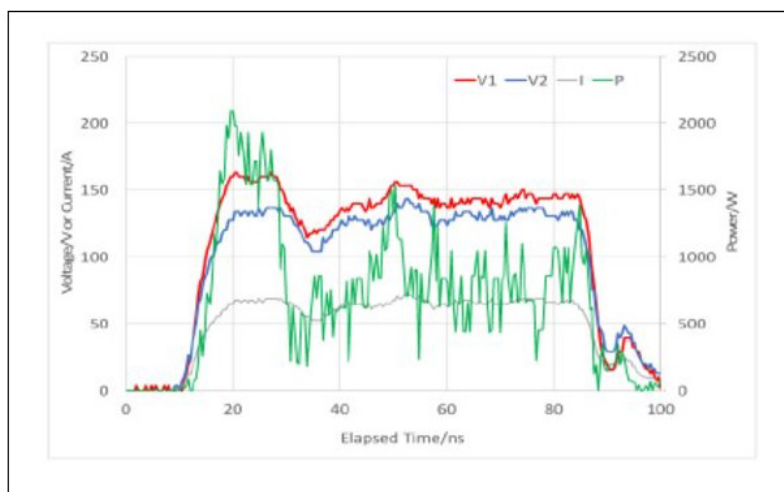


Figure 5. Measurement of the Q -pulse power across the catalyst.

rms voltage by the rms current. This calculated power is referred to as Core Q Power.

In compensation calorimetry the heater power is varied to keep either the catalyst or inner block at constant temperature, which generally also keeps the other at a constant, but slightly different, temperature. The difference between the heater power with and without stimulation determines the effect of the stimulation. If this difference is greater than the stimulation that reaches the catalyst, then energy is being produced in the catalyst. Approximately 70 different parameters are collected allowing for calculation of Reaction Power (the power produced by the process induced by the pulse stimulation). Several calculation methods are possible from these parameters. In addition, two different stimulation sequences are used. In Section 2.4, we describe these two sequences and the calorimetry method used for each of them.

2.3. Operation

A description of the data acquisition system with a copy of the graphical interface has been described earlier [2]. The program has several panes allowing for control of temperature, pressure, pulse voltage, pulse power, pulse width, and pulse repetition rate and gas composition. The program also collects the heater power, the pulse power at the generator (as well as at the catalyst), all temperatures, water flow rates, and gas pressure. The concentration of hydrogen and oxygen in the argon blanket are collected and measured. In all, more than 70 different parameters are collected and stored every 10 s. A sequence file can be used to automatically change any or all of the input parameters at specified intervals over a multi-day or multi-week period.

The sheath containing the catalyst is operated with a static fill of hydrogen, and occasionally helium or argon, gas held at constant pressure up to 15 bar. The temperature of the catalyst, and its substrate, is held constant using the embedded heater and thermocouple and controlled from 100°C to 600°C. The outer block (outer cylindrical perimeter of the calorimeter) temperature is held at 25°C using water flow from a Neslab[®] recirculating constant-temperature chiller.

The power emanating from the Q -pulse generator board, or that applied directly to the catalyst, is held constant

as chosen by the program's front panel or the sequence file. Generally, the pulse amplitude (voltage) and pulse width are chosen. The repetition rate is adjusted automatically to maintain the chosen pulse power or temperature. Only a minor fraction of this power from the generator board reaches the catalyst as most of it is lost as heat in the termination resistor. This is necessary to get an accurate measure of energy actually dissipated in the catalyst and to match the load impedance to that of the generator thus preventing reflections that could cause measurement errors. Of that reduced power only a portion of it influences the heater power as explained in Section 2.2. The actual pulse power is measured directly via the methodology presented above.

During this time period several stimulation methods were tried to find one that can act as a blank (no excess power) using similar Core Q Power. Ideally these methods need to be compatible with the data collection's software's calculation designed for the low duty cycle Q -Pulse square waves and not require hardware changes. Some of the methods tried were: (1) straight sine waves; (2) low duty cycle square waves; (3) large pulse widths with long rise times. Ultimately, calibration runs used Q -Pulse parameters that were known not to produce LENR heat (low voltage, long length pulses at lower repetition rates) but impart the same power to the catalyst as parameters expected to show LENR heat (high voltage, short length pulses at higher repetition rates).

Operating in power compensation mode, the computer generally keeps the heat spreader (inner block) temperature constant at its set point. This generally keeps the calorimeter output power constant. When power is imparted from the Q -Pulse, the heater power is reduced, or removed completely to compensate and maintain a constant temperature. Hence, the catalyst substrate temperature and the inner and outer block temperatures are all held constant while using the same gas. When the inner block temperature is held constant the output mass flow calorimetry power reaches the same output power whether using heater or pulse input power. This allows for calibration using only heater power. When using lower voltage, lower repetition rate pulses, the calorimetric power is equal to that measured using only the heater.

In addition to applying DC power to the heater inside the tube, DC current was occasionally passed only through the outer metal coating for thermal calibration. Operating at constant gas pressure, a sequence stepped the reactors from 100°C to 300°C in 50°C intervals. At each temperature a given DC power was applied to the outer metal coating on the substrate, as opposed to pulses driven between the outer metal and Cu coatings. This process was then repeated but applying constant power pulses between the Cu and outer metal while varying pulse width at each temperature. The pulse repetition rate was adjusted at each temperature to keep the temperature constant.

Two major methods of operation were employed, each requiring a different analysis method. The first method operated with the reactor at a steady-state temperature and input powers, which we refer to as the mass flow calorimetry (MFC) method. In our second approach, the heat flow (HF) method, we calibrate the system using heater steps as described above, but measure the output power using redundant thermocouples situated at three different locations from inside the reactor catalyst's substrate to the outer reactor boundary. The HF method was developed to allow for many Q -pulse parameters to be tested in less time.

2.4. Analysis

The earlier report [5] describes the two different analysis methods employed in the effort. Here we describe the stimulation and analysis methods employed most recently.

2.4.1. MFC method

The steady-state stimulation method was now operated in MFC mode, where the computer kept the temperature constant at either the catalyst substrate or the inner block. Then power was imparted from the Q -pulse replacing the heater power and adjusting the pulse repetition rate automatically to keep the inner block at the same temperature maintained

using the heater. Hence, when the inner and outer block temperatures are held constant, the substrate temperature will respond to the stimulation. The output power (calculated from the water flowing through outer block) did not change as the input power compensates for the total power emanating from the catalyst. The total output power included the stimulation power and the power due to reaction heat (i.e. LENR power).

In this method heater power necessary to maintain the inner block at constant temperature for four hours without Q -pulses present was applied. We realize that only a fraction of the heater power may be imparted to the catalyst because the heater/thermocouple combination has temperature-dependent losses to the rest of the calorimeter and to the environment. The steady state is achieved during the 4-hour heater step and the inner block temperature remains constant during the subsequent Q -Pulse steps. During these Q -Pulse steps the system is instructed to apply chosen pulse width and pulse amplitude at each step while the system adjusts the repetition rate as needed to maintain constant inner block temperature. Figure 6 shows an example of a heater calibration run. The 70% efficiency has been improved as the calorimeter has been modified to capture more of the input power. The latest analyses use a temperature-dependent calorimeter efficiency.

As the thermocouple inside the catalyst substrate is more closely coupled to the heater, its temperature is hotter when using the heater than when applying pulses even though the inner block is held constant because the thermocouple is imbedded in the heater assembly. Since both of these input power steps are allowed to achieve a steady state, the calorimetric efficiency of the Q -Pulse power is taken to be equal to thermal efficiency of the heater at the same temperature. As expected, the MFC output power varies with the inner block temperature such that the source of the heat does not affect the output power at the same inner block temperature.

Another calibration was performed using DC joule heating along the length of the metal outer coating. It is assumed that DC current will not stimulate the MH_x material to yield excess power as proposed to happen with the Q -Pulses.

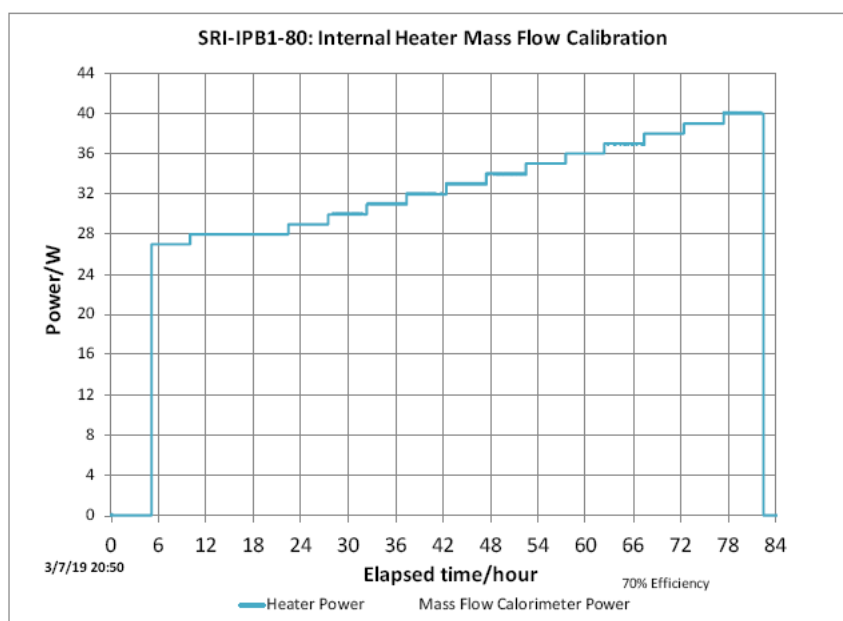


Figure 6. Reactor calibration using a heater inside the reactor tube. The MFC power matches best the input power when a 70% efficiency of the heater power is taken into account.

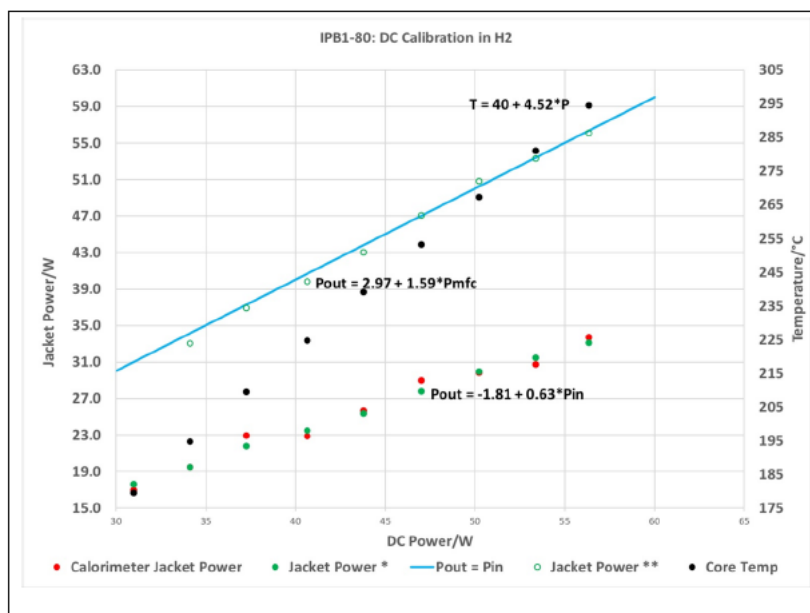


Figure 7. Reactor calibration using DC joule heating along the metal outer coating.

A summary of the DC heating steps is shown in Fig. 7 where input power is plotted on the horizontal axis and output power is plotted on the left vertical axis. The red dots are an average of the final 5 min of the raw calorimeter output power taken at the end of each power step. The green dots are that same power adjusted for the effect of the diurnal change of room temperature. The green circles are the output power adjusted for calorimeter efficiency to best fit the $P_{out} = P_{in}$ blue line. The black dots represent the temperature inside the catalyst substrate plotted against the right vertical axis.

Using pulse stimulation and inputting the same power, or holding the same block temperatures, as used in the calibration we use the efficiency calculated from the calibration to calculate the ratio of P_{out}/P_{in} . Also, using low voltage and high voltage steps at same power we can examine the effect of different pulse amplitudes and width. We have examined different pulse amplitudes and lengths at different temperatures and concluded that the lower amplitude, longer length pulses result in less output power. We then call this our calibration stimulation, even though it may not produce zero excess power, but yields conservative excess power measurement.

2.4.2. HF method

The HF method employs a model with several components, each representing individual components of the calorimeter, shown schematically in Fig. 8. This analysis utilizes a simplified version of the system identification (SI) model reported by Berlinguette and Fork [6–8]. Linkages between these components (and from a component to the reference room temperature) are either conductive or storage. Temperatures are on the inside of the catalyst substrate and on the outside of the cylindrical heat spreader (inner block). The five differential equations in time shown in Eqs. (1)–(5), model the heat imparted to the catalyst using a function of the difference of the catalyst and inner block temperature, a function of the ability of the substrate and inner block to store heat, and the difference between the substrate and

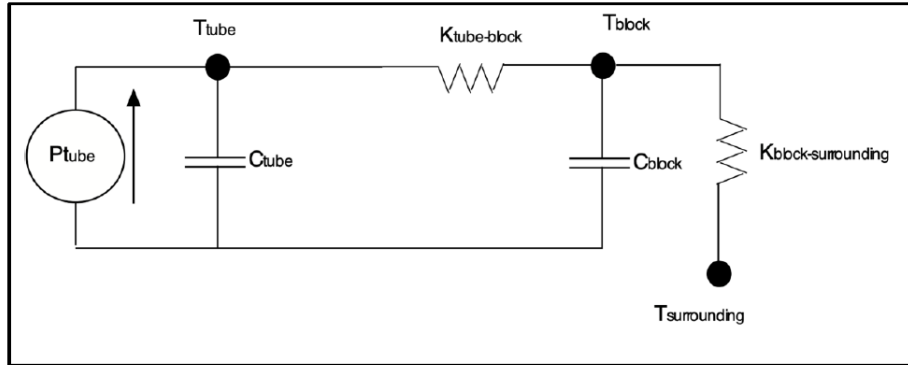


Figure 8. Heat flow calorimetry model of isoperibolic reactor, where “Tube” refers to the catalyst.

ambient temperatures. Each of these four components has three coefficients, each in the form of a third order equation. These coefficients are determined by fitting the temperature data to the actual power measured using low voltage pulses or heater power. The model then yields a simple set of equations that can be solved analytically for input power, being equal to output power during low voltage pulses or joule heating.

$$dT_{\text{tube}}/dt = (1/C_{\text{tube}})(P_{\text{tube}} - k_{\text{t-b}}(T_{\text{tube}} - T_{\text{block}})), \quad (1)$$

$$dT_{\text{block}}/dt = (1/C_{\text{block}})(k_{\text{tube-block}}T_{\text{tube}} - T_{\text{block}}) - k_{\text{block-surrounding}}(T_{\text{block}} - T_{\text{surrounding}})), \quad (2)$$

$$P_{\text{in}} = P_{\text{tube}}(\text{pulse, DC or internal heater}), \quad (3)$$

$$P_{\text{out}} = k_{\text{block-surrounding}}(T_{\text{block}} - T_{\text{surrounding}}), \quad (4)$$

$$P_{\text{stored}} = C_{\text{tube}}(dT_{\text{tube}}/dt) + C_{\text{block}}(dT_{\text{block}}/dt). \quad (5)$$

These coefficients are represented as four simple 3-coefficient binomial equations, yielding 12 possible parameters. These parameters are then used to calculate the amount of heat emanating from the catalyst during an attempt to produce LENR heat. A comparison between the calculated power emanating from the catalyst during an active run and that from the calibration run at the same temperature and with the same Core Q Power is used to determine the amount, if any, LENR heat was produced. The computer application MatLab[®] is used to determine the best fit parameters, although other applications can be used to solve these simple equations.

3. Results and Discussion

A tabulation of all experiments run to date in the IPB calorimeters is available on the Brillouin Energy web site [5].

Table 1. Summary of COP calculations from mass flow calorimetry runs.

Temperature (°C)	COP IPB1
200	1.30
220	1.41
260	1.46
270	1.26
275	1.40

3.1. Mass flow calorimetry results

The runs detailed in this analysis of MFC runs generally used a 100 ns pulse width with similar Q power on the catalyst at different voltages. The data acquisition and control system kept the Core Q Pow relatively constant at each temperature.

Table 1 summarizes the COP results from recent MFC runs performed in two identical reactors. COP was calculated by dividing the $P_{\text{out}}/P_{\text{in}}$ from the reactor with an active catalyst and one with an inactive catalyst. These catalysts were chosen based on previous results. Comparing the active catalyst to the inactive catalyst the COP was between 1.26 and 1.41 with no obvious dependence on temperature. The COP's were calculated from the average $P_{\text{out}}/P_{\text{in}}$ of several runs at the same temperature. A total of 65 $P_{\text{out}}/P_{\text{in}}$ calculations at different temperatures were used to create Table 1. Output powers from less than 10 W at lower temperatures to approximately 30 W at the highest temperatures were measured.

3.2. Heat flow calorimetry results

Figure 9 shows the results of a calibration run using the HF method. The left chart plots the measured and calculated temperatures from 11 steps in heater power. The right chart shows the control and measured heater power during this calibration run. Although the heater power quickly reaches a steady state, the time constant of the calorimeter prevents its temperature from reaching the steady state. In order to perform this experiment using MFC we would need to wait three time-constants which would take much longer than the time needed in this HF run. By solving Eqs. (1)–(5) using the measured temperatures and input power we find the coefficients shown in Table 2. Using these coefficients to calculate the temperatures from the known powers yields plots of both block and substrate temperatures indistinguishable from their respective measured values.

Figure 10 plots the input power and output power calculated using the measured temperatures and Eqs. (1)–(5) during an active run. It is obvious that this analysis yields a COP of up to 1.5 at higher temperatures and power.

Table 3 lists the coefficients found from a calibration run on a different catalyst in a different reactor. For this active excitation run the Q -pulse power was scanned from 0 to 43 watts in a sine-squared function versus time. Using the coefficients from Table 3 the output power curve was calculated from the measured temperatures. The input power and calculated output power are plotted versus time in Fig. 11. It can be seen from this plot that the COP was greater than 1.5.

Table 2. Heat flow coefficients found from calibration run in Fig. 9, where “Tube” refers to the catalyst.

Coefficient	Value	Coefficient	Value	Coefficient	Value	Coefficient	Value
ctube0	106.87	cblock	4213	Kb-s	0.22	Kt-b	0.31
ctube1	−0.403	cblock	−6.1	Kb-s	0.000489	Kt-b	−0.00030
ctube2	0.000461	cblock	0.0107	Kb-s	−1.92E-0	Kt-b	6.62E-07

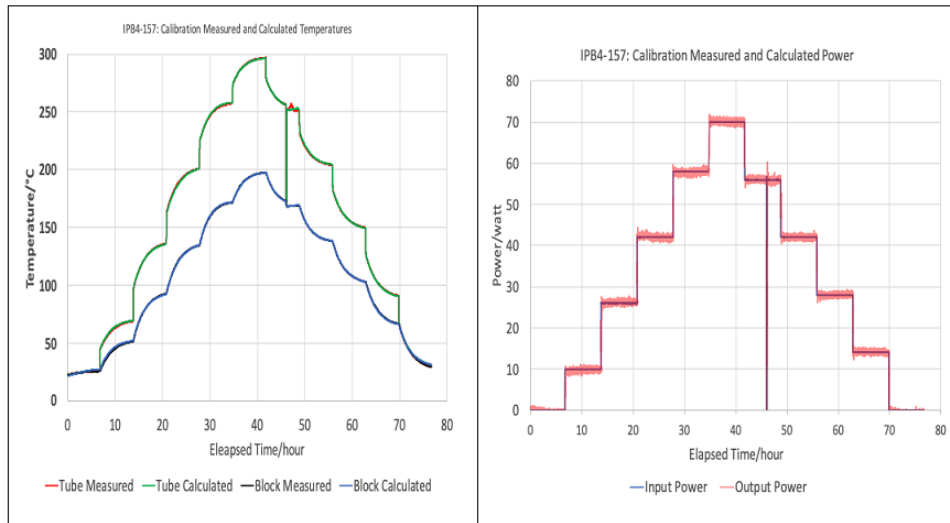


Figure 9. Calibration run using the heat flow method.

4. Conclusions

LENR can produce thermal power when hydrogen-absorbing, catalytic metal-coated substrates are stimulated using fast rise-time pulses. These experiments operated in H_2 gas from 200°C to 350°C. Comparative thermal measurements were performed between heater-only power and heater and pulse power. These runs were performed in isoperibolic

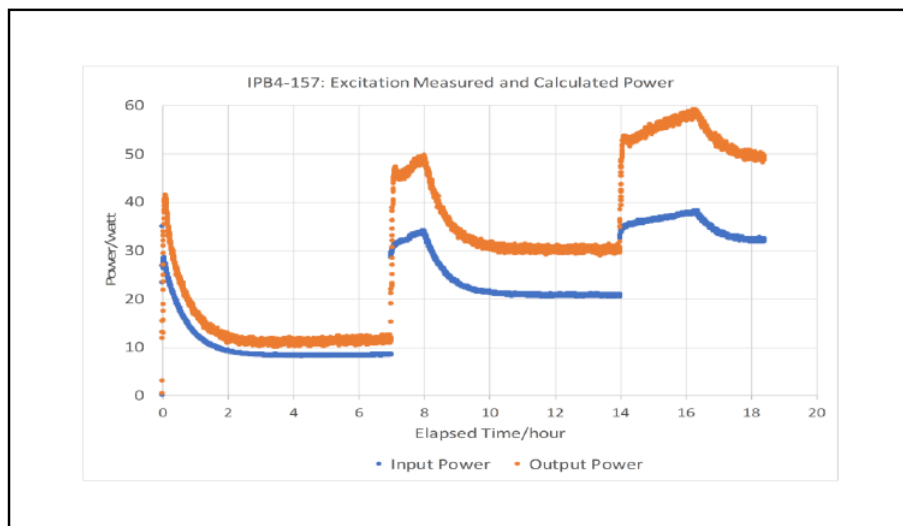


Figure 10. One example of an excitation run using the heat flow method.

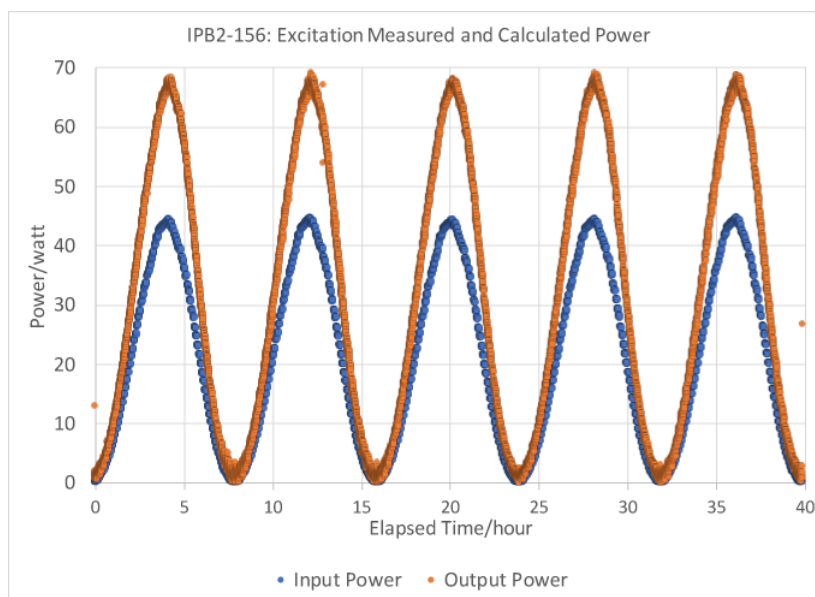


Figure 11. Another example of an excitation run using the heat flow method.

Table 3. Heat flow coefficients found from calibration run in a different reactor.

Coefficient	Value	Coefficient	Value	Coefficient	Value	Coefficient	Value
ctube0	$3.76 \times 10^{+01}$	cblock	$2.16 \times 10^{+04}$	Kb-s	4.00×10^{-01}	Kt-b	1.80×10^{-01}
ctube1	-9.14×10^{-02}	cblock	$-9.79 \times 10^{+01}$	Kb-s	-5.62×10^{-04}	Kt-b	2.54×10^{-04}
ctube2	1.22×10^{-04}	cblock	1.31×10^{-01}	Kb-s	1.15×10^{-06}	Kt-b	1.93×10^{-07}

calorimeters operated in steady-state mode, where the heater adjusts its power to keep the inner block (heat spreader) temperature constant. After stepped constant-power calibrations, non-steady-state excitation pulse powers were imparted to the outer metal coating on the substrate.

Over 600 runs were performed on over 100 different catalysts using different calorimetric methods in four different isoperibolic reactors. Additional catalysts were also tested for other experimental purposes. The reproducibility of recent results has been considerably better than those reported earlier. Earlier reports have shown that catalyst can be transported between different laboratories and using different reactors to achieve very similar positive results.

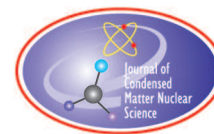
Calibrations and active runs have recently been performed comparing all thermal output to all electrical power input. Encouraging results have been seen and will be presented in the future.

Acknowledgements

We would like to acknowledge Dr. Michael McKubre for his work on the calorimeter design and thank Brillouin Energy engineers Mike Beaver, Ron Gremban, Mark Bowles, and Dave Correia for their aid in the calorimetric analysis. ERC also acknowledges the Anthropocene Institute. for their generous support of this work.

References

- [1] R. Godes, R. George, F. Tanzella and M. McKubre, Controlled electron capture and the path to commercialization, *J. Condensed Matter Nucl. Sci.* **13** (2015) 127.
- [2] R. Godes, R. George and F. Tanzella, Nanosecond pulse stimulation in the Ni-H₂ system, *J. Condensed Matter Nucl. Sci.* **29** (2019) 202–210.
- [3] R. Godes, Drive circuit and method for semiconductor devices, US Patent 8,624,636, 2014.
- [4] <http://www.rfcafe.com/references/electrical/skin-depth.htm>.
- [5] F. Tanzella, Isoperibolic hydrogen hot tube reactor studies, Final progress report from SRI International, July 2018, www.brillouinenergy.com/.
- [6] C.P. Berlinguette, Y.-M. Chiang, J.N. Munday, T. Schenkel, D.K. Fork, R. Koningstein and M.D. Trevithick, Revisiting the cold case of cold fusion, *Nature* **270** (2019) 45–51, <https://doi.org/10.1038/s41586-019-1256-6>.
- [7] B.P. MacLeod, P.A. Schauer, K. Hu, B. Lam, D. K. Fork and C.P. Berlinguette, High-temperature high-pressure calorimeter for studying gram-scale heterogeneous chemical reactions, *Rev. Sci. Instrum.* **88** (2017) 084101.
- [8] B.P. MacLeod, D.K. Fork, B. Lam and C.P. Berlinguette, Calorimetry under non-ideal conditions using system identification, *J Thermal Analysis and Calorimetry* **138** (2019) 3139, <https://doi.org/10.1007/s10973-019-08271-z>.



Research Article

Progress Toward an Understanding of LENR–AHE Effects in Coated Constantan Wires in D₂ Atmosphere: DC/AC Voltage Stimulation

Francesco Celani ^{*,†}, C. Lorenzetti, G. Vassallo[‡], E. Purchi, S. Fiorilla, S. Cupellini, M. Nakamura, R. Burri, P. Boccanera, P. Cerreoni and A. Spallone[§]

International Society for Condensed Matter Nuclear Science (ISCMNS_LI), Via Cavour 26, 03013 Ferentino (FR), Italy

Abstract

This paper presents a summary and some deeper details about the experiments presented at the 22nd International Conference on Condensed Matter Nuclear Science (ICCF22). It reports on the experimental study of LENR phenomena in Constantan (Cu₅₅Ni₄₄Mn₁) from its inception in 2011 to the most recent experiments. Using an empirical approach we identified the effect of surface modification of the Constantan wires with coatings comprised of elements that enhance the absorption behavior, and oxides with low work function for electron emission. We also explored certain geometrical arrangements of the wires such as knots and coils in order to induce local thermal gradients and predictable hot-spots. Moreover, the DC polarization of the wires by a counter-electrode proved to be a versatile approach to induce non-equilibrium conditions that are essential for Anomalous Heat Effects (AHE), especially when a dielectric barrier discharge (DBD) is produced. From the review of experiments summarized in this article, we obtain indications that the main parameter controlling the AHE is the *flux* of reactive species through the surface of the loaded material. As a consequence, all other external conditions of the reactor core (voltage–current, temperature, pressure, electric field stimulations, DC and/or AC external fields), can be seen as co-factors that enable a flux of active species through surfaces and in the bulk of the materials. Although most of the tests are in agreement with a possible flux model, some results still lack an interpretation, probably due to limits of the experimental setup.

© 2020 ISCMNS. All rights reserved. ISSN 2227-3123

Keywords: Anomalous Heat Excess (AHE), Cu–Ni–Mn alloy, Deuterium, Dielectric barrier discharges (DBD), Hydrogen, Low work function coatings, Nickel–Copper alloys, Nickel hydrides and deuterides

*Corresponding author. E-mail: franzcelani@libero.it.

[†] Also at: Ist. Naz. Fis. Nuc.-Lab. Naz. Frascati (INFN-LNF), Via E. Fermi 40, 00044 Frascati(RM), Italy.

[‡] Also at: DIIS, University of Palermo, 901298 Palermo (PA), Italy.

[§] Also at: Ist. Naz. Fis. Nuc.-Lab. Naz. Frascati (INFN-LNF), Via E. Fermi 40, 00044 Frascati(RM), Italy.

1. Introduction

Our group has studied Anomalous Heat Effects (AHE) in nickel–copper alloys for several years [1–10]. Apart from some initial speculation [5] one of the motivations for the choice of these materials came from the work of Romanowski [11] who showed their remarkable capability at promoting the dissociation of molecular hydrogen (H_2). Moreover we came across the work of Bruckner [12] who observed a reduction of electrical resistance of the alloys when exposed to hydrogen as well as the pioneering experiments of Ahern with Ni–Cu multilayer structures [13].

Among various Ni–Cu alloys, Constantan ($Cu_{55}Ni_{44}Mn_1$) wires became in particular the focus of our studies because of their low cost, versatility and robustness in various experimental setups. To sum up, Constantan resembles palladium (which has been more extensively studied) in that both require loading with D_2 or H_2 , and conditions of *non-equilibrium* to produce AHE.

Under certain conditions indeed, absorption and/or desorption, of D (or H), are associated with exothermic phenomena exceeding by orders of magnitude the enthalpy of conventional chemical reactions.

Still, when non-equilibrium conditions are absent, AHE are either reduced or they tend to decline over time. This observation led our group to investigate ways to increase non-equilibrium conditions through years of trial and error. In a typical experiment, a 200 μm Constantan wire is oxidized by heating it in air with direct current or with a sequence of short duration, low repetition rate pulses of high peak power. These repeated oxidations create a sub-micrometric texture of oxides featuring a large surface area. The oxides are then easily reduced and the resulting porous layer enables the quick absorption of D (or H). Significant improvements in reproducibility and AHE magnitude were made by modifying this porous layer with low work function oxides [4] comprised of strontium, potassium, iron, and manganese. An SEM analysis of wires after treatment and reduction shows a sub-micrometric texture of heterogeneous composition where areas rich in nickel and copper respectively can be easily distinguished, iron and manganese instead appear in isolated islands whereas potassium and strontium oxides are uniformly distributed.

That being said, the experiments are conducted by direct constant-current heating of the wires in a D_2 atmosphere. Typically they are allowed to saturate at a pressure of 2 bar for a few days at a temperature between 300 and 500°C, then the pressure is gradually reduced below 100 mbar. In general, AHE occurs if a series of conditions previously reported [3,4] are met. AHE proves indeed to be *correlated with the amount of absorbed deuterium as well as with the presence of non-equilibrium conditions that we speculate promote a flux* [14] *or migration of active species at the interfaces of the spongy wire.*

Initially, changes in pressure, temperature, voltage, current, and the arrangement of the wires showing thermal gradients (i.e. hot spots), were introduced with a certain degree of success [6,12].

Quite interestingly the authors also found a remarkable empirical association among the thermionic emission of the wires and the occurrence and intensity of AHE [6]. Despite a lack of a clear mechanism, this peculiar correlation quickly became the focus of much experimental work. This turned our attention to electric stimuli such as the introduction of a voltage with a second wire acting as counter electrode, and even a low frequency alternating polarization (50 Hz). Afterward, a new setup was designed to isolate and explicate the effects of the thermionic emission from the hot wires and electric stimuli, hence in the most recent experiments, strong thermal gradients were avoided with respect to the knotted wire design described in [8]. In fact, above a certain temperature, thermal gradients, although particularly effective at increasing AHE magnitude, proved to be insufficient at obtaining a longlasting effect without the use of additional stimuli (changes in pressure, current, etc.).

In general we face the need to maximize the thermionic emission of the wires as well as their deuterium loading. Unfortunately these two parameters require opposite operating conditions: thermionic emission increases at low pressures, but low pressures cause the wire to unload (i.e. it allows excessive release of stored deuterium) hence leading invariably to the suppression of AHE after some time [10]. This issue was initially tackled by conducting experiments at a pressure that could prevent excessive release of deuterium from the wires while still allowing electrons to be

emitted from the Constantan wires coated with low work function elements. Also, the distance between the active wire and the counter electrode was kept as low as practically possible to promote electron emission without using an excessive voltage which could lead to localized arcs.

Such conditions are in agreement with the Child-Langmuir equation for the transport of electrons in vacuum [15,16]. Although to date a working model is not available, our speculations include a role for ionized deuterium and its interaction with electrons [9,10].

2. Chronology of the Experiments with Constantan Wires

Chronology of the experiments with Constantan wires is shown in Table 1 and the Experimental Design is shown in Fig. 1.

3. Wire Treatment and Effect of Diameter and Length on AHE

To prepare the wires, including the oxidation and coating steps, we used the same procedures described in previous papers [4]. We would like to emphasize that thinner wires consistently provide higher AHE. This was observed in several experiments where we compared 100, 200 and 350 μm wires. The AHE magnitude observed in multiple experiments seems to fit qualitatively with the ratio between the section area of the oxidized layer formed during the preparation of the wires and the area of the non-oxidized core. Figure 2 shows these ratios for wires of different diameters based on SEM observations. We think that the porous and spongy oxidized layers at sub-micrometric dimensionality, upon reduction, provides a porous region/skin which may be more receptive for deuterium (or hydrogen).

Moreover thinner wires, when heated by direct current in the reactor, feature a significantly higher current density and a larger voltage drop along their ends (similarly to NEMCA [17] or Preparata [18] effects).

Table 1. Chronology of experiments with Constantan wires.

Year	Main achievement	Reference
2011	Beginning of experiments with oxidized wires, of Nickel–Copper alloys in pure H_2 , D_2 or H_2/Ar , D_2/Ar mixture atmosphere, first measures of AHE in Constantan	[1]
2013	Reproducibility of AHE occurrence enhanced after coating the wires with low work function materials (SrO) and inserting the wires in sheaths of borosilicate glass fibers	[1,2,4]
2015	AHE occurrence associated with Fe impurities on Constantan wires	[4]
	Further improvements in reproducibility after adding Fe, Mn and K to the low work function main coating of the wires	
	Observation of thermionic emission from the wires in accordance with Richardson law and related Child–Langmuir law	
2017	AHE magnitude increased through geometrical arrangements to create thermal gradients along the wires	[6]
	Air flow calorimetry introduced for better AHE measures	
2018	AHE occurrence empirically associated with thermionic emission of the wires, a counter electrode is introduced to enhance electron emission and AHE	[6–8]
2019	AHE effects stabilized (from hours to days) through high voltage and alternating current stimuli. Observation of the effect of dielectric barrier discharge on AHE occurrence and magnitude	[9,10]

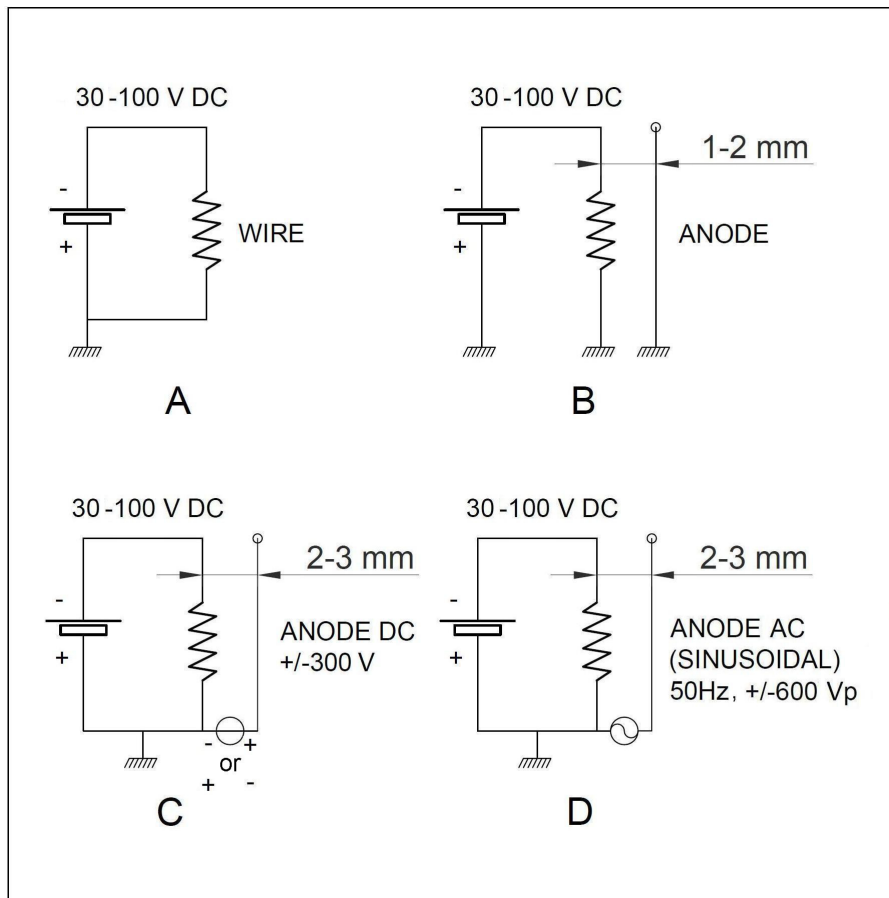


Figure 1. Evolution of the experimental set-up: Constantan wire reactor (A); grounded counter-electrode is added (B); counter-electrode is polarized with direct current (C); counter-electrode polarized with alternating current (D).

Giuliano Preparata, in particular studied the AHE generation as function of the *total voltage drop along the wire*, assuming that it may behave as if in a coherent state. The coherence phenomena and their relation to LENR, although controversial, are still the object of investigations [19].

4. Richardson and Child–Langmuir Laws

In 2014, the authors added an independent wire in close proximity to the active Constantan and observed, at high temperatures, a weak electrical current flowing when powering the first wire [4].

This current proved to be strongly related to the temperature of Constantan wire and unmistakably the consequence of thermionic emission (where the treated Constantan is a cathode and the second wire an anode), in close agreement with the Richardson law [8,9,20]. The recorded current follows a pattern in accordance with the Child–Langmuir law. Further details can be found in [15].

Later, our experiments showed that the thermionic effect and the spontaneous voltage between the two wires were

correlated to AHE occurrence. To date no clear model can explain the association of the thermionic effect and AHE occurrence, but the consistency of the relationship among the two phenomena has been confirmed in multiple experiments. Also, as mentioned above, the presence of thermal and chemical gradients is considered as being particularly relevant, especially when interpreting the large effect of knots on AHE magnitude.

5. Knots and Thermal Gradients

In 2018, mostly following a trial and error approach, attempts to further increase AHE focused on the study of different types of knots, leading eventually to the choice of the Capuchin type (see Fig. 3).

This knot design leads to several hot spots along the wire and comprises three areas characterized by a temperature difference up to several hundred degrees. The temperature difference between the external spires of the knot and the internal straight segments may also induce voltage between the spires arising from an ohmic drop along the wire, and from the different temperatures between the inner and external part of the knot.

We must emphasize that a large AHE rise was observed when introducing an extra voltage between the active wire (cathode) and a second close wire (anode) through an external power supply.

6. Coil Design

As anticipated, after the study of the wires with strong thermal gradients induced by knots, we realized they have mechanical and aging limitations, so we initiated various experiments focusing on the use of electric stimuli only. The

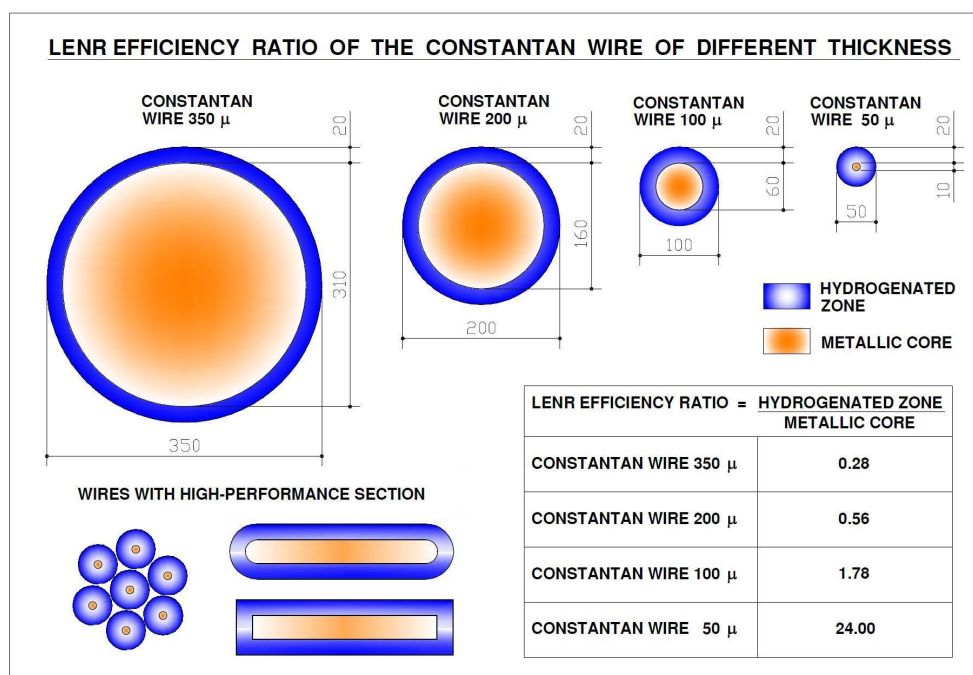


Figure 2. Section of wires of different diameter after oxidation and additional treatments. We observe the formation of a porous oxidized layer that later is reduced by deuterium. The resulting porous skin is especially prone to enhanced deuterium absorption (*blue area*). These schematic figures are based on measurements taken by Scanning Electron Microscopy. The highly loaded zone is in the range of 15–25 μm .

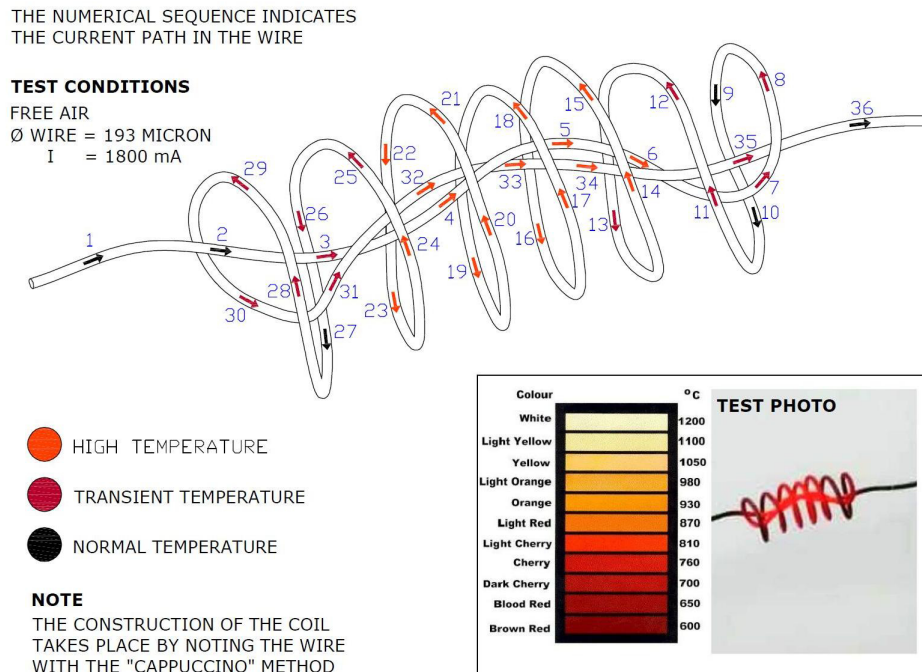


Figure 3. A knot comprised of eight loops heated in air with a direct current ($\Phi = 193 \mu\text{m}$, $I = 1900 \text{ mA}$). The external diameter of the coil is 15–20 mm. Based on a color analysis, the darker area is likely to be at a temperature of $<600^\circ\text{C}$, the external spires at about 800°C , while the innermost straight section may reach 1000°C . The wire used in experiments is 200 cm long and may have 4–8 knots of this type.

strong empirical association between AHE and thermionic emission guided us toward the use of a second wire with a positive polarization, to enhance electron emission from the active wire. In a more recent setup, shown in Fig. 4, a $200 \mu\text{m}$ (or $350 \mu\text{m}$) Constantan wire is oxidized and coated with a low work function oxide (SrO). The wire is then inserted in an original sheath (made by SIGI-Favier) comprised of borosilicate glass fibers (each fiber has $\Phi = 5 \mu\text{m}$) tightly woven with quartz-alumina fibers (the latter to enhance the temperature resistance of the sheath). The sheath is also impregnated with the same solution of low work function elements used to treat the wires. The sheathed wire is then coiled on an iron tube insulated with a thin sheath of quartz-alumina fibers only. The Pt wire has the same geometrical configuration as the Constantan wires, except for the missing surface treatments and sheath impregnation. In this configuration the iron tube is used as a counter-electrode to study the effect of voltage bias on AHE occurrence and magnitude.

A schematic of the assembly is shown in Fig. 4.

7. Reactor Assembly

The reactor consists of a borosilicate glass tube (Schott type 3.3); dimension: $\Phi = 33\text{--}40 \text{ mm}$, $L = 400 \text{ mm}$. A SS-304 tube (carefully cleaned to exclude sulfur), is used as central support to hold in place the coils of wires (V1, V2, V3 in Fig. 5). This tube encloses an additional thermocouple to measure the mean gas temperature inside the reactor.

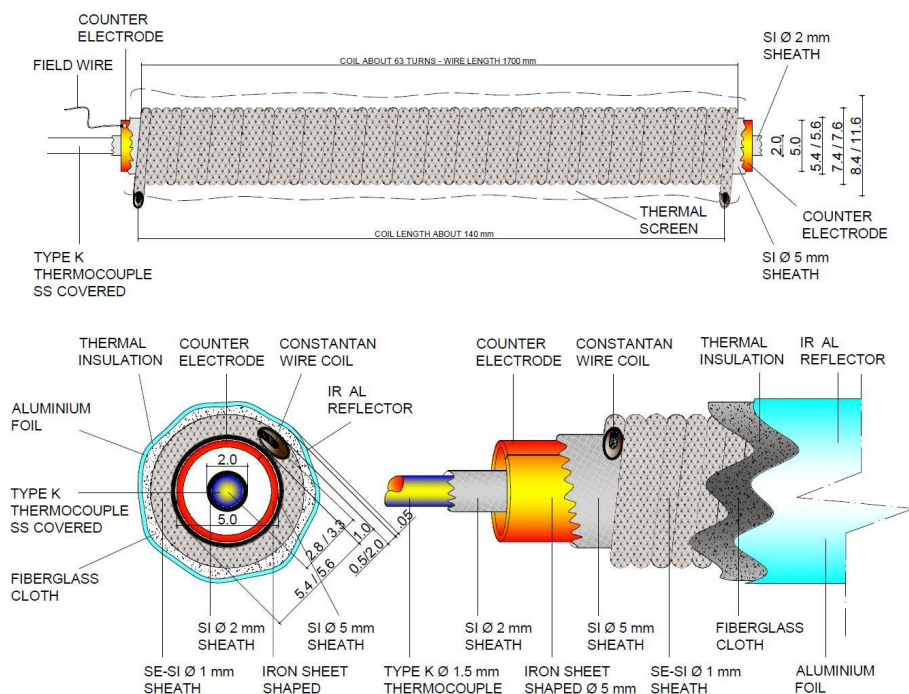


Figure 4. Details of a coil in its final assembly. The counter-electrode is a Fe tube covered by an electrical insulating, thin quartz-alumina fiber sheath. The details of construction are the same for Pt and Constantan wires. (Please note that the Constantan coils have an internal thermocouple contained in a SS tube, the internal thermocouple is not used for the platinum coil whose temperature is measured from its variation of resistance.)

On the outside of the reactor we positioned a sealed source of gamma radiation (Fig. 6) comprised of WTh2% TIG electrodes (Thoriated Tungsten alloy). This source is located inside a hermetically sealed, 2 mm thick, SS304 tube and has a nominal maximum intensity of 33 kBq. Only X-gamma radiation, specifically from thorium decay, can pass through the stainless steel tube and reactor wall to reach the Constantan wire (15 mm away from the source outer wall). In fact, the use of gamma sources is well known to facilitate electron emission as well as a trigger for avalanche ionization phenomena especially in the presence of static potential (see addendum B for further information on the source).

8. Direct Current (DC) Electric Stimuli

Wires are heated by different DC constant-currents at various power levels (usually 40–120 W). The AHE occurs usually in the range of temperatures of 650–850°C, after loading the wires at 2 bar of D₂ for 2–4 days at 300–500°C, and inducing non equilibrium conditions. This can be executed by decreasing the pressure, up to a minimum of approximately 10 mbar. In a typical experiment the AHE may last up to one day but then it slowly vanishes. This behavior may be attributed to: (a) desorption of deuterium from the wire and (b) decrease of effectiveness of the non-equilibrium conditions that may have triggered AHE release in the first instance.

To reactivate AHE release, usually, a new loading cycle at high pressure is needed.

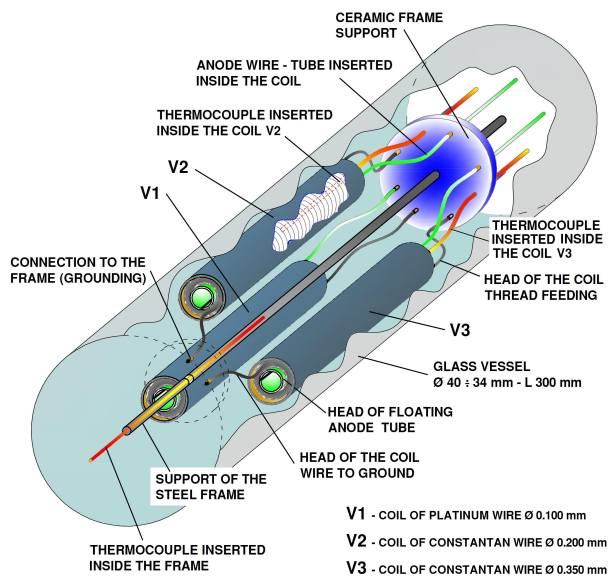


Figure 5. Assembly of the reactor including three coil cartridges, V1 is a platinum coil used mainly for calibrations, V2 and V3 are two active coils comprised of treated Constantan wires. The V1 temperature is measured using its variation of resistance; the V2 and V3 coil temperatures are measured by thermocouples inside the coil. An additional thermocouple (*in red*) is inside a SS tube used as support for the steel frame holding in place the three coils. This thermocouple is used to estimate the mean internal temperature of the reactor. All the thermocouples are type K, SS screened; insulated by MgO: 1200°C maximum temperature.

In the last two years, we have found that a practical approach to reducing the AHE decline and increasing the AHE magnitude is the application of a voltage (bias) between the wire and a counter electrode. As already mentioned, we observed an AHE increase by applying a static positive polarization to the Constantan wire (cathode); later we also witnessed an effect with a negative polarization.

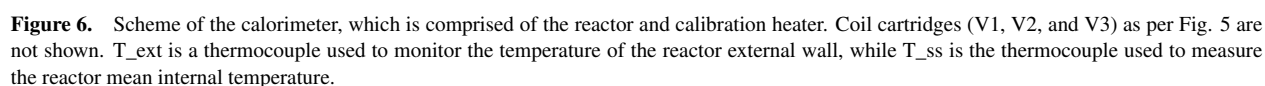
This led eventually to the choice of an AC stimulus (Fig. 1D) between the Constantan wire and the counter electrode. Figure 5 shows the electrical connections of each coil used in the latest reactor assembly. The wires are inserted in their sheaths (Figs. 4 and 5) and then wound on a tubular Fe support, macroscopically insulated by a porous and thin-wall sheath of quartz-alumina fibers.

The excitation voltage is applied between the main wire (which is always heated by direct current, whether it is Pt or Constantan) and the Fe counter-electrode.

The deuterium loading of the wires is monitored continuously by a dedicated circuit shown in Fig. 7. This allows us to measure the ratio between the actual resistance (R) of the wire and its resistance (R_0) before the first deuterium loading. The circuitry is based on JFET J511 (Constant Current silicon diode, three in parallel, each providing 4.7 mA of current) and operates at low power only.

The same approach is used also when higher power is applied to the wires (up to 120 W in some experiments, up to 3 A of current with a 350 μ m wire). Both circuits are operated in parallel, self-decoupled by a network of high voltage diodes, as a sum node. To put it in a few words, when Constantan absorbs hydrogen or deuterium, the wire resistance decreases; the larger the decrease, the larger is the loading.

A second section is designed for the low power (0.1–5 W, ± 600 V_p), used to feed the alternating current excitation



(AC). It includes several protection networks (based on back to back 150 V, 5 W Zener diodes shown in Fig. 7) put on each end of the active wires (Constantan and Pt) in parallel to the coaxial connector, to avoid potential failures, to the main power supply and acquisition system, due to couplings of the high voltage AC pulses. The $\pm 600 V_p$ are applied to promote both Richardson–Child–Langmuir (only the positive region of the wave, lower pressures) and Paschen regimes (corresponding to a pressure of 30–40 mbar in our geometrical configuration, featuring a distance of 2–3 mm between the electrodes). The rationale of the circuitry is keeping the wires always polarized by a proper amount of

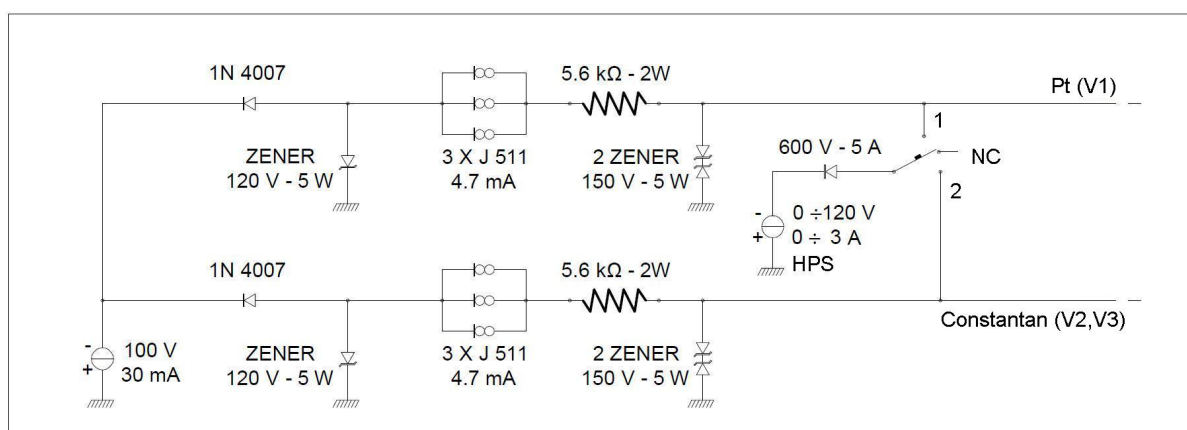


Figure 7. Scheme for the circuitry adopted for R/R_0 measurements.

current, this in order to measure the temperature of platinum wire (V1) and Resistance Ratio (i.e. R/R_0) in the case of Constantans (coils V2 and V3).

This reduction of resistance, with respect to the value of Constantan before absorption (R_0), is likely related to the amount of H (or D) absorbed by the wire similarly to what observed with palladium above a certain loading [21]. That being said, a precise correlation among absorbed H (D) and resistance is not yet available nor fully understood for the case of Constantan wires (which as shown in Fig. 2 show nonhomogeneous absorption across their section).

Also, the minimum current injected to maintain the wires polarization, is about 14 mA and is feed by the three constant current diodes (CCD) in parallel (J511 in the scheme of Fig. 7). When higher current needs to be injected, a High Power Supply is used (HPS: –120 V, 0–3 A). Appropriate high voltage diodes prevent the current from going back to the low power supply section (when the high current path is active). The output of HPS has three positions: 1, connected to Pt (connector V1); 2, connected to the Constantan (connector V2 or V3); three unconnected (NC).

Among others, some explorative tests were made with: (a) unipolar half-wave, positive or negative pulses (see Appendix A for the circuits used in this case). The Richardson regime, with the related Child–Langmuir current, occurs at a rather low pressure and the emission intensity of electrons at the surface of the material depends both on the temperature and the value of the work function of the material. We recall that the electrons boil-off at the *surface* of the low work function materials: they create a spatial-charge localized in close proximity of the surface until some external field of positive polarization is applied removing them [3,6,20].

Concerning the *Paschen* regime, with respect to the original formula developed in 1889 by Friedrich Paschen [22–28] in free air and parallel plates, we must consider that the use of low work function materials and the presence of the thoriated tungsten source outside the reactor is likely to influence the discharge initiation.

Under these conditions, we think that the breakdown voltage would be significantly reduced.

9. Alternating Current Electric Stimuli

The AC circuitry that generates 1200 V_{pp} was applied to the counter-electrode. It is based on two 50 Hz, multiple output transformers in cascade. This allows us to increase the 230 V_{rms} (i.e. 324 V_p) of the line to 610 V_p as measured by oscilloscope.

The current needed for the excitation is rather low, with a limit at 60 mA due to a 10 k Ω limiting resistor. Usually the current does not exceed 10–20 mA because the triggering voltage of the Paschen effect is approximately 400–500 V and RMS values up to 5–6 mA, as measured by a Fluke 187 multimeter (BW=100 kHz). The RMS voltage is in the range 250–280 V, as measured by a Tektronix DMM916 multimeter (BW=20 kHz). For higher accuracy, and better understanding of waveforms, especially the higher frequency components, the signal at the end of a 10 k Ω resistor is sent to a Fluke 198C Digital Scope (BW=100 MHz). Some of the most significant operating situations are reported in Figs. 10–12.

Figure 10 shows in particular a typical waveform corresponding to a limited coupling between the counter electrode and the active wire (under high pressure or pure deuterium). As deduced from Fig. 8, the addition of Ar is able to reduce significantly the voltage needed to initiate a discharge. Figure 11 shows instead the waveform observed using a 1:1 molar mixture of Ar and D₂ at a pressure compatible with discharge occurrence (as per Fig. 8). In these conditions AHE is substantially increased compared to the case presented in Fig. 10.

Finally Fig. 12 shows the remarkable occurrence of a dielectric barrier discharge, and it is definitely the most effective at producing AHE. However, it is rather difficult to maintain and the materials (especially the insulating sheaths) shows signs of degradation after few hours, probably due to arcing. According to the literature, an increase of frequency (from present 50 Hz up to values of 10–40 kHz) and optimization of tension and wave form, could limit the drawback and it is currently under investigation.

That being said, due to the high voltage needed for AC excitation, the injection circuitry and measuring set-up

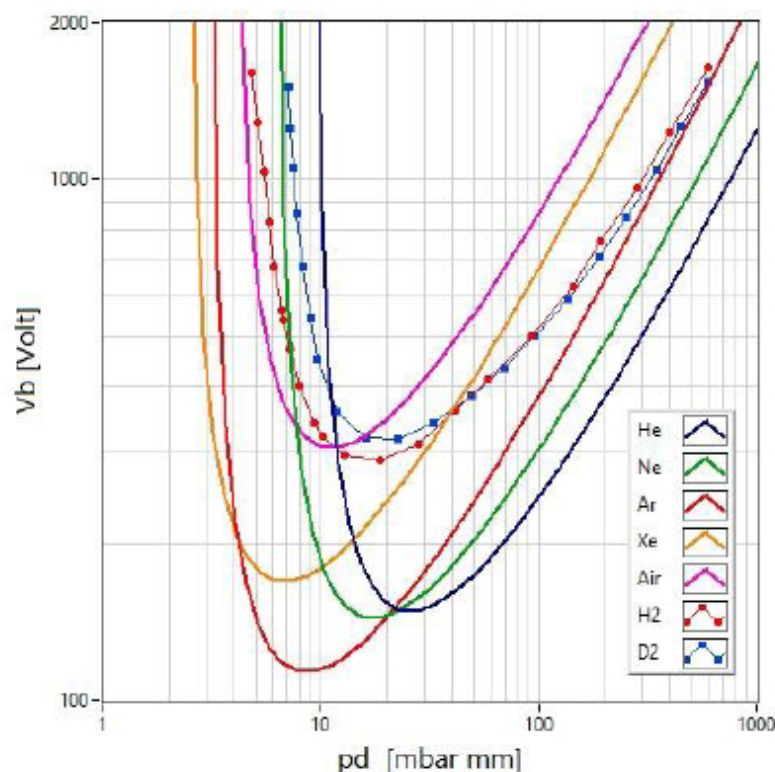


Figure 8. Direct current breakdown tension (V_b) of several gases versus pressure and distance between electrodes ($p \cdot d$) [29]. The addition of argon to deuterium clearly enables discharges at lower tension.

is currently being improved. This is in order to reduce the value of the 10 k Ω limiting resistor and to boost the peak current at high voltage. Non-linear circuitry with overall improved high frequency performance, is under consideration.

Some of the waveforms observed by the oscilloscope are reported in Figs. 10–12. Curves in Fig 12 seem to be associated with the highest AHE. In these conditions a dielectric barrier discharge is clearly occurring.

10. Calorimetry

AHE occurrence was studied using air-flow calorimetry.

The calorimeter consists of an insulated case made of double walls (6.5 cm in total), thick polystyrene whose each internal surface is covered with multiple reflective thin aluminum foil. This apparatus is calibrated using a Nichrome heater inside the calorimeter case or a platinum wire coil inside the reactor (V1 in Fig. 5) under inert gas (He).

The Ni–Cr heater is contained in a borosilicate tube having dimensions similar to the active reactor. Both the heater and the reactor are placed in close proximity. They are covered by several corrugated layers of 40 μm thick Al foils with one black side. An overview of the assembly is shown in Fig. 6. The fan is 5 cm wide, operates in suction mode, and has a nominal air flow of 4.445 l/s at normal pressure and temperature (NPT), and it rotates at 75 Hz. Its revolution rate is monitored, and the measurement is logged in the acquisition system. The overall average coefficient of heat exchange during calibrations (e.g. in the restricted power range of 90–110 W) with the Ni–Cr heater or platinum wire is

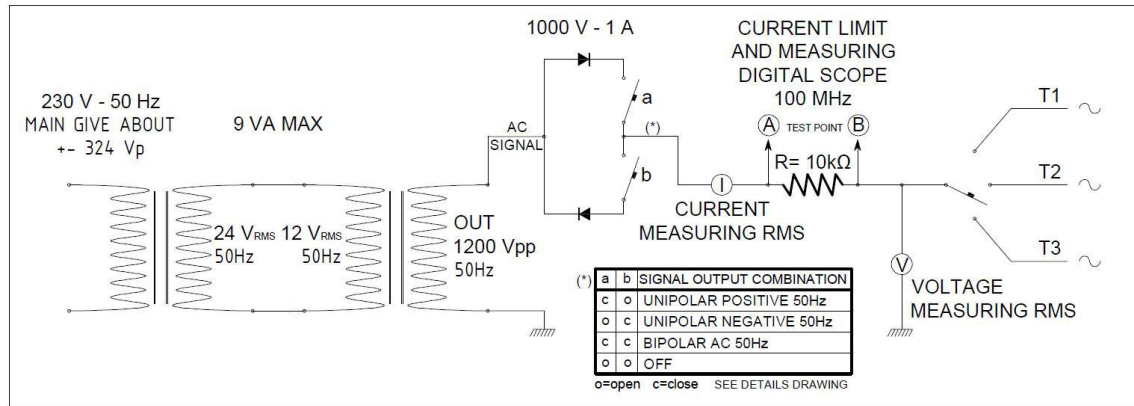


Figure 9. Scheme of the high voltage-low current circuitry adopted for AC excitation. The R limit and current measuring resistance usually has a value of 10 k Ω (T1, T2, and T3 refer to the counter electrodes of each coil which is the iron tube shown in Fig. 4).

approximately 0.20°C/W and is consistent with the values of air flow, density, pressure and air humidity (which is kept almost stable at 45–55% of RH by the air conditioning system of the laboratory) and heat capacity in the range of air temperature inside the calorimeter (20–60°C). Precautions to increase internal air turbulence are also taken to prevent air stratification which could affect the measures. A selection of over 80 tests are reported in Table 2, Appendix B.

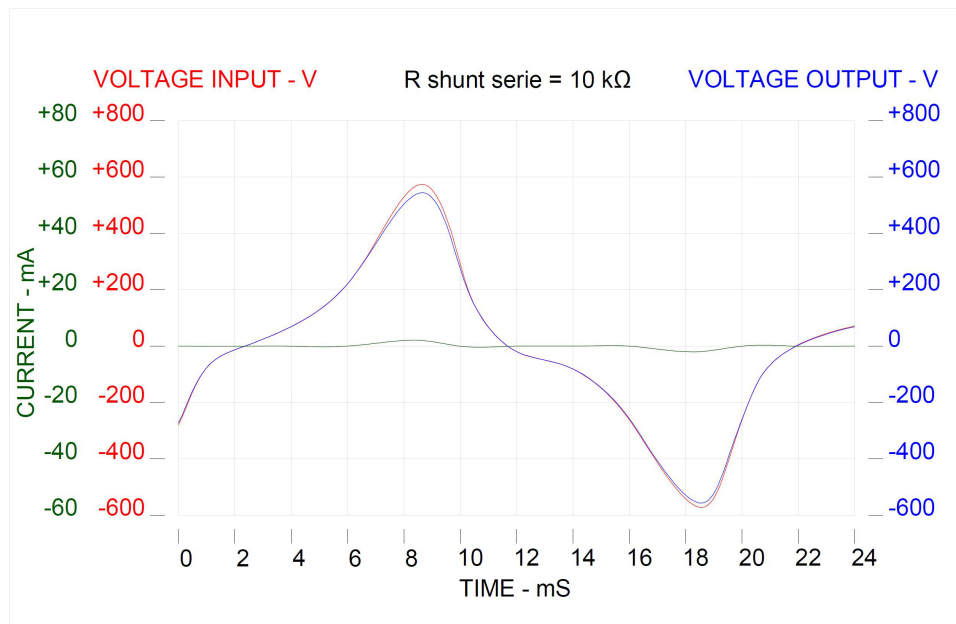


Figure 10. Voltage drop along the limiting-measuring resistor of 10 k Ω . Red is at test point A, blue at test point B. Current is the green color line. Typical waveforms in mild condition of excitation, i.e. not Dielectric Barrier Discharge (DBD) conditions. Even the Paschen regime (starting from about 400 V) looks self-quenched, perhaps due to the excessive value of the resistance (10 k Ω resistor in Fig. 10).

AHE is estimated as follows:

$$A1 = \frac{T_{\text{out}} - T_{\text{in}}}{P_{\text{in}}} (^\circ\text{C/W}) \text{ Calibration values,} \quad (1a)$$

$$A2 = \frac{T_{\text{out}} - T_{\text{in}}}{P_{\text{in}}} (^\circ\text{C/W}) \text{ Active wire values,} \quad (1b)$$

$$\text{AHE} = \frac{A2 - A1}{A1} P_{\text{in}} (W), \quad (1c)$$

where T_{out} and T_{in} are the air temperatures measured at the outlet and inlet of the calorimeter, respectively, as shown in Fig. 6.

Further details on the adopted calorimetric technique can be found on the paper summarizing the presentation at ICCF21[5,6].

11. Results

In a particularly impressive experiment, 18 W of AHE were observed for an input power of 99.7 W (line #38 of Table 2 in Appendix B), recorded when using a 200 μm wire (coil V2 in Fig. 2) at a temperature of 716°C. The counter-electrode excitation consists of +270 V bias and 3 mA current, the behavior of R/R_0 was oscillating over time. The effect lasted over 5 h.

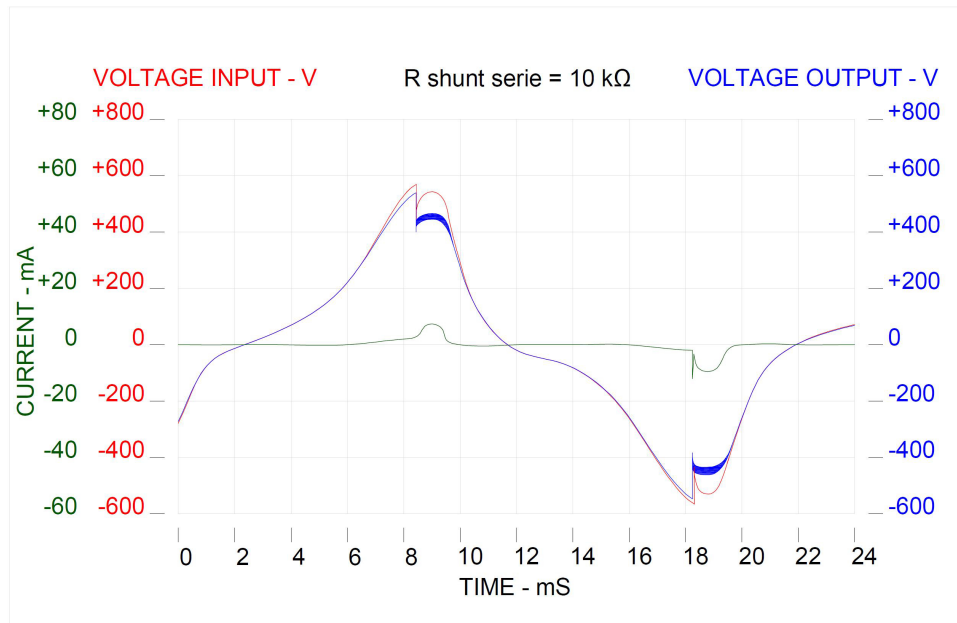


Figure 11. Similar to the case of Fig. 10 but with larger current. The current starts at a voltage value close to 400 V, as expected according to the threshold voltage of the gas involved.

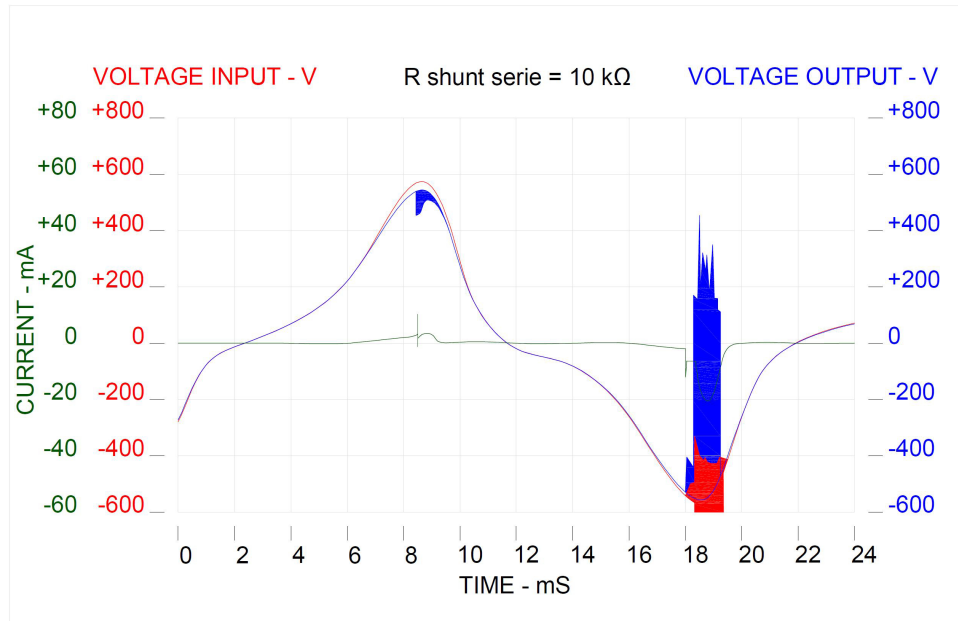


Figure 12. Typical waveform that seems to be the most efficient to increase the AHE.

Afterward AHE decreased to 9.5 W (line #39), perhaps due to air intake from a leak. In fact, the pressure increased from about 300 up to about 316 mbar. Anyway, the effect had a remarkable time span of over 15 h. When the polarity was changed from positive to negative (line #40), AHE decreased from 9.5 to 7.4 W. The shift (line #41) from unipolar negative to bipolar oscillation ($\pm 600 V_p$, 50 Hz) increased AHE from previous 7.4 to 10.7 W, the effect lasted about 4 h. Reducing the pressure from 341 to 98 mbar (line #42) the effect increased from 10.7 to 14.5 W, always under AC oscillation and current (rms value) of 2–3 mA. The effect lasted 4 h. After the interruption of the AC stimulus (line #43) leakage was observed, causing a pressure increase from 98 to 250 mbar, this was followed by a reduction of AHE from 14.5 to 2.4 W. AHE slowly vanished following stabilization of R/R_0 (that was unstable and oscillating proportionately to AHE).

When AC oscillation (line #44) was resumed at a constant pressure of 250 mbar, AHE rise again, from 2.4 to 9.2 W. In general, much lower AHE values were observed when using the larger diameter wire coil V3 (350 μm). Eventually the only way to recover large values of AHE (i.e. 14.4 W, line #59), was to power 200 μm wire (V2) add some Ar to the gas mixture, keep the pressure relatively low (36 mbar), and use AC excitation to the counter electrode.

12. Conclusions

From the collected data the following conclusions can be drawn.

- The AHE occurrence is correlated with fast loading or unloading of the wire. In the case of unloading however, after a short time, the AHE vanishes.
- When loading/unloading occurs slowly, AHE is significantly reduced.
- A state of oscillation seems to be the most efficient since it produces AHE for a longer time with respect to fast loading or unloading (especially when a dielectric barrier discharge occurs).

- (d) Loading and unloading occurrence, as assumed from R/R_0 and variation in reactor pressure, strongly support the key role of deuterium flux (see [14] for a definition of flux).

There are additional external conditions, such as high temperature, low pressure, purity of the gas that facilitate the AHE. In any case, after some time, even the optimal conditions described above are not sufficient to maintain AHE release. That being said, the major finding we would like to emphasize is the ability of the counter-electrode stimulus to keep the AHE active for longer times, perhaps indefinitely.

Also, the role of non-equilibrium conditions and flux were suggested by several researchers [30–38] since the beginning of Cold Fusion experiments. Convincing proofs being said, the set of experiments summarized in Table 2 of the present work consistently shows a strong correlation between a change in loading/pressure and the occurrence of AHE, hence providing a strong support to the flux model or hypothesis. Also, although most of the tests here described are in agreement with the flux model, some results are still difficult to interpret. We think that this could be due to accidental contamination of the deuterium due to an insufficiently air-tight glass reactor, especially at high temperature and low pressure.

Moreover, a critical analysis of the data collected in Table 2 (Appendix B) allows us to highlight a series of observations or possible generalizations on the best conditions enabling AHE release for the selected reactor geometry:

- (1) Temperature must be as high as possible, provided that sintering of the spongy surface does not occur. Also, high temperature is one of the key factors for electron emission from low work function materials. We speculate that a high intensity emission may interact with deuterium (or hydrogen) leading to useful phenomena. This last statement is purely based on associations during experiments (i.e. between thermionic emission and AHE).
- (2) Low pressure is useful to increase the e^- emissions. However, below a certain pressure the effect may be deleterious due to excessive deuterium release (unloading) from the wires. We would like to highlight that the occurrence of a dielectric barrier discharge (Fig. 13) is associated with a remarkably intense AHE. Although at this stage we would like to avoid venturing into a discussion of possible reaction mechanisms, we recognize some analogies with previous work and that of Randell Mills [39–42] and Jacques Dufour [43,44].
- (3) The addition of low-thermal conduction noble gases (like Ar or Xe) is generally useful to increase the temperature inside the reactor core and promote the Paschen regime, when the counter-electrode has sufficiently high voltage.
- (4) High DC voltages along the active wire are useful (perhaps due to NEMCA and/or Preparata effects). As a consequence, thinner wires are usually more efficient at producing AHE.
- (5) The effect of AC has to be fully explored in all of its potential (varying frequency, voltage, waveform, bias, and/or asymmetries). Nevertheless, we observed an unexpected but clear correlation with the negative side of AC wave and an increase of the temperature in the reactor core when certain conditions of temperature and pressures are fulfilled. In general, AC stimuli seems to counteract the AHE decline observed in previous experimental projects.
- (6) The *flux of deuterium through the active material (Constantan)* seems to be the most important factor driving the AHE generation. Based on experimental observations, we speculate that *inducing oscillations of flux* may be the best method for triggering or increasing AHE.
- (7) Contamination of the reactor atmosphere (e.g. by air and/or degradation of glassy sheaths) has a deleterious effect on AHE. Unfortunately, due to budget constraints, up to now we could not afford a Residual Gas Analyzer (RGA) placed in-line with the reactor to diagnose this problem.

Our present work aims at preventing the issues of the described experimental setup such as the frequent leakages and poor control of gas compositions. This will be achieved with a new stainless steel reactor equipped with residual gas analysis (RGA). We are also working at optimizing the electronics used as AHE stimulus and for DBD plasma

generation, as well as at finding the optimal operating conditions both with conventional high tension, medium-high frequency generators, as well with pulsed DC power supplies.

Acknowledgments

The experimental work described in this paper was presented at ICCF22 Conference (Assisi, September 8–13, 2019). This work was carried out at INFN-LNF while some trials were conducted at the premises of a Metallurgical Company of North Eastern-Italy with independent instruments and personnel. This Company has also has provided some financial support since 2011. SIGI (Società Italiana Guaine Isolanti) Favier, France, designed and produced dedicated glass fiber sheaths in close collaboration with the above-mentioned Metallurgical Company. From October 2017 Lega Nord, an important political Group in Italy, enabled the continuation of F. Celani's experiments in the Frascati Laboratory of INFN. Special thanks to Francesco Malagoli, Filippo Panini, Paolo Varini. All have followed LENR development for many years, in line with a political program focused on the protection of the environment. Antonino Cataldo and Stefano Bellucci (NEXT collaboration) performed SEM and EDX analysis at INFN-LNF. Some of the expenses to perform experiments and for travel and food, were supported by IFA group-Italy. We thank the Anthropocene Institute, USA (i.e. Carl Page and Frank Ling) for providing economic support so that two of our collaborators could attend the ICCF22. We thank Hideki Yoshino, CEO of Clean Planet Company, Japan, for providing economic support enabling another of our collaborators to attend the ICCF22. We are indebted to Luca Gamberale, one of the last collaborators of Prof. Giuliano Preparata still active in the LENR –AHE field, for the critical reading of our manuscript. We are also indebted to Jed Rothwell for proofreading the manuscript, for his scientific suggestions and for improving the English grammar, as he has done for several years.

References

- [1] F. Celani, E.F. Marano, A. Spallone, A. Nuvoli, B. Ortenzi, S. Pella, E. Righi, G. Trenta, F. Micciulla, S. Bellucci, S. Bartalucci and M. Nakamura, Experimental results on sub-micro structured Cu–Ni alloys under high temperatures hydrogen/deuterium interactions, *Chem Material Res* **3** (3) (2013) 25–76.
- [2] F. Celani, E.F. Marano, B. Ortenzi, S. Pella, S. Bartalucci and S.B. F. Micciulla, Cu–Ni–Mn Alloy wires, with improved sub-micrometric surfaces, used as LENR device by new transparent, dissipation-type calorimeter, *J. Condensed Matter Nucl. Sci.* **13** (2014) 56–67.
- [3] F. Celani, G. Vassallo, E. Purchi, S. Fiorilla, L. Notargiacomo, C. Lorenzetti, A. Calaon, B. Ortenzi, A. Spallone, M. Nakamura, A. Nuvoli, P. Cirilli, P. Boccanera and S. Pella, Improved stability and performance of surface-modified Constantan wires, by chemical additions and unconventional geometrical structures, *J. Condensed Matter Nucl. Sci.* **27** (2018) 9–21.
- [4] F. Celani, A. Spallone, B. Ortenzi, P.S. E. Purchi, F. Santandrea, S. Fiorilla, A. Nuvoli, M. Nakamura, P. Cirilli, P. Boccanera and L. Notargiacomo, Observation of macroscopic current and thermal anomalies, at high temperatures, by hetero-structures in thin and long constantan wires under H₂ gas, *J. Condensed Matter Nucl. Sci.* **19** (2016) 29–45.
- [5] F. Celani, C. Lorenzetti, L. Notargiacomo, E. Purchi, G. Vassallo, S. Fiorilla, B. Ortenzi, M. Nakamura, A. Spallone, P. Boccanera, S. Cupellini and A. Nuvoli, LENR phenomena in Constantan; a steady progress toward practical applications: observation of Zener-like behaviour, in air atmosphere, of Constantan submicrometric wires after D₂–Xe loading–deloading and related AHE, in *12th Int Workshop on Anomalies in Hydrogen Loaded Metals*, Asti, 2017.
- [6] F. Celani, B. Ortenzi, A. Spallone, C. Lorenzetti, E. Purchi, S. Fiorilla, S. Cupellini, M. Nakamura, P. Boccanera, L. Notargiacomo, G. Vassallo and R. Burri, Steps to Identify main parameters for AHE generation in sub-micrometric materials: measurements by isoperibolic and air-flow calorimetry, *J. Condensed Matter Nucl. Sci.* **29** (2019) 52–74.
- [7] F. Celani and C. Lorenzetti (Eds.), Electrically induced anomalous thermal phenomena in nanostructured wires, in *Cold Fusion*, Chap 7, Elsevier, Amsterdam, 2020, pp. 101–113.
- [8] F. Celani, C. Lorenzetti, G. Vassallo, E. Purchi, S. Fiorilla, S. Cupellini, M. Nakamura, P. Boccanera, R. Burri, B. Ortenzi, A. Spallone and P. Cerreoni, First evaluation of coated Constantan wires comprising Capuchin knots to increase anomalous heat and reduce input power at high temperatures, *J. Condensed Matter Nucl. Sci.* **30** (2020) 25–35.

- [9] F. Celani, C. Lorenzetti, G. Vassallo, E. Purchi, S. Fiorilla, S. Cupellini, M. Nakamura, P. Boccanera, R. Burri, P. Cerreoni and A. Spallone, Effects of super-Capuchin knot geometry, and additional electric fields, on hydrogen/deuterium absorption: related AHE on long and thin Constantan wires with sub-micrometric surfaces at high temperatures, in *2019 LANR/CF Colloquium at MIT-USA*, Cambridge, MA 02139 (USA), March 23–24, 2019.
- [10] F. Celani, C. Lorenzetti, G. Vassallo, E. Purchi, S. Fiorilla, S. Cupellini, M. Nakamura, P. Cerreoni, P. Boccanera, R. Burri and A. Spallone, Unexpected effects due to voltage waveform at anode, in gaseous LENR experiments based on sub-micrometric surface coated Constantan wires., in *Terzo Convegno Assisi nel Vento, Domus Laetitiae*, Assisi (PG), Italy, May 17–19, 2019.
- [11] S. Romanowski, W. M. Bartczak and R. Wesołkowski, Density functional calculations of the hydrogen adsorption on transition metals and their alloys. an application to catalysis, *Langmuir* **15** (18) (1999) 5773.
- [12] W. Brückner, S. Baunack, G. Reiss, G. Leitner and T. Knuth, Oxidation behavior of Cu–Ni(Mn) (constantan) films, *Thin Solid Films* **258** (12) (1995) 252.
- [13] B.S. Ahern, K.H. Johnson and H.R. Clark, Method of maximizing anharmonic oscillations in deuterated alloys. Patent US5411654A, 1995.
- [14] D. Ugura, A.J. Storm and R. Verberk, Quantification of the atomic hydrogen flux as a function of filament temperature and H₂ flow rate, *J Vacuum Sci. Technol* **30** (3) (2012) 1–6.
- [15] K. Jensen, *Introduction to the Physics of Electron Emission, Child–Langmuir Law*, Chap. 16, Wiley 2017.
- [16] Y.L.Y. Lau, Electron emission: from the Fowler–Nordheim relation to the Child–Langmuir law, *Phys Plasmas* **1** (1994) 2082–2085.
- [17] C.G. Vayenas, S. Bebelis, I.V. Yentekakis, S. Neophytides and J. Yi, Ion spillover as the origin of the NEMCA effect, *Studies in Surface Science and Catalysis* **77** (1993) 111–116.
- [18] M. Cola, E.d. Giudice, A.D. Ninno and G. Preparata, A Simple Model of the Cohn-Aharonov Effect in a Peculiar Electrolytic Configuration, Vol. 70, Lericci (SP)-Italy, SIF Bologna, 2000, pp. 349–358.
- [19] Luca Gamberale, Dynamical realization of coherent structures in condensed matter, in *Invited paper at IWAHLM13, October 5–8, 2018*, Greccio (RI)-Italy, 2018.
- [20] O.W. Richardson, Thermionic Phenomena and the Laws which Govern Them. Nobel lecture, 1929.
- [21] Y. Sakamoto, K. Takai, I. Takashima and M. Imada, Electrical resistance measurements as a function of composition of palladium–hydrogen(deuterium) systems by a gas phase method, *J Phys.: Condensed Matter* **8** (19) (1996) 3399–3411.
- [22] F. Paschen, Ueber die zum Funkenübergang in Luft, Wasserstoff und Kohlensäure bei verschiedenen Drucken erforderliche Potentialdifferenz, *Annalen der Physik* **273** (5) (1889) 69–75.
- [23] D. Marić, M. Savić, J. Sivoš, N. Škoro, M. Radmilović-Radjenović, G. Malović and Z. Petrović, Gas breakdown and secondary electron yields, *Eur. Phys. J. D* **68** 155 (2014) 1–7.
- [24] L.F. Berzak, S.E. Dorfman and J. Smith, *Paschen's Law in Air and Noble Gases*, Berkley, USA, 2006, pp.1–14.
- [25] E.M. Bazelyan and Y.P. Raizer, *Spark Discharge*, CRC Press, Boca Raton, FL, USA, 1998, 1998.
- [26] I. Donko and Z. Korolov, Breakdown in hydrogen and deuterium gases in static and radiofrequency, *Phys. Plasmas* **22** (9)(2015).
- [27] M.W. Childs, Ion generator apparatus, United States Patent US10398015B2, 27 8 (2019).
- [28] D. Fisher and J.d. Bitetto, Townsend ionization coefficients and uniform field breakdown, *Phys. Rev.* **104** (1956) 1213.
- [29] M.A. Lieberman and A.J. Lichtenberg, in *Principles of Plasma Discharges and Materials*, Vol. 1, 2nd Edn, Wiley Blackwell, 2005, p. 700.
- [30] F. Celani, Talk at the first workshop on cold nuclear fusion, in *Summary by Richard L. Garwin, Nature* **338** (1989) 616–617 <https://doi.org/10.1038/33861>, E. Majorana Centre for Scientific Culture, Erice (Italy), 1989.
- [31] M. Swartz, Quasi-one-dimensional model of electrochemical loading of isotopic fuel into a metal, *Fusion Technol.* **22** (2) (1992) 296–300.
- [32] G.C. Fralick, A.J. Decker and J.W. Blue, Results of an attempt to measure increased rates of the reaction D₂ + D₂ yields He-3 + n in a nonelectrochemical cold fusion experiment, NASA-TM-102430, E-5198, NAS 1.15:102430, Cleveland, 1989.
- [33] Y. Arata and Y.C. Zhang, Reproducible cold fusion reaction using a complex cathode, *Fusion Technol.* **22** (2) (1992) 287–295.
- [34] Y. Iwamura, T. Itoh and M. Sakano, Nuclear products and their time dependence induced by continuous diffusion of deuterium through multi-layer palladium containing low work function material, in *8th Int Conf Cold Fusion*, Lericci (La

- Spezia),2000.
- [35] M.C.H. McKubre, S. Crouch-Baker, A.M. Riley, S.I. Smedley and F.L. Tanzella, Excess power observations in electrochemical studies of the D/Pd system; the influence of loading, in *Frontier of Cold Fusion, Proc. ICCF3 Nagoya*, 1992.
 - [36] Y. Iwamura, T. Itoh, M. Sakano, S. Sakai and S. Kuribayashi, Low energy nuclear transmutation in condensed matter induced by D₂ gas permeation through Pd complexes: correlation between deuterium flux and nuclear products, in *Proc. of ICCF10, Condensed Matter Nuclear Science*, Cambridge, MA, 2006.
 - [37] Y. Iwamura, T. Itoh and N. Gotoh, Characteristic X-ray and neutron emission from electrochemically deuterated palladium, in *Proc. 5th Int. Conf. Cold Fusion, Monte Carlo*, Monaco, 1995.
 - [38] T.O. Passell, Use of helium production to screen glow discharges for low energy nuclear reactions (LENR), in *American Physical Society. APS March Meeting 2011*, March 21–25, 2011, Abstract ID Y33.008.
 - [39] R.L. Mills, W.R. Good, J. Phillips and A.I. Popov, Lower-energy hydrogen methods and structures, Patent US6024935A, 1997.
 - [40] R.L. Mills and P. Ray, Spectral emFractional quantum energy levels of atomic hydrogen from a helium–hydrogen plasma and the implications for dark matter, *Int. J. Hydrogen Energy* **27**(3) (2002) 301–322.
 - [41] R.L. Mills, P.C. Ray, M. Nansteel, X. Chen, R.M. Mayo, J. He and B. Dhandapani, Comparison of excessive Balmer α line broadening of inductively and capacitively coupled RF, microwave, and glow-discharge hydrogen plasmas with certain catalysts, *IEEE Trans Plasma Sci* **31** (3) (2003) 338–355.
 - [42] B. Holverstott, *Randell Mills and the Search for Hydrino Energy*, KRP History, 2016.
 - [43] J. Dufour, J. Foos and J.P. Millot, Measurement of excess energy and isotope formation in the palladium–hydrogen system, in *5th Int Conf on Cold Fusion*, Monte-Carlo, Monaco, 1995.
 - [44] J. Dufour, J. Foos and J.P. Millot, Excess energy in the system palladium/hydrogen isotopes. measurement of the excess energy per atom hydrogen, in *5th Int Conf on Cold Fusion*, MonteCarlo, Monaco, 1995.

Appendix A. Auxiliary Circuitry for Explorative Tests

Auxiliary circuitries were developed to study:

- (A) the effects of unipolar excitation at 50 Hz, both positive and negative. Schematic shown in Fig. 13
- (B) current flowing between cathode and anode. DC level at maximum allowable voltages, ± 600 V. Sketch shown in Fig. 14

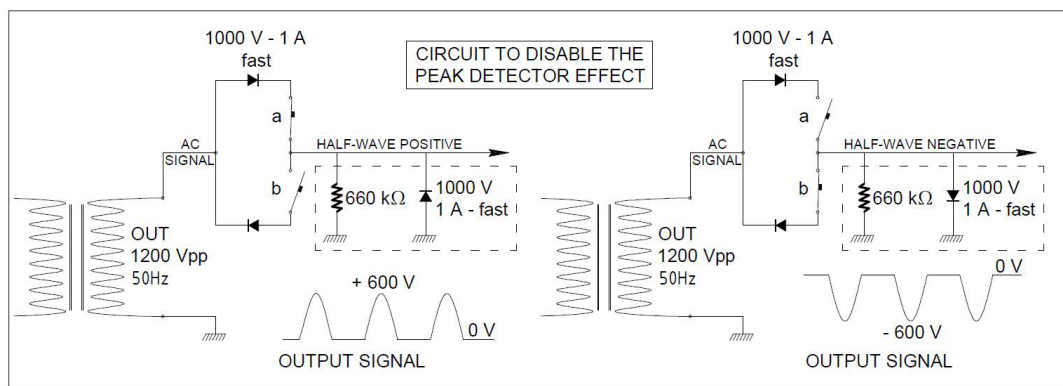


Figure 13. Circuitry to generate unipolar pulses, at 50 Hz, by a network of fast diodes and R (660 k Ω grounded). Such circuitries allowed to evaluate the effect of repetitive unipolar pulses from the point of view of AHE stimulation. The results were used to optimize the operating conditions of the reactor (gas, temperature and pressure).

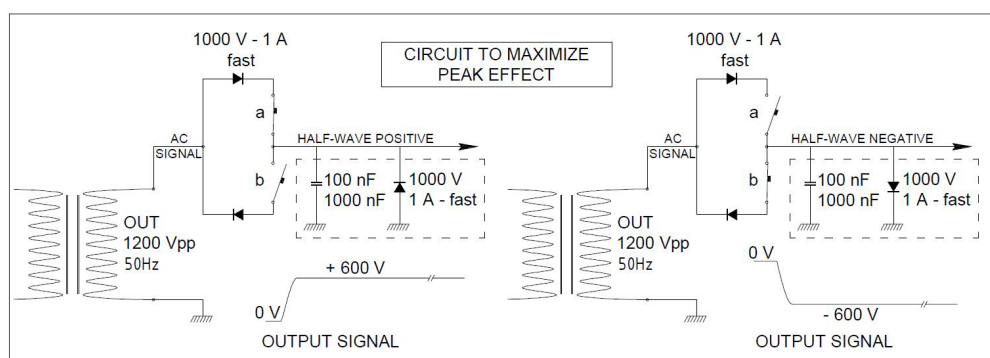


Figure 14. The simple circuitry used to generate unipolar high voltages in DC, by means of a peak detector system (D, Capacitor). Adding an ammeter between the output of the circuitry and the counter electrode it was possible to measure the current, in DC conditions, between the two wires of the reactor while changing gas, temperature and pressure.

Appendix B.

Table 2 summarizes over 80 tests performed during two months of experiments using Constantan wires, 1.7 m long, with a diameter of 200 or 350 μm . During these experiments the active wire polarity was kept negative and the extremity of each wire was grounded; the power supply was operated in the constant-current mode. The table includes the following data:

- C1** Identification of the experiment, time [s] since the start of specific data logging.
- C2** Wire diameter (mm).
- C3** Electric input power (W), Voltage along the wire (V), Current (A).
- C4** Gas type, pressure (mbar).
- C5** Temperature at the core of each tube/cartridge used for the Constantan wires (inside the Fe counter-electrode); the R/R_0 value of the wire; the trend of its variation over time (reported on the last 10 ks) as observed in the plot of raw data.

The wire loading during the experiments was classified, as follows:

- C5.1** Increase of Loading (IL), corresponds to a R/R_0 decrease; it can be Slow (S) or Fast (F) (e.g. IL_S means slow increase of loading).
- C5.2** Decrease of Loading (DL), corresponds to a R/R_0 increase; it can be Slow (S) or Fast (F).
- C5.3** Oscillation. The R/R_0 values oscillate around a certain mean value. The larger is the amplitude of oscillations, the larger AHE is.
- C5.4** Constant. The R/R_0 not varying significantly over time. In this conditions AHE is absent.

We assume that these behaviors are closely correlated with a flux of the active species thorough the surface and/or bulk of the wire;

- C6** Electric conditions of the counter-electrode, i.e. V , I , in DC or AC.
- C7** AHE values (W), calculated using Eq. (1)(1–3). Maximum value measured was +18 W with 100 W input.
- C8** Short comments on the experimental conditions and results.

Table 2. Summary of the most important operating conditions and results collected over two months of experiments.

C1	C2	C3	C4	C5	C6	C7	C8
Test # *Timer (s)	Wire, diameter (mm)	* P_{w_in} (W) * V (V), I (A)	Gas type, pressure (mbar)	* T_{core} (°C); * R/R_0 wire; *loading varia- tion	Counter electrode, V , A ; DC or 50 Hz AC (rms)	AHE (W)	Notes
#1 599280	0.350	40.6 19.5, 2.08	D ₂ 1810	318 0.885 DL_S		-0.7	10 July 2019. File started 03 July 2019, 16 h 44 m af- ter several calibrations using nichrome and platinum heaters
#2 616410	0.350	60.6 24.1, 2.51	D ₂ 1770	427 0.905, DL_F		+8.7	Gas leak. Fast deuterium de- loading. Higher temperatures and fast unloading effective to get AHE
#3 691100	0.350	80.6 28.6, 2.8	D ₂ 1100	544 0.9524 DL_F		+7.8	Gas leak. Fast de-loading
#4 767700	0.350	97.4 31.6, 3.08	D ₂ 1100	630 0.964 DL_S		+0.5	Gas leak. Slow unloading. The <i>rate</i> of unloading is a key factor to get AHE.
#5 1005840	0.350	49.4, 22.2, 2.2	Ar/D ₂ = 1.34 1160	483 0.945 C		+0.2	R/R_0 almost constant. No AHE observed
#6 1015360	0.350	59.8, 24.6, 2.43	Ar/D ₂ = 1.34 1210	546 0.953 DL_F		+4.5	Fast unloading. AHE recov- ered
#7 1020670	0.350	70.2, 26.7, 2.62	Ar/D ₂ = 1.34 1230	603 0.961 IL_S		+2.8	Low speed loading, reduced AHE
#8 1029100	0.350	80.5, 28.7, 2.80	Ar/D ₂ = 1.34 1270	656 0.966 IL_S O		+8.6	Increasing loading, noisy R/R_0 . The AHE increased largely, perhaps due to R/R_0 oscilla- tions
#9 1037080	0.350	90.5, 30.6, 2.96	Ar/D ₂ = 1.34 1300	702 0.972 C O		+6.6	R/R_0 almost flat but with sev- eral instabilities. AHE present
#10 1097810	0.350	97.7, 31.7, 3.08	Ar/D ₂ = 1.34 1310	725 0.972 C O		+4.4	R/R_0 almost flat but with in- stabilities. Also the oscillations are useful to get AHE
#11 1340 New file			D ₂ fresh 1960	22 0.926			Calorimeter opened and re- closed to repair a large gas leak. New file 170719_12:01
#12 18350	0.350	59.9, 24.4, 2.46	D ₂ 2610	420 0.906 IL_S		-0.5	In almost static conditions and high pressure no AHE, al- though some loading
#13 24230	0.200	60.4, 40,1.51	D ₂ 2440	439 0.949 IL_S O		+0.8	Gas leak. P_w at V2. Very slow loading. Some R/R_0 instabil- ity. Similar to test #12 but some weak oscill

						Table 2 continued
#14 92900	0.200	60.1, 39.8, 1.51	D ₂ 2050	433 0.946 C	−0.7	Gas leak. 50 ks measurement. R/R_0 flat. No AHE
#15 172570	0.200	61.1, 40.1, 1.52	D ₂ 2610	438 0.947 C		Very long measures, 180 ks. R/R_0 flat. No AHE
#16 185120	0.200	80.5, 46.5, 1.73	D ₂ 2670	529 0.962 C		Long duration measures. R/R_0 flat. No AHE
#17 195370	0.200	99.7, 52.1, 1.91	D ₂ 2710	607 0.977 DL_S O	+5.3	R/R_0 slowly increased. Some oscillations were the source of AHE
#18 196100	0.200	99.9, 52.2, 1.91	D ₂ 1970	611 0.978 O	+10.1	Forced pressure reduction. R/R_0 quite unstable: origin of AHE. <i>Short time test</i>
#19 196550	0.200	100.0, 52.3, 1.91	D ₂ 1470	617 0.978 DL_F O	+9.7	Forced pressure reduction. R/R_0 increased. <i>Short test</i>
#20 196960	0.200	100.0, 52.3, 1.91	D ₂ 1040	634 0.981 DL_F	+7.7	Forced pressure reduction. <i>No thermal equilibrium</i>
#21 197320	0.200	100.4; 52.4, 1.91	D ₂ 660	636 0.982 NA	+6.0	Forced pressure reduction. <i>No thermal equilibrium</i>
#22 198070	0.200	100.2; 52.5, 1.91	D ₂ 440	659 0.986 NA	+4.0	Forced pressure reduction. <i>No thermal equilibrium</i>
#23 198600	0.200	100.6; 52.7, 1.91	D ₂ 300	685 0.990 NA	+5.9	Forced pressure reduction. <i>No thermal equilibrium</i>
#24 199160	0.200	100.2; 52.7, 1.90	D ₂ 196	713 0.995 NA	+5.5	Forced pressure reduction. <i>No thermal equilibrium</i>

Table 2 continued

#25 199860	0.200	99.9; 52.7, 1.89	D ₂ 156	733 0.997 NA		+8.1	Forced pressure reduction. <i>No thermal equilibrium</i>
#26 431190	0.200	81.2; 47.2, 1.72	D ₂ + air 216	612 0.983 C		+0.5	Long measurement (>60 h). Leakage: air intake, initial 158 mbar at same temperatures. Some oscill.
#27 432920	0.200	81.2; 47.1, 1.72	D ₂ + air 214	612 0.982 O	+300 V, 0.250 mA	+3.1	Counter electrode has positive Polarization: some AHE, at least at for short time.
#28 443190	0.200	81.1; 47.1, 1.72	D ₂ + air 209	613 0.983 C	−300 V 0.210 mA	−2.1	Counter electrode Negative Polarization: AHE vanished, <i>even endothermic effects</i>
#29 451110	0.200	81.0; 47.1, 1.72	D ₂ + air 218	614 0.983 C	−300 V 0.200 mA	−0.9	Pol. Neg. long time (>2 h). Slowly AHE endothermic region vanished
#30 598310	0.200	98.9; 52.1, 1.90	D ₂ + air 330	688 0.983 IL_S		+1.7	Long measurement. Slow improvement of loading: some AHE
#31 77.7 616520	0.200	79.9; 46.5, 1.72	D ₂ + air 270	596 0.969 C		+1.1	Leakage air intake observed. After an initial improvement, later R/R_0 flat
#32 620080	0.200	80.1; 46.6, 1.72	D ₂ + air 184	609 0.972 O	±300 V 0.5–2 mA	+3.4	Forced pressure reduction. Several test with DC field $P_{os.}$ and Neg. Indications that a change of polarity could be useful to get AHE
#33 623680	0.200	80.0; 46.6, 1.72	D ₂ + air 211	613 0.973 O		+5.9	Abrupt temperature increase. DC field removed

Table 2 continued

#34 626380	0.200	80.2; 46.7, 1.72	D ₂ + air 168	628 0.975 DL_S		+2.5	Forced pressure reduction
#35 630540	0.200	80.4; 46.8, 1.72	D ₂ + air 187	631 0.976 DL_F	+296 V, 2.7 mA	+2.8	Pressure reduction and recovery. Fast increase R/R_0 DC field
#36 683800	0.200	80.7; 46.8, 1.72	D ₂ + air 183	628 0.975 IL_S O	+296 V, 2.7 mA	+3.2	Long time with field. R/R_0 noisy. First time observed AHE not decreasing over time with power constant
#37 697670	0.200	89.7; 49.5, 1.81	D ₂ + air 230	672 0.981 DL_F O	+297 V, 2 mA	+4.0	P_w increased from 80 to 90 W. Fast increase of R/R_0 , oscillations of R/R_0
#38 716220	0.200	99.7; 52.3, 1.90	D ₂ + air 300	716 0.985 DL_F O	+290 V, 3.2 mA	+18.0	P_w increased from 90 to 100 W. Fast increase of R/R_0 . Osc. large AHE observed
#39 771310	0.200	99.7; 52.2, 1.91	D ₂ + air 316	709 0.981 IL_S O	+297 V 3.15 mA	+9.5	Long duration 50 ks, at 100 W, DC field +300 V. R/R_0 decreased
#40 775060	0.200	99.6; 52.2, 1.91	D ₂ + air 317	707 0.981 O	−297 V, −3.5 mA	+7.4	Test with negative field. Slowly decreasing AHE: Negative field effect
#41 789230	0.200	99.3; 52.1, 1.90	D ₂ + air 341	706 0.981 O	AC, 260 V 2–3 mA	+10.7	AC stimulation, first time. RMS values. R_{equiv} : 100 k Ω . AHE recovered
#42 803300	0.200	100.2; 52.6, 1.90	D ₂ + air 98	767 0.989 DL_F	AC, 260 V 2–3 mA	+14.5	Pressure reduced several times. AC on. Large R/R_0 increase

Table 2 continued

#43 1029400	0.200	99.2; 51.9, 1.91	D ₂ + air 250	708 0.973 IL_S O		+2.4	Long time meas. Air intake: Press. increased. Temp. decreased. AHE decreased slowly. Loading Oscillations
#44 1032030	0.200	99.2; 51.9,1.91	D ₂ + air 252	708 0.973 O	AC, 280 V 1–2 mA	+9.2	AC stimulation: recovered partially AHE, i.e. 2.4–9.2 W
#45 1114330	0.350	60.7; 24.7, 2.45	D ₂ +air 118	531 0.922 IL_S	AC, 260 V 5–6 mA	+0.2	Active wire 0.35 mm. First time
#46 1130570	0.350	79.8; 28.6, 2.79	D ₂ +air 163	634 0.934 DL_S	AC, 262 V 5 mA	–1.1	R/R_0 slowly decreased. No AHE
#47 1143330	0.350	90.1; 30.4, 2.96	D ₂ +air 190	678 0.939 O	AC, 262 V 5 mA	+6.5	Several spikes at AC, R/R_0 noisy. Increasing P_w and temperature were useful
#48 1203690	0.350	60.4; 24.7, 2.45	D ₂ +air 104	539 0.921 DL_S	AC 260 V, 7 mA	+0.7	Regular oscillations. Weak AHE, although AC oscillation
#49 1215750	0.350	60.9; 24.9, 2.44	D ₂ +air 90	557 0.930 DL_S	AC, 263 V 5.8 mA	+0.9	Forced pressure re- duction. No effect to recover AHE
#50 1219320	0.350	60.7; 24.8, 2.45	D ₂ +air 85	576 0.927 IL_S O	AC, 262 V 6.0 mA	+2.1	Forced pressure reduction. Increase of internal temperature and AHE
#51 1289670	0.200	61.2; 40.4, 1.51	Ar=D ₂ 87	575 0.956 O	AC, 293 V ≪1 mA	+3.1	After vacuum new gas (Ar=D ₂ 70 mbar at RT), Wire switch (V3 to V2). Smaller wire diameter, i.e. higher DC voltage, increased AHE
#52 1306580	0.200	80.15; 46.6,1.72	Ar=D ₂ 80	684 0.970 DL_S	AC, 293 V ≪1 mA	+2.2	Forced pressure reduction R/R_0 stable last 2 h

							Table 2 continued
#53 1319520	0.200	100.1; 52.3, 1.91	Ar=D ₂ 90	770 0.980 DL_F O	AC, 293 V ≪1 mA	+9.1	Forced pressure reduction. AHE improved
#54 1321510	0.200	100.1; 52.4, 1.91	Ar=D ₂ 72	777 0.982 DL_S O	AC, 293 V ≪1 mA, self-pulse at HF	+11.3	Forced pressure reduction <i>R/R</i> noisy. Further increase of AHE. HF self-pulses look useful
#55 1370080	0.200	99.7; 52.0, 1.92	Ar=D ₂ +air 125	734 0.974 IL_S	AC, 299 V ≪0.5 mA	+9.8	Leakage air intake. Several pressure reductions. AC current almost vanished Still AHE
#56 1374840	0.200	100.6; 52.5, 1.92	Ar= D ₂ +air 45	799 0.982 D-I-L O	AC, 299 V ≪0.5 mA	+10.2	Several forced pressure reduction. AHE correlated with fast <i>R/R</i> ₀ variation, oscill. high temperature
#57 1393640	0.200	99.5; 52.0, 1.91	Ar= D ₂ +air 94	750 0.974 O	AC, 299 V ≪0.5 mA	+8.7	Leakage air intake. Reducing local temperature decreases AHE
#58 1395760	0.200	101.3; 52.9, 1.92	Ar= D ₂ +air 41	854 0.991 IL_F O	NO AC	+6	Forced pressure reduction. One of co-factor effects for AHE generation is AC stimulation, although HT increased (750–854)
#59 1403770 02/08/20 17:57	0.200	99.9; 52.2, 1.91	Ar= D ₂ + air 36	778 0.978 IL_F O	AC, 290 V 2–4 mA	+14.4	Forced pressure reduction. Large AHE. Geiger-Muller gamma detector several times in alarm (>>4 BKG). <i>R/R</i> ₀ decreased
#60 1447460	0.350	41.0; 20.3, 2.02	Ar= D ₂ +air 66	510 0.917 C		−0.7	New file: 19082019, 13:37 Over 15 days operation at low power. No AHE
#61 1456770	0.350	41.1 20.4, 2.02	Ar= D ₂ + air 30	547 0.924 DL_S	AC, 247 V 5.5 mA	+0.1	Reducing pressure and adding AC stimulation induced some AHE
#62 1461380	0.350	41.0 20.3, 2.01	Ar= D ₂ + air 45	534 0.922 C	AC, 270 V 2–3 mA	−0.1	AC excitation ended 2 h before measurement. AHE vanished
#63 1522010	0.350	50; 22.5, 2.22	Ar= D ₂ + air 57	582 0.926 DL_S	NO AC	−1.4	Without AC the weak AHE disappeared

Table 2 continued

#64 1549730	0.350	50; 22.5, 2.22	Ar= D ₂ +air 50	576 0.927 DL_S	AC, 247 V 4.9 mA	+0.6	Forced pressure reduction. AC field from 20 ks. No HF discharge. Weak AHE
#65 1554010	0.350	49.9; 22.5, 2.22	Ar= D ₂ +air 46	574 0.925 IL_S		+1.6	Pressure reduction. AC off since 1 h. R/R_0 decreased but AHE weak
#66 1610150	0.350	50; 22.5, 2.22	Ar= D ₂ +air 55	578 0.927 DL_S		−1.3	AC off since 16 h. Pressure increased, AHE vanished
#67 1627860	0.350	50; 22.3, 2.22	Ar= D ₂ +air 60	582 0.928 Osc.	AC, 290 V 1 mA	+1.5	AC field since 4 h R/R_0 noisy. Recovering of AHE
#68 1633300	0.350	50; 22.5, 2.22	Ar= D ₂ +air 41	578 0.925 IL_S	NO AC	+0.1	Pressure reduced. AC stopped: AHE vanished.
#69 1640820	0.350	50.2; 22.6, 2.22	Ar= D ₂ +air 20	600 0.930 IL_S Osc	AC, 290 V 1–2 mA	+2.6	Forced pressure reduction, AC ON since 2 h. AHE resumed
#70 1695500	0.350	60.5; 24.8, 2.43	Ar= D ₂ +air 60	632 0.932 C		−1.8	NO AC. Pressure increased. R/R_0 stable; AHE absent
#71 1713770	0.350	60.5; 24.9, 2.43	Ar= D ₂ +air 30	660 0.936 IL_S	AC, 280 V 2–3 mA	+1.2	Forced pressure reduction. AHE improved
#72 1780200	0.350	80.1; 28.7, 2.79	Ar= D ₂ +air 75	700 0.937 IL_S	AC, 253 V 4.5 mA. NO HF	−1.3	AC seems NOT effective to stimulate AHE without HF component
#73 1787240	0.350	80.0; 28.6, 2.79	Ar= D ₂ +air 85	692 0.937 IL_F O	AC, 253 V 4.5 mA. Some HF	+3.2	AC ON, sometimes HF. R/R_0 noisy
#74 1806940	0.350	97.8; 31.7, 3.08	Ar= D ₂ + air 150	757 0.942 IL_F O		+4.8	R/R_0 decreasing. Absolute value of local high temperature (760°C) is also important
#75 1812230	0.350	98.2 31.9, 3.08	Ar= D ₂ 62	802 0.946 IL_F O	AC, 260 V 4 mA	+7	AC ON, some spontaneous HF. Forced pressure reduction. Combined effect of higher temperature, low pressure-AC excitation is

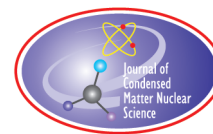
Table 2 continued

#76 2043780	0.350	97.4 31.6, 3.08	Ar= D ₂ +air 146	719 0.935 IL_S	AC, 290 V <1 mA	+2.8	AC ON, leakage air intake. AHE reduction (7.2–2.8) because: pressure increasing, lower AC, lower temperature
#77 76650 New file 260827, 11:27	0.350	40.6; 20.1, 2.02	D ₂ fresh 440	336 0.906 IL_S O	AC, 290 V 1–2 mA	+1.8	After vacuum, fresh D ₂ (380 mbar at RT). Increasing of loading. Noisy. Some AHE, although low power and temperature. Flux of D ₂ looks important
#78 26480 New file 270819, 10:18	0.200	40.5; 32.4, 1.25	D ₂ , 480	463 0.929 IL_S	AC, 300 V <0.5 mA NO HF	–0.3	Re-activated V2. Slow loading speed. No AHE, although AC oscillation but no HF components. Pressure excessive and temperature not sufficient for AHE
#79 37570	0.200	60.7; 40.1, 1.51	D ₂ 15	580 0.959 O	AC, 290 V <0.6 mA	+4.9	Forced pressure reduction. R/R_0 noisy: combined effects with HT. AHE resumed
#80 89.1 116590	0.200	81.5; 47.0, 1.73	D ₂ 26	720 0.971 IL_F Osc.	AC, 290 V 0.3–1 mA	+115	Forced pressure reduction. R/R_0 noisy and decreasing. HT, low pressure, oscill.: ingredients to get AHE
#81 174740	0.200	81.2; 46.7, 1.73	D ₂ +air 34	691 0.964 IL_F O	AC, 290 V 0.4 mA	+8.3	AC polarization started. Leakage, air intake observed. Reduction of temperature decreases AHE (11.5–8.3)
#82 195640	0.200	100.4; 52.2, 1.92	D ₂ + air 75	764 0.970 IL_F O	AC, 290 V 0.2–1 mA	+13.0	AC always active. R/R_0 noisy and decreasing fast. The AC keeps AHE stable over time
#83 204780	0.200	101; 52.6, 1.92	D ₂ +air 30	808 0.981 IL_F O	AC, 290 V 0.2–1 mA	+12.8	Several pressure reduction steps. AC always active. R/R_0 noisy and decreasing. Although air intake AHE almost stable

							Table 2 continued
#84	0.200	100.3;	D ₂ +air	753	AC, 290 V	+11.2	Long duration measures. AC ON. Leakage and air intake occurred. R/R_0 noisy and decreasing. The combined effect of high temperature, AC oscillation and sufficiently low pressure overcome the deleterious effect of air intake even for long times (>14 h). <i>Last measurement before ICCF22</i>
257660		52.1, 1.92	50	0.97	0.2–0.5		
				IL_F	mA		
				Osc.			

Addendum

- (1) After the ICCF22 conference we received enquiries whether we have a theory supporting the correlation between AHE occurrence and electron emission. Unfortunately to date we can only speculate that electron emission may cause D⁺ ions in gaseous phase to move toward the surface of the Constantan wire, possibly contributing to the D flux or inducing extreme localized gradients beneficial to the manifestation of AHE (especially on the nanostructures present on the surface of the wire).
- (2) The gamma source contains 10 g of ²³²Th in form of Thoriated Tungsten (i.e. electrodes used for TIG welding). Thorium is dispersed at 2% concentration w/w in a matrix of W. The specific activity of ²³²Th is 4.07×10^3 Bq/g, mostly alpha and beta radiations. In addition there are several gamma, even at high energies (2614 keV), due to his decay products (²²⁸Ac, ²¹²Bi, ²¹²Pb, ²¹²Po, ²²⁴Ra, ²²⁸Ra, and ²⁰⁸Tl). The tube where the material is inserted is a 2 mm thick stainless steel tube, hermetically closed. In short, the measured gamma activity, measured using just a simple Geiger Muller detector, is over 10 times larger of local background (35–40 μ Rem/h). Moreover, a 3×3 inch NaI(Tl) detector was successfully used to identify the ²³²Th gamma peaks up to 2 MeV of energy.



Research Article

The Thermoneutral Potential in Electrochemical Calorimetry for the Pd/D₂O System

Melvin H. Miles*

College of Science and Technology, Dixie State University, St George, UT 84770, USA

Abstract

The thermoneutral potential (E_H) for any electrochemical reaction corresponds to the enthalpy change (ΔH) for that reaction. The D₂O electrolysis reaction produces an enthalpy change of $\Delta H = 294.600$ J/mol of D₂O which yields a thermoneutral potential of $E_H = -1.5267$ V ($-\Delta H/2F$). This thermoneutral potential will apply throughout a Pd/D₂O calorimetric experiment except for the first day or two where the loading of deuterium into the palladium cathode occurs. The changes in ΔH and E_H during loading and their effect on measurements of excess power will be presented. It is concluded that the changes in E_H during deuterium loading do not explain the very early excess power measurements for Pd–B cathodes. Furthermore, boron may be a critical component for the excess power effect in the palladium – D₂O system.

© 2020 ISCMNS. All rights reserved. ISSN 2227-3123

Keywords: Boron, Deuterium, Electrochemistry, Enthalpy, Excess power, Loading, Palladium, Palladium–Boron alloys, Thermoneutral potential

1. Introduction

The loading of deuterium into palladium is an exothermic reaction that occurs readily up to a value of $x = 0.6$ (mol D/mol Pd) as represented by the reaction



which forms the beta phase of palladium deuteride. This value of $\Delta H = -35.10$ kJ/mol D₂ for PdD_{0.6} was reported by Balej and Divisek in 1990 [1] and confirmed by China Lake experiments [2]. Similar values of $\Delta H = -34.6$ kJ/mol D₂ were reported by Flanagan [3] and $\Delta H = -34.2$ kJ/mol D₂ by Sakamoto [4]. The value of $\Delta H = -35.10$ kJ/mol D₂ will be used in this study.

It is confusing that this ΔH value is often expressed in various ways such as kJ/mol D and kJ/mol Pd. From Eq. (1), $\Delta H = -35.10$ kJ/mol D₂ = -17.55 kJ/mol D = -10.53 kJ/mol Pd at $x = 0.6$. This follows from 1 mol D₂ = 2 mol D and 1 mol Pd = 0.3 mol D₂ for PdD_{0.6} formation. More generally, 1 mol Pd = $0.5x$ mol D₂ for PdD _{x}

*E-mail: mhmiles1937@gmail.com.

formation. The use of either kJ/mol D₂ or kJ/mol D is convenient because ΔH is then constant over a range of D/Pd from 0 to 0.6 [3,4]. At higher loadings, the magnitude of these exothermic enthalpies decline markedly with increasing deuterium content [3,4].

Sakamoto [4] reports the equation for bulk Pd

$$\Delta H(\text{kJ/mol D}) = 49.69 [\text{D/Pd}] - 50.75 \quad (2)$$

for D contents in the range of $0.7 < x < 0.85$ where $x = \text{mol D/mol Pd}$. Mathematically, this is a straight-line equation, $y = ax - b$, where $y = \text{kJ/mol D}$, $a = 49.69$, $b = 50.75$ and $x = \text{mol D/mol Pd}$. Assuming this equation applies over a wide range of x -values, then $y = 0$ at $x = b/a = 1.021$ and any higher loading would be endothermic. Sakamoto reports a similar equation for studies of palladium in the form of a black powder where $a = 41.89$ and $b = 44.99$ [5]. Therefore, $y = 0$ at $x = 1.074$. Fleischmann [6] postulated a new gamma-phase for Pd–D at high loading where further loading would be endothermic (ΔH positive). Therefore, higher temperatures would favor higher loadings leading to a positive feedback effect where the anomalous excess power would increase markedly with the cell temperature. For the calculation of E_H at the beginning of a Pd/D₂O calorimetric experiment, the value for ΔH is needed for small x -values.

2. Determination of ΔH at Different Loadings

Publications by Balej, Flanagan and Sakamoto [1–3] all report that ΔH in mol/D or mol/D₂ remains constant from $x = 0$ to about $x = 0.6$. This seems logical because each increment of D involves the same reaction with the palladium. One can use either $-35.10 \text{ kJ/mol D}_2$ or -17.55 kJ/mol D over this x range. However, the value for kJ/mol Pd will depend on the extent of loading. For deuterium loadings greater than about 0.6 mol D/mol Pd, then Sakamoto's equation (2) can be used. The results for ΔH at various values of x are given in Table 1. The results for kJ/mol D₂ are displayed in graphical form in Fig. 1.

Note that Sakamoto's equation (2) is in the form of a straight line as shown in Fig. 1, where the y -intercept is at $x = 1.021$ and further loading would be an endothermic process. This straight line equation gives $y = -35.10 \text{ kJ/mol D}_2$ at $x = 0.6681$. Further loading then becomes more difficult and less exothermic in a linear fashion. Figure 1 appears to be an accurate display of how ΔH (kJ/mol D₂) changes during deuterium loading and gives a reasonable merging of the Sakamoto's results for high loadings with results for lower x -values.

Table 1. The values for ΔH at various deuterium loadings.

x (mol D/mol Pd)	kJ/mol D (y)	kJ/mol D ₂ ($2y$)	kJ/mol Pd (xy)
0.01	−17.55	−35.10	−0.1755
0.10	−17.55	−35.10	−1.7550
0.20	−17.55	−35.10	−3.5100
0.30	−17.55	−35.10	−5.2650
0.40	−17.55	−35.10	−7.0200
0.50	−17.55	−35.10	−8.7750
0.60	−17.55	−35.10	−10.5300
Sakamoto, Eq. (2)			
0.60	−20.94	−41.88	−12.56
0.70	−15.97	−31.94	−11.18
0.80	−11.00	−22.00	−8.80
0.90	−6.03	−12.06	−5.43
1.00	−1.06	−2.12	−1.06
1.10	+3.91	+7.82	+4.30

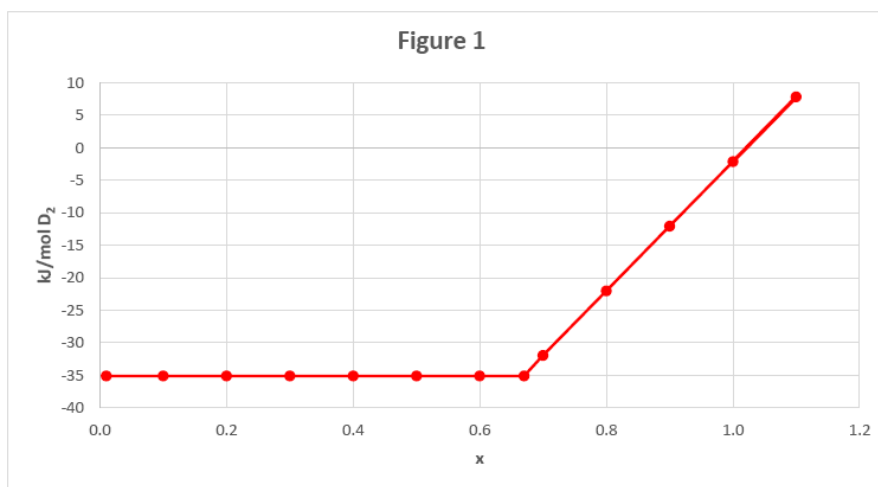


Figure 1. The enthalpy change (kJ/mol D₂) versus x (mol D/mol Pd) for the formation of PdD_x.

Table 1 results for kJ/mol Pd are shown in Fig. 2 for various x -values. The magnitude of ΔH per mole of palladium increases linearly with the loading between $x = 0$ and $x = 0.6681$ and then decreases at higher loadings.

At lower x -values, ΔH (kJ/mol Pd) = $x(-17.55 \text{ kJ/mol D})$ and at high loadings, Sakamoto's equation yields ΔH (kJ/mol Pd) = x (kJ/mol D) = $ax^2 - bx$. Mathematically, this is the equation for a parabola ($z = xy = ax^2 - bx$) where $z = 0$ at $x = 0$ and at $x = b/a = 1.021$. The largest magnitude for ΔH is given by $dz/dx = 2ax - b = 0$ where $x = b/2a = 0.5107$ and $\Delta H = -12.96 \text{ kJ/mol Pd}$. Based on Table 1 and Figs. 1 and 2, the thermoneutral potential can be calculated at any value of x for the Pd – D₂O system. Figure 2 shows that kJ/mol Pd = 0 at $x = 0$

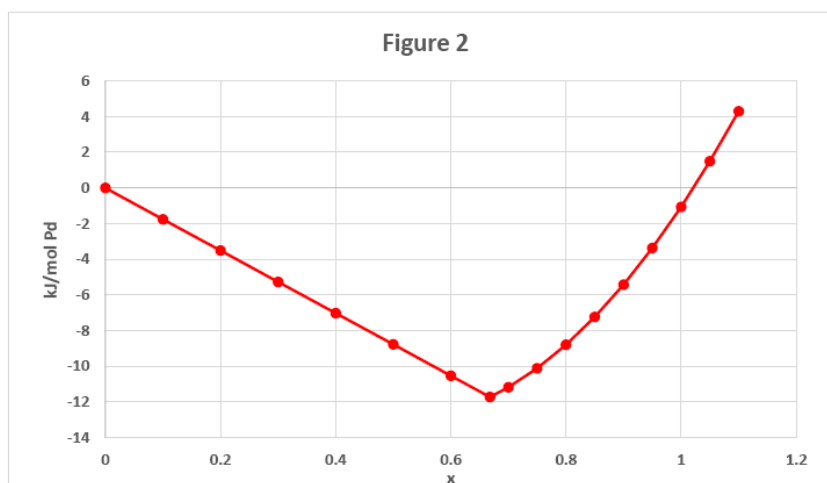


Figure 2. The enthalpy change for PdD_x formation in units of kJ/mol Pd for various x -values.

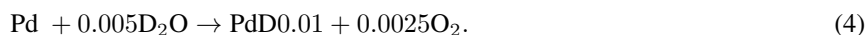
because there would be no reaction with deuterium. However, this makes both kJ/mol D_2 and kJ/mol D indeterminate (0/0) at $x = 0$. This simply means that there is zero enthalpy production for palladium when no deuterium is available.

3. The Thermoneutral Potential for Pd/ D_2O Electrolysis

For the initial electrolysis of D_2O on Day 1 assuming that all of the D_2 generated is used for the palladium loading, the net reaction can be expressed as



The enthalpy change is then ΔH (kJ/mol Pd) = ΔH_f (PdD_{0.6}) – 0.3 ΔH_f (D_2O). Therefore, ΔH (kJ/mol Pd) = $-10.530 - 0.3(-294.600) = +77.850$ kJ and $E_H = -\Delta H/0.6 F = -1.3448$ V. A similar thermoneutral potential of $E_H = -1.336$ V during the initial reaction period has been previously reported [7]. If the same calculation is carried out for the very early electrolysis period where $x = 0.01$, then the reaction is expressed by



This gives $\Delta H = -0.1755 - 0.005(-294.600) = 1.2975$ kJ/mol Pd and $E_H = -\Delta H/0.01 F = -1.3448$ V (the same E_H value). The thermoneutral potential is defined as the cell potential where no heat is given off and no heat is absorbed from the surroundings.

Assuming 100% of D_2 produced by electrolysis is used for palladium loading, then E_H remains equal to -1.3448 V for any x -value up to the formation of PdD_{0.6}. This is because $\Delta H = -35.10$ kJ/mol D_2 remains constant for the initial formation of PdD _{x} (see Table 1). If $E_H = -1.5267$ V is used for this initial loading, then the maximum excess power due to the deuterium loading is given by Eq. (5).

$$P_X = (1.5267 - 1.3448)I. \quad (5)$$

This equation is correct as long as 100% of the D_2 is used for loading rather than exiting the cell. This is more likely to be correct when small cell currents are used initially.

For the Pd–B studies reported previously [8,9] using a current of $I = 0.1500$ A, then the maximum early excess power due to the loading would be $P_X = 0.0273$ W or 27.3 mW from Eq. (5). This is the same maximum excess power as calculated by other methods [9]. Therefore, the early excess power exceeding 27.3 mW reported for the Pd–0.5B experiment [9] cannot be explained by any change in the thermoneutral potential. The previous report of $E_H = 0.9204$ V during the deuterium loading [9] was a calculation error due to the use of -35.10 kJ/mol D_2 in reaction (3) rather than the correct value of -10.53 kJ/mol Pd. These errors are frequent in the literature where incorrect units are used in ΔH calculations for the Pd–D system. For the 100% use of D_2 for loading, $E_H = -1.3448$ V during this loading process. The magnitude for E_H cannot be less than this value during D_2O electrolysis. The use of Eq. (5) provides a simple method of calculating the maximum excess power expected due to the exothermic reaction of deuterium with palladium to form PdD _{x} at any cell current used. The Pd–B experiments produce excess power effects that significantly exceeded the maximum values expected for the deuterium loading process [8,9]. The explanation for this very early excess power for Pd–B cathodes remains unknown. Most chemical reactions of boron with deuterium would be endothermic and not a source for excess heat.

4. Applications for Electrochemical Calorimetry

After the first day or two of electrolysis in D_2O using a palladium cathode, the palladium is essentially loaded with deuterium to give PdD _{x} where $x = 0.6$ or higher. The electrolysis reaction then becomes



where $\Delta H = 294,600 \text{ J/mol}$ and $E_H = -\Delta H/2F = -1.5267 \text{ V}$. There is no change expected in E_H for the rest of an experiment. Small increases or decreases in the loading may occur over time, but these are insignificant compared to Reaction (6). The thermoneutral potential (E_H) provides a simple method for determining the rate of chemical enthalpy ($E_H I$) carried outside an open calorimetric cell by the D_2 and O_2 electrolysis gases [2,7,8].

The best way to analyze the initial electrolysis period is to follow Fleischmann's method [8] and simply use $E_H = -1.5267 \text{ V}$. The excess power (P_X) due to loading cannot be larger than that expressed by Eq. (5) which assumes that 100% of the D_2 generated reacts with palladium rather than exiting the cell. Accurate measurements of excess power during the initial loading would require measurements over time of the fraction of D_2 that reacts with palladium. For the H_2O electrolysis system, Storms [10] reports that this fraction is initially near 100% but declines steadily with time to near zero after 6 or 7 h of electrolysis at $I = 0.1 \text{ A}$.

The Fleischmann–Pons Dewar glass cell used in Japan [8] permitted the direct observation of D_2 gas evolution from the Pd–0.5B cathode using $I = 0.150 \text{ A}$. Initially, there was only a slight gas evolution from the cathode (about 5% of expected). Even after 98 min, the gas evolution at the cathode was still very small indicating that most of D_2 generated was being used for loading. It was not until 220 min that vigorous gassing was observed at the Pd–0.5B cathode. Assuming that 100% of the cell current (0.150 A) was used for deuterium loading, it would require 254 min to load this Pd–0.5B cathode ($V = 0.350 \text{ cm}^3$) to give $x = 0.6 \text{ mol D/mol Pd}$.

Interest in this initial electrolysis period stems from the experiment in Japan [8] and another in the US [9] using this same Pd–0.5B alloy cathode (0.5 wt.% B) prepared by Dr. Imam at the Naval Research Laboratory (NRL). Both experiments gave significant excess power effects during the first day of electrolysis using $D_2O + LiOD$ electrolytes [8,9]. The early excess power results for the Ridgecrest, California experiments [9] are presented in Fig. 3.

Note that the experimental excess power immediately exceeds the expected $P_X = 27.3 \text{ mW}$ (dash lines) due to loading and reaches a peak of 118 mW at 8 min. The excess power remains significantly higher than expected based on Eq. (5) for several hours. A discussion of the calorimetry used in this experiment has been reported elsewhere [11]. The excess power later decreased to zero for Days 2 and 3 [11] before again increasing up to 36 mW at Day 10. Much larger excess power effects near 10 W were observed during a boil-off of the D_2O in the Japan experiment [8].

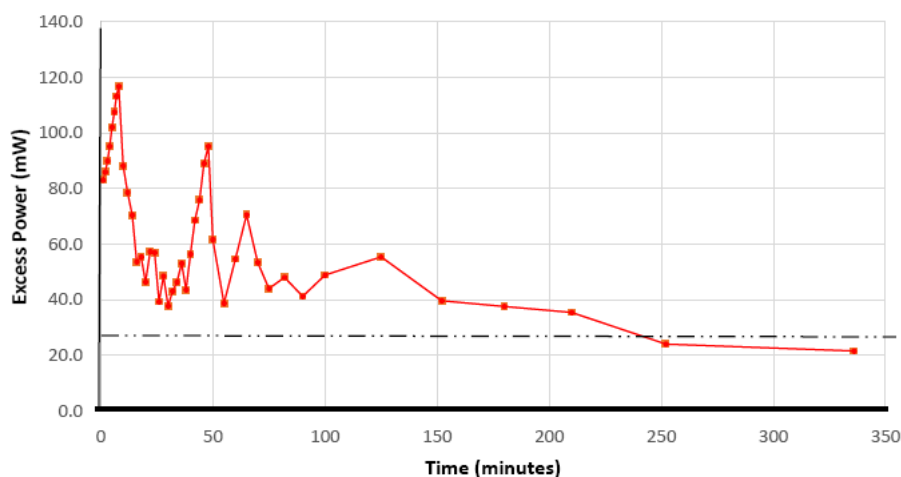


Figure 3. Early excess power for a Pd–0.5 B rod ($0.47 \times 2.01 \text{ cm}$). The peak excess power was 118 mW at 8 min. The dashed line shows the maximum excess power expected for 100% deuterium loading at the cell current of $I = 0.150 \text{ A}$.

The very early excess power is quite unusual for the Pd/D₂O electrolysis system because most calorimetric experiments using palladium cathodes require weeks or even month of electrolysis before any significant excess power effects are observed [2]. The addition of small amounts of boron to the palladium must have some major unknown effect for the excess power. A previous explanation involving the thermoneutral potential does not appear to be correct [9]. The initial formation of the α -phase for PdD_x where x is less than 0.017 also fails as an explanation of the early excess power effect for this Pd–0.5 B electrode.

Is boron a critical component for the palladium in these experiments which takes a long time to be transferred from the Pyrex glass cell in an LiOD electrolyte to the palladium in most calorimetric Pd/D₂O experiments? Perhaps, most Pd/D₂O experiments fail to produce any excess power effects due to the lack of sufficient electrolysis time for the boron transfer from the glass cell or even due to the lack of a boron source in a cell not made of glass. The use of an LiOD electrolyte and its attack on the glass over time likely facilitates this boron transfer. Some results have suggested a nuclear fusion process involving boron as the source for the excess heat [12]. Seven of eight Pd–B cathodes previously investigated produced excess enthalpy [2,9]. It should be noted that a Pd–B cathode that produced excess power at the China Lake Navy laboratory was one of 18 experiments that produced both excess power and helium-4 [2,13,14]. It is an experimental fact, however, that most studies of the Pd–D₂O system do not produce any excess power effects [2,15]. This suggests that certain impurities such as boron may be essential in palladium cathodes for the electrochemical excess power effects using D₂O + LiOD electrolytes.

5. Summary

The value of the enthalpy change for D₂O electrolysis to form PdD_x remains constant at $\Delta H = -35.10$ kJ/mol D₂ (or -17.55 kJ/mol D) during the deuterium loading up to about $x = 0.6$. The value for ΔH then sharply declines in magnitude for $x > 0.7$ and even becomes endothermic near $x = 1.0$. The thermoneutral potential (E_H) for D₂O electrolysis is normally $E_H = -1.5267$ V but it may decrease in magnitude somewhat during the initial deuterium loading to $E_H = -1.3448$ V. The maximum excess power (P_X) due to the exothermic reaction of deuterium with palladium to form PdD_x is given by $P_X = (1.5267 - 1.3448)I$, where I is the cell current in amps. This effect does not explain the early excess power exceeding 100 mW using Pd–B cathodes. It is postulated that boron may be a critical component for excess power in the Pd–D₂O system. The role of boron in producing the excess power effect remains unknown.

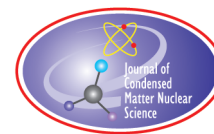
Acknowledgements

Support for this work was received from an anonymous fund at the Denver Foundation through the Dixie Foundation at Dixie State University. An Adjunct Faculty position at the University of LaVerne in California and a Visiting Professor position at Dixie State University in Utah are also acknowledged. The author also thanks Jed Rothwell for his help with the references.

References

- [1] J. Balej and J. Divisek, Energy balance of D₂O electrolysis with a palladium cathode: Part 1. theoretical relations, *J. Electroanal. Chem.* **278** (1990) 85–98.
- [2] M.H. Miles, B.F. Bush and K.B. Johnson, Anomalous effects in deuterated systems, Naval Air Warfare Center Weapons Division, NAWCWPNS TP8302, September 1996, 98 pages (see <http://lenr-canr.org/acrobat/MilesManomalousea.pdf>).
- [3] T.B. Flanagan, W. Luo and J.D. Clewley, Calorimetric enthalpies of absorption and desorption of protium and deuterium by palladium, *J. Less Common Metals* **172–174**, Part A (1991) 42–55.
- [4] Y. Sakamoto, M. Imoto, K. Takai, T. Yanaru and K. Ohshima, Calorimetric enthalpies for palladium-hydrogen (deuterium) systems at H(D) contents up to about $[H]/[D]/Pd = 0.86$, *J. Phys.: Condens. Matter* **8** (1996) 3229–3240.

- [5] Y. Sakamoto, M. Imoto, K. Takai and T. Yanaru, Calorimetric enthalpies in the β -phase regions of Pd black – H(D) systems in, *The Sixth Int. Conf. on Cold Fusion, Progress in New Hydrogen Energy*, M. Okamoto, Chairperson, Lake Toya, Japan, Vol. 1, 1996, pp. 162–170.
- [6] M. Fleischmann in Letters From Martin Fleischmann to Melvin Miles, Jed Rothwell, Editor, LENR-CANR.org, pp. 410,411,438, May 2018 (see <https://www.lenr-canr.org/acrobat/Fleischmannlettersfroa.pdf>).
- [7] N.A. Godshall, E.P. Roth, M.J. Kelly, T.R. Guilinger and R.I. Ewing, Calorimetric and thermodynamic analysis of palladium–deuterium electrochemical cells, *J. Fusion Energy* **9** (2) (1990) 229–237.
- [8] M.H. Miles, M. Fleischmann and M.A. Imam, Calorimetry analysis of a heavy water electrolysis experiment using a Pd-B alloy cathode, Naval Research Laboratory Report, NRL/MR/6320-01-8526, March 26, 2001, 155 pages (see <http://lenr-canr.org/acrobat/MilesMCalorimetrd.pdf>).
- [9] M.H. Miles and M.A. Imam, Excess power measurements for palladium–boron cathodes, *J. Condensed Matter Nucl. Sci.* **29** (2019) 12–20.
- [10] E. Storms, The enthalpy of formation of PdH as a function of H/Pd atom ratio, *J. Condensed Matter Nucl. Sci.* **29** (2019) 275–285.
- [11] M.H. Miles, Electrochemical isoperibolic calorimetry for D₂O electrolysis, *ChemRxiv*, 17.11.(2019), November 17, 2019. DOI: 10.26434/chemrxiv.10269713.
- [12] T.O. Passell, Search for nuclear reaction products in heat-producing Pd, in *ICCF-7 Proceedings*, Vancouver, Canada, April 19–24, 1998, pp. 309–313 (see <http://www.lenr-canr.org/acrobat/ENECOftheseventh.pdf#page=309>).
- [13] M.H. Miles, Correlation of excess enthalpy and helium-4 production: a review, in *Condensed Matter Nuclear Science, ICCF-10 Proceedings*, P.L. Hagelstein and S.R. Chubb (Eds.), World Scientific, Hackensack, NJ, 2006, pp. 123–131, ISBN 981-256-564-7 (see <https://www.lenr-canr.org/acrobat/MilesMcorrelatioa.pdf>).
- [14] M.H. Miles, Production of helium in cold fusion experiments, in *Cold Fusion: Advances in Condensed Matter Nuclear Science*, Chapter 1, Jean-Paul Biberian (Ed.), Elsevier, 2020. ISBN 9780128159446.
- [15] C.P. Berlinguette, Y.M. Chiang, J.N. Munday, T. Schenkel, D.K. Fork, R. Koningstem and M.D. Trevithick, Revisiting the cold case of cold fusion, *Nature* **570** (2019) 45–51.



Research Article

Active LANR Systems Emit a 327.37 MHz Maser Line

Mitchell R. Swartz*

JET Energy Inc., Wellesley Hills, MA 02481, USA

Abstract

Active LANR systems, both aqueous and dry preloaded nanomaterials, emit very narrow bandwidth radio frequency (RF) hyperfine emission peaks (ca. 327.37 MHz) very close to the Deuterium Line (DL). In a Fabry–Perot structure, two electrically driven PdD–ZrO₂ preloaded components produce a solid state DL maser when driven above a threshold voltage, and below their electrical avalanche breakdown voltage. When the systems are electrically driven at higher applied voltage, a superhyperfine structure of sidebands appears with significant local in situ information. The RF emission proves that D is the LANR fuel and demonstrates that the deuteron, in the excited pre-⁴He state, is a free radical emitting from an FCC vacancy.

© 2020 ISCMNS. All rights reserved. ISSN 2227-3123

Keywords: Active site, Deuteron line, Deuterium line, LANR maser, Maser, Zeeman splitting

1. Introduction – D-Line Maser Emission from Active CF/LANR Components

Active lattice assisted nuclear reaction (LANR) systems, both aqueous and dry nanomaterial, emit very narrow bandwidth radiofrequency (RF) emission peaks (ca. 327.37 MHz), in the Deuterium-line (“DL”; 327.348 MHz) region. Figure 1 shows a very narrow bandwidth RF emission peak ($Q > 1.2 \times 10^6$) from a preloaded ZrO₂PdD NANOR[®]-type LANR component [1–12] operated below its avalanche voltage in a well-grounded resonant Fabry–Perot chamber. Maser activity is seen by the bright curved line.

In Fig. 1, emission occurred immediately after electrical drive (bottom left); followed by an exponential-like drift of the frequency to a slightly lower, more stabilized, monochromatic frequency. The high- Q (ultra-narrow bandwidth) and positive Zeeman response of the emitted radiation (Fig. 1) is consistent with maser activity, and only appeared when the components were in their active electrically driven state. The other lines are from a variety of signals commonly observable, mainly military and cosmic. The RF CF/LANR maser line is 1–4 dB greater in intensity than all of the others lines.

The LANR active state’s emission creates a new method to observe LANR systems. It also gives possible further information about LANR’s difficult-to-attain most desired mode because higher applied voltages have revealed superhyperfine structure (hyperfine sidebands). Most importantly, the D-line emission frequency of these observations also

*Mitchell R. Swartz ScD, MD, EE, ACIER, E-mail: drswartz@nanortech.com.

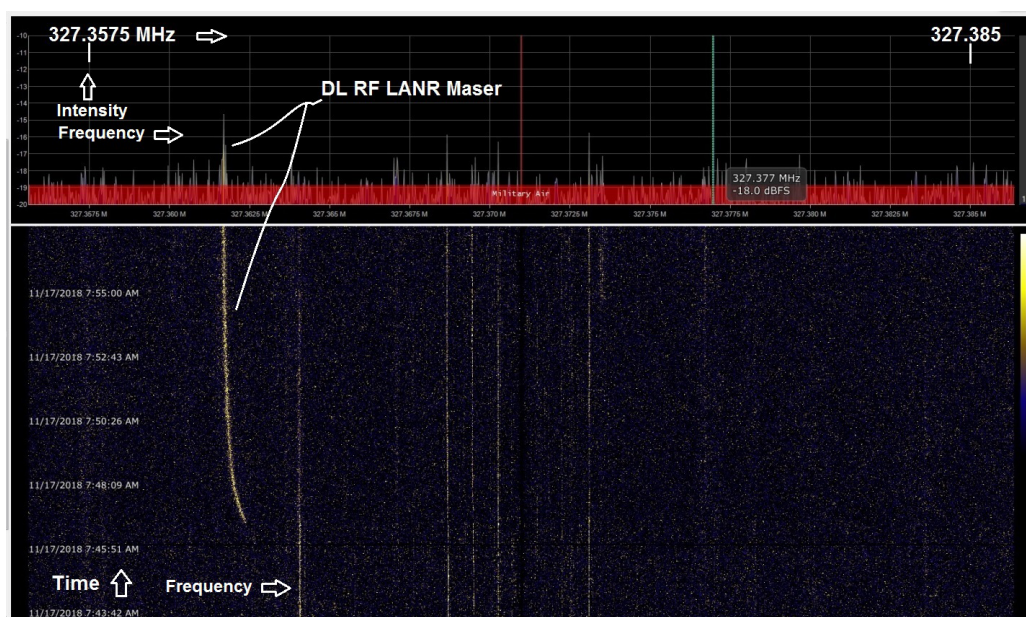


Figure 1. Software defined radio identification of LANR hyperfine line maser emission. In this dual graph, there are two regions; in both, the frequency increases from left to right. The upper portion shows RF intensity peaks as a function of frequency (horizontal) at a single moment in time. On the bottom, each peak appears as a dot on a horizontal line for each one moment in time. Time increases from top to bottom, as in a waterfall. The DL RF CF/LANR maser emission line is indicated in both portions of the display.

confirms the role of deuterium in LANR [13,14]. Analysis of the nearest neighbor resonance of those superhyperfine emission peaks has revealed the nature of the LANR active site (a face center cubic (FCC) vacancy), and with positional lattice changes around the active site during the active mode. D-loaded active nickel is far more complex. This confirms the prediction (ICCF-4 [15]) which also relates to the mechanism of fuel entering the active site. Using the known stereoconstellations, the analyses indicate a possible loss of coordination number (CN) from, and a new interaction with a paramagnetic ion causing an apparent change in magnetic properties of, the fourth and second closest neighbors, respectively. It also identifies connections between the loaded deuterons [13].

2. Background

2.1. Hyperfine emission in radioastronomy

This effort links CF/LANR with the tools and methods of the science of radioastronomy, which studies the universe by measuring radiofrequency emissions from several MHz to the far infrared [16]. Historically, the field of radioastronomy began in the 1930s when a daily hissing sound was heard on radios. By the 1940s, Jan Oort recognized the importance of these astronomical radio frequency (RF) emission lines [17]. Although study of deuterium came later, in 1944, Hendrik van de Hulst predicted that neutral hydrogen could be detected at 1420.4058 MHz [18], the hydrogen line (HL) was thereafter first detected in 1951 by Ewen and Purcell [19]. The impact is that the hydrogen hyperfine line (HL) emission at 1.4 GHz and the 327 MHz hyperfine line of the deuteron (DL) radically changed astronomy by making objects – unseen by conventional optical telescopes – become visible (Fig. 2), and by even enabling the determination of some of the galactic distributions and concentrations of H and D. Those determinations were only possible

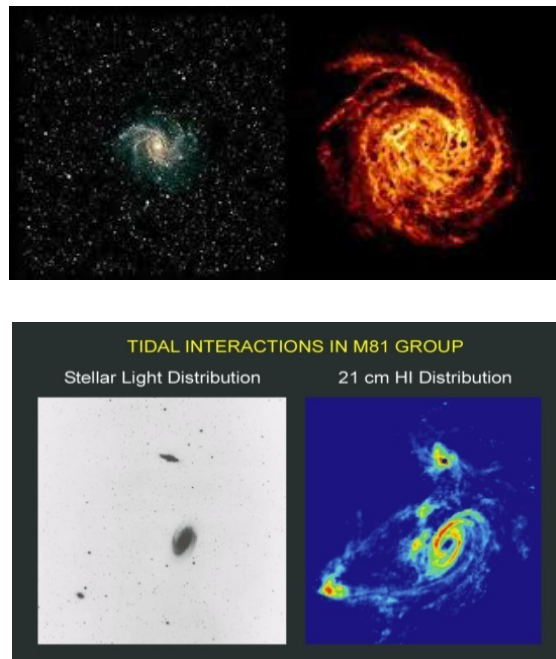


Figure 2. DL and HL observations improve galactic understanding.

because fortunately, the 21 cm line (1.42 GHz in the L band) is in the “microwave window” and passes through the Earth’s atmosphere.

Together, the HL and DL have provided understanding of the matter distribution through the known universe (Fig. 2) – providing information from post-Big Bang times just after recombination through reionization to the present. These are a few of the findings. First, examinations of the incoming HL and DL have revealed that hydrogen atoms are NOT uniformly distributed throughout the galaxy (although they were much more homogeneous 13.6 billion years ago). After 1952 the first maps of the neutral hydrogen in the Milky Way Galaxy were made, and these revealed for the first time the beautiful spiral structure of our galaxy. The HL has even revealed, by Doppler shift (ca. 200 MHz to 9 MHz), the relative speed and rotation of each arm.

As an example of the time-scanning power of this technique, after deuterium was discovered in space, its semi-quantitative levels were sought to determine the local photon to baryon ratio and the cosmological baryon density, thus giving a further peek into the “dark ages”. As another example of the sensitivity of this technique, deuterium hyperfine line investigations have also indicated an upper limit for D/H and 8×10^{-5} [20]. This was much higher than both UV and optical measurements of $\sim 2 \times 10^{-5}$ [21]. This difference is important and reflects the facts that the isotope shift of the astronomical optical lines of D and H is too small for precise measurements, and that the optical lines do not reflect all of the H and D content. Therefore, the DL and HL are used instead (0.327 and 1.42 GHz) showing another importance of DL and HL in astronomy [16].

In radioastronomy, DL and HL observations have greatly improved human understanding of the extent, and interactions of galaxies, both now and back to a few hundred thousand years after the Big Bang. They make the invisible visible. Two galaxies are shown above. For each, the optical image is on the left. The HL image on the right reveals the interactions of groups of matter in a fashion, impossible to see by conventional stellar light and optical telescopes.

2.2. Hyperfine emission from free radical hydrogen

The word deuterium indicates the deuteron has positive charge, but it is a charge neutral free radical (with an unpaired electron). Deuterium is light enough that isospin is a good symmetry. The proton and neutron are both fermions, and a state containing two of them must be antisymmetric under exchange. The nuclear spin results from the fact that the proton and neutron interact by strong force. Because parallel electric currents attract, the parallel magnetic dipole moments (i.e. with antiparallel spins) has the lowest energy. This creates two states at two different energy levels and that is what actually emits the detected RF signal(s). Two closely spaced energy levels in the ground state (1s) of the heavy hydrogen atom result. The transition in H has an energy difference of $5.87433 \mu\text{eV}$ (D has $1.3528 \mu\text{eV}$). The difference is a photon at 1420 MHz for hydrogen and 327.348 MHz for deuterium.

Precisely, characteristic, identifying, RF emissions of atomic hydrogen including DL emission at 327 MHz results from energy transitions within the hyperfine structure (Fig. 3). The energy states result from the interaction between the deuteron's electron's spin and its own nuclear spin. Figure 3 shows the analysis for the more commonly examined hydrogen free radical.

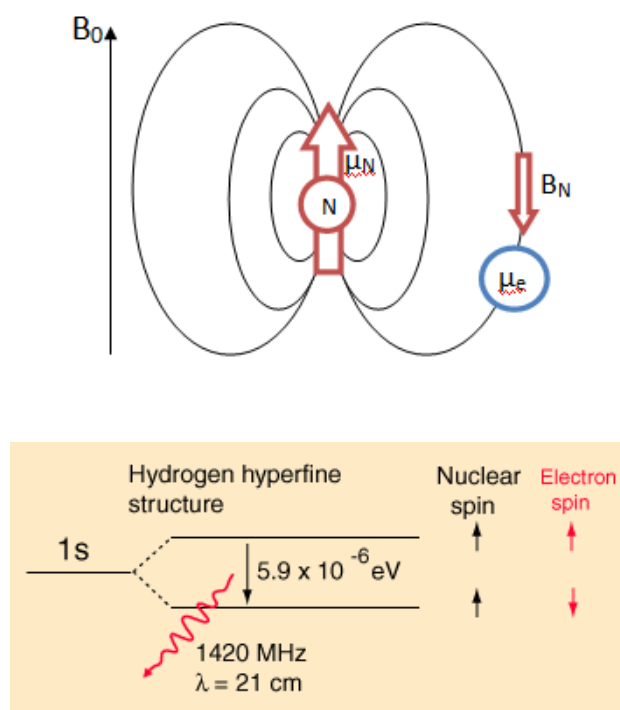


Figure 3. Origin of the HI and DL RF hyperfine spectra. This schematic figure of a free radical (atomic) hydrogen atom and corresponding energy diagram show the origin of the HI and DL RF hyperfine structure. The left portion shows the atomic orientation of the nuclear and electron magnetic spins, which can be either in parallel or antiparallel magnetic states. The right portion shows the energy level differences of those two states. The difference is a photon at 1420 MHz for hydrogen and 327.348 MHz for deuterium.

2.3. Long emission times herald narrow bandwidth

Because atomic deuterium and atomic hydrogen have no electric moment, the energy transition between the two states, shown in Fig. 3, is highly forbidden; meaning that there is an extremely small transition rate of $\sim 2.9 \times 10^{-15}$ /s, which correlates to a mean lifetime of the excited state of ca. 10 million years. Simply put, a spontaneous transition between these states does not normally occur on Earth – unless induced using a hydrogen maser. But it is observed in astronomy. As a corollary, because of the long mean lifetime, the line has an extremely small natural width. Broadening, therefore, is due to Doppler shifts. There is also significant shift of the main signal due to relativistic Doppler shifts from very far away galaxies emitting at times up to about 13.8 billion years ago.

3. Experimental Materials

3.1. Overview

There were three active electrically driven LANR systems tested. The aqueous Ni–ordinary water system and two different solid state preloaded ZrO_2 –PdNiD nanomaterial components. The maser RF outputs, and the one from the aqueous nickel system in the active CF/LANR state, each show significant operating significance from these new RF findings. As discussed below, and in detail in [13,14]. The data were examined to determine what type of loaded Group VIII lattice structure would produce the observed superhyperfine sideband structure. This is shown for an active XSH-producing aqueous nickel LANR system and for two dry preloaded palladium zirconia CF/LANR components (NANOR[®] type) [1–12].

It is important to recognize and to control the two different electrically driven modes for both aqueous and nanostructured CF/LANR systems. Only one state is the active, desired, excess heat (XSH)-producing state “mode”. This was demonstrated by presenting calorimetry and other measurements of both modes during a single run, and by confirmation using CMORE spectroscopy. It is fortunate that LANR systems, when active, have distinct calorimetric and CMORE antiStokes-XSH linked signatures, because it explains why some CF/LANR systems fail to create XSH, and reveals unwanted reactions, XSH-quenching reactions and pathways [24].

3.2. Aqueous nickel LANR system

Our first recent set of experimental RF surveys began with preliminary amateur radio and LANR investigations that examined and resolved, for the first time, the apparent absence of HL and presence of DL emissions from the MOAC (“Mother of all Cathodes”) LANR (ordinary water) aqueous system electrically driven during its active mode [22–24]. The MOAC cell has a 3 l capacity with a cathode weighing 2.132 kg (#46 hard drawn smooth nickel wire with an area of ca. 240,000 cm²). The electrolyte was a dilute carbonate solution in laboratory distilled deionized “ordinary” water. For the calorimetry, calibration was determined by ohmic controls and other methods, as discussed elsewhere [25–37]. Careful results have revealed a loss of deuterium (more precisely, “deuterons”) from ordinary water when excess heat is observed [23]. The exit gas, from the enclosed electrolytic cell, had an HD/H₂ isotopic ratio (3/2 ratio) which was significantly less than originally. When using $V * I$ as electrical input power, the maximum incremental power gain was ~ 4 times electrical input; this occurred at lower electrical input power. The maximum excess power was ca. 5 W.

3.3. Dry ZrO_2 –PdNiD NANOR[®]-type components

The second investigations were a set of experiments looking for possible RF output, and then solid-state LANR maser action at 327.7 MHz (such as in Fig. 1) resulting from electrically driving ZrO_2 PdD preloaded NANOR[®]-type LANR components [1–12], carefully below their avalanche voltage [10,24] when excess heat is known to cease.

This new generation of CF/LANR quantum electronic devices have at their core nanostructured $\text{ZrO}_2\text{-PdNiD}$, and exhibit considerable energy gain. These important novel devices feature two terminals with a cylindrical shape and active CF/LANR core and self-contained superior handling properties enabling portability and transportability. Most importantly, the activation of the cold fusion/lattice assisted nuclear reaction is, for the first time, separated from loading. These NANOR[®]-type preloaded components are dry, sealed into an electrically conductive (high impedance) configuration. Thus, they are potentially incredibly very useful and have demonstrated a more reproducible CF/LANR behavior.

The two terminal component, after the component is placed in a holder, is positioned to fix and maintain the orientation, while holding the connecting cables and component connectors safely and reliably. The dry, preloaded nanocomposite components have at their core $\text{ZrO}_2\text{-PdD}$ nanostructured material. They are smaller than 2 cm length, with 30–200 mg of active LANR material. Although small in size, the LANR excess power density is more than 19,500 W/kg of nanostructured material. The small, preloaded, dry components have enabled the way to higher instantaneous power gain, total energy gain, imaging, emissions, open demonstrations, and a better understanding of the impact of applied magnetic fields, and electrical transconduction [1–12].

One nanostructured material is $\text{ZrO}_2\text{-(Pd Ni D)}$ with Zr (65%), Ni (30%), and Pd (5%) by weight. However, generally speaking several types of $\text{ZrO}_2\text{-(Pd}_x\text{Ni}_{1-x})$, with D addition can be used. The ratios are chosen for those which absorb the greatest amount of deuterium or hydrogen gas and greatest effect, and those which create the greatest desired effects. For simplicity in description, after loading, all of these nanostructured materials in the core will henceforth simply be referred to as $\text{ZrO}_2\text{-PdD}$, $\text{ZrO}_2\text{-NiHD}$, and $\text{ZrO}_2\text{-PdNiD}$. These are the symbols used below even though the actual variation of composition in the nanostructured material in the core can vary considerably. The nanostructured material has a composite distribution of nanostructured ferromagnetic “islands” separated among a vast dielectric zirconia “ocean”. The dielectric zirconia embeds uncountable numbers of nanostructured metal ternary alloy islands of the material containing now NiPdD. The appearance is like a chocolate chip cookie on the nanoscale. The “chips” are hydrided palladium nickel metallic alloy embedded in a zirconium oxide dielectric matrix (“cookie”). The $\text{ZrO}_2\text{-(Pd Ni)D}$ is prepared in a complicated process that begins by oxidizing a mixture of zirconium oxide surrounding metallic palladium, nickel, or Pd–Ni islands. The desired nanostructure islands of NiPdD have characteristic widths of 5–20 nm size. This nanostructure size is selected because it can react cooperatively, generating large amplitude, low frequency oscillations. These size structures tend to be Raman active, with the islands having anharmonic terahertz vibrations [11,12,22]. Furthermore, the storage capacity decreases rapidly when the nanostructure size is greater 30 nm. It is not unreasonable to see rapid drop off in LANR success if sizes are larger than 30 nm. The vibrations of nanostructured materials are very important for activity. Attention is directed to the fact that palladium as one of the elements within the zirconia nanostructured material. Other types of materials can also be used. All of them involve the solubility of D and H in palladium and less so in nickel and the other active metals and alloys.

Our previous studies and reports have been directed to both avoiding the avalanche voltage and approaching the optimal operating point (OOP) of the system [37]. Most importantly, we have demonstrated that several electrical transconduction states exist, but that only one is active, desired, and capable of producing “excess heat” [10,24]. The other is DEAD, with no desired excess heat. Beyond the region of electrical avalanche, the previously active preloaded LANR quantum electronic components give a thermal output similar to a standard ohmic control (a carbon composition resistor). Despite driving at higher input electrical power, on other side of the electrical avalanche, these NANOR[®]-type components act as little more than electrical resistors which – when in electrical avalanche mode- are conventionally dissipative, not over-unity, and therefore are functionally “dead” with respect to producing excess heat.

The activated loaded nanomaterial package (i.e. called an NANOR[®]-type component which is a working LANR device in its active electrically driven mode) can be monitored by several methods for verifiable scientific data. Compared to the 2003 LANR open demonstration at MIT, the second open demonstration at MIT in 2012, for several months using these components featured a more complicated calorimeter shown at the MIT RLE laboratory. It had

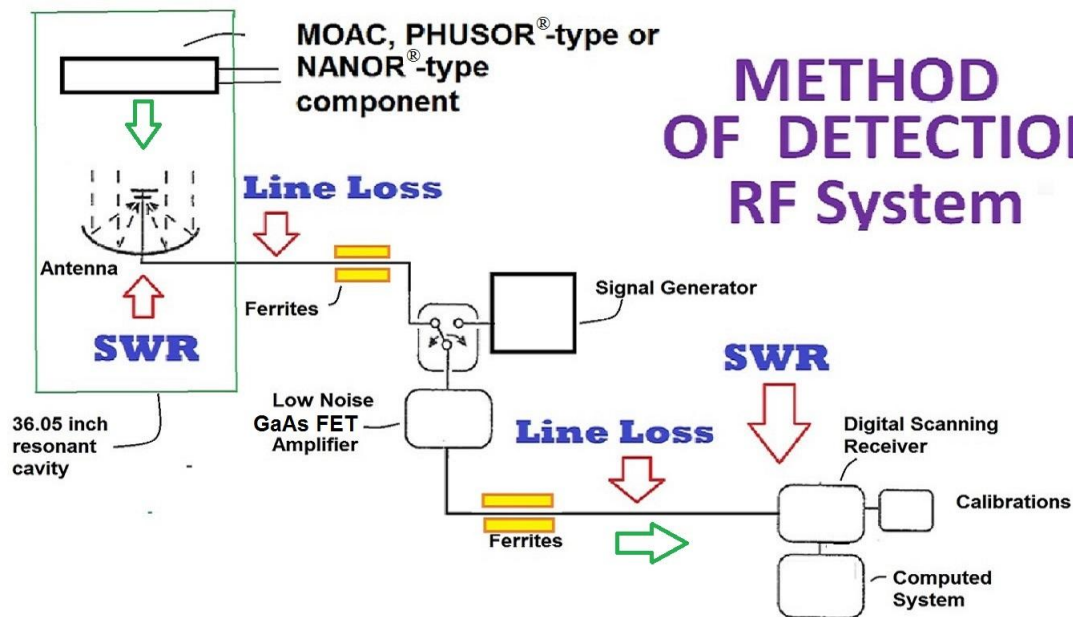


Figure 4. Block diagram of the system used for the HL and DL receiver system.

additional monitoring diagnostics for improved verification, such as the measurement of heat flow, to thereby provide for three independent ways of monitoring excess heat semiquantitatively compared to a thermal ohmic control. Like its 2003 (ICCF-10) predecessor demonstration at MIT, this preloaded NANOR®-type LANR device also showed excess energy and also obvious improvements of size, response time, diagnostics, and total output energy (energy gain 14.1 in 2012 vs. an energy gain ~ 2.7 in 2003 [27,30]).

3.4. Experimental methods – overview

There are multiple parts and systems for inducing, controlling, detecting, analyzing, and presenting the data, including the CF/LANR superhyperfine structure. First, the RF emissions are collected. Second, they are examined as a function of frequency, electric drive state, using ohmic and other controls. Third, finally, the data is examined, including to determine what type of loaded D-loaded Group VIII lattices produce the observed superhyperfine sideband structure. Figure 4 shows in a schematic block diagram the arrangement for inducing and then detecting the RF emissions. The examination focuses on a material containing a free radical which emits radiofrequency (RF) photons.

Beginning in the top left, it shows the electrical driving system, used to activate a MOAC-type, PHUSOR®-type or NANOR®-type component to its active, excess heat-producing state, the resonant enclosure box, antenna, transmission lines, ferrites, signal generator, low noise amplifier (LNA), receiver, calibration equipment, computation system and imaging output. Also identified are the transmission lines which can insert very serious line loss, and the very relevant standing wave ratios (SWR) which must be adjusted for an impedance match, if the subsequent computation and analysis are to work.

The figure shows a block diagram representation for the CF/LANR emitter, the antenna, the line feeds and transmission lines (including serious line loss), the ferrites, the control signal generator, the GaAs FET (field effect transistor)

amplifier, the most relevant standing wave ratio (SWR) points to match, computation and software defined (digital scanning) receiver (SDR).

3.5. Emission, driving the emitted

As presented below, there are two types of active sites in the active XSH-producing aqueous nickel CF/LANR system (MOAC type), and for two dry preloaded palladium zirconia CF/LANR components (NANOR[®]-type component) examined. In order to get emissions, the sample comprises a means to electrically drive the free radical, which is capable of achieving an excited state and, in the appropriate conditions as taught herein, releasing a radiofrequency photon. This emitted photon is characterized by a specific wavelength which is the DL. To achieve this, the free radical is located in a nanostructured a component containing a ZrO₂-PdD preloaded nanostructured material. It is in a two terminal component which is used to couple it, and the material within it, to an external electrical power source.

The circuit must be built very carefully using platforms that have insulation resistance that are very high. Some exceptional NANOR[®]-type components have electrical resistances up to 30 GΩ, so conventional circuit boards have been out of the question. An Arduino microprocessor and associated sketch are used. In constant driving systems, the complete activator and driver consists of a power supply. That driver consists of a power supply run by a programmable controlled-microprocessor (such as an Arduino, itself controlled by a sketch design either evaluate the LANR material or to also exploit the LANR material (“evaluation sketch” or “exploiter sketch”). The Arduino Uno (designed at MIT’s Media Lab) can be obtained and a pulse wave modulated (PWM) Arduino Uno microcomputer can be used with paired MOSFET drivers on the controller board (one for the ohmic control). MOSFET drivers include UCC27424, MIC4422YN, and MCP1407. Schottkey diodes, such as 1N5817, can be put across the MOSFET for protection, if not already built in. MOSFETs can be equivalent be substituted for by photoFETs, which are more advanced MOSFETs. Similar to a Panasonic solid state relay (AQV258). This Photo FET is a 20 mA, 1500 V switch. As an alternative, to have less loss (due to resistance across the switch), if the NANOR[®] has low enough electrical resistance, a Panasonic Solid State Relay (AQV254) 150 mA, 400 V, switch can be used. To double check, drive the reactions through pairs of electrodes using a controlled electric current source, and a Keithley 225 at low input, with $\pm 1\%$ accuracy. Electrical voltage sources might included HP/Harrison 6525A for transsample potentials up to 3000 V ($\sim \pm 0.5\%$ accuracy).

Electrically, the response of the component, and similar nanomaterials, is even more complex. The zirconia dielectric matrix is insulating at low voltage and keeps the nanoscale metal islands electrically separated. It also prevents the aggregation of the islands. Each nanostructured island acts as a short circuit elements during electrical discharge. These allow deuterons to form a hyperdense state in each island, where the deuterons are able to be sufficiently close together. In addition, the nanomaterial lattice of Pd is expanded by Zr, and also, but less so, by the H and D.

3.6. Detection and transmission

Beginning with the detection of the RF signal, the signal emitted by the material is received first by an antenna, and then a receiver to measure the intensity of emission, and range of frequencies of the photons. Hence, connecting the two is done by a transmission line used to coupling the antenna to the receiver. The signals are weak, and therefore the antenna is made with an aperture as large as possible, and the collection is for as long a time as possible because one key to success is time. The sensitivity of this detection system (SNR) is proportional to $A \times \sqrt{t}$, where A is the antenna’s collecting area, and t is the integration time. What is not explicitly shown in Fig. 1, but is therefore quite important, is that the data is meticulously collected over several minutes to hours, as it is integrated/analyzed over time and as a function of frequency.

Current investigations use one of three antennae: reflector, Yagi, and a convenient “duck” antenna system. Only the latter fits easily into the resonance chamber. The “duck” is a “normal-mode helix” which is an enclosed wire helix.

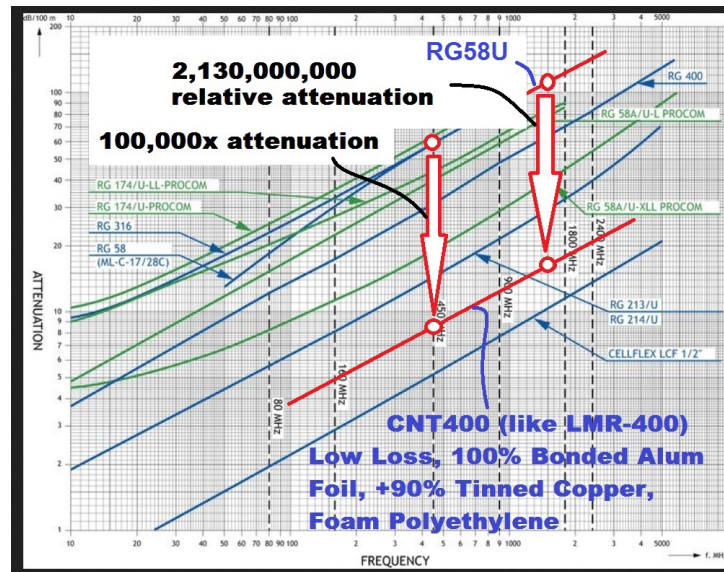


Figure 5. Antenna feed line loss as a function of frequency for various cables.

This type of antenna is 4–15% of a wavelength long. It's name came from the US Secret Service after its naming “rubber ducky” by the former first daughter Caroline Kennedy. This is electrically a very short quarter-wave antenna which is capacitive and the matching inductor is moved from base to be part of the antenna itself. Its current distribution is not sinusoidal unlike a dipole, but it has a high- Q factor (narrow bandwidth) with use over a wide frequency range of 100–500 MHz. The best designs have $\sim 50 \Omega$ impedance at the feed-point.

For this to work, transmission lines must be closely examined. Although often ignored, the antenna feed line loss was significant and had to be addressed for this iteration of experimental runs. In addition, the use of military grade coax (CNT400) decreased the transmission line loss by +90 dB per standardized length over RG58U (Fig. 5). (http://cablexperts.com/cfdocs/tech_data.cfm?BSKT=0&USA_ship=1#AttenuationChart) [38].

There must be a matching of the SWR to 2–3. When supplied and conventional antennae were checked by the use of antenna analyzers, it was found important to decrease the SWR (from ca. >20 for some) to ~ 2 –3. The inclusion of a low noise amplifier enabled an additional ~ 20 dB gain. Copious ferrites are used to minimize shield currents and RF interference (RFI) near active equipment.

The receiver is a software defined radio (SDR). SDR receivers (RTL-brand and the like) were used because of their high dynamic range, high bandpass stability, and excellent out-of-band rejection. The images shown are dynamic gradient with time markers on the left-hand side. The sample rate was 3.2 million samples per second (MSPS). Upper sideband (USB) was used to minimize imaging. Resolution was the highest achievable with a Blackman–Harris 4 window, although Bo Gardmark [39] suggests using Hann or Hamming windows for improved SNR along with a AD8317 log detector. The radio, or software defined radio, is capable of separating the received signal, or signals, received by the antenna. It functionally acts as a computation system to derive the Fourier transform of the signal. Other transforms can be used, but the frequency (Fourier) system is preferred.

Figures 1, 8–17 are based on what were first received by said receiver. Two types of images are shown in the figures. In one type, an instantaneous emission result is shown, with the frequency increasing from left to right. There, the RF intensity is shown as a function of frequency (horizontal). This is a single moment in time. The vertical axis

is relative intensity, in dB. In the second type, usually on the bottom of many figures, each peak appears as a dot on a line for each one moment in time, and time increases from top to bottom, as in a waterfall; after which the display type is named. The images shown are dynamic gradient with time markers on the left hand side in each case, with the data extending over a fraction of an hour. The brightness, or color, is qualitatively associated with the intensity of the signal. The sample rate was 3.2 MSPS. The USB was used to minimize imaging. Resolution was the highest achievable with a Blackman–Harris 4, Hann or Hamming window for improved SNR.

In Fig. 5, antenna feed line loss is shown as a function of frequency for various cables. The use of military grade coax (CNT400) decreased the transmission line loss by +90 dB, as shown, over RG58U. The RG58U relative attenuation line is at the origin (flat upper portion of the arrows in the figure) of the two arrows.

3.7. Analysis: calorimetry

The PHUSOR[®]-type, NANOR[®]-type, and MOAC components were extensively examined by calorimetry and electrical conduction to observe their active states thereby avoiding the inactive/electrical avalanches in the dry components [4], and H₂ exhaust in the aqueous ones [24]. In each of these cases, measurements were taken by at least one or more of three methods. Most importantly, for good, calibrated measurement, the electrically driven active components were compared to an ohmic control. Then, calorimetry and input-power-normalized delta-*T* are used to semiquantitatively ascertain energy produced, and infer specific activity.

Specifically, first, the energy produced is instantaneously and kinematically determined by the ratio of the input power normalized temperature increase, called by the symbol “delta T/P_{in} ” referring to the increase of temperature (delta T), divided by the input electrical power (P_{in}). Second, it is instantaneously and kinematically evaluated over a wide area by the ratio of the input power normalized heat flow leaving it, called by the symbol “HF/ P_{in} ” referring to the heat flow (HF) divided by the input electrical power (P_{in}). Third, it is examined by calorimetry, calibrated by the thermal ohmic control, and confirmed by long-term time integration. These three methods of verification are pooled to derived very useful information.

As one example, a working NANOR[®]-type device containing active preloaded LANR material was shown at MIT during the months of January 30 through March 2012 [3]. The excess heat, which this preloaded NANOR[®]-type LANR device demonstrated, was monitored three ways by class members. The duty cycle was split with control sequences and an ohmic control portion. A carefully controlled electrical DC pulse was applied into an ohmic resistor which was used to thermally calibrate the calorimeter. The dry preloaded LANR component was able to generate excess energy (clean efficient energy production, which is a matter of incredibly important utility) and to convert conventional thermometry into more useful calorimetry to observe and monitor it. The preloaded NANOR[®]-type LANR device demonstrated an average energy gain (COP) of $\sim 14 \times$ ($\sim 1412\%$) the input for a duration of several hours that it was observed (and levels of that order continued). The semiquantitatively measured output energy IS a significant energy gain which has always been a goal post for cold fusion, and beyond the realm for hot fusion on Earth by engineering means.

This demonstration was an improvement of incremental power gain over the previous open demonstration of the PHUSOR[®]-type LANR devices including BOTH at MIT and when he later developed larger systems (ca. 2004–2006 involving paired Stirling engines driven by LANR systems which showed 19 W of excess power [1,29,30].

3.8. Analysis: coherent Raman scattering

Classical Raman spectroscopy involves the inelastic scattering of light which generates new frequencies which result from the interaction of light the irradiated matter [40]. Raman–Stokes scattering transfers some of the energy from the incident light to excited states in the irradiated material, and thus some of the reflected wavelengths are red-shifted.

Raman anti-Stokes scattering results when the irradiated material already contains excited states, and the reflected photons are blue-shifted by the difference in energy between the excited states returning to their ground state. The major problem of the Raman effect is that it produces very weak signals because the photon conversion efficiencies are less than 10^{-18} . Therefore, Sir Raman stated that the effect has “excessive feebleness” [40]. This small signal results because the proportionality constant $\chi(3)$, known as the “third-order susceptibility”, is only linearly proportional to the local oscillator density. However, that is not the case when irradiation is made using coherent lasers which yield a much larger signal because with coherent illumination there results phase-matching conditions and quadratic dependence on the number of local oscillators. Thus, even with the same selection rules, the coherent irradiation Raman effect yields a much greater signal intensity, about 10^6 times greater [41,42].

The CMORE spectra detect the active modes of nanomaterials [11,12,24] and aqueous CF/LANR systems [22]. Those involving ZrO_2 preloaded active nanomaterial demonstrating power gain have been the most studied. The spectra show reflected optical intensity as a function of wavelength, initially from two incident coherent optical beams but then reflected by backscatter along with the initial optical beams from the nanomaterial. The CMORE spectra reveal different types of activity states from the same sample, observed by the same diagnostic. Specifically, they saliently show that for the same NANOR[®]-type component electrically driven there are two states (the unwanted electrical avalanche mode [10,24] and the optimal operational state, the desired, active XSH mode, where excess energy is being released), and “off”. There is diversity in outcome. Characteristic anti-Stokes peaks only appear when the electrical drive generates excess heat but differ in energy, amount, and in what stimulates their appearance. When driven in the avalanche mode, the anti-Stokes peaks differ considerably from those which appear during the excess heat-producing or desired mode.

3.9. Energy and flux units

The terms used in the physics of RF electromagnetic radiation analysis is very close to those used in calorimetry. Here, the rate of change of energy is called Luminosity.

$$L = dE/dt \quad (\text{Watts} = \text{J/s}). \quad (1)$$

With these emitters and antenna, radial and spherical volume corrections are made, therefore correcting the luminosity thereby – which becomes the irradiation flux.

$$\text{Irradiation flux } f(R), \quad S = L/4\pi R^2 \quad (\text{W/m}^2). \quad (2)$$

When account is taken of the frequency, this becomes the irradiation flux density, where the density refers not to a solid volume but frequency space itself

$$\text{Irradiation flux density } S(\lambda) = dS/d\lambda \quad (\text{W/m}^2/\text{Hz}). \quad (3)$$

For normalization, irradiation flux density, $S(\lambda)$ is compared to the reference unit, the Jansky. Two radioastronomic targets are listed below it, in those preferred units.

$$1 \text{ Jy} = 10^{-26} \text{ W/m}^2/\text{Hz} = 10^{-23} \text{ erg/s/cm}^2/\text{Hz}. \quad (4)$$

Sun: $4 \times 10^{-22} \text{ W/m}^2/\text{Hz}$ @ 100 MHz, Cas A: $2 \times 10^{-22} \text{ W/m}^2/\text{Hz}$ @ 100 MHz.

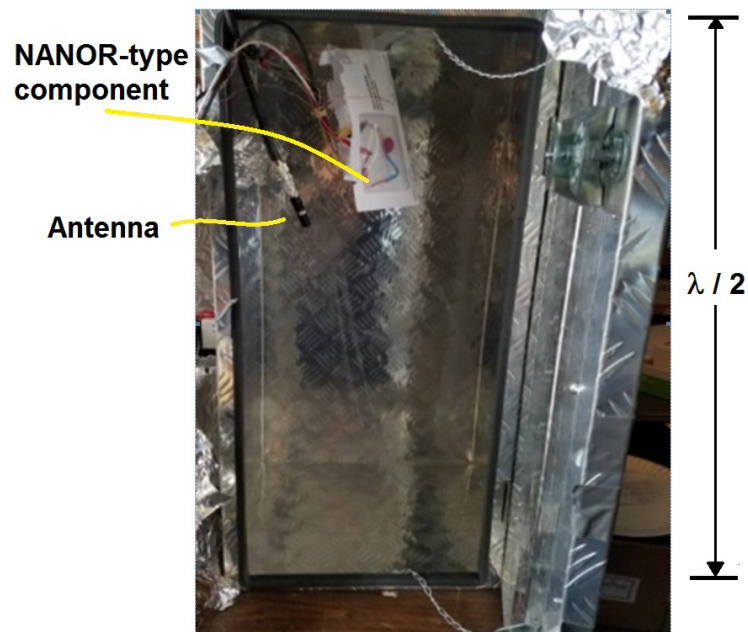


Figure 6. Resonant Fabry–Perot maser cavity.

3.10. Resonant chamber

To achieve a functioning system, a maser was created requiring the electrically driven material to be contained in a Fabry–Perot container. The protected frequency(ies) require that it also be contained within a Faraday cage. Therefore, the active emitting portion is held and contained within a box of electrically conductive surfaces which is used to act as a resonant cavity. Therefore, for a resonant cavity the length of the box must be equal to a half wavelength, in at least one direction, of the desired emitted photon.

The 36.05-inch long metallic case used as the resonant cavity with the half wavelength set vertically. Shown – while open and the second Faraday cage removed – are the antenna, beginning of transmission line, and NANOR[®] type component. A white envelope is seen, surrounding the NANOR[®]-type CF/LANR component to easily detect, and to protect against, falling or extravasated nanomaterials. It also in the photograph better shows the depth into the rhombic shaped cavity. For the experiment, the door was shut, sealed, covered with multiple layers of aluminum foil and wiring with all connected to a driven copper rod driven into the Earth as ground.

Figure 6 shows the resonator box used to surround the NANOR[®] type component which was required to make a functional maser. For this, a 36-inch long metallic case was used as the resonant cavity with the half wavelength set vertically. For each experiment/run, the door was shut, sealed, covered with aluminum foil and connected to a driven copper rod driven into the Earth. This essentially made a double Faraday cage to avoid interference. Figures 1, 9, and 10 show the impact of adding the resonator box: blazing maser output.

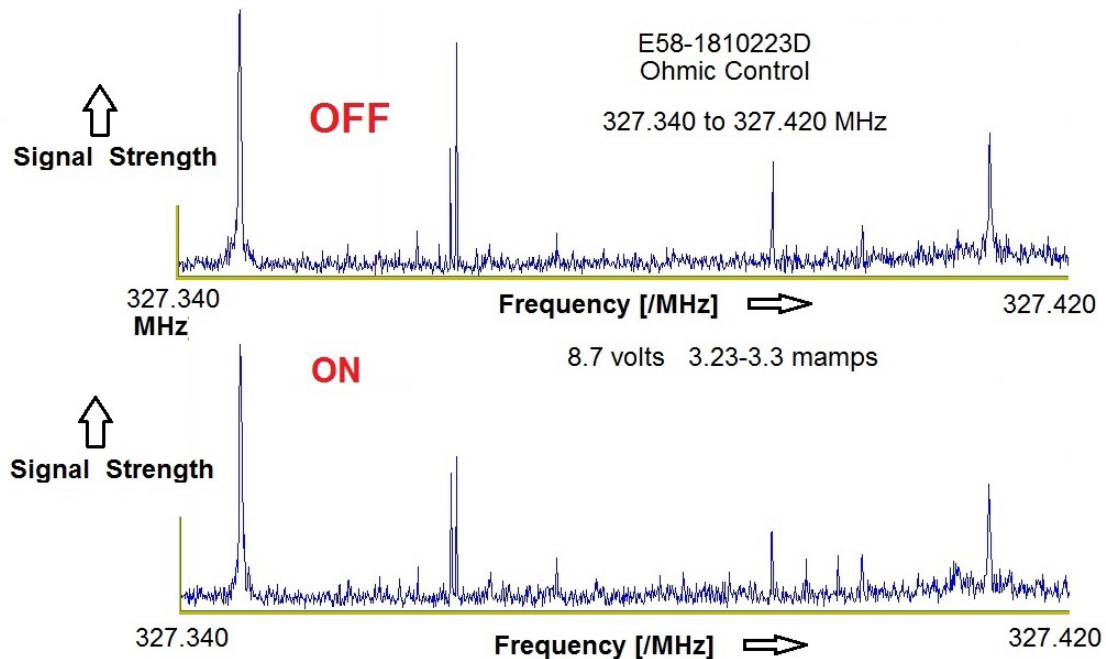


Figure 7. RF intensity in the DL region as a function of frequency for two ohmic controls showing no significant change.

4. Results

4.1. Galactic controls, cosmic background

Interference has been considered, and minimized, by monitoring over several weeks, and comparison to known frequency dispersions and examination of bandwidth. Changes as a function of time and/or frequency have led to the identification of modulated (military in this band) signals, and galactic input. Possible television transmitters, cell phones, microwave appliances, and ionospheric noise (QRN) have not been a significant problem at these frequencies given the long term monitoring and pre-identification.

For each experiment, attention has been necessarily made to the location of the Galactic center, and, when possible, measurements have been made when the Earth is optimally shielding emissions from the galactic center. This was found to be much less needed once the resonator box was correctly grounded. As background, the Galactic center continuum is reported to have nonthermal background of ~ 500 K (with a 25-element sub-array, 23 dB gain, 12° beam width, 12 m^2 effective aperture). The Galactic anticenter has a nonthermal background of ~ 70 K and, therefore, any deuterium excitation temperature ≥ 130 K causes appearance of RF emissions.

Investigators should use two well-ground Faraday cages, and are advised that it may take weeks to understand the background. However, not having a detailed understanding of the vast background does not preclude using the DL to monitor and better understand CF/LANR and other emitters.

4.2. Ohmic controls yield no RF DL emission

The possibility of RF emissions from ohmic controls was examined in driven samples. None were ever seen. Figure 7 shows the RF emissions in the region from 327.340 to 327.420 MHz (the DL region) for two ohmic (thermal) controls. There were no peaks directly associated with driving the ohmic controls even at much higher electrical input power levels. “ON” refers to the application of electrical power; after it is “OFF”. Simply put, multiple RF intensity vs. frequency plots taken in the DL region demonstrate the apparent absence of similar RF emission activity from such ohmic controls. Only the original galactic background was seen unchanged from electrically driving the ohmic controls. This was unlike the active CF/LANR components which received less than 0.1% of the power delivered to the ohmic controls but instead gave forth blazing maser outputs (Figs. 1, 8–17). In this case, for this paper, the controls included having nothing in the Faraday cage with full double shielding as discussed above, and included having the NANOR[®]-type component present in the cage but being NOT electrically driven. In addition, controls included having in the same electrical circuit an electrically driven ohmic control instead of the NANOR[®]-type component. In this case, the ohmic control consisted of a carbon resistor, but in the future both wire-wound and film resistors should also also be examined.

4.3. Narrow bandwidth RF emissions

Unlike the result from the ohmic resistors (e.g. Fig. 7), there is a clear LANR-related narrow bandwidth solid state DL MASER emission at 327.7 MHz resulting ONLY from electrically driving some of these ZrO₂PdD preloaded NANOR[®]-type LANR components (7-4 and 7-5; [1–12]), carefully below their avalanche voltage [4] which is a regime where excess heat has been shown to suddenly cease and desist. These very narrow bandwidth emission peaks (some singular, and others with sidebands) are hundreds of Hertz wide in a frequency band of 327 MHz. The narrow bandwidth RF emission peaks which appear with electrical drive are located very close to the expected emission of deuterium. This is not Doppler shift because both are in the same frame-of-reference, and confirming that there is no evidence of broadening (vide infra). This is reproducible solid-state LANR maser action.

These control RF intensity plots (Fig. 7) taken in the DL region demonstrate the salient absence of RF emission activity for ohmic controls at the relevant range of frequencies. The original galactic background was seen unchanged from electrically driving the ohmic controls.

Figures 1, 9, and 10 show the maser at its stabilized frequency ca. 327.364 MHz. It was found that electrical potential inputs of 1.05–2.4 V were sufficient to drive the maser. It shows three curves which plot the hyperfine RF output from a prefilled nanostructured PdD–ZrO₂ material, at three moments of time. Figure 10 shows the appearance of the DL emission acting as a maser at its stabilized frequency ca. 327.364 MHz. These three graphs which show the instantaneous intensity of the RF emissions in the region from 327.360 to 327.370 MHz (the DL region) as a function of frequency and applied electrical potential to the NANOR[®] type component N7-4. The first graph (top) has the component wired up but no applied driving voltage. The second graph (middle) had the component received 1.02 V electric potential across it. The third (bottom) had the component with 2.4 V potential across it. It was found that electrical potential inputs of 1.02–2.4 V were sufficient to drive the maser. A high-*Q* output $>1.2 \times 10^6$ is seen at 327.364 MHz consistent with maser activity. These maser RF outputs in the active CF/LANR state occurred nearly reproducibly for at least two slightly different types of LANR components. The other RF emission line on the right is galactic in origin, in the three graphs. It is important that the RF DL hyperfine emissions come only from LANR (CF) active cells containing high loaded levels of deuterons. First, it proves that D is the fuel. Second, the RF emission demonstrates that the deuteron, in the excited pre-⁴He state is a D free radical. Third, the emission is normally forbidden on Earth, and here it shows up ONLY when there is excess heat. Thus, this is important because it is a signal for working, active LANR systems, providing information on the activity.

4.4. Resonant chamber improved stimulated emission

As a result of these positive findings: maser action consistent with excess-heat-producing active modes for these CF/LANR components, efforts were made to improve the system using a well-grounded resonant chamber which would also act as a second Faraday cages to further protect the radio environment. Once in the resonator cavity, there was blazing, spectacular success after it was slowly learned how to better turn on and control the maser. In addition, it was found that a well-grounded resonant (Fabry–Perot in at least one direction) chamber greatly improved output (cf. Figs. 1,9,10, and 17), offered improved clarity of the output emissions with removal of most of the interfering emissions. Thus, this arrangement achieved resonant-chamber-NANOR[®]-type components which have yielded low voltage, electron current controllable blazing LANR masers (Figs. 1,9,10,11, and 17).

First, these radiofrequency DL LANR emissions (327.37 MHz) herald an excited state of deuterium being present in lattice assisted nuclear reaction (LANR) active states, in both aqueous and dry preloaded systems. Second, this new solid state D-MASER was observed to have characteristic emissions exhibiting very narrow bandwidth, as well as other, possibly larger energy emissions over a much wider bandwidth also in the DL region (Figs. 13 and 14). This is similar to other observed masers' action. Surprisingly, it also enabled the facile determination of superhyperfine structure – there were sets of RF emission peaks, and not just a single peak. This is seen in Figs. 12 and 15.

In Figs. 7 and 8 also other figures, galactic DL are seen. Although there could be near complete exclusion, some input is on rare occasion allowed and used for calibration, yet still greatly diminished in amplitude by the electrically well-grounded resonant cage (Fabry–Perot cavity in one direction where $\lambda/2$ is ca. 36 inches).

4.5. Deuteron line RF LANR maser

In Figs. 1 and 9, maser activity is seen by the bright curved line using Software Defined Radio (SDR) Identification of the LANR DL maser emission. The images show the hyperfine output using a prefilled nanostructured PdD–ZrO₂ material, including an instantaneous intensity vs. frequency output on top, and a waterfall image of intensity, at various times, vs. frequency. In this dual graph, there are two regions. The DL RF CF/LANR maser emission line is indicated in both portions of the display. In both, the frequency increases from left to right. Markers of the frequencies (in MHz) are shown.

The top, upper portion is a graph which shows RF intensity peaks as a function of frequency (horizontal) at a single moment in time; in a single sweep. The relative intensity, in decibels (dB), is shown on the left-hand side. On the bottom, each peak appears as a dot on a line for each one moment in time, and time increases from top to bottom, as in a waterfall; after which the display type is named. The timestamp is on the left-hand side. This is an integrated graph over a fraction of an hour. The color in both portions, top and bottom, is qualitatively associated with the intensity of the signals. The gradient scale is shown. Depending upon the resonant cavity, and in the limited, attenuated galactic background, the main peak for deuteron RF emission can be clearly seen (Fig. 1), along with those other peaks (Figs. 1, 11, and 12). The other lines are from a variety of signals commonly observable, mainly military and cosmic. The DL RF CF/LANR maser line is 1–4 dB greater in intensity than all of the others lines. It is unclear why the emission frequency is not precisely the same as for free radical deuterium. It may be perturbations of the electron orbits in D secondary to the Ni or Pd in which it is a binary alloy. It may also arise from magnetic Ni or Pd atoms which impact the hyperfine, and now superhyperfine, splitting. Pd¹⁰⁵ (abundance 22%) has a nonzero nuclear magnetic moment, and we have discussed some of these magnetic Pd effects in this magnetized LANR components [10].

4.6. Initial superhyperfine line (sideband) drift

There is an initial drift for the major central peak and the sidebands. Figures 1 and 9 show the temporally controlled turn-ons and the slow drift of the RF maser output to lower frequencies. Note that the RF emission occurred imme-

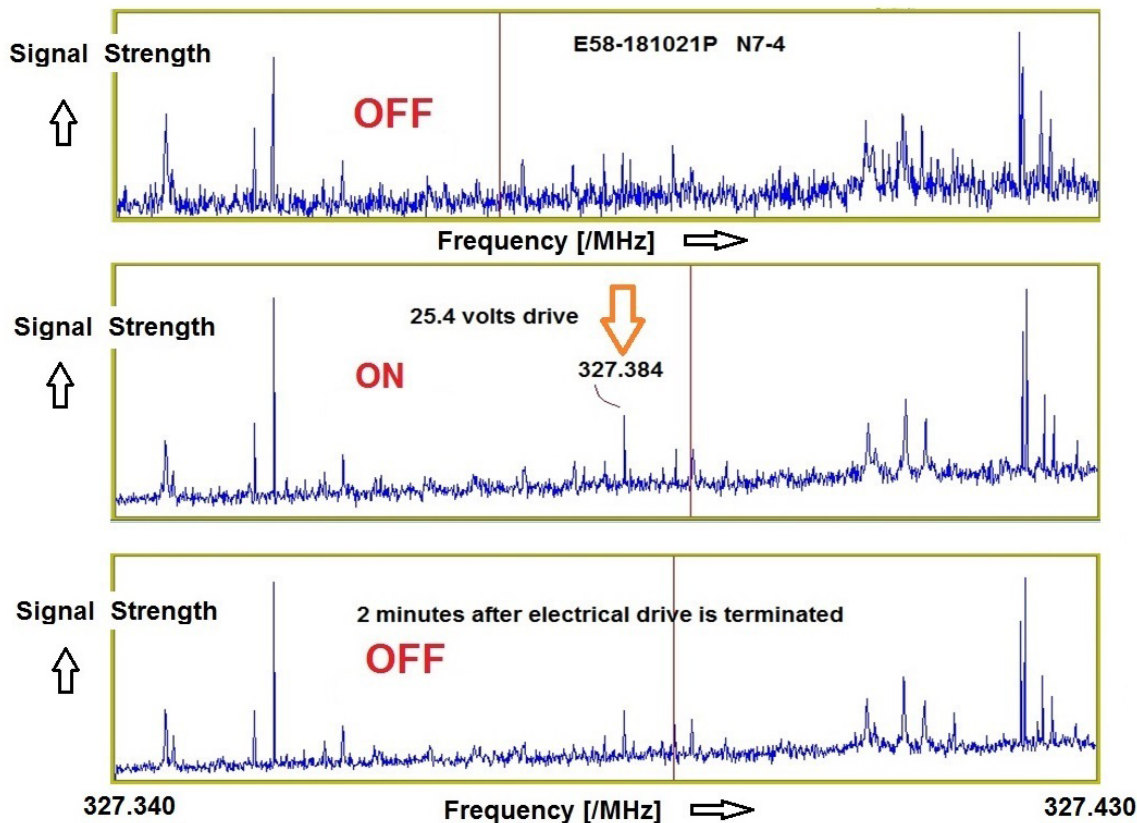


Figure 8. RF intensity as a function of frequency without resonant Cavity.

diately after electrical drive (1.2 V) (bottom left); followed by an exponential-like drift of the frequency to a slightly lower, more stabilized, monochromatic frequency. This drift toward a stable frequency, and other interesting behaviors were noted for these solid state LANR masers. The reason for this drift until stabilization remains unclear. Such behaviors have included hunting, drift, and chirping maser behavior,

4.7. Evanescent fall off of the peaks

The new narrow bandwidth RF emission peaks disappear with removal of the applied voltage. Despite a much faster rise time when maser action first appears after initiating electrical drive, there is a slower fall-off of the RF emissions within several (~ 3 – 4) minutes after electrical drive is terminated (Figs. 11,13, and 14). What controls the evanescent behavior as the maser output slowly disappear has neither yet been resolved nor understood. They may herald conditions within the loaded lattice, before its stereoconstellation re-attains equilibrium.

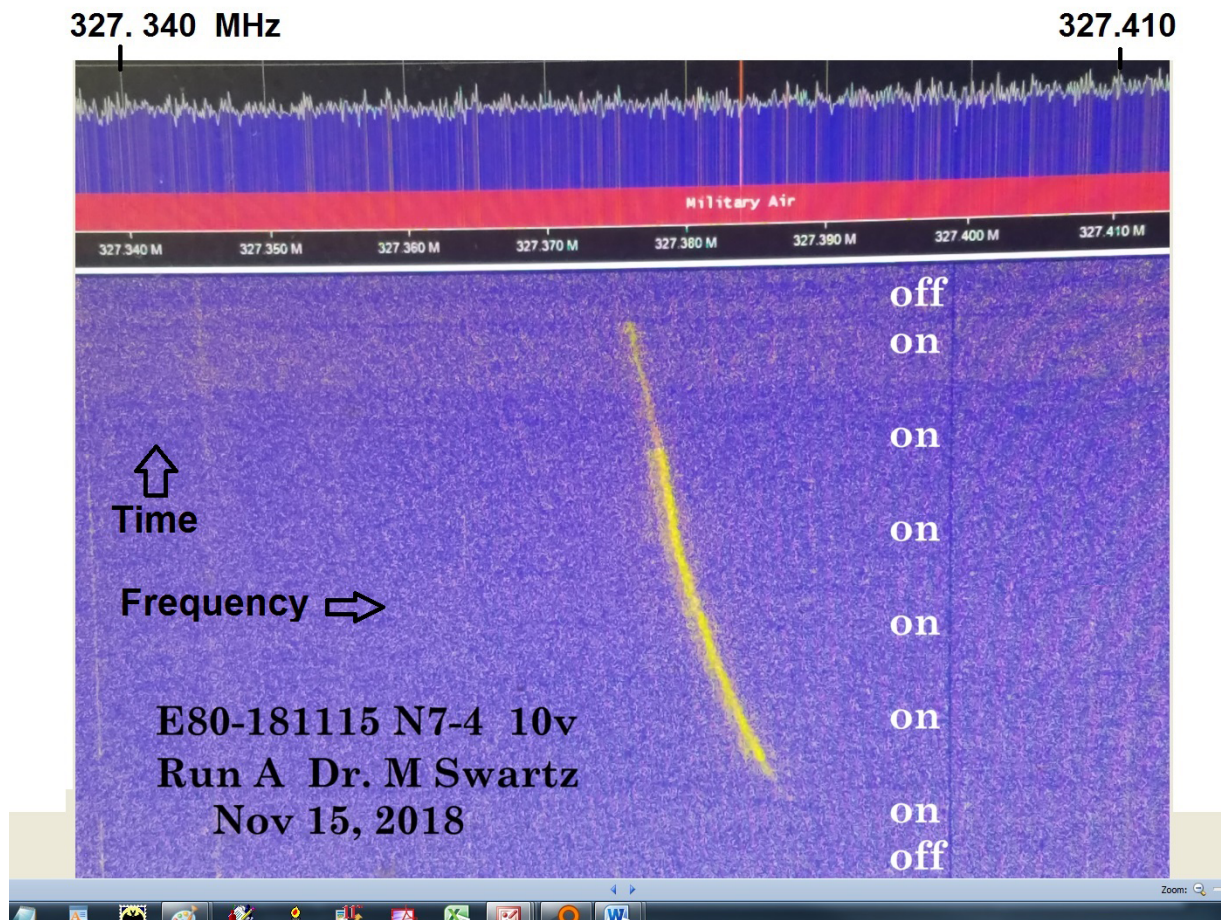


Figure 9. SDR identification of the first LANR DL emission (E58-181115A). On the bottom, time increases from top to bottom, and CF/LANR maser activity is seen by a bright curved line, with a sudden turn-on after electrical drive (10 V) initiated. This was followed by a drift to lower monochromatic frequencies. This is a photograph of the monitor from the very first maser emission achieved from an active CF/LANR device. It is a ZrO_2PdD NANOR[®]-type component, operated carefully in the resonance cavity below its avalanche voltage.

4.8. Wideband RF emissions

As described below, these solid state D-MASERS were observed to have characteristic emissions exhibiting very narrow bandwidth, as well as another very low energy emission over a much wider bandwidth, and also in the DL region. This can be seen in Figs. 16 and 17 semiquantitatively. For example, Figs. 13 and 14 show the RF intensity in the DL from 327.3 to 327.45 MHz presented as a function of time, with notation of the times during which the NANOR[®]-type component was electrically driven. This data does not count any of the RF main or RF sideband peaks (superhyperfine structure) which have all been subtracted. The derived RF emission density demonstrates a low level time dependent wide band contribution.

First, note that the low-level wideband RF emission is also evanescent. The RF high- Q peaks and the low level wider band emissions are linked, and both act similarly with respect to time.

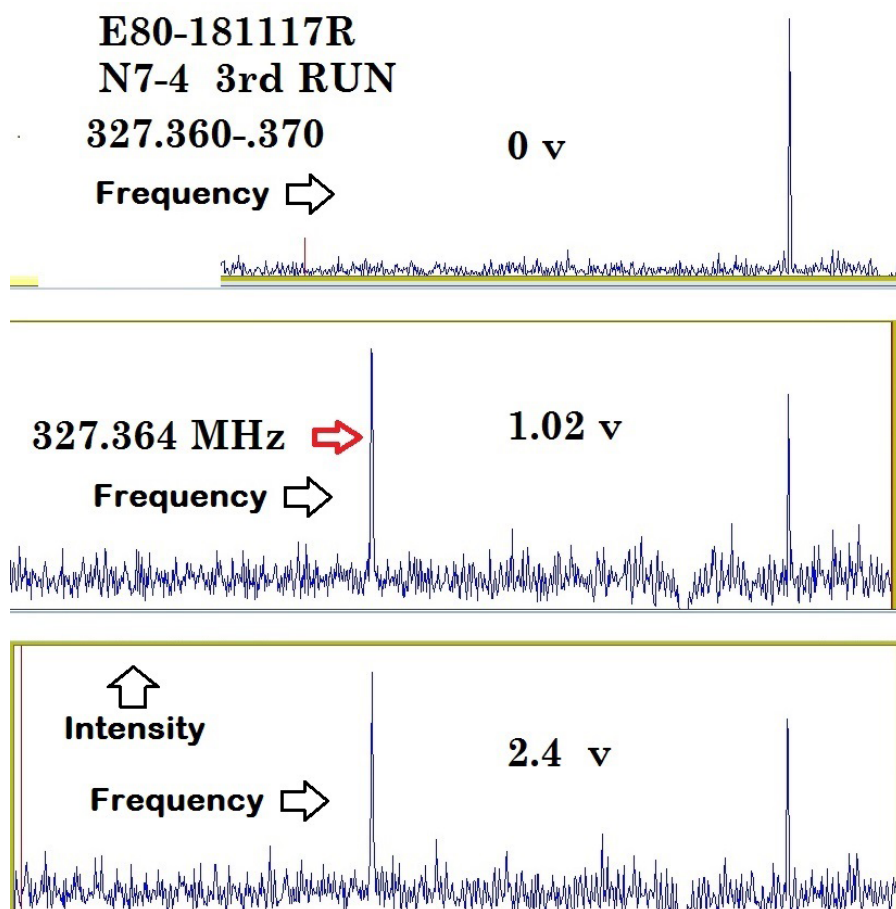


Figure 10. Appearance of maser line. Shown is the Intensity of the RF emissions in the region from 327.360 to 327.370 MHz (the DL region) as a function of frequency and applied electrical potential to the NANOR[®] type component N7-4. A high-*Q* output is seen at 327.364 MHz. The other RF emission line on the right is galactic in origin.

Second, because the bandwidth of an emission is related to the lifetime of the excited state, the wider bandwidth emissions may herald a second pathway with faster rates of de-excitation for some reason undetermined at this time. It is unclear what controls the wider band emissions from masers, but that must be investigated. Analysis of the wider bandwidth emissions may yield information on the Einstein A and B coefficients of de-excitation in these systems.

This lower energy wideband emission is similar to other observed masers' action [43].

In Fig. 8, comparison of the RF emissions in the region from 327.340 to 327.430 MHz (the DL region). The first graph was obtained with the NANOR[®]-type component N7-4 undriven ("off"). The second graph was obtained where the component was then electrically driven. The lowest graph is the return to "off", two minutes after termination of the electrical drive, but before the requisite time to have all the stimulated emission cease.

In Fig. 13, the energy in the RF band NOT INCLUDING THE PEAKS from 327.3 to 327.45 MHz obtained from NANOR[®]-type component N7-4, driven by 50.7 V applied, is presented as a function of time. A large magnet

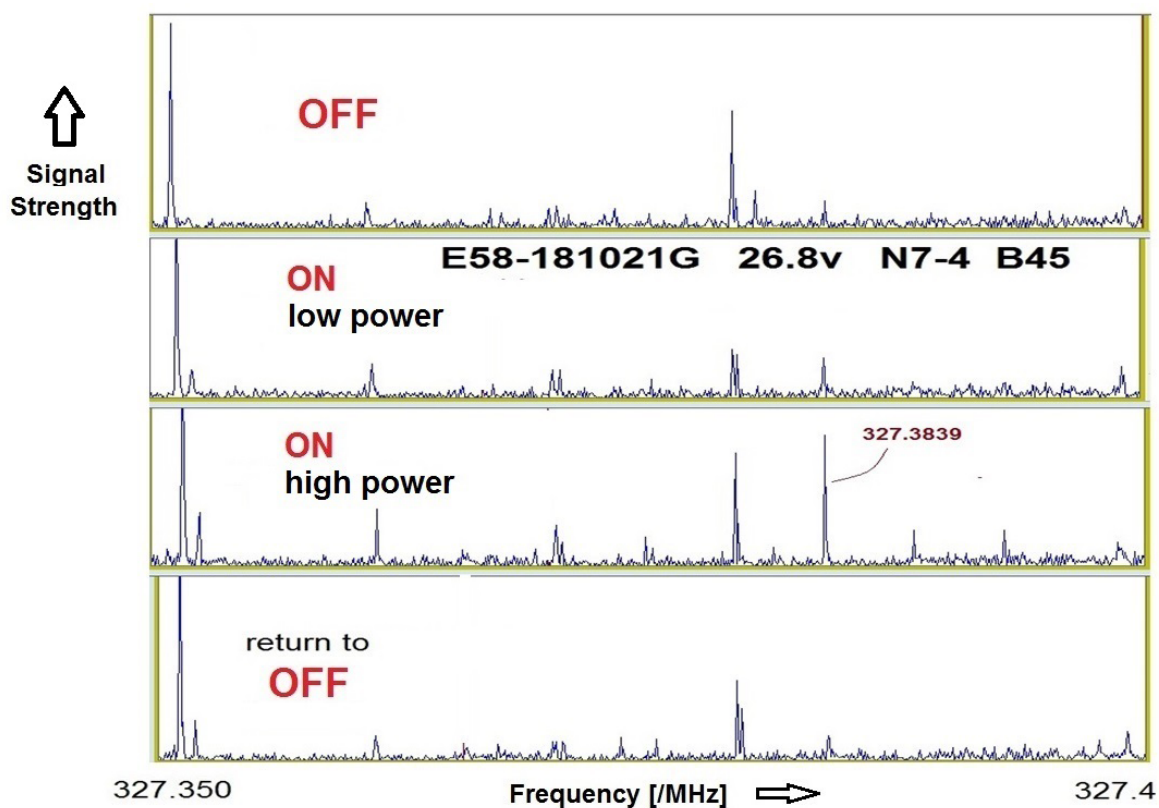


Figure 11. RF intensity as a function of frequency and electrical input power. Shown for comparison are the RF emissions in the region from 327.350 to 327.400 MHz (the DL region) obtained from NANOR[®]-type component N7-4. The top curve is undriven (“off”). The second graph was obtained where the component was then electrically driven. At higher electrical input power, some peaks (to the right of the identified increasing peak – 327.3839 MHz) also increase in amplitude and additional peaks appear. “ON” refers to the application of electrical power; after it is “OFF”. The lowest graph is the return to “off”.

was placed above the resonator box for this experimental run. The time scale is shown below it, along with the actual output in the regions without addition of the hyperfine and superhyperfine peaks. It is clear that there is some wideband emission and it is also evanescent with a time constant of minutes.

In Fig. 14, the energy in the RF band NOT INCLUDING THE PEAKS obtained from NANOR[®]-type component N7-5, driven by first 26.7 V, and then 50.4 V applied. A large magnet was placed above the resonator box for this experimental run. To the left is the integrated wide band output from 327.350 to 327.430 MHz with all peaks removed, presented as a function of time. The time scale is shown without addition of the hyperfine and superhyperfine peaks. It is clear that there is some wideband emission and it is also evanescent with a time constant of minutes.

4.9. RF emissions from active aqueous Ni MOAC

These experimental survey radio and LANR investigations examined and resolved, for the first time, the apparent absence of significant HL and the presence of DL emissions from the MOAC LANR (ordinary water) aqueous system

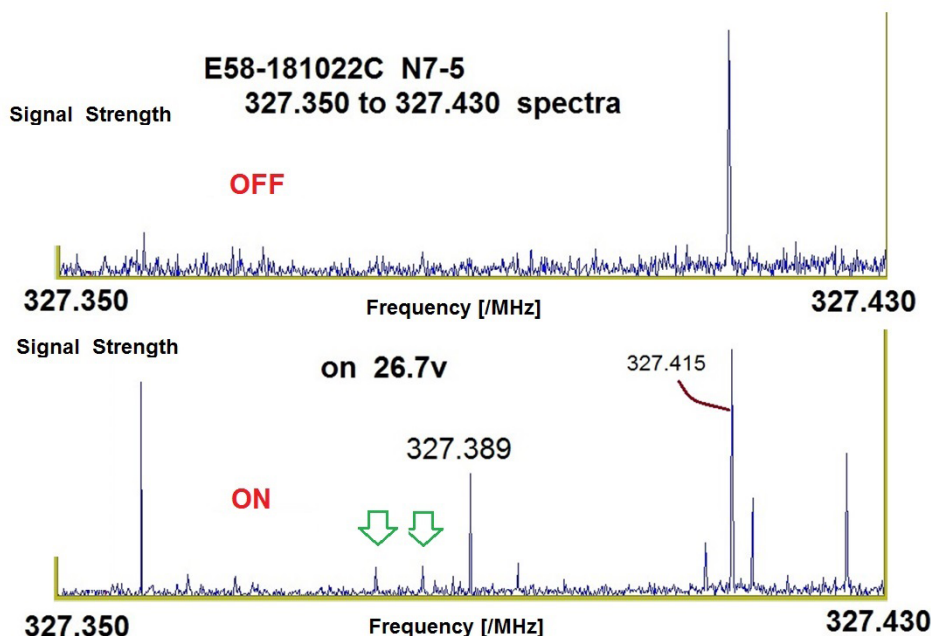


Figure 12. RF intensity as a function of frequency and electrical input power. Shown for comparison are the RF emissions in the region from 327.350 to 327.430 MHz (the DL region) obtained from NANOR[®]-type component N7-5. The top curve is undriven (“off”). The second graph was obtained where the component was then electrically driven at 26.7 V. An identified CF/LANR-derived peak is seen at 327.389 MHz, along with other smaller sideband peaks. A galactic peak at 327.415 is seen.

electrically driven during its active mode [13,14]. The HL and DL were the regions which were examined with the MOAC turned off over several hours. The initial HL results were inconclusive but with recent improvements in sensitivity and selectivity, further investigations are warranted. However, the DL investigation results showed something else.

Figure 15 shows these RF emissions from an active aqueous Ni MOAC using the present invention. Figure 15 is composed of three curves showing the output of the present invention using an aqueous Ni/H₂OD₂O/Pt system MOAC-type, at three moments in time, at three moments in time; post-loading no further electrical input, electrical drive at the optimal operating point, and just beyond that input power.

Figure 16 shows a clear comparison of the DL RF emissions from the aqueous MOAC in three different electrical current drives; each separated by vertical lines during three different times and electrical input powers (0, 450 mV, and 4 W). The first on the left is where MOAC was “OFF”. The second two were electrically driven at two input power levels. The central curve had its electrical drive point was very close to the peak of the optimal operating point (OOP) manifold. Figure 15 compares the emission in the RF region between ~ 327.25 and ~ 327.5 MHz (the DL region) for the MOAC while “off” and while it was electrically driven at two levels (top of OOP), and just to the “right” of the peak. The upper curves are a brief waterfall display. The central peaks are labeled by an arrow at 327.3 MHz). Attention is directed to the fact that there are distinguishable differences in both the integrated amplitude near that region, and in the nature of the superhyperfine structure (sidebands). The increased emission in the DL region is apparent. These sidebands are analyzed [13,14]. Because of the positive results in the aqueous system, it was elected

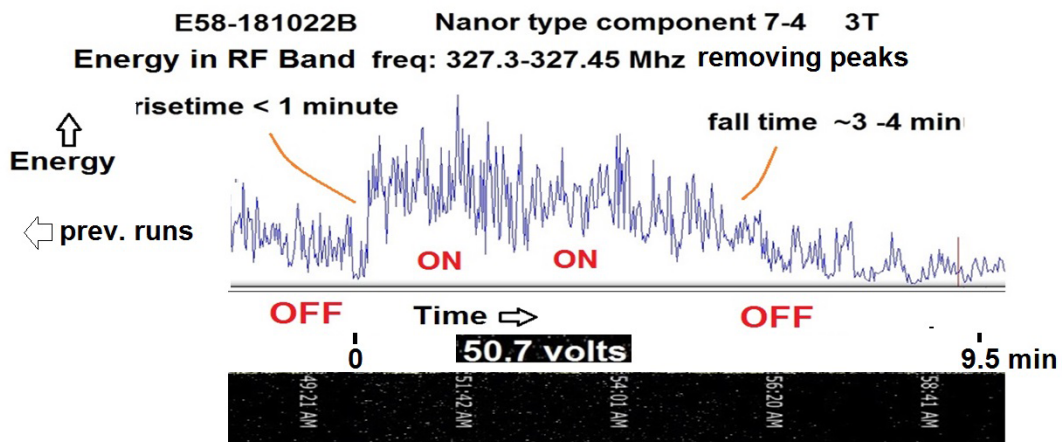


Figure 13. Wideband RF emissions in the DL region as a function of time.

to further investigate the dry, preloaded NANOR[®]-type components for possible RF emission, too.

4.10. Larger voltages reveal superhyperfine spectra

There are voltage-dependent peaks. The applied voltage increase yielding this display of superhyperfine sideband structure can be seen in Fig. 13. At higher electrical input power, some peaks increase in amplitude (327.3839 MHz) and additional peaks appear. The newly appearing peaks, like the previous LANR-active RF D-L peaks are evanescent

E58-181022F Nanor 7-5
3T 327.350 - .430
Dr. M Swartz 10/22/18



Figure 14. Wideband RF emissions in the DL region as a function of time.

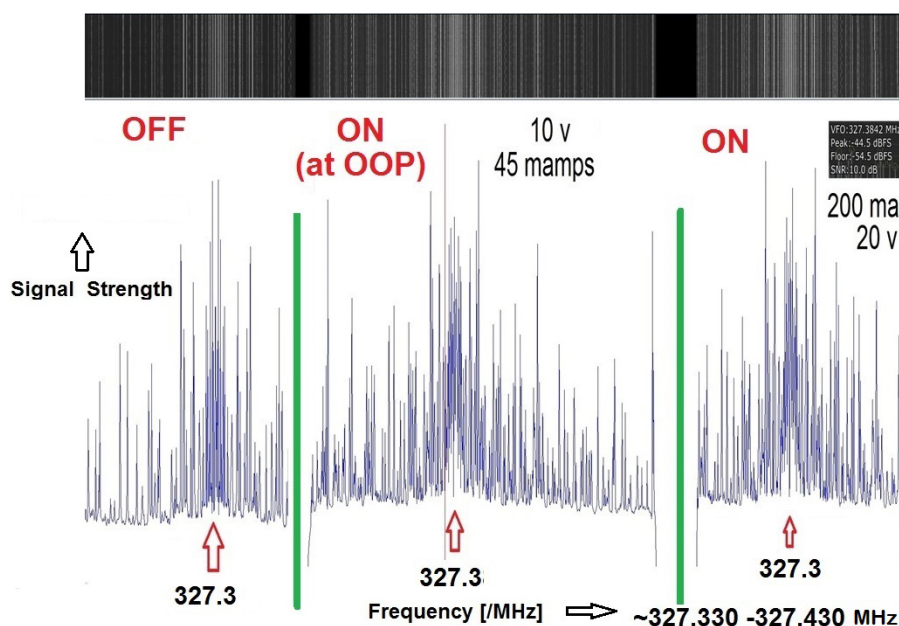


Figure 15. Comparison of the DL RF emissions from the aqueous MOAC in three different electrical current drives; each separated by vertical lines. These focus on the region from 327.3 to 327.43 MHz (the DL region) during three different times and electrical input powers (0, 450 mV, and 4 W). The first on the left is where MOAC was “OFF”. The second two were electrically driven at two input power levels. The central curve had its electrical drive point was very close to the peak of the OOP manifold [24,25,37]. The increased emission in the DL region is apparent with widening + increased amplitude.

when the power is turned off; and can be seen to disappear in the lowest graph (the return to “off”).

This needs to be further investigated as a function of input current, as well as power, because analysis may yield information on the collisions which lead to the desired reactions, as well as the material science. It might be important to note that the RF maser emission occurred at lower driving voltages than had been used to elicit other diagnostic techniques such as CMORE spectroscopy looking for antiStokes lines. It is unclear the reason, or why higher trans-sample voltages below threshold electrical avalanche voltage, elicited the superhyperfine lines (DL sidebands) appear.

4.11. Analysis of non-Zeeman superhyperfine line splitting for PdD

In the following papers [13,14] it will be shown that these energy and matter-magnetic field intensity power spectra can be analyzed to give metallurgical and material science information not otherwise available. The superhyperfine lines (SHFL) LANR-induced RF DL-emissions yield insight into LANR active site, the LANR active excited state, and the periodic magnetic locations surrounding the RF emitter. Most importantly, the next paper reports that the superhyperfine line structure of some of these LANR DL emissions appear consistent with the RF-emitting deuteron being located in an FCC vacancy [13]. This is important, and it also reveals insight into the stereoconstellation surrounding the LANR active site.

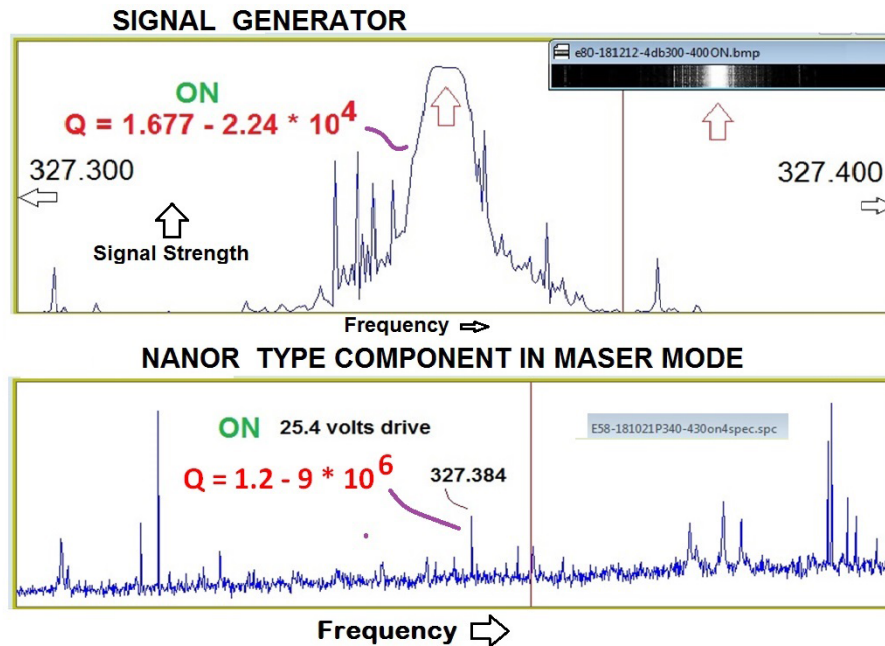


Figure 16. RF intensity in the DL region for a signal generator showing the normal Q (bandwidth) of a conventional oscillator.

4.12. Signal generator control

Figure 16 shows an emission control consisting of a signal generator (Fig. 4) employed to check frequency and normal bandwidth. Under a Faraday cage, signal generator controls were employed to check frequency and normal bandwidth. It shows the RF emissions in the region from 327.300 to 327.400 MHz (the DL region). The arrows show the frequencies (in MHz) of the far-right, and far-left of the figure. Figure 16 contains two curves which clearly show the very high- Q of the hyperfine output by plotting, at two moments of time, the instantaneous intensity vs. frequency. The figure shows RF intensity plots taken in the DL region for both the signal generator (on top) which has the normal Q (bandwidth) of a conventional oscillator, and the NANOR[®]-type component (on the bottom).

These demonstrate the amazing difference between the output of the signal generator and the NANOR-type component. This is thus a control which consists of the output of a signal generator added in the first upper, run. The upper curve has a brief waterfall display (on the very top). For this, a ZrO₂PdD preloaded NANOR[®]-type LANR component, operated carefully below the avalanche voltage, did emit very narrow bandwidth RF emission peaks ($Q > 1.2 \times 10^6$) in the DL (DL; 327.37^{+/-1} MHz) region. The high- Q (ultra-narrow bandwidth) of the emitted radiation (Figs. 3–8) is consistent with maser activity, and only appeared when the components were in their active electrically driven state.

In Fig. 16, these RF intensity plots taken in the DL region demonstrate the difference between the output of the signal generator (a conventional oscillator; top) and the NANOR[®]-type component (bottom). The arrows show the frequencies (in MHz) of the far-right, and far-left of the figure. Attention is directed to the fact that the signal generator had a Q less than 2.3×10^4 .

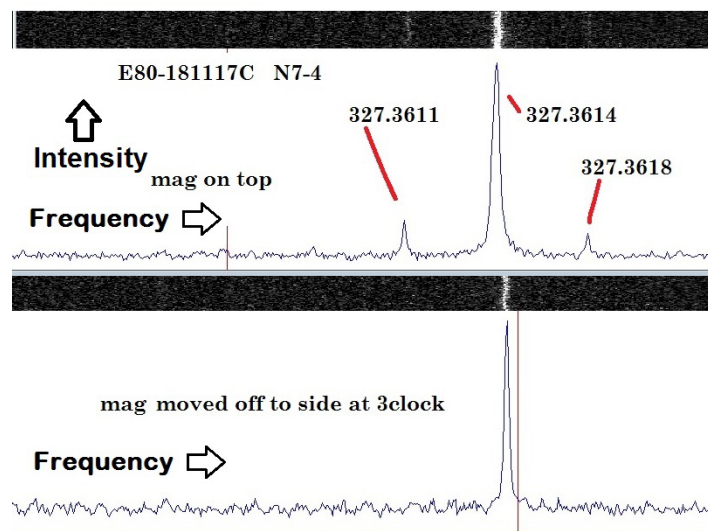


Figure 17. Impact of direction of applied magnetic field intensity. Shown for comparison are the RF emissions in the region from 327.350 to 327.430 MHz (the DL region) obtained from NANOR[®]-type component N7-4, with a large magnet placed above (top curve) and to the side (bottom curve) of the resonator box. A magnetic field parallel to the cavity axis causes Zeeman splitting and which decreases when moved perpendicular (and, after which, was then removed entirely) is shown in Fig. 15. There was splitting when the magnet was placed only above the box. These Zeeman effects/observations are consistent with reports of masers [44].

4.13. Positive Zeeman effect by an external magnetic field

Figure 17 shows Zeeman splitting of the emission peak by an external applied magnetic field. The figure shows two curves which demonstrate the Zeeman effect by plotting the hyperfine output at two successive moments of time with a large applied magnetic field intensity above the long axis, and to the side of the long axis; with each showing instantaneous intensity vs. frequency. Specifically it shows the impact of the direction of said applied magnetic field intensity to an active CF/LANR system being monitored by the present invention. Shown for comparison are the RF emissions in the region from 327.350 to 327.430 MHz (the DL region) obtained from NANOR[®]-type component N7-4, with a large magnet placed above (top curve) and to the side (bottom curve) of the resonator box. The baselines are otherwise relatively flat in the dual Faraday cage/Fabry–Perot resonant cavity (aluminum). The upper curve and lower curve, each have a brief waterfall display (above each).

It was found that a magnetic field parallel to the major resonant cavity axis caused clear Zeeman splitting of the main peak (at 327.3614 MHz) to a triplet (paired peaks added to the side of the main peak). The intensity of the doubled decreased – and then disappeared – when the magnetic field intensity was moved perpendicular to the major axis, as shown in Fig. 17. There was splitting when the magnet was placed only above the box. These Zeeman effects/observations are consistent with reports of masers. First, it was found that a magnetic field parallel to the major resonant cavity axis caused clear Zeeman splitting and which decreased when the magnetic field was moved perpendicular to the major axis, as shown in Fig. 17. Second, because of the potential interference, thereafter, all additional external magnetic fields were removed, although the Earth's field was not corrected for by the use of Helmholtz coils.

5. Interpretation

5.1. Consistencies with earlier reports

The RF emission may be consistent with some early reports, although they appear to have been at other frequencies [45].

5.2. Analysis of Q factor

The resonance of a system can partially be described by the Quality Factor (Q factor). This is a non-dimensional number. It is also an inverse measure of the strength of the damping of a system's oscillations, and it shows up as the system's relative (frequency normalized) linewidth. Although originally used for electronic LC circuits, it has since been useful for microwave cavity and optical resonators. There are actually two different connotations of the Q factor.

5.2.1. Definition of Q involving energy storage

The Q factor is 2π times the ratio of the stored energy to the energy dissipated per oscillation.

5.2.2. Definition of Q as defined by resonance bandwidth

The Q factor is the ratio of the resonance frequency to the full width at half-maximum (FWHM) bandwidth vicinal to the resonance.

These two different definitions are only the same for weakly damped oscillations (high- Q) such as the case here. The Q factor equals 2π times the exponential decay time of the stored energy times the optical frequency.

5.3. Analysis of broadening and shift

As suggested by Lawrence Forsley at the 2019 MIT Colloquium, bandwidth may yield Doppler information regarding velocity and other information. The CF/LANR maser must now be considered for both broadening and shift. As in NMR spectroscopy, the lifetime of the excited state of $^4\text{He}^*$ creating the D which then emits RF at the DL is relatively long, so in both cases the lines are very sharp, producing the possibility of high-resolution superhyperfine CF/LANR spectra.

5.3.1. Analysis of line shape

Analysis shows that the RF output curve is Lorentzian in shape, and not Gaussian. This heralds an exponential energy decay of the excited state rather than a step function because the Fourier transform of an exponential time function is a Lorentzian in the frequency domain.

5.3.2. Natural broadening

The uncertainty principle connects the lifetime of the excited state of D^* (due to spontaneous or stimulated RF decay or the Auger process) with the uncertainty of the energy of the transition. This produces natural broadening and there is no associated shift.

5.3.3. Doppler broadening

Analysis of bandwidth includes looking for Doppler information regarding velocity, Doppler broadening results from atoms in a gas emitting radiation while the atoms have a distribution of velocities. Thermally, the higher the gas temperature, the broader the spectral line emission. This broadening effect is described by a Gaussian profile and there is no associated shift. This is not significantly seen here.

5.3.4. Collision broadening

Impact pressure broadening or collisional broadening results from collisions which interrupt the emission, and increase the uncertainty in the energy emitted. The broadening effect produces a Lorentzian profile and there may be an associated shift. There is no apparent pressure change here – except perhaps initially.

5.3.5. Resonance broadening

Perhaps the most important is resonance broadening. Resonance broadening occurs when the perturbing particle is of the same type as the emitting particle and it introduces the possibility of energy exchange processes. The resonance broadening goes as $1/r^3$.

$$\Delta E_{RB} \sim 1/r^3. \quad (5)$$

This is importantly observed, and appears to give rise to the discovered superhyperfine splitting (discussed in detail in [13,14]). Also, resonance broadening may reveal information within periodic lattices.

5.4. Is this maser activity?

It is important to consider and confirm if this is really maser action. There are several characteristics and evidence consistent with maser action by these two solid state CF/LANRF components. Consider the following seven reasons beyond the fact that the signals are temporally linked to the excitation. First, the emissions have very narrow bandwidth. The Q (frequency over half power bandwidth) has ranged from 1.2×10^6 to some measurements at high as 9×10^6 . This high- Q is consistent with maser activity.

Second, microwave emission occurs and can be either spontaneous or stimulated emission, and the energy transit from the excited (2) state to the lower, de-excited (1) state is described by the Einstein A_{21} and B_{21} coefficients, respectively. Therefore, such emissions are “forbidden”.

$$\frac{A_{21}}{B_{21}} = \frac{8\pi h\nu^3}{c^3}. \quad (6)$$

Because the ratio of their contribution is very (third order) frequency dependent, then in the microwave region, at the DL line, spontaneous emission can be neglected. Therefore, this is also consistent, given the RF emissions, with maser activity.

Third, masers use materials (here heavy hydrogen, D) and move them into their metastable excited state. From their excited state they release a photon and move to the de-excited state. This use of LANR components which activate acoustic phonons for the desired state also heralds collisions between deuterons and palladium and zirconia, and that too is consistent with maser activity because in galactic masers, the pumping mechanisms are in part hydrogen/deuteron collisions. That is what we see when the NANOR[®]-type components enter the desired quantum electronic state producing excess heat (which is not the avalanche state).

Fourth, furthermore, that this is very probable maser action is supported by the fact that atomic deuterium as occurs in Group VIII binary metals has no electric dipole moment. Thus, in the palladium lattice where the desired reactions occur, deuterium and hydrogen are atomic. As in outer space, because atomic deuterium and hydrogen have no electric moment, this transition between these two states is highly forbidden with an extremely small transition rate. This makes the excited state long lived.

This also suggests that spontaneous transitions do not occur in the absence of a deuterium maser. This lack of transitions makes the excited state long lived, which is a *sine qua non* for achieving a population inversion. This may also enable further control of these reactions.

Also supporting this, the population inversion has also been seen indirectly by the antiStokes signature of ZrO_2PdD in the desired active state [11,12,24].

Sixth, further supporting that this is maser activity is that the input was very low power, and as the figures indicate the output has extremely low noise in this region, consistent with the role(s) of masers for low noise amplifiers, and very precise oscillators.

Finally, the emissions are supplemented by other larger intensity emissions over a much wider bandwidth. This is similar to the other observed masers. Nonetheless, these complex factors deserve further analysis to understand the nature and ratio of the two emissions. In summary, this brief analysis of the observations and their expectations shows that the characteristics are consistent with active state CF/LANR maser action.

5.5. Analysis of relationship to electron spin resonance

Atomic hydrogen is a free radical. This could also produce an ESR signal [46]. However, what is observed is linked but not like that signal. This is because a 300 Hz wide signal, normally appearing between 40 MHz and 4 GHz has a 1 in 20,000 chance of being in the correct zone of ± 2 MHz near the DL. And, the applied magnetic field induced splitting but did not shift it as would be expected for an ESR signal. This is being further examined because the electrophysics may be linked in one or more of the electronic states (“off”, subthreshold, excess-heat producing, avalanche).

6. Conclusions

6.1. LANR RF DL and maser findings

- (1) Active lattice assisted nuclear reaction (LANR) systems, both aqueous and preloaded nanomaterial, emit very narrow bandwidth RF hyperfine emission peaks (ca. 327.37 MHz) very close to the theoretical Deuterium Line (DL: 327.7 vs. 327.8 MHz).
- (2) There is a very large RF radiation flux density for the very small electrical input.
- (3) There is an initial DL, and sideband linked, frequency drift/shift until equilibrium.
- (4) There is a fall-off of both types within minutes (~ 3 min) immediately after electrical drive is terminated.
- (5) In addition to the characteristic RF DL emissions of very narrow bandwidth there are, in addition, other emissions of much lower intensity with wider bandwidth.
- (6) Active electrically driven LANR PdD-ZrO_2 preloaded components in a Fabry–Perot structure yield a low voltage solid state DL RF maser.
- (7) An active electrically driven LANR aqueous Ni-ordinary water system also emits at the DL. The two different solid state maser RF outputs, and the one from the aqueous MOAC in the active CF/LANR state show significant operating significance.
- (8) The DL RF emissions exhibit a large Q ($>1.2 \times 10^6$ – 9×10^6), which is the ratio of the bandwidth at half power to the frequency.
- (9) The solid state DL RF maser exhibits a positive Zeeman effect.

- (10) When electrically driven, at higher applied voltage, a superhyperfine structure of sidebands appears.

6.2. Confirmation of LANR fuel

- (11) These radiofrequency Deuteron-Line (DL) LANR emissions (327.37 MHz) herald an excited state of deuterium being present in LANR active states, in both aqueous and dry preloaded systems.
- (12) Most importantly, the DL emission frequency of these observations confirms the role of deuterium in CF/LANR systems making helium-4 which generates the observed excess energy in the active state [22,23, 47].

6.3. Derivation of active site

- (13) This method also gives more insight into the volume and stereoconstellation around the active CF/LANR site.
- (14) Analysis using putative nearest neighbors indicates a possible location of the deuteron free radical during its RF emission. The fuel generates the fusion product and at least some of these reactions occur in face center cubic (Pd FCC) vacancy for palladium (in PdD) or Zr (in ZrO₂).
- (15) Thus, vacancies, as predicted at ICCF-4 [15], are apparently the site of some of the desired reaction in these active systems. The coordination number is qualitatively associated with what is seen, except for some possibly very important changes. The second closest neighbors are now different. And this appears to have come from interaction with half of the fourth closest neighbors, with either that interaction of additional paramagnetic (possible lattice Zr in Pd contamination) factors, changing the singlet to multiplet. The results in nickel are more complex and demonstrate a range of both FCC and BCC vacancies, possibly heralding new metallurgic phases.

6.4. Possible elucidation of intralattice effects

- (16) These radiofrequency DL LANR emissions (327.37 MHz) identify connections between the loaded deuterons.
- (17) One important implication is that in active CF/LANR systems, the loaded deuterons work together from their vacancy sites and enable the desired XSH-producing reactions within the loaded Group VIII metal while emitting RF radiation at the Deuterium-line heralding the inverted population

6.5. New active state detection system

- (18) In addition, this system may have a future as a very improved LANR active-state detection system, perhaps able to give possible further information about LANR's difficult-to-attain most desired mode.
- (19) Recognition of CF/LANR RF emission from the active state is important because not only is the location active site is clearer, including surroundings which appear altered, but because now methods of detection can be aimed at the phenomena to discern the desired active XSH-producing driven state.

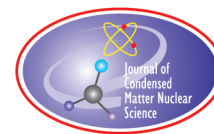
Acknowledgments

The author gratefully acknowledges and thanks David Nagel, Bo Gardmark, Gayle Verner, Peter Hagelstein, Lawrence Forsley, Louis Dechiaro, Isidor Straus, Joshua Gyllinsky, and Dan Steinberg for their very helpful comments, editorial assistance, and additional material. The author also thanks Brian Ahern, Alan Weinberg and the late Charles W. Haldeman for their construction, early testing, modifications, and transfer of the MOAC. This effort has been supported by JET Energy Inc., Nanortech Inc., and Anthropocene Institute, LLC.

References

- [1] M.R. Swartz, G. Verner and J. Tolleson, Energy gain from preloaded ZrO_2 -PdNi-D nanostructured CF/LANR quantum electronic components, *J. Condensed Matter Nucl. Sci.* **13** (2014) 528, www.iscmns.org/CMNS/JCMNS-Vol13.pdf.
- [2] M.R. Swartz, G. Verner, J. Tolleson and P.L. Hagelstein, Dry, preloaded NANOR[®]-type CF/LANR components, *Current Sci.* **108** (4) (2015) 595.
- [3] M.R. Swartz and P.L. Hagelstein, Demonstration of energy gain from a preloaded ZrO_2 -PdD nanostructured CF/LANR quantum electronic device at MIT, *J. Condensed Matter Nucl. Sci.* **13** (2014) 516, www.iscmns.org/CMNS/JCMNS-Vol13.pdf.
- [4] M.R. Swartz, P.L. Hagelstein and G. Verner, Impact of electrical avalanche through a ZrO_2 -NiD nanostructured CF/LANR component on its incremental excess power gain, ICCF-19, *J. Condensed Matter Nucl. Sci.* **19** (2016).
- [5] M.R. Swartz, Optical detection of phonon gain distinguishes an active cold fusion/LANR component, *J. Condensed Matter Nucl. Sci.* **20** (2016) 29–53, www.iscmns.org/CMNS/JCMNS-Vol20.pdf.
- [6] M.R. Swartz and P.L. Hagelstein, Increased PdD anti-Stokes peaks are correlated with excess heat mode, *J. Condensed Matter Nucl. Sci.* **24** (2017) 130–145.
- [7] M.R. Swartz, G. Verner, J. Tolleson, L. Wright, R. Goldbaum and P.L. Hagelstein, Imaging of an active NANOR[®]-type LANR component using CR-39, *J. Condensed Matter Nucl. Sci.* **15** (2015) 81, www.iscmns.org/CMNS/JCMNS-Vol15.pdf.
- [8] M.R. Swartz, Incremental high energy emission from a ZrO_2 -PdD nanostructured quantum electronic component CF/LANR, *J. Condensed Matter Nucl. Sci.* **15** (2015) 92, www.iscmns.org/CMNS/JCMNS-Vol15.pdf.
- [9] M.R. Swartz, G. Verner, J. Tolleson, L. Wright, R. Goldbaum P.L. Hagelstein, Amplification and restoration of energy gain using fractionated magnetic fields on ZrO_2 -PdD nanostructured components, *J. Condensed Matter Nucl. Sci.* **15** (2015) 66, www.iscmns.org/CMNS/JCMNS-Vol15.pdf.
- [10] M.R. Swartz, P.L. Hagelstein and G. Verner, Impact of electrical avalanche through a ZrO_2 -NiD nanostructured LANR component on its incremental excess power gain, ICCF-19, *J. Condensed Matter Nucl. Sci.* **19** (2016) 287–297.
- [11] M.R. Swartz, Optical detection of phonon gain distinguishes an active cold fusion/LANR component, *J. Condensed Matter Nucl. Sci.* **20** (2016) 29–53, www.iscmns.org/CMNS/JCMNS-Vol20.pdf.
- [12] M.R. Swartz and P.L. Hagelstein, Increased PdD anti-Stokes peaks are correlated with excess heat mode, *J. Condensed Matter Nucl. Sci.* **24** (2017) 130–145.
- [13] M.R. Swartz, Superhyperfine line structure of ZrO_2 PdD RF emission heralds a deuteron in an FCC vacancy, *J. Condensed Matter Nucl. Sci.* (2019), to appear.
- [14] M.R. Swartz, Pulsatile 327.37 MHz superhyperfine line heralds lattice mass–energy movements, *J. Condensed Matter Nucl. Sci.* (2019), to appear.
- [15] M.R. Swartz, Catastrophic active medium (CAM) theory of cold fusion, *Proc. ICCF4* **4** (1993) 255, sponsored by EPRI and the Office of Naval Research.
- [16] Important radioastronomical RF monochromatic spectral lines, <http://www.astrosurf.com/luxorion/radioastronomy-lines2.htm>.
- [17] J.H. Oort, The development of our insight into the structure of the galaxy between 1920 and 1940, *Ann. NY Acad. Sci.* **198** (1972) 255–266.
- [18] H. Hulst, C. Van DE, The solid particles in interstellar space, *Rech. Astr. Obs. Utrecht XI*, part 2 (1949).
- [19] E.M. Purcell, The lifetime of the 22 S112 state of hydrogen in an ionized atmosphere, *Ap. J.* **116** (1952) 457.
- [20] S.I. Weinreb, *Nature* **195** (1972) 367.
- [21] A.K. Dupree, S.L. Baliunas and H.L.I. Shipman, *Astrophys. J.* **218** (1977) 361.
- [22] M.R. Swartz, Increase of an anti-Stokes peak at the cathode of an electrically-driven, active aqueous nickel/H₂O/Pt system, *J. Condensed Matter Nucl. Sci.* **22** (2018) 279.
- [23] M.R. Swartz, B. Ahern, C. Haldemann and A. Weinberg, Excess heat is linked to deuterium loss in an aqueous nickel LANR system, *Proc. ICCF-21*, Fort Collins, CO, 6/3/18 (2018), *J. Condensed Matter Nucl. Sci.* **29** (2019) 169.
- [24] M.R. Swartz, Aqueous and nanostructured CF/LANR systems each have two electrically driven modes, *Proc. ICCF-21*, Fort Collins, CO, 6/3/18 (2018), *J. Condensed Matter Nucl. Sci.* **29** (2019) 177.
- [25] M.R. Swartz, Survey of the observed excess energy and emissions in lattice assisted nuclear reactions, *J. Scientific Explor.* **23** (4) (2009) 419–436.

- [26] M.R. Swartz, Improved electrolytic reactor performance using p-notch system operation and gold anodes, *Trans. Amer. Nucl. Assoc.* **78** (1998) 84–85, Nashville, TN, Meeting, (ISSN:0003-018X publisher LaGrange, Ill).
- [27] M.R. Swartz, Can a Pd/D₂O/Pt device be made portable to demonstrate the optimal operating point?, *Condensed Matter Nuclear Science, Proc. ICCF-10*, P.L. Hagelstein, S.R. Chubb (Eds.), World Scientific, NJ, ISBN 981-256-564-6, 29-44; 45-54 (2006).
- [28] M.R. Swartz, Investigations of “Heat after Death”, analysis of factors which determine the tardive thermal power and HAD enthalpy, *J. Condensed Matter Nucl. Sci.* **31** (2020) 20–41.
- [29] M.R. Swartz, Excess power gain using high impedance and codepositional LANR devices monitored by calorimetry, heat flow, and paired stirling engines, *Proc. ICCF14* **1** (2008) 123, ISBN: 978-0-578-06694-3, 123, (2010); www.iscmns.org/iccf14/ProcICCF14a.pdf.
- [30] M.R. Swartz and G. Verner, Excess heat from low electrical conductivity heavy water spiral-wound Pd/D₂O/Pt and Pd/D₂O–PdCl₂/Pt Devices, *Condensed Matter Nuclear Science, Proc. ICCF-10*, World Scientific, NJ, ISBN 981-256-564-6, 29-44; 45-54 (2006).
- [31] M.R. Swartz and G. Verner, The Phusor[®]-type LANR cathode is a metamaterial creating deuteron flux for excess power gain, *Proc. ICCF14* **2** (2008) 458, D.J. Nagel and M.E. Melich (Eds.), ISBN: 978-0-578-06694-3, 458, (2010), www.iscmns.org/iccf14/ProcICCF14b.pdf.
- [32] M.R. Swartz, G. Verner and A. Weinberg, Non-thermal near-IR emission from high impedance and codeposition LANR devices, *Proc. ICCF14* **1** (2008) 343, D.J. Nagel and M.E. Melich (Eds.), ISBN: 978-0-578-06694-3, 343, (2010); www.iscmns.org/iccf14/ProcICCF14a.pdf.
- [33] M.R. Swartz, Photoinduced excess heat from laser-irradiated electrically-polarized palladium cathodes in D₂O, *Condensed Matter Nuclear Science, Proc. ICCF-10*, ISBN 981-256-564-6, 213-226 (2006).
- [34] M.R. Swartz, Consistency of the biphasic nature of excess enthalpy in solid state anomalous phenomena with the quasi-1-dimensional model of isotope loading into a material, *Fusion Technol.* **31** (1997) 63–74.
- [35] M.R. Swartz, G.M. Verner and A. H. Frank, The impact of heavy water (D₂O) on nickel-light water cold fusion systems, *Proc. ICCF9*, China, Xing Z. Li (Ed.), May 2002, pp. 335–342.
- [36] M.R. Swartz, Codeposition of palladium and deuterium, *Fusion Technol.* **32** (1997) 126–130.
- [37] M.R. Swartz, Optimal operating point manifolds in active, loaded palladium linked to three distinct physical regions, *Proc. ICCF14* **2** (2008) 639, ISBN: 978-0-578-06694-3, 639, (2010).
- [38] RF cable attenuation composite includes,
http://cablexperts.com/cfdocs/tech_data.cfm?BSKT=0&USA_ship=1#AttenuationChart.
- [39] Personal communication, Bo Gardmark (2018).
- [40] C.V. Raman, Scientific papers of C.V. Raman, Vol. 1, S. Ramaseshan (Ed.), Indian Academy of Sciences, Bangalore, India, The Scattering of Light, 1988.
- [41] Ji-xin Cheng, Eric O. Potma and Sunney X. Xie, Coherent anti-Stokes Raman scattering correlation spectroscopy: probing dynamical processes with chemical selectivity, *J. Phys. Chem. A* **106** (2002) 8561–8568.
- [42] L.C. Evans and X. Sunney Xie, Coherent anti-Stokes Raman scattering microscopy: chemical imaging for biology and medicine, *Ann. Rev. Anal. Chem.* **1** (2008) 883–909.
- [43] M. Miles, Correlation of excess power and helium production during D₂O and H₂O electrolysis using palladium cathodes, *J. Electroanal. Chem.* **346** (1993) 99–117.
- [44] D.J. Wineland and N.F. Ramsey, Atomic deuterium maser, *Phys. Rev. A* **5** (1972) 821.
- [45] R.L. Plante, K.Y. Lo, R.M. Crutcher and N.E.B. Killeen, The magnetic field at the galactic center: detection of HI Zeeman splitting, American Astronomical Society, 183rd AAS Meeting, id.116.05; *Bull. Amer. Astron. Soc.* **25** (1993) 1467, AAS...18311605P.
- [46] Personal communication, Louis Dechiaro (2018).
- [47] Personal communication, P.L. Hagelstein (2018).



Research Article

Pulsatile Superhyperfine Lines at 327.37 MHz Herald LANR Activity and Possible Mass–Energy Transfer

Mitchell R. Swartz*

JET Energy Inc., Wellesley Hills, MA 02481, USA

Abstract

Active lattice assisted nuclear reaction (LANR) systems, both aqueous and dry preloaded nanomaterials, emit very narrow bandwidth hyperfine radiofrequency (RF) emission peaks at 327.37 MHz. This is located very close to the theoretical Deuteron-Line (DL; 327.348 MHz) region. At higher applied driving voltages, a complex superhyperfine line structure of sidebands appears. At least some of their emitting RF radiation superhyperfine line peaks, heralding the inverted population, are observed to be apparently pulsing. This may be a sign of real time mass-energy transfers within the high loaded Group VIII lattice.

© 2020 ISCMNS. All rights reserved. ISSN 2227-3123

Keywords: Atomic deuteron, Deuterium, LANR hyperfine lines, Pulsing superhyperfine line, Superhyperfine spectra, Resonance broadening, Vacancy active site

1. Introduction – CF/LANR RF Deuterium Line Emissions

Active cold fusion/lattice assisted nuclear reactions (CF/LANR) systems, both nanomaterial [1–14] and aqueous [13–29] emit very narrow bandwidth radiofrequency (RF) emission peaks (ca. 327.37 MHz), in the Deuteron-Line (DL; 327.348 MHz) region [30]. This paper reports that within the maser spectrum are pulsatile superhyperfine RF lines (PSHFL) with periods of minutes. It is unlike everything else examined over two years from Earth and galactic origin, and only associated with XSH from an ordinary water nickel CF/LANR system. The superhyperfine sideband line (SHFL) structure (Fig. 1) has been analyzed for this aqueous nickel CF/LANR system in its active mode. It may herald quantum mechanical movements or even perforation through the Coulomb barrier.

2. Experimental

2.1. Aqueous nickel LANR system

The high Q ($> 1.2 \times 10^6$) and Zeeman response indicate maser action. There is the appearance of maser line sidebands (superhyperfine lines) with increasing voltage (Fig. 1). They appear separated by resonance broadening and energy

*Mitchell R. Swartz ScD, MD, EE, ACIER, E-mail: drswartz@nanortech.com.

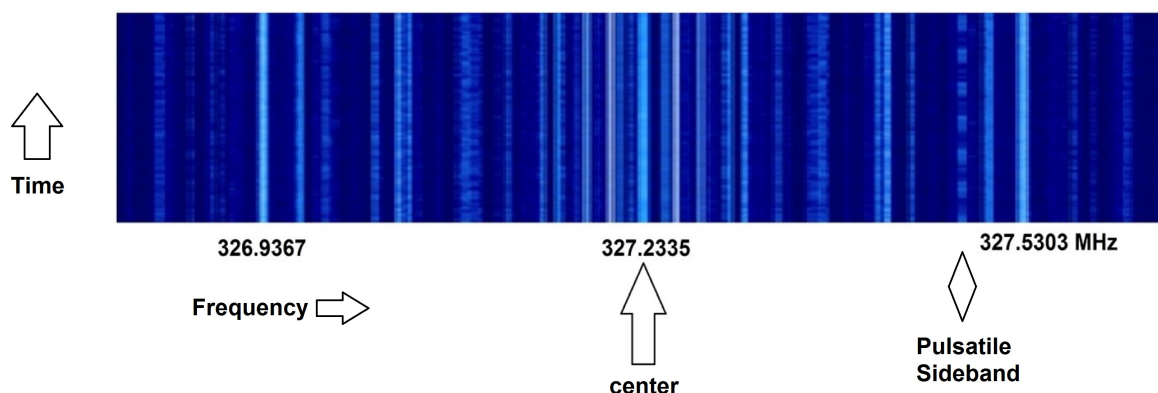


Figure 1. Pulsatile RF emissions in a background of other RF SHF lines. The radiofrequency superhyperfine DL spectrum of this nickel hydrogen loaded LANR system during its active state (40 V, 200 mA). This is a “waterfall” plot and intensity is shown as a function of frequency. Note the central arrow appears to almost be a vertical mirror along the horizontal axis. The largest amplitude pulsatile RF line is clearly visible on the right-hand side, and is marked by a star.

exchange processes [30,31]. Resonance broadening occurs when the perturbing particle is of the same type as the emitting particle and it introduces the possibility of energy exchange processes. The resonance broadening goes as $1/r^3$. The data uniquely shows the nearby sites surrounding the active site in an active nickel CF/LANR system studied. The Mother of all Cathodes (MOAC) cell has a 3 l capacity with a cathode weighing 2.132 kg (#46 hard drawn smooth nickel wire with an area of ca. 240,000 cm²). The electrolyte was a dilute carbonate solution in laboratory distilled deionized ordinary water. These studies used Deuterium Line (DL) emissions from the MOAC LANR (ordinary water) aqueous system electrically driven during its active mode [30,31]. For the calorimetry, calibration was determined by ohmic controls and other methods, as discussed elsewhere [13–29].

2.2. Methods – RF emission detection system

The previous paper [30] discussed in detail the arrangement of detecting the RF emissions. Software defined radio (SDR) receivers were used because of their high dynamic range, high bandpass stability, and excellent out-of-band rejection. The sample rate was 3.2 million samples per second (MSPS). Upper sideband (USB) was used to minimize imaging. Resolution was the highest achievable with a Blackman–Harris 4 window, Hann or Hamming windows.

The sensitivity of this detection system (signal to noise ratio: SNR) is proportional to $A * \sqrt{t}$, where A is the antenna’s collecting area, and t is the integration time. The signals are weak, and therefore the antenna is made with an aperture as large as possible, using a duck antenna system because of its easy fit into the resonance chamber. The use of antenna analyzers and matching decreased the standing wave ratio (SWR) from circa 20+ to 2 to 3. The use of military grade coax (CNT400) decreased the transmission line loss by +90 dB, and the low noise amplifier (LNA) provided an additional +20 dB gain. Ferrites are used to minimize shield currents and radio frequency interference (RFI) near active equipment.

3. Results

3.1. RF emissions from active aqueous Ni MOAC

This experimental survey began with preliminary amateur radio and LANR investigations that examined and resolved, for the first time, the apparent absence of Hydrogen Line (HL) and presence of DL emissions from the MOAC LANR (ordinary water) aqueous system electrically driven during its active mode [30,31]. The HL and DL were regions were examined with the MOAC off over weeks, to learn the galactic (followed by the zodiac) rhythm. The initial HL results were inconclusive but with recent improvements in sensitivity and selectivity, further investigations are warranted.

The DL results showed something else. Figure 2 shows these RF DL emissions from an active aqueous Ni MOAC. The figure shows the data for experiment E31=180 503 with the driving power off, and then at 10 V and 45 mA electrical current, and then at 20 V and ~ 200 mA electrical current. Figure 2 is composed of three curves showing the output of an aqueous Ni/H₂OD₂O/Pt system MOAC-type, at three moments in time, at three moments in time; post-loading no further electrical input, electrical drive at the optimal operating point, and just beyond that input power. Figure 2 compares the emission in the RF region between 327.25 and 327.5 MHz (the D-line region) for the MOAC while off and while it was electrically driven at two levels (top of OOP), and just to the right of the peak. The upper curves are a brief waterfall display. The central peaks are labeled by and arrow at 327.3 MHz). The figure shows a clear comparison of the D-line RF emissions from the aqueous MOAC in three different electrical current drives; each separated by vertical lines during three different times and electrical input powers (0, 450 mW, and 4 W). The first on the left, is where MOAC was OFF. The second two were electrically driven at two input power levels. The central

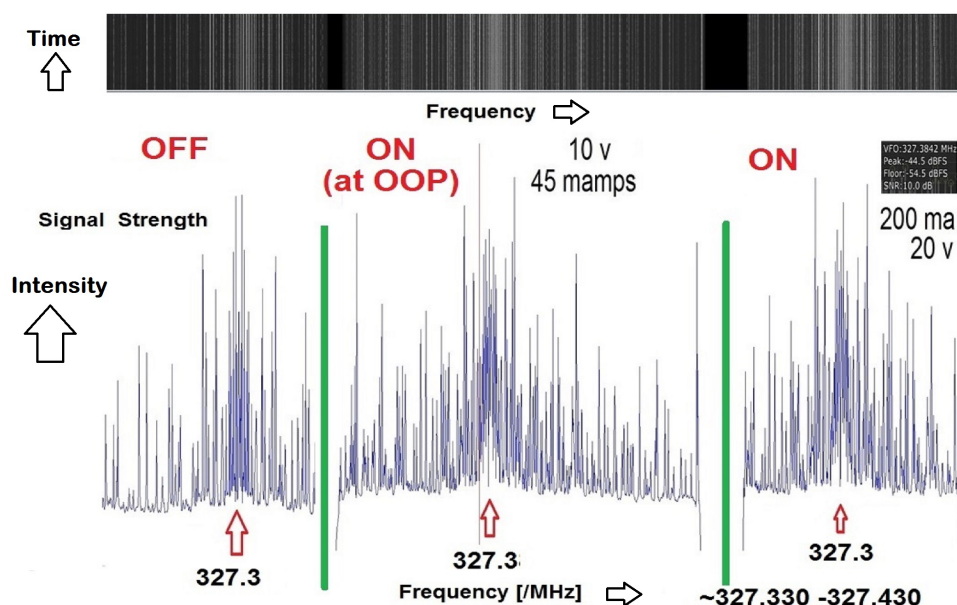


Figure 2. Comparison of the D-line RF emissions from the aqueous MOAC in three different electrical current drives; each separated by vertical lines. These focus on the region from 327.3 to 327.43 MHz (the D-line region) during three different times and electrical input powers (0, 450 mW, and 4 W). The first on the left, is where MOAC was OFF. The second two were electrically driven at two input power levels. The central curve had its electrical drive point was very close to the peak of the optimal operating point (OOP) manifold [29,15]. The increased emission in the D-Line region is apparent.

curve had its electrical drive point was very close to the peak of the optimal operating point (OOP) manifold.

Attention is directed to the fact that there are distinguishable differences in both the integrated amplitude near that region, and in the nature of the superhyperfine structure (sidebands). The increased emission in the D-line region is apparent. These sidebands are analyzed below.

Because of the positive results in the aqueous system, it was elected to further investigate the dry, preloaded NANOR[®]-type components for possible RF emission, too.

3.2. Pulsing deuterium line from active aqueous Ni/H₂O/Pt system

A unique pulsatile superhyperfine RF line (PSHFL) is evident with periods of minutes, and is associated with XSH from an ordinary water nickel, very large cathode, LANR system. In Figs. 1–3 are shown is the superhyperfine DL spectrum of the hydrogen loaded nickel MOAC in its active state (40 V, 200 mA).

In Fig. 1, the frequencies of the widest, and central, peaks are identified by angular frequency. The center is

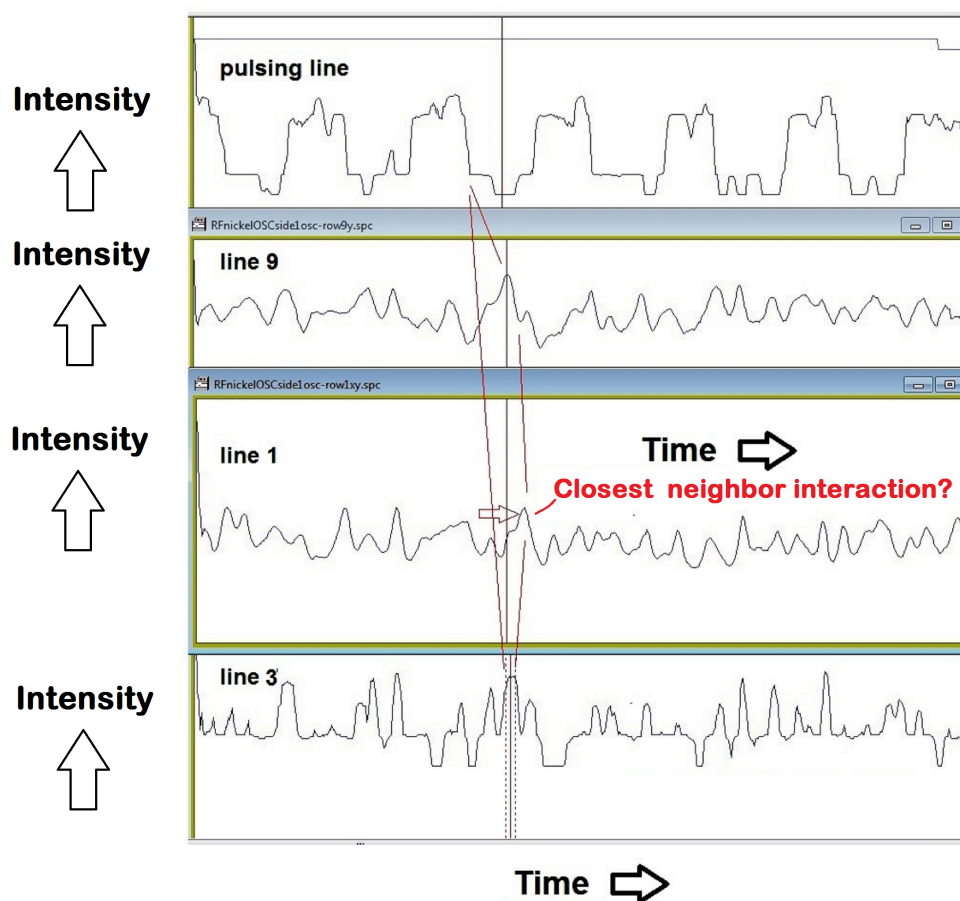


Figure 3. Amplitude of pulsatile RF line and three other time-matched RF lines.

identified by the arrow. There is very reasonable symmetry, more so than for the active electrically driven nanostructured $\text{ZrO}_2\text{-PdD}$ [1–12]. Analysis of the amplitude and positions as a function of frequency strongly suggest that the hydride nickel has changed; perhaps a in part a phase change from a simple face centered cubic (FCC) lattice [30,31]. Attention is drawn to the pulsatile RF line.

Figure 3 shows a blow up of the pulse, and three other pulses, as function of time. What was vertical in Fig. 1 is now horizontal in Fig. 2. This shows a possible connection between some of the SHFL sidebands.

Does the deuteron density actually move to other regions during this event?

4. Interpretation

4.1. Pulsing sideband at 327.37 MHz is not mode locking

This is not mode-locking. Mode-locking was first reported by Gurs and Muller [36,37] on ruby lasers, and Statz and Tang [38] on He–Ne lasers, and reviewed by Herman Haus [39]. The author first did mode-locking experiments with a He–Ne laser in 1967 with Dr. Hermann Haus at MIT. It is the author's belief that these pulsatile densities in the RF spectrum of the 327 MHz CF/LANR maser are unlikely to be mode locking.

4.2. Background – mode locking

Mode-locking is a laser technique to create pulses of light of extremely short duration, circa picoseconds to femtoseconds. The concept of mode-locking describes enforcing coherence between multiple axial modes in a resonant laser cavity so that pulses of laser light result – observed as changes in the intensity of selected longitudinal modes. The process creates a fixed-phase relationship between modes created by the laser's chemistry and the Fabry Perot cavity. The pulses arrive in a train as the laser becomes “phase-locked” (also called “mode-locked”). Although these pulses are slower than the overall energy exchange between atoms emitting the radiation and the sea of photons in which they immersed, they are picoseconds or less. Mode-locking engineering over 6 decades has involved making the pulses shorter while increasing the understanding of the electrical engineering process.

4.3. Reason 1 – Spatial reason disproving that this is not mode locking

First, in laser mode locking, the resonant cavity's length, L , is such that it is much greater than the wavelength of the light, λ . In mode locked lasers, there are usually at least 100 half wavelengths, enabling interaction of different mode orders, i.e. n and $n+1$. Laser mode locking involves hundreds of half-wavelengths, enabling superposition of different modes (e.g. half wavelength, full wavelength, ..., etc.). This occurs in lasers where the resonant cavity's length, L , is much greater than the wavelength of the light, λ . This is multi-mode operation.

By contrast, the 327 MHz LANR RF maser has only single-mode (half wavelength) operation. The resonant rhombic metallic box used to make the simple cavity allows modes which have the separation distance of the mirrors between 0 and L (i.e. length of the resonant box) equal to an exact multiple of half wavelengths.

4.4. Reason 2 – Temporal reason disproving that this is not mode locking

Second, in laser mode locking, the mode orders are periodically constructively interfere to create a single pulse of light. The pulses are separated in time by $\tau = 2L/c$, the time for one path back and forth across the Fabry–Perot laser cavity. By contrast, the 327 MHz LANR RF maser's unique pulsing sidebands are characterized by times which are minutes long.

4.5. Reason 3 – Pulse shape reason disproving that this is not mode locking

Third, in laser mode locking, the pulses have a Gaussian shape, although for femtosecond pulses a hyperbolic-secant-squared (sech²) pulse shape is assumed. By contrast, the 327 MHz LANR RF maser's pulses appear almost as step functions. This could however also be a result of the qualitative analysis of intensity, although it is unlikely because the RF frequency examined does not significantly change.

4.6. An intralattice kinetoscope

One important implication is that in active CF/LANR systems the loaded deuterons work together from their vacancy sites and enable the desired XSH-producing reactions within the loaded Group VIII metal while emitting RF radiation at the Deuterium-line heralding the inverted population. Is this the first intralattice movie of what occurs?

Efforts are underway to examine this further, including intensities, pulsations and transfer-movements. Taken together, they suggest a need for an intralattice kinetoscope. Two types are being examined.

4.7. Possible lattice interactions

The 327.37 MHz RF emission peaks, specifically the pulsatile superhyperfine structure may yield information of these desired reactions unlike everything examined previously. Do the pulsed RF superhyperfine bands herald one or more of these collective excitations enabling the desired reactions? It is a fact that thirty years of data demonstrate that deuterons loaded into Group VIII metals DO work together in active LANR systems to generate *de novo* ⁴He. But how? The RF emissions show that there are inverted populations of atomic D [30] with RF D-line emission sidebands [31] and this RF pulsing from active LANR systems might indicate part of an active-necessary deuteron redistribution in the lattice.

These pulsing RF D-L bands directly herald active LANR activity. They may also herald, and allow further exploration of, deuteron (energy–mass) movements between, and to other, lattice regions, as revealed by the PSHFL (and interpreted, depending upon the model used: Band States, Bose–Einstein condensates, and other quasiparticles), including redistributions between lattice specific periodic lattice regions. Is such redistribution a *sine qua non* for successful movement through the Coulomb barrier?

4.8. Possible sign of loss of Coulomb barrier

Vladimir Dubinko has proposed Nuclear Fusion of Hydrogen Isotopes Induced by the Phason Flips in Pd and Ni nanoclusters [44]. These involve changes in the amplitude of mass–energy components giving rise to a calculated lower Coulomb barrier. The RF superhyperfine pulses, the redistribution in the RF superhyperfine spectrum, and the excess heat and antiStokes observed support his theory.

4.9. Implications of d-line shfl pulsing discovery

4.9.1. Detection of ion band states, Bose–Einstein states, or Phusons?

In one way, this is retrospectively even expected. Unlike quasiparticles, collective excitations result from the ORGANIZED aggregate behavior of the object (usually a lattice). A coherent collective excitation is one which is united and forms an entire uniform constant phase relationship. The pulsing RF signal may be that. It may reveal some of those factors that contribute to increase the likelihood of possible fusion. These might include electrical charging of the cathode to a high negative voltage, or the deuteron or ion band structure, or Bloch-symmetric Bose–Bloch condensates

[40–43], or plasmon exchange, or electron screening, or the increased effective mass of the deuterons due to polarons which occur in the crystalline lattice and other dielectrics used. They may also be tied to Phusons (***) [34,35], or other reported/theoretical ideas in CF/LANR used to enable successful movement through the Coulomb barrier, and therefore towards successful CF/LANR.

These other theoretical ideas include Lou Dechiaro's recognition of coherence among self-sustained maser longitudinal modes in a CF/LANR system which might well related to the Fourier components of the nuclear quantum wavefunctions as taught by Vyssotsky, Adamenko, and Dubinko.

4.9.2. Detection of Coulomb barrier loss?

It may be that such resonance(s) involving wavefunction coherence, as now detected [30,31], may also lead to quantum mechanical movements, perhaps even along with the disappearance of the Coulomb barrier under the right conditions (ICCF22 [44]).

4.10. Phuson theory (***)

The Phuson theory incorporates the observed products and the energy levels, and explains the branching ratios based on the thermal energies available [34]. It also explains the origin of the excess heat in active LANR systems. In addition, it explains why there is a relative absence of strong neutron and gamma ray emissions in LANR. The gamma emission branch from the excited state of $^4\text{He}^*$ is actually spin-forbidden for both hot and cold fusion. However, at higher hot fusion temperatures the restriction is lifted slightly so that some gammas are seen, and not zero. This spin-forbiddenness of gamma emission is therefore consistent to what is seen for both hot and cold fusion. The Phuson theory also correctly describes the relative absence of neutrons emissions in LANR.

The only nuclear branches available are those whose band gaps are surmountable by the available activation energy (limited by the ambient temperature and incident radiation). The neutron emission branch is more than 1 MeV above the first excited state ($^4\text{He}^*$). Hot fusion has large activation energies available (it is hot). LANR does not. In LANR, given the actual much smaller amount of thermal energy, $k_B * T$ available for LANR ($\sim 1/25$ eV), absence of adequate activation energy decisively means that the branch is NOT available, as it is for hot fusion. There results: lattice heating (excess heat) and de novo ^4He . Neutrons are not observed, helium 4 production is in its stead [34,15].

5. Conclusion

5.1. RF findings summary

- (1) Active CF/LANR systems, both aqueous and nanomaterial, emit very narrow bandwidth RF emission peaks (ca. 327.37 MHz), in the DL; 327.348 MHz region [30]. The high $Q(> 1.2 \times 10^6)$ and Zeeman response indicate maser action.
- (2) There is the appearance of maser line sidebands (superhyperfine lines) with increasing voltage. They appear by resonance broadening and energy exchange processes [30,31]. Resonance broadening occurs when the perturbing particle is of the same type as the emitting particle and it introduces the possibility of energy exchange processes. The resonance broadening goes as $1/r^3$. The data uniquely show the nearby sites surrounding the active site in an active nickel CF/LANR system. The superhyperfine sideband line (SHFL) structure (Fig. 1) has been analyzed for the aqueous nickel MOAC system in its active mode [31].
- (3) We report this unique pulsatile superhyperfine RF line (PSHFL) with periods of minutes. It is unlike everything else examined over two years from Earth and galactic origin, and only associated with XSH from an ordinary water nickel CF/LANR system.

- (4) These pulses are not the result of mode locking. Laser mode locking involves hundreds of half-wavelengths, enabling interaction of different mode orders; but this 327 MHz LANR maser has only single-mode (half wavelength) operation. Laser mode locked pulses are separated by the Fabry–Perot cavity transit time but the 327 MHz LANR maser pulsing sideband is characterized by times which are minutes. Finally, laser mode locked pulses have a Gaussian or a hyperbolic-secant-squared (sech²) pulse shape but the 327 CF/LANR maser's pulses appear as near step functions.
- (5) It may herald quantum mechanical movements or even perforation through the Coulomb barrier.

5.2. Complete LANR model based on RF LANR findings

The complete model involves the saturation of the Pd by D. This is the expected full amount that can be contained therein, and is a function of temperature. The fractional saturation and its interactions with the phonons and the interstitials and vacancies within the palladium better explain how LANR works. Simply put, there is injection of deuterons into the vacancies by the sudden catastrophic desaturation of highly loaded Pd. That is followed by a quasiparticle which drives the desired reaction by coupling to the lattice.

The first step is that successful LANR begins with loading of the lattice, the kinetics of which can be described by the quasi-1-dimensional model of loading [16,19,31,32]. LANR, after loading, then has at least two coherent excitation/quasiparticles in its successful action. These sections will describe the pathway to successful activity in LANR. What is described here is a multistep process to LANR. Then there occurs a coherent excitation involving the catastrophic active media forming deuteron flux and very rapidly filling of the vacancies (CAM theory). Under some circumstances, as discussed by Takahashi, Scott and Talbot Chubb and others, there can occur in the lattice the formation of *de novo* helium 4 (⁴He*). Finally, in the fourth irreversible step there is the de-excitation through the PHUSON coherent particle [34,35]. These steps, and the energy levels explain the observations of LANR – including the excess heat, and the lack of significant emissions.

5.3. Quasi-one-dimensional loading model

As discussed at ICCF-4, we suggest a series of reversible reactions which lead up to a final irreversible step. The series includes an intermediate state which is called apo-⁴He* (meaning that which occurs before the ⁴He* is seen). apo-⁴He* is on the way to becoming the excited helium state, ⁴He*, located about 22 MeV above the ground state of helium. If the conditions are perfect, ⁴He* can then become *de novo* ⁴He and heat the lattice, where it appears as excess heat. If successful, then in the highly loaded lattice (n D within the Pd, which is ignored in this equation):

The LANR reaction begins in the extremely difficult-to-achieve highly-loaded Group VIII lattice. There is a critical content of loaded Pd for activity, generally described as a requirement of $>\sim 0.85$ [15]. Understanding this system requires continuum electromechanics as well as electrochemistry.

5.4. Loading requires positive deuteron flux

Deuteron flux is examined here by the quasi-1-dimensional model of loading which shows that conventional electrolysis is WRONG and a red herring, and is why many have trouble achieving successful LANR. The quasi-1-dimensional equations [32,33] also show the way to optimal results. These equations explain some of the difficulties from 1989 on, and they DO NOT DEPEND upon equilibrium conditions, and in fact they make successful predictions (both unlike the relatively useless Nernst equation). There are several components of deuteron flux. They must be considered, including entry into the metal (J_E), movement to gas evolution (J_G), and an extremely tiny loss by potential fusion reactions (J_F). J_{IP} is a pathway afforded by the high impedance spiral PHUSOR[®]-type LANR component (not to be confused with the PHUSON).

At the cathodic metal surface, several components of deuteron flux must be considered; entry into the metal (J_E), movement to gas evolution (J_G), and an extremely tiny loss by potential fusion reactions (J_F). J_{IP} is a pathway afforded with a metamaterial [22].

$$J_D = B_D \frac{d[D(z, t)]}{dz} - \mu_D [D(z, t)] \frac{d\Phi}{dz}. \quad (1)$$

Equation (1) describes the flow. J_D is the flux of deuterons, B_D is their diffusivity, and μ_D is their electrophoretic mobility. The deuterons can enter the metal forming a binary alloy. Deuterons which enter (load) into the palladium lattice drift from shallow to deeper sites within the palladium, obstructed by ordinary hydrogen at interfaces and grain boundary dislocations. The quasi-1-dimensional model begins with the Navier-Stokes equations which describe flow for fluids and other materials in continuum electrodynamics [45]. Dividing each flux by the local deuteron concentration yields the first order deuteron flux constants, k_E , k_G , and k_F (cm/s), respectively. They are linked as follows through Gauss' law and integral equations.

$$k_E = (\mu_D * E) - (k_G + k_F). \quad (2)$$

This shows absolutely clearly that LANR can be missed by insufficient loading, contamination (affecting k_E , e.g. by protium), and by the evolution of D_2 gas, which all inhibit the desired reactions. This also shows that the first order deuteron loading rate equation teaches that the deuteron gain by the lattice depends on the applied electric field MINUS the loss of deuterons from gas evolution (k_G) and fusion (k_F). (consistent with conservation of mass).

Furthermore, when the deuteron flux equation is modified by the Einstein relation, the first term now has geometric, material factors, and the ratio of two energies [the applied electric energy organizing the deuterons divided by $k_B T$, thermal disorder). The modified deuteron flux equation reveals how competitive gas evolving reactions destroy the desired reactions, and how the ratio of the applied electric field energy to thermal energy ($k_B * T$) are both decisive in successful LANR experiments [21,15].

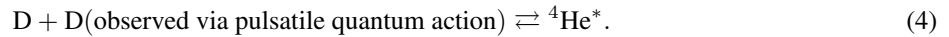
Step 1: (A reversible step) Loading of palladium by deuterons

$$k_E = \frac{B_D * qV}{L[k_B * T]} - (k_G + k_F). \quad (3)$$

5.5. Catastrophic Active Medium driven deuterons and Anderson focusing

The next key movements on the road to successful cold fusion (i.e. LANR) begin with the D within the highly loaded Pd. The deuterons are driven by catastrophic desaturation following local temperature increase. This desaturation and the rise time to produce by positive feedback are described by the CAM (catastrophic active media) model. Briefly, after loading (Step 1), there can –under some conditions– occur Step 2 which is the CAM-driven filling of vacancies.

Step 2: (A reversible step) CAM formation of apo- $^4\text{He}^4$ in hyperloaded vacancies



In summary, the CAM reactions drive the loaded deuterons to the vacancy sites. Catastrophic Active Medium (CAM) model [16] of LANR considers the deuteron solubility in, and the unusual solubility–temperature relationship with, palladium. Unlike most metals characterized by low solubility (\sim one deuteron per 10,000 metal atoms), the deuteron solubility in palladium is quite large and decreases with temperature.

Second, the model adds in the fact that the Pd is an active medium capable of rapid desorption of deuterons, thus with recruitment potential of even more deuterons. This can happen in a paroxysmal and catastrophic way with feedback effects. This has a profound impact on increasing deuteron recruitment, which means the increase of heat produces even more suddenly available deuterons by desorption of D from the Pd (positive feedback [46]). Third, the model reflects that the metallic Pd lattice is heterogeneous, and the model considers *all* types of sites in which the intraelectrode deuterons can reside, including deeper traps supplementing the octahedral and tetrahedral sites. Most importantly, the model documents that the loaded Pd is an active medium capable of rapid deuteron desorption and redistribution (shown in Fig. 4 by τ_C), and that there can also be movements into vacancies, and Anderson focusing (a solid state effect which focuses D flux into vacancies).

The model shows that although the deuteron fugacity ($\Theta_{D,Pd}$) (where fugacity is related to the deuteron pressure rises slightly, thereafter the deuteron saturation curve in Fig. 4 falls rapidly for the loaded palladium. There is a 7-fold decrease in content from 5 to 50°C. Prior to destruction of the lattice through cracks and dislocations and rupture, this desaturation creates an increase in the intrinsic pressure (fugacity) which follows the intraelectrode deuteron flux from redistribution. Because of the fractional saturation-temperature effect, dynamic inversion of $\Gamma_{D,Pd}(t)$ occurs as

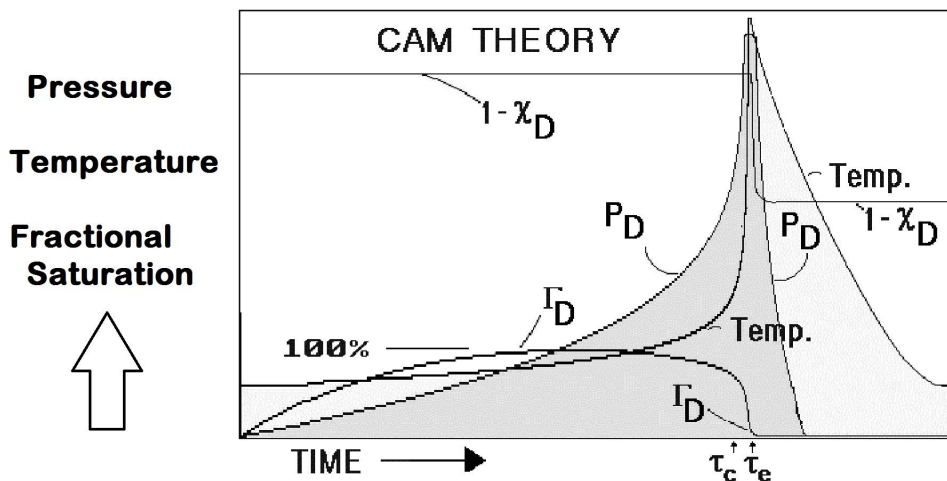


Figure 4. Catastrophic redistribution of deuterons (described by CAM theory). Temperature and loading as a function of time – the theoretic results of a sudden CAM desaturation of a palladium electrode with respect to deuterons. As the palladium heats up (in positive feedback), the solubility of the D in it decreases, leading to a massive falloff of the fractional saturations ($D/(PdD)$ % defined as Γ_D). This drives the deuterons by the CAM catastrophic desaturation into the vacancies which are the site of the LANR reactions.

$\Theta_{D,Pd}(t)$ and temperature reach crescendo levels. As a result, after sufficient time, the active site (compartment 2) is suddenly and catastrophically fed deuterons from the large vicinal volumes of the crystalline palladium lattice (compartment 1), further increasing the likelihood of additional temperature-incrementing reactions. Eventually, however, the crystal lattice is unable to survive intact, and instead the surface energy normally is required to prevent the palladium from escaping, becomes insufficient and the reactants continue to move from their normal sites to accumulate in compartment 2 by the catastrophic reactions and thereby maintain close contact for the desired reactions.

The surface energy required to rupture the palladium prevents the escape of the reactants as they continue to accumulate by the catastrophic reactions and thereby maintain close contact for the desired reactions. Positive feedback comes from the catastrophic behavior secondary to the saturation-temperature relationship. However, when the internal pressures are able to exceed the energy needed to create fresh new surfaces in the palladium, leakage then occurs and the sample becomes, at best, locoregionally inactive.

5.6. Phusons and successful LANR

The lattice enables this reversible reaction through internal conversion [40–43]. The critical reaction proceeds and is described by either band states and/or Bose–Einstein states, and other interaction models. It is enabled by the collective excitations of phonons. In addition, it is reasonable to assume that conditions may enable formation of $^4\text{He}^*$ if and when there is sufficient activation energy [27, 47–49].

Looking closer at the phonons and their role: Cold fusion is enabled by the collective excitations of phonons. After adequate containment time and flux, there is near commensurate amount of excess heat observed in LANR, with the ash which is *de novo* He^4 . Phonon de-excitation modes apparently produce transitional times significant for enabling $^4\text{He}^*$ to ^4He transitions which involving recruitment of sufficient numbers of lattice sites and their associated phonons. The temperature rise occurs as the acoustical and optical phonons are eventually unable to carry off all the momentum and the excess energy of the reactions appears and grows. This process is the unique feature that allows LANR to occur with energy transfer to the lattice which does enable the desired reactions if and when there is sufficient activation energy [27,47–49] The penultimate critical (~ 20 MeV) transition shown above is enabled by the coherent Phuson, enabled by phonons, Hagelstein's lossy spin bosons, and magnons [9,15]. Hagelstein incorporates the optical phonons in his theory. Swartz at ICCF20 has shown these to also, obvious by coherent antiStokes spectroscopy, include acoustic phonons [11,12,18].

5.7. Phuson quasiparticle enables coherent collective de-excitation

The pulsing RF superhyperfine bands interacting may be the Phuson quasiparticle. The coherent means of excitation of the lattice, the Phuson [34,35], enables LANR by coherent transfer of energy from $^4\text{He}^*$ to the lattice in a process which is consistent with conventional physics, and where it appears as excess heat [15] and *de novo* ^4He . As discussed in the original paper, the PHUSON theory has a mechanism which incorporates the observed products, and the energy levels to all those branches. As a result, it succinctly explains the differences in observed outputs, including the observed excess heat as T rises. It also explains the different branches observed near room temperature (LANR) and at hot fusion temps. The temperature rise occurs as the acoustical and optical phonons become unable to carry off all the momentum and excess energy of the reactions. In this step (Step 3), there is a critical IRREVERSIBLE (~ 20 MeV) transition that is coherent by PHUSON, enabled by phonons and magnons. The Phuson is a coherent particle of the lattice. Simply put, the Phusons, coherent excitation objects/particles cooperatively transfer energy from the megavoltage energy of the $^4\text{He}^*$ to the lattice.

Step 3: (An irreversible step) de-excitation by Phuson/Phonons (in lattice) to He^4

$${}^4\text{He}^* [\text{via PHUSON-coherent transfer}] = (*) \Rightarrow {}^4\text{He} \quad (5)$$

(*) requires phonons and magnons

The coherent de-exciting PHUSON enables the massive energy loss by way of lossy spin bosons processes involving phonons and (as we have shown at ICCF-18) magnons. There are many factors that contribute to increase the likelihood of possible fusion: electrical charging of the cathode to a high negative voltage, the deuteron band structure, Bloch-symmetric Bose–Bloch condensates, plasmon exchange, electron screening, and the increased effective mass of the deuterons due to polarons which occur in the crystalline lattice and other dielectrics used.

6. Conclusions

6.1. LANR RF emission summary

Active CF/LANR systems, both aqueous and nanomaterial, emit very narrow bandwidth hyperfine RF emission peaks (ca. 327.37 MHz), which are located very close to the theoretical DL; 327.348 MHz) region, and they exhibit a large $Q(> 1.2 \times 10^6)$, which is the ratio of the bandwidth at half power to the frequency. RF identification and recognition of CF/LANR RF emission from the active state is important. In the future, RF detection, like coherent antiStokes spectroscopy [11–13,18] can be used, aimed at the phenomenon's location, to discern the conditions of the desired active XSH-producing driven state.

6.2. Confirmation of fuel – Deuterons free radicals

These results confirm that in active CF/LANR systems deuterons are making helium-4 which generates the observed excess energy in the active state [50,17].

6.3. Derivation of the active site – FCC vacancies

At higher applied driving voltages, a superhyperfine line structure of sidebands appears, and that this revelation gives more insight into the volume and stereoconstellation around the active site. The fuel generates the fusion product and at least some of these reactions occur in face center cubic (Pd FCC) vacancy for palladium (in PdD) or Zr (in ZrO₂). Vacancies, as predicted at ICCF-4 [46], are the site of some of the desired reaction in these active systems.

6.4. Real time mass–energy intralattice spectroscopy

In active CF/LANR systems, the loaded deuterons work together from their vacancy sites to enable continuation of the desired XSH-producing reactions within the loaded Group VIII metal. At least some of their emitting RF radiation superhyperfine line peaks, located at the DL heralding the inverted population, are observed to be pulsing. This action may herald quantum movements of energy and matter within an active XSH-producing PdD lattice. With the new information derived from the RF superhyperfine pulsing data and analysis, one can uncover where the highest energy precursor to the final state spatially occurs and observe in real time mass-energy transfers within the high loaded Group VIII lattice.

Acknowledgments

The author gratefully acknowledges and thanks David Nagel, Bo Gardmark, Gayle Verner, Peter Hagelstein, Lawrence Forsley, Louis Dechiaro, Isidor Straus, and Joshua Gyllinsky for their very helpful comments, editorial assistance,

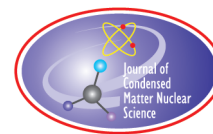
and additional material. He also thanks Brian Ahern, Alan Weinberg and the late Charles W. Haldeman for their construction, early testing, and transfer of the MOAC. This effort has been supported by JET Energy Inc., Nanortech Inc., and the Anthropocene Institute, LLC.

References

- [1] M.R. Swartz, G. Verner and J. Tolleson, Energy gain from preloaded ZrO_2 -PdNi-D nanostructured CF/LANR quantum electronic components, *J. Condensed Matter Nucl. Sci.* **13** (2014) 528, www.iscmns.org/CMNS/JCMNS-Vol13.pdf.
- [2] M.R. Swartz, G. Verner, J. Tolleson and P.L. Hagelstein, Dry, preloaded NANOR[®]-type CF/LANR components, *Current Sci.* **108** (4) (2015) 595.
- [3] M.R. Swartz and P.L. Hagelstein, Demonstration of energy gain from a preloaded ZrO_2 -PdD nanostructured CF/LANR quantum electronic device at MIT, *J. Condensed Matter Nucl. Sci.* **13** (2014) 516, www.iscmns.org/CMNS/JCMNS-Vol13.pdf.
- [4] M.R. Swartz, P.L. Hagelstein and G. Verner, Impact of electrical avalanche through a ZrO_2 -NiD nanostructured CF/LANR component on its incremental excess power gain, ICCF-19, *J. Condensed Matter Nucl. Sci.* **19** (2016) 287–297.
- [5] M.R. Swartz, Optical detection of phonon gain distinguishes an active cold fusion/LANR component, *J. Condensed Matter Nucl. Sci.* **20** (2016) 29–53, www.iscmns.org/CMNS/JCMNS-Vol20.pdf.
- [6] M.R. Swartz and P.L. Hagelstein, Increased PdD anti-Stokes peaks are correlated with excess heat mode, *J. Condensed Matter Nucl. Sci.* **24** (2017) 130–145.
- [7] M.R. Swartz, G. Verner, J. Tolleson, L. Wright, R. Goldbaum and P.L. Hagelstein, Imaging of an active NANOR[®]-type LANR component using CR-39, *J. Condensed Matter Nucl. Sci.* **15** (2015) 81.
- [8] M.R. Swartz, Incremental high energy emission from a ZrO_2 -PdD nanostructured quantum electronic component CF/LANR, *J. Condensed Matter Nucl. Sci.* **15** (2015) 92.
- [9] M.R. Swartz, G. Verner, J. Tolleson, L. Wright, R. Goldbaum and P.L. Hagelstein, Amplification and restoration of energy gain using fractionated magnetic fields on ZrO_2 -PdD nanostructured components, *J. Condensed Matter Nucl. Sci.* **15** (2015) 66, www.iscmns.org/CMNS/JCMNS-Vol15.pdf.
- [10] M.R. Swartz, P. Hagelstein and G. Verner, Impact of electrical avalanche through a ZrO_2 -NiD nanostructured CF/LANR component on its incremental excess power gain, ICCF-19, *J. Condensed Matter Nucl. Sci.* **19** (2016) 287–297.
- [11] M.R. Swartz, Optical detection of phonon gain distinguishes an active cold fusion/LANR component, *J. Condensed Matter Nucl. Sci.* **20** (2016) 29–53, www.iscmns.org/CMNS/JCMNS-Vol20.pdf.
- [12] M.R. Swartz and P.L. Hagelstein, Increased PdD anti-stokes peaks are correlated with excess heat mode, *J. Condensed Matter Nucl. Sci.* **24** (2017) 130–145.
- [13] M.R. Swartz, Aqueous and nanostructured CF/LANR systems each have two electrically driven modes, *J. Condensed Matter Nucl. Sci.* **29** (2019) 177.
- [14] M.R. Swartz, Comparison of NANOR[®]-type LANR components to ^{238}Pu as a heat source for space flight, *J. Condensed Matter Nucl. Sci.* **29** (2019) 238.
- [15] M.R. Swartz, Survey of the observed excess energy and emissions in lattice assisted nuclear reactions, *J. Sci. Exploration* **23** (4) (2009) 419–436.
- [16] M.R. Swartz, Excess power gain using high impedance and codepositional LANR devices monitored by calorimetry, heat flow, and paired stirling engines, *Proc. ICCF 14*, **1** (2008) 123; ISBN: 978-0-578-06694-3, 123, (2010); www.iscmns.org/iccf14/ProcICCF14a.pdf.
- [17] M.R. Swartz, Charles Haldemann, Alan Weinberg and Brian Ahern, Possible deuterium loss during excess heat from ordinary water-carbonate electrolyte using nickel, *J. Condensed Matter Nucl. Sci.* **29** (2018) 169.
- [18] M.R. Swartz, Increase of an anti-Stokes peak at the cathode of an electrically-driven, active aqueous nickel/ H_2O /Pt system, *J. Condensed Matter Nucl. Sci.* **29** (2018) 22.
- [19] M.R. Swartz, Consistency of the biphasic nature of excess enthalpy in solid state anomalous phenomena with the quasi-1-dimensional model of isotope loading into a material, *Fusion Technol.* **31** (1997) 63–74.
- [20] M.R. Swartz, Codeposition of palladium and deuterium, *Fusion Technol.* **32** (1997) 126–130.
- [21] M.R. Swartz and G. Verner, Excess heat from low electrical conductivity heavy water spiral-wound Pd/ D_2O /Pt and Pd/ D_2O -

- PdCl₂/Pt devices, Condensed matter nuclear science, *Proc. ICCF-10*, World Scientific, NJ, ISBN 981-256-564-6, 29-44; 45–54 (2006).
- [22] M.R. Swartz and G. Verner, The Phusor[®]-type LANR cathode is a metamaterial creating deuteron flux for excess power gain, *Proc. ICCF-14*, **2** (2008) 458, ISBN: 978-0-578-06694-3, 458 (2010).
- [23] M.R. Swartz, G. Verner and A. Weinberg, Non-thermal near-IR emission from high impedance and codeposition LANR devices, *Proc. ICCF 14*, D.J. Nagel and M.E. Melich (Eds.), **1** (2008) 343, ISBN: 978-0-578-06694-3, 343, (2010), www.iscmns.org/iccf14/ProcICCF14a.pdf.
- [24] M.R. Swartz, Improved electrolytic reactor performance using π -notch system operation and gold anodes, transactions of the American nuclear association, Nashville, Tenn. Meeting, (ISSN:0003-018X publisher LaGrange, Ill) **78** (1998) 84–85.
- [25] M.R. Swartz, Can a Pd/D₂O/Pt Device be Made Portable to Demonstrate the Optimal Operating Point? Condensed Matter Nuclear Science, *Proc. ICCF-10*, P.L. Hagelstein and S.R. Chubb (Eds.), World Scientific, NJ, ISBN 981-256-564-6, 29-44; 45–54 (2006).
- [26] M.R. Swartz, Investigations of heat after death, *J. Condensed Matter Nucl. Sci.* **31** (2020) 20–41.
- [27] M.R. Swartz, Photoinduced excess heat from laser-irradiated electrically-polarized palladium cathodes in D₂O, Condensed Matter Nuclear Science, *Proc. ICCF-10*, NJ, ISBN 981-256-564-6, 213-226 (2006).
- [28] M.R. Swartz, G. M. Verner and A.H. Frank, The impact of heavy water (D₂O) on nickel-light water cold fusion systems, *Proc. ICCF 9*, China, Xing Z. Li (Ed.), May 2002, pp. 335–342.
- [29] M.R. Swartz, optimal operating point manifolds in active, loaded palladium linked to three distinct physical regions, *Proc. ICCF14*, D.J. Nagel and M.E. Melich (Eds.), Vol. 2, 2008, p. 639, ISBN: 978-0-578-06694-3, 639, (2010).
- [30] M.R. Swartz, Deuterons in active LANR systems emit a 327.37 MHz hyperfine maser line, *J. Condensed Matter Nucl. Sci.* (2019), to appear.
- [31] M.R. Swartz, Superhyperfine line structure of ZrO₂PdD RF emission heralds a deuteron in a FCC vacancy, *J. Condensed Matter Nucl. Sci.* (2019), to appear.
- [32] M.R. Swartz, Quasi-one-dimensional model of electrochemical loading of isotopic fuel into a metal, *Fusion Technol.* **22** (2) (1992) 296–300.
- [33] M.R. Swartz, Isotopic fuel loading coupled to reactions at an electrode, *Proc. ICCF4* **2** (1993) 429, *Fusion Technol.* **26** (4)T (1994) 74–77.
- [34] M.R. Swartz, Phusons in nuclear reactions in solids, *Fusion Technol.* **31** (1997) 228–236.
- [35] M.R. Swartz, Quasiparticles, collective excitations and higher-order collective quasi-excitations in lattice assisted nuclear reactions, *J. Condensed Matter Nucl. Sci.* with excess heat mode, *J. Condensed Matter Nucl. Sci.* **24** (2017) 130–145.
- [36] K. Gurs and R. Muller, Breitband-modulation durch Steuerung der emission eines optischen masers (Auskopple-modulation), *Phys. Lett.* **5** (1963) 179–181.
- [37] K. Gurs, Beats and modulation in optical ruby lasers, in *Quantum Electronics* III, P. Grivet and N. Bloembergen (Eds.), Columbia University Press, New York, 1964, pp. 1113–1119.
- [38] H. Stutz and C.L. Tang, Zeeman effect and nonlinear interactions between oscillating laser modes, in *Quantum Electronics* III, P. Grivet and N. Bloembergen (Eds.), Columbia University Press, New York, 1964, pp. 469–498.
- [39] H.A. Haus, Mode-locking of lasers, *IEEE J. on selected topics in Quantum Electronics*, Vol. 6, No. 6, November/December 2000, p. 1173.
- [40] T.A. Chubb and S.R. Chubb, *Ion Band States: What they are, and How they Affect Cold Fusion*, Cold Fusion Source Book, *ibid.*, 75, (1994).
- [41] T.A. Chubb and S.R. Chubb, The role of hydrogen ion band states in cold fusion, *Trans. Fusion Technol.* **26**(4T) (1994) 414.
- [42] T.A. Chubb and S.R. Chubb, An explanation of cold fusion and cold fusion by-products, based on lattice induced nuclear chemistry, in *Second Annual Conference on Cold Fusion, The Science of Cold Fusion*, Como, Italy, Societa Italiana di Fisica, Bologna, Italy, 1991.
- [43] T.A. Chubb and S.R. Chubb, Bloch-symmetric fusion in PdD_x, *Fusion Technol.* **17** (1990) 710.
- [44] V. Dubinko, Nuclear fusion of hydrogen isotopes induced by the phason flips in Pd and Ni, *J. Condensed Matter Nucl. Sci.* (2019), to appear.
- [45] J. Melcher, *Continuum Electromechanics*, MIT Press, Cambridge, 10. 13-10. 18 (1981).
<https://www.google.com/url?sa=t&rct=j&q=&esrc=s&source=web&cd=4&cad=rja&uact>

- =8&ved=2ahUKEwj8pc7XrIjjAhVorlkKHfQjBI4QFjADegQIBhAC&url=https%3A%2F%2Focw.mit.edu%2Focw%2Fresources%2Fmelcher%2Fresized%2Fcem_811.pdf&usq=AOvVaw1ityC4BWlIPTM792pP5DX7.
- [46] M.R. Swartz, Catastrophic active medium (CAM) theory of cold fusion, *Proc. ICCF 4*, **4** (1993) 255, sponsored by EPRI and the Office of Naval Research.
 - [47] D. Cravens, D. Letts and P.L. Hagelstein (Progress on two-laser experiments, *Proc. ICCF 15* (2009); <http://lenr-canr.org/acrobat/Hagelsteinprogresson.pdf>) deuterium-heavy water system, *Electroanal. Chem.* **287** (1990) 293.
 - [48] D. Letts and D. Cravens, Laser stimulation of deuterated palladium: past and present, *Proc. 10th Int. Conf. on Cold Fusion*, 2003.
 - [49] D. Letts and P.L. Hagelstein, Stimulation of optical phonons in deuterated palladium. in *ICCF-14 Int. Conf. on Condensed Matter Nucl. Sci.*, 2008, Washington, DC, D. Letts, D. Cravens and P.L. Hagelstein (Eds.), *Thermal Changes in Palladium Deuteride Induced by Laser Beat Frequencies*, in *Low-Energy Nuclear Reactions Sourcebook*, J. Marwan and S. Krivit (Eds.), 2008, Oxford University Press, Oxford, D. Letts and D. Cravens, Laser stimulation of deuterated palladium: past and present, in *Tenth Int. Conf. on Cold Fusion*, 2003, Cambridge, MA.
 - [50] M. Miles, correlation of excess power and helium production during D₂O and H₂O electrolysis using palladium cathodes, *J. Electroanal. Chem.* **346** (1993) 99–117.



Research Article

FCC Vacancies in ZrO_2PdD are the Active LANR Site

Mitchell R. Swartz*

JET Energy Inc., Wellesley Hills, MA 02481, USA

Abstract

Active lattice assisted nuclear reaction (LANR) systems emit very narrow bandwidth hyperfine radiofrequency (RF) emission peaks (ca. 327.37 MHz) signaling their LANR activity. This RF frequency is very close to the theoretical Deuteron-Line (DL; 327.348 MHz) proving that D is the fuel. Neither the maser emission, nor the revealing sidebands (superhyperfine structure) appear when the components are electrically driven at subthreshold voltage or when driven in electrical avalanche mode. The RF emission sidebands provide unique information about the conditions of the desired active LANR state.

© 2020 ISCMNS. All rights reserved. ISSN 2227-3123

Keywords: Cold fusion maser, Deuterium, Deuterium line, Free radical deuteron, Resonance broadening, Spectra, Superhyperfine, Superhyperfine lines, Vacancies

1. Overview of CF/LANR D-Line Hyperfine RF Emissions

Active lattice assisted nuclear reactions (LANR) systems, both aqueous and nanomaterial (ZrO_2 PdD preloaded Nanor[®]-type LANR components [1–12] operated carefully below their avalanche voltage[4]), emit very narrow bandwidth radiofrequency (RF) emission peaks (ca. 327.37 MHz), in the Deuteron-Line (DL; 327.348 MHz) region [13,14]. The high Q ($1.2\text{--}9 \times 10^6$) and Zeeman response indicate maser action. Higher applied voltages have revealed sidebands (superhyperfine line (SHFL) structure). These are non-Zeeman splitting because there are no additional significant applied H-fields. Analysis of the positions of the non-Zeeman SHFL splittings yields great insight into the LANR active site not otherwise available (Fig. 1). It is important that the RF DL hyperfine emissions come only from LANR (CF) active cells containing high loaded levels of deuterons.

Figure 1 is a four section analysis of the superhyperfine structure of Nanor[®]-type component 7-4 using a frequency–time plot. The top shows the actual SHFL sideband structure for Nanor[®]-type component #7-4, driven at ~10 V. This is a “waterfall” plot and intensity is shown as a function of frequency. The exact width of the SHFL splitting’s displacement, as a function of frequency, results from resonance broadening (RB) which occurs from perturbing deuterons located elsewhere, such as other vacancies, through energy exchange processes. RB impact was derived for the first four closest neighbor sites using the fact that the RB interaction decreases as $1/r^3$. As discussed in detail below, analysis such as shown in Fig. 1 demonstrates this nearest neighbor RB analysis. Here, the Nanor[®]-type

*Mitchell R. Swartz ScD, MD, EE, AC1ER, E-mail: drswartz@nanortech.com.

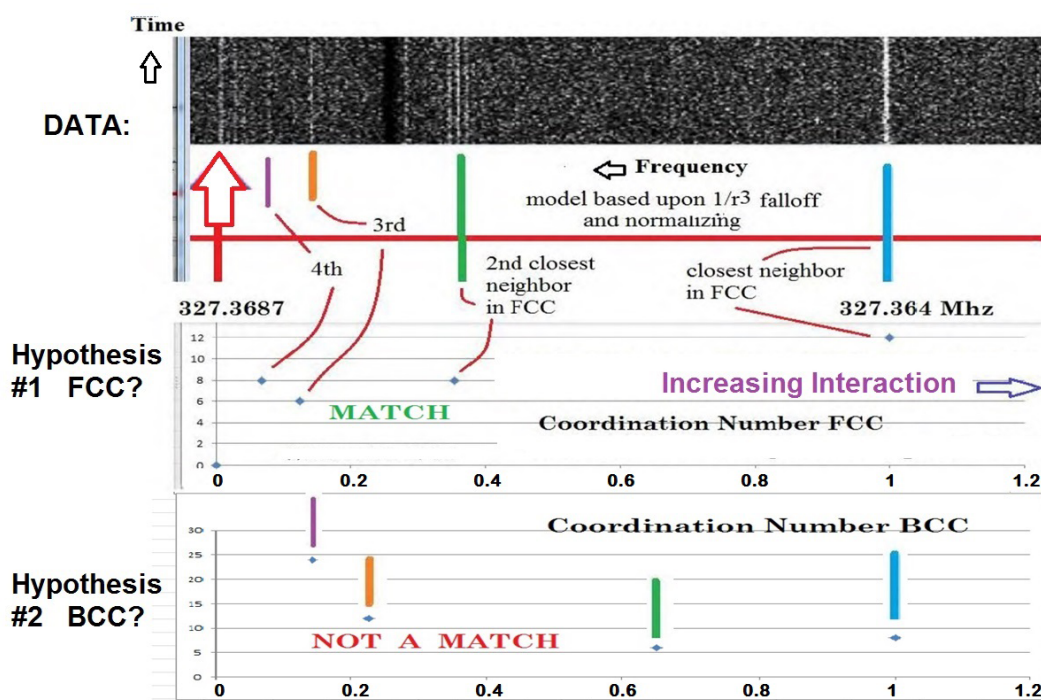


Figure 1. Analysis of an active ZrO_2PdD component's frequency–time plot.

component 7-4 is driven at sufficient voltage so that the additional SHF lines appear. Below, this is followed by assignments (labeled “Hypothesis”) based upon nearest neighbor location and the expected resonance broadening falloff. The middle and bottom of the figure show the expected results for two different gendanken active sites: face and body centered cubic (FCC, BCC), respectively, both the coordination numbers (height) and expected deviation (to the right for frequency) are shown based upon known locations for both FCC and BCC lattice arrangements.

Figure 1 shows considerable overlap of the expected locations (in solid color) in the midgraph and the frequency singularities above them for the FCC lattice, but not the BCC lattice. It thus reveals that the key D^* reactions occur in a lattice which is face center cubic (FCC). In Fig. 1, note the better overlap of the expected FCC locations in the midgraph, unlike the BCC lattice. The coordination numbers (CN) also better match for the FCC lattice. The location of the excited state deuterium is a vacancy within a slightly modified FCC lattice. The multiplet near the second nearest neighbor might herald that this is a zirconia at a rhombic corner (one phase of ZrO_2 is isoequivalent to a FCC vacancy) or an atom of zirconium (or other magnetic impurity) within the PdD lattice. This appears to confirm the prediction (ICCF-4 [16]) which also relates to the mechanism of fuel entering the active site – being a vacancy.

The results in nickel are more complex and demonstrate a range of FCC and body centered cubic (BCC) vacancies, possibly heralding new metallurgic phases. These discoveries add semiquantitative material science supporting theories that cite vacancies [16] as the site of the desired LANR reactions, with deuterons as its “fuel” to form *de novo* 4He .

Importantly, the D-line emission RF from active LANR systems confirms the role of atomic deuterium in LANR. It also heralds, and here identifies, the lattice connections between the loaded deuterons. This demonstrates that LANR active state's RF emission creates a new method to observe LANR systems, and especially LANR's difficult-to-attain

most-desired mode. The remainder of this paper is discussed these energy and matter power spectra.

2. Background

2.1. Hyperfine emission in radioastronomy

This effort links CF/LANR with the tools and methods of the science of radioastronomy which studies the universe by measuring RF emissions from several GHz to the far infrared. Together, the H-L and DL have provided understanding of the matter distribution through the known universe; providing information from post-Big Bang times just after recombination through reionization to the present. In radioastronomy, DL and HL observations have greatly improved human understanding of the extent, and interactions of galaxies, both now and back to a few hundred thousand years after the Big Bang.

2.2. Hyperfine emission from free radical hydrogen

The word deuterium indicates the deuteron has positive charge, but it is a charge neutral free radical with an unpaired electron. The energy states result from the interaction between the deuteron's electron's spin and its own nuclear spin. Deuterium is light enough that isospin is a good symmetry. The proton and neutron are both fermions, and a state containing two of them must be antisymmetric under exchange. The nuclear spin results from the fact that the proton and neutron interact by strong force. Because parallel electric currents attract, the parallel magnetic dipole moments (that is with antiparallel spins) has the lowest energy. The difference is a photon at 1420 MHz for hydrogen and 327.348 MHz for deuterium.

2.3. Long emission times heralded by narrow bandwidth

Because atomic deuterium and atomic hydrogen have no electric moment, the energy transition between the two states is highly forbidden. That means there is an extremely small transition rate of $\sim 2.9 \times 10^{-15}$ per second, which correlates to a mean lifetime of the excited state of ca. 10 million years. Therefore, simply put, a spontaneous transition between these states does not normally occur on Earth – unless induced using a hydrogen maser. But it is observed in astronomy. As a corollary, because of the long mean lifetime, the line has an extremely small natural width – as uniquely seen here.

3. Experimental

3.1. Materials – Aqueous nickel LANR system

There are three parts to the detection and analysis of the CF/LANR superhyperfine structure. First, the RF emissions are collected. Second, they are examined as a function of frequency, electric drive state, using ohmic and other controls. Finally, the data was examined to determine what type of loaded Group VIII lattice structure would produce the observed superhyperfine sideband structure. This is shown below for an active XSH-producing aqueous nickel CF/LANR system (MOAC type; “Mother of all Cathodes”), and for two dry preloaded palladium zirconia CF/LANR components (NANOR[®]-type).

Our first experimental surveys began with preliminary amateur radio and LANR investigations that examined and resolved, for the first time, the apparent absence of Hydrogen Line (HL) and presence of Deuterium Line (DL) emissions from the MOAC LANR (ordinary water) aqueous system electrically driven during its active mode [17,18]. The MOAC cell has a 3 l capacity with a cathode weighing 2.132 kg (#46 hard drawn smooth nickel wire with an area of ca. 240,000 cm²). The electrolyte was a dilute carbonate solution in laboratory distilled deionized “ordinary” water. For the calorimetry, calibration was determined by ohmic controls and other methods, as discussed elsewhere [19–32].

3.2. Dry, preloaded LANR NANOR[®]-type components

The second investigations were a preliminary set of experiments looking for possible solid-state LANR maser action at 327.7 MHz (such as in Fig. 1) resulting from electrically driving ZrO₂PdD preloaded Nanor[®]-type LANR components [1–12], carefully below their avalanche voltage [4] when excess heat is known to cease. These LANR systems examined are two-terminal component with a cylindrical shape and active CF/LANR core.

The dry, preloaded nanocomposite components have at their core ZrO₂–PdD nanostructured material. They are smaller than 2 cm length, with 30–200 mg of active LANR material. Although small in size, the LANR excess power density is more than 19,500 W/kg of nanostructured material. The small, preloaded, dry components have enabled the way to higher instantaneous power gain, total energy gain, imaging, emissions, open demonstrations, and a better understanding of the impact of applied magnetic fields, and electrical transconduction [1–12].

Our previous studies and reports have been directed to both avoiding the avalanche voltage and approaching the optimal operating point (OOP) of the system [31]. Most importantly, we have demonstrated that several electrical transconduction states exist, but that only one is active, desired, and capable of producing “excess heat” [10,18,25]. Beyond the region of electrical avalanche, the previously active preloaded LANR quantum electronic components give a thermal output similar to a standard ohmic control (a carbon composition resistor). Despite driving at higher input electrical power, on other side of the electrical avalanche, these NANOR[®]-type components act as little more than electrical resistors which – when in electrical avalanche mode – are conventionally dissipative, not over-unity, and therefore are functionally “dead” with respect to producing excess heat.

3.3. Methods – RF emission detection system

Figure 2 shows the arrangement of detecting the RF emissions. SDR receivers (RTL-brand and the like) were used because of their high dynamic range, high bandpass stability, and excellent out-of-band rejection. The images shown are dynamic gradient with time markers on the left-hand side. The sample rate was 3.2 million samples per second (MSPS). Upper sideband (USB) was used to minimize imaging. Resolution was the highest achievable with a Blackman–Harris 4 window, although Bo Gardmark suggests using Hann or Hamming windows for improved signal to noise ratio (SNR) along with a AD8317 log detector.

The sensitivity of this detection system (SNR) is proportional to $A\sqrt{t}$, where A is the antenna’s collecting area, and t is the integration time. What is not explicitly shown in Fig. 4, but is therefore quite important, is that the data is meticulously collected over several minutes to hours, as it is integrated/analyzed over time and as a function of frequency.

The LANR-emitted RF signals are weak, and therefore the antenna is made with an aperture as large as possible, and the collection is for as long a time as possible. Current investigations use three antennae: reflector, Yagi, and a convenient “duck” antenna system. The latter fit easily into the resonance chamber. Although often ignored, the antenna feed line loss was significant and had to be addressed for this iteration of experimental runs. The coaxial improvement for this version (CNT400) was significant with 90 db gain per standardized length.

3.4. Resonant chamber

A 36 inch long metallic case was used as the resonant cavity with the half wavelength set vertically. It contains the antenna, beginning of transmission line, and NANOR[®] type component. A white envelope is used, surrounding the NANOR[®]-type CF/LANR component to easily detect, and to protect against, falling or extravasated nanomaterials. For the experiment, the door was shut, sealed, covered with aluminum foil and connected to a driven copper rod driven into the Earth.

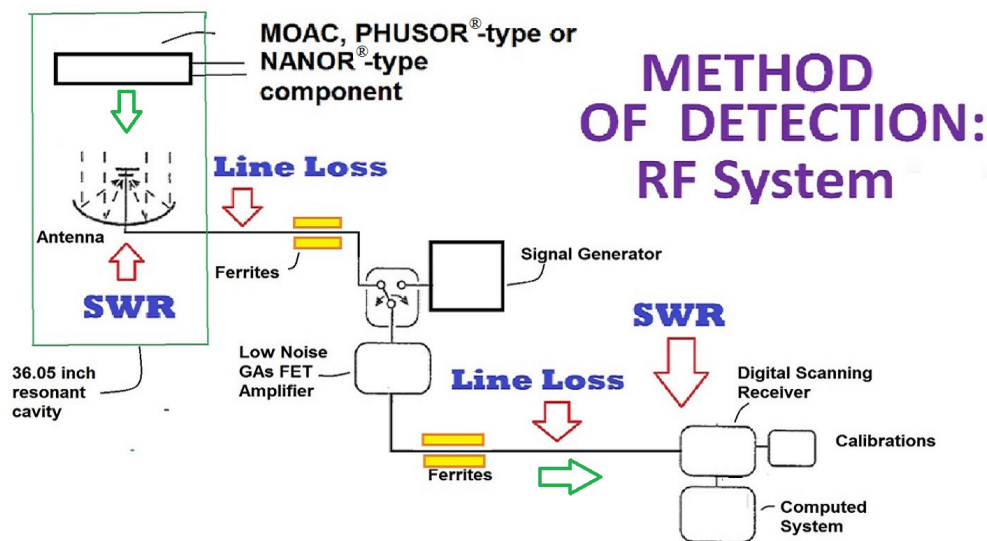


Figure 2. Block diagram of the system used for the HL and DL receiver system. Shown is a block diagram representation for the CF/LANR emitter, the antenna, line feeds and transmission lines (including serious line loss), the ferrites, the control signal generator, the Gas FET amplifier, the most relevant standing wave ratio (SWR) points to match, computation and software defined receiver (SDR). The use of antenna analyzers and matching decreased the SWR from ca. 20+ to 2–3. The use of military grade coax (CNT400) decreased the transmission line loss by +90 db, and the low noise amplifier (LNA) provided an additional +20 db gain. Ferrites are used to minimize shield currents and radio frequency interference (RFI) from nearby active equipment.

3.5. Galactic control

Interference has been considered, and eliminated, by monitoring over several weeks, and comparison to known frequency dispersions and examination of bandwidth. Changes as a function of time and/or frequency have led to the identification of modulated (military in this band) signals, and galactic input. Possible television transmitters, cell phones, microwave appliances, and ionospheric noise (QRN) have not been a significant problem at these frequencies given the long term monitoring and pre-identification. Investigators should use well-ground Faraday cages, and are advised that it may take weeks to understand the background. However, not having a detailed understanding of the vast background does not preclude using the D-line to monitor and better understand CF/LANR.

For each experiment, attention has been necessarily made to the location of the Galactic center, and, when possible, measurements have been made when the Earth is optimally shielding emissions from the galactic center. This was found to be much less needed once the resonator box was correctly grounded. As background, the Galactic center continuum is reported to have nonthermal background of ~500 K (with a 25 element sub-array, 23 dB gain, 12° beam width, 12 m² effective aperture). The Galactic anticenter has a non-thermal background of ~70 K and, therefore, any deuterium excitation temperature ≥ 130 K causes appearance of RF emissions.

3.6. Ohmic controls

In this case, for this paper, the controls included having nothing in the Faraday cage with full double shielding as discussed above, and included having the NANOR[®] type component present in the cage but being NOT electrically driven. In addition, controls included having in the same electrical circuit an electrically driven ohmic control instead

of the NANOR[®] type component. In this case, the ohmic control consisted of a carbon resistor, but in the future both wire-wound and film resistors should also be examined.

The possibility of RF emissions from ohmic controls were observed in the driven samples. None were seen. Figure 7 shows the RF emissions in the region from 327.340 to 327.420 MHz (the D-Line region) for two ohmic (thermal) controls. There were no peaks directly associated with driving the ohmic controls even at much higher electrical input power levels. Only the original galactic background was seen unchanged from electrically driving the ohmic controls – unlike the CF/LANR components which received less than 0.1% of the power delivered to this ohmic controls and gave blazing maser outputs. What was not used for this paper was a NANOR[®] type component loaded with ordinary hydrogen. That must also be done in the future.

3.7. Signal generator control

Under a Faraday cage, signal generator controls were employed to check frequency and normal bandwidth. These RF intensity plots taken in the D-Line Region demonstrate the difference between the output of the signal generator (a conventional oscillator) and the NANOR[®]-type component. The signal generator had a Q less than 2.3×10^4 . By contrast, the RF emissions obtained from the NANOR[®]-type component had a Q greater than 1.2×10^6 . This narrow bandwidth (high Q) heralds maser activity.

3.8. Zeeman splitting of peak by an external magnetic field

It was found that a magnetic field parallel to the major resonant cavity axis caused clear Zeeman splitting and which decreased when the magnetic field was moved perpendicular to the major axis. This Zeeman effects/observation is consistent with reports of masers [33].

3.9. Evanescent peaks and wideband emissions

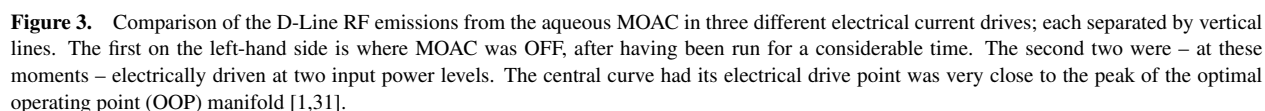
The new narrow bandwidth RF emission peaks disappear with removal of the applied voltage. Despite a much faster rise time when maser action first appears after initiating electrical drive, there is a slower fall-off of the RF emissions within several (~3–4) minutes after electrical drive is terminated. The emissions are also characterized by a much smaller amount of energy disturbed over a region of wider bandwidth. This is similar to other observed masers [34].

4. Results

4.1. RF emissions from active aqueous Ni MOAC

This experimental survey began with preliminary amateur radio and LANR investigations that examined and resolved, for the first time, the apparent absence of HL and presence of DL emissions from the MOAC LANR (ordinary water) aqueous system electrically driven during its active mode [13]. The HL and DL were regions were examined with the MOAC off over weeks, to learn the galactic (followed by the zodiac) rhythm. The initial HL results were inconclusive but with recent improvements in sensitivity and selectivity, further investigations are warranted.

The DL results showed something else. Figure 3 is composed of three curves showing the output of an aqueous Ni/H₂OD₂O/Pt system MOAC-type, at three moments in time, at three moments in time; post-loading no further electrical input, electrical drive at the optimal operating point, and just beyond that input power. Figure 3 shows these RF emissions from an active aqueous Ni LANR system. The figure shows the data for experiment E31 = 180 503 with the driving power off, and then at 10 V and 45 mA electrical current, and then at 20 V and ~200 mA electrical current. Figure 3 compares the emission in the RF region between ~327.25 and ~327.5 MHz (the D-Line region) for



Attention is directed to the fact that there are distinguishable differences in both the integrated amplitude near that region, and in the nature of the superhyperfine structure (sidebands). The increased emission in the D-Line region is apparent.

This is important for several reasons. First, it proves that D is the fuel. Second, the RF emission demonstrates that the deuteron, in the excited pre-⁴He state is a D free radical. Third, the emission is normally forbidden on Earth, and here it shows up ONLY when there is excess heat. Thus, this is important because it is a signal for working, active LANR systems, providing information on the activity. For that information these sidebands are analyzed below. Because of the positive results in the aqueous system, it was also elected to further investigate the dry, preloaded NANOR[®]-type components for possible RF emission, too.

4.2. RF emissions from preloaded Pd NANOR[®]-type components

There were also positive results (analyzed below) from the dry preloaded NANOR[®]-type components.

Unlike the result from the ohmic resistors, there is a clear LANR-related narrow bandwidth maser line emission resulting ONLY from electrically driving some of these ZrO₂PdD preloaded Nanor[®]-type LANR components (7-4,7-5, and others) below the avalanche voltage (e.g. Fig. 4 and see [10,13]). These very narrow bandwidth emission peaks (some singular, and others with sidebands) are hundreds of Hertz wide in a frequency band of 327 MHz. The narrow bandwidth RF emission peaks which appear with electrical drive are located very close to the expected emission of

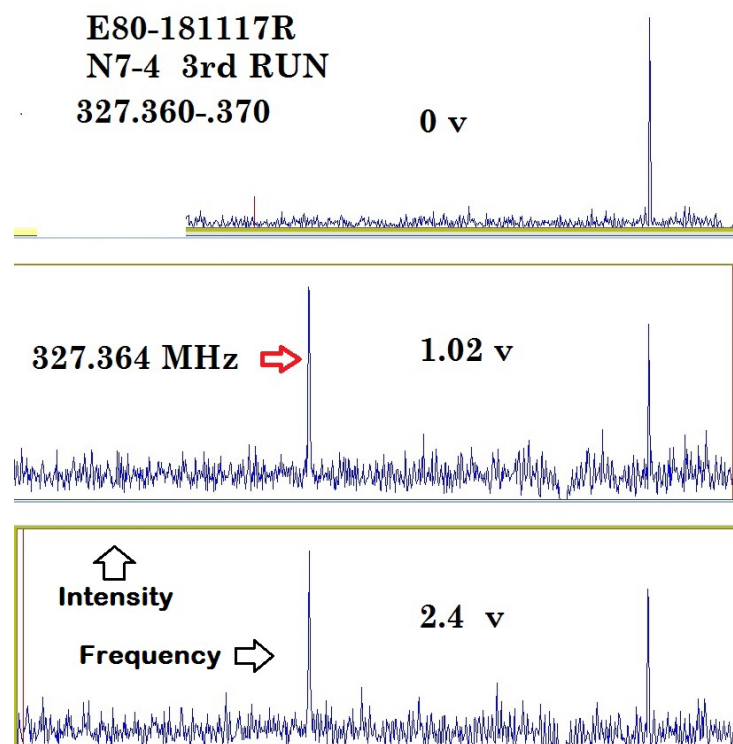


Figure 4. Appearance of maser line. Shown is the Intensity of the RF emissions in the region from 327.360 to 327.370 MHz (the D-Line region) as a function of frequency and applied electrical potential to the NANOR[®] type component N7-4. A high Q output is seen at 327.364 MHz. The other RF emission line on the right is galactic in origin.

deuterium.

Figures 1, 5, and 7 are the images showing the superhyperfine output a prefilled nanostructured PdD–ZrO₂ material. Figure 1 shows the instantaneous intensity vs. frequency output on top, and a waterfall image of the superhyperfine structure with intensity at various times, vs. frequency.

This is important for several reasons. First, it proves that D is also the fuel for the dry preloaded LANR components. Second, the RF DL emission again appears ONLY when there is excess heat and NOT when they are subthreshold voltage and NOT when they are in avalanche mode. As importantly, the RF maser emission and sidebands ONLY occur for several LANR components and NOT when other components are substituted for them. As with the aqueous LANR system, this is important because it is a signal for working, active nanomaterial LANR systems, providing information on the activity.

4.3. Larger voltages reveal superhyperfine line spectra

There are voltage dependent sub-hyperfine (hereinafter called “superhyperfine”) peaks. The applied voltage increase yielding this display of superhyperfine sideband structure can be seen in Fig. 5. At higher electrical input power, some peaks increase in amplitude (327.3839 MHz) and additional peaks appear. The newly appearing peaks, like the previous LANR-active RF DL peaks are evanescent when the power is turned off; and can be seen to disappear in the

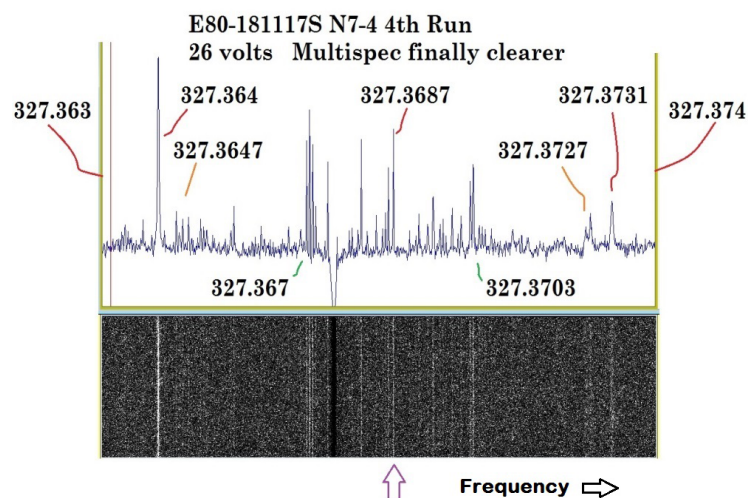


Figure 5. Superhyperfine structure of RFDL-LANR emission. This is a frequency–time plot of the driven LANR component. Note the appearance of a central maser line which is NOT the highest amplitude. Shown is the RF intensity as a function of frequency in the D-Line region for the NANOR[®]-type component N7-4, and increased drive potential was used to bring out the peaks. Improved grounding was used to maximally remove may other interfering signals (QRM) and atmospheric noise (QRN). The null to the right of the 327.367 MHz complex is an error in the equipment/receiver that usually is placed outside of the examined region.

lowest graph (the return to off).

It might be important to note that the RF maser emission occurred at lower driving voltages than had been used to elicit other diagnostic techniques such as CMORE spectroscopy looking for antiStokes lines. It is unclear the reason, or why higher trans-sample voltages below threshold electrical avalanche voltage, elicited the superhyperfine lines (DL sidebands) appear.

This needs to be further investigated as a function of input current, as well as power, because analysis may yield information on the collisions which lead to the desired reactions, as well as the material science.

This analysis begins with attention directed to Figures 1, 5 and 7. They show the superhyperfine structure of the RF DL-LANR emission of D-loaded Pd in its active state. It is an image showing the superhyperfine output of a prefilled nanostructured PdD–ZrO₂ material. It has an instantaneous intensity vs. frequency output of the driven active LANR component on top, and a waterfall image of the superhyperfine structure with intensity at various times, vs. frequency. Shown is the RF Intensity as a function of frequency in the D-Line region for the NANOR[®]-type component N7-4, and increased drive potential was used to bring out the peaks. Improved grounding was used to maximally remove may other interfering signals (QRM) and atmospheric noise (QRN). The main peak (at 327.3687 MHz) and several peaks of the superhyperfine structure (sidebands) are shown. A receiver artifact is shown. This null to the right of the 327.367 MHz complex is an error in the equipment/receiver that usually is placed outside of the examined region.

Figures 1, 5, and 7 have information which enables analysis of the D-Line RF emission using the superhyperfine structure. These RF emission lines are first analyzed for symmetry (Fig. 7), and then for their amplitude and positions as a function of frequency (Fig. 1). Figure 1 is an image showing the superhyperfine output of a prefilled nanostructured PdD–ZrO₂ material, with intensity vs. frequency output on top, and two hypothetical (gendanken) exceptions of locations of said outputs when resonance broadening and location in the lattice are both considered.

Only after the LANR components are electrically driven into the active XSH-producing state, the data is collected.

The information is obtained by an analytical system which measures, or derives, the coordination numbers determined by the normalized intensities of the superhyperfine peaks, and the resonance broadening determined by the translational distance of each of the superhyperfine peaks from the central peak. This is important for at least three reasons. First, the superhyperfine structure does NOT appear when the components are at subthreshold driving voltage, and NOT when they are in electrical avalanche mode, nor when other components are substituted for them. Second, the RF emission provides unique information about the driving/controlling/limiting conditions of the desired state of active CF/LANR. Third, it yields characteristics regarding the location within the lattice.

5. Interpretation

5.1. Analysis of superhyperfine line spectra

The emissions have very narrow bandwidth. The Q (frequency over half power bandwidth) has ranged from 1.2×10^6 to some measurements at high as 9×10^6 . This is because in the microwave region, at the DL line, spontaneous emission can be neglected [26] supported by the fact that atomic deuterium as occurs in Group VIII binary metals has no electric dipole moment. As in outer space, because atomic deuterium and hydrogen have no electric moment, this transition between these two states is highly forbidden with an extremely small transition rate.

It is unclear why the emission frequency is not precisely the same as for free radical deuterium. It may be perturbations of the electron orbits in D secondary to the Ni or Pd in which it is a binary alloy. It may also arise from magnetic Ni or Pd atoms which impact the hyperfine, and now superhyperfine, splitting. The Pd^{105} (abundance 22%) has a nonzero nuclear magnetic moment, and we have discussed some of these magnetic Pd effects in this magnetized LANR components [10].

This paper reports that the LANR induced RF DL-emissions yield insight into LANR active site, the LANR active excited state, and the periodic magnetic locations surrounding the RF emitter. As a result, as shown below, these energy and matter-magnetic field intensity power spectra can be analyzed to give metallurgical and material science information not otherwise available.

It is believed that the separations results because of resonance broadening which occurs when the perturbing particle is of the same type as the emitting particle and it introduces the possibility of energy exchange processes. The resonance broadening goes as $\frac{1}{r^3}$, where r is the distance from the active CF/LANR site.

Most importantly, this paper reports that the hyperfine structure of some of these LANR DL appear consistent with the RF-emitting deuteron being located in an FCC vacancy for Pd systems. This is important, and it also reveals insight into the stereoconstellation surrounding the LANR active site.

5.2. Asymmetry analysis of PdD superhyperfine structure

These RF emission lines have been analyzed first for asymmetry, and then for their amplitude and positions as a function of frequency. This analysis begins with attention directed to Fig. 7. Start with the arrow and focus on that line above the arrow: note the near mirror appearance of the singlets and the multiplet. The arrow marks appear is the actual central line around which all the lines and spacings are somewhat symmetric. Note that this is by spacing. Unlike “normal” spectroscopy, it is not symmetric by intensity. In this case, the arrow marks the central CF/LANR RF maser D-Line which is NOT the highest amplitude. The asymmetry is 7% for the 1st closest position. For the more complex range of the superhyperfine structures the variation is $\sim 10 \pm 5\%$. It is 13% for the third closest position.

These are actually far smaller than the 50% discussed and noted in the literature for some other Zeeman splitting [15,35].

In Fig. 6, also note that during drift towards a stable monochromatic frequency, the sidebands in the superhyperfine structure move together.

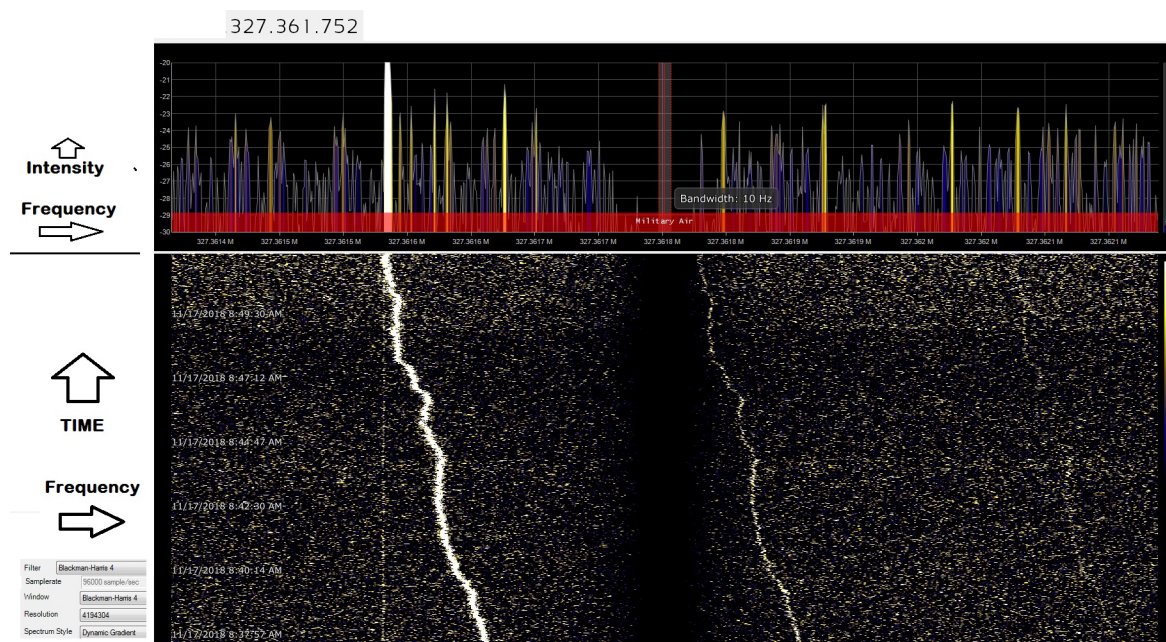


Figure 6. Connected drift of superhyperfine structure of RFDL-LANR emission. This is a frequency–time plot of a driven LANR component showing drift and shift (hunting) behavior. Shown is the RF intensity emission, before stabilization, as a function of frequency in the D-Line region for the NANOR[®] type component N7-4, and increased drive potential was used to bring out the peaks. Improved grounding was used to maximally remove other interfering signals and QRN.

5.3. Identification of PdD closest neighbors

Figure 1 shows that the LANR induced RF DL-emissions yield insight into LANR active site and the LANR active excited state. As a result, as shown below, these energy and matter-magnetic field intensity power spectra can be analyzed to give metallurgical and material science information not otherwise available.

Understanding the analysis of the superhyperfine structure of the D-line emission of the LANR active state begins with an examination of the closest neighbors in the palladium lattice – which is face centered cubic. Consider, within the lattice, the first four levels of closest neighbors which exist, and are now examined, around a gendanken FCC Pd vacancy. In such an FCC lattice, at any point, there are 12 first closest neighbors. They each have a distance of $1/2$ lattice spacing away. Therefore, it is said that the coordination number (CN) is 12 and the separation distance, d , is $a/2$.

First closest neighbor $CN = 12$, $d = a/2$, where a is the lattice spacing.

Next, there are 8 s closest neighbors. These are located on opposite walls of the unit cell. The distance of separation, d , in this case, is the unit cell distance divided by the square root of two.

Second closest neighbor $CN = 8$, $d = a/\sqrt{2}$.

Then, there are six third closest neighbors. They are located one lattice space away in each of the six directions. That makes d equal to a , the lattice spacing.

Third closest neighbor $CN = 6$, $d = a$.

Finally, the fourth closest neighbors are eight in number, and located at the opposite vertices of the two units abutting the face centered cubic palladium site under analysis. In this case, the separation distance, d , is the lattice spacing

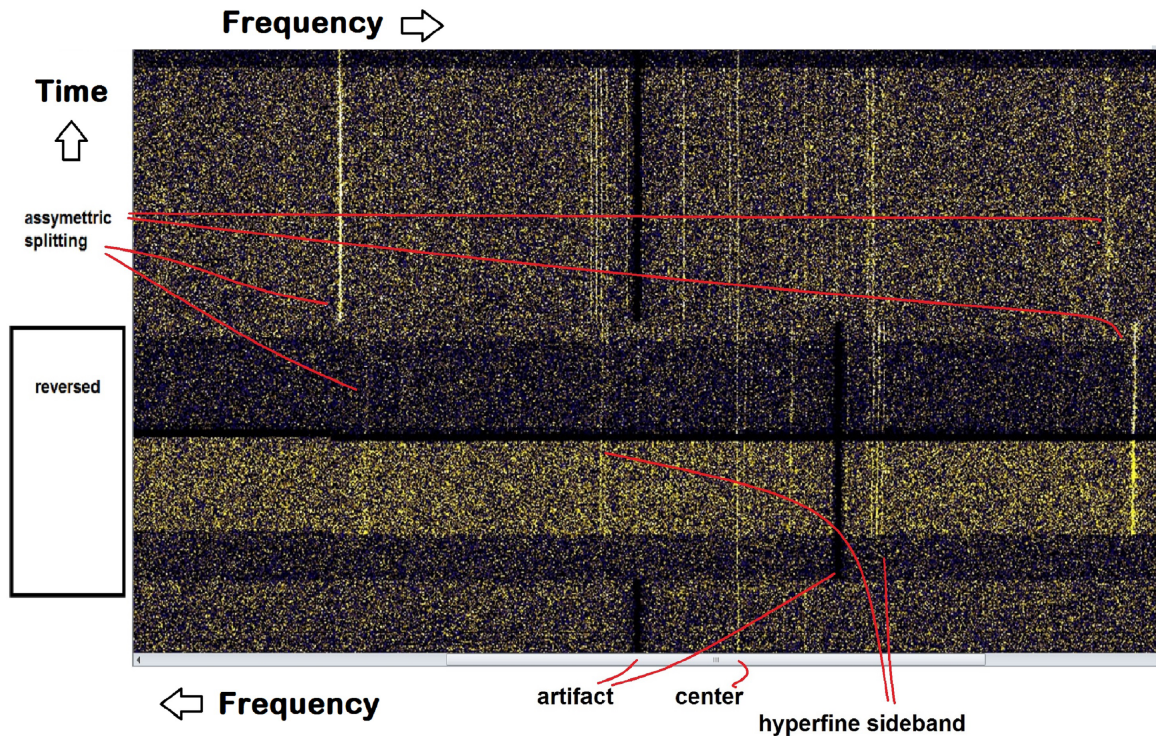


Figure 7. Asymmetry analysis of Pd superhyperfine splitting. Shown is the superhyperfine spectrum of D-loaded Pd in its active state. The bottom half is optically mirror-reversed around the center, showing that there is not exact symmetry.

times the square root of $3/2$.

Fourth closest neighbor $CN=8$, $d = a\sqrt{3/2}$.

5.4. Impact of closest neighbors on superhyperfine spectrum

Resonance broadening occurs when the perturbing particle (in this case deuterons in other vacancies) is of the same type as the emitting particle (a deuteron emitting at the D-line), and that will introduce the possibility of an energy exchange process. Using the results of Table 1, specifically the resonance broadening (or relative magnetic field intensities depending upon the model) which should be directly proportional to the hyperfine splitting. Thus, the ratios of the impact of resonance broadening (or magnetic impact) were derived for the first four closest neighbor sites, and then superposition used.

These ratios, derived in Table 1, are shown semiquantitatively in Fig. 8 normalized to the strongest (putative closest neighbor) line. Incidentally, the variation in distance in the Column 3 should come into play in the Dicke narrowing contributing to the high Q .

Resonance broadening falls off as the cube root of the distance. Thus, the $1/r^3$ characterizes the falloff of the resonance interaction, and the constellation of these superhyperfine peaks are a means to identify, where in the lattice from where they come. This is done by examining the overlap of expected peaks/lines and actual derived peaks (superhyperfine lines) as a function of said frequency.

Thus, the ratios of RB impact were derived for the first four closest neighbor sites, and then superposition used. The first column in Table 1 are the nearest neighbors by position for Pd. The second column normalizes the lattice spacing. The third column is therefore the relative distance, followed by the coordination number in column four. The final column contains the expected resonance broadening, which like derived relative magnetic field intensities, falls off as $1/r^3$. Normalization was made to the largest observed line. Incidentally, the variation in distance in the Column 3 should come into play in the Dicke narrowing contributing to the high Q . Attention is now made to determine the lattice geometric parameters and which phase (such a FCC or BCC) the lattice is comprised.

5.5. Vacancy (FCC) is the active site

These CF/LANR-induced RF emission lines, superhyperfine lines, have been analyzed (Fig. 1). It is an image showing the superhyperfine output of a prefilled nanostructured PdD–ZrO₂ material, Nanor[®]-type component 7-4. The figure shows the lattice analysis of this active PdD component from its RF emission frequency-time plot.

At the top of Fig. 1 is the intensity as a function of frequency plot, in a waterfall presentation of the experimental findings by frequency horizontally, as a function of time vertically. Here, the Nanor[®]-type component 7-4 is driven at sufficient voltage that the additional lines appear. In the middle of Fig. 1, some of the peaks are identified. This is simplified in that, for example, the triplet is treated as a single peak. At the bottom of Fig. 1, shown are the coordination number and expected deviations by calculated resonance broadening at each putative active site based upon known locations for both FCC and BCC lattice arrangements. The expected resonance broadening has falloff which does decrease as $1/r^3$.

Attention is directed to the two hypothetical (gedanken) expectations of locations of said outputs when resonance broadening and location in the lattice are both considered for a FCC lattice vs. a BCC lattice, for comparison. Each compares the expected findings for four nearest neighbors. Each has the horizontal distance related to the inverse cube of the distance, d . Also shown is the coordination number, for each. The figure shows considerable overlap of the expected locations in the mid-graph and the frequency singularities above them for the FCC lattice, but not the BCC lattice. The FCC locations and BCC locations respectively must be compared with what is observed. The normalizations for each are made for the first closest neighbor.

FCC is a much closer match than BCC, and thus the actual lattice of Pd heralds the location of the active site. Thus, most importantly, analysis of the amplitude and positions as a function of frequency of the superhyperfine structure of these LANR DL emissions appear consistent with the RF-emitting deuteron being in an excited atomic state and being in a slightly modified palladium (Pd) vacancy within the Pd FCC lattice vacancy. This is important, and it also reveals insight into the stereoconstellation surrounding the LANR active site. The data uniquely shows the positions of nearby sites vicinal to an emitter, and they appear to be at nearest neighbor FCC locations, which closely match what is observed (Fig. 1). Simply put, the results in Fig. 8 show that the palladium vacancy is, as predicted at ICCF-4 (Swartz), the site of the desired reaction in these active systems.

Furthermore, for the lower RF frequencies, there is another indication that the coordination number is qualitatively

Table 1. Impact of resonance broadening from nearest neighbor locations in Pd FCC normalized to the first closest neighbor.

Nearest neighbor	Spacing	Rel distance to vacancy	CE coordination number	Rel. resonance broadening field intensity at DL emission location
First	1	0.50	12	1
Second	1	0.7072	8	0.3533
Third	1	1.0	6	0.125
Fourth	1	1.2248	8	0.06801

associated with what is seen. The output qualitatively appears to match the intensity of some of the lines for the FCC lattice.

If the magnitudes of the received outputs are qualitatively related to the expected emissions by coordination number, then the band at 327.364 MHz (blue band) is in fact the largest at the lower frequencies, as expected. This may explain why the center peak is NOT the highest in magnitude (unlike Zeeman splitting).

5.6. Other changes observed in ZrO_2 -PdD

5.6.1. *Fourth closest neighbor merged with second closest neighbor*

Furthermore, upon close inspection, the spectra provide information on the interactions between active sites, in situ. Specifically, the lower RF frequencies also suggest that the coordination number is qualitatively associated with what is seen – except for the following.

The second closest neighbors are now different. Also this comes from interaction with half of the fourth closest neighbors. Analysis of the superhyperfine structure is consistent with what appears to be loss of coordination number (CN) meaning a change in structure with fewer in that position and some of the elsewhere including a new interaction causing an apparent change in magnetic properties of, the fourth and second closest neighbors, respectively (Figs. 1 and 7). Specifically, it appears that part of the fourth nearest neighbors are now interacting with the second closest neighbors creating a superhyperfine structure within (green band).

5.6.2. *Third closest neighbor demonstrates multiplet substructure*

The superhyperfine structure indicates a multiplet at the position of, and possibly due to a new, second nearest neighbor. This might mean that this results from the active site being near, or in, the zirconium oxide, at a rhombic corner. That location is magnetically closely isoequivalent to an FCC vacancy (Fig. 1). Alternatively, it might mean that an atom of zirconium (or impurity therein the oxide) may have entered the Pd lattice, as has been suggested [30].

5.7. Analysis of non-Zeeman superhyperfine splitting for NiD

The RF emission lines have been analyzed more closely of the data derived from the aqueous nickel MOAC system in its active mode (Figs. 9 and 10). Figure 9 shows the asymmetry analysis. It is much closer to a theoretical mirror, than for the Pd system.

5.8. Identification of NiD closest neighbors

Figure 10 shows the experimental findings on the top. This presents the data by frequency horizontally, as a function of time vertically. The graph on the bottom shows the expected relative resonance effect (or alternatively magnetic field intensity) for each of the closest neighbors, and has the horizontal distance related to the inverse cube of the distance, d , for BOTH an FCC lattice, and BCC lattice. Analysis of the amplitude and positions as a function of frequency strongly suggest that the hydride nickel has changed in phase from a simple FCC lattice.

The data uniquely shows the nearby sites surrounding the active site in an active nickel CF/LANR system. Note that some locations appear to have further splitting, and there are what appear to be two slightly different layers within the new phase, or two new phases.

The minority report must include that the vacancy might be in rhombic ZrO_2 which is also an FCC.

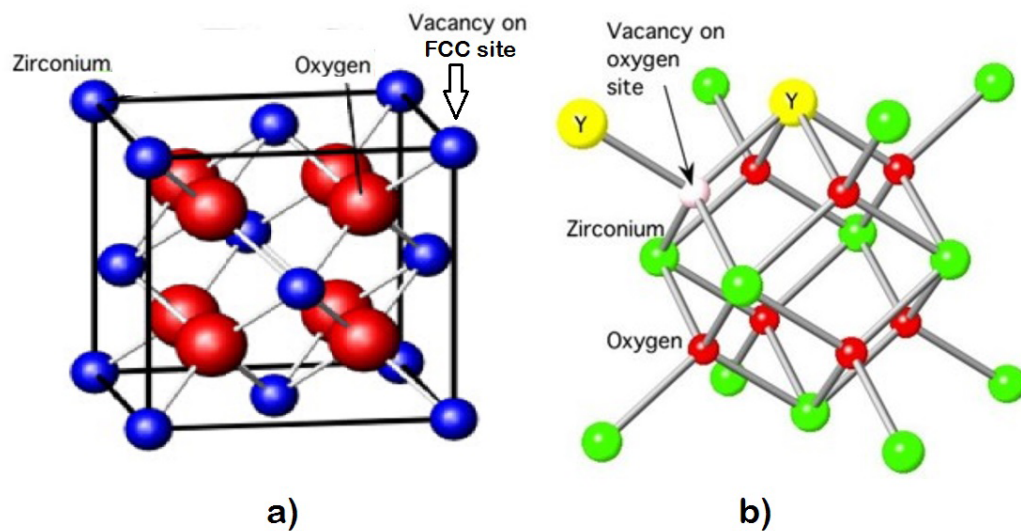


Figure 8. Possible vacancy sites to consider on ZrO₂. The first possible site is in the rhombic formation, which is near FCC in stereoconstellation (*left*). Oxygen vacancies should be considered even though inconsistent with the present group of sidebands (superhyperfine lines; *right*).

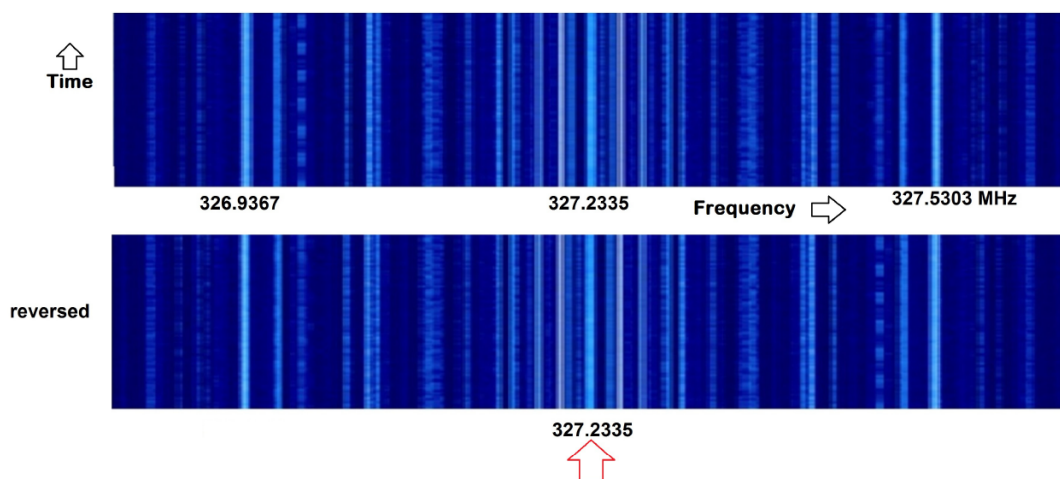


Figure 9. Asymmetry analysis of nickel superhyperfine splitting. Shown is the superhyperfine DL spectrum of the hydrogen loaded nickel MOAC in its active state (40 V, 200 mA). Note that the bottom half is simply reversed horizontally around the arrow to enable comparison of the left and right. The frequencies of the widest, and central, peaks are identified. For both cases, in this instance, the center is identified by the arrow. Attention is directed to the symmetry.

6. Conclusions

Active CF/LANR systems, both aqueous and nanomaterial, emit very narrow bandwidth RF emission peaks (ca. 327.37 MHz), which are located very close to the theoretical Deuteron-Line (DL; 327.348 MHz) region, and they exhibit a large Q ($>1.2 \times 10^6$), which is the ratio of the bandwidth at half power to the frequency [13]. This paper demonstrates that at higher applied driving voltage, a superhyperfine line structure of sidebands appears, and this revelation gives more insight into the volume and stereoconstellation around the active site.

6.1. Confirmation of fuel

These results confirm that in active CF/LANR systems deuterons are making helium-4 which generates the observed excess energy in the active state [17,37]. This excess energy has a very large specific density making it comparable to other systems [38]. The fuel generates the fusion product and at least some of these reactions occur in face center cubic (Pd FCC) vacancy for palladium (in PdD) or Zr (in ZrO₂).

6.2. Derivation of the active site

Analysis using putative nearest neighbors indicates a possible location of the deuteron free radical during its RF emission. Vacancies, as predicted at ICCF-4 [16], are apparently the site of some of the desired reaction in these active systems. The coordination number is qualitatively associated with what is seen, except for some possibly very important changes. The second closest neighbors are now different. And this appears to have come from interaction with half of the fourth closest neighbors, with either that interaction of additional paramagnetic (possible lattice Zr in Pd contamination) factors, changing the singlet to multiplet.

The results in nickel are much more complex and demonstrate a range of both FCC and BCC vacancies, possibly heralding new metallurgic phases.

6.3. Summary

Detection, RF identification and recognition of LANR RF emission from the active state are important. The reasons include information about the activity, location of, and changes to, the active site.

In the future, RF detection, like coherent antiStokes spectroscopy [11,12,32], can be used to detect the active – rate-limiting–excited (desired) state. These also discern data from the phenomenon's location, including some of the conditions requisite to attain the desired active XSH-producing driven state.

In the next paper [14], another important detail of the superhyperfine line structure of sidebands will be discussed. It appears that in active CF/LANR systems, the loaded deuterons work together from their vacancy sites, disappearing two at a time from those deuterons decorating the binary alloy, to enable continuation of the desired XSH-producing reactions within the loaded Group VIII metal. At least some of their emitting RF radiation superhyperfine line peaks, located at the DL heralding the inverted population, are observed to be pulsing. This action may herald quantum movements of energy and matter within an active XSH-producing PdD Lattice.

Acknowledgments

The author gratefully acknowledges and thanks David Nagel, Bo Gardmark, Gayle Verner, Peter Hagelstein, Lawrence Forsley, Louis Dechiaro, Isidor Straus, Joshua Gyllinsky, Brian Ahern, John Wallace and Dan Steinberg for their very helpful comments, editorial assistance, and additional material. The author also thanks Brian Ahern, Alan Weinberg and the late Charles W. Haldeman for their construction, early testing, modifications, and transfer of the MOAC. This effort has been supported by JET Energy Inc., Nanortech Inc., and Anthropocene Institute.

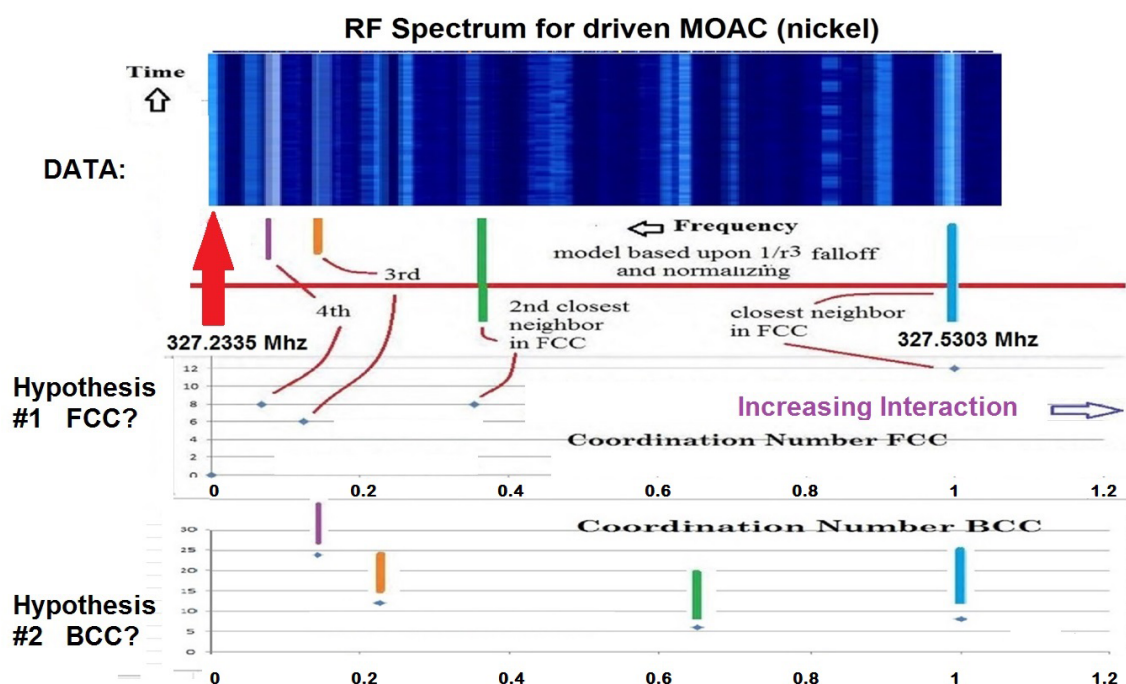


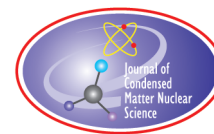
Figure 10. Lattice analysis of active MOAC's frequency–time plot. This figure shows an analysis of the active MOAC's (nickel cathode) super-hyperfine structure using a frequency–time plot and, below it, implied assignment based upon nearest neighbor location and the expected magnetic field intensity (falloff– $1/r^3$ model). *Top:* Intensity as a function of frequency in a Waterfall. Here, the MOAC is electrically driven to produce excess power. *Middle:* Some of the peaks (those for FCC, for simplicity) identified. *Bottom:* Coordination number and expected deviation for each calculated magnetic field strength at the putative active site based upon known locations for both FCC and BCC lattice arrangements. The figure shows considerable overlap of the expected locations for the FCC lattice, and the BCC lattice. This may be consistent with the new phases seen for electrochemically loaded nickel [36].

References

- [1] M.R. Swartz, G. Verner and J. Tolleson, Energy gain from preloaded ZrO_2 –PdNi–D nanostructured CF/LANR quantum electronic components, *J. Condensed Matter Nucl. Sci.* **13** (2014) 528, www.iscmns.org/CMNS/JCMNS-Vol13.pdf.
- [2] M.R. Swartz, G. Verner, J. Tolleson and P. Hagelstein, Dry, preloaded NANOR[®]-type CF/LANR components, *Current Sci.* **108** (4) (2015) 595.
- [3] M.R. Swartz and P.L. Hagelstein, Demonstration of energy gain from a preloaded ZrO_2 –Pd nanostructured CF/LANR quantum electronic device at MIT, *J. Condensed Matter Nucl. Sci.* **13** (2014) 516, www.iscmns.org/CMNS/JCMNS-Vol13.pdf.
- [4] M.R. Swartz, P.L. Hagelstein and G. Verner, Impact of electrical avalanche through a ZrO_2 –NiD nanostructured CF/LANR component on its incremental excess power gain, ICCF-19, *J. Condensed Matter Nucl. Sci.* **19** (2016) 287–297.
- [5] M.R. Swartz, Optical detection of phonon gain distinguishes an active cold fusion/LANR component, *J. Condensed Matter Nucl. Sci.* **20** (2016) 29–53, www.iscmns.org/CMNS/JCMNS-Vol20.pdf.
- [6] M.R. Swartz and P.L. Hagelstein, Increased Pd anti-Stokes peaks are correlated with excess heat mode, *J. Condensed Matter Nucl. Sci.* **24** (2017) 130–145.
- [7] M.R. Swartz, G. Verner, J. Tolleson, L. Wright, R. Goldbaum and P.L. Hagelstein, Imaging of an active NANOR[®]-type LANR component using CR-39, *J. Condensed Matter Nucl. Sci.* **15** (2015) 81, www.iscmns.org/CMNS/JCMNS-Vol15.pdf.
- [8] M.R. Swartz, Incremental high energy emission from a ZrO_2 –PdD nanostructured quantum electronic component CF/LANR,

- J. Condensed Matter Nucl. Sci.* **15** (2015) 92, www.iscmns.org/CMNS/JCMNS-Vol15.pdf.
- [9] M.R. Swartz, G. Verner, J. Tolleson, L. Wright, R. Goldbaum and P.L. Hagelstein, Amplification and restoration of energy gain using fractionated magnetic fields on ZrO_2 –Pd nanostructured components, *J. Condensed Matter Nucl. Sci.* **15** (2015) 66, www.iscmns.org/CMNS/JCMNS-Vol15.pdf.
 - [10] M.R. Swartz, P.L. Hagelstein and G. Verner, Impact of electrical avalanche through a ZrO_2 –NiD nanostructured CF/LANR component on its incremental excess power gain, ICCF-19, *J. Condensed Matter Nucl. Sci.* **19** (2016) 35–46.
 - [11] M.R. Swartz, Optical detection of phonon gain distinguishes an active cold fusion/LANR component, *J. Condensed Matter Nucl. Sci.* **20** (2016) 29–53, www.iscmns.org/CMNS/JCMNS-Vol20.pdf.
 - [12] M.R. Swartz and P.L. Hagelstein, Increased PdD anti-Stokes peaks are correlated with excess heat mode, *J. Condensed Matter Nucl. Sci.* **24** (2017) 130–145.
 - [13] M.R. Swartz, Deuterons in active LANR systems emit a 327.37 MHz hyperfine maser line, *J. Condensed Matter Nucl. Sci.* (2019), to appear.
 - [14] M.R. Swartz, Pulsatile 327.37 MHz superhyperfine line heralds lattice mass–energy movements, *J. Condensed Matter Nucl. Sci.* (2019), to appear.
 - [15] G.W. Walker, On asymmetry of the Zeeman effect, The London, Edinburgh, and Dublin Philosophical Magazine, *J. Sci. Series 6* **3** (14) (1902) 247–251, <https://doi.org/10.1080/14786440209462760>.
 - [16] M.R. Swartz, Catastrophic active medium (CAM) theory of cold fusion, *Proc. ICCF4*, 4, 1993, p. 255, sponsored by EPRI and the Office of Naval Research.
 - [17] M.R. Swartz, Charles Haldemann, Alan Weinberg and Brian Ahern, Possible deuterium loss during excess heat from ordinary water-carbonate electrolyte using nickel, *J. Condensed Matter Nucl. Sci.* **29** (2018) 169.
 - [18] M.R. Swartz, Aqueous and nanostructured CF/LANR systems each have two electrically driven modes, *J. Condensed Matter Nucl. Sci.* **29** (2019) 177.
 - [19] M.R. Swartz, Consistency of the biphasic nature of excess enthalpy in solid state anomalous phenomena with the quasi-1-dimensional model of isotope loading into a material, *Fusion Technol.* **31** (1997) 63–74.
 - [20] M.R. Swartz, Codeposition of palladium and deuterium, *Fusion Technol.* **32** (1997) 126–130.
 - [21] M.R. Swartz and G. Verner, Excess heat from low electrical conductivity heavy water spiral-wound Pd/D₂O/Pt and Pd/D₂O–PdCl₂/Pt devices, *Condensed Matter Nuclear Science, Proc. ICCF-10*, World Scientific, NJ, ISBN 981-256-564-6, 29-44; 45-54 (2006).
 - [22] M.R. Swartz and G. Verner, The Phusor[®]-type LANR cathode is a metamaterial creating deuteron flux for excess power gain, *Proc. ICCF-14*, Vol. 2, D.J. Nagel and M.E. Melich (Eds.), 2008, p. 458, ISBN: 978-0-578-06694-3, 458, (2010); www.iscmns.org/iccf14/ProcICCF14b.pdf.
 - [23] M.R. Swartz, G. Verner and A. Weinberg, Non-thermal near-IR emission from high impedance and codeposition LANR devices, *Proc. ICCF14*, Vol. 1, D.J. Nagel and M.E. Melich (Eds.), 2008, p. 343, ISBN: 978-0-578-06694-3, 343, (2010); www.iscmns.org/iccf14/ProcICCF14a.pdf.
 - [24] M.R. Swartz, Excess power gain using high impedance and codepositional LANR devices monitored by calorimetry, heat flow, and paired stirling engines, *Proc. ICCF14* **1** (2008) 123, ISBN: 978-0-578-06694-3, 123, (2010), www.iscmns.org/iccf14/ProcICCF14a.pdf.
 - [25] M.R. Swartz, Survey of the observed excess energy and emissions in lattice assisted nuclear reactions, *J. Scientific Explor.* **23** (4) (2009) 419–436.
 - [26] M. Swartz, Improved electrolytic reactor performance using π -notch system operation and gold anodes, Transactions of the American Nuclear Association, Nashville, TN, Meeting, ISSN:0003-018X publisher LaGrange, Ill, Vol. 78, 1998, 84–85.
 - [27] M. Swartz, Can a Pd/D₂O/Pt device be made portable to demonstrate the optimal operating point?, Condensed Matter Nuclear Science, *Proc. ICCF-10*, P.L. Hagelstein and S.R. Chubb (Eds.), World Scientific, NJ, ISBN 981-256-564-6, 29-44; 45-54 (2006).
 - [28] M. Swartz, Investigations of heat after death: analysis of factors which determine the tardive thermal power and HAD enthalpy, *J. Condensed Matter Nucl. Sci.* **31** (2020) 20–41.
 - [29] M. Swartz, Photoinduced excess heat from laser-irradiated electrically-polarized palladium cathodes in D₂O, Condensed Matter Nuclear Science, *Proc. ICCF-10*, P.L. Hagelstein and S.R. Chubb (Eds.), World Scientific, NJ, ISBN 981-256-564-6, 213-226 (2006).

- [30] M. Swartz, G.M. Verner and A.H. Frank, *The Impact of Heavy Water (D₂O) on Nickel-Light Water Cold Fusion Systems*, Proc. ICCF9, Xing Z. Li (Ed.), China, 2002, pp. 335–342.
- [31] M.R. Swartz, Optimal operating point manifolds in active, loaded palladium linked to three distinct physical regions, *Proc. ICCF-14*, Vol. 2, D.J. Nagel and M.E. Melich (Eds.), 2008, pp. 639, ISBN: 978-0-578-06694-3, 639, (2010).
- [32] M.R. Swartz, Increase of an anti-stokes peak at the cathode of an electrically-driven, active aqueous nickel/H₂O/Pt system, *J. Condensed Matter Nucl. Sci.* **279** (2018) 22.
- [33] R.L. Plante, K.Y. Lo, R.M. Crutcher and N.E.B. Killeen, The magnetic field at the galactic center: detection of HI Zeeman splitting, American Astronomical Society, 183rd AAS Meeting, id.116.05, *Bull. Amer. Astronomical Soc.* **25** (1993) 146, 7AAS...18311605P.
- [34] D.J. Wineland and N.F. Ramsey, Atomic deuterium maser, *Phys. Rev. A* **5** (1972) 821.
- [35] J.E. Mack and O. Laporte, Asymmetric Zeeman effect patterns in a complex spectrum, *J. Archive, Phys. Rev.* **51** (1937) 291, DOI:<https://doi.org/10.1103/PhysRev.51.291.2>.
- [36] M.R. Staker, Coupled calorimetry and resistivity measurements, in conjunction with an emended and more complete phase diagram of the palladium – isotopic hydrogen system, *ICCF-21*, June 5, 2018, <https://www.youtube.com/watch?v=4FeMnRjTtr0>.
- [37] M. Miles, Correlation of excess power and helium production during D₂O and H₂O electrolysis using palladium cathodes, *J. Electroanal. Chem.* **346** (1993) 99–117.
- [38] M.R. Swartz, Comparison of NANOR-type LANR components to ²³⁸Pu as a heat source for space flight, *J. Condensed Matter Nucl. Sci.* **29** (2019) 238.



Research Article

Elliptic Tracks: Evidence For Superluminal Electrons?

Keith A. Fredericks*

Restframe Labs, 310 W. 52nd St., New York, NY 10019, USA

Abstract

In the literature of Low-Energy Nuclear Reactions (LENR), particle tracks in photographic emulsions (and other materials) associated with certain electrical discharges have been reported. Some Russian and French researchers have considered these particles to be magnetic monopoles. The mechanisms of energy deposition and track formation, while among the most important properties, are contradictory and the least understood of all of the observations. Our method of producing these tracks differs markedly from most other studies in that no electrical discharge is used as a source. Rather, tracks are created with a simple uniform exposure to photons. This simpler method of producing exactly the same tracks supports a more comprehensive exploration of particle track properties. Out of 750 exposures with this method, *elliptic particle tracks* were detected, 22 of which were compared to Bohr–Sommerfeld electron orbits in an idealized model. Ellipses fitted to the tracks were found to have quantized semi-major axis sizes with ratios of $\simeq n^2/\alpha^2$ to corresponding Bohr–Sommerfeld hydrogen ellipses. This prompts inquiry relevant to magnetic monopoles due to the n^2/α^2 force difference between magnetic charge and electric charge using the Schwinger quantization condition. Analogy with the electron indicates that the elliptic tracks could be created by a bound magnetically charged particle with mass $m_m = 1.45 \times 10^{-3}$ eV/c², yet with superluminal velocities. Using a modified extended relativity model, m_m becomes the relativistic mass of a *superluminal* electron, with $m_0 = 5.11 \times 10^5$ eV/c², the fine structure constant becomes a mass ratio and charge quantization is the result of two states of the electron. Relevance of this new model is considered in light of the observed inconsistencies in track formation.

© 2020 ISCMNS. All rights reserved. ISSN 2227-3123

Keywords: Elliptic orbits, Faster-than-light, Kepler orbits, LENR, Monopoles, Particle tracks, Photographic emulsion, Strange radiation, Superluminal, Tachyons

1. Introduction

In this paper evidence is reported for quantized elliptic tracks in photographic emulsions with sizes expected of bound magnetic monopoles, yet *requiring* velocities greater than the speed of light, indicating particles with superluminal electric charge.

Preliminary measurement of the first recognized elliptic track detection showed a size difference, to within a few percent of $137^2 n^2 \simeq n^2/\alpha^2$ larger than an $n = 7$ Bohr–Sommerfeld hydrogen electron orbit, α^{-2} being the difference

*E-mail: keith@restframe.com.

in force between electrons and magnetic monopoles using Schwinger quantization, i.e. Eq. (2). This runs contrary to current expectations suggesting magnetic monopole bound states with *smaller* (e.g. 7.2×10^{-18} m) orbit sizes [1] than bound electrons in hydrogen.

Additional experiments provided a collection of elliptic track candidates that were fitted to ellipses. The resulting track fits were quantized according to semi-major axis size, (see Fig. 1) and therefore energy, (see Section 5.3) according to $E^{(n)} = h\nu^{(n)}$, indicating a new particle exhibiting properties of magnetic monopoles. Analogy with the electron and orbit sizes suggest faster-than-light velocities.

Analysis of the results leads to a new model of extended relativity restricted to bound states using a scale transformation rather than the usual superluminal Lorentz transformation (SLT), resulting in the fine structure constant as a mass ratio and a new proposed explanation for charge quantization.

2. Elliptic Tracks

In earlier work [2], properties of new and unusual tracks in photographic emulsions were analyzed and classified. The source of the tracks was unidentified. Analysis showed track configurations clearly distinct from those observed before in nuclear track studies [3], but directly corresponding to tracks from certain studies including:

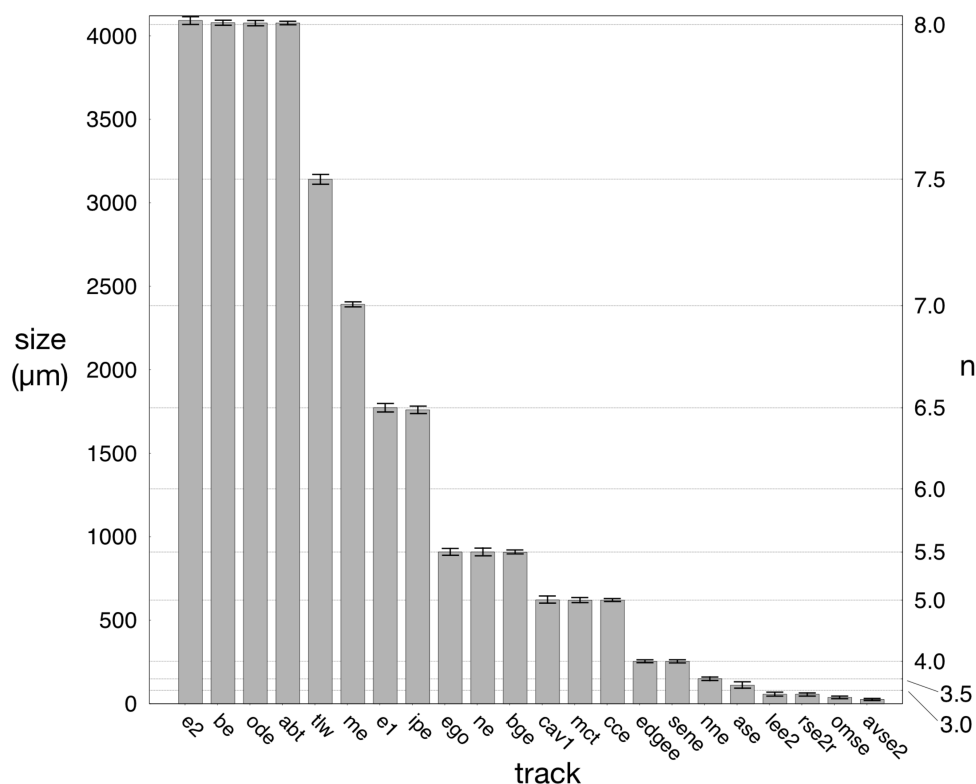


Figure 1. Quantized ellipse semi-major axis sizes. Ellipses between $n = 8$ and $n = 3.5$ are shown to be quantized as half integer values. Ellipses less than $n = 3.5$ are quantized by quarter integer values. Error bars represent the combined standard uncertainty of the semi-major axis size.

- (1) exposure of emulsions during bombardment by low-energy ions in electric explosion of metallic wires and thin foils [4–7],
- (2) exposure of emulsions during low-energy discharges in water and excitation of beta-decay products by a magnetic field [8],
- (3) exposure of emulsions and Pd electrodes during glow discharge plasma processes [9],
- (4) exposure of special semiconductor layers during the super-compression of solid targets using electron beams [10], and,
- (5) exposures of photographic emulsions, CR-39 (with and without etching), PMMA, and glass during picosecond laser irradiation of electrodes [11].

Ivoilov [8] called this unknown source a *control background*.

Using a simple brief uniform amplifying exposure of photons on photographic emulsions exposed to the environment (as in e.g. a cosmic ray study) duplicates virtually all of the track types presented in the list of studies above. This technique is called photon amplification.

The advantages of photon amplification are:

- (1) Tracks can be readily seen in the plastic layer as well as the emulsion layer of photographic films.
- (2) Compared to electric discharge sources, simple conditions of the exposure to light bypasses the need for elaborate laboratory setups and hence more data can be gathered (hundreds of exposures) and the phenomenon can be studied more deeply.
- (3) Amplification or sensitization of the photographic emulsion due to the uniform photon exposure increases the sensitivity of the photographic emulsion to photons and charged particles.
- (4) Detector sensitivity is *re-zeroed* at a higher level by the uniform photon exposure so as to react to tearing down as well as building up of latent image. *White tracks* are detected as well as black tracks.
- (5) The light sensitive volume element of the photographic emulsion registers track images of usual time-like particles, which travel through space and, (if they were to exist and are detectable), space-like particles, which would travel through time, since the detector is continually active until the time of development.

This study is concerned primarily with tracks, in photographic emulsions coated on a plastic base, produced during (or after) brief exposures to light. These exposures to light produce a uniform background density on development. Tracks in emulsion are registered against this background density in addition to tracks registered in the plastic base.

Supplemental uniform exposures of photons followed by or combined with imagewise fluxes of particles (traditionally photons) can enhance the sensitivity of photographic emulsions [12]. Giving the supplemental exposure prior to the imagewise exposure is called pre-exposure [13] or pre-flashing. Giving the supplemental exposure during the same time interval is called *concurrent photon amplification* [14]. These techniques were used experimentally by photographic scientists and practically in astronomy and in autoradiography, but (outside of the present study) apparently never used with emulsions for detection of charged particle tracks (nuclear track studies). One of the critical questions to be answered is how is it possible that a particle, responsible for these tracks, has so far evaded detection, especially with a history of perhaps 150 years of the scientific use of photographic emulsions. Here are some possible explanations:

- (1) Since the tracks are generally microscopic effects, they would not normally be recognized in non-uniform (standard pictorial photography) backgrounds and, if seen, they would be easy to dismiss or ignore as a processing errors, light leaks or other artifacts.
- (2) Since (apparently) no nuclear track studies, that is where emulsions were scanned by greater than $\sim 250\times$ magnification, used supplementary photon exposures as amplification, the probability of these new types of tracks remaining unrecognized would be increased.

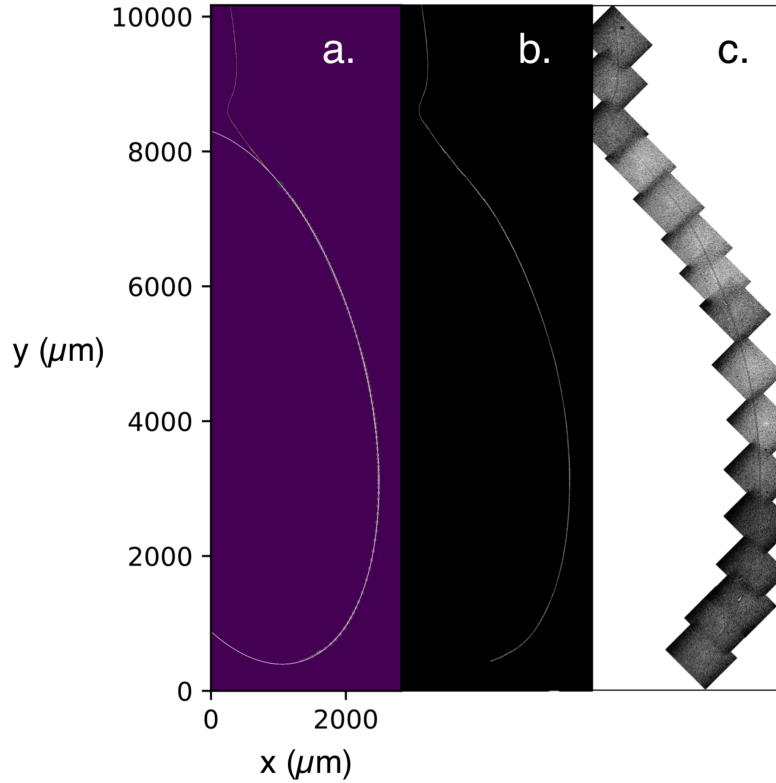


Figure 2. Track *be* (see also Table 1). The semi-major axis size of $a_m = 4078.6 \pm 14.6 \mu\text{m}$ is related to the semi-major axis size of an $n = 8$ electron in hydrogen, a_e by $a_m/137^2 n^2 \simeq a_e$. a.) Least-squares fit of x, y track coordinates to ellipse overlaid on processed track image. b.) Track after image processing and background eradication. c.) Photo montage of track.

- (3) In the case where no supplemental photon exposure is required to create a baseline background of clear tracks (in plastic base or gelatin), and where magnification greater than $\sim 250\times$ was used to scan emulsions, these tracks may well have not been the object of the search or not of interest, being clear rather than black, or they may have been mistaken for something else like surface damage (cf. [7]).
- (4) In the case where no supplemental photon exposure is used and where black tracks, as were reported here, were registered on the film and the film was scanned with greater than $\sim 250\times$ magnification, then it is possible that these tracks were treated as unidentified and never looked at in a deeper way.
- (5) In general, the rate of detection/recognition and the flux (see Section 3.7) was reduced and more capricious compared to objects being studied, decreasing the chance of recognition.

For electrically (magnetically) charged particles, it is expected that magnetic fields (electric fields) applied perpendicularly to the plane of particle motion will produce helical curvature and it is expected that electric fields (magnetic fields) applied transversely to the plane of particle motion will produce parabolic curvature. In [2] the possibility of parabolic curvature in magnetic fields for these tracks was incorrectly asserted. In a large number of experiments using applied magnetic fields from $\sim 6.0 \times 10^{-4}$ to ~ 0.7 T, and electric fields from $\sim 1 \times 10^5$ to 2×10^5 V/m, these particles have not, so far, appeared to follow helical or parabolic paths. Rather, they appear to move in other unpredictable ways.

During these experiments, however, repeatable evidence has been found for tracks with elliptic curvature occurring in the presence *or absence* of applied electric and/or magnetic fields (see Figs. 2–7 and 10). Detection of elliptic curvature is probably the most significant breakthrough in the study of these tracks, providing the possibility to compute, under certain assumptions, via *purely geometrical considerations*, properties of particles capable of creating these tracks.

3. Experimental

3.1. Technique

Experiments between May 2014 and December 2017 used uniform photon amplification of films with applied magnetic and electric fields in various configurations. Results were scanned for curved tracks.

Film types Arista Ortho Litho 3.0 or Rollei Ortho 25 were exposed both in $10.2\text{ cm} \times 12.7\text{ cm}$ and $3\text{ cm} \times 12.7\text{ cm}$ sheets. LED and applied electric and magnetic field exposures were controlled using an Arduino Uno.

3.2. LED exposure

Two or four white LEDs at a 3–6 cm distance from the film plane were turned on simultaneously for a 50–2000 ms exposure. Various white LED lamps were used for the uniform amplifying exposure. These LEDs have a typical luminous intensity of $1250 \pm 15\%$ mcd.

3.3. Applied fields

Abbreviations in boldface appear in the legend of Table 1.

- **DM** Permanent magnet.
 - N45 NdFeB Disc magnet,
 - flux density = 1.32 T,
 - radius = 9 mm,
 - height = 3 mm.
- **BM** Permanent magnet.
 - N40 NdFeB block magnet,
 - flux density = 1.26 T,
 - $50\text{ mm} \times 50\text{ mm} \times 20\text{ mm}$.
- **YM** Permanent magnet
 - N42 NdFeB Yoked magnet,
 - flux density = 0.5 T (center line between poles perpendicular to the x,y plane of the film),
 - $100\text{ mm} \times 6\text{ mm} \times 9\text{ mm}$.
- **AH** Anti-Helmholtz Coil.
 - number of turns = 10,
 - current per coil = 3.0 A,
 - coil radius = 12.7 cm,
 - H Field at center = 0.0 A/m,

- flux density at center = 0.0 T,
 - 15.96 m of 14 AWG wire,
 - aligned with horizontal vector of earth's magnetic field.
- **S1 Solenoid.**
 - turns = 2703,
 - length = 0.76 m,
 - radius = 0.053 m,
 - Amperes = 3.0,
 - flux density = 1.35×10^{-2} T,
 - aligned with horizontal vector of earth's magnetic field and at vertical angle between 0° and 68° ,
 - oriented with the negative side of the coil closest to the exposure.
- **S2 Solenoid.**
 - turns = 2703,
 - length = 0.76 m,
 - radius = 0.053 m,
 - Amperes = 5.0,
 - flux density = 2.24×10^{-2} T,
 - aligned with horizontal vector of earth's magnetic field and at vertical angle between 0° and 68° ,
 - oriented with the negative side of the coil closest to the exposure.
- **E1 Electric Field.**
 - 1.4×10^5 V/m,
 - copper electrodes,
 - 3 cm separation,
 - in direction of orbital plane.
- **E2 Electric Field.**
 - 2.4×10^5 V/m,
 - copper electrodes,
 - 3 cm separation,
 - in direction of orbital plane.

3.4. Handling, development and processing

Film was handled only using vinyl gloves. Under recommended safelight illumination, the film was marked to indicate orientation and placed onto the exposure stage, normally in a north-south direction.

Film was then developed for 90 s immediately after exposure. Development was stopped with a water bath, normally fixed and dried. Using a Leitz Metalloplan microscope with a large stage, developed film was scanned at low magnification. At higher magnifications, selected tracks were measured using an eyepiece reticle calibrated with a stage micrometer and photographed using plano objectives and a calibrated Peltier-cooled 12 MP Jenoptik ProgRes C14 camera. Selected images were then aligned in mosaics, processed, measured and analyzed using ImageJ microscopy software and a set of custom track processing routines written in Python.

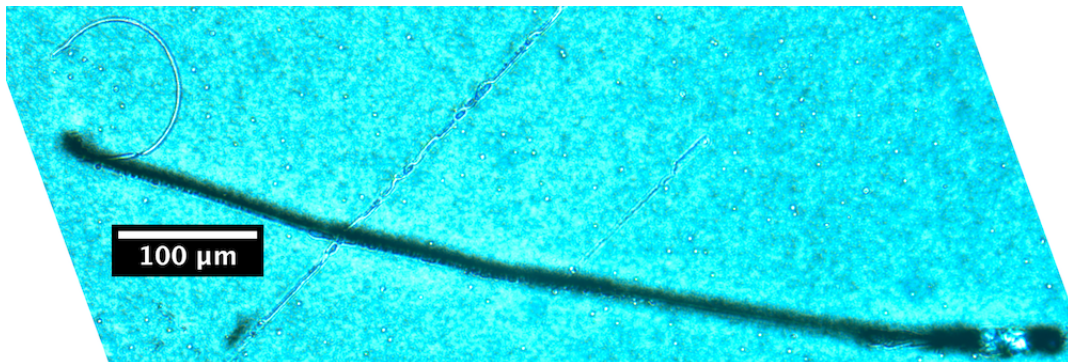


Figure 3. Track *lee2*, $n = 2.75$ showing ellipse at “end” of track. “Clear” ellipse emerges as if ejected from straight track with both clear and darkened components. Photographed at $160\times$ using a Leitz PL $16\times$ objective.

3.5. Observations

Experiments were performed with various electric and magnetic field configurations and various levels of light amplification of more than 750 exposures comprising a total photosensitive area of more than 2.85 m^2 . No repeatable curvature resulting from the application of electric or magnetic fields was observed. It is possible that the conditions for electric or magnetic curvature of the particles was outside of the applied field strengths. It is also possible that applied fields played a role in the production of elliptic tracks. 102 of these tracks were candidates for elliptic curvature analysis. About 20% of the track candidates showed excellent unambiguous fits to ellipses.

The elliptic track type is a partial ellipse (ellipse segment) and can be described as a *comma* track. This type of curvature is observed either in standalone tracks or tracks indicating a particle decay event or a series of decays. If not a stand alone track, ellipses commonly appear at one end of a track (see Fig. 3) or as an intermediary component of a compound track, which may be a series of partial ellipses. Partial ellipses also commonly occur in pairs, multiples and swarms as do non-ellipse tracks (cf. [2] and see Section 9.1. Partial ellipses can be registered as black tracks or white tracks in the emulsion layer or clear tracks in the plastic base. On examination with $400\times$ magnification, along with the darkening or bleaching of AgBr grains, many tracks show physical formation of voids, damage and/or ionization along $\sim 90\%$ of the track indicating particle traversal cutting a channel on the surface or directly through the AgBr/gelatin layer and/or plastic base of the film. Daviau et al. [7] using confocal and scanning electron microscopes, make the same point about particles cutting a groove or *tunneling* through layers of the emulsion and base. Due to the length and smooth curvature of the tracks, this indicates a particle detection with unusual characteristics and appears to rule out known charged particles.

In each case the elliptic tracks can be viewed as classical capture into and escape from a Kepler elliptic orbit in the plane of the film. In Fig. 5 (Bottom), the initial particle, P_1 decays into P'_1 and P_2 . P_2 is then captured into and subsequently escapes from an elliptic orbit.

In analogy with the gravitational case, we assume orbital capture of (charged) particle P_2 with mass m is possible due to a massive (charged) particle at the focus, F , of the ellipse in Fig. 5 (Bottom) with mass $M \gg m$ (and opposite charge). It is not clear why the particle escapes from the elliptic orbit.

Elliptic trajectories where $n > 3$ are observed to escape before aphelion. When $n < 3$, some ellipses are observed to continue on until almost complete.

3.6. Measurement

After creating a photomosaic of the track at high magnification, image processing is used to eradicate the background and x, y coordinates are extracted. Entry and exit points are determined by test hand-fitting followed by automated fitting using a progressive least-squares algorithm.

The procedure for measuring these tracks is as follows:

- (1) Scan entire film for elliptic tracks using a microscope with $25\times$ magnification.
- (2) Locate elliptic track candidate and change to higher ($\geq 160\times$) magnification.
- (3) Locate, measure and record fiducial points near to track.
- (4) Photograph the track in sections.
- (5) Reconstruct track using mosaic (photomontage) software.
- (6) Scale x, y track coordinates to x, y image coordinates.
- (7) Threshold track image (image processing).
- (8) Eradicate background (image processing).
- (9) Get track center x, y coordinates (image processing).
- (10) Determine ellipse entry and exit points.
- (11) Fit ellipse to x, y coordinates.
- (12) Report result as size of ellipse axes \pm error. See Table 1.

3.7. Particle flux

Based on an average exposure and processing time of 180s with a detector square area of $\sim 3.8 \times 10^{-3} \text{m}^2$ and a nominal five total tracks per exposure, these particles have a differential flux of $\sim 1.2 \text{ m}^{-2} \text{ s}^{-1} \text{ sr}^{-1}$. This compares with $1 \text{ m}^{-2} \text{ s}^{-1} \text{ sr}^{-1}$ for 500 MeV electrons and $1.1 \text{ m}^{-2} \text{ s}^{-1} \text{ sr}^{-1}$ for 500 MeV photons at sea level [15].

About 750 exposures with these parameters were carried out. Of these, 22 final ellipses were found, putting the total ellipse track flux at $\sim 1.8 \times 10^{-6} \text{ m}^{-2} \text{ s}^{-1}$.

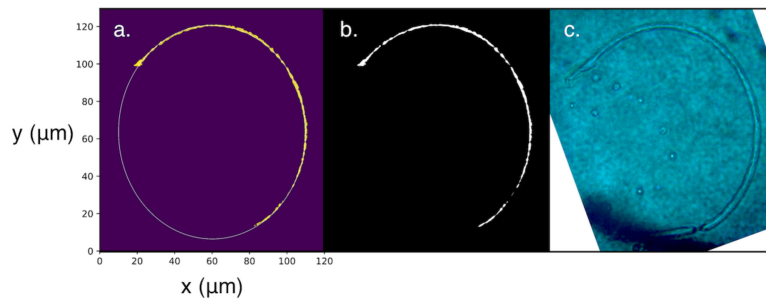


Figure 4. Track *lee2*, $n = 2.75$. (a) Ellipse fitted to track, semi-major axis size, $a = 56.9 \pm 13.0 \mu\text{m}$. (b) After processing and background eradication. (c) Photo at $1000\times$ using Leitz PL $100\times$ objective.

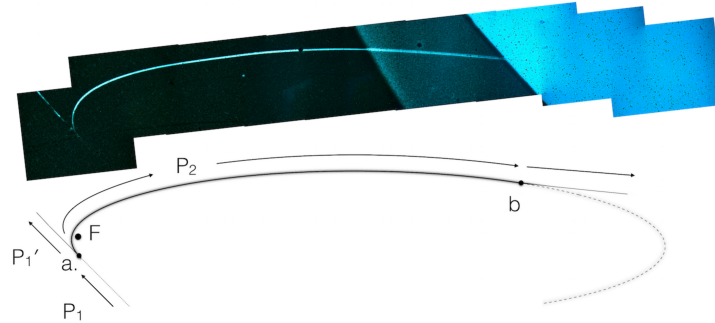


Figure 5. Track me , $n = 7$. *Top.* Semi-major axis size $a = 2391.6 \pm 16.1 \mu\text{m}$. Ten tile photomosaic at $160\times$ using a Leitz PL $16\times$ objective. See Fig. 6 for closeup of track. *Bottom.* Capture into and escape from an elliptic orbit. (1) Initial particle, P_1 , trajectory. (2) At point a . Particle decays into P_1' , continuing on initial trajectory and P_2 , which is captured into an elliptic orbit. (3) at point b . Particle escapes from the elliptic orbit.

4. Framework for Analysis

4.1. $1/r^2$ force tracks in film

A $1/r^2$ central force and an orbiting particle are required to create an elliptic particle track in a nuclear track detector. The central force involved is active over a range from $\sim 2.54 \times 10^{-5}$ to 4.07×10^{-3} m. The strong force, weak force and gravity are negligible at these distances. Electrostatic central force is within the range with the largest known electron orbits of order $n \sim 1000$ in Rydberg atoms with radius 10^{-4} m [16], but is ruled out by the inability of tracks of known charged particles to register smooth curvature in emulsions. The remaining possibility is magnetostatic central force, i.e. a magnetic charge orbiting an opposite magnetic charge.

It is not possible for any *known* charged particle to record a significant part of an elliptic particle track or *any* track with appreciable smooth curvature with attainable magnetic fields in photographic emulsions. In this sense, these tracks are more like tracks in bubble chambers, that is, cutting through the relatively high density photographic emulsion like a hot knife through butter. So, we have the unusual situation of a particle traveling through a detector material as if that material had a much lower density than its known density and yet depositing very high levels of energy [2,4,5,7,10].

For known charged particles, scattering of the particle obscures any curvature and the most that can be expected of

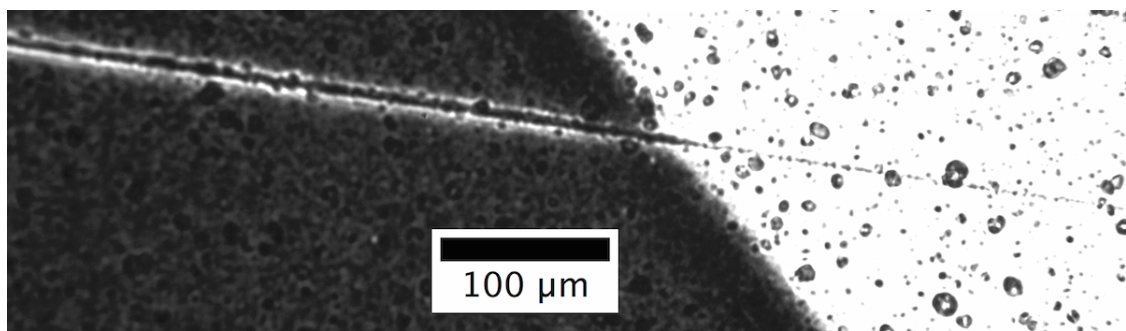
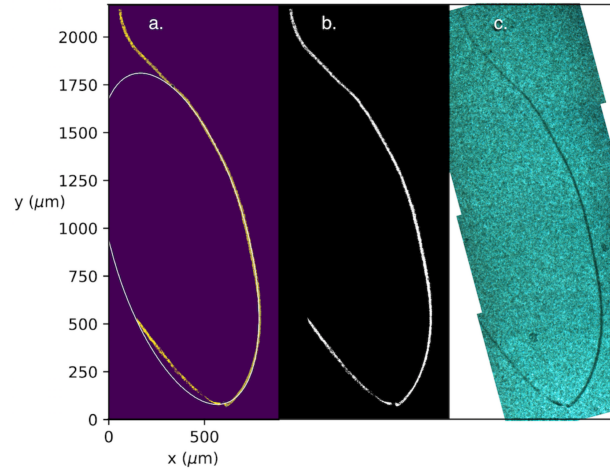


Figure 6. Detail of the $n = 7$ track showing track as blackened grains in dark area and as voids in plastic or gelatin in clear area. Note the *conventional* pattern similar to an ionizing particle in an emulsion (cf. periodic tracks in [2] and references therein).

Table 1. Ellipse semi-major, a , and semi-minor, b , axis measurements for each track along with associated quantum number, applied field setup, film type and associated applied field effect.

No.	track	$a(\mu\text{m})$	$b(\mu\text{m})$	n	Setup	Film	Effect
1	e2	4091.7 ± 22.5	2241.3 ± 22.5	8.00	trans BM	Rollei	Stark
2	be	4078.6 ± 14.6	1996.0 ± 14.6	8.00	E1+S1@26°	Arista	Zeeman
3	ode	4077.0 ± 16.1	1129.4 ± 16.1	8.00	no field	Arista	none
4	abt	4076.6 ± 10.3	1053.6 ± 10.3	8.00	E2+S1@68°	Arista	Zeeman
5	tlw	3141.0 ± 30.5	1474.4 ± 30.5	7.50	no field	Arista	none
6	me	2391.6 ± 16.1	549.3 ± 16.1	7.00	AH@0° DM	Arista	Stark
7	e1	1773.2 ± 24.9	1100.5 ± 24.9	6.50	trans BM	Rollei	Stark
8	ipe	1760.0 ± 23.1	615.3 ± 23.1	6.50	S1@68°	Arista	Stark
9	ego	908.9 ± 21.8	505.8 ± 21.8	5.50	S1@53°	Arista	Stark
10	ne	909.0 ± 25.7	367.2 ± 25.7	5.50	E1+YM	Rollei	Zeeman
11	bge	907.5 ± 11.6	284.3 ± 11.6	5.50	S1@53°	Arista	Stark
12	cav1	622.1 ± 21.1	300.7 ± 21.1	5.00	S1@32°	Arista	Stark
13	mct	619.9 ± 16.2	192.7 ± 16.2	5.00	DM+S1@68°	Arista	Stark
14	cce	621.1 ± 7.3	173.8 ± 7.3	5.00	S1@65°	Arista	Stark
15	edgee	254.2 ± 7.4	104.8 ± 7.4	4.00	S1@28°	Arista	Stark
16	sene	253.6 ± 9.8	202.2 ± 9.8	4.00	S1@65°	Arista	Stark
17	nne	149.8 ± 13.1	83.0 ± 13.1	3.50	S1@68°	Arista	Stark
18	ase	111.1 ± 20.6	72.1 ± 20.6	3.25	S1@53°	Arista	Stark
19	lee2	56.9 ± 13.0	49.8 ± 13.0	2.75	S1@68°	Arista	Stark
20	rse2	56.7 ± 9.5	31.5 ± 9.5	2.75	S1@65°	Arista	Stark
21	omse	38.1 ± 6.2	36.0 ± 6.2	2.50	S1@65°	Arista	Stark
22	avse2	25.6 ± 6.4	15.9 ± 6.4	2.25	S2@18°	Arista	Stark

Applied field legend: AH is the anti-Helmholtz, S1 the Solenoid – 1.35×10^{-2} T, S2 the Solenoid – 2.24×10^{-2} T, BM the Block Magnet – 1.26 T, DM the Disc Magnet – 1.32 T, YM the Yoked Magnet – 0.5 T, E1 the 1.4×10^5 V/m, and E2 is the 2.4×10^5 V/m. See Section 3.3 for applied field details.

**Figure 7.** Track ne , $n = 5.5$. (a) Ellipse fitted to track, semi-major axis size, $a = 909.0 \pm 25.7 \mu\text{m}$. (b) Track after processing and background eradication. (c) Mosaic of track photographed with Leitz PL 16× objective.

measurements of curvature occurring entirely within photographic emulsions due to applied magnetic fields is to find the sign of charge [17].

Earlier studies [2,18] have detailed a catalog of tracks and associated properties such as have never been seen before in nuclear track studies. Properties include track lengths of more than 6.6 cm, lack of visible delta rays (indicating unconventional exposure), random motion trajectories (each containing dozens of extremely rare large-angle deflections) [3], smoothness and uniformity of track width over most of a given track, regular periodic structure [2] observation on many different film types and detector materials (see Section 2) correlated tracks and swarms [2], and bundles or tracks with internal structure [2].

An *idealized model* is created, analyzing geometry of tracks, neglecting scattering and energy loss of the particle as it travels through the detector material. Neglecting scattering could be considered as good approach based on the visual observation of smooth curved tracks in emulsions.

4.2. Geometric analysis

Ordinarily calibration with a known particle track type is done in nuclear emulsions for particle identification via particle energy loss. Since only geometric analysis of the tracks is being done in this case, this type of calibration is not required.

4.3. Magnetic monopoles

Dirac [19] showed that quantized magnetic charges (hereafter *monopoles*) could explain the quantization of electric charge and bring symmetry to Maxwell's equations. But the symmetry is not complete since the value of magnetic charge does not equal the value of electric charge.

The Dirac quantization condition [19],

$$g_D^{(n)} = \frac{ecn}{2\alpha}, \quad n = (0, \pm 1, \pm 2, \pm 3, \dots), \quad (1)$$

where $\alpha = k_e e^2 / \hbar c$ and $k_e \equiv (4\pi\epsilon_0)^{-1}$ with $n = 2$ gives

$$g = 2g_D = \frac{ec}{\alpha}, \quad (2)$$

and is equivalent to the $n = 1$ *Schwinger Quantization* ($g = 2g_D$) condition [20]. The Schwinger formulation removed Dirac's thin solenoid and gained *rotational* symmetry.

Using Eq. (1) with $n = 1$, the force between north and south magnetic poles is $\epsilon_0\mu_0(g_D/e)^2$ or 68.5^2 times stronger than the force between electric charges and using Eq. (2), the force difference or *ratio* between magnetic and electric charges is

$$\epsilon_0\mu_0 \left(\frac{g}{e}\right)^2 = \frac{n^2}{\alpha^2} \quad (g = 2g_D), \quad (3)$$

or, with $n = 1$, $\alpha^{-2} = 137^2$.

If it exists, a classical monopole will move in an elliptic orbit around an oppositely charged pole at one focus and that pole should have a mass much greater than the orbiting pole.

Based on analogy with the electron and using $g = 2g_D$, the magnetic coupling constant

$$\alpha_m = \alpha^{-1} = k_m \frac{g^2}{\hbar c} \quad (k_m \equiv \mu_0/4\pi), \quad (4)$$

where subscripts of m indicate magnetic, is just the reciprocal of the fine structure constant, α .

5. Particle Properties

In our idealized model, neglecting scattering and other perturbations to particle motion in the emulsion, fitted ellipses are compared to Bohr–Sommerfeld ellipses and various particle properties are computed.

The semi-major axes of the fitted ellipses, a_m , differ from the semi-major axes, a_e , of corresponding Bohr–Sommerfeld ellipses for hydrogen by $\simeq 137^2 n^2$. Using $g = 2g_D$,

$$137^2 n^2 \simeq \frac{a_m^{(n)}}{a_e^{(n)}} = \frac{n^2}{\alpha^2}, \quad (5)$$

where subscripts of e stand for the electron and superscripts of (n) denote principal quantum numbers. Semi-major axis sizes and quantum numbers for the magnetic ellipses are determined using

$$a_m^{(n)} = a_e^{(n)} \frac{n^2}{\alpha^2} \quad (\alpha = ec/g), \quad (6)$$

where α is the Schwinger quantization from (2). See Table 2. These are compared with the collection of fitted ellipses. In Fig. 1 measured ellipse sizes are shown to be quantized by half integer values from $n = 8$ to $n = 3.5$. Below $n = 3.5$, ellipse sizes appear to be quantized by quarter integer values.

5.1. Monopole mass

All orbits including the Bohr radius follow the same relation as Eq. (5), so that with $n = 1$,

$$\frac{a_{0m}}{a_{0e}} = \frac{1}{\alpha^2}. \quad (7)$$

Using the formula for Bohr radius, $a_{0e} = \hbar/m_e c \alpha$, the analogous $a_{0m} = \hbar/m_m c \alpha_m$ and Eq. (7), monopole mass can be written as

$$m_m = \frac{m_e \alpha^3}{\alpha_m}, \quad (8)$$

and from Eq. (4), $\alpha_m = \alpha^{-1}$, so

$$m_m = m_e \alpha^4 = 1.45 \times 10^{-3} \text{ eV}/c^2, \quad (9)$$

which leads to the fine structure constant, $\alpha = (m_m/m_e)^{1/4}$, as a mass ratio.

This value agrees with our independent prediction of monopole mass [21] based on $g = 2g_D$ (see Section 6.3).

Table 2. Ellipse semi-major axis size, a_m , energy, E , velocity, v and momentum, p for $n = \{1 - 8\}$. Mass, $m_m = 1.45 \times 10^{-3} \text{ eV}/c^2$.

n	$a_m(\text{m})$	$E(\text{eV})$	$v(\text{m/s})$	$p(\text{eV}/c)$
1	9.93×10^{-07}	1.36×10^{01}	$4.11 \times 10^{+10}$	1.99×10^{-01}
2	1.59×10^{-05}	8.51×10^{-01}	$8.22 \times 10^{+10}$	2.48×10^{-02}
3	8.04×10^{-05}	1.68×10^{-01}	$1.23 \times 10^{+11}$	7.36×10^{-03}
4	2.54×10^{-04}	5.32×10^{-02}	$1.64 \times 10^{+11}$	3.11×10^{-03}
5	6.21×10^{-04}	2.18×10^{-02}	$2.05 \times 10^{+11}$	1.59×10^{-03}
6	1.29×10^{-03}	1.05×10^{-02}	$2.46 \times 10^{+11}$	9.20×10^{-04}
7	2.38×10^{-03}	5.67×10^{-03}	$2.88 \times 10^{+11}$	5.80×10^{-04}
8	4.07×10^{-03}	3.32×10^{-03}	$3.29 \times 10^{+11}$	3.88×10^{-04}

5.2. Monopole velocity

The ground state orbital velocity of the electron in hydrogen is $v_{0e} = k_e e^2 / \hbar = c\alpha$ and the analogous ground state orbital velocity of the bound monopole

$$v_{0m} = k_m \frac{g^2}{\hbar} = c\alpha^{-1}, \quad (10)$$

where $v_{0m} > c$, once seen as required yet unphysical [22] is postulated as required, physical and aptly symmetric [21] with the electron, i.e. $v_{0e} = c\alpha$ below c and $v_{0m} = c\alpha^{-1}$ above c (see also Table 3).

5.3. Quantized energy levels

For the electron in hydrogen, energy is quantized according to

$$E_e^{(n)} = -k_e \frac{e^2}{2a_{0e}n^2} = \frac{E_{0e}}{n^2} = h\nu^{(n)}, \quad (11)$$

and for the bound monopole,

$$E_m^{(n)} = -k_m \frac{g^2}{2a_{0m}n^4} = \frac{E_{0m}}{n^4} = h\nu^{(n)}. \quad (12)$$

Note the n^{-2} vs. n^{-4} difference between the electron and monopole.

5.4. Kepler period

Using $g = 2g_D$, the Kepler period for an electron in hydrogen and the monopole in a magnetic hydrogen analog,

$$\tau_m^{(n)} = \frac{2\pi a_{0m}n^3}{v_{0m}} = \frac{2\pi a_{0e}n^3}{v_{0e}} = \tau_e^{(n)} \quad (13)$$

are equal.

6. A New Superluminal Transformation

6.1. Extended relativity

The concept of special relativity extended to superluminal velocities was perhaps best put by Corben [23] where our world is bifurcated at the speed of light with one sector (our regular world) moving at $v^2 < c^2$ and the other sector moving at $v^2 > c^2$ relative to us. The two sectors of the world are symmetric since what we observe as bradyons from the $v^2 < c^2$ sector will be observed as tachyons from the $v^2 > c^2$ sector and vice-versa. Observations by physicists in each world are defined as equivalent, but with rest frames at different relative velocities.

A cornerstone of the work done by Recami and others to extend special relativity to superluminal velocities is the superluminal Lorentz transformation or SLT [24,25] that connects observations made in a $v^2 > c^2$ frame with observations made in the $v^2 < c^2$ frame. A superluminal particle property observed by a subluminal observer needs to be transformed by an SLT to correspond to something that we would normally observe.

Using an SLT, length, time, momentum, energy and mass can all be transformed between $v^2 < c^2$ and $v^2 > c^2$ frames. Time-like vectors are transformed into space-like vectors and vice-versa. Velocity is transformed simply as $\beta \rightarrow 1/\beta$ where $\beta = v/c$.

In this framework, an electron from a $v^2 > c^2$ frame seen by an observer in a $v^2 < c^2$ frame is interpreted as an electron with superluminal Lorentz-transformed properties and *magnetic charge* of $g = -ec$ (bringing a more complete symmetry to Maxwell's equations). Slower-than-light monopoles are not predicted in this theory.

The collinear bi-dimensional (x, t) SLT works without problems, but, when extended to four dimensions (x, y, z, t) , it leads to imaginary quantities for certain measurements of $v^2 > c^2$ objects and problems of how to interpret these physically. It is possible to use a six-dimensional space for the SLT, but there can be difficulties with the physical interpretation of two additional time dimensions.

If length is contracted using a collinear bi-dimensional transcendent [24] SLT along the x -axis and further (isotropic scale) contracted by an EM shift of α in accordance with the Schwinger quantization condition where $a_m^{(n)} = x$, $a_e^{(n)} = x'$, $b_m^{(n)} = y$, $b_e^{(n)} = y'$,

$$\begin{cases} a_m^{(n)}(\alpha\gamma) = a_e^{(n)} \\ b_m^{(n)}(\alpha) = b_e^{(n)} \end{cases} \quad (\gamma = (\beta^2 - 1)^{-1/2}, \quad \beta > 1). \quad (14)$$

As an example using theoretical $n = 8, \ell = 2$ ellipse data, ellipse size, orientation and eccentricity ($\mathcal{E} = 0.95 \rightarrow \mathcal{E}' = 0.99$) radically changes as a result of this *hybrid* SLT.

Using Recami's multidimensional approach, the SLT simply inverts the quadratic form sign [26] of an object and the shape of the monopole ellipse becomes

$$0 \geq -\frac{x^2}{a_m^{(n)2}} + \frac{y^2}{b_m^{(n)2}} \geq -1 \quad (15)$$

consisting of the area between an on-central-axis conic section,

$$\frac{y^2}{b_m^{(n)2}} = \frac{x^2}{a_m^{(n)2}}, \quad (16)$$

and a hyperbola,

$$\frac{y^2}{b_m^{(n)2}} = \frac{x^2}{a_m^{(n)2}} - 1, \quad (17)$$

greatly distorted from the original ellipse with eccentricity, $\mathcal{E}' > 1$, as shown in Fig. 8.

A real (vs. complex) SLT by Rajput et al. [27] results in an ellipse with the same semi-major axis size, same eccentricity,

The elliptic particle tracks we observe, (do they share geometrical properties of superluminal electrons?), do not share the same semi-major axis size as their (presumed) subluminal counterparts and do not appear to be distorted. That is, they appear to be scaled instead of stretched.

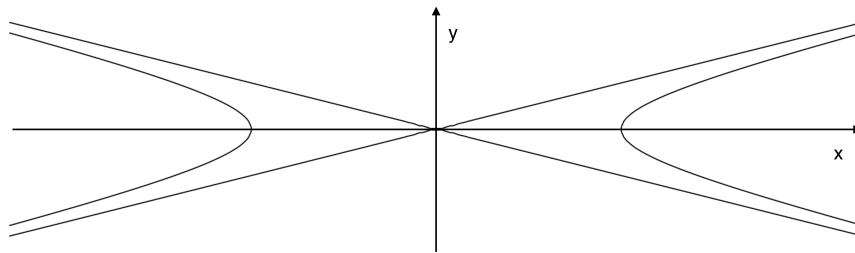


Figure 8. Recami type SLT of a theoretical $n = 8, \ell = 2$ monopole ellipse.

6.2. The Coulomb flip

If measured eccentricity corresponds to pure Bohr-Sommerfeld eccentricity, then, due to the α^{-2} size change, the transformation of ellipses in general needs to be an isotropic *scale* transformation instead of a translation along one axis.

The ratio of measured eccentricity, \mathcal{E}_μ to Bohr-Sommerfeld eccentricity, \mathcal{E}_τ

$$\frac{\mathcal{E}_\mu}{\mathcal{E}_\tau} = \frac{(1 - b^2/a^2)^{1/2}}{n^{-1} (n^2 - \ell(\ell + 1))^{1/2}} \quad (18)$$

as a ratio of averages over the 22 track values, $\langle \mathcal{E}_\mu \rangle / \langle \mathcal{E}_\tau \rangle = 0.99$, and measured eccentricity corresponds well to Bohr-Sommerfeld electron orbit eccentricity. This implies that the superluminal transformation, for this restricted case of bound particles, should be a scale transformation.

The required transformation is just the force ratio, from Eq. (3), a scale ratio, dilatation (α^{-2}) or contraction (α^2) between magnetic and electric force strengths, which could be called the *Coulomb flip*.

The one-dimensional basis Coulomb flips from $\beta > 1$ to $\beta < 1$ are

$$\alpha_{\text{EM}} : \quad \alpha_m (\alpha^2) = \alpha_e, \quad (19a)$$

$$a_0 : \quad a_{0m} (\alpha^2) = a_{0e}, \quad (19b)$$

$$v_0 : \quad \alpha_m c (\alpha^2) = \alpha_e c, \quad (19c)$$

$$q^2 : \quad k_m g^2 (\alpha^2) = k_e e^2. \quad (19d)$$

Combining the basis transformations, Eqs. (19b)–(19d), and assuming \hbar is Coulomb flip invariant, transformations for momentum, energy and mass are

$$\frac{\hbar}{a_{0m}} \xrightarrow{\alpha^2} \frac{\hbar}{a_{0e}}, \quad p_m (\alpha^{-2}) = p_e, \quad (20a)$$

$$-\frac{k_m g^2}{2a_{0m}} \xrightarrow{\alpha^2} -\frac{k_e e^2}{2a_{0e}}, \quad E_m (\alpha^0) = E_e, \quad (20b)$$

$$\frac{\hbar}{a_{0m} \alpha_m c} \xrightarrow{\alpha^2} \frac{\hbar}{a_{0e} \alpha_e c}, \quad m_m (\alpha^{-4}) = m_e, \quad (20c)$$

and the monopole and electron properties can be transformed into one another using Coulomb flips with $g = 2g_D$. In the ground state, time, in Eq. (13) and energy in Eq. (20b) remain invariant.

The 2-dimensional Coulomb flip scales the standard equation of the monopole ellipse (upper ellipse in Fig. 9), by the factor $(n^2 \alpha^{-2})^2$,

$$\left(\frac{n^2}{\alpha^2} \right)^2 \left(\frac{x^2}{a_m^{(n)^2}} + \frac{y^2}{b_m^{(n)^2}} \right) = 1, \quad (21)$$

to the electron ellipse (lower ellipse in Fig. 9).

Since measurements made on the $v^2 < c^2$ and $v^2 > c^2$ sides of the world use (x, y, z) quantities all scaled by the same real factor, $(n^2 \alpha^{-2})$, extending Eq. (21) to three dimensions, imaginary quantities do not enter the equations as they do in the determination of lengths orthogonal to the boost axis in the usual SLT. This scale transformation, resulting from interpretation of experiments, may, as a side-effect, solve the imaginary quantities problem [28] of SLTs.

The relativistic scale transformation could be termed a *Lorentz zoom* as opposed to a Lorentz boost. Relativistic scale transformations have been investigated by Nottale [29].

6.3. Equivalence of charges

Even though a superluminal particle's observed (by a subluminal observer) charge state is magnetic, it *should* possess exactly the same amount of charge in its own rest frame (the $v^2 < c^2$ frame) where the charge state is electric. This is to say that $v^2 > c^2$ electric charge is observed by normal subluminal observers to be magnetic charge and that subluminal magnetic charge does not exist [30,31].

As noted earlier, equivalence of charge along with considerations of special relativity prompted Recami et al. to set $g = -ec$ and abandon the Dirac quantization condition with respect to magnetic monopoles. In light of $g = 2g_D$ it is possible to reconsider this issue.

The basis Coulomb flip for charge in Eq. (19d) shows that, after transformation, the magnetic charge is equivalent to the electric charge in a $v > c$ frame observed from a $v < c$ frame. Solving for g in (19d) with $k_m/k_e = 1/c^2$ yields $g = ec/\alpha$, which is the Schwinger quantization condition. So the Coulomb flip for charge is just the Schwinger quantization condition.

In an analysis of the Dirac quantization condition, Datta [22], found a new hierarchy of fundamental *monopole* lengths, $a_{0m}, \lambda_{cm}, r_{0m}$, (Bohr radius, Compton wavelength and classical 'electron' radius) and pointed out that monopole bound states require superluminal ground state orbital velocities, but rejected the superluminal velocities as unphysical.

With *acceptance* of the required superluminal velocities and $g = 2g_D$, a new hierarchy of fundamental lengths and corresponding velocities [21] (see Table 3) reproduces the extended relativity spacetime structure, but, in the restricted case of bound states, and due to the experimental result of Eq. (18), requires Coulomb flip scale transformations between subluminal and superluminal sides rather than SLTs.

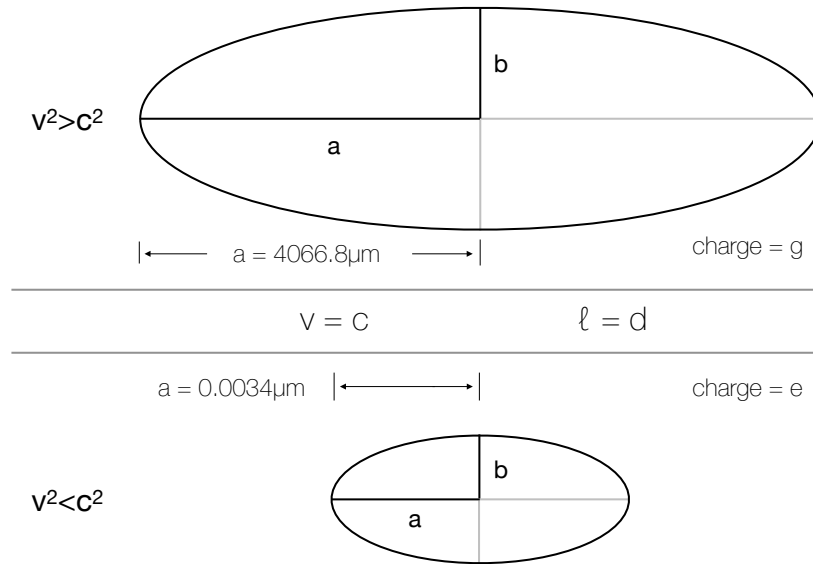


Figure 9. How a $v^2 < c^2$ observer sees a $v^2 < c^2$ electron orbit and an $n = 8, l = 2$ $v^2 > c^2$ monopole orbit. The $v^2 > c^2$ orbit is transformed to the $v^2 < c^2$ orbit using the 2-dimensional Coulomb flip Eq. (21) (not to scale).

Table 3. Velocity and length sequence alignment [21].

Velocity (m/s)			Length (m)		
4.11×10^{10}	v_{0m}	$c\alpha^{-1}$	$\lambda_{ce}\alpha^{-5}$	r_{0m}	1.86×10^{-2}
			$\lambda_{ce}\alpha^{-4}$	λ_{cm}	1.36×10^{-4}
			$\lambda_{ce}\alpha^{-3}$	a_{0m}	9.93×10^{-7}
2.99×10^8	c	$c\alpha^0$	$\lambda_{ce}\alpha^{-2}$	d	7.25×10^{-9}
2.19×10^6	v_{0e}	$c\alpha^1$	$\lambda_{ce}\alpha^{-1}$	a_{0e}	5.29×10^{-11}
			$\lambda_{ce}\alpha^0$	λ_{ce}	3.86×10^{-13}
			$\lambda_{ce}\alpha^1$	r_{0e}	2.82×10^{-15}

7. Applied Field Effects

As mentioned in Section 9, two main categories of tracks are distinguished, the predominant type and decays, which include the elliptic tracks. Effects of the electric and magnetic fields have not been observed for the predominant tracks. The central focus here is on the effect of the applied fields on the elliptic tracks.

In a similar manner to the way the electric charge is transformed to the magnetic charge and vice-versa using Coulomb flips (see Eq. (19d) and Section 6.3) applied electric and magnetic fields will also reverse roles.

If the applied electric field, now transformed to a magnetic field, is in a direction perpendicular to a superluminal electron orbiting a superluminal proton, it is possible that the Zeeman effect can occur. This is referred to as the *flipped* Zeeman effect. In the case of the Zeeman effect, both the semi-major and the semi-minor axes are affected by the magnetic field [32], so for tracks 2, 4 and 10 in Table 1, even though the field was not applied perpendicular to the orbit, but in the plane of the orbit, the principal quantum number *could* differ from the principal quantum number in the case of zero applied magnetic field and therefore the principal quantum number for these tracks may not be correct.

If the applied magnetic field, now transformed to an electric field, is in the direction of the plane of the orbit, it is possible that the Stark effect can occur. This is referred to as the flipped Stark effect. In the case of the Stark effect, only the semi-minor axis, related to changes in angular momentum, will be affected [33]. The principal quantum number will not be affected. Therefore the principal quantum numbers for tracks 6–9 and 11–22 in Table 1 should be correct, while the eccentricity and semi-minor axis size of these ellipses will be distorted with respect to the zero field case.

Tracks 3 and 5 had no applied electric or magnetic fields and so the principal quantum number should be correct as shown in Table 1.

So, the principal quantum number of tracks 3, 5–9 and 11–22 should be correct as shown in Table 1. Due to the flipped Zeeman effect, tracks 2, 4 and 10 *could* possess a different primary quantum number than that of an elliptic track without an applied magnetic field and as a result can be ignored in the analysis (although it does not change the main conclusions).

8. Track Formation Mechanism Inconsistencies

The mechanism of track formation is unknown and extremely unusual. We pointed out earlier [2] that the mechanism of track exposure is not clear. As mentioned in Section 2, tracks are observed on a number of materials besides the photographic emulsion (comprised of a dispersion of AgBr in gelatin on a polyester base), including Pd electrodes, MDS, (a semiconductor sandwich of Si, SiO₂ and Al), CR-39 (etched and unetched), PMMA, metal (Pb, W, and Al) foils, and glass. Commonly, the mechanism of track formation in photographic emulsions is ionization and to a lesser extent radiation [13]. The mechanism for (etchable) track formation in dielectrics and some semiconductors is ionization [34]. Etchable ion track formation in metals has been observed only using low-temperature GeV heavy ion

irradiation [35].

A number of contradictions exist in the observations of properties associated with track formation for the particles under consideration:

- (1) Particle tracks in photographic emulsions with smooth curvature are not known to occur for any known particle, yet these are commonly observed for the tracks under consideration. Coulomb scattering should dominate the process of energy deposition while suppressing any possibility of smooth curvature, and remain relatively constant along the track. Coulomb scattering in nuclear tracks has a characteristic look [3], which is not seen for these tracks. The only clear evidence of scattering that is seen is the large-scale scattering *in the observed capture process itself* (see Fig. 5), a relatively rare event.
- (2) In the case of Bohr–Sommerfeld ellipses, we should see no energy loss from an elliptic orbit. By definition, these orbits have no dissipation and no energy loss. Furthermore, there is no known way to directly record an orbiting particle on a material detector, that is, where the particle would actually traverse the material. Yet, energy loss is large, in the elliptic tracks that fit with the Bohr–Sommerfeld model, as it is in all of these tracks.
- (3) Analyses of energy deposition for these particles indicate very high energies (yet in the current study there is no known high energy source). In our 2013 study [2], we reported an average energy deposition estimate (linear stopping power) based on a grain density method developed by Katz [36] of ~ 250 GeV/cm. Other studies used high-energy discharges, byproducts of discharges or laser illumination in electric and magnetic fields as sources of the tracks. Daviau et al. [7], based on comparison with alpha particle tracks, computed the energy necessary to carve the tracks in the MeV range. Adamenko and Vysotskii reported a value of 10^6 GeV/cm total energy release for the track type created in their study [10]. On the basis of the developed density of a track in the emulsion, assuming Coulomb braking, deposited energy was estimated at 700 MeV by Urutskoev and coworkers [4]. Skvortskov has estimated an energy loss of $\sim 10^4$ GeV based on the amount of material removed from tracks in metals [11].
- (4) The “hairy rope” [36], track thickening toward the end of tracks, or other properties normally associated with ionization of high energy particles in emulsions is not seen.
- (5) Monopoles should leave tracks similar to heavy nuclear fragments in emulsions [37], but these are not seen.
- (6) Monopoles should exhibit constant track width over the entire track [38] and *thinning* [39,40] instead of thickening at the end of tracks. This *is* seen in our studies [2] (see also Fig. 10).
- (7) Particles are either tunneling through AgBr/gelatin/plastic or digging deep trenches to make tracks [2,7].
- (8) Adamenko and Vysotskii have forwarded a theory of track formation by nuclear reactions related to the passage of a magnetic monopole through a multilayer sandwich of Al, SiO₂ and Si because currently accepted theories of track formation apparently are not relevant.

The topic of mechanism of formation of these tracks is completely problematic. Our normal understanding of track formation *does not apply*. The entire question of energy deposition of these tracks is *completely unresolved*. With respect to how the tracks are formed, so far no scientific consensus has been reached.

If Coulomb scattering would be operative for formation of the elliptic tracks, it is reasonable to expect that the track geometry and the particle properties derived therefrom in this study would be different from the *actual* particle properties. But, it is *simply not possible* to achieve the level of Coulomb scattering normally associated with particle tracks in these tracks under consideration, which commonly exhibit smooth curvature in high density detectors like photographic emulsions because (for the most part) *scattering prohibits* [17] *measurable curvature* (and completely excludes *smooth* curvature).

In light of the preceding, any additional information on the behavior of these tracks occurring in materials is a welcome addition to the existing knowledge on the subject. The concept that the elliptic tracks could be formed in

approximate agreement with the presented idealized model cannot be evaluated based on an area of research that is inconsistent, *i.e.* the existing evidence for formation of these tracks in materials.

9. Discussion

These particles have been a mystery from the first known detection in 1979 (see [2]), using the photon amplification technique, to the experiments by Urutskoev and coworkers in 2000 and the various other experiments mentioned above in the ensuing years.

9.1. Earlier findings

The analyses of these experiments up to now have been based on certain observed particle properties such as the length of tracks, the curving of the tracks, the energy required to create a track in a certain material, etc.

Overall there has been agreement in the conjecture that these tracks are caused by monopoles [2,4–8,10,11,18,21,41,42]. Until now we have known about certain particle properties:

- (1) *Periodicity*, visible in some (but not all) tracks, clearly indicates *regular oscillation* of the particle (or particle system) causing the track [2,4,5,7,9,11,18,41,42]. Orderly helical-like tracks as well as complex periodic tracks have been observed.
- (2) *Penetration*, is apparent as many of the tracks possess very long track lengths, up to and more than ~ 7 cm through photographic emulsions and other materials [2,4–7,41].
- (3) *Random motion*, where the track undergoes many large-angle deflections like Brownian motion [2,7,18].
- (4) *Correlation of tracks* [2,8,11,18,43] indicates a common origin of particles that are likely entangled. This also includes correlated random motion tracks and swarms [2].
- (5) *Central force* evident from conformation of multiple correlated particle tracks [2,7,8,18,41]. Track geometry of correlated tracks indicates coordinated response arising from a central force.
- (6) *Tracks in various materials*, *i.e.* plastic, gelatin, metals, semiconductors and glass [2,9–11] gives information about the energy of these particles.
- (7) *Large angles of curvature* or abrupt changes of directions of tracks [2,8,41] may give information about the mass, charge and decay of particles.
- (8) *White tracks* in addition to black tracks indicate a tearing down of the latent image. These tracks can only be a result of exposure after or during the supplemental photon exposure, thus constraining the exposure time to the elapsed time after photon exposure till start of development. These tracks have only been observed in Fredericks [2]. The AgBr emulsion, re-zeroed at a higher level of sensitivity, able to respond in two directions, may be exactly the type of detector Terletskii [44] suggested as necessary to detect a negative energy particle.

Skvortsov has made mass estimates in a range of $\sim 10^{-3} \text{ eV}/c^2$ [45] and $\sim 10^{-2} \text{ eV}/c^2$ [11], based on the peak-to-peak amplitude of a periodic (clear) track in CR-39 (etched for 20 min. in an alkali solution). Mass shown in Eq. (9), $1.45 \times 10^{-3} \text{ eV}/c^2$, is within this range.

9.2. New findings

The series of experiments culminating in detection of elliptic curvature of new tracks in emulsions and the subsequent analysis brings a new critical set of particle properties:

- (1) Tracks show decay events, some of which are elliptic tracks emitted from a central track (see Fig. 10), showing two distinct track types, *i.e.* decays, which include elliptic tracks, and predominant tracks, which include everything else.

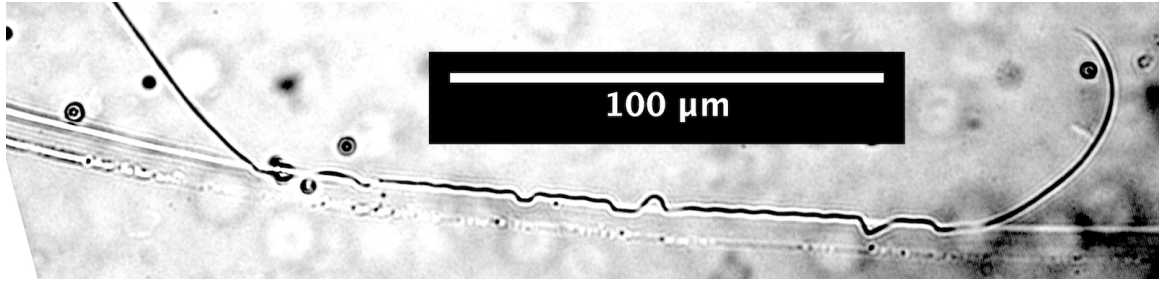


Figure 10. Track *rse2*, $n = 2.75$ showing elliptic track decay event. Photo at $400\times$ using Leitz PL $40\times$ objective. Notice also constant track width over the entire range [38] and track thinning [39,40] at the end of the track.

- (2) Exposures with and without applied electric and/or magnetic fields show nearly identical results in terms of overall track curvature. Predominant tracks are observed as curving one way and then the other or as long straight tracks. These particles (or composite particle systems) appear to behave as if neutral or the applied electric and magnetic fields are not in the right range to repeatably affect the particles.
- (3) Partial elliptic tracks show quantized semi-major axis sizes $a_m^{(n)}$, $n^2\alpha^{-2}$ larger than Bohr–Sommerfeld hydrogen with quantized energy levels $E^{(n)} = h\nu^{(n)}$.
- (4) Ground state velocity based on the elliptic tracks and analogy with the electron is α^{-2} greater than the electron ground state velocity in hydrogen, and therefore superluminal.
- (5) Coulomb flips of the new particle momentum, energy and mass match with a superluminal electron with $m_0 = 5.11 \times 10^5 \text{ eV}/c^2$.
- (6) The Coulomb flip of Eq. (19a) constitutes a single EM coupling constant, α_{EM} , which inverts with velocity

$$\alpha_{EM} = \begin{cases} \alpha & \text{if } \beta < 1 \\ \alpha^{-1} & \text{if } \beta > 1 \end{cases} \quad (22)$$

- (7) Mass, m_m , based on the elliptic tracks and analogy with the electron, which is the relativistic mass of the electron, is $m_e\alpha^4$ smaller than the electron rest mass, giving a mass ratio equal to the fine structure constant from Eq. (9), $\alpha = (m_m/m_e)^{1/4}$.
- (8) Charge quantization based on special relativity, *i.e.* Dirac's cause of quantization is the presence of magnetic charge, which is satisfied by the corresponding superluminal charge state of the electron, which to the subluminal electron is indistinguishable from magnetic charge.

The key point is item 5 that, using the Coulomb flip, the particle tracks correspond directly to the geometry of electrons from a superluminal frame.

Application of electric and magnetic fields during exposures that create these tracks shows no hard evidence of affecting predominant track curvature. This seems to be contradictory since only charged particles should be recorded and, if recorded, should respond to magnetic and/or electric fields. However, the particle (or composite particle system) behaves as if neutral. Decay events, where particle tracks emerge from a main track, however, do exhibit repeatable curvature, may be susceptible to EM fields, and, as mentioned in item 1, show two specific particle types. Note that Daviau and coworkers [7] earlier referred to this decay as *branching*.

According to the Heisenberg uncertainty principle, our elliptic orbits should be smeared or diffuse, not sharp tracks. This question is beyond the current scope but the subject of an upcoming investigation.

9.3. Theoretical approaches

Georges Lochak [41,42] has investigated these tracks and has looked specifically at the tracks produced in experiments by Urutskoev et al. [4,5], Ivoilov [8,46], Daviau et al. [7], Bardout et al. [47] and Priem et al. [6,48] and suggests that these are light leptonic monopoles that are magnetically excited neutrinos. Lochak believes that these particles are linked to composite particles following de Broglie's theory of light [42]. Writing the equations for a nonlinear massive monopole, Lochak shows (as an aside) how tachyon states appear and that these states exist also for the nonlinear neutrino. Lochak cites Recami and Mignani in relation to this hypothesis. He also believes, based on work by Urutskoev and coworkers and Ivoilov, that these particles are extremely numerous.

Independent of the particle track data, Stumpf [49] elaborates on Lochak's ideas of the light leptonic magnetic monopole and composite particles on the basis of Urutskoev et al.'s [4,5] use of discharges in water as the source of low-energy nuclear reactions. Stumpf is in agreement with Lochak regarding the magnetically excited neutrino hypothesis and looks to extend the standard model to include these types of particles.

In the track images where a decay is taking place, i.e. a particle is seen flying off at an angle to a main trajectory, one can assert the idea of two or more particles traveling together, but then separating when a certain energetic conditions are met. The composite particle system concept may well fit with the physical evidence seen in these types of tracks.

9.4. The Coulomb lens

The Coulomb flip likely provides a superluminal transformation without the introduction of imaginary quantities, allowing switching between electric and magnetic worlds and transforming all of the ellipses in the study from monopole to electron orbits. This would mean that superluminal objects could provide a portal of magnification, analogous to gravitational lensing, into our own world, that electron orbits could be examined in a way never before available, like looking at partial atomic electron orbits using the $\alpha^{-2} \times (\sim 1.88 \times 10^4 \times)$ magnification using what might be called a Coulomb lens.

10. Concluding Remarks

It should not be possible for any *known* particle to create the type of smooth elliptic tracks in photographic emulsion shown in Figs. 2,3,5,6, and 10 and the ranges of possible central forces suggests the elimination of all but magnetic force as the cause of these tracks. Using an idealized analysis based on analogy between the electron and magnetic monopole and the track geometry, a modification to extended relativity is developed, resulting in the Coulomb flip to transform between $v^2 < c^2$ and $v^2 > c^2$ frames.

Using a geometrical analysis and analogy with the electron, these particles are shown to possess a (relativistic) mass of $1.45 \times 10^{-3} \text{eV}/c^2$ and a superluminal velocity. A related yet independent analysis [21] based on the Schwinger quantization condition shows that due to the size of the orbits these particles must possess superluminal velocities and a mass of $1.45 \times 10^{-3} \text{eV}/c^2$. Using a new extended relativity model, the experimental results appear to be consistent with the detection of superluminal electrons with $m_0 = 5.11 \times 10^5 \text{eV}/c^2$.

The idealized model adds new information to the overall understanding of these new types of particle tracks. Inconsistencies in the understanding of track formation mechanisms for these tracks precludes the application of any error arising from track formation that might affect the idealized model since one cannot say exactly what that error is. Additional work needs to be done to determine track formation mechanisms and particle interactions so as to understand what error should be taken into consideration in the geometric analysis of these tracks.

A new model builds upon The Dirac/Schwinger quantization condition, Recami and Mignani's extended theory of relativity and Coulomb's law to bring a simple superluminal scale transformation presumably without imaginary quantities in the Coulomb flip. Distortion observed by subluminal observers may well be that of a uniform scale change

and not a shape change as a result of a translation. Detection of superluminal objects may open a path to substantial magnification of submicroscopic objects analogous to, but with a much greater magnification than, gravitational lensing for astronomical objects.

Acknowledgments

The author thanks Jacques Consiglio for essential help and stimulating discussions and is also grateful to Moses Fayngold, Giovanni Modanese and Leonid Urutskoev for important suggestions and interest in this work.

References

- [1] L. Epele, H. Fanchiotti, C. Garcia Canal and V. Vento, *Euro. Phys. J. C* **56** (2008) 87.
- [2] K.A. Fredericks, *Eng. Phys.* **6** (2013) 15.
- [3] C.F. Powell, *The Study of Elementary Particles by the Photographic Method*, Pergamon, London, 1959; W.H. Barkas, *Nuclear Research Emulsions*, Vol. 1: *Techniques and Theory*, Academic Press, New York, 1963; W.H. Barkas, *Nuclear Research Emulsions*, Vol. 2: *Particle Behavior and Emulsion Applications*, Academic Press, New York, 1973.
- [4] L.I. Urutskoev, V.I. Liksonov and V.G. Tsinoev, *Ann. Fond. L. de Broglie* **27** (2002) 701, arXiv:physics/0101089.
- [5] L.I. Urutskoev, *Ann. Fond. L. de Broglie* **29** (2004) 1149.
- [6] D. Priem, C. Daviau and G. Racineux, *Ann. Fond. L. de Broglie* **34** (2009) 103.
- [7] C. Daviau, D. Fargue, D. Priem and G. Racineux, *Ann. Fond. L. de Broglie* **38** (2013) 139.
- [8] N.G. Ivoilov, *Ann. Fond. L. de Broglie* **31** (2006) 115.
- [9] B. Rodionov and I. Savvatimova, in *Proc. 12th Int. Conf. on Cold Fusion*, A. Takahashi, K. Ota and Y. Iwamura (Eds.), World Scientific, Singapore, 2005, Chap. 44, pp. 421–429; I. Savvatimova and J. Dash, in *The 9th Int. Conf. on Cold Fusion, Condensed Matter Nuclear Science*. 2002. Tsinghua Univ., Beijing, China, Z.Z. Li (Ed.), Tsinghua Univ. Press, 2002.
- [10] S. V. Adamenko and V. I. Vysotskii, in *Proc. 14th Int. Conf. on Condensed Matter Nuclear Science on Cold Fusion (ICCF-14)* 10–15 August 2008, Washington DC, D.J. Nagel and M.E. Melich (Eds.), New Energy Foundation Inc., 2008, p. 484; S.V. Adamenko and V.I. Vysotskii, *Ann. Fond. L. de Broglie* **33** (2008) 13.
- [11] V.A. Skvortsov and N.I. Vogel, in Exotic nuclei: EXON-2014, *Proc. of Int. Symposium*, Y. Penionzhkevich and Y. Sobolev (Eds.), World Scientific, Singapore, 2015, pp. 457–463.
- [12] H.D. Ables, *AAS Photo-Bull.* **3** (1971) 18T. A. Babcock, *AAS Photo-Bull.* **13** (1976) 6.
- [13] T.H. James, *The Theory of the Photographic Process*, Fourth Edn. Macmillan, New York, 1977.
- [14] R.P. Czwakiel and E.C. Scott, *Proc. SPIE* **0058** (1975) 192.
- [15] G. Kaye, T. Laby and N.P.L.G. Britain, *Tables of Physical & Chemical Constants*, 16th Edn. 1995, 2.7.7 Cosmic Rays, Kaye & Laby Online. Version 1.0 (2005), National Physical Laboratory, 2005.
- [16] V. Lebedev and I. Beigman, in *Physics of Highly Excited Atoms and Ions*, Springer, Berlin, Heidelberg, 1998, pp. 1–9.
- [17] C. Dilworth, S. Goldsack, Y. Goldschmidt-Clermont and F. Levy, *Philos. Mag.* **41** (1950) 1032, I. Barbour, *Phys. Rev.* **78** (1950) 518, M. Merlin, *Nuovo Cimento* **11** (1954) 218.
- [18] K.A. Fredericks, *J. Condensed Matter Nucl. Sci.* **15** (2015) 203.
- [19] P.A.M. Dirac, *Proc. Royal Soc. A* **133** (1931) 60, P.A.M. Dirac, *Phys. Rev.* **74** (1948) 817.
- [20] J. Schwinger, *Phys. Rev.* **144** (1966) 1087.
- [21] K.A. Fredericks, *Phys. Essays* **30** (2017) 269.
- [22] T. Datta, *Lett. Nuovo Cimento* **37** (1983) 51.
- [23] H.C. Corben, *Int. J. Theoret. Phys.* **15** (1976) 703.
- [24] E. Recami and R. Mignani, *Nuovo Cimento* **4** (1974) 209, E. Recami, *Nuovo Cimento* **9** (1986) 1.
- [25] L. Parker, *Phys. Rev.* **188** (1969) 2287.
- [26] A. Barut, G. Maccarrone and E. Recami, *Nuovo Cimento A* **71** (1982) 509.
- [27] B.S. Rajput, P. Joshi and O.P.S. Negi, *Lett. Nuovo Cimento* **35** (1982) 147.
- [28] H.C. Corben, *Lett. Nuovo Cimento* **11** (1974) 533.

- [29] L. Nottale, *Found. Sci.* **15** (2010) 101.
- [30] R. Mignani and E. Recami, *Lett. Nuovo Cimento* **9** (1974) 367.
- [31] E. Recami and R. Mignani, *Lett. Nuovo Cimento* **9** (1974) 479.
- [32] W.-D.R. Stein, *J. Russ. Laser Res.* **34** (2013) 553.
- [33] J. C. Solem, *Am. J. Phys.* **55** (1987) 906, <https://doi.org/10.1119/1.14951>.
- [34] R. Fleischer, P. Price and R. Walker, *Nuclear Tracks in Solids: Principles and Applications*, University of California Press, USA, 1975.
- [35] A. Barbu, H. Dammak, A. Dunlop and D. Lesueur, *MRS Bull.* **20** (1995) 29–34.
- [36] R. Katz, *Nucl. Instrum. Meth. B* **40–41** (1989) 1271.
- [37] E. Bauer, *Math. Proc. Cambridge* **47** (1951) 777–789.
- [38] R. Katz and J.J. Butts, *Phys. Rev.* **137** B (1965) 198.
- [39] R. Katz and D.R. Parnell, *Phys. Rev.* **116** (1959) 236.
- [40] H.J.D. Cole, *Math. Proc. Cambridge* **47** (1951) 196–206.
- [41] G. Lochak, *Z. Naturforsch. A* **62** (2007) 231, arXiv:0801.2752 (quant-ph) .
- [42] G. Lochak, in *The Leptonic Magnetic Monopole Theory and Experiments, Advances in Imaging and Electron Physics*, Vol. 189, P.W. Hawkes (Ed.), Elsevier, Amsterdam, 2015, pp. 1–172.
- [43] V.A. Skvortsov and N.I. Vogel, in Exotic nuclei: EXON-2014, *Proc. Int. Symposium*, Y. Penionzhkevich and Y. Sobolev (Eds.), World Scientific, Singapore, 2015, pp. 465–470.
- [44] Y.P. Terletsii, *Paradoxes in the Theory of Relativity*, Plenum, New York, 1968, pp. 102–104.
- [45] V.A. Skvortsov and N.I. Vogel, in *Proc. 29th EPS Conference on Plasma Phys.*, ECA **26** B (2002) D-5.013.
- [46] N.G. Ivoilov and L.I. Urutskoev, *Ann. Fond. L. de Broglie* **29** (2004) 1177.
- [47] G. Bardout, G. Lochak and D. Fargueb, *Ann. Fond. L. de Broglie* **32** (2007) 551.
- [48] D. Priem, G. Racineux, G. Lochak, C. Daviau, D. Fargue, M. Karatchentcheff and H. Lehn, *Ann. Fond. L. de Broglie* **33** (2008) 129.
- [49] H. Stumpf, in The leptonic magnetic monopole theory and experiments, *Advances in Imaging and Electron Physics*, Vol. 189, P.W. Hawkes (Ed.), Elsevier, Amsterdam, 2015, pp. 173–314.



Research Article

Condensed Plasmoids (CPs) – A Quantum-Mechanical Model of the Nuclear Active Environment of LENR

Lutz Jaitner*

85405 Nandlstadt, Germany

Abstract

Researchers have long been puzzled about the basic nuclear reaction mechanisms of low-energy nuclear reactions (LENR). Usually the crystal lattice or nano-particles (among others) are assumed to be the nuclear active environment that catalyzes the reaction somehow. In contrast, the author has built a quantum-mechanical model of the nuclear active environment in LENR, where this environment is modeled as an ultra-dense plasmoid, i.e. a “condensed plasmoid” (CP). The computed properties of CPs are so exotic that CPs qualify as a previously unknown aggregation state of matter. The quantum-mechanical model of CPs is based on the cylindrical symmetry of a very thin (i.e. about 40 pm) plasma “wire”. (The quantitative properties given in the abstract depend on the configuration of the CP; these are just examples.) The electrons of a CP are fully delocalized and decoupled from the nuclei. They are moving with high velocity (10–80% of light speed) against the nuclei. This results in an intrinsic current of about 9 kA in the CP with a mean current density of approximately 2.5 A/pm^2 . The magnetic field from this current reaches 50 MT (magatesla) and creates a confinement pressure of more than 10^{21} Pa . The electrons are compressed by the strong z -pinch condition to a mean density of about $0.15 \text{ electrons/pm}^3$. The creation of a CP is an endothermic process (i.e. it takes in energy from an external source), which typically requires discharges with high voltages and high currents. Once created, these objects can be long-living (lasting hours). The minimum distance of hydrogen nuclei in a CP is only about 2 pm, which enables tunneling of nuclei through the Coulomb barrier, i.e. nuclear fusion. The barrier is also much screened by the dense electrons.

© 2020 ISCMNS. All rights reserved. ISSN 2227-3123

Keywords: Charge clusters, EVs, EVOs, LENR, Nuclear active environment, Pease–Braginskii current, Plasmoids, Radiative collapse, Strange radiation, z -Pinch

1. General Description

This article is an extract from a much more comprehensive document on the author’s web site [1]. The term “condensed plasmoid” was recently coined, and is presented in this document for the first time, thus a definition is given here. A CP is defined to be a plasmoid (i.e. a self-consistent structure of a current-carrying plasma and magnetic fields), which meets all of the following criteria.

*Web: www.condensed-plasmoids.com. E-mail: lutz.jaitner@t-online.de.

- The plasmoid is compressed by a strong z-pinch condition. “Strong” in this sense means that the internal current is larger than 200 A; the radius of the plasma channel is less than 200 pm; and the length of the plasma channel is at least several micrometers. These numbers are based on the computational results of the current modeling. For yet unknown reasons CPs might exist with lower intrinsic currents.
- All electrons of the containing atoms (not merely the outer electron shells) are delocalized, i.e. the electrons are all contributing to the current and they can freely move between the atomic nuclei. The delocalization is caused by the small inter-nucleic distance (i.e. less than 10 pm in case of hydrogen).
- The electrons reside in orbitals, which are at (or near) the quantum-mechanical ground state of the CP. For this to be true, the temperature of the CP must be low enough that the thermal pressure of the plasma is smaller than the magnetic pressure enforced on the moving electron gas by the Lorentz force.

A direct consequence of this definition is that CPs are representing mesoscopic objects of matter. “Mesoscopic” means “in between quantum-mechanical and macroscopic”. The properties of CPs therefore do not always follow the conventional wisdom of plasma physics. For example, cooling down a CP will not produce electron-ion recombinations and ordinary molecules.

CPs exist in different topologies.

- The open-ended configuration of a CP exists under transient conditions in the presence of a strong electric field. An open-ended CP loses electrons at the negative end. The positive end of an open-ended CP is often connected to a cathode, which replaces the electrons lost at the other end.
- The closed-loop configuration of a CP is the long-lasting form, where the internal current is flowing in a circular manner. Closed-loop CPs can exist even in the absence of an external electric field. Based on the microscopic evidence, there are various mechanisms by which closed-loop CPs can develop. These mechanisms are typically supported by the electrostatic attraction between the electrons and the cations. The positive and negative charges will rapidly find a path to meet if the loop is not yet closed. Along this path the plasmoid then condenses. Another mechanism would be, if a CP is spawning a closed loop by overlapping with itself.

Imprints of CPs have been observed in LENR experiments both at the surface of cathodes and as images on x-ray films or nuclear emulsions. In the latter case CPs were emitted by LENR experiments (sometimes called “strange radiation”), which exposed the films/emulsions.

Imprints of ring-shaped CPs have been documented by different research groups in the following images (Fig. 1):

The primary structure of CPs has a cylindrical shape, i.e. it is a plasma “wire”, which is long, very thin and rotational symmetric. Most, but not all, properties of CPs can be derived from the cylindrical structure. At longer



Figure 1. CP rings on X-ray film, diameter = 0.2 mm by Claude Daviau et al. [2] (left) and by B. Rodinov and I. Savvatimova [3] (middle). CP ring on an electrode by T. Matsumoto [4] (right).

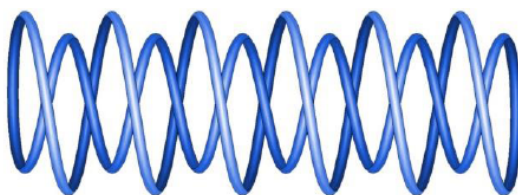


Figure 2. Drawing of a CP coiling up in a two-layered closed-loop solenoid via magnetic self-interaction.

CPs the ultra-strong magnetic field of CPs is deforming the plasma-wire, leading to a secondary structure, i.e. CPs are tending to coil up in two-layered closed-loop solenoids is shown in Fig. 2.

Imprints of the helical secondary structure of CPs were documented by B. Rodinov and I. Savvatimova (Fig. 3). CPs can create significant erosion craters at the cathode (Fig. 4): The author believes that the patterns left by CPs are not merely a strange side effect of LENR, but they provide the experimental core evidence of the presence of CPs in such experiments. The term “nuclear-active environment” has been coined by Edmund Storms [7] in an attempt to characterize the properties of the zone where the nuclear reactions of LENR actually happen. Taking this concept

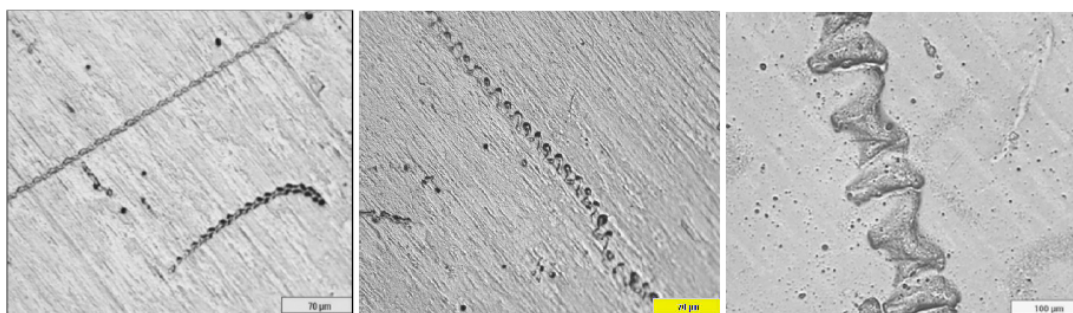


Figure 3. Quasi-periodic patterns from helical CPs produced by glow discharge. *Left and middle:* Pd cathode, *right:* nuclear emulsion [3].

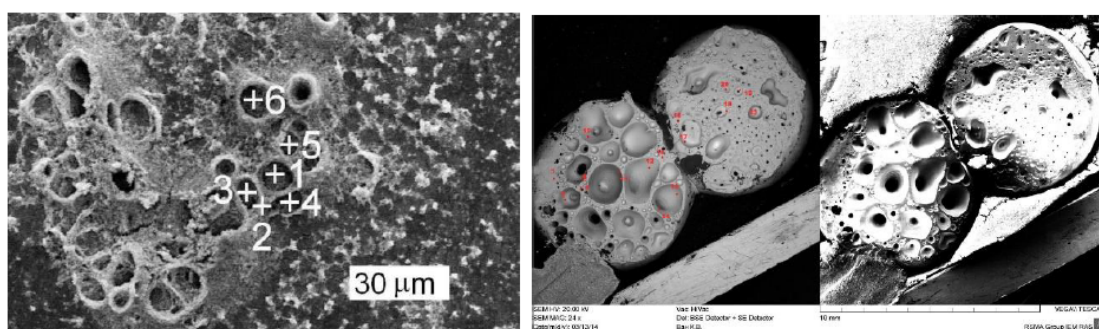


Figure 4. Volcano-like structures at the palladium cathode surface after electrolysis of heavy water, W.-S. Zhang and J. Dash [5] (*left*); Erosion craters in the nickel cathode of the plasma vortex reactor of A. Klimov et al. [6] (*right*).

to the next step, the nuclear active environment is equated here with CPs. Without CPs there can be no excess heat, because the nuclei can fuse only in the dense environment of CPs.

The main idea of this theory on CPs is as follows. The azimuthal component of the magnetic field at the surface of a plasma wire is inversely proportional to the radius of the conducting channel (and proportional to the CPs intrinsic current). Therefore, the more the magnetic field compresses the plasmoid, the stronger the magnetic field becomes and the stronger the plasmoid is compressed. It is a *positive feedback mechanism*: When the current divided by the plasmoid radius increases beyond a critical threshold, there will be a rapid compression of the plasmoid (“condensation”).

However, not all plasmoids will readily condense. For example, an electric arc is often too hot and the ionized channel is often too wide for the condensation to take place. The continuing current heats the plasmoid by resistive losses, which negatively affects the ability of the plasmoid to condense.

If the temperature is kept low enough, only the degeneracy pressure of the electron gas will hinder a total collapse of the matter. The degeneracy pressure is a quantum-mechanical result of the Pauli Exclusion Principle. It increases with increasing electron density.

A quantum-mechanical model of CPs had to be established in order to compute the equilibrium radius (and other properties) of CPs. (This refers to the equilibrium between the magnetic pressure and the quantum-mechanical pressure of the electron gas.) The scope of the model is to describe the stationary state after the compression of the plasmoid, rather than modeling the dynamic aspects of the compression.

During condensation the matter density increases dramatically and the scattering probability of the electrons decreases to almost zero. Electron scattering in CPs differs from electron scattering in ordinary plasmoids by the fact that most of the lower-energy orbitals of CPs are already occupied and there is no energy available for scattering electrons into higher-energy orbitals. As a result, the resistance of the CP drops to levels very close to zero (a phenomenon not necessarily related to superconductivity), and the current in a close-looped CP can flow for a very long time.

There is a minimum length of a CP, which is believed to be a few micrometers. Based on this length, CPs contain at least a hundred million electrons. There is no maximum length, i.e. CPs can be made arbitrarily long.

W.H. Bennett in 1934 [8] showed that there is an equilibrium between the thermal pressure of a plasma channel and the magnetic pressure of a pinched plasmoid, if the so called Bennett relation is met:

$$k_B (N_e T_e + N_i T_i) = \frac{\mu_0}{4\pi} I^2, \quad (1)$$

where N_e is the number of electrons per unit length of the plasma channel, N_i the number of ions per unit length of the plasma channel, I the total current, μ_0 the vacuum permeability, k_B the Boltzmann’s constant, T_e the electron temperature and T_i is the ion temperature.

This relation assumes that the velocity distribution of the electrons and ions obey the Boltzmann statistics of an ideal gas. This assumption is invalid in the case of CPs, because their plasma is fully degenerate (Fermi gas) and the temperature is low.

The possibility of radiative collapse in pinched linear discharges was first studied independently by Pease [9] and Braginskii [10,11] in 1957 for pure hydrogen or deuterium plasmas. When radiation losses by bremsstrahlung exceed Ohmic heating at high currents, they predicted shrinking of the plasma channel, which may even result in a collapse of the channel to extremely high densities. They derived a critical current value (i.e. the Pease–Braginskii current) that has to be exceeded to achieve a collapse:

$$\frac{I_{PB}}{MA} \approx 0.27 \sqrt{\ln \Lambda} \left(1 + \frac{1}{Z} \right), \quad (2)$$

where $\ln \Lambda$ is the Coulomb logarithm, MA stand for megaampere and Z is the charge of the ions.

Formula (2) is assuming an infinitely long plasma channel and $T_e = T_i$. It is based on Spitzer resistivity (first formulated by Lyman Spitzer [12] in 1950), where the resistivity of the plasma channel is proportional to $T_e^{-3/2}$.

There were many later attempts in the literature to refine the original formula of Pease and Braginskii, but the issues at low temperatures were not addressed, as far as the author is aware of.

Spitzer resistivity is built upon classical electron–ion collisions (this can be seen as a high-temperature approximation), whereas at low temperatures the scattering behavior of the electrons can only be understood by a quantum-mechanical analysis. With Spitzer resistivity one would conclude that the plasma channel becomes non-conductive (and Ohmic losses would diverge) when the temperature approaches zero. In reality the resistivity of a CP is lowest at the lowest temperatures. The physical reason for this discrepancy is that electron–ion scattering is energetically hindered at low temperatures in CPs. Instead the resistivity of a CP is mainly based on electron–phonon scattering, which also becomes negligible at very low temperatures.

Also, the Pease–Braginskii formula merely considers Bremsstrahlung as the cooling mechanism, where in reality line radiation of heavier atoms, heat transport by delocalized electrons, stimulated cyclotron radiation, and direct thermal conduction to the environment contribute to the cooling during the condensation phase.

The Pease–Braginskii current is typically computed as being in the order of 1.5 MA for hydrogen. It decreases to about 100 kA for elements like Ar, Kr and Xe, because line radiation dominates over Bremsstrahlung and the radiative cooling thus becomes more efficient.

With peak currents in the range of 150–200 kA evidence for radiative collapse has been found [13]: Low-inductance vacuum sparks produced by discharging a capacitance of 10–30 μF (charged to 10–20 kV) through a circuit inductance of 50–100 nH achieves pulse lengths of 1.5–2 μs . The sparks are producing small, point-like regions in the plasma that are called plasma points, bright spots, or hot spots. (Similar observations have been made in plasma focus devices and in gas puffs.)

The first phase of the discharge creates a plasma with material eroded from the electrodes. In the next phase of the discharge the current increases as prescribed by the electrode voltage and the inductance of the circuit. On top of the smoothly rising current there appear short (<100 ns) single or multiple dips in the current. These current dips are accompanied by intense bursts of X-rays with photon energies of 5–150 keV. The current dips are correlated with the appearance of plasma points. The points are often less than 10 μm in size.

It is remarkable that the maximum X-ray photon energy is much higher than the theoretical maximum energy of the electrons traversing the electric field between the electrodes. The maximum photon energy also exceeds the K-shell energy of the plasma ions. These high photon energies can be explained by electron relaxation in CPs, which have a Fermi energy (i.e. the energy difference between the highest and the lowest occupied orbital) of up to 200 keV.

The observed current dips can be interpreted as the condensation phase of the CPs: When the radius of the CPs is shrinking the magnetic flux of the CPs is compressed. This is electromagnetically inducing a high voltage counter to the externally applied voltage. During the current dips compression work is applied to the CPs by means of the external field. At the end of the compression phase (i.e. the end of the current dip) the current continues to rise and the generated CPs continue to exist, but the electron relaxation is mostly complete and the X-ray emission fades.

The fact that sometimes multiple current dips have been observed during the same discharge can be interpreted to mean that several CPs have been created in parallel, which successively condensed. This could be due to a filamentation instability of the initial plasmoid.

J. Va'vra et al. determined the smallest possible spark current, which is still consistent with the X-ray production and the development of plasma points [14]. Their generator used a spark gap operating at low pressure (0.1–1 Torr) and low discharge voltages between 0.8 and 2.1 kV. The charging capacitance was 75 nF, the circuit inductance was about 1000 nH, the stored energy amounted to 0.024–0.17 J per pulse, the peak spark currents were 200–500 A and the total capacitor charge was between 4×10^{14} and 10^{15} electrons. The spark gap was 1 mm.

The observed X-ray energies were between 2 and 10 keV even at the lowest sparking voltage of about 0.8 kV (depending on the gas). The maximum observed X-ray energy (~ 10 keV), generated at the lowest voltage (~ 0.8 kV), is above K-shell energy of typical gases used in the tests, and materials used in the spark electrodes. The X-ray

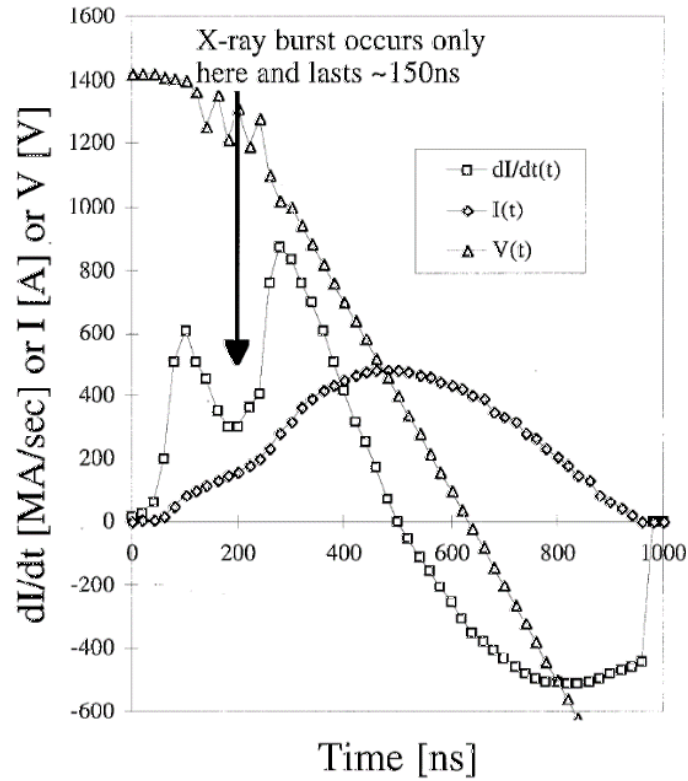


Figure 5. Current and voltage development in a low-pressure spark discharge according to J. Vařva et al. [14].

production persisted even for the carbon electrodes which have the smallest K-shell energy (0.284 keV). The spark current and the electrode voltage were measured as follows (Fig. 5).

The radiative collapse of the plasmoid (which can be equated with the condensation of a CP) occurred during the dip of the $dI/dt(t)$ curve, which lasted about 150 ns. It is very interesting that this collapse occurs already at a current of about 200 A.

2. CP Quantum Mechanics

2.1. Basic assumptions

Modeling of CPs is based on the following basic assumptions:

- CPs contain ensembles of atomic nuclei densely packed in a long and very narrow channel.
- The distances between the nuclei are so small, that all electrons bound to these nuclei are delocalized along the channel. In other words, even in their electronic ground state CPs do not consist of individual atoms. Instead, CPs form a quasi-one-dimensional plasma (Fig. 6).

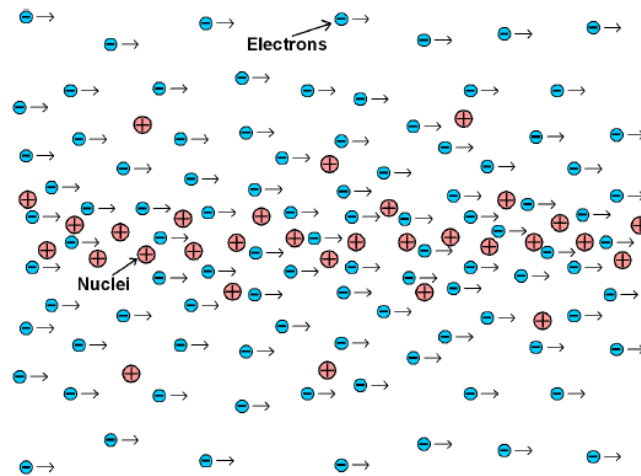


Figure 6. Basic model of a CP. The CP similarly extends to the left and to the right of this picture.

2.2. The cylindrical model of CPs

The shape and quantum mechanical state of CPs can be very complicated. In order to obtain a simple quantum mechanical description of CPs, the following simplifications are used, which will subsequently be called “the cylindrical model of CPs”.

- (c) The CP is perfectly straight and cylindrically symmetric, i.e. it is not bent to rings, helices, etc. The CP is oriented in parallel to and centered on the z axis of the modeling cylindrical coordinate system.
- (d) The CP has the length \bar{L} and contains a total nuclear charge Q in its core.
- (e) The electron wave functions of the CP are confined in the interval $0 \leq z < \bar{L}$. At $z = \bar{L}$ these wave functions are continuously extended to their value and gradient at $z = 0$, as if the CP were a ring. However, this is meant to describe only the *circular boundary condition* of the wave functions at $z = \bar{L}$, not the shape of the CP.
- (f) No external field is applied to the CP.
- (g) A *jellium* model is used for the spatial distribution of the nuclear charge. This means, for the purpose of computing the spatial distribution of the electrons, the positive charges of the nuclei are modeled as a uniform “positive jelly” background, rather than point charges with distances in between. The nucleic charge density is assumed to be constant in axial and azimuthal direction, but it depends on the radial distance.
- (h) The nucleic charge distribution of the jellium is modeled by means of a two-dimensional distribution function in radial direction. This function is to be determined, such that the total energy of the CP is minimized.
- (i) The core area of the CP (i.e. the space defined by the extent of its electron orbitals) is surrounded by a charge compensation layer (“halo”) consisting of cations. The charge of the halo compensates the surplus negative charges of the electrons in the core. The halo is modeled as a cylindrical shell of positive charge. The halo radius has to be larger than the core radius.
- (j) The CP is assumed to reside in a vacuum. Interaction of the CP with surrounding matter is thus neglected.
- (k) Only stationary states are modeled, as the goal is to describe the ground state of a CP. Consequently, the model assumes there is no electron scattering, i.e. there is no momentum transfer between electrons and the nuclei.
- (l) The time-independent Klein–Gordon equation is used for modeling the electron wave functions, thereby

neglecting the magnetic moments of electron spins. The Klein–Gordon equation takes care of the sizable relativistic effects occurring in CPs. (Clearly, the Dirac equation would be more adequate for modeling CPs. However, the involved complexities of such approach are avoided here.) For comparing the formulas and simulation results with the ones obtained from a non-relativistic Hamiltonian, also the Schrödinger equation is used.

- (m) The magnetic field of the azimuthal electron orbits is neglected.
- (n) Magnetic field from nuclear spins is neglected.
- (o) The electron wave functions are modeled in an inertial frame of reference, where no magnetic field is created by any collinear movements of the nuclei. This simplification amounts to an approximation in cases where the nucleic velocities are position dependent.
- (p) The multi-electron system is approximated by computing a collection of one-electron orbitals, whereby each electron orbital is subjected to the mean electric potential and magnetic vector potential created by the total charge density and total current density of all other occupied orbitals and the nuclei (independent particle model). The Pauli Exclusion Principle is used for determining orbital occupations of the ground state. Exchange and correlation energies are neglected.
- (q) Quantum field theory is not engaged. Particle count is conserved.
- (r) Eigen states are excluded from occupation, where the corresponding total energy eigenvalue (including the electron's rest energy) of the electron is negative. This shall ensure that the mass defect per electron doesn't exceed the electrons rest energy.
- (s) The kinetic energy of the electrons is always positive, i.e. states with a negative kinetic energy are ignored.

2.3. The Klein–Gordon equation of a CP

Initial calculations of a CP with the Schrödinger equation have shown that the spectrum of the axial electron velocities can reach 80% of the speed of light. This provided a reason for engaging a relativistic Hamiltonian and a Lorentz-covariant quantum mechanical equation to model CPs. Assuming that the electron spins have only minor effects on the results, the Klein–Gordon equation was chosen for the modeling instead of the more complicated 4-component Dirac equation.

At the non-relativistic limit the Klein–Gordon equation is equivalent to the Schrödinger equation, which was also used for comparison.

In relativistic electrodynamics with the so-called minimal coupling the Hamiltonian (total energy) of a particle with charge q moving in the presence of a static (external) electromagnetic potential is

$$\hat{H} = c\sqrt{\left(\vec{P} - q\vec{A}\right)^2 + m_e^2 c^4} + q\Phi, \quad (3)$$

where c is the speed of light, Φ the electric potential, \vec{A} the magnetic vector potential, $\vec{P} = \gamma m_e \vec{v} + q\vec{A}$ the electron's canonical momentum, m_e the electron rest mass and γ is the Lorentz factor. All formulas are written in SI units, unless otherwise noted.

By quantizing the canonical momentum via the del operator $\vec{P} \equiv -i\hbar\nabla$ and applying both sides to an electron wave function Ψ , Eq. (3) transforms to the *stationary Klein–Gordon equation of an electron in a static electromagnetic potential*:

$$(\bar{E} + e\Phi + m_e c^2)^2 \Psi = \left[\left(-i\hbar c \nabla + e c \vec{A} \right)^2 + m_e^2 c^4 \right] \Psi, \quad \text{where } \bar{E} \equiv \hat{H} - m_e c^2 \quad (4)$$

is the total energy minus the rest energy, \hbar is the reduced Planck constant, e is the elementary charge and $i = \sqrt{-1}$.

Due to simplification (q), Ψ is called here a “wave function”, rather than a “quantum field”.

The term $\bar{E} + m_e c^2$ represents the total energy of the electron. Usually the Klein–Gordon equation is written such that the total energy is sought as the eigenvalue of this differential equation. However, this document deviates from the customary approach. Instead, the quantity \bar{E} is sought here as the eigenvalue (both approaches are equivalent in their results).

Some authors prefer the term “relativistic Schrödinger equation” for Eq. (4). Here, these terms are used interchangeably. In quantum mechanics a multi-electron system is correctly described by a single wave function $\Psi(\vec{r}_1, \vec{r}_2, \dots, \vec{r}_N)$ depending on the positions of the N electrons.

By means of the mean-field approach (assuming the particles are independent) a multi-particle wave function is usually formed as a Hartree product of wave functions:

$$\Psi(\vec{r}_1, \vec{r}_2, \dots, \vec{r}_N) = \chi_1(\vec{r}_1) \cdot \chi_1(\vec{r}_2) \cdots \chi_1(\vec{r}_N).$$

In order to take care of the fermionic nature of the electrons one typically has to engage a Slater determinant (or a linear combination of several Slater determinants) to ensure anti-symmetry and the Pauli Exclusion Principle [15]:

$$\Psi(\vec{r}_1, \vec{r}_1, \dots, \vec{r}_N) = \frac{1}{\sqrt{N!}} \begin{vmatrix} \chi_1(\vec{r}_1) & \chi_2(\vec{r}_1) & \cdots & \chi_N(\vec{r}_1) \\ \chi_1(\vec{r}_2) & \chi_2(\vec{r}_2) & \cdots & \chi_1(\vec{r}_2) \\ \vdots & \vdots & \ddots & \vdots \\ \chi_1(\vec{r}_N) & \chi_2(\vec{r}_N) & \cdots & \chi_1(\vec{r}_N) \end{vmatrix}. \quad (5)$$

According to simplification (p) a rigorously simpler approach is used here for modeling CPs, requiring only moderate computer power:

So, instead of using a multi-electron Klein–Gordon equation describing the pair-wise interaction between N electrons, the cylindrical model uses N *single-electron Klein–Gordon equations with N wave functions* $\Psi(\vec{r})$, each describing a single electron in the *mean potential* of all other electrons and the nuclei. Of course, this is merely an independent particle approximation. For example, the approach does not account for the exchange energy and the correlation energy usually deemed important in quantum chemistry.

At first glance this looks still challenging to compute, because there are N Klein–Gordon equations to be solved. Fortunately, large numbers of these equations can be computed in groups, because they produce nearly the same charge density distributions and current density distributions.

According to simplifications (l) and (k) the magnetic field of the electron spins and of the azimuthal movement of the electrons is neglected. Thus, the only source of the magnetic field is the current carried by the electrons moving in the z -direction. Therefore, the vector potential is everywhere oriented in the z -direction:

$$\vec{A} = \bar{A}_z \vec{e}_z \quad (6)$$

Transforming to cylindrical coordinates, using $\nabla \cdot \vec{A} = 0$ (Lorentz gauge in the static case) and inserting Eq. (6) into Eq. (4) is resulting in the *stationary Klein–Gordon equation of an electron in the mean potential of a CP’s all other electrons and the nuclei*:

$$\left\{ \frac{-\hbar^2}{2m_e} \left[\frac{1}{\rho} \frac{\partial}{\partial \rho} \left(\rho \frac{\partial}{\partial \rho} \right) + \frac{1}{\rho^2} \frac{\partial^2}{\partial \phi^2} + \frac{\partial^2}{\partial z^2} + 2 \frac{e\bar{A}_z}{\hbar} i \frac{\partial}{\partial z} - \frac{e^2 \bar{A}_z^2}{\hbar^2} \right] - \frac{m_e c^2}{2} \left(\frac{\bar{E} + e\Phi}{m_e c^2} + 1 \right)^2 + \frac{m_e c^2}{2} \right\} \Psi = 0, \quad (7)$$

where ρ is the radial distance from the z -axis, ϕ is the azimuth and z is the coordinate of the z -axis.

With simplification (f) the electric potential Φ is depending solely on the electron charge density $\bar{\sigma}_e(\rho)$ and the nuclear charge density $\bar{\sigma}_n(\rho)$. The magnetic vector potential \bar{A}_z is solely dependent on the electric current density $\bar{J}_z(\rho)$. The electron charge density and the electric current density are derived from the modulus square of the other electron's wave functions. This approach has *similarities with the density functional theory (DFT)* used in quantum chemistry modeling, except that the exchange and correlation energies are not accounted for. Equation (7) therefore can be seen as the Kohn–Sham equation [16].

2.4. Boundary conditions for solutions of the Klein–Gordon equation

Care must be taken according to simplification (r), that *the total energy $\bar{E} + m_e c^2$ of an eigenstate is always positive*, therefore:

$$\bar{E} > -m_e c^2. \quad (8)$$

Requirement (8) can be fulfilled by *excluding eigenstates with a negative total energy during orbital occupation*. The wave function amplitude must disappear at infinite radial distances:

$$\lim_{\rho \rightarrow \infty} \Psi(\rho) = 0. \quad (9)$$

As required by simplification (e) the wave function has to meet circular boundary conditions:

$$\Psi(z=0) = \Psi(z=\bar{L}) \quad \text{and} \quad \frac{\partial \Psi(z=0)}{\partial z} = \frac{\partial \Psi(z=\bar{L})}{\partial z}. \quad (10)$$

For computing observables the Klein–Gordon electron wave functions have to be *normalized* such that:

$$1 = \|\Psi\| = \iiint_{\mathbf{R}^3} |\Psi|^2 d\vec{r}. \quad (11)$$

2.5. Observables of the Klein–Gordon electron wave function

The potential energy of an electron is solely stemming from the Coulomb field:

$$\bar{E}_{\text{pot}}(\vec{r}) = -e\Phi(\vec{r}). \quad (12)$$

The local kinetic energy of the electron is what's left when the potential energy is subtracted from \bar{E} :

$$\bar{E}_{\text{kin}}(\vec{r}) = \bar{E} + e\Phi(\vec{r}). \quad (13)$$

By using modulus square factorization (31) the *volume charge density distribution* of all N electrons of the CP computes as

$$\bar{\sigma}_e = -e \sum_{i=1}^N |\Psi_i|^2 = -\frac{e}{2\pi\bar{L}} \sum_{i=1}^N |\Psi_{\rho,i}|^2, \quad (14)$$

where $\Psi_{\rho,i}$ is the radial wave function of electron number i

The *current density distribution* of all N electrons of the CP is

$$\vec{J} = \frac{-e}{m_e} \sum_{i=1}^N \left[-\frac{i\hbar}{2} (\Psi_i^* \nabla \Psi_i - \Psi_i \nabla \Psi_i^*) + e\vec{A} |\Psi_i|^2 \right]. \quad (15)$$

Using product ansatz (29), modulus square factorization (31) and Ψ_z -solution (33), the z -component (in cylindrical coordinates) of the *current density* (15) in a CP computes as

$$\bar{J}_z = \frac{-e}{m_e} \sum_{i=1}^N \left[-\frac{i\hbar}{2} \left(\Psi_i^* \frac{\partial \Psi_i}{\partial z} - \Psi_i \frac{\partial \Psi_i^*}{\partial z} \right) + e\bar{A}_z |\Psi_i|^2 \right] = \frac{-e}{2\pi m_e \bar{L}} \sum_{i=1}^N \bar{p}_{z,i} |\Psi_{\rho,i}|^2, \quad (16)$$

where

$$\bar{p}_{z,i} = \bar{P}_{z,i} + e\bar{A}_z = \hbar k_i + e\bar{A}_z \quad (17)$$

is the z -component of the electron's kinetic momentum \hat{p} .

The total *current* in z -direction carried by all electrons of the CP can be computed by integrating (16) over all radius values and azimuth values:

$$\begin{aligned} I_z &= \int_{\phi=0}^{2\pi} \int_{\rho=0}^{\infty} \bar{J}_z(\rho) \rho \, d\rho \, d\phi = \frac{-e}{m_e \bar{L}} \int_0^{\infty} \sum_{i=1}^N \bar{p}_{z,i} |\Psi_{\rho,i}(\rho)|^2 \rho \, d\rho \\ &= \frac{-e}{m_e \bar{L}} \sum_{i=1}^N \int_0^{\infty} [\hbar k_i + e\bar{A}_z(\rho)] |\Psi_{\rho,i}(\rho)|^2 \rho \, d\rho, \end{aligned} \quad (18)$$

The expectation value of the *electron group velocity's z -component* (averaged over all N electrons of the CP) can be computed from the z -component of the total current:

$$\langle v_z \rangle = \frac{I_z \bar{L}}{-Ne}. \quad (19)$$

The *expectation value of the electron orbit radius* for eigenstates of Eq. (7) is

$$\langle \rho \rangle = \int_0^{\infty} |\Psi|^2 \rho^2 \, d\rho. \quad (20)$$

The *total formation energy* \bar{E}_B of a CP is

$$\bar{E}_B = \bar{E}_n + \sum_{i=1}^N \left(\bar{E}_i - \frac{1}{2} \langle \bar{E}_{C,e} \rangle_i \right), \quad (21)$$

where \bar{E}_B is the nuclear repulsion energy defined in (40), $\langle \bar{E}_{C,e} \rangle_i = \langle -e\Phi_e \rangle_i$ is the expectation value of the electron–electron Coulomb energy for electron number i and Φ_e is the potential of all electrons.

2.6. Electromagnetic potential and field of a CP

The electric potential of a CP splits as follows:

$$\Phi = \Phi_n + \Phi_e + \Phi_h, \quad (22)$$

where Φ_n is the electric potential of the nuclear jellium in the core according to simplification (g), Φ_e is the electric potential of the electrons, and Φ_h is the electric potential of the halo (44).

The charge density of a CP splits as follows:

$$\bar{\sigma}(\rho') = \bar{\sigma}_n(\rho') + \bar{\sigma}_e(\rho') + \bar{\sigma}_h(\rho'), \quad (23)$$

i.e., the sum of the nuclear charge density in the core, the electron charge density and the charge density of the halo (43)

The *electric potential* of the CP (in Lorentz gauge, static case) is

$$\Phi(\rho) = \frac{1}{4\pi\epsilon_0} \int_0^\infty \bar{\sigma}(\rho') G(\rho, \rho') \rho' d\rho', \quad (24)$$

where

$$G(\rho, \rho') = \begin{cases} 4\pi \left[\ln \left(\bar{L}/2 + \sqrt{\bar{L}^2/4 + \rho'^2} \right) - \ln \rho' \right] & \text{for } \rho \leq \rho', \\ 4\pi \left[\ln \left(\bar{L}/2 + \sqrt{\bar{L}^2/4 + \rho^2} \right) - \ln \rho \right] & \text{for } \rho > \rho'. \end{cases} \quad (25)$$

Replacing $\bar{\sigma}(\rho')/\epsilon_0$ with $\mu_0 \bar{J}_z(\rho')$ in (24) provides the *z*-component of the CP's *magnetic vector potential* (in Lorentz gauge, static case):

$$\begin{aligned} \bar{A}_z(\rho) &= \frac{\mu_0}{4\pi} \int_0^\infty \bar{J}_z(\rho') G(\rho, \rho') \rho' d\rho' \\ &= -\frac{e\mu_0}{8\pi^2 m_e \bar{L}} \int_0^\infty \sum_{i=1}^N [\bar{P}_{z,i} + e\bar{A}_z(\rho')] |\Psi_{\rho',i}|^2 G(\rho, \rho') \rho' d\rho', \end{aligned} \quad (26)$$

where μ_0 is the vacuum permeability, $\bar{J}_z(\rho')$ is the *z*-component of the current density and $\bar{P}_{z,i} = \hbar k_i$ is the *z*-component of the electron's canonical momentum.

Note that \bar{A}_z is depending on itself in Eq. (26). Therefore, the values of \bar{A}_z and \bar{J}_z need to be determined iteratively until self-consistency. Based on the circular boundary condition, (7) the electric potential (24) and the vector potential (26) are made constant in *z*-direction. This approximation is required for maintaining the full cylindrical symmetry of the model.

The radial and azimuthal (see simplification (m)) components of the vector potential and the current density are zero everywhere. Due to simplification (o) the nuclear jellium is not contributing to the current density. The *radial electric field* of a CP computes as

$$\varepsilon_\rho = -\frac{\partial}{\partial \rho} \Phi(\rho). \quad (27)$$

The *azimuthal magnetic field* of a CP computes as

$$B_\phi = -\frac{\partial}{\partial \rho} \bar{A}_z(\rho). \quad (28)$$

2.7. Product ansatz

The following *product ansatz* is made to factorize the electron wave function:

$$\Psi(\rho, \phi, z) = \Psi_\rho(\rho) \Psi_\phi(\phi) \Psi_z(z) \quad \text{or in short :} \quad \Psi = \Psi_\rho \Psi_\phi \Psi_z. \quad (29)$$

The wave function of a single electron is supposed to be normalized and it represents a stationary state. In azimuthal direction and in axial direction the electromagnetic potential is constant. Therefore, the modulus square of Ψ_ϕ and Ψ_z is also constant:

$$|\Psi_\phi|^2 = \Psi_\phi^* \Psi_\phi = \frac{1}{2\pi} \quad \text{and} \quad |\Psi_z|^2 = \Psi_z^* \Psi_z = \frac{1}{L}. \quad (30)$$

Hence the *modulus square* of the entire wave function factorizes as

$$|\Psi|^2 = \Psi_\rho^*(\rho) \Psi_\rho(\rho) \Psi_\phi^*(\phi) \Psi_\phi(\phi) \Psi_z^*(z) \Psi_z(z) = \frac{1}{2\pi L} |\Psi_\rho(\rho)|^2. \quad (31)$$

The *normalization criteria* (11) could then be carried out as

$$1 = \|\Psi\| = \int_0^\infty |\Psi_\rho(\rho)|^2 \rho \, d\rho. \quad (32)$$

2.8. Separation of the Klein–Gordon equation

The following *wave function* is solving the *z-dependent part* of (29):

$$\Psi_z = \sqrt{\frac{1}{L}} e^{ikz}, \quad \text{where } k \in \mathbf{R}. \quad (33)$$

Due to simplification (e) the energy eigenvalues are quantized to a discrete spectrum, because wave number k has to meet the following boundary condition:

$$k = l \frac{2\pi}{L}, \quad (34)$$

where integer l acts as an *axial quantum number*.

The following *wave function* is solving the ϕ -dependent part of (29):

$$\Psi_\phi = \sqrt{\frac{1}{2\pi}} e^{im\phi}, \quad (35)$$

where integer m is the *azimuthal quantum number*

Inserting Eqs. (17), (29), (33) and (35) into Eq. (7) provides the *radial Klein–Gordon equation* of a CP:

$$\left\{ \frac{\hbar^2}{2m_e} \left[-\frac{1}{\rho} \frac{d}{d\rho} \left(\rho \frac{d}{d\rho} \right) + \frac{m^2}{\rho^2} \right] + \frac{\vec{p}_z^2}{2m_e} - \frac{m_e c^2}{2} \left(\frac{\bar{E} + e\Phi}{m_e c^2} + 1 \right)^2 + \frac{m_e c^2}{2} \right\} \Psi_\rho = 0. \quad (36)$$

At the *non-relativistic limit* Eq. (36) becomes the *radial Schrödinger equation* of a CP:

$$\left\{ \frac{\hbar^2}{2m_e} \left[-\frac{1}{\rho} \frac{d}{d\rho} \left(\rho \frac{d}{d\rho} \right) + \frac{m^2}{\rho^2} \right] + \frac{\vec{p}_z^2}{2m_e} - \bar{E} - e\Phi \right\} \Psi_\rho = 0. \quad (37)$$

The eigenstates of differential equation (36) or (37) provide the radial wave functions Ψ_ρ . The eigenvalues \bar{E} of bound states are discrete, i.e. they are countable by a principal quantum number n , the azimuthal quantum number m and the axial quantum number l . The *principal quantum number* $n = 1, 2, 3, \dots$ is defined here analogous to the hydrogen atom: n equals one plus the number of node lines of $\Psi_\rho \Psi_\phi$, therefore $n \geq |m| + 1$. (In a stricter sense, Ψ_ϕ has no node lines. However, a standing wave of two superposed azimuthal wave functions, differing only in the sign of quantum number m , has m node lines.)

Principal quantum number n has no explicit representation in (36) or (37) or in any of the following formulas. It is useful however, as an ordering scheme for computational results. One has to keep in mind, that the eigenvalues \bar{E} , the eigenstates Ψ_ρ , Ψ_ϕ and Ψ_z , as well as the quantum numbers n , m and l are generally distinct for each electron of the CP. In order to ease readability, the electron number as an index has been omitted from these symbols, unless the index is needed in a summation.

2.9. The jellium model of the nuclear charge distribution

According to simplification (g) the charge of the nuclei is treated as if it were a uniform “positive jelly” background, rather than point charges with distances in between. The nuclear charge density distribution $\bar{\sigma}_n(\rho)$ of the core jellium has cylindrical symmetry, i.e. it does not depend on φ and z . It is a function of the radial distance ρ .

According to Eqs. (22), (0) and (24) the *electric potential of the core nuclear jellium* is

$$\Phi_n(\rho) = \frac{1}{4\pi\epsilon_0} \int_0^\infty \bar{\sigma}_n(\rho') G(\rho, \rho') \rho' d\rho'. \quad (38)$$

An infinitesimal charge element $\bar{\sigma}_n(\rho') \rho' d\rho' d\phi dz$ brought into potential Φ_n has the potential energy:

$$d\bar{E}_n = \bar{\sigma}_n(\rho) \Phi_n(\rho) \rho d\rho d\phi dz. \quad (39)$$

Integrating (39) over the entire space and dividing the result by two yields the *nuclear self-repulsion energy*:

$$\begin{aligned} \bar{E}_n &= \bar{E}_{n,h} + \bar{E}_{h,h} + \frac{1}{2} \int_0^{\bar{L}} \int_0^{2\pi} \int_0^\infty \bar{\sigma}_n(\rho) \Phi_n(\rho) \rho d\rho d\phi dz \\ &= \bar{E}_{n,h} + \bar{E}_{h,h} + \pi \bar{L} \int_0^\infty \bar{\sigma}_n(\rho) \Phi_n(\rho) \rho d\rho, \end{aligned} \quad (40)$$

where $\bar{E}_{n,h}$ is the halo-core repulsion energy according to Eq. (46) and $\bar{E}_{h,h}$ is the halo self-repulsion energy according to Eq. (47). The division by two in (40) takes care of the fact that the jellium is interacting with itself and the repulsion energy must not be accounted for twice during integration. According to simplification (h) the *nucleic charge distribution in the core* is modeled by means of a two-dimensional distribution function in radial direction.

After studying the computational results of the radial electron density distribution, it became apparent that the charge distribution function can be modeled like this

$$\bar{\sigma}_n(\rho) = \text{Height} \cdot \exp \left(-\frac{\rho^2}{2\bar{s}^2} - \frac{\rho^5}{\text{Slope}^5} - \frac{\rho^{16}}{\text{Cutoff}^{16}} \right). \quad (41)$$

Parameter Height has to be computed such that the distribution function (41) is normalized to the core nuclear charge Q . Parameters Slope and Cutoff should be adjusted, such that the total energy of the CP is minimized.

2.10. The CP halo (i.e. the charge compensation layer)

The computational results achieved with the cylindrical model show that the core of a CP can carry excess negative charge (e.g. 2% more electrons than nuclear charges). Typically, the surplus negative charge of the CP has to be compensated by a surrounding layer of cations. This layer contains room charge, which terminates the electrical field around the CP core. Throughout this document the charge compensation layer of cations is designated as the “halo” of the CP, whereas the nuclei and the electrons comprising the CP (without the halo) is designated as the “core” of the CP. The halo can also be modeled as a jellium, like the core. If the halo is fully compensating the charge of the core, the *linear charge density of the halo* is

$$\bar{\lambda}_h \equiv \frac{Q_h}{L} = -\bar{\lambda}_e - \bar{\lambda}_n, \quad (42)$$

where Q_h is the total charge of the halo, $\bar{\lambda}_n = Q/L$ is the linear charge density of the nuclei in the core and $\bar{\lambda}_e$ is the linear charge density of the electrons in the core. For the purpose of computing the electric potential in the core, the easiest way is to assume a homogeneously charged cylindrical shell with a radius ρ_h , which is larger than the radial extent of the electron orbits and the extent of the nuclear charge distribution of the core (simplification (i)). The shell shall be concentric to the z -axis and have an infinitesimal wall thickness of $\delta\rho$. The *charge density of the halo* cations then is

$$\bar{\sigma}_h = \frac{\bar{\lambda}_h}{2\pi\rho_h\delta\rho}. \quad (43)$$

The potential summands sourced by the nuclei and the electrons had been specified in Eq. (22). The *contribution of the halo to the Coulomb potential* computes as

$$\Phi_h = \frac{1}{4\pi\epsilon_0} \int_0^\infty \bar{\sigma}_h(\rho') G(\rho, \rho') \rho' d\rho' = \frac{\bar{\lambda}_h}{8\pi^2\epsilon_0} \int_{\rho_h}^{\rho_h+\delta\rho} \frac{1}{\rho'\delta\rho} G(\rho, \rho') \rho' d\rho' = \frac{\bar{\lambda}_h}{8\pi^2\epsilon_0} G(\rho_h, \rho_h). \quad (44)$$

The *contribution of the halo to the Coulomb energy of a single electron* is

$$\bar{E}_{C,h} \equiv -e\Phi_h = -\frac{e\bar{\lambda}_h}{8\pi^2\epsilon_0} G(\rho_h, \rho_h). \quad (45)$$

The additional charge of the halo increases the self-repulsion energy between the nuclear charges, as mentioned in Eq. (40). In particular: The *core-halo repulsion energy* can be computed via:

$$\bar{E}_{n,h} = Q\Phi_h. \quad (46)$$

The *halo self-repulsion energy* is

$$\bar{E}_{h,h} = \frac{1}{2} Q_h \Phi_h. \quad (47)$$

The result in the above equation was divided by two, because the halo charges are interacting with themselves.

2.11. Approximate solution of the radial wave function

The following *ansatz* will be used for approximating the *radial wave function*:

$$\rho_0 \Psi_\rho \equiv R(r) = f(r) \cdot \exp(-\zeta r), \quad (48)$$

where $r \equiv \rho/\rho_0$ is the relative radius, $\rho_0 \equiv a_0/\sqrt{\lambda_n}$ is the reference radius, $f(r)$ is assumed to be a polynomial and $\zeta \in \mathbf{R}^+$ is a tunable scaling factor.

The value of the *exponential scaling factor* ζ can be determined by analyzing the asymptotic behavior of the wave function R at $r \rightarrow \infty$

$$\zeta = \sqrt{\frac{1}{\lambda_n} (P_z^2 - \alpha^2 E^2 - 2E)}. \quad (49)$$

Therefore,

$$E = \frac{1}{\alpha} \sqrt{P_z^2 - \lambda_n \zeta^2 + \frac{1}{\alpha^2}} - \frac{1}{\alpha^2},$$

where $\lambda_n \equiv Qa_0/e\bar{L}$ is the linear nuclear charge density of the core in natural units, $E \equiv \bar{E}/\bar{E}_h$, $\bar{E}_h \equiv \hbar^2/m_e a_0^2$ is the Hartree energy, $\alpha \equiv \hbar/m_e c a_0$ is the fine structure constant and $P_z \equiv a_0 \bar{P}_z/\hbar$ is the axial canonical momentum of the electron in natural units

At the *non-relativistic limit* the *exponential scaling factor* computes as

$$\zeta = \sqrt{\frac{1}{\lambda_n} (P_z^2 - 2E)}, \quad (50)$$

thus

$$E = \frac{1}{2} (P_z^2 - \lambda_n \zeta^2).$$

Inserting (48) and (49) into radial Klein–Gordon equation (36) leads to:

$$\begin{aligned} & -\frac{\lambda_n}{2} f'' + \frac{\lambda_n}{2} \left(2\zeta - \frac{1}{r} \right) f' \\ & + \left[\frac{\lambda_n \zeta}{2r} + \frac{\lambda_n m^2}{2r^2} + \frac{p_z^2}{2} - \frac{\alpha^2}{2} \left(\frac{1}{\alpha} \sqrt{P_z^2 - \lambda_n \zeta^2 + \frac{1}{\alpha^2}} - E_C \right)^2 + \frac{1}{2\alpha^2} - \frac{\lambda_n \zeta^2}{2} \right] f = 0, \end{aligned} \quad (51)$$

where $E_C \equiv -e\Phi/\bar{E}_h$ is the Coulomb energy in natural units and $p_z \equiv a_0 \bar{p}_z/\hbar$ is the axial kinetic momentum in natural units

For the non-relativistic limit the Schrödinger equation (37) leads to:

$$-\frac{\lambda_n}{2} f'' + \frac{\lambda_n}{2} \left(2\zeta - \frac{1}{r} \right) f' + \left(\frac{\lambda_n \zeta}{2r} + \frac{\lambda_n m^2}{2r^2} - P_z A_z + \frac{A_z^2}{2} + E_C \right) f = 0. \quad (52)$$

Solutions to differential equation (51) or (52) consist of eigenvalues of ζ and eigenstates of polynomial f . These solutions can then be used to compute the eigenvalues of \bar{E} and eigenstates of Ψ_ρ of the radial Klein–Gordon equation (36) or Schrödinger equation (37).

Function $f(r)$ can be approximated by a polynomial of r as follows:

$$f(r) \approx \sum_{j=0}^J c_j r^{|m|+j} \quad \text{for } c_j \in \mathbf{R} \quad (53)$$

Generally, constants c_j and ζ are depending on quantum numbers n , m and l . For simplicity reasons, this dependency is not reflected in the respective indices of these constants.

In Eq. (57) a number of terms can be approximated by a polynomial of degree P :

$$\frac{p_z^2}{2} - \frac{\alpha^2}{2} \left(\frac{1}{\alpha} \sqrt{P_z^2 - \lambda_n \zeta^2 + \frac{1}{\alpha^2}} - E_C \right)^2 + \frac{1}{2\alpha^2} - \frac{\lambda_n \zeta^2}{2} \approx \sum_{p=0}^P b_p r^p, \quad (54)$$

where $P \leq J - 1$ and $b_p \in \mathbf{R}$

At the non-relativistic limit (54) simplifies to:

$$-P_z A_z + \frac{A_z^2}{2} + E_C \approx \sum_{p=0}^P b_p r^p, \quad (55)$$

where $P \leq J - 1$ and $b_p \in \mathbf{R}$

A good approximation accuracy has been achieved with $P = 8$. The coefficients c_j can be computed by the iterative formula from the value of c_0 :

$$c_j = \frac{1}{(2|m|j + j^2)} \left\{ \zeta (2|m| + 2j - 1) c_{j-1} + \frac{2}{\lambda_n} \sum_{p=0}^P b_p c_{j-p-2} \right\}, \quad (56)$$

where $c_i = 0$ for $i < 0$

Note, that the coefficients c_j are all proportional to each other. Formula (56) stays the same at the non-relativistic limit. The last coefficient c_J is zero, only in case ξ is an eigenvalue. All eigenvalue can be found this way. The value of coefficient c_0 can be determined from ζ by normalization of the wave function R . The normalization condition (32) requires:

$$1 = \|R\| = \int_0^\infty |R(r)|^2 r dr = \int_0^\infty \left(\sum_{j=0}^J c_j r^{|m|+j} \right)^2 \exp(-2\zeta r) r dr. \quad (57)$$

That means, one has to scale all c_j proportionally, such that (57) yields the value 1.

2.12. Grouping, orbital occupation, self-consistent field iterations

The electron configuration of a CP consists of many orbitals, which are characterized by the quantum numbers n , m and l . According to the Pauli Exclusion Principle each orbital can only be occupied by a maximum of two electrons (one with spin up and one with spin down).

There are too many electrons in a CP to compute all occupied orbitals individually. Instead, ranges of orbitals with contiguous values for l are grouped together. Within a group all orbitals have the same quantum numbers n and m . These orbitals of such groups differ in quantum number l . The arithmetic mean of the quantum numbers l represents the group during computation. Equations (14) and (16) are computed by letting the summation run over the occupied number of groups. Each summand is multiplied by the number of electrons it represents. For ground state computations of the occupation should start with the lowest energy. It should progress to groups with successively higher energy until the targeted number of electrons “found their orbital”.

Equations (14), (16) and (56), as well as the occupation process are depending on each other in a circular manner. Thus, they can be computed only *iteratively* until reaching *self-consistency between eigenstates, potential and occupation*. Within each of these SCF-iterations (self-consistent field iterations) there is a need for sub-iterations:

According to (16) and (26) the axial current density J_z and the vector potential A_z are mutually dependent on each other. Sub-iterations are required for making these quantities consistent with each other, while leaving the eigenstates unchanged.

3. Computational Results from the Cylindrical Model

3.1. The physical properties of the “Golden Configuration”

The author has programmed a “simulator” tool [17], which implements the mathematics of the cylindrical model described in Section 2. Many different configurations of CPs have been simulated successfully with this tool. In the current section, only one of these configurations will be described, which the author believes is among the most stable ones. This configuration is called the “golden configuration” throughout this document.

The golden configuration of a CP is characterized by the following *input parameters*:

- The computation was relativistic, i.e. the Klein–Gordon equation was engaged.
- A template with 14 750 orbital groups was used. The template specifies the quantum numbers n , m and l for groups of electrons. The orbitals (i.e. eigenvalues and eigenstates) of these groups were calculated as candidates for occupation. 7375 of these groups were actually occupied in the order of the computed eigenvalues.
- The length of the CP was set to 9.6 mm.
- The nuclei in the jellium had a mean charge of 48 elementary charges.
- The linear charge density of the nuclei λ_n was set to 500 elementary charges per picometer length of the CP.
- The number of electrons was set to be 102% of the total number of elementary charges contained in all the core nuclei combined.
- A halo of cations was configured to reside at a distance of $150\rho_0 = 48.8$ pm, such that the total charge of the CP is zero (neutral).
- The core nuclear charge distribution was computed according to Eq. (60) with a standard deviation of $\bar{s} = 90\rho_0 = 29.3$ pm, a slope parameter of $\text{Slope} = 105\rho_0 = 34.2$ pm and a cutoff parameter of $\text{Cutoff} = 115\rho_0 = 37.4$ pm.
- The maximum number of coefficients c_j of the wave function polynomial was set to 2150.
- The axial velocity of the electrons was limited to $10\% \leq v_z \leq 80\%$ of the speed of light.

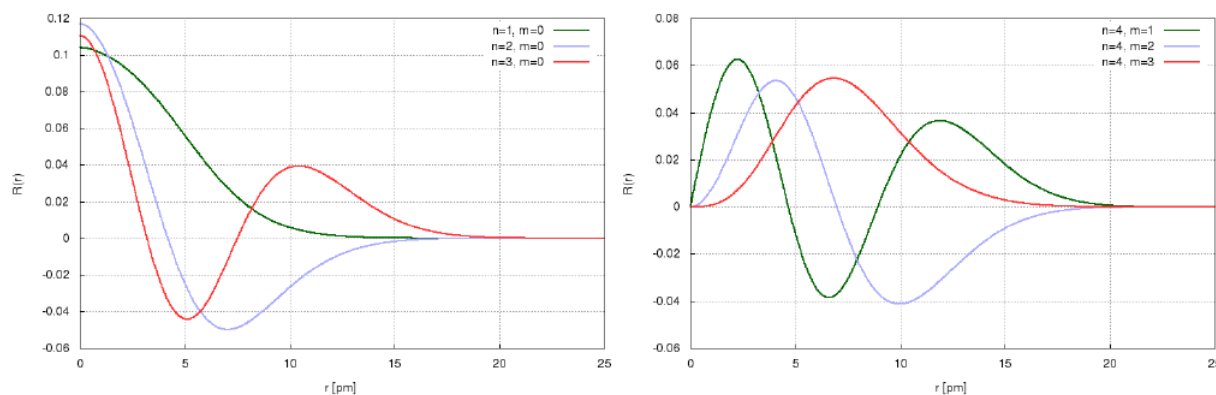


Figure 7. Plots of three radial wave functions $R(r)$ against the radius r ; *Left:* With principle quantum numbers $n = 1, 2$ and 3 and azimuth quantum number $m = 0$. *Right:* With principle quantum numbers $n = 4$ and azimuth quantum number $m = 1, 2$ and 3 .

The simulator tool in this case had to compute 44 iterations before reaching a self-consistent field status, where the field of the electron charge distribution was self-consistent with the eigenstates of the occupied groups. The tool lists the resulting eigenvalues (in eV) of the groups ordered by their quantum number in a huge triangular table.

The eigenvalues within a single field of the table are distinguished by quantum number l , i.e. the electrons of the respective groups have different axial velocities. Each eigenvalue has a hyperlink, which upon clicking opens a detailed description of the respective eigenstate, including a plot of the wave function. Plots with samples of the computed wave functions are shown in Fig. 7:

As can be seen from Fig. 7, the number of zeros of the wave functions equals $n - m$, whereby the last zero is at infinite radii. The radial extent of the wave functions generally increases with principal quantum number n . The eigenvalues of wave functions with identical n and l but different m are non-degenerate (i.e. they are different): The

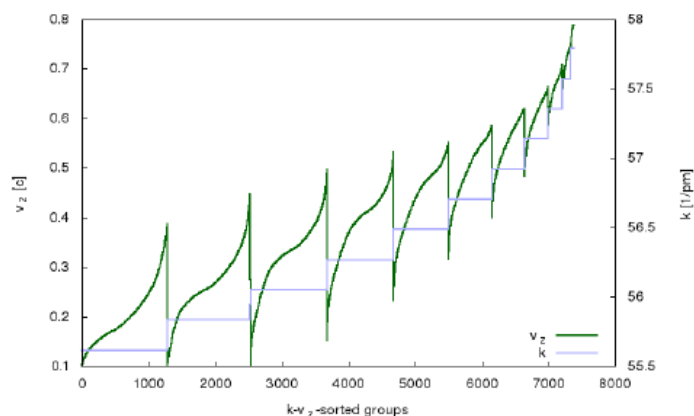


Figure 8. Distributions of the electron's axial velocities (v_z) and axial wave numbers (k). The occupied groups have been sorted at first by wave number. Within the ranges of constant wave numbers the groups have then been sorted by velocity.

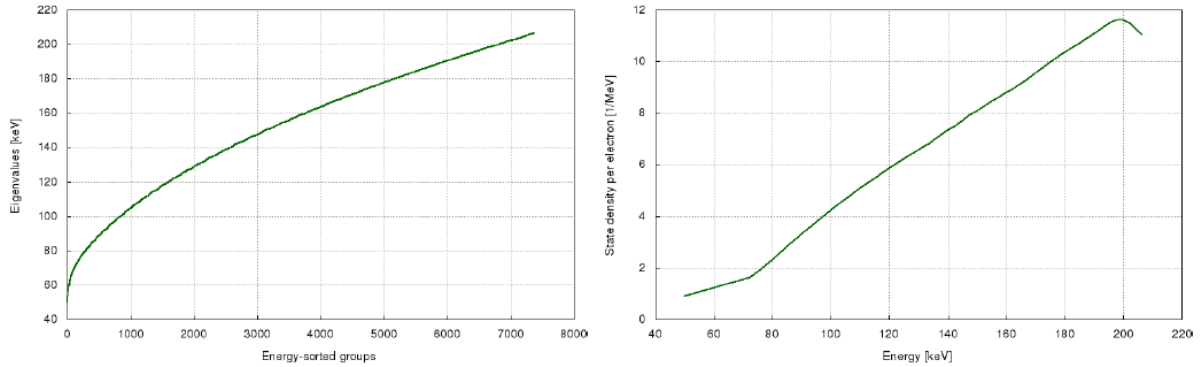


Figure 9. *Left:* Electron eigenvalue distribution. The occupied groups have been sorted by energy eigenvalue; *Right:* Electron state density distribution. It has been computed by exchanging the x and y axes of the left figure and then forming the first derivative via numerical derivation. The state density measures, how many quantum states per electron exist in an infinitesimal energy interval.

radial extent of a wave function (with a fixed n) decreases and the eigenvalue decreases with increasing m .

The symmetry of the axial velocity distribution is broken, i.e. it is not centered symmetrically on zero. The axial velocity correlates with the wave number of the axial de Broglie waves. The wave number distribution is also asymmetric. Both distributions can be seen in Fig. 8:

- The total nuclear charge of the CP core is 7.69×10^{-7} C.
- The total charge of the halo cations is an additional 1.54×10^{-8} C.
- The CP contains 100 billion nuclei.
- There are 4.90×10^{12} electrons in the CP.
- Each electron group contains 664 million electrons.
- The maximum matter density in the CP core is 647 kg/cm^3 for cadmium, 92.0 kg/cm^3 for oxygen and 5.80 kg/cm^3 for hydrogen. For cadmium this is about 75,000 times denser than ordinary metal.

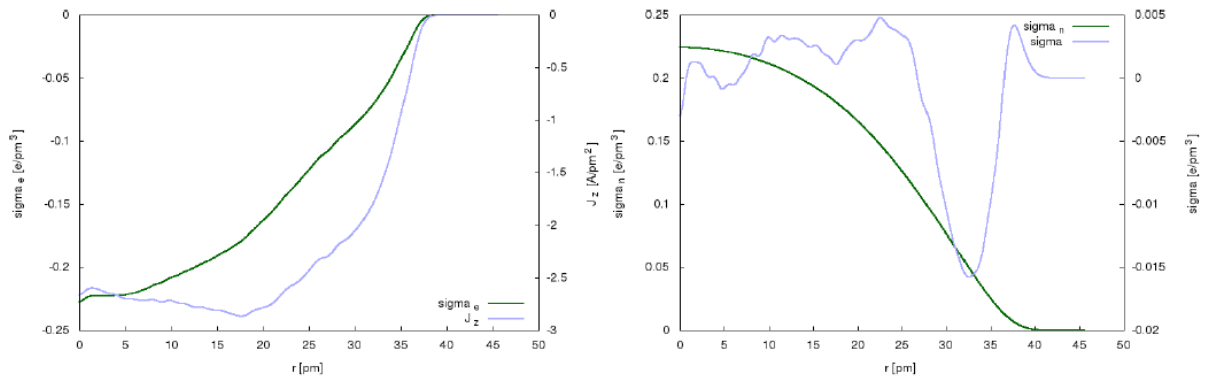


Figure 10. *Left:* Radial distributions of the electron charge density (σ_e) and the current density (J_z). *Right:* Radial Distributions of the core nuclear charge density (σ_n) versus the total charge density (σ).

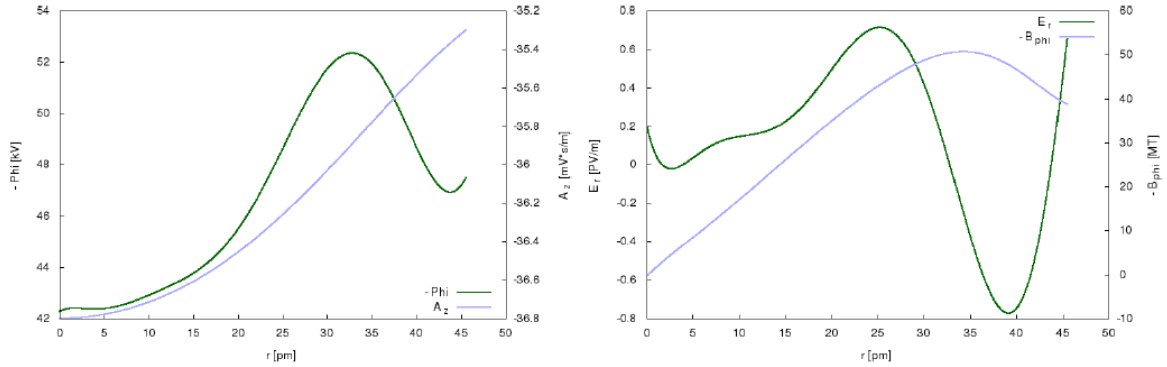


Figure 11. Left: Electric potential (φ) and magnetic potential (A_z). Right: Radial electric field (E_r) and azimuthal magnetic field (B_{ϕ}).

- The kinetic energy of the electrons ranges from 1.9 to 155 keV, stemming mostly from the axial movement
- The axial de Broglie wavelength of the electrons ranges from 0.108 to 0.113 pm

3.2. Varying the input parameters

The most prominent changes of the simulation results occur when the linear charge density of the core λ_n is varied. The total number of nuclei and electrons in the CP has been kept constant for this comparison: Other key properties of a CP also change significantly, when the linear charge density of the core nuclei λ_n is varied (Table 1):

Varying λ_n strongly changes the eigenvalue distribution: The minimum axial velocity also has strong influence on the properties of the CP, mainly because it changes the axial current of the CP: Varying the minimum axial velocity is changing the eigenvalues, because of the differences in the axial kinetic energy. Other key properties changing with the minimum axial velocity are as follows (Table 2).

The staircase shape of the wave number graph is an artifact from electron grouping: A whole range of wave numbers is represented by its mean value of the group. With a larger number of groups in the simulation template, the

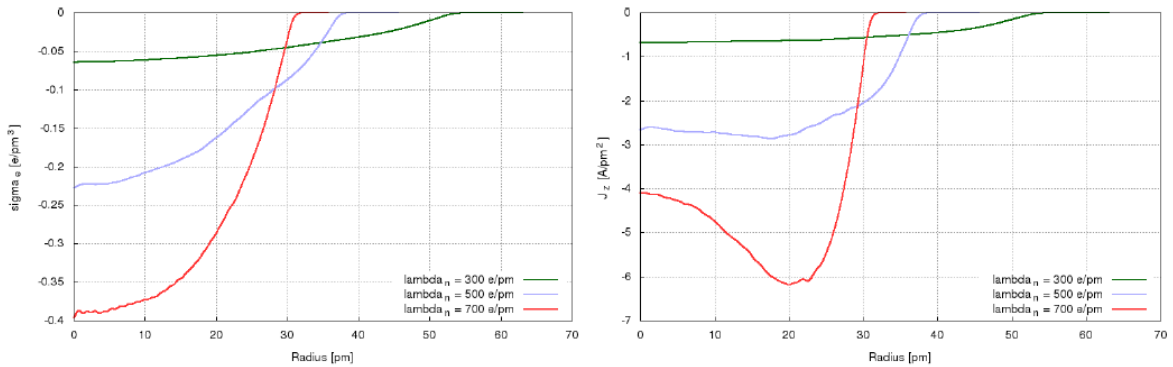


Figure 12. Electron charge density distribution (top) and current density distribution (bottom) at different values for the linear charge density λ_n of the nuclei.

Table 1. Changes of key properties, when the linear charge density of the core nuclei λ_n is varied (the “golden configuration” is marked bold).

Linear charge density of the core (e/pm)	100	200	300	400	500	600	700	800
CP length (mm)	48	24	16	12	9.6	8	6.86	6
Reference radius (pm)	0.727	0.514	0.420	0.364	0.325	0.297	0.275	0.257
Mean expectation value of the electron radius (pm)	66.2	39.6	29.2	23.7	20.2	17.8	17.0	16.3
Mean expectation value of the electron charge density (e/pm ³)	−0.0029	−0.0159	−0.0433	−0.0875	−0.150	−0.231	−0.297	−0.374
Mean expectation value of the current density (A/pm ²)	−0.0222	−0.160	−0.529	−1.24	−2.48	−4.06	−5.26	−6.81
Formation energy per electron (keV)	9.79	24.4	43.4	65.2	92.3	118	136	158
Min. electric potential of the core (kV)	−7.36	−18.3	−27.9	−39.5	−52.3	−60.7	−66.6	−79.6
Total axial current (kA)	−0.779	−2.08	−3.90	−6.15	−9.21	−12.0	−14.2	−16.7
Mean axial velocity (c)	0.159	0.213	0.265	0.314	0.376	0.409	0.414	0.426
Max. magnetic flux density (MT)	1.43	6.24	15.3	29.3	50.7	74.8	94.6	119
Characteristic Impedance (Ω)	653	673	684	692	698	703	705	706
Inductance (nH)	165	85.1	57.7	43.8	35.3	29.7	25.5	22.4
Capacitance (fF)	388	188	123	91.5	72.5	60.0	51.4	44.8
Magnetic flux (μ Wb)	129	177	225	269	326	356	362	373
Energy of the magnetic flux per electron (MeV)	0.0639	0.235	0.560	1.06	1.91	2.72	3.28	3.98
Minimum nuclear distance ($Z_m = 48, 8$ and 1) (pm)	27.8	15.7	11.2	8.80	7.42	6.52	6.16	5.83
	15.3	8.64	6.16	4.84	4.08	3.59	3.39	3.21
	7.65	4.32	3.08	2.42	2.04	1.79	1.69	1.60
Lowest occupied orbital eigenvalue (keV)	8.35	15.5	22.9	28.5	49.9	58.3	72.4	87.3
Highest occupied orbital eigenvalue (keV)	26.4	61.5	102	147	206	258	298	350
Max. state density per electron (1/MeV)	114	42.9	25.7	18.2	11.6	8.83	7.56	6.03

steps get smaller. The velocity ranges for neighboring wave number values are overlapping, which results in the saw teeth shape of the velocity distribution graph. The energy eigenvalues of the occupied orbitals is distributed according to Fig. 9. The charge density distribution and the current density distribution computed as follows.

At radius values around 32 pm the electron charge density exceeds the nuclear charge density. The resulting total charge density distribution can be seen at the right side of Fig. 10. The electric and magnetic potentials, as well as the electric and magnetic fields as a function of the radius is shown here.

Other computation results for the golden configuration are listed in column “500” in Table 1. Additionally, the following values have been computed. The following diagrams compare the results of non-relativistic simulations (via the Schrödinger equation) with relativistic simulations (via the Klein–Gordon equation).

As can be seen above, there is virtually no difference in the electron charge distributions for both types of simulation runs. The same is true for the individual wave functions. However, the eigenvalue distribution changes markedly

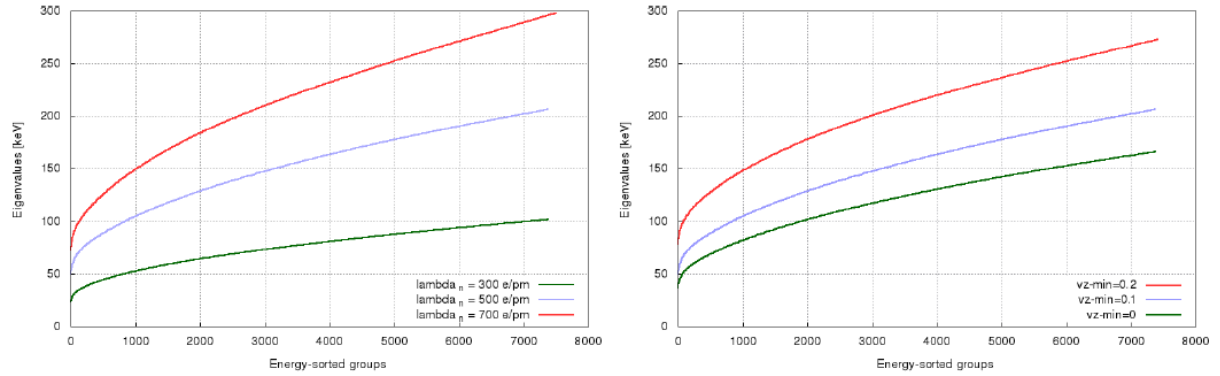


Figure 13. Top: Changes of the eigenvalue distribution, when λ_n is varied. Bottom: Changes of the eigenvalue distribution, when the minimum axial velocity is varied.

between non-relativistic versus relativistic simulations. These changes lead to a higher (i.e. more endothermic) formation energy and a lower state density at non-relativist runs. Except for the purpose of this comparison here, all properties of CPs were obtained by relativistic simulations. The length of a CP and the number of electrons in the CP core have only minor influence on the resulting properties. Therefore, no details are shown here.

3.3. Confinement, stability, formation energy, electron scattering

According to Fig. 11 the electric potential in the CP core is below -47.5 keV with an electron surplus of 2% against the nuclear charges. The potential is repulsive to the electrons and attractive to the nuclei. *The electric potential safely confines/traps the nuclei inside the core.* The negative potential is a direct result of the electron surplus in the CP core. The larger this surplus is, the more negative the potential will become. It is believed that there is an equilibrium of diffusion for the nuclei: If the core potential is becoming too negative, nuclei from the surrounding matter will be pulled into the core. If the core potential is becoming less negative, nuclei from the core will diffuse out and will

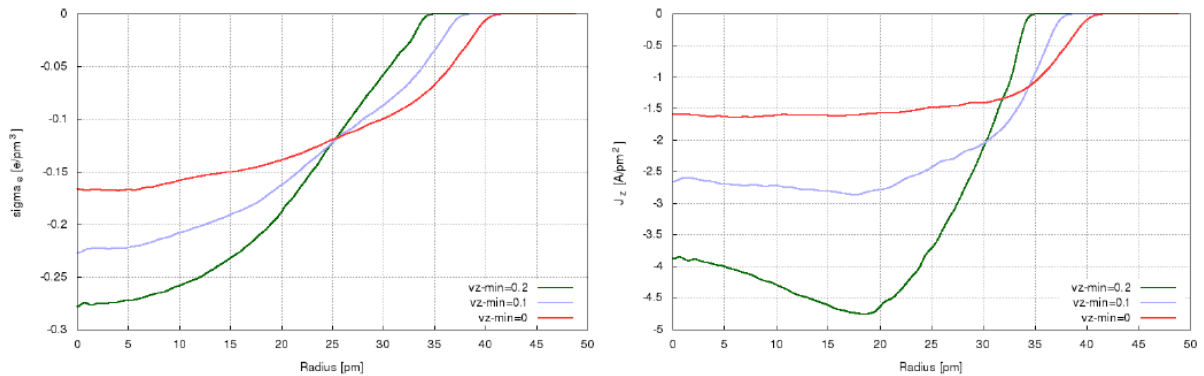


Figure 14. Electron charge density distribution (left) and current density distribution (right), at different values of the minimum axial velocity (in units of the light speed) of the electrons.

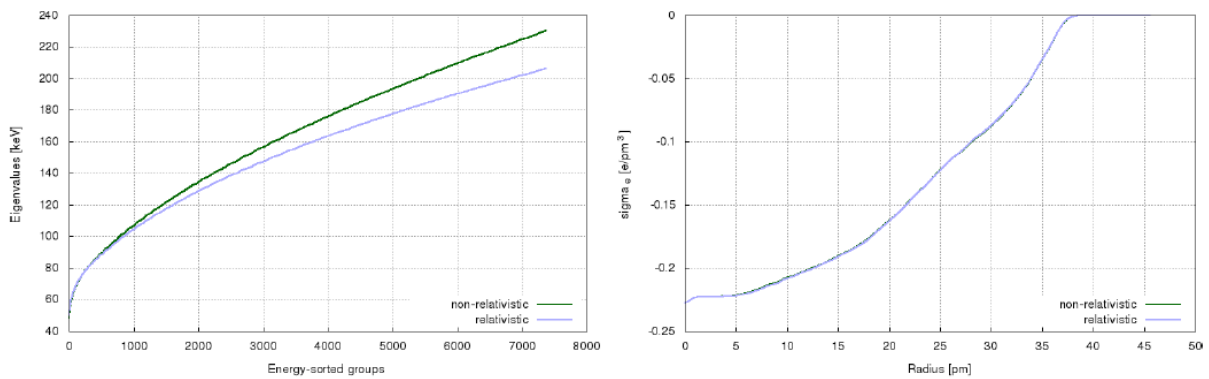
Table 2. Changes of key properties, when the minimum of the axial velocity of the electrons is changed is varied.

	$v_{z,\min} = 0$	$v_{z,\min} = 0.1 \cdot c$	$v_{z,\min} = 0.2 \cdot c$
Formation energy	66.1 keV	92.3 keV	132 keV
Total axial current	−6.38 kA	−9.21 kA	−12.2 kA
Mean axial velocity	0.260 c	0.376 c	0.498 c
Mean expectation value of the electron radius	22.7 pm	20.2 pm	18.0 pm
Mean expectation value of the electron charge density	−0.120 (e/pm ³)	−0.150 (e/pm ³)	−0.190 (e/pm ³)
Mean expectation value of the current density	−1.43 (A/pm ²)	−2.48 (A/pm ²)	−4.05 (A/pm ²)
Min. electric potential of the core	−48.5 kV	−52.3 kV	−63.3 kV
Max. magnetic flux density	−32.6 MT	−50.7 MT	−74.4 MT
Minimum nuclear distance ($Z_m = 48$)	8.15 pm	7.42 pm	6.92 pm
Lowest occupied orbital eigenvalue	36.9 keV	49.9 keV	78.1 keV
Highest occupied orbital eigenvalue	166 keV	206 keV	273 keV

recombine with electrons from the surrounding matter. A quantitative analysis of this equilibrium is not available, however.

The magnetic potential confines the electrons in radial direction safely, because the axial velocity of the electrons is in positive z -direction. Therefore, the electrons will be compressed against the z -axis (z -pinch). The confinement of the electrons in axial direction exists only, if the CP has formed a *closed loop*, i.e. the electrons cannot escape at the ends. In open-ended configurations of a CP, the electrons will be emitted at one end of the CP, while the other end will be depleted from electrons. It is clear, that open-ended CP configurations are not stable. However, they can exist in a transient manner, e. g. while being attached to a cathode and in the presence of a strong electric field. The cathode in this case has to replace the electrons at the positive end of the CP, at the same rate the electrons are emitted at the negative end. Within the current framework of the cylindrical model the *length stability of a CP* remains enigmatic. In consequence it is uncertain at which densities CPs are most stable. On one hand, there is ample experimental evidence available showing that CPs are either energetically metastable or dynamically stable with lifetimes sometimes exceeding one hour. On the other hand, a CP with the binding energies according to Table 1 would just elongate itself and decay, because the binding energies fall monotonically with the CP length.

Could the length stability be caused by a yet unknown term of the Hamiltonian, which lowers the formation energy at higher densities? Arguments exist as to why the resistive losses in a CP at low or moderate temperatures are expected to be extremely small: Small-angle scattering of the electrons would need to occupy higher-energy orbitals or would

**Figure 15.** Eigenvalue distribution and electron charge density distribution, non-relativistic versus relativistic.

result in orbitals, which are already occupied. Thus, one can say that small-angle *scattering is quantum mechanically suppressed*.

Large-angle scattering (such as the reflection of electrons by the core nuclei) is also suppressed, because the resulting orbitals would run in negative z -direction. The resulting eigenvalues would be higher than before the reflection, i.e. the reflection will not occur. Only at very high temperatures (above hundreds or thousands Kelvin) will there be sizable electron-phonon scattering (both, small-angle and large-angle). Some of the resulting eigenstates will have negative axial velocities. These electrons will be repelled from the CP by the electric field (i.e. they will be lost). In other cases, the resulting eigenstates will relax back (under electromagnetic radiation) to the lower-energy eigenstates, which were populated before the scattering occurred.

Interestingly, the electrons, which will be accelerated in positive z -direction, cannot relax back to lower velocities, because linear movement of charges does not radiate. In effect, very high temperatures in the core can increase the mean axial velocity of the electrons. In order for the model proposed here to account for stable CPs, the resistive loss will need to be very low. The reasons given above are thought to be plausible as to how this might come about. However, further analysis or experimentation is required for clarification.

If the resistive losses are indeed very small, the magnetic flux of a CP is expected to be virtually constant in a sub-millisecond timeframe. Over a longer time span the flux can potentially change slowly (in both directions, depending on the external conditions). For a CP to decay, the axial movement of the electrons has to slow down. This, however, takes a long time because of the said lack of electron scattering and because the magnetic flux can change only very slowly.

4. Summary and Conclusions

Previously known as “strange radiation”, a novel aggregation state of matter has been characterized and named “condensed plasmoids” (CP). A quantum-mechanical model of CPs was built, a computer program was designed, and computer calculations were used to obtain the properties of CPs. The computed properties are well-aligned with many experimental findings in LENR, including the strange patterns left by CPs on the surfaces of electrodes and x-ray films.

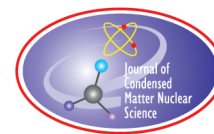
CPs compress matter magnetically to such high densities that atomic nuclei can tunnel through the Coulomb barrier, thereby enabling fusion. The current modeling is seen as being incomplete, because no length stability of CPs was found and because the calculated intrinsic current of CPs appears to be larger than what can be concluded from the experiments. This is probably caused by inaccuracies in the relativistic Hamiltonian.

Hopefully, the theory on CPs will reinvigorate the scientific discourse between research groups, startup companies and other organizations, which lately were working on their patents and LENR reactor designs in an understandably closed-lipped fashion. Without an open scientific dialogue on CPs however, the completion of this theory cannot be achieved. Hopefully, the theory on CPs will be instrumental in the technical development of *reliable, durable and safe* LENR reactors and timely commercialization.

References

- [1] Lutz Jaitner, *The Physics of Condensed Plasmoids and Low-Energy Nuclear Reactions (LENR)*, comprehensive article at the author's web site, 2015–2019, http://condensed-plasmoids.com/condensed_plasmoids_lenr.pdf.
- [2] Claude Daviau, Daniel Fargue, Didier Priem and Guillaume Racineux, *Tracks of magnetic monopoles, Annales de la Fondation Louis de Broglie* **38** (2013), <http://aflb.enscm.fr/AFLB-381/aflb381m778.pdf>.
- [3] B. Rodinov and Irina Savvatimova, *Unusual Structures on the Material Surfaces Irradiated by Low Energy Ions*, archived at

- LENR-CANR.org., 2005,
<http://www.lenr-canr.org/acrobat/RodionovBunusualstr.pdf>.
- [4] Takaaki Matsumoto, Bulletin of the Faculty of Engineering, Hokkaido Univ., No. 175, 1995, p. 73.
 - [5] W.-S. Zhang and J. Dash, Excess heat reproducibility and evidence of anomalous elements after electrolysis in $\text{Pd/D}_2\text{O}+\text{H}_2\text{SO}_4$ electrolytic cells, *13th Int. Conf. Condensed Matter Nucl. Sci.*, 2007,
<http://www.lenr-canr.org/acrobat/ZhangWSexcessheat.pdf>.
 - [6] A. Klimov et al., Interaction of hydrogen atoms and ions with erosive metal clusters in heterogeneous plasmoid, *12th IWAHLM*, Italy, 2017,
<http://www.iscmns.org/work12/KlimovAinteractionof.pdf>.
 - [7] Edmund Storms, *The Nature of the Nuclear-Active-Environment Required for Low Energy Nuclear Reactions*, Submitted to Infinite Energy, 2002,
<http://www.lenr-canr.org/acrobat/StormsEthenatureoa.pdf>.
 - [8] W.H. Bennett, Magnetically self-focusing streams, *Phys. Rev.* **45** (1934) 890.
 - [9] R.S. Pease, Equilibrium characteristics of a pinched gas discharge cooled by bremsstrahlung radiation, *Proc. Roy. Soc. London Ser. B* **70** (1957) 11–13.
 - [10] S.I. Braginskii, On the behavior of a completely ionized plasma in a strong magnetic field, *Zhur. Eksptl'. i Teoret. Fiz.* **33** (1957) 645.
 - [11] S.I. Braginskii, Contribution to the theory of spark channels, *Sov. Phys. JETP* **6** (1957) 494–501.
 - [12] Robert S. Cohen, Lyman Spitzer and Paul McR. Routly, The electrical conductivity of an ionized gas, *Phys. Rev.* **80** (2) (1950) 230–238,
<http://ayuba.fr/pdf/spitzer1950.pdf>.
 - [13] K.N. Koshelev and N.R. Pereira, Plasma points and radiative collapse in vacuum sparks, *J. Appl. Phys.* **69**(10) (1991) R21–R44,
https://www.researchgate.net/publication/224546528_Plasma_points_and_radiative_collapse_in_vacuum_sparks.
 - [14] J. Va'vra, J.A. Maly and P.M. Va'vra, Soft X-ray production in spark discharges in hydrogen, nitrogen, air, argon and xenon gases, SLAC-PUB-7683, *Nucl. Instr. Methods Phys. Res. Section A* **418** (2,3) (1998) 405–419,
<https://www.slac.stanford.edu/pubs/slacpubs/7500/slac-pub-7683.pdf>
 - [15] P.W. Atkins, *Molecular Quantum Mechanics*, Parts I and II: *An Introduction to Quantum Chemistry*, Vol. 1, Oxford University Press, Oxford, ISBN 0-19-855129-0, 1977.
 - [16] Kohn Walter and Sham Lu Jeu, Self-consistent equations including exchange and correlation effects, *Phys. Rev.* **140** (4A) (1965) A1133–A1138.
 - [17] Lutz Jaitner, *CP Simulator*, online program, 2016–2019,
https://condensed-plasmoids.com/dyn?cmd=retrieve_simulation_form.



Research Article

The Electromagnetic Considerations of the Nuclear Force

N.L. Bowen*

Colorado Mountain College, Glenwood Springs, Colorado, USA

Abstract

This paper explores how the electromagnetic energies of the quarks within the nucleus affect the behavior of the Nuclear Force. By examining the electromagnetic energies and forces, many questions about nuclear behavior can be answered and many insights into the nucleus can be gained. Previous theoretical models for the nuclear force include only the Coulomb electric force of the protons, but with little or no consideration of the electromagnetic characteristics of the quarks. By incorporating the electromagnetic energies and forces into nuclear theory, this model has been able to achieve predictions of binding energy better than any previous model, doing so by using only one variable instead of five. This model unifies the nuclear force to the electromagnetic force.

© 2020 ISCMNS. All rights reserved. ISSN 2227-3123

Keywords: Electromagnetic force, Nuclear binding energy, Nuclear bonding, Nuclear force, Nucleon–Nucleon force, Quarks

1. Introduction

1.1. Electromagnetics and the nuclear force

The development of a proper theory of the nuclear force has occupied nuclear physicists for over eight decades and has been one of the main topics of physics research in the 20th and 21st centuries. The focus of this paper is the role of electromagnetic energies within the nucleus and how these energies affect nuclear behavior. The emphasis of this paper is electromagnetics, since this has been largely disregarded in previous models of the nuclear force. Although the emphasis is on electromagnetics, this paper does not ignore quantum physics in any way, and the concepts of quantum physics are included in this paper.

Currently, there is no one model of the nuclear force that can explain the majority of nuclear behaviors [1–4]. Here is a brief list of the more salient nuclear behaviors that a successful model of the nuclear force should address:

- Particle decay – this includes alpha decay, beta-delayed alpha decay, proton decay, beta-delayed proton decay, neutron decay, beta-delayed neutron decay, spontaneous fission, and beta-delayed spontaneous fission. (Beta decay and gamma decay are not considered as particle decay.)
- The shape of binding energy curve.

*E-mail: nbowen@coloradomtn.edu.

- Large quadrupole moments.
- Why and how excited energy states exist.

In this paper, the lowest energy configuration of hundreds of nuclides, from ^2H to ^{208}Pb , have been computer-modeled and simulated, by applying the laws of electromagnetics to the quarks inside of the nucleus. The binding energies of these nuclides have been calculated and compared to experimental data. Using only electromagnetics to compute the binding energies, the calculated binding energies agree with the experimental binding energies within a few percent. These computations are done by using only one variable, rather than five variables. (The Weizsäcker formula, which is a curve-fitting equation, uses five variables plus conditional logic to empirically curve-fit the experimental data.) No other current theoretical model of the nuclear force has been able to demonstrate such a tight prediction of binding energy for all the nuclides from ^2H to ^{208}Pb with only one variable. This achievement is an unprecedented success and strongly indicates the correctness of this new model.

This model assumes the laws of electromagnetics are valid inside a nucleus, and that these laws should not be disregarded. This model asserts that is the electromagnetic properties of the quarks within the nucleus that create the nuclear force and hold the nucleons in a nucleus together. The electromagnetic forces and energies cause the nuclides to fall into the lowest energy state and configuration. It is asserted that this electromagnetic energy and the specific lowest energy configurations of the nuclides are features that give the nuclides certain behaviors, such as binding energy, large quadrupole moments, excited states, and particle decay.

The electromagnetic forces inside a nucleus, when taken into full account rather than being disregarded and ignored, can explain much about nuclear behavior. A better understanding of nuclear behavior can be gained by applying the knowledge and insight provided by the electromagnetic force. The role of electromagnetics within the nucleus is a field that deserves further research and serious analysis by theoretical nuclear physicists. This paper serves as the introduction and encouragement of further on-going theoretical investigations into the electromagnetic considerations of the nuclear force.

1.2. Definition and clarification of terms

The “Nuclear Force” is that force which binds together the nucleons in the nucleus. Historically, the nuclear force was called the “Strong Nuclear Force”, and was considered to be one of the four forces of nature, along with the gravitational force, the electromagnetic force and the weak nuclear force. Soon after the discovery of quarks, the force which holds the quarks together in a nucleon was called the “Chromo Dynamic Force”. This chromo dynamic force, which is a sub-nucleon force, is considered to be much larger than the nuclear force. Later, the chromo dynamic force was redefined as the strong nuclear force, which is now considered to be a sub-nucleon force responsible for the behavior and interactions of sub-nucleon particles. The force which hold the nucleons together in a nucleus was renamed as the “Nuclear Force”. To add to the confusion even more, there is a model of the nuclear force, which is called the residual chromo dynamic force. This model is a model of the nuclear force, that force which holds the nucleons together inside a nucleus. Because of this model, it is presumed that the nuclear force is simply a subset of the strong nuclear force. Because of this association, it is still claimed that there are only four forces in nature: The strong nuclear force, the electromagnetic force, the gravitational force, and the weak nuclear force. the strong nuclear force has two parts, the chromo dynamic force which is sub-nucleon, and the nuclear force, which is that force holding the nucleons together in a nucleus.

For clarity to the reader in this paper, the term strong nuclear force will not be used. Rather the term chromo dynamic force will be used to reference that force which holds together the quarks inside a nucleon. The term nuclear force will be used to describe that force which holds together the nucleons in a nucleus. The term residual chromo dynamic force will be used to describe one of the models of the nuclear force, and it will be emphasized in italics as the *residual* chromo dynamic force, to avoid any confusion of this force with the chromo dynamic force.

1.3. Current concepts regarding the chromo dynamic force

The chromo dynamic force is thought to be much stronger than the nuclear force, by several orders of magnitude. However, an actual definitive measurement of the strength of this force has not been made because particle physicists have been unable to separate the quarks inside a nucleon. Presently there are numerous models, some of which are quite complex and confusing, about what is inside a nucleon. These models attempt to describe the number of quarks inside a nucleon, what components make up the bulk mass of a nucleon, and what gives a nucleon its spin. Particle physicists believe that there could be several hundred non-valence quarks inside a nucleon. Suffice it to say, particle physicists are not presently concerned about applying uncertainty principles to these hundreds of quarks. The motion of the non-valence quarks is presumed to contribute to the orbital angular momentum of the nucleon, along with the massless gluons that hold them together; however, this has not been confirmed experimentally. It is not the intention of this paper to be a critique or review of the models of the sub-nucleon chromo dynamic force. In this paper, only the three valence quarks are considered.

2. Brief Review of Current Models

There are numerous models for the nuclear force. Each model can provide some explanation of certain properties of nuclei in their ground state, but no single model can explain all the properties. No complete theory exists which fully describes the structure and behavior of the nuclear force and of the nuclei which it controls [1–4]. Listed below are brief descriptions of the more-commonly known nuclear models.

2.1. Gamow's alpha decay model

One of the first descriptions for nuclear behavior was developed in 1928 by Gamow [5] to explain the observed alpha decay for the large nuclides. This proposed mechanism uses the Schrödinger equation to describe how an alpha particle can overcome its potential barrier via quantum tunneling. Gamow's proposed mechanism is valid only for the larger nuclides and does not apply to the near-instantaneous alpha decay seen in several of the smaller nuclides. Although the tunneling mechanism serves as a good description for the process of large-A alpha decay, it assumes the alpha particle is pre-formed inside the nucleus, an idea contrary to the independent particle models.

2.2. Weizsäcker formula and the liquid drop model

The Weizsäcker formula [6] is simply a mathematical equation used to curve-fit the experimental binding energy data. This formula is also known as the semi-empirical mass formula, meaning that the variables are chosen to curve-fit the data empirically. It uses five variables and conditional logic to obtain the best fit to the experimental binding curve. Although this curve-fitting formula is not a model *per se*, it is used in conjunction with the liquid drop model.

The liquid drop model, developed by Gamow in 1929 [7], states that nucleons bind only to their closest neighbors, as in a drop of liquid. This concept is based on the experimental binding energy curve, for which the energy per nucleon is relatively constant; this behavior is caused by the limited number of times that a nucleon can bind with other nucleons. (Interestingly, this limitation is also true of the atomic bond within crystals. An atom in a crystal can bond only to its nearest neighbors, thus the number of bonds which can be formed by a single atom is limited.) The liquid drop model assumes the nucleus is spherical. In conjunction with the curve-fitting Weizsäcker formula, the liquid drop model can predict the experimental binding energies to within a few percent. The liquid drop model offers only a conceptual explanation for spontaneous fission, but it does not offer a rigorous mathematical description for this behavior. For example, it cannot explain why certain nuclides such as ^{237}Cf exhibit fission, but other larger ones, such as ^{275}Hs do not. The liquid drop model does not consider excited states, large quadrupole moments, or other types of nuclear particle decay.

2.3. Meson exchange model

In 1935, Hideki Yakawa proposed that the nuclear interaction was mediated by an exchange of mesons [8]. This meson exchange model served, for many years, as a good description for the underlying mechanism of nuclear binding. However, the model itself does not attempt to explain binding energies, particle decay, excited states, or large quadrupole moments.

2.4. Alpha cluster model

The alpha-cluster model was developed in 1938 [9] to explain the stronger binding energy that is experimentally observed for nuclei with an integer number of alpha particles. When used in conjunction with the alpha decay model [5], together these models can explain the mechanism for alpha decay of the large isotopes, as well as correlating the experimentally observed energy of the emitted alpha particles to the half-life of the alpha decay. Recently, there has been much experimental evidence that excited states of nuclides are indeed made of clusters of alpha particles [10–15], as well as other building blocks. More recent theoretical refinements of the alpha-cluster model have provided increasing insight into these experimental observations [16–23].

2.5. Independent particle model

There are several independent particle models of the nuclear force, of which the Fermi gas model [24] is the simplest. These models hypothesize that nucleons move independently, confined inside a three-dimensional energy well, and that the nucleons do not interact with each other to any significant extent. By using this concept, these independent particle models are much easier to solve mathematically than an n -body problem of the nucleus. The more complex independent-particle models alter the shape of the potential energy well, from that of the Fermi gas model, by using numerous variables depending on the nuclide being studied. This alteration is done to predict the excited states of the nuclide. However, these independent-particle models cannot explain large quadrupole moments, unless a non-radial energy well is pre-assumed for the Hamiltonian. These models do not attempt to explain the binding energy curve or particle decay.

2.6. Shell model

The nuclear shell model was first hypothesized in 1932 and further developed in 1949 [25–27]. It is considered to be an independent-particle model, based on a concept similar to the electronic shell structure of atoms. The model is an attempt to explain the minor deviations that have been observed between experimental data and the Weizsäcker formula. This model assumes there is a passive nuclear core of nucleons, beyond which only the valance nucleons contribute to the nuclear behavior. The shells are based on “magic” numbers. When experimental data is compared to the Weizsäcker formula, the inconsistencies are observed to be larger at these magic numbers. Another experimental observation of magic numbers, unrelated to the Weizsäcker formula, is that for the lowest excited spin-2 state of the even-even nuclides, the energy is higher for the nuclides with magic numbers than for nuclides with non-magic numbers. Another experimental observation of magic numbers is that the neutron separation energy has a slight step for the nuclides when N is equal to a magic number.

Theoretically, to get these magic numbers, the shell model starts from a potential well called the “Woods–Saxon” potential. This potential energy well lies somewhere between the abrupt square well and the smooth harmonic-oscillator well; it also asymptotically approaches a zero energy at the well boundary. To this Woods–Saxon potential, a spin–orbit term is added, in an attempt to duplicate the observed magic numbers. However, the result does not coincide with these magic numbers unless an empirical spin–orbit coupling is also added. The shell model does not explain

any type of particle decay or large quadrupole moments [28]. The shell model uses the Pauli Exclusion Principle to predict spins; however, it can only do this accurately if the Nilsson terms are included [28]. The Nilsson term is not a “term” in the strict mathematical sense of the word; rather it is at least two or three different variables, with values that are dependent on the nucleus being studied. These are often referred to as “spaghetti plots” due to their complicated natures. When the Nilsson terms are included into the spin-orbit coupling constant, a better prediction of the nuclear spins can be achieved [29].

2.7. Collective model

Another model is the Bohr–Mottelson model, also known as the collective model [30–34]. This model is described as a combination the essential features of the liquid drop model and the shell model. In the shell model, one regards the primary form of motion as the orbital motion of the individual nucleons in the average nuclear field. However, in the liquid-drop model one looks at the simple collective motions of the nucleons. Both of these forms of motions are observed experimentally in nuclei to some extent. Thus, the Bohr–Mottelson model is a more general description of nuclear structure, one that considers the total state of motion as a superposition of these two basic components of motion. Such a description is regarded as a generalization of the shell model, in which the nuclear field is no longer considered to be considered constant, but rather to be considered to be a dynamic variable, in that the net nuclear potential undergoes deformations away from a spherical well. The Schrödinger equation is solved for non-spherical net nuclear potential. This variation of the collective nuclear field is linked with the vibrating shape of the nucleus. By using this dynamically-variable nuclear field the Bohr-Mottelson model can more closely estimate magnetic dipole moments and large electric quadrupole moments.

2.8. Collective-motion model

The collective-motion model (not to be confused with the collective model) is more of an experimental observation than a model. The experimentally-measured spin energies of the nucleus indicate that the nucleus is not a collection of independent particles moving randomly with respect to each other, but rather the rotational moment of inertia of the nucleus is similar to a rigid structure. This behavior is referred to as an apparent collective motion of the nucleus [35,36] whereby the nucleons within the nucleus appear to move with a collective motion.

2.9. Effective field model

Several other models are grouped together under the term “effective field models” [37]. These models incorporate an approximation for the overall Hamiltonian, often times using as many as 40 or more variables to curve fit the predicted results to the observed experimental data [38]. These effective field models are used to explain results from scattering experiments.

2.10. Residual chromo dynamic model

The residual chromo dynamic model [39], similar to the meson exchange model of 1935, postulates that the nuclear force is caused by the exchange of virtual light mesons, such as the virtual pi-mesons (aka pions). In this model, the nuclear force is produced by a potential energy well that is a residual short-range force of the chromo dynamic force. The chromo dynamic force is the force that holds the quarks together inside the nucleon, in which dissimilar colors are attracted to each other, but similar colors are not. Conversely, the residual chromo dynamic force occurs outside the nucleon. It is postulated that this residual force bonds the quarks in one nucleon to a quark in another nucleon. The

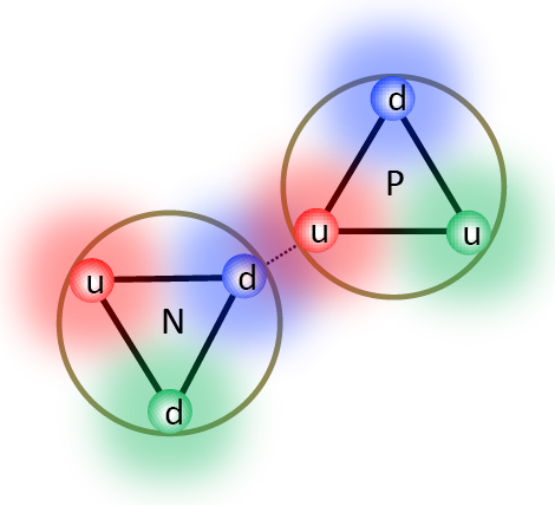


Figure 1. The nuclear binding of deuterium, as hypothesized by the residual chromo dynamic force.

residual chromo dynamic force thereby binds the two nucleons together. In other words, the residual chromo dynamic force is an inter-nucleon force between two quarks. The residual chromo dynamic force is often compared to the Van der Waals force, a force that is electromagnetic in nature, due to the electric dipole moment of the molecules. Figure 1 depicts the residual chromo dynamic force for a deuterium nucleus, showing the quarks (red, blue and green). The chromo dynamic forces are represented in Fig. 1 by the bond black lines, and the residual chromo dynamic force is represented by the gray dotted line.

The proton is composed of one down quark and two up quarks; the neutron is composed of one up quark and two down quarks. The quarks are shown in the colors of red, green, and blue. The chromo dynamic force is represented by the darker coils in the nucleons. The lighter coils represent the residual chromo dynamic force, between the nucleons. With regard to quantum chromo dynamics, the word “color” has no relation to visible color. Also, the terms “up” and “down” have no relationship to vertical direction. Similar to the liquid drop model, the residual chromo dynamic model clarifies why a nucleon is bonded only to its nearest neighbors. Corresponding to the meson exchange model of the 1930s, the residual chromo dynamic model hypothesizes that the nuclear force is due to an exchange of virtual particles. This model is one of the few models of the nuclear force that takes quarks into consideration. However, mathematically, it is very difficult to derive the nuclear force from the quantum chromo dynamics using the Schrödinger equation [40], even for a system of only two nuclides. This difficulty arises because each nucleon consists of three quarks, such that the system of two nucleons is a six-body problem.

2.11. Electromagnetic hydrogen model

An electromagnetic model of the nuclear force was proposed [41], which can accurately give the binding energy for a few of the hydrogen isotopes, but this model has yet to be extended to larger nuclides. It is based on an assumed dipole moment of a bonded neutron (as opposed to a free neutron).

2.12. Model summary

In summary, the current models focus on specific aspects of the nuclear force, most of them relatively secondary behaviors, rather than focusing on the more salient behaviors, such as particle decay. The following is a partial list of some very basic questions that should be answered by a good model. Currently, no one model can answer them all.

- Why do certain medium-sized isotopes, such as ^{150}Dy , exhibit alpha radiation, and yet certain larger isotopes, such as ^{208}Pb , do not?
- Why is ^8Be so extremely unstable, and why does it exhibit alpha radiation?
- Considering the daughter nuclides after the fission of ^{235}U , why is there an extreme double-humped curve?
- Why do certain light isotopes (such as ^4He , ^8Be , ^{12}C , ^{16}O , ^{20}Ne , etc.) have a spike in their binding energy per nucleon?
- Why does ^4He have a zero thermal nuclear cross section?
- Why is ^5He so extremely unstable?
- Why are the magnitudes of quadrupole moments so much larger than any model predicts?
- What causes a nucleus to eject a neutron (aka neutron decay) in certain nuclides?
- What causes proton decay in certain nuclides?
- What causes alpha decay in certain nuclides?
- What causes spontaneous fission in certain nuclides?
- What causes beta-delayed neutron decay in certain nuclides?
- What causes beta-delayed proton decay in certain nuclides?
- What causes beta-delayed alpha decay in certain nuclides?
- What causes beta-delayed spontaneous fission in certain nuclides?

For most of these questions, the current models cannot offer any *theoretical* answer, other than to say, “because experimental energy levels allow the transition.” This response is not a valid theoretical answer, and is merely an experimental observation in support of the laws of thermodynamics. However, all of these questions can be answered with a better understanding of electromagnetic forces within the nucleus.

3. Recent Changes in Our Understanding of Nucleons

3.1. Quarks

In 1964, the existence of quarks was proposed independently by Gell-Mann and Zweig [42–45], changing the concept of the proton and neutron from homogeneously-charged particles to particles having electrical inhomogeneity. A proton is made up of three valence quarks, two up quarks and one down quark. A neutron is also made up of three valence quarks, two down quarks and one up quark. (Other non-valence quarks may exist inside the nucleons.) Up quarks have an electrical charge which is $2/3$ of an elementary charge. Down quarks have a charge which is $-1/3$ of an elementary charge. Since these concepts about quarks were introduced, we now know that the electrical charge and magnetic moments of a nucleon are confined to the quarks, rather than being homogeneously distributed throughout the nucleon. Illustrated in Fig. 2 are three shorthand symbolic representations, showing the up and down quarks, and the electric charges associated with them. In the first representation, the up quarks, in red, have a $++$ charge ($2/3$ of an elementary charge), and the down quarks, in blue, have a $-$ charge ($1/3$ of an elementary charge). The second symbolic shorthand representation shows just the $++$ and $-$ electric charges associated with the quarks. The third symbolic shorthand representation shows just the quarks as red and blue dots. (Please note that the colors in these figures do not relate in any way to the chromo dynamic force.) The magnetic moments of the up quarks are out of the page, and the magnetic moments of the down quarks are into the page; these moments are not shown.

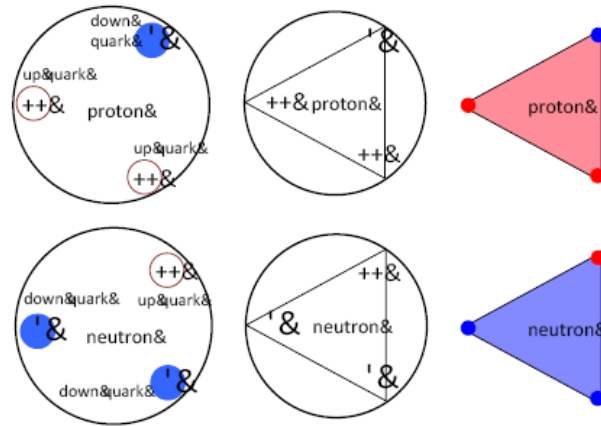


Figure 2. Three shorthand simplified representations of protons and neutrons.

3.2. Angular momentum and mass of quarks

Prior to the 1980s, particle physicists believed that the spin angular momentum of the quarks was the only contribution to the angular momentum of the proton and neutron. However, experiments proved this concept to be wrong, creating what was called the nucleon spin crisis [46–51].

Further, it was recently learned that the rest mass of the three valence quarks make up a small percentage, approximately 1% or less, of the total mass of a nucleon [52]. Quarks are now considered to be point-like particle, similar to electrons, having no physical dimensions. (Thus in the drawing in Fig. 2, the circles representing the quarks are not meant to represent their actual physical dimensions, nor is the ratio of their radius to the radius of the nucleon meant to be drawn to scale.)

Since mass of the quarks is extremely small, they do not carry much, if any, kinetic energy related to their intrinsic angular momentum. Quarks have an intrinsic spin of $1/2$, but similar to the electron, there is no classical radial speed at which the particle is spinning. In a free nucleon, one that is not bonded inside of a nucleus, it was assumed prior to the 1980s, that the quarks were free to move around with no net orbital angular momentum, and the sum of the spin of the quarks was assumed to be equal to the spin of the nucleon. However, it was found experimentally that the spin of the nucleon is not equal to the sum of the spin of the quarks [46].

Particle physicists now believe there is a net orbital component to the movement of the quarks, rather than random motion. It is currently postulated by particle physicists that the spin of the nucleon, as well as the bulk of its mass, is due to the collective motion of the hundreds of energetic quarks and gluons inside a nucleon. There is another issue concerning these quarks and massless gluons confined within the nucleus, related to uncertainty, forcing the quarks to be extremely energetic. Exacerbating this issue even more, in 2013 as a result of better experimental measurements, the charge radius of the nucleon was corrected to a smaller value of 0.84087 fm [53]. Calculations for the *residual* chromo dynamic model circumvent this issue by using unrealistically large values for the masses of the quarks in their calculations, and then extrapolating down to the more realistic smaller values [54]. (This unrealistically large value used for the quark mass also helps the convergence of the computer solution, but it also creates potentially large errors in the resultant answers.)

Recall that the chromo dynamic force is considered to be large enough to confine and bind together the energetic

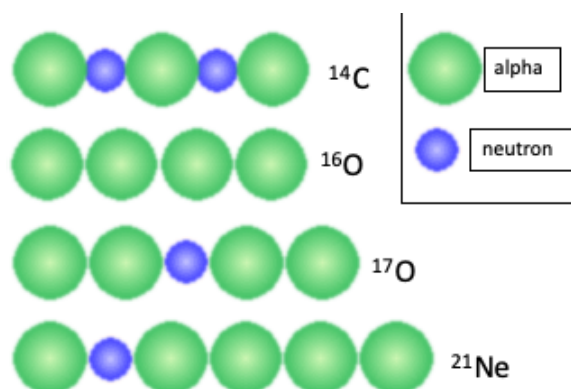


Figure 3. Ikeda diagrams of four simple nuclides.

quarks, despite their energetic vibrating circular motion. Random motion of the quarks inside a bonded nucleus need not be assumed, especially since the orbital angular momentum of the quarks is considered to contribute a significant part of the proton's spin.

3.3. Recent experimental and theoretical progress of the cluster model

The recent research regarding the clustering model has shown that clustering structures do indeed exist within nuclei [55–60], confirming the concept of an actual structure inside a nucleus. Recent research in the clustering structure of nuclides further corroborates the experimentally observed collective motion of nuclei, strongly suggesting that nucleons do not move independently inside a nucleus. Clustering is observed as a general phenomena at high excitation energies in light alpha-like nuclei, and clustering is a general feature not only observed in light neutron-rich nuclei, but also in less common systems, such as ^{11}Li and ^{14}Be [23]. The alpha-cluster model has now been extended beyond just the alpha nuclei, with much study and research in the field of cluster structure and of the so-called “nuclear molecules”. These “nuclear molecules” can be thought of as being built from building blocks or segments, which are linked together to form chain-like structures, called “nuclear molecules.”

These nuclear molecules are illustrated graphically in Ikeda diagrams [60]. A sample of Ikeda diagrams are shown in Fig. 3, to familiarize the reader with this type of diagram for nuclear structure.

As can be seen from the Ikeda diagrams, the nuclear segments form chain-like configurations, to create the nuclear molecules of the nucleus. Again, this is long chain-like shape is verified both experimentally and theoretically within the nuclear cluster model. (It is possible that this chain-like shape curls up to form a more elliptical overall shape, like a coiled chain.)

4. A Slight Conceptual Change to the Residual Chromo Dynamic Force

The *residual* chromo dynamic force postulates that the nuclear force is a residual effect of the chromo dynamic force and the “color charge” of the quarks. The *residual* chromo dynamic force is postulated to be an exchange of pions between the quarks of different nucleons. However, one simple extension to this hypothesis makes an interesting difference in our understanding of the forces involved within the nucleus. If this force is dependent upon the up/down polarity of quarks, rather than the color charge of the quarks, then many questions can immediately be answered. The concept here is that a down quark is attracted to an up quark, but not to another down quark. Similarly, an up quark is

attracted to down quark, but not to another up quark. The nuclear force is then simply the attraction of the up quark in one nucleon to the down quark in another nucleon—an inter-nucleon force between two quarks. When a bond is made between these two different quarks in two different nucleons, the nucleons themselves are thus bonded, and the nucleus is at a lower overall energy than the sum of the constituent parts. (Thus, it has a higher binding energy.)

This simple change of concept, that the nuclear force is dependent upon the up/down polarity rather than the color charge of the quark, easily explains why a system of six protons and six neutrons is at a lower energy (and at a higher binding energy) than five protons and seven neutrons. It is because six protons and six neutrons can form one bond for every pair of up-down quarks. There are 18 up quarks and 18 down quarks in the system of six protons and six neutrons, thus there could be 18 pairs of up-down quarks, and 18 bonds. However, for five protons and seven neutrons, there are 19 down quarks and 17 up quarks, thus only 17 bonds could be formed. The nucleus with five protons and seven neutrons would be at a higher overall energy (and at a lower binding energy) than the system of six protons and six neutrons. With this simple change, we can also now understand why a nucleon can only bond to its nearest neighbors. Specifically, a nucleon can only bond to three other nucleons because it only has three valence quarks with which to bond. The quarks involved in the bonding must be of opposite up/down polarity. This single concept immediately explains the asymmetry force of the Weizsäcker formula, because the greatest number of bonds occurs when there are equal numbers of up quarks and down quarks, which in turn means an equal number of protons and neutrons.

This new concept explains why there is a limited number of bonds for each nuclide in the nucleon, clarifying in a definitive explanation the first term of the Weizsäcker formula. Also, as a direct result, there is a definitive explanation of the asymmetry force—because unequal numbers of neutrons and protons form fewer bonds. The Coulomb energy term of the Weizsäcker formula is also easily explained as being related to the electrical energy of the net positive charges. For this one simple change in the residual chromo dynamic model, we can understand three of the five terms of the Weizsäcker formula as being a direct results of the quark-to-quark inter-nucleon binding. Thus, this simple variation of the residual chromo dynamic force, based on up-to-down polarity rather than color charge, associates the residual chromo dynamic model with the conceptual terms of the semi-empirical Weizsäcker formula.

Quick calculations have been made to test this hypothesis [61]. These calculations show that this concept of inter-nucleon up-to-down quark bonding reproduces the binding energy curve surprisingly well, using only one variable – the strength of the bond. Such good replication, achieved with simple mathematics, points toward the correctness of this concept. The quick calculation of this concept did not assume any particular type of force for the bond; it only assumed that a bond was formed between an up quark and a down quark. If the electromagnetic force is assumed to be the force between the up and down quarks, then a more rigorous and detailed calculation can be done; this is the topic to be explored in this paper.

First, a brief review of the electromagnetic force is given.

4.1. Electromagnetic forces within a nucleus

As outlined above, if the residual chromo dynamic force is related to the up/down quark polarity (such that a bond can form between an up quark in one nucleon to a down quark in another nucleon) then this simple concept explains many aspects about nuclear behavior in an understandable manner.

Recall that the electrical charges and magnetic moments of the nucleons are contained within the quarks. Due to the inverse-square-law dependence with distance for this force, the electromagnetic forces between an up quark and a down quark can be extremely strong, if they are close enough. The purpose of this paper is to determine if the electromagnetic forces can be sufficiently strong to hold the nucleons together in the nucleus.

Shown in Fig. 4 is a representation of an electromagnetic bond.

In other words, the force binding these two nucleons is the electromagnetic force between the quarks.

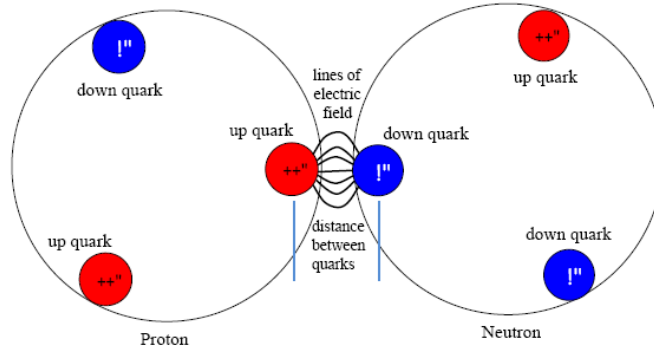


Figure 4. The electromagnetic bond between quarks.

4.2. Brief review of the electric energy

The electric energy [62–65] between two electrically charged particles is shown in Eq. (1), where r_{12} is the distance between particles 1 and 2, and q_1 and q_2 are the charges on particles 1 and 2, respectively. U_{E12} is the electric energy.

$$U_{E12} = \frac{-q_1 q_2}{((4\pi\epsilon_0)(r_{12}))}. \quad (1)$$

For additional charges, the electrical energies are simply summed for every pair of charges, as shown in Eq. (2).

$$U_{\text{electric total}} = \sum_{i=1}^{n-1} \sum_{j=i+1}^n \frac{-q_i q_j}{((4\pi\epsilon_0)(r_{ij}))}. \quad (2)$$

4.3. The magnetic energy

The magnetic energy [66–72] between two magnets is more complicated than the electric energy because it has vector and position dependence. Given two magnets, with magnetic moments μ_1 and μ_2 , the magnetic field of magnet₁ must be determined at the location of magnet₂. This magnetic field is symbolized as B_{12} . The resultant energy, $U_{\text{magnetic } 12}$, is the negative dot-product of the vector μ_2 with the vector B_{12} , as shown in Eq. (3).

$$U_{\text{magnetic } 12} = -\vec{\mu}_2 \cdot \vec{B}_{12}. \quad (3)$$

For a collection of magnets, the total magnetic energy is the double summation over all magnet pairs, as shown in Eq. (4).

$$U_{\text{magnetic total}} = \sum_{i=1}^{n-1} \sum_{j=i+1}^n -\vec{\mu}_i \cdot \vec{B}_{ij}, \quad (4)$$

where \vec{B}_{ij} is the vector magnetic field established by the i th magnet at the location of the j th magnet.

The equation for \vec{B}_{ij} is

$$\vec{B}_{ij} = \frac{\mu_0}{4\pi} \left\{ \frac{3 (\vec{\mu}_j \cdot \vec{r}_{ij}) \vec{r}_{ij} - r_{ij}^2 (\vec{\mu}_j)}{r_{ij}^5} \right\}. \quad (5)$$

Due to the vector properties of this energy, the lowest energy configuration for two magnets is a stacked bond, in which the magnetic moments of the magnets are aligned, in a stacked orientation with respect to each other, and as close as physically possible. Another way for two magnets to bond is a side-by-side bond, with the magnetic moments anti-parallel, oriented side-by-side, and as close as physically possible. An angled bond, in between a stacked and a side-by-side bond, will give intermediate results.

Combining Eqs. (2), (4), and (5), we see that the total electromagnetic energy of a distribution of charges and magnets is shown in Eq. (6).

$$U_{\text{EM total}} = \sum_{i=1}^{n-1} \sum_{j=i+1}^n \frac{-q_i q_j}{((4\pi\epsilon_0)(r_{ij}))} + \sum_{i=1}^{n-1} \sum_{j=i+1}^n \frac{-\mu_0}{4\pi} \left\{ \frac{3 (\vec{\mu}_j \cdot \vec{r}_{ji}) (\vec{\mu}_i \cdot \vec{r}_{ji}) - r_{ji}^2 (\vec{\mu}_i \cdot \vec{\mu}_j)}{r_{ji}^5} \right\}. \quad (6)$$

From quantum field theory we know that quarks behave like point-like Dirac particles, each having their own inherent magnetic moment, rather than having a magnetic moment caused by a current loop of spinning charge [73,74].

4.4. The limitation of the electromagnetic force

Prior to the 1960s, the proton was incorrectly thought to be homogeneously charged and to have a radius of about 1.2 fm. As a result, the strongest electrical energy between two such protons was thought to be 9.6×10^{-15} J.

The energy required to free a single nucleon from a nuclide is experimentally much larger than this. For this reason, the nuclear force was believed to be much stronger than the electric force. As a result, this incorrect concept of a homogeneously charged proton created an incorrect limitation of the electric force. Unfortunately, this incorrect concept is still often perpetuated even today, completely ignoring the electrical characteristics of quarks.

If the minimum quark-to-quark distance (defined as the minimum distance of one quark in one nucleon to a second quark in another nucleon) is 1/10 the radius of a proton, the electrical energy between the two quarks is 6.1×10^{-13} J. This value is made even larger by including the magnetic energy. Mathematically, in the limit as the distance goes to zero, the electromagnetic energy goes to infinity. Hence, the electromagnetic energy can be extremely large if the quarks are close enough to each other. Since the charge of the nucleons resides within the quarks, it is obvious that a quark from one nucleon could bond electromagnetically with a quark in another nucleon, and that the resultant electromagnetic force between two such quarks can be extremely large.

4.5. Short-range vs. long-range forces

Since there is no indication of a nuclear force at large distances, it was previously thought that the nuclear force must be a short-range force. Due to the misconception that protons were homogeneously charged, it was thought that the electromagnetic force could not be same as the nuclear force; thus the existence of a force, different from the electromagnetic force, was postulated. Given the understanding that the nuclear force is electromagnetic, the requirement of a short-range force is no longer necessary.

4.6. Brief review of the nuclear electric quadrupole moment

The electric quadrupole moment of a distribution of charge is a frequently misunderstood topic that deserves review before proceeding [75–77].

A monopole moment is the net charge of an object, assuming the object has a spherical distribution of charge with radial symmetry. Any distribution of charge with radial symmetry will have only an electric monopole moment. If the distribution has a polarity of positive and negative charges, then the object will also have an electric dipole moment. If the distribution of charge has an ellipsoidal shape, instead of a spherical shape, then the object will have an electric quadrupole moment. The quadrupole moment is related to the eccentricity of the charge distribution, and it can be either prolate (positive, cigar shaped) or oblate (negative, pancake shaped). The quadrupole moment of a non-spinning object is referred to as its “intrinsic” quadrupole moment, and this moment is different from the “measured” quadrupole moment, if the object is spinning.

If a *prolate* object (with an intrinsic quadrupole moment Q_0) is spinning, then depending on the axis of spin, the measured quadrupole moment may be smaller than the intrinsic quadrupole moment, and it can even be negative. However, the measured quadrupole moment cannot be larger than the intrinsic quadrupole moment. Thus for an intrinsically prolate charge distribution, the measured quadrupole moment can be smaller in absolute value than the intrinsic quadrupole moment, and it can be either positive or negative. It cannot be larger in absolute value.

Correspondingly, if an *oblate* object (with an intrinsic quadrupole moment $-Q_0$) is spinning, then depending on the axis of spin, the measured quadrupole moment can be smaller in absolute value, all the way to zero. The measured quadrupole moment cannot be positive, and it cannot have a larger absolute value than the intrinsic quadrupole moment. Thus, for an intrinsically oblate charge distribution, the measured quadrupole moment can be smaller in absolute value than the intrinsic quadrupole moment, and it can be either zero or negative.

To reiterate, the absolute value of the measured quadrupole moment of a spinning object can never be larger than the absolute value of the intrinsic quadrupole moment. *Thus, if a nuclear model predicts a small intrinsic quadrupole moment, smaller than the measured quadrupole moment, then this model is inherently flawed and incorrect.* Conversely, if a nuclear model predicts a large intrinsic quadrupole moment, one that is larger than the measured quadrupole moment, then this can easily be explained as being due to the angle of the spin axis.

Taken into the quantum realm, similar principles apply. The measured quadrupole moment, Q_{measured} , is related to the intrinsic quadrupole moment, $Q_{\text{intrinsic}}$, as shown in Eq. (7)

$$Q_{\text{measured}} = Q_{\text{intrinsic}} \left(\frac{3K^2 - J(J+1)}{(J+1)(2J+3)} \right), \quad (7)$$

where K is the projection of the spin axis onto the symmetry axis and J is the total spin of the nucleus [76].

There is a common misconception that large quadrupole moments only exist in isolated sections of the nuclear table; however, the data for nuclear quadrupole moments and the nuclear deformation parameters show that this concept is not true. Figure 5 shows all the experimental quadrupole moments for all nuclides from $A = 0$ to 250 for those nuclides with a spin. The blue line in Fig. 5 shows the predicted maximum quadrupole moments of the shell model. (All data for Fig. 5 extracted from [78].)

Figure 6 shows the quadrupole moments for the nuclides with even–even values of Z and N , all of which have 0 spin. In Fig. 6 note that all of these quadrupole moments are much larger than what the shell model can explain, which is again indicated by the blue line. (All data for Fig. 6 are extracted from [79].)

A quantity similar to the quadrupole moment is the deformation parameter. Figure 7 shows all the experimentally known deformation parameters. If the shell model were correct, then all of the deformation parameters seen in Fig. 7 should be less than one, indicated by the blue line. However, they are much higher. (All data for Fig. 7 are extracted from [79].)

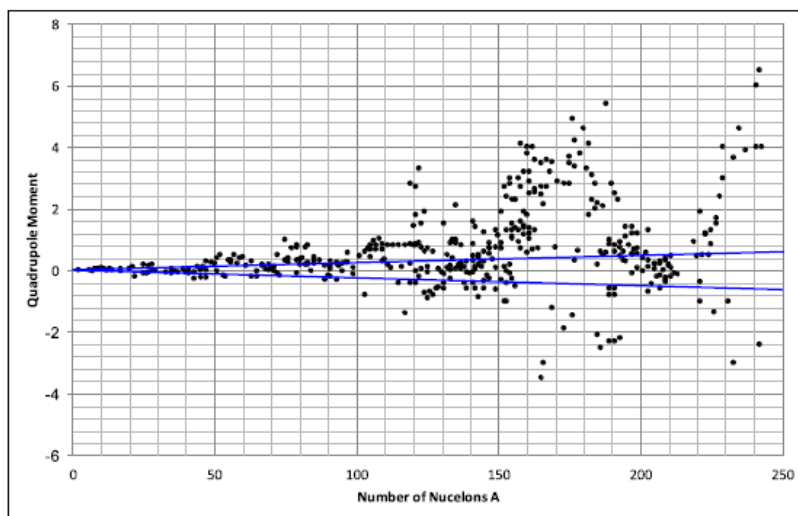


Figure 5. Experimental quadrupole moment. The predicted maximum quadrupole moment of the shell model is shown by the blue lines.

As can be seen, the quadrupole moments and the deformation parameters are much larger than the shell model can explain. As shown in Figs. 5–7, almost all nuclei have a quadrupole moment and deformation parameter that are much larger than what the shell model can explain. The distortion is not just in a few isolated regions of the nuclear table, but covers the entire range. The large experimentally measured quadrupole moments for the vast majority of nuclides

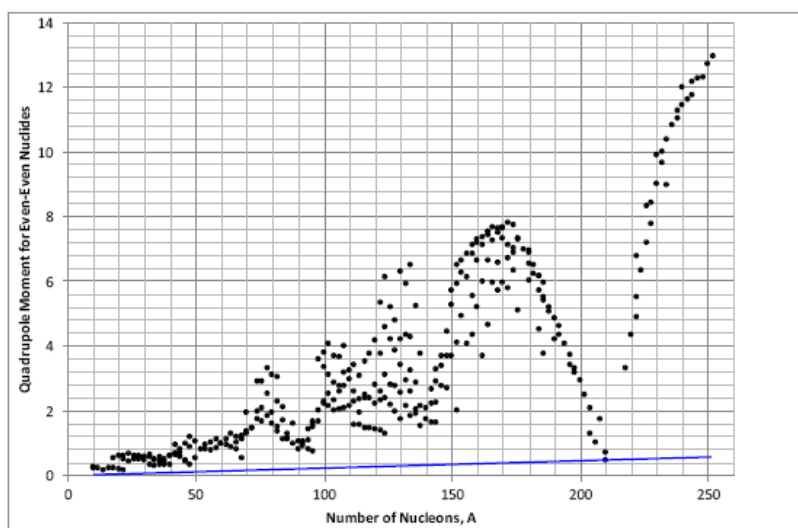


Figure 6. Experimental quadrupole moment of even-even nuclides. The predicted maximum quadrupole moment of the shell model is shown by the blue line.

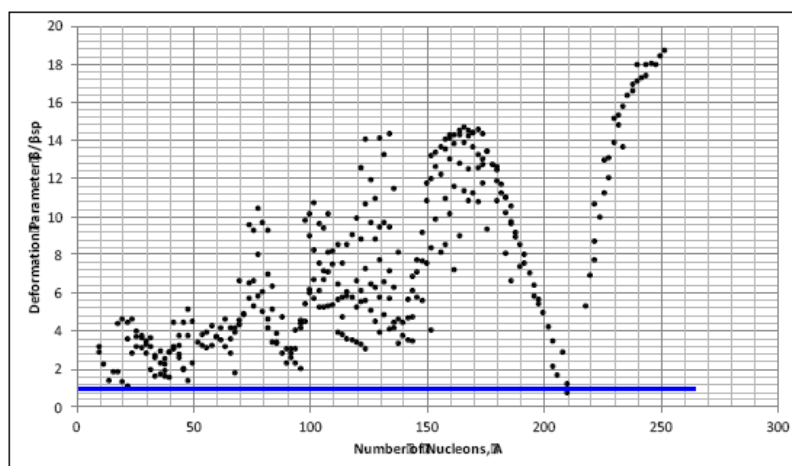


Figure 7. The ratio of the experimental nuclear deformation parameter divided by the predicted deformation parameter of the shell model, indicated by the blue line at the value 1.

negates any concept of spherical nuclides. These large quadrupole moments are in direct conflict with any model that pre-assumes a spherical shape.

With the exception of analyzing quadrupole moments, presently when researchers interpret the data from an experimentally probed nucleus, the shape of the nucleus is pre-assumed to be a spherical shape. Then, for this pre-assumed spherical shape, the best value of its radius R is forced-fit to the data, without any attempt to examine a different shape [80–82]. For example, the interpretation of the electron scattering data only considers the electric monopole moment. The interpretation of this data is then normalized over the charge density to force-fit the charge inside a sphere. A Gaussian curve is assumed as the skin of the nuclide. So regardless of the actual shape, the forced-fit normalized data makes the nucleus appear to be spherical in shape with a Gaussian skin. Even the so-called model-independent interpretations of scattering data still assume a spherical shape [83]. The experimental data is force-fit to be spherical to match the models, and most of the current nuclear models pre-assume a spherical shape, perpetuating the misconception regarding a spherical nucleus. As can be readily seen in Fig. 5, there is very little experimental justification for a spherical shape.

4.7. The Schrödinger equation

The Schrödinger equation [84] is a useful tool and has been successful in many areas of quantum physics, especially for the behavior of atomic electrons. The Schrödinger equation is a second-order differential equation that can only be solved for a given potential energy, kinetic energy, and initial conditions. Thus it is inherently difficult to use. Previous nuclear models have tried to model the nuclear potential, using different formulas for the Hamiltonian to obtain the probability function of the particle in question. However, the Schrödinger equation has proven to be extremely difficult and almost intractable to use for the nuclear force, especially for large nuclides.

If the Schrödinger equation is to be used properly for the nuclear force, the correct solution can only be obtained if the Hamiltonian is related to the electromagnetic energy of each individual quark in the nuclide. The proper potential energy well must take into account an energy that can be both attractive and repulsive, as well as taking into account the vector properties of the energy. However, even without polarity and vector dependence, the quark-based solution for

even ^2H has proven to be extremely difficult [28]. Fortunately the electromagnetic equations are more easily applied.

4.8. The concept of a nuclear bond similar to an atomic bond

For the electromagnetic model, the nuclear bond is an energy well between the two quarks forming the bond. The energy well is between the up quark of one nucleon and the down quark of another nucleon. It is this bond between the quarks that lowers the overall energy of the nucleus. This aspect is similar to the electronic bonds between the atoms of a molecule. In atomic bonding, one atom cannot bond to an indefinite number of other atoms. Similarly, one nucleon cannot bond to an indefinite number of other nucleons. Rather the number of bonds is limited by the number of quarks available for bonding. Thus each nucleon, with only three valence quarks, can only bond to three other nucleons. Two quarks are needed for one bond.

4.9. Summary of the electromagnetic force within the nucleon

The following is a review of the basic concepts for the proposed electromagnetic model.

- The electromagnetic force is valid inside the nucleon.
- The electric charge and the magnetic moment of the nucleons are contained within the quarks.
- The quarks of the nucleons have a spatial quantum probability distribution associated with the nucleon in which they are located. (An equilateral triangle is assumed for simplicity.)
- There are three possible bonds per nucleon, one for each valence quark. After three bonds, the nucleon cannot bond to a fourth nucleon.
- A pair of quarks, one from two different nucleons, is needed for one bond.

All of the above considerations are used in this electromagnetic model, along with the following quantum considerations.

- The kinetic energy of the quantum angular momentum of the nucleus [85–87] is also properly taken into account. (Note that this kinetic energy of the nuclear angular momentum strongly correlates to the energy of the pairing term in the Weizsäcker formula.)
- The lowest energy configuration is assumed for the ground state.
- There is a minimum distance between two quarks of two different nucleons, consistent with the Pauli Exclusion principle and the hard core repulsion.
- The hard core repulsion of the nucleons prevents any given nucleon from bonding more than once to another given nucleon. Any nucleon that attempts to bond twice to another nucleon is involved in a “double-nucleon bond”. A double-nucleon bond is not allowed; an attempted “double-nucleon bond” will break both bonds.
- A quark that attempts to bond to more than one other quark is engaged in a “triple-quark bond”. This triple-quark bond is not allowed, and an attempted triple-quark bond will break the bonds.

5. The Nuclear Configurations of the Lowest Energy States

For every nuclide in this paper, the position of each quark is defined in a matrix with xyz spatial coordinates and an electric charge value of either $-1/3$ or $+2/3$ of an elementary charge. The value of the magnetic moment, for either the up or down quark, and the three dimensional vector direction of each magnetic moment for each quark are also included in the matrix. Stacked magnetic bonds, angled magnetic bonds, or side-by-side magnetic bonds are determined, depending on the physical constraints of the configuration. Every nuclide in this paper is placed into

its lowest energy state in accordance with the rules for electromagnetic energies and the electromagnetic equations. Double-nucleon bonds or triple-quark bonds are not allowed, due to the hard core repulsion of the nucleons. This matrix file is used to calculate the change in the electromagnetic energy from the original constituent parts, and the result is then used to calculate the nuclear binding energy.

Here are some simple considerations to recognize when the nucleons form into segments.

- When a bond is formed the net charge of the bond is $+1/3$ of an elementary charge. This net positive charge is present at every bond.
- The nucleons cluster into segments, similar to the segment clusters described in the cluster model. This clustering is due to the electromagnetic force situating the nuclide into its lowest energy configuration.
- Due to the consideration that the nucleons can only bond three times, the nucleons will tend to cluster into alpha particle segments, each segment consisting of two protons and two neutrons. A segment consisting of two protons and two neutrons is the dominant type of segment, and is called an alpha segment.
- Another type of segment that is possible is a tri-nucleon segment consisting of one proton and two neutrons, called a tritium segment.
- Another type of segment that is possible is a tri-nucleon segment consisting of two protons and one neutron, called a He3 segment.
- Another segment is made of one neutron, called a single-neutron segment.
- Another segment is made of one proton, called a single-proton segment.
- Another segment is made of one proton and three neutrons, called an H4 segment.
- In the lowest energy state, each segment can bond only to one or two other segments.

5.1. Basic pattern for the configurations of stable nuclides with $A \geq 12$

The electromagnetic model has successfully computer simulated both stable and unstable nuclides, all the way up to californium ^{250}Cf , using only the electromagnetic equations and the equations for quantum angular momentum. From carbon ^{12}C upwards, the stable nuclides follow a relatively simple pattern. This basic pattern is *not* mere speculation, but rather the pattern is due to the lowest energy configuration of the nucleons, when taking into consideration the laws of electromagnetics. The pattern is as follows:

- There is one alpha particle segment for every two protons and two neutrons.
- An open alpha particle segment is in the middle of the configuration. This open alpha particle segment has two unbonded down quarks, and the negative charge of the unbonded down quarks offsets the high Coulomb energy in the middle of the nuclide. It also allows the net positive charge of the nuclide to be spread out a bit further.
- When there are more neutrons than protons, and Z is even, then the extra neutrons are single neutron segments, interspersed between the alpha segments.
- When Z is odd, and there are one or two more neutrons than protons, then the odd proton combines with the two extra neutrons to form an H3 segment. (An H3 segment is comprised of two neutrons and one proton.)
- If there are enough extra neutrons, then three of the extra neutrons will bond with a proton to form an H4 segment. This bonding pattern will occur only once for odd Z , and only twice for even Z . These H4 segments are on the end of the configuration.
- When there is an equal number of protons and neutrons, and this number is odd, such as nitrogen ^{14}N , then there is a single neutron segment plus a single proton segment. This situation occurs infrequently in the stable nuclides, but more frequently in the unstable nuclides.

5.2. Basic pattern for the radioactive nuclides

For the radioactive nuclides, there are two more considerations for their lowest energy configurations. Again, these patterns are not mere speculation, but rather the patterns emerge as a direct result of the electromagnetics energies.

- When there are more protons than neutrons, then the one extra proton will form either a single proton segment or an He3 segment. (A He3 segment is comprised of one neutron and two protons.)
- Any nuclide with more single neutron segments than alpha segments will double-up the single neutron segments in pairs, without an alpha segment between them. These doubled-up single neutron segments tend to be near the middle of the nuclide. There are no stable nuclides with doubled-up neutron segments in the ground state.

5.3. Particle decay

Particle decay is defined as alpha decay, neutron decay, proton decay, spontaneous fission, and the beta-delayed reactions of the same. An in-depth analysis of the electromagnetic causes of particle decay will be covered in subsequent papers of this series. Briefly stated, in the smaller nuclides, all particle decay occurs when the electromagnetic force within the nuclide pulls or pushes on the unbonded quarks in such a way as to cause either a double-nucleon bond or a triple-quark bond – both of which are not allowed. If the energy transference is large enough when there is an attempt to form either of these prohibited bonds, then the bonds will break and particle decay results.

The alpha decay exhibited by the larger nuclides, $A > 150$, is a statistical mechanism, different from the near-instantaneous alpha decay seen in the smaller nuclides. The alpha decay of the larger nuclides is a topic that will be covered in subsequent papers of this series. Briefly, the mechanism is similar to Gamow's model of alpha decay for the larger nuclides, in that it is dependent on random statistical parameters. However, the electromagnetic model can predict the half life of alpha decay, based on *theoretical* parameters rather than simply correlating two experimentally observed parameters. The likelihood of alpha decay is correlated to the strength of the net repulsive electric energy seen by the end-most alpha-particle segment in the configuration.

5.4. The smaller nuclides, $A < 12$

The nuclides smaller than ^{12}C cannot follow the pattern outlined above, simply because they do not have enough nucleons to do so. Also, the energy of the quantum angular momentum is a much larger percentage of the overall energy for the lighter nuclides. Both of these characteristics contribute to the more unusual nuclear behaviors of the smaller nuclides. An in-depth analysis of the nuclear behaviors of the smaller nuclides, $A < 12$, is covered in subsequent papers of this series.

6. An Example Calculation for ^2H

For every nuclide in this paper, the position of each quark is defined in a matrix with xyz spatial coordinates and an electric charge value of either $-1/3$ or $+2/3$ of an elementary charge. For example, the nuclide of ^2H is composed of one proton and one neutron, with three quarks in each nucleon, for a total of six quarks, three up quarks and three down quarks. Within each nucleon, the quarks form an equal-lateral triangle. Using the symbolic shorthand representations similar to those shown in Figs. 1 and 2 the configuration for the example for ^2H is shown in Fig. 8. Note in Fig. 8 the distance between two internucleon quarks is 2.11083×10^{-16} m, and the separation of the quarks in the nucleon is 1.27385×10^{-15} m. The radius of the nucleon is 0.841×10^{-15} m. The orientation of the xyz coordinate system is also shown.

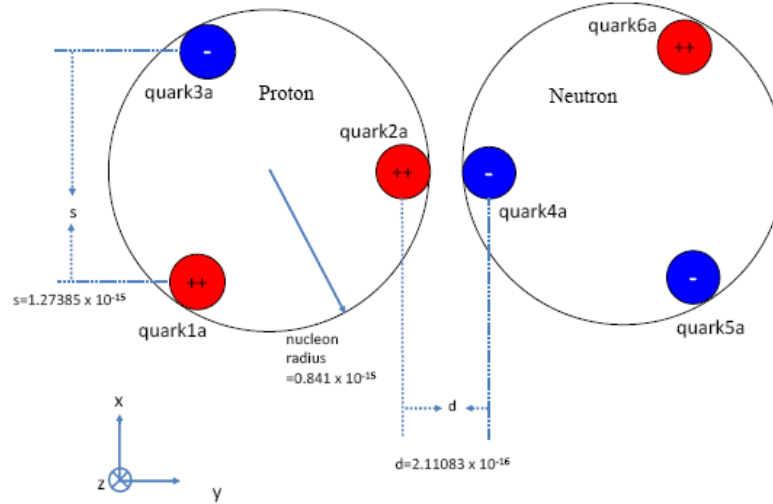


Figure 8. Short-hand simplified graphic of ^2H .

Listed in Table 1 are the name of the quark, the (x, y, z) location coordinates in meters, the quark value in units of elementary charge, the magnetic dipole vector, and the magnetic dipole moments in units of nuclear magnetons.

The bond is between quark2a and quark4a. The vector orientation of magnetic bond is a side-by-side bond, with the up quark magnetic moment going into the page, and the down quark magnetic moment going out of the page.

6.1. An example of the electric energy calculation

The electric energy of this configuration is calculated using Eq. (2), the double summation. For six quarks, the summation includes 15 terms, where each U_{Eij} term represents the electric energy between the i th and j th quark.

$$U_{\text{electric_total}} = U_{E12} + U_{E13} + U_{E14} + U_{E15} + U_{E16} + U_{E23} + U_{E24} + U_{E25} + U_{E26} + U_{E34} + U_{E35} + U_{E36} \\ + U_{E45} + U_{E46} + U_{E56}.$$

Table 1. Quark names, charge, location, and magnetic parameters.

Quark name	Quark location	Quark value	Magnetic vector	Magnetic dipole moment
Quark 1a	(0,0,0)	0.666	(0,0,1)	1.85
Quark 2a	$(6.36926 \times 10^{-16}, 1.10319 \times 10^{-15}, 0)$	0.666	(0,0,1)	1.85
Quark 3a	$(1.2738 \times 10^{-15}, 0, 0)$	-0.333	(0,0,-1)	-0.97
Quark 4a	$(6.36926 \times 10^{-16}, 1.31427 \times 10^{-15}, 0)$	-0.333	(0,0,-1)	-0.97
Quark 5a	$(0, 2.41745 \times 10^{-15}, 0)$	-0.333	(0,0,-1)	-0.97
Quark 6a	$(1.27385 \times 10^{-15}, 2.41745 \times 10^{-15}, 0)$	0.666	(0,0,1)	1.85

To fill in these values we use Eq. (1), using the number values from Table 1, and solving for the r_{ij} value first:

$$r_{12} = \sqrt{[(6.36926 \times 10^{-16} - 0)^2 + (1.10319 \times 10^{-15} - 0)^2 + (0 - 0)^2]},$$

$$r_{12} = 1.27385 \times 10^{-15} \text{ m.}$$

Using this value of r_{12} to solve for the electrical energy from quark 1 to 2:

$$U_{E12} = (-1)(8.98755 \times 10^9)(2/3)(2/3)(1.602 \times 10^{-19})^2 / (1.2738 \times 10^{-15}),$$

$$U_{E12} = -8.04935 \times 10^{-14} \text{ J.}$$

The negative sign denotes that it is a repulsive energy. The other values are similarly calculated:

$$U_{E13} = +4.02468 \times 10^{-14},$$

$$U_{E14} = +3.5104 \times 10^{-14},$$

$$U_{E15} = +2.12076 \times 10^{-14},$$

$$U_{E16} = -3.75243 \times 10^{-14},$$

$$U_{E23} = +4.02468 \times 10^{-14},$$

$$U_{E24} = +2.42883 \times 10^{-13},$$

$$U_{E25} = +3.5104 \times 10^{-14},$$

$$U_{E26} = -7.02079 \times 10^{-14},$$

$$U_{E34} = -1.7552 \times 10^{-14},$$

$$U_{E35} = -9.38107 \times 10^{-15},$$

$$U_{E36} = +2.12076 \times 10^{-14},$$

$$U_{E45} = -2.01234 \times 10^{-14},$$

$$U_{E46} = +4.02468 \times 10^{-14},$$

$$U_{E56} = +4.02468 \times 10^{-14}.$$

The sum of this electric energy is 2.70207×10^{-13} J. Notice that the dominant contribution to this energy is from the bond seen at U_{24} . This is the electric energy *after* a nucleus is forms from a proton and a neutron. However, in order to properly calculate the bonding energy, the electric energy before the proton and neutron forms a nucleus must

be subtracted from this sum. In other words, the energy of all the individual isolated protons and neutrons must be subtracted from this sum. The electric energy of one individual isolated proton is

$$U_{E12} + U_{E13} + U_{E23} = 0 \text{ J.}$$

The electric energy of one individual isolated neutron is:

$$U_{E45} + U_{E46} + U_{E56} = 6.03701 \times 10^{-14} \text{ J.}$$

This then gives the net electric energy as

$$U_{\text{net electric energy}} = (2.70207 \times 10^{-13}) - (6.03701 \times 10^{-14}) = 2.0984 \times 10^{-13} \text{ J.}$$

This value is used below in the calculation for total binding energy. As seen by the sign, it is an attractive force and an attractive energy.

6.2. An example of the magnetic energy calculation

Now the magnetic energy for this configuration of quarks must be calculated, using Eqs. (3)–(5). This involves vector math.

$$U_{\text{magnetic total}}$$

$$U_{\text{magnetic total}} = U_{M12} + U_{M13} + U_{M14} + U_{M15} + U_{M16} + U_{M23} + U_{M24} + U_{M25} + U_{M26} + U_{M34} \\ + U_{M35} + U_{M36} + U_{M45} + U_{M46} + U_{M56}.$$

Here U_{Mij} now represents the magnetic energy between the i th quark and the j th quark.

To do this calculation, the magnetic field of the i th quark must be calculated in the vicinity of the j th quark, must be calculated first, using Eq. (5) and vector math. For this example, we will calculate U_{M14} . From Table 1, the vector values for μ_1 , μ_4 , and r_{14} are:

$$\mu_1 = (0, 0, 9.34407 \times 10^{-27}),$$

$$\mu_4 = (0, 0, -4.899 \times 10^{-27}),$$

$$r_{14} = (6.36926 \times 10^{-16}, 1.31427 \times 10^{-15}, 0).$$

Plugging this value into Eq. (5), to find the magnetic field vector, yields:

$$\mathbf{B}_{14} = (0, 0, 1.57273 \times 10^{11}).$$

Plugging this vector into Eq. (4), yields:

$$U_{M14} = +1.46957 \times 10^{-15} \text{ J.}$$

Here, the positive sign denotes that it is an attractive energy. The other values are similarly calculated. listed below:

$$U_{M12} = -4.22392 \times 10^{-15},$$

$$U_{M13} = +2.2147 \times 10^{-15},$$

$$U_{M14} = +1.46957 \times 10^{-15},$$

$$U_{M15} = +3.24037 \times 10^{-16},$$

$$U_{M16} = -2.24373 \times 10^{-16},$$

$$U_{M23} = +2.2147 \times 10^{-15},$$

$$U_{M24} = +4.86762 \times 10^{-13},$$

$$U_{M25} = +1.46957 \times 10^{-15},$$

$$U_{M26} = -2.8028 \times 10^{-15},$$

$$U_{M34} = -7.70534 \times 10^{-16},$$

$$U_{M35} = -1.17644 \times 10^{-16},$$

$$U_{M36} = +3.24037 \times 10^{-16},$$

$$U_{M45} = -1.16122 \times 10^{-15},$$

$$U_{M46} = +2.2147 \times 10^{-15},$$

$$U_{M56} = +2.2147 \times 10^{-15}.$$

The sum for all of these is $+4.89704 \times 10^{-13}$ J, which is a net attractive energy. As before with the electric energy, in order to find the magnetic binding energy, we must subtract the magnetic interaction energy of the isolated independent neutrons and protons prior to them being combined in a nucleus. The magnetic interaction energy of a proton is

$$U_{M12} + U_{M13} + U_{M23} = 2.05488 \times 10^{-16}$$

and the magnetic interaction energy of a neutron is

$$U_{M45} + U_{M46} + U_{M56} = 3.30392 \times 10^{-15}$$

For the ^2H nucleus, this energy is subtracted from the previously calculated sum of the magnetic energies, and the net magnetic binding energy is:

$$U_{\text{netmagneticenergy}} = (+4.89704 \times 10^{-13} \text{ J}) - (2.05488 \times 10^{-16}) - (3.30392 \times 10^{-15}),$$

$$U_{\text{netmagneticenergy}} = 4.8623 \times 10^{-13} \text{ J}.$$

Similar to the net electric energy, the net magnetic energy is dominated by the magnetic energy of quark2a to 4a, where the bond is located.

6.3. An example for the calculation of the kinetic energy of the orbital angular momentum

For ^2H , the proton is assumed to be spin 1/2, and the neutron is assumed to be spin 1/2 in the same direction, so that the sum of these two spins is 1. The net spin, of spin angular momentum plus orbital angular momentum of ^2H is 1. This gives the orbital spin as a net zero. Thus for this nuclide, the orbital kinetic spin energy is zero.

Had there been a net orbital spin associated with the nuclide, however, the example of how it is calculated is shown. First we must calculate the center of mass in three dimensions, in Eq. (8).

$$\text{Center of mass} = (X_{\text{center of mass}}, Y_{\text{center of mass}}, Z_{\text{center of mass}}),$$

where

$$\begin{aligned} X_{\text{center of mass}} &= \sum_{i=1}^n (X_i) (m_i), \\ Y_{\text{center of mass}} &= \sum_{i=1}^n (Y_i) (m_i), \\ Z_{\text{center of mass}} &= \sum_{i=1}^n (Z_i) (m_i), \end{aligned} \quad (8)$$

where X_i is the x location of nucleon i , and m_i is the mass of nucleon i . Similarly for Y_i and Z_i . The axis of spin goes through the center of mass, at an angle θ with respect to the y -axis. An arm radius, which is defined as the closest distance of that nucleon to the axis of spin, must be found for each nucleon in the configuration of the nucleus. Using simple trigonometry, this arm radius is shown in Eq. (9), for when theta is defined with respect to the y -axis.

$$\text{Radius}_{\text{Arm}_i} = \sqrt{[\Delta x_i^2 + (\Delta y_i \sin(\theta) + \Delta z_i \cos(\theta))^2]}, \quad (9)$$

where Δx_i is the X_i minus the $X_{\text{center of mass}}$, for the i th nucleon. Similarly for Δy_i and Δz_i .

At this point, the arm radius is known for every nucleon in the nucleus. Next the spin inertia I_{spin} for each nucleon must be found. The spin inertia is the arm radius squared multiplied by the mass of the nucleon. This is summed together to get the spin inertia of the entire nucleus, as shown in Eq. (10).

$$I_{\text{spin}_i} = (m_i)(\text{Radius}_{\text{Arm}_i})^2 \quad I_{\text{spin_total}} = \sum_{i=1}^n (m_i)(\text{Radius}_{\text{Arm}_i})^2. \quad (10)$$

Once the total spin inertial $I_{\text{spin_total}}$ is found, the energy of the orbital angular momentum, as shown in Eq. (11) is calculated. One must know the value of the orbital angular momentum, which is denoted by the small letter l .

$$E_{\text{orbital angular momentum}} = \frac{(l)(l+1)\hbar^2}{2 \times I_{\text{spin_total}}}. \quad (11)$$

This calculation is done for every nucleus with an orbital angular momentum. For smaller nuclides, $A < 12$, this energy can be a considerable of the bonding energy. For medium to large nuclides, this energy is quite small and could be ignored, but it is done for all nuclides regardless in the computer calculations, just to be thorough.

6.4. An example for the calculation of the total binding energy

Binding energy reduces the overall energy of the configuration of nucleons in a nucleus. Similarly, it reduces the overall mass nucleus as compared to the constituent nucleons.

Total Binding energy = Electric Binding Energy + Magnetic Binding Energy – Orbital Angular Momentum energy.

For this example,

$$E_{\text{binding_total}} = (2.0984 \times 10^{-13} \text{ J}) + (4.8623 \times 10^{-13} \text{ J}) - 0, \quad E_{\text{binding_total}} = 4.34452 \text{ MeV}.$$

The total electromagnetic bonding energy is the sum of the electric and magnetic bonding energies. This is $(2.0984 \times 10^{-13} \text{ J}) + (4.8623 \times 10^{-13} \text{ J}) = 6.9607 \times 10^{-13} \text{ J}$, which is 4.34452 MeV. The actual binding energy for ^2H is 2.22476 MeV. Thus, this calculation is high by a couple of MeV.

6.5. Summary of the calculations for the total binding energy of all the nuclides

For every nuclide in the paper, every quark is defined in a matrix with its location in three dimensional space, its value, its magnetic moment and the three dimensional vector direction of each magnetic moment, and these detailed calculations are done as shown in this section. Stacked magnetic bonds, angled magnetic bonds, or side-by-side magnetic bonds are determined, depending on the physical constraints of the configuration.

For large nuclides such as lead ^{208}Pb , which has 624 quarks in it, the calculations for the electric and magnetic binding energy are quite complicated and lengthy, requiring large amounts of memory for the computer program to run. Even so, it only takes a matter of minutes to run a large nuclide such as ^{208}Pb . All of these calculations are done for each and every nuclide in this paper. The numbers in Table 2 and in the graphs of Fig. 7 are not rough estimates or simple guesses. They are the result of detailed and rigorous calculations.

Every nuclide in this paper is placed into its lowest energy state in accordance with the rules for electromagnetic energies and the electromagnetic equations. Double-nucleon bonds or triple-quark bonds are not allowed, due to the hard core repulsion of the nucleons.

Finding the lowest energy configuration for a nuclide requires trial and error to determine which configuration is the lowest energy. For example, for lithium ^6Li , 26 different configurations were examined to determine what was the lowest energy configuration. In order to determine the lowest energy configuration for a nuclide, several configurations are tried, and the one with the lowest energy is used. The configuration that is used is not something that is selected based on which configuration gives the best answer, but rather it is selected based on which configuration is the lowest energy.

7. Results and Conclusions

Once the lowest energy configurations are found using electromagnetic equations, there remains only one variable to be selected for the best fit to the binding energy data; namely, the minimum distance between the two quarks of the two different nucleons, called the “minimum quark-to-quark distance”. This model has only one variable to determine. The Weizsäcker formula uses five variables and a conditional logic statement to achieve its mathematical curve-fitting. The electromagnetic model of the nuclear force proposed herein is able to get comparable results with only one variable.

Over a thousand different configurations for different nuclides have been computer modeled using this method to calculate the binding energy based on electromagnetics. These include stable and unstable, large, medium, and small, and ground and high energy states. These detailed calculations have been done for every nuclide listed in Table 2. Each nuclide is placed in the lowest energy configuration; then, using this configuration, the electro-magnetic energy is calculated and the binding energy is determined.

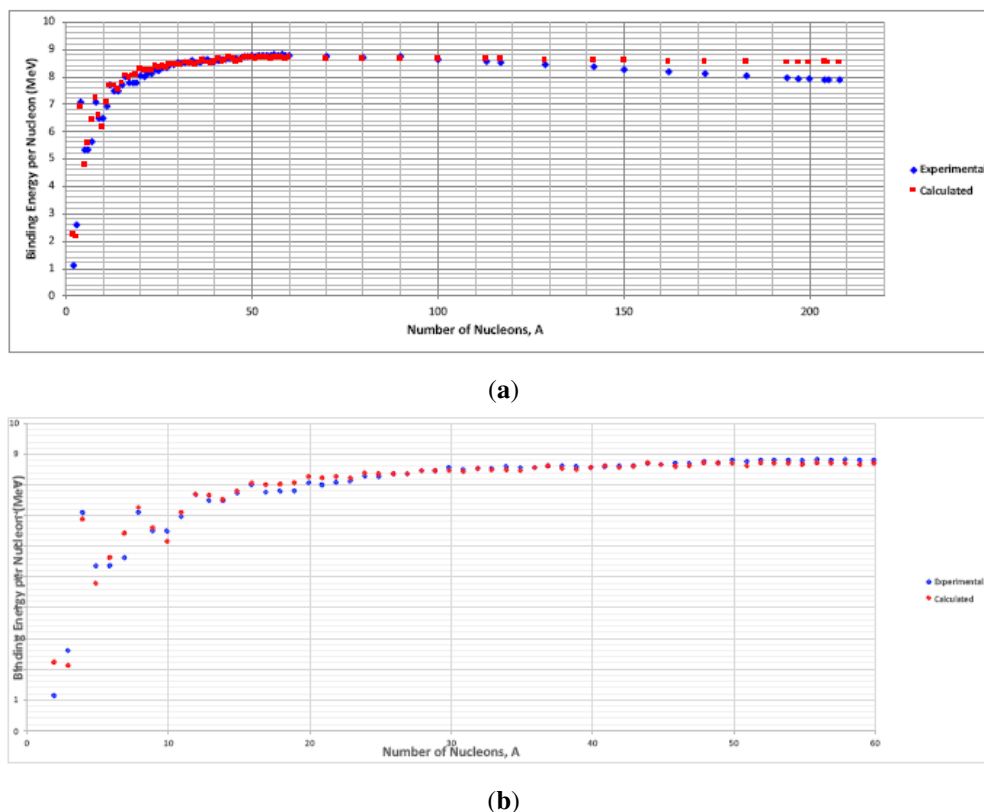


Figure 9. (a) Binding energy per nucleon vs. A , for both calculated and experimental data, from $A = 2$ to $A = 208$. (b) Binding energy per nucleon vs. A , for both calculated and experimental data, showing detail for the smaller nuclides, from $A = 2$ to $A = 60$.

The value for the minimum distance between quarks was selected to be 2.11082×10^{-16} m. It is the only variable that is selected. This value was not selected by trial and error in order to obtain the best fit to the data, but rather it was selected to give close to zero error for ^{40}Ca , allowing the rest of the nuclides to fit where they would.

Using this value for the minimum distance between quarks, the resulting bonding energy curve is shown in Fig. 9(a,b). For comparison, two sets of values are shown: the calculated binding energy, shown in red circles, and the experimental binding energy, shown in blue diamonds. Figure 9(a) shows all the points from $A = 2$ to $A = 208$. Figure 9(b) shows only the points from $A = 2$ to $A = 60$, for ease of viewing the details of this curve. (Note that the binding energies for the stable nuclides with $A = 2, 3, 6$ and 7 are more dependent on spin and the angle of the axis of spin.) As can be seen in Fig. 9(b), there is excellent agreement in the reproduction of the experimental data. The downward curve for the smaller nuclides is reproduced and the peaks at the alpha particle nuclides are reproduced.

These data are also presented in Table 2, and show excellent reproduction of the experimental binding energy; most of the nuclides fall within a one or two percent error. For the nuclides with large A , the predicted downward slope is not as severe as is experimentally observed. For these nuclides, the worst error is 8.32% for ^{204}Pb .

No other theoretical model has been able to achieve such a tight prediction of binding energy (numerical curve-fitting of the semi-empirical formula is not a theoretical model) with only *one* variable. This feature is an unprecedented

Table 2. Comparison of experimental and calculated binding energy.

Nuclide	A	Z	N	Experimental binding energy, EBE (MeV)	Calculated bind- ing energy, CBE (MeV)	% Error	EBE/A	CBE/A
H ²	2	1	1	2.22	4.41318	98	1.11	2.21
He ³	3	2	1	7.72	6.350778513	−17.72	2.57	2.12
He ⁴	4	2	2	28.30	27.5109714	−2.77	7.07	6.88
He ⁵	5	2	3	26.63	23.84432281	−10.45	5.33	4.77
Li ⁶	6	3	3	31.99	33.55664463	4.88	5.33	5.59
Li ⁷	7	3	4	39.24	44.82377489	14.22	5.61	6.40
Be ⁸	8	4	4	56.50	57.7602052	2.23	7.06	7.22
Be ⁹	9	4	5	58.17	59.23945254	1.85	6.46	6.58
B ¹⁰	10	5	5	64.75	61.33238839	−5.28	6.48	6.13
B ¹¹	11	5	6	76.20	77.75612889	2.04	6.93	7.07
C ¹²	12	6	6	92.16	91.84852621	−0.34	7.68	7.65
C ¹³	13	6	7	97.11	99.46746342	2.43	7.47	7.65
N ¹⁴	14	7	7	104.66	105.1179975	0.44	7.48	7.51
N ¹⁵	15	7	8	115.49	116.4347726	0.82	7.70	7.76
O ¹⁶	16	8	8	127.62	128.5307189	0.71	7.98	8.03
O ¹⁷	17	8	9	131.76	135.4333122	2.79	7.75	7.97
O ¹⁸	18	8	10	139.81	144.2829922	3.20	7.77	8.02
F ¹⁹	19	9	10	147.80	152.8740704	3.43	7.78	8.05
Ne ²⁰	20	10	10	160.65	164.8561421	2.62	8.03	8.24
Ne ²¹	21	10	11	167.41	172.5446382	3.07	7.97	8.22
Ne ²²	22	10	12	177.77	180.8086775	1.71	8.08	8.22
Na ²³	23	11	12	186.56	188.9156486	1.26	8.11	8.21
Mg ²⁴	24	12	12	198.26	200.6161192	1.19	8.26	8.36
Mg ²⁵	25	12	13	205.59	208.3377118	1.34	8.22	8.33
Mg ²⁶	26	12	14	216.68	216.8794256	0.09	8.33	8.34
Al ²⁷	27	13	14	224.95	224.6324319	−0.14	8.33	8.32
Si ²⁸	28	14	14	236.54	236.2369786	−0.13	8.45	8.44
Si ²⁹	29	14	15	245.01	244.4662386	−0.22	8.45	8.43
Si ³⁰	30	14	16	255.62	252.7252293	−1.13	8.52	8.42
P ³¹	31	15	16	262.92	260.5887444	−0.89	8.48	8.41
S ³²	32	16	16	271.78	271.5706273	−0.08	8.49	8.49
S ³³	33	16	17	280.42	279.7819366	−0.23	8.50	8.48
S ³⁴	34	16	18	291.84	288.1957519	−1.25	8.58	8.48
Cl ³⁵	35	17	18	298.21	295.667157	−0.85	8.52	8.45
Ar ³⁶	36	18	18	306.72	306.7118673	0.00	8.52	8.52
Cl ³⁷	37	17	20	318.78	318.087543	−0.22	8.62	8.60
Ar ³⁸	38	18	20	327.34	323.4884506	−1.18	8.61	8.51
K ³⁹	39	19	20	333.72	330.7573498	−0.89	8.56	8.48

Table continued

Ca ⁴⁰	40	20	20	342.05	341.9080812	−0.04	8.55	8.55
K ⁴¹	41	19	22	351.62	352.903988	0.37	8.58	8.61
Ca ⁴²	42	20	22	361.90	358.8434157	−0.84	8.62	8.54
Ca ⁴³	43	20	23	369.83	368.8924248	−0.25	8.60	8.58
Ca ⁴⁴	44	20	24	380.96	382.3032576	0.35	8.66	8.69
Sc ⁴⁵	45	21	24	387.85	388.0794464	0.06	8.62	8.62
Ti ⁴⁶	46	22	24	398.19	393.4074295	−1.20	8.66	8.55
Ti ⁴⁷	47	22	25	407.07	403.491218	−0.88	8.66	8.58
Ti ⁴⁸	48	22	26	418.70	417.0568753	−0.39	8.72	8.69
Ti ⁴⁹	49	22	27	426.84	425.5071529	−0.31	8.71	8.68
Ti ⁵⁰	50	22	28	437.78	434.0477448	−0.85	8.76	8.68
V ⁵¹	51	23	28	445.84	439.4862366	−1.43	8.74	8.62
Cr ⁵²	52	24	28	456.34	451.6674486	−1.02	8.78	8.69
Cr ⁵³	53	24	29	464.29	460.2097234	−0.88	8.76	8.68
Cr ⁵⁴	54	24	30	474.01	468.7637783	−1.11	8.78	8.68
Mn ⁵⁵	55	25	30	482.08	474.1977824	−1.63	8.77	8.62
Fe ⁵⁶	56	26	30	492.26	486.479967	−1.17	8.79	8.69
Fe ⁵⁷	57	26	31	499.91	494.9566096	−0.99	8.77	8.68
Fe ⁵⁸	58	26	32	509.94	503.2991831	−1.30	8.79	8.68
Co ⁵⁹	59	27	32	517.31	508.7045784	−1.66	8.77	8.62
Ni ⁶⁰	60	28	32	526.84	520.6395297	−1.18	8.78	8.68
Ge ⁷⁰	70	32	38	610.52	606.4072667	−0.67	8.72	8.66
Kr ⁸⁰	80	36	44	695.44	691.549535	−0.56	8.69	8.64
Zr ⁹⁰	90	40	50	783.89	776.6805842	−0.92	8.71	8.63
Ru ¹⁰⁰	100	44	56	861.93	862.4006397	0.05	8.62	8.62
Cd ¹¹³	113	48	65	963.56	972.230688	0.90	8.53	8.60
Sn ¹¹⁷	117	50	67	995.62	1005.905022	1.03	8.51	8.60
Xe ¹²⁹	129	54	75	1087.65	1107.556296	1.83	8.43	8.59
Nd ¹⁴²	142	60	82	1185.15	1216.64027	2.66	8.35	8.57
Sm ¹⁵⁰	150	62	88	1239.25	1284.443313	3.65	8.26	8.56
Dy ¹⁶²	162	66	96	1324.11	1385.331685	4.62	8.17	8.55
Yb ¹⁷²	172	70	102	1392.76	1469.133262	5.48	8.10	8.54
W ¹⁸³	183	74	109	1465.53	1561.208977	6.53	8.01	8.53
Pt ¹⁹⁴	194	78	116	1539.58	1652.970554	7.37	7.94	8.52
Au ¹⁹⁷	197	79	118	1559.40	1673.675529	7.33	7.92	8.50
Hg ²⁰⁰	200	80	120	1581.21	1702.923901	7.70	7.91	8.51
Pb ²⁰⁴	204	82	122	1605.34	1738.948651	8.32	7.87	8.52
Tl ²⁰⁵	205	81	124	1615.09	1740.84469	7.79	7.88	8.49
Pb ²⁰⁸	208	82	126	1636.44	1769.027241	8.10	7.87	8.50

success for the electromagnetic model in obtaining such results. The numbers for the calculated binding energy are generated from the computer simulation of each nuclide using the electromagnetic equations. (Experimental data are extracted from [88].) Current nuclear models using the *residual* chromo dynamic model and the Schrödinger

equation have trouble modeling ^2H with six quarks. However, using electromagnetic equations, nuclides as large as copernicium²⁸³Cn have easily been modeled.

This model has applied the laws of electromagnetics directly to the quarks, and combined this feature together with aspects of the *residual* chromo dynamic model and the cluster model.

This model assumes the laws of electromagnetics are valid inside a nucleus, and that these laws should not be disregarded. This model asserts that is the electromagnetic properties of the quarks within the nucleus that create the nuclear force and hold the nucleons in a nucleus together. The electromagnetic forces and energies cause the nuclides to fall into the lowest energy state and configuration. It is asserted that this electromagnetic energy and the specific lowest energy configurations of the nuclides are features that give the nuclides certain behaviors, such as binding energy, large quadrupole moments, excited states, and particle decay.

Rather than disregarding the electromagnetic forces and energies of the quarks, when taken into full account and understanding, the electromagnetic forces inside a nucleus can explain much about nuclear behavior. By applying this knowledge and insight, a better understanding of the nuclear behaviors can be gained through this model. Only the slight decrease in binding energy per nucleon that is seen for the largest nuclides cannot be explained by the electromagnetic force. The role of electromagnetics within the nucleus is a research field that deserves further analysis and serious consideration by theoretical nuclear physicists. This paper serves as the introduction to such theoretical investigations into the electromagnetic considerations of the nuclear force.

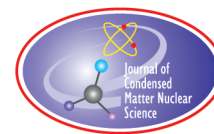
In conclusion, a significantly large part of the Nuclear Force, that force which binds together the nucleons in a nucleus, has been directly unified to the Electromagnetic Force.

References

- [1] K.N. Mukhin, *Experimental Nuclear Physics, Volume I, Physics of Atomic Nucleus*, Mir, Moscow, 1987, p. 120.
- [2] S. Sharma, *Atomic and Nuclear Physics*, Dorling Kindersley, New Delhi, 2008, p. 286.
- [3] R. Eisberg and R. Resnick, *Quantum Physics of Atoms, Molecules, Solids, Nuclei, and Particles*, Wiley, New York, 1985, pp. 509–549.
- [4] J. Lilley, *Nuclear Physics Principles and Applications*, Wiley, Chichester, 2001, p 35.
- [5] G. Gamow, Quantum theory of the atomic nucleus, *Z. Phys.* **51** (1928) 204.
- [6] C.F. von Weizsäcker, Zur theorie der kernmassen, *Zeitschrift für Physik* (in German) **96** (7–8) (1935) 431–458.
- [7] G. Gamow, Gamow’s description of the “liquid drop model” of the atomic nucleus, *In the Proc. Roy. Soc. London Series A. Vol. CXXIII, “Discussion on Structure of Atomic Nuclei”*, Gamow’s contribution of pp. 386–387, Royal Society, London, 1929, pp. 373–390.
- [8] H. Yukawa, On the interaction of elementary particles, *Proc. Phys. -Math. Soc. Japan* **17** (1935) 48.
- [9] L.R. Hafstad and E. Teller, The alpha-particle model of the nucleus, *Phys. Rev.* **54** (1938) 681.
- [10] A.H. Wuosmaa et al., Evidence for alpha-particle chain configuration in ^{24}Mg , *Nucl. Phys. A* **553** (1993) 563c–566c.
- [11] A.H. Wuosmaa et al., Evidence for alpha-particle chain configuration in ^{24}Mg , *Phys. Rev. Lett.* **68** (9) (1992) 1295–1298.
- [12] B.M. Nyakó et al., *Phys. Rev. Lett.* **52** (1984) 507.
- [13] S.P.G. Chappell et al., *Phys. Rev. Lett.* **B 444** (1998) 260.
- [14] M. D’Agostino, Focus: rod-shaped nucleus, *Phys. Rev. Focus* **28** (2011) 10.
- [15] H. Horiuchi and K Ikeda, *Progr. Theoret. Phys.* **40** (1968) 277.
- [16] I. Hamamoto and B. Mottelson, Shape deformations in atomic nuclei, *Scholarpedia* **7**(4) (2012) 10693.
- [17] H. Horiuchi, Coexistence of cluster states and mean-field-type states, *J. Phys. G: Nucl. Part. Phys.* **37** (2010) 064021.
- [18] A.C. Merchant and W.D.M. Rae, Systematics of alpha-chain states in 4 N-nuclei, *Nucl. Phys. A* **549** (1992) 431–438.
- [19] N. Itagaki et al., Exotic cluster structure in light nuclei, *J. Phys.: Conf. Serie* **420** (2013) 012080.
- [20] T. Ichikawa, J.A. Maruhn, N. Itagaki and S. Ohkubo, Linear chain structure of four- α clusters in ^{16}O , *Phy. Rev. Lett.* **107** (2011) 112501.

- [21] L. Zamick and D.C. Zheng, Linear α -chain states in nuclei, *Zeitschrift für Physik A Hadrons and Nuclei* **349** (3,4) (1994) 255–257.
- [22] B.R. Fulton, The six alpha chain state story – from Strasborg to Rab, in *Proc. 7th Int. Conf. Clustering Aspects of Nuclear Structure and Dynamics*, M. Korolija, Z. Basrak and R. Caplar (Eds.), World Scientific, London, 2000, pp. 122–129.
- [23] C. Beck, State of the art in nuclear cluster physics, *J. Phys. Conf. Series* **569** (2014) 012002, doi: 10.1088/1742-6596/569/1/012002.
- [24] K.N. Mukhin, *Experimental Nuclear Physics*, Volume 1, *Physics of Atomic Nucleus*, Mir, Moscow, 1987, p. 133.
- [25] D.D. Ivanenko, The neutron hypothesis, *Nature* **129** (3265) (1932) 798.
- [26] M.G. Mayer, *Phys. Rev.* **75** (1949) 1969.
- [27] M.G. Mayer and J.H.D. Jensen, *Elementary Theory of Nuclear Shell Structure*, Wiley, New York, 1955.
- [28] S.G. Nilsson, Binding states of individual nucleons in strongly deformed nuclei, *Kgl. Danske Videnskab. Selskab., Mat.-fys. Medd.* **29** (16) (1955).
- [29] B.A. Brown and B.H. Wildenthal, Status of the nuclear shell model, *Ann. Rev. Nucl. Part. Sci.* **38** (1988) 29–66.
- [30] A. Bohr and R.B. Mottelson, *Nuclear Structure*, Vol. I, W.A. Benjamin, 1969, World Scientific, Singapore, 1998.
- [31] A. Bohr and R.B. Mottelson, *Nuclear Structure*, Vol. II, W.A. Benjamin, 1975, World Scientific, Singapore, 1998.
- [32] A. Bohr, Rotational motion in nuclei, *Rev. Mod. Phys.* **48** (1976) 365.
- [33] B. Mottelson, Elementary modes of excitation in the nucleus, *Rev. Mod. Phys.* **48** (1976) 37.
- [34] R. Eisberg and R. Resnick, *Quantum Physics of Atoms, Molecules, Solids, Nuclei, and Particles*, Wiley, New York, 1985, pp. 545–549.
- [35] K.S. Krane, *Introductory Nuclear Physics*, Wiley, New York, 1988, pp.134–146.
- [36] J.D. McGervey, *Introduction to Modern Physics*, Academic Press, New York, 1971, pp. 498–499.
- [37] H. Georgi, Effective field theory, *Ann. Rev. Nucl. Particle Sci.* **43** (1993) 209–252.
- [38] R.B. Wiringa, V.G.J. Stoks and R. Schiavilla, Accurate nucleon–nucleon potential with charge-independence breaking, *Phys. Rev. C* **51** (1995) 38.
- [39] G. Vayenas and S. Souentie, *Gravity, Special Relativity and the Strong Force*, Springer, New York, 2012, pp. 25–27.
- [40] R. Machleidt, Nuclear forces, *Scholarpedia* **9** (1) (2014) 30710.
- [41] Bernard Schaeffer, Electric and magnetic coulomb potentials in the deuteron, *Adv. Electromagnetics J.* **2** (2013) 69–72.
- [42] Gell-Mann, A schematic model of baryons and mesons, *Phys. Lett.* **8** (3) (1964) 214–215, doi: 10.1016/S0031-9163(64)92001-3.
- [43] G. Zweig, An SU(3) model for strong interaction symmetry and its breaking (PDF), CERN-TH-401 (1964).
- [44] G. Zweig, An SU(3) model for strong interaction symmetry and its breaking: II, CERN-TH-412 (1964).
- [45] M. Gell-Mann, The eightfold way: a theory of strong interaction symmetry, in M. Gell-Mann and Y. Ne’eman (Eds.), *The Eightfold Way*, Westview Press, 2000, 1964, p. 11, ISBN 978-0-7382-0299-0.
Original: M. Gell-Mann, The eight-fold way: a theory of strong interaction symmetry, Synchrotron Laboratory Report CTSL-20. California Institute of Technology, 1961, doi:10.2172/4008239.
- [46] J. Ashman, EMC Collaboration, A measurement of the spin asymmetry and determination of the structure function g_1 in deep inelastic muon–proton scattering, *Phys. Lett. B* **206** (2) (1988) 364.
- [47] R.L. Jaffe, Where does the proton really get its spin? *Phys. Today* **24** (1995).
- [48] S. Brodsky, J. Ellis and M. Karliner, Chiral symmetry and the spin of the proton, *Phys. Lett. B* **206** (1988) 309.
- [49] X. Zheng, J.P. Chen and Z.-E. Meziani, The spin structure of the nucleon in the valence quark region, *Phys. Rev. C* **65** (2002) 065205.
- [50] A.V. Belitsky, Xiangdong Ji and Feng Yuan, *Phys. Rev. Lett.* **91** (2003) 092003.
- [51] A. Thomas, Interplay of spin and orbital angular momentum in the proton, *Phys. Rev. Lett.* **101** (10) (2008) 102003.
- [52] C.T.H. Davies et al., Precise charm to strange mass ratio and light quark masses from full lattice QCD, *Phys. Rev. Lett.* **104** (13) (2010) 132003.
- [53] A. Antognini et al., Proton structure from the measurement of 2S-2P transition frequencies of muonic hydrogen, *Science* **339** (6118) (2013) 417.
- [54] Sinya Aoki et al., Lattice QCD approach to nuclear physics (2012), arXiv: 1206.5088 (hep-lat).
- [55] D.M. Brink, History of cluster structure in nuclei, *J. Phys.: Conf. Ser.* **111** (2008) 012001.

- [56] S.A. Afzal, A.A.Z. Ahmad and S. Ali, Systematic survey of the alpha-alpha interaction, *Rev. Mod. Phys.* **41**(1) (1969) 247–273.
- [57] M. Freer, The clustered nucleus – cluster structures in stable and unstable nuclei, *Reports Progr. Phys.* **70** (2007) 2149.
- [58] B.R. Fulton, Clustering in nuclei: nuclear chains, nuclear molecules and other exotic states of nuclear matter, *Contemporary Phys.* **40** (1999) 299–311.
- [59] T. Kawabata et al., $2\alpha + t$ cluster structure in ^{11}B , *Phys. Lett. B* **646** (2007) 6–11.
- [60] K. Ikeda, N. Tagikawa and H. Horiuchi, The Ikeda diagram. *Progr. Theoret. Phys. Suppl.* extra number (1968) 464.
- [61] N.L. Bowen, a simple calculation of the inter-nucleon up-to-down quark bond and its implications for nuclear binding, *J. Condensed Matter Nucl. Sci.* **29** (2019) 249–259.
- [62] D. Halliday and R. Resnick, *Fundamentals of Physics*, Wiley, New York, 1974, p. 477.
- [63] P. Lorrain and D. Corson, *Electromagnetic Fields and Waves*, Freeman, San Francisco, 1970, pp. 72–76.
- [64] D. Giancoli, *Physics Principles with Applications*, Prentice Hall, Upper Saddle River, NJ, 1998, pp. 509–510.
- [65] G.E. Owen, *Electromagnetic Theory*, Allen and Bacon, Boston, 1963, pp. 21–26.
- [66] D. Halliday and R. Resnick, *Fundamentals of Physics*, Wiley, New York, 1974, pp. 537–571.
- [67] P. Lorrain and D. Corson, *Electromagnetic Fields and Waves*, Freeman, San Francisco, 1970, pp. 292–299.
- [68] D. Giancoli, *Physics Principles with Applications*, Prentice Hall, Upper Saddle River, NJ, 1998, pp. 588–612.
- [69] G.E. Owen, *Electromagnetic Theory*, Allen and Bacon, Boston, 1963, p. 205.
- [70] K. Yosida, *Theory of Magnetism*, Springer, New York, 1996, p. 13.
- [71] D.J. Griffiths, *Introduction to Electrodynamics*, 3rd Edn., Prentice Hall, Upper River Saddle, NJ, 2007, p. 281.
- [72] D. Halliday and R. Resnick, *Fundamentals of Physics*, Wiley, New York, 1974, p. 571.
- [73] M.E. Peskin and D.V. Schroeder, *An Introduction to Quantum Field Theory*, Perseus, Reading, MA, 1995, pp. 175–198.
- [74] D.H. Perkins, *Introduction to High Energy Physics*, Addison Wesley, Reading, MA, 1982, pp. 201–202.
- [75] P. Lorrain and D. Corson, *Electromagnetic Fields and Waves*, Freeman, San Francisco, 1970, pp. 64–70.
- [76] A.J. Buchmann et al., Intrinsic quadrupole moment of the nucleon, arXiv:hep-ph/0101027, Feb. (2008).
- [77] G. Neyens, Nuclear magnetic and quadrupole moments for nuclear structure research on exotic nuclei, *Reports Progr. Phys.* **66** (2003) 633.
- [78] N.E. Holden, *Table of the Isotopes*, D.R. Lide (Ed.), *CRC Handbook of Chemistry and Physics*, 84th Edn., CRC Press, Boca Raton, FL, 2004.
- [79] S. Raman, C.W. Nestor and P. Tikkanen, Transition probability from the ground to the first $2+$ state of even-even nuclides, B. Pritychenko (Ed.), *Atomic Data and Nuclear Data Tables*, Vol. 78, Elsevier, Cambridge, MA, 2001, pp. 1–128.
- [80] K.N. Mukhin, *Experimental Nuclear Physics, Volume 1, Physics of Atomic Nucleus*, Mir, Moscow, 1987, pp. 62–68.
- [81] J.D. McGervey, *Introduction to Modern Physics*, Academic Press, New York, 1971, pp. 470–475.
- [82] K.S. Krane, *Introductory Nuclear Physics*, Wiley, New York, 1988, pp. 49–57.
- [83] H. De Vries, C.W. De Jager and C. De Vries, Nuclear charge-density-distribution parameters from elastic electron scattering *Atomic Data and Nuclear Data Tables* **36** (1987) 495–536.
- [84] E. Schrödinger, An undulatory theory of the mechanics of atoms and molecules, *Phys. Rev.* **28** (6) (1926) 1049–1070.
- [85] K.S. Krane, *Introductory Nuclear Physics*, Wiley, New York, 1988, p. 144.
- [86] J.D. McGervey, *Introduction to Modern Physics*, Academic Press, New York, 1971, p. 498.
- [87] C.A. Bertulani, *Nuclear Physics in a Nutshell*, Princeton University Press, Princeton, NJ, 2007, p. 155.
- [88] National Nuclear Data Center, information extracted from the NuDat 2 database, <http://www.nndc.bnl.gov/nudat2/>.



Research Article

An Examination of the Updated Empirical Data in Support of the Shell Model

N.L. Bowen*

Colorado Mountain College, Glenwood Springs, Colorado, USA

Abstract

This paper is an examination of the updated experimental data, as is currently known in 2020, in support of the shell model and its concepts. The shell model of the nuclear force is considered to be the fundamental and foundational model of the nuclear force – that force which binds the nucleons together in a nucleus. The shell model was developed in the late 1940s, and it is based on the experimentally known nuclear data at that time, data which supported the concept of nuclear shells. Most textbooks, even the current ones, present this experimental data from the 1940s when discussing the validity of the shell model. However, a large amount of nuclear data has since been collected over the past 70 years, and a re-examination of the experimental data in support of the shell model is long overdue.

© 2020 ISCMNS. All rights reserved. ISSN 2227-3123

Keywords: Liquid drop model, Nuclear bonding, Nuclear force, Nuclear stability. Separation energy, Shell model

1. Introduction

The first nuclear shell model was proposed by Dmitry Ivanenko in 1932 soon after the discovery of the neutron [1]. The model was further developed in 1949 by several physicists, most notably Maria Goeppert Mayer, J. Hans D. Jensen, and Eugene Paul Wigner, who shared the 1963 Nobel Prize in physics for the development of the model [2,3]. The nuclear shell model is similar to the concept of the electronic shell structure of atoms, in that it proposes a similar shell-like structure for the protons and neutrons within a nucleus.

When the nuclear shell model was first proposed, there were immediate objections to it, mainly because the nuclear shell model is based on a centrally-located force. However, as inferred by the experimental nuclear binding curve, the nuclear force is not a centrally-located force. As the number of nucleons A increases, a centrally located force would have a parabolically increasing curve for binding energy vs. A , but experimentally, this is not seen. Rather, the nuclear force is commonly referred to as a saturated force, in which the (binding energy/ A) vs. A is relatively flat, or “saturated”. Another reason for the initial objections to the shell model was due to its underlying differences with the liquid drop model. The shell model is based on the concept that the nucleons within a nucleus move independently,

*E-mail: nbowen@coloradomtn.edu.

and interact with one another only rarely, if at all. Rather the nucleons interact with an energy well, that is used by the Schrödinger equation to determine the nuclear behavior. Quite opposite of this concept, the liquid drop model is based on the concept that there is a collective motion of the nucleus, with a bonding interaction between neighboring nucleons, similar to a drop of liquid.

The shell model includes certain “magic” numbers, numbers that were found by examining the empirical data, comparing it to the liquid drop model, and searching for discrepancies. It was found, from the nuclear data of the 1940s, that there were slight discrepancies in the nuclear behavior when either Z or N is equal to 2, 8, 20, 28, 50, 82, and 126. The nuclear shell model asserts that the explanation for these discrepancies is the existence of nuclear shells.

To get these magic numbers theoretically, a complicated theoretical process is involved. The shell model uses an average potential energy well with a spherically symmetric square well with rounded edges. To this potential, an empirical spin–orbit coupling must be added. These additional variables, which account for geometrical considerations, vibrations, rotational excitations, and pairing properties are used when employing the Schrödinger equation [4]. There are other models that offer more refinements to the shell model, such as the collective model [5,6]. The collective model is described by Bohr as being a generalization of the shell model, in which the nuclear field is no longer considered to be considered constant, but rather to be considered to be a dynamic variable, in that the net nuclear potential undergoes deformations away from a spherically-symmetric square well. Other more recent models for the nuclear force include the nuclear cluster model [7], the residual chromodynamic force model [8] and the electromagnetic model [9].

In this paper, the latest and most updated nuclear databases are used to examine the empirical nuclear data [10] in support of the shell model. This updated data is used to reconstruct the diagrams, graphs, and other empirical evidence in support of the claims of the shell model.

Claim 1. There are incongruities in the binding energy per nucleon when comparing experimental data to the predictions of the semi-empirical formula.

When comparing the binding energy per nucleon to the predicted value from the semi-empirical formula of the liquid drop model, one can see a slight bump at $Z = 28, 50, 82$ and at $N = 28, 50, 82$, and 126. Figure 1(a,b) shows the difference between the semi-empirical formula calculations and the actual binding energy per nucleon, vs. Z and N . As can be seen, this incongruity is small. Usually, the left-hand sides of these graphs are not shown, to hide the very large discrepancies there. These charts shown in Fig. 1(a,b) are generated by inserting the values of Z, N , and A into the semi-empirical equation, and then subtracting the experimental values binding energy for each nuclide. The slight discrepancies seen at the magic numbers seem to be little more than a minor variation, especially when compared to the large discrepancies of the smaller nuclides.

Claim 2a. There are more known isotopes and more stable isotopes, when Z is a magic number.

A second claim for evidence of shells is that there are more known isotopes and more stable isotopes when the number of protons Z is equal to a magic number. Shown in Fig. 2(b) is a plot of the number of known isotopes and the number of stable isotopes vs. Z [10]. By looking at the magic numbers of 2, 8, 20, 28, 50, and 82 on the x -axis, and comparing the number of known isotopes (*blue dots*) for that magic number, it can be seen that there are very slight, rather unremarkable, bumps at Z equal to 28 and 50. There are also bumps at 56 and 80, but these are not magic numbers. There are no apparent bumps at any of the other magic numbers. For the number of stable isotopes (*red dots*) shown in Fig. 2(a), a small effect can be seen for $Z = 20$ and 50, but again the other magic numbers do not have any variation in the number of stable isotopes.

For protons, the updated data shows this claim to be true for only two magic numbers, and even then, it is a rather insignificant effect.

Claim 2b. There are more known isotones and more stable isotones, when N is a magic number.

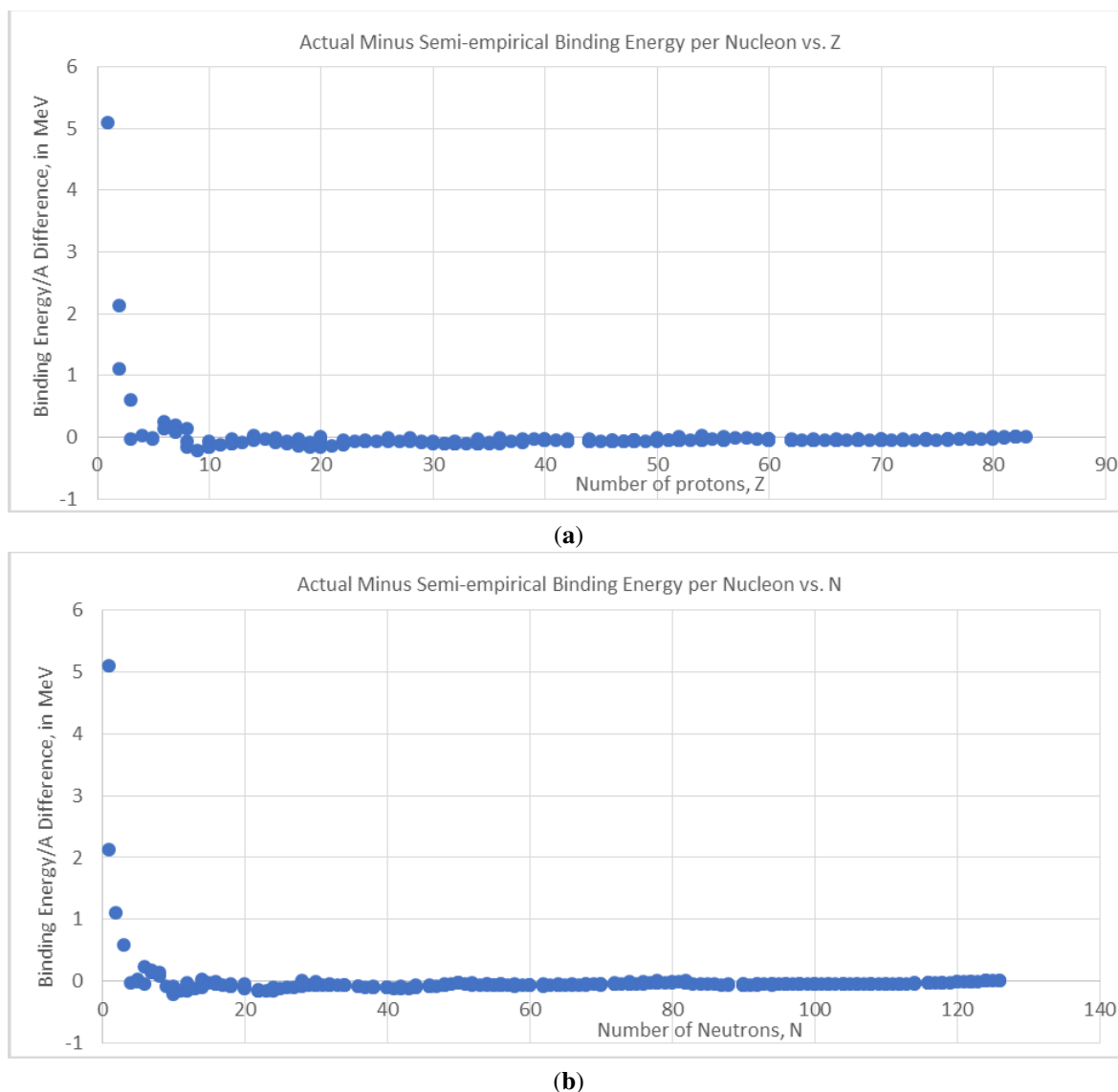


Figure 1. (a) Difference between semi-empirical formula and actual binding energy per nucleon, vs. Z . (b) Difference between semi-empirical formula and actual binding energy per nucleon, vs. N .

The second part of this second claim is that there are more known isotones and more stable isotones when the number of neutrons N is equal to a magic number. Shown in Fig. 2(b), on a similar vertical scale as Fig. 2(a) for easier comparison, is a plot of the number of known isotones and the number of stable isotones vs. N [10]. By looking at the magic numbers of 2, 8, 20, 28, 50, and 82 on the x -axis, and comparing the number of known isotones (*blue dots*) for that magic number, it can be seen that there is a very slight bump of one additional isotone at $N = 20$. There are similar slight bumps at 85, 88, 91, and 97, but these are not magic numbers. There are no bumps at any of the other

magic numbers. For the number of stable isotones (red dots), a small effect can be seen for $Z = 20, 28, 50$, and 82 , but again the other magic numbers of $2, 8$, and 126 do not have any notable variation in the number of stable isotopes.

Thus similar to protons, the updated data for neutrons shows this claim to be only partially true for only four of the magic numbers. Again, it is only a slight effect, and not what one should consider to be a significant indicator of nuclear shell structure.

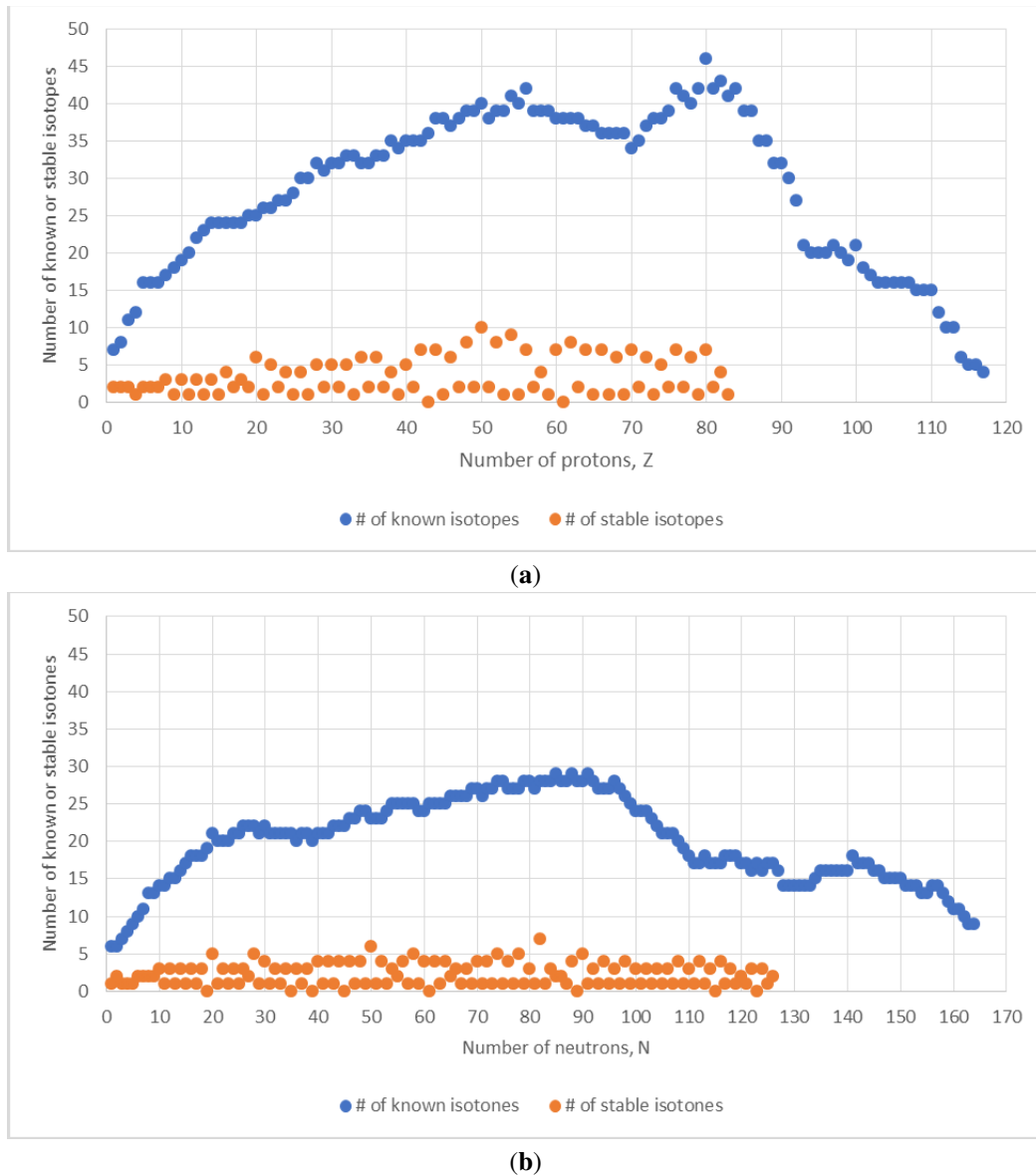


Figure 2. (a) The number of known and stable isotopes vs. Z . (b) The number of known and stable isotones vs. N .

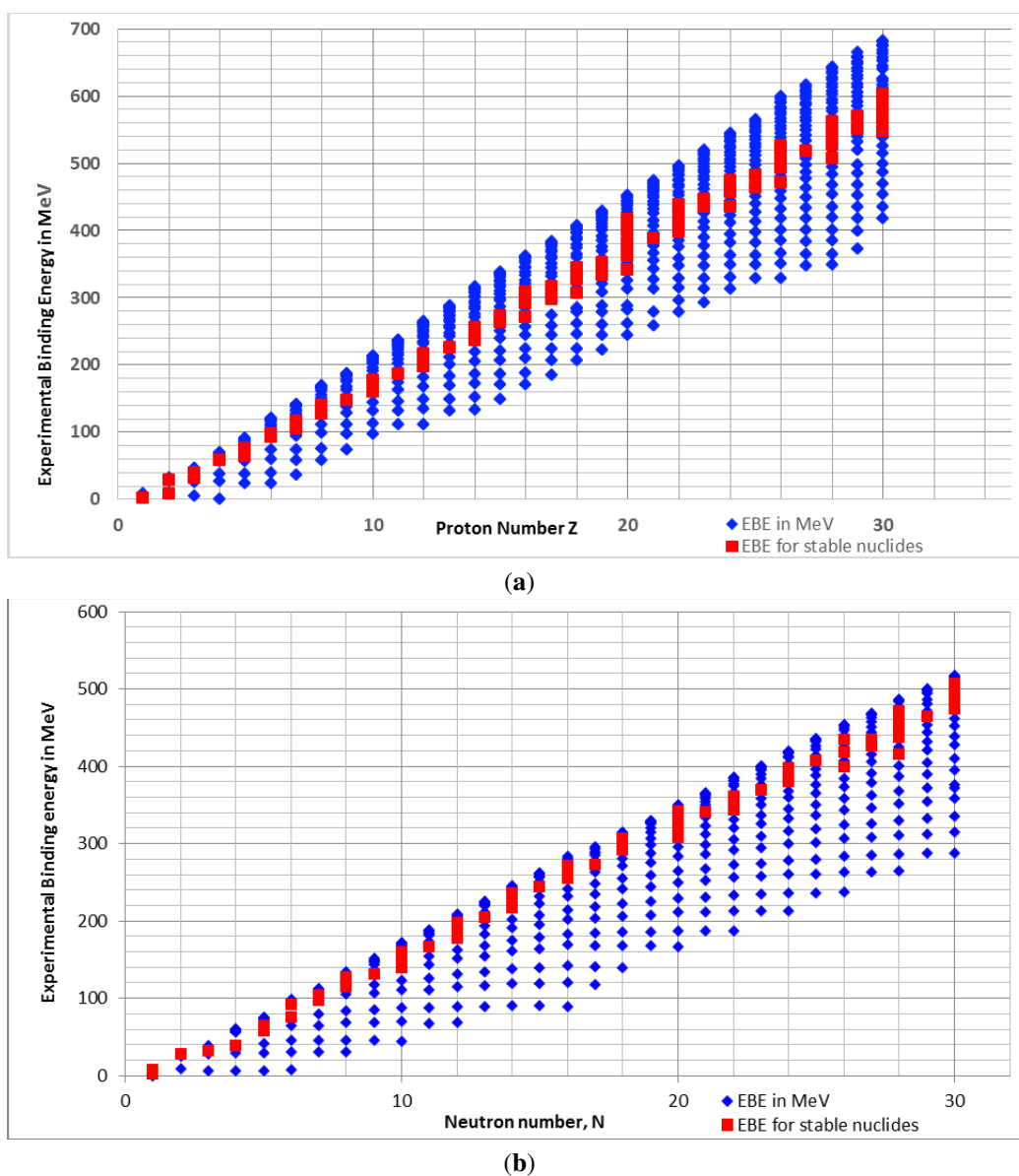


Figure 3. (a) Experimental binding energy per nucleon vs. Z . (b) Experimental binding energy per nucleon vs. N .

There is another inconsistency in this second claim of there being more stable nuclides for magic numbers. When the mode of decay of an unstable nuclide is due to beta decay rather than particle decay, then the instability of the nuclide is due to the weak nuclear force. If the shell model is claiming to be able to predict the behaviors of the weak nuclear force, then there are many other more salient behaviors of the weak nuclear force that should be answered that are unrelated to magic numbers or shells. For example, why do nuclides with odd Z tend to have only one or two

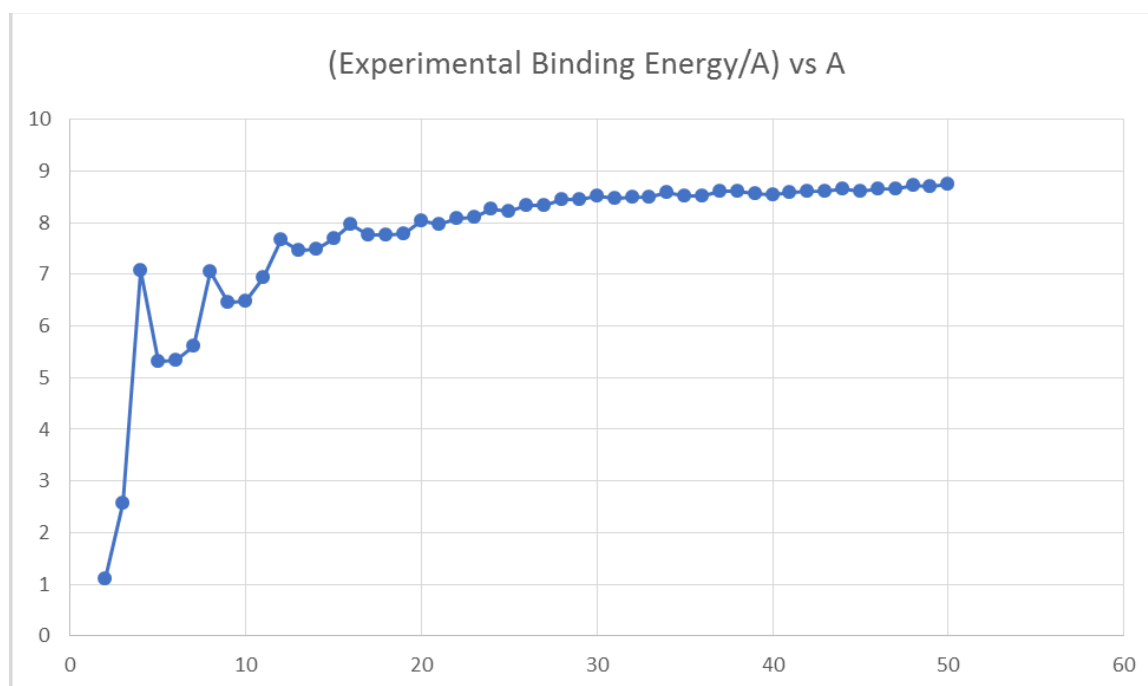


Figure 4. Experimental binding energy per nucleon vs. A for the first 50 stable nuclides.

stable isotopes, and similarly, why do nuclides with the odd N tend to have only zero or one stable isotone? There are many other behaviors of the weak nuclear force that show no correlation to the magic numbers of the shell model. Thus, it would be incorrect to imply that the shell model is a model for the weak nuclear force. Given that, the number of stable isotopes or isotones for a given Z or N should be considered as being more relevant to the weak nuclear force, rather than being considered as evidence in support of the nuclear shells.

Claim 3. Nuclei with a magic number for Z or N have a higher binding energy than non-magic nuclei.

Another claim of the shell model is that nuclei with either Z or N equal to a magic number have a higher binding energy than non-magic nuclei. Figure 3(a,b) shows the experimental binding energy for all the nuclides, stable and unstable. Figure 3(a) shows the binding energy vs. Z , and Fig. 3(b) shows the binding energy vs. N . As is seen in the figures, there is not a higher binding energy for the magic numbers. The evidence of there being higher binding energy for nuclides with magic numbers at 2, 8, 20 or 28 is not evident in either graph, and going out further to larger values of Z or N also shows no such effect in binding energy.

As seen in Fig. 3(a,b), the nuclides with a magic number of either 2, 8, 20 or 28 are not more tightly bound than the other nuclides near them. For example, all nuclides of Helium have the magic number of $Z = 2$, but other than ^3He and ^4He they are not stable. Furthermore, ^3He is not tightly bound. Helium-5 is extremely unstable, even though it has a magic number for the number of protons. As another example, the nuclides with $N = 8$, such as ^{11}Li , are not more tightly bound nor more stable than the non-magic values of N .

Another related claim to this one suggests that the “doubly magic” nuclides are more stable and more tightly bound, such as ^4He and ^{16}O . However, ^4He and ^{16}O are not distinct in their binding energy per nucleon, when compared other

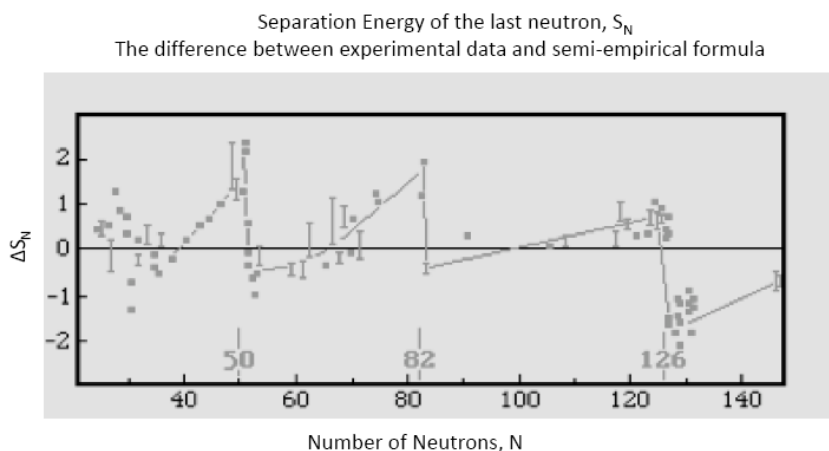


Figure 5. A graph of the binding energy of last neutron vs. N , data from the 1940s.

alpha-particle nuclides, such as ^{12}C , ^{20}Ne , ^{24}Mg , ^{28}Si , ^{32}S , ^{36}Ar , or ^{40}Ca . This is shown in Fig. 4 for the Experimental Binding Energy per nucleon vs. A .

All of the alpha-particle nuclides (in which Z is even, and $N = Z$) have a slightly higher binding energy than

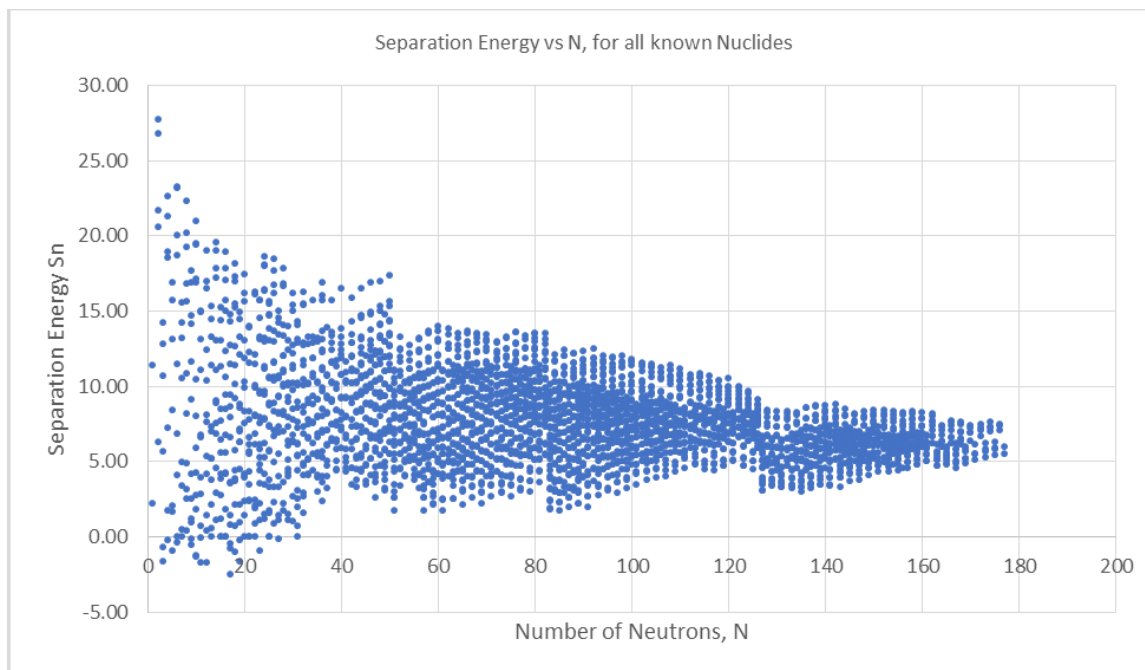


Figure 6. Separation energy, S_n , vs. N , for all known nuclides.

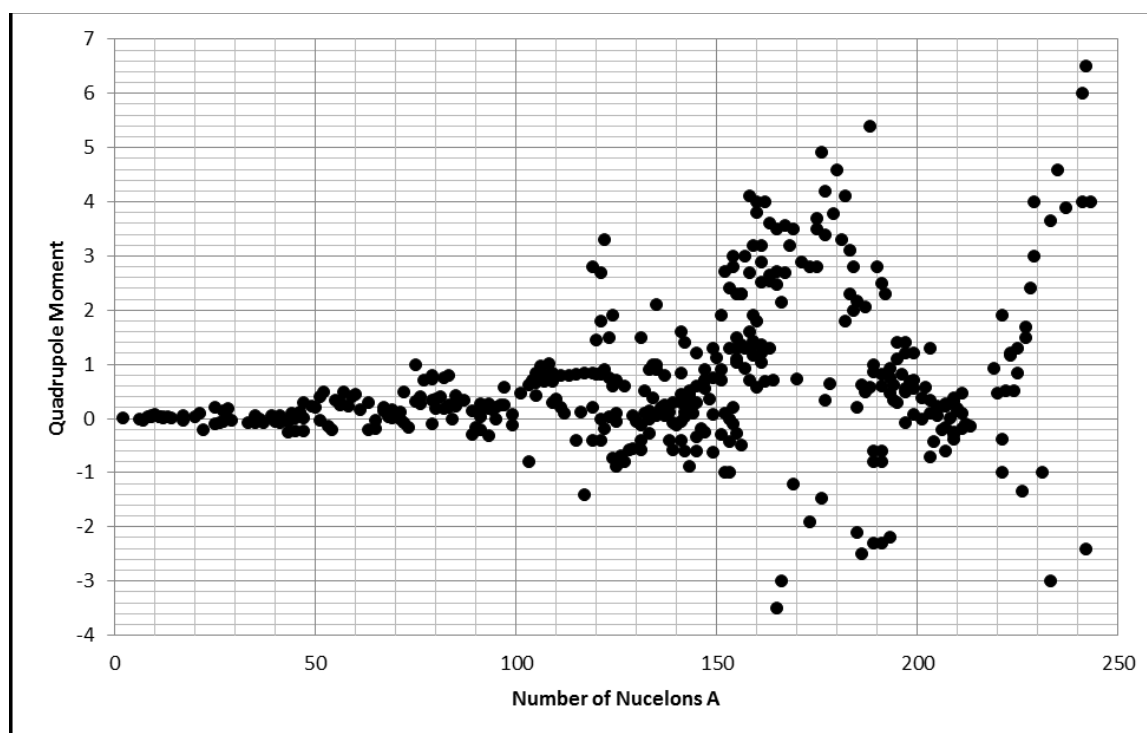


Figure 7. Experimental quadrupole moment. The predicted deformation parameter of the shell model is shown by the blue lines.

the nuclides near them. Thus, this higher binding energy per A at the values of $A = 4, 8, 12, 16, 20, 24, 28$, and 32 supports the cluster model more than the shell model. Also, the claim that doubly magic nuclides are more stable is not valid, as can be seen when examining all the doubly magic nuclides. There are 12 known nuclides that are doubly magic: ${}^4\text{He}$, ${}^{10}\text{He}$, ${}^{16}\text{O}$, ${}^{28}\text{O}$, ${}^{40}\text{Ca}$, ${}^{48}\text{Ca}$, ${}^{48}\text{Ni}$, ${}^{56}\text{Ni}$, ${}^{78}\text{Ni}$, ${}^{100}\text{Sn}$, ${}^{132}\text{Sn}$, and ${}^{208}\text{Pb}$. However, only five of them are stable: ${}^4\text{He}$, ${}^{16}\text{O}$, ${}^{40}\text{Ca}$, ${}^{48}\text{Ca}$, and ${}^{208}\text{Pb}$. The remaining seven nuclides are unstable. Thus, being doubly magic does not endow a nuclide with a higher propensity for being more stable.

Claim 4. Neutron separation energies show a distinct zigzag pattern associated with magic numbers, characteristic of shells.

Another claim in support of shell model numbers is an old graph, reproduced in Fig. 5, showing the separation energy vs. neutron number N . Figure 5 is a reproduction of a graph using data from the 1940s. The separation energy, S_n , is the energy required to remove one neutron from a nuclide. This graph in Fig. 5 attempts to emphasize the effect of magic numbers. To obtain this graph, the binding energy of the two nuclides A_N and A_{N-1} , are subtracted. Note that these binding energies go up to 1800 MeV for the larger nuclides. Thus the difference between the two nuclides A_N and A_{N-1} , illustrated in this figure, is a very small difference between two much larger numbers. This difference, obtained from the experimental data, is then compared to the predictions of the semi-empirical formula of the liquid drop model, and the resulting difference of the differences, is plotted as shown in Fig. 5. Similar graphs of this separation energy are seen in numerous text books, claiming that this is strong evidence in support of nuclear shells and magic numbers [11–14].

The reason this graph is considered to support the nuclear shell model is due to the zigzag effect seen in this data. For the atomic shell model for electrons, there is a strong zigzag effect seen in the ionization energy of electrons. A plot of the ionization energy of the electrons around an atom vs. the number of electrons displays this zigzag pattern. As the electronic shells are filled around an atom, the ionization energy exhibits a definite and strongly evident zigzag pattern. If nuclear shells existed within a nucleus, similar to the electronic shells around an atom, then this same zigzag effect should be seen as well.

One obvious problem with this graph in Fig. 5 is that it does not include all the nuclides. Nor does it even include, at the very least, all the stable nuclides. There are over 3200 known nuclides that should be plotted on this graph, and yet the data shown in Fig. 5 only shows a smattering of selected points.

Also, the graph in Fig. 5 is the *difference* between the empirical separation energy and what is predicted by using the semi-empirical model, with no justification for doing that. The electronic shell model data for electron ionization energy is simply a plot of the ionization energy; it is not the difference between the actual ionization energy and another theory's predictions. Thus, the experimental data for the nuclear separation energy should show a zigzag pattern, without having to subtract it from another model's theoretical predictions. Another very evident problem with the graph shown in Fig. 5 is that it cuts off at $N < 20$, obscuring the data for the smaller nuclides. When the nuclides from 1 to 20 are included, the resulting spread is extremely large. This large spread is unrelated to magic numbers. Hence, for all these reasons, the graph in Fig. 5 is not a true representation of the separation energy S_n vs. N .

Figure 6 shows all the actual separation energy S_n of all the known nuclides. (All data for S_n have been extracted from [10].) As can be seen by comparing Figs. 5 and 6, there is much difference between what is purported to be proof of a shell-like structure in a nucleus in Fig. 5, and what is actually seen in the updated empirical data for neutron separation energy.

In Fig. 6, there are, indeed, discontinuities at $N = 50$, $N = 82$, and $N = 126$. These discontinuities are considerably small, around 1–2 MeV, and they are minor compared to the overall spread, 30 MeV, of the experimental data for S_n that is seen in Fig. 6. Furthermore, these 1–2 MeV discontinuities are insignificant when compared to the overall binding energies (over 1800 MeV) for the larger nuclides. Even more problematic is that no such effect occurs with regard to magic numbers for the separation energy of a proton, S_p , and its absence implies that nuclear shells are not a credible explanation.

There is no question that the small steps in S_n at $N = 50$, 82, and 126 exist. What is in question, however, is whether steps are the result of shells and magic numbers within the nucleus. With regards to the shell model, the term “magic” is very much a misnomer. Physicists know that magic is not really the explanation for nuclear behaviors. Rather, the word “magic” might be best explained as a short-cut way of saying, “There is a phenomenon occurring at these numbers which we can not yet explain.” At some future time physicists may understand why those small steps occur at $N = 50$, 82, and 125 for the separation energy S_n . However, there is no question that such a future understanding would be an explanation of something other than magic.

Claim 5. There are deformations in the shape of the nuclei, as seen by the electric quadrupole moment, that occur when a nuclei is far away from a magic number.

Another claim of the shell model is that there are deformations in the shape of the nuclei when the nuclei is far away from a magic number. With regard to the concept of a spherical nuclides, it is claimed that these deformations exist in small clusters within the nuclear chart, occurring in small islands far from the magic numbers. The experimental data for the electric nuclear quadrupole moments, which is directly correlated to the nuclear deformations, shows that this claim is not valid. If the shell model were correct, all of these quadrupole moments, seen in the Fig. 7, should be less than what is indicated by the blue line. (All data extracted from [10,15].)

As can be seen in Fig. 7, there are large deformations in the shape of the nuclides, much larger than can be predicted or explained by the shell model. These deformations exist for the majority of nuclides, not just for small islands far

from the magic numbers. Hence the claim that the data for the electric nuclear quadrupole moment support the shell model is not supported by the updated empirical data; rather it is quite contradictory to the shell model. Most of the nuclides are far above the blue lines, the maximum quadrupole moment predicted by the shell model. (The collective model is able to reproduce the large quadrupole moments by adding two to three empirically selected variables for each nuclide. In the collective model, the potential energy well of the Schrödinger equation is not spherically symmetric, but rather it is ellipsoidal, to better match the experimentally observed quadrupole moments.)

2. Discussion

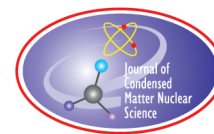
The updated experimental data for nuclides indicate that certain magic numbers may not be as cogent as previously assumed. This is an unanticipated result, but one which is difficult to deny when examining the updated experimental data. Thus, upon reexamination of updated data, the shell model appears to be less of a fundamental model to explain nuclear behavior than was previously believed in the 1940s. Experimental evidence in support of the shell model has diminished in the test of time.

3. Conclusion

It would be misleading for anyone to claim that the shell model is a foundational model, or that nuclear structure is based on nuclear shells, with strong empirical data to support this concept. To be more precise, the nuclear shell model is substantiated only by weak and/or insignificant experimental data. Also, considering that the shell model requires the inclusion of other theoretical models, such as the collective model, to more accurately predict experimental behavior, the shell model seems to be obsolete, both empirically and theoretically. It is suggested that the shell model should only be taught in the context of its historical interest, but it should not be taught as an underlying foundational model of nuclear structure.

References

- [1] D.D. Ivanenko, The neutron hypothesis, *Nature* **129** ((1932) 3265), 798.
- [2] M.G. Mayer, *Phys. Rev.* **75** (1949) 1969.
- [3] M.G. Mayer and J.H.D. Jensen, *Elementary Theory of Nuclear Shell Structure*, Wiley, New York, 1955.
- [4] B.A. Brown and B.H. Wildenthal, Status of the nuclear shell model, *Ann. Rev. Nucl. Part. Sci.* **38** (1988) 29–66.
- [5] A. Bohr and R.B. Mottelson, *Nuclear Structure*, Vol. I, W.A. Benjamin, 1969; World Scientific, Singapore, 1998.
- [6] A. Bohr and R.B. Mottelson, *Nuclear Structure*, Vol. II, W.A. Benjamin, 1975; World Scientific, Singapore, 1998.
- [7] D.M. Brink, History of cluster structure in nuclei, *J. Phys.: Conf. Ser.* **111** (2008) 012001.
- [8] G. Vayenas and S. Souentie, *n Gravity, Special Relativity and the Strong Force*, Springer, New York, 2012, pp 25–27.
- [9] N.L. Bowen, The electromagnetic considerations of the nuclear force, *J. Condensed Matter Nucl. Sci.* Dec. 2020.
- [10] *National Nuclear Data Center*, information extracted from the NuDat 2 database, <http://www.nndc.bnl.gov/nudat2/>.
- [11] R. Eisberg and R. Resnick, *Quantum Physics of Atoms, Molecules, Solids, Nuclei, and Particles*, Wiley, New York, 1985, pp. 530.
- [12] J. Lilley, *Nuclear Physics Principles and Applications*, Wiley, Chichester, 2001, p. 45.
- [13] K.S. Krane, *Introductory Nuclear Physics*, Wiley, New York, 1988, pp. 119.
- [14] S. Sharma, *Atomic and Nuclear Physics*, Dorling Kindersley, New Delhi, 2008, pp. 295–296.
- [15] S.G. Nilsson, Binding state of individual nucleons in strongly deformed nuclei, *Mat. Fys. Medd. Dan. Vid. Selsk.* **29** (1955) 16.



Review Article

Review of Seebeck Calorimeters Used in LENR Experiments

Bengisu Sisik and David J. Nagel*

The George Washington University, 725 23rd Street NW, Washington DC 20052, USA

Abstract

Cold Fusion is the name initially applied to what are now called, more generally, Low Energy Nuclear Reactions (LENR). Such reactions produce nuclear products and generate thermal energy. Calorimeters are the instruments used to measure the energy production. They can be based on either mass or heat flow. Some heat flow calorimeters use the Seebeck effect in particular materials, where temperature differences produced by LENR generate measurable voltages from thermoelectric devices. This paper is a review of Seebeck calorimeters that have been used in LENR experiments. Compilations of their characteristics and performance are provided. The scaling of the performance of Seebeck calorimeters with their size is considered. The equations that govern the behavior of both mass flow and heat flow calorimeters are given.

© 2020 ISCMNS. All rights reserved. ISSN 2227-3123

Keywords: Calorimeters, Isoperibolic calorimeters, LENR, Low energy nuclear reactions, Mass flow calorimeters, Seebeck calorimeters

1. Introduction

The Low Energy Nuclear Reaction (LENR) experiments produce a few minor and two major effects. The lesser outputs are some energetic radiations, infrared emission and sound production. The major results are reaction products and thermal energy. The transmutation products are scientifically useful, since they indicate which reactions might have occurred. They are measured with a wide variety of analytical techniques [1]. It is unclear now whether or not the reaction products will be commercially important. The thermal energy has great practical promise as a new source of clean energy. It is quantified by the use of calorimeters of various designs and properties.

This review considers reports where Seebeck calorimeters were used for quantification of LENR thermal power. To set such calorimeters in context, the next section surveys calorimetry in general and, more specifically, the types of calorimeters that have been used in LENR experiments. Seebeck calorimeters are based on thermoelectric materials that exhibit the Seebeck effect and its inverse, the Peltier effect. In the latter, the application of voltages to devices containing thermoelectric materials makes it possible to pump heat from one face of the device to the other. In the Seebeck effect, a temperature difference across the device faces results in an output voltage. One device can be used for both of the reciprocal effects. The third section reviews thermoelectric devices and closely related thermocouples.

*Corresponding author. E-mail: nagel@gwu.edu.

With that background, LENR papers about Seebeck calorimeters are summarized in the fourth section. Their physical and other characteristics, and measures of their performance, are the subject of the fifth section. A simple analytical approach to the geometrical scaling of Seebeck calorimeters is given in Section 6. The last section sketches the characteristics of a new Seebeck calorimeter being built for our LENR laboratory.

2. Types and Features of LENR Calorimeters

Calorimetry is both an old and widely used approach to measuring the release of energy. It is employed for assessment of energy released by physical processes, notably radioactive decay. Calorimetry is most commonly used for the quantification of heat from chemical reactions. Foods can be thought of as unreacted chemicals. Measurement of the energy content of foods is routine in some countries, where the caloric content of foods must be on packages.

In general terms, a calorimeter is a vessel in which some heat-releasing reaction occurs, leading to an increase in temperature of the contents of the calorimeter. The temperature increase is usually referenced to some constant-temperature part of the overall calorimeter system. The increase in temperature can be quantified in a variety of ways. A major and universal limitation of calorimeters is their relatively slow response to sudden heat releases due to the time it takes for heat transfer from the source to the calorimeter or from the calorimeter to the surrounding media. The response time constants of most LENR calorimeters are in the range of tens of minutes. Consider the cooling of a cup of hot coffee on a table to gain some appreciation of the slow response time of calorimeters.

Many different types of calorimeters were used in the years following the 1989 announcement by Fleischmann and Pons that they were able to use (low) chemical energies to trigger (high) nuclear energies. They performed “cold fusion” experiments within electrochemical cells inside of calorimeters [2]. The electrochemical cells contained heavy water, which was electrolyzed into deuterium and oxygen. The deuterium interacted with a metal cathode, usually palladium, to produce heat-releasing LENR reactions. The calorimeter was calibrated to permit quantification of the power and energy from the LENR. A review of many of those types of calorimeters was featured in a session of the *14th International Conference on Cold Fusion* in 2008 [3]. Both books by Storms have useful discussions of calorimeters employed in LENR experiments [4,5]. There are many published or posted papers on the design and performance of diverse LENR calorimeters. We will not consider all known possibilities, but instead will review the most used and important types of LENR calorimeters. The Appendix contains a qualitative comparison of the three major types of the LENR calorimeters.

During the past thirty years of the experimental study of LENR, a few basic calorimeter designs have stood the test of time, and are still in use. They fall into two major categories, Mass Flow Calorimeters and Heat Flow Calorimeters. Each is considered in the remainder of this section.

2.1. Mass flow calorimeters

In mass flow systems, the heat produced by electrical, chemical or nuclear means is transferred directly to a liquid that surrounds and flows past the reaction volume. Figure 1 is a simple schematic of such a system. The energy ΔE produced and transferred by conduction to the liquid raises the temperature of the liquid ΔT . The governing equation is

$$\Delta E = M C_p \Delta T \quad \text{or} \quad \Delta P = \frac{dM}{dt} C_p \Delta T, \quad (1)$$

where dM is the mass of the liquid that flows through the calorimeter in time period dt , C_p is the specific heat of the liquid and P is the transferred thermal power. Measurements of the flow rate (dM/dt) and the input and output temperatures of the liquid enable calculation of the generated power ΔP , all as a function of time.

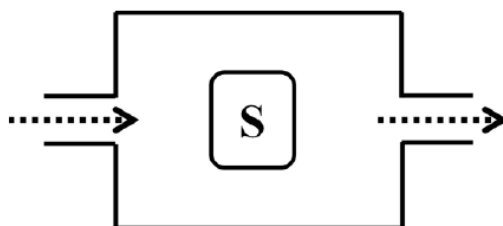


Figure 1. Schematic of a mass flow calorimeter, showing the liquid flowing into and out of a chamber surrounding the heat source S. Not shown are the temperature sensors at the inlet and outlet, or the means of measuring the flow rate.

The mass flow rate can be determined with flow meters, or more precisely, by weighing. The temperatures of the liquid are measured by any temperature sensors, such as thermocouples (TC) or resistance thermal detectors (RTD). Modern mass flow calorimeters use digital scales, and digitize the temperature readings for computer recording. Mass flow calorimeters with water as the working fluid have been used extensively by McKubre and his colleagues [6]. Oil flow systems are employed for operation at temperatures higher than the boiling point of water. They are employed by a Japanese collaboration, which is using nano-scale materials for LENR experiments in the range of 200–300°C [7]. The response time of mass flow calorimeters is determined by the time needed to transport thermal energy from within the calorimeter to the surrounding flowing liquid. Mass flow calorimeters have an important advantage, since they do not require a stable temperature reference.

2.2. Heat flow calorimeters

These systems can be contrasted with mass flow calorimeters in two ways. The first is the fact that they require a stable temperature reference. It is often a water bath, but can also be solids, the temperature of which is controlled by an active (feedback) thermoelectric system. And, they seek to either restrict or exploit energy flow to their surroundings. The result of internal energy releases of any kind within a heat flow calorimeter is an increase in temperature of the contents of the reaction vessel. There are two major types of LENR Heat Flow calorimeters, Isoperibolic calorimeters [2] and Seebeck calorimeters [3,4]. Both have constant temperature surroundings, but they differ in what is measured to determine LENR power production. With Isoperibolic calorimeters, the temperature of the contents of the LENR cell provides the data to compute the rate of nuclear energy generation as a function of time [8]. They can be used with closed LENR cells, where a recombiner catalyzes the combination of any hydrogen (deuterium) and oxygen to avoid explosions, or in an open configuration, where the gases are permitted to escape from the cell and calorimeter. For Seebeck calorimeters, the produced LENR energy is conducted through active thermoelectric elements, providing the raw voltage data for power history determinations [9,10]. Such calorimeters are generally used with closed LENR cells having recombiners. Such calorimeters are named after Thomas Seebeck, an Estonian, German physicist, who discovered in 1821 that the junctions between dissimilar metals produce voltages when they are heated [11]. Both variants of heat flow calorimeters are considered in the following paragraphs.

2.2.1. Isoperibolic calorimeters

Figure 2 contains a simple schematic of an isoperibolic calorimeter. Heat flows from the source to the gas or liquid inside of the calorimeter, and thence, through the insulation to the constant temperature region. Measurements of the internal cell temperature as a function of time can be converted into data on the internally generated power, also as a function of time. The simplest equation for an isoperibolic heat flow calorimeter is:

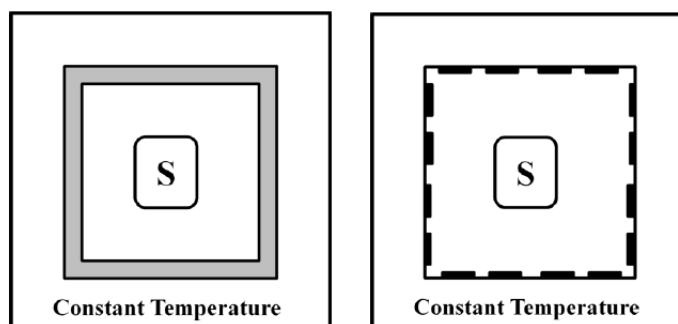


Figure 2. Schematics of two types of heat flow calorimeters surrounding a heat source S, an Isoperibolic calorimeter on the *left* and a Seebeck calorimeter on the *right*. The Isoperibolic calorimeter consists of a thermal barrier, shown in *grey*. The interior air or liquid of the calorimeter is heated by the source, which raises the internal temperature. That temperature as a function of time is the output data. The Seebeck calorimeter consists of walls held at constant temperature, which are covered by small thermoelectric elements shown in *black*. Their voltage, also measured as a function of time, constitutes the output signal. It depends on the temperature difference between the interior of the Seebeck calorimeter and the colder outside temperature.

$$MC_p \frac{dT}{dt} = \text{Input powers} - \text{Output thermal power}, \quad (2)$$

where M is the mass of the contents of the reaction vessel, C_p is the specific heat of those contents and (dT/dt) is the rate of change of the internal temperature. The input electrical power needed to free the protons from light water or the deuterons from heavy water can be written as $I(V_c - V_h)$, where I is the usually constant electrical current, V_c is the voltage across the electrochemical cell and V_h is the thermoneutral potential for electrolysis of water. Any power due to LENR is also part of the input power.

The output thermal power term is different for conductive or radiative losses. In the case of conduction, it is $K_c (T - T_b)$, where K_c is a “cell constant” in $W/^\circ C$, which can be determined in multiple ways. They include (a) measuring the slope of the cell temperature vs. input electrical power calibration curve, (b) fitting an analytical equation to the cooling history of a cell after the input power is turned off or (c) computing the constant from the conductivity and geometry of the thermal barrier. The T_b is the temperature of the usually water bath surrounding a heat flow calorimeter.

Conductive heat flow calorimeters have been used often in LENR experiments by Miles and others [12]. Radiative heat loss, without significant conduction is possible by the use of Dewar calorimeters, which have two walls with a vacuum between them, and cannot support conduction. The original Fleischmann and Pons calorimeters were such Dewars [2]. For them, the output thermal power term is $K_r (T^4 - T_b^4)$, where K_r is the coefficient for radiative heat transfer and the fourth power dependence is due to the Stefan–Boltzmann law. Like conductive systems, the radiative systems also required a stable outside temperature, usually a water bath. For both conductive and radiative heat flow calorimeters, the response times (time constants) are determined by the time it takes for the contents of the system to be transferred from the interior to the surroundings.

Equation (2) has two types of deficiencies. The first deals with the existing terms. There are multiple materials within the calorimeter. For electrolytic experiments, they include the electrolyte, metal electrodes and leads, plastic holders and electrical lead covers, a glass test tube and the oil. For Seebeck systems, they include those items, and also the air within the calorimeter. So, the first term is actually a sum of MC_p products, $\sum M_i C_{p_i}$. V_h is not constant

and varies during loading. And, the cell constant is sensitive to the electrolyte level. Secondly, there are two missing terms, one for work done on the atmosphere by the bubbles and the other for energy carried out of the open cell by the gases. These terms are small for low input powers and temperatures [13].

Given the above considerations, the equation for an isoperibolic calorimeter can be written, for low power operation, as:

$$\sum M_i C_{pi} \frac{dT}{dt} = I(V - V_h) + P_{LENR} - K_c (T - T_b). \quad (3)$$

The only unknown in this equation is P_{LENR} . The masses, specific heats and V_h are known from construction and tables. The cell constant is known from any of the methods already noted above. During a run, the input electrolysis current and voltage are measured. Both the cell temperature T and the bath temperature T_b are also measured as a function of time. If temperature readings from the cell are taken frequently, such as every second, then it is possible to smooth the $T(t)$ readings and fit them with an analytical curve to obtain good values for (dT/dt) .

2.2.2. Seebeck calorimeters

Figure 2 contains a schematic of a Seebeck heat flow calorimeter. Such heat flow calorimeter systems are containers, the walls of which are covered with thermoelectric devices or thermocouples (both called TE elements). Heat flows from the source to the interior air, and then through the thermoelectric elements to the constant temperature region. Experiments performed within Seebeck Calorimeters produce heat by (a) the electrolysis needed to free protons or deuterons for LENR, (b) one or more fans that are always on to produce a uniform internal air temperature, (c) resistive heaters to provide calibrations before, during or after LENR runs, and (d) the LENR. The action of these heat sources raises the temperature of one side of the TE devices relative to the other side, which is heat-sinked to the exterior reference temperature. Walls with water cooling or other means of producing a uniform temperature, such as the use of TE elements as heat pumps, are common. The voltages produced by individual TE elements are added by connecting them in series. The resistance of the TE elements is ignorable because virtually no current flows through them due to the high impedance of voltage measuring devices.

Like most instruments, Seebeck calorimeters have advantages and disadvantages. They can have larger internal volumes than other calorimeters. Seebeck calorimeters provide an alternative means of calorimetry, with a few different challenges to accurate measurements. Thermoelectric Devices and Thermocouples can respond quickly to changes in temperature. Like all calorimeters, Seebeck systems require understanding and calibration. The response time is set by thermal conductivity out of the LENR cell into the air within the Seebeck calorimeter.

Storms published an equation for performance of Seebeck calorimeters [14]. He wrote “Excess power (EP) is calculated according to the equation:

$$EP = A + B * V + C * V^2 - V_c * I_c - V_f * I_f \quad (4)$$

where V is the Seebeck voltage, V_c the voltage between the anode and cathode, I_c the current passing through the cell, V_f the voltage applied to the fans, I_f the current passing through the fans, and A , B , and C are constants obtained from calibrations”.

Another approach to the equation for a Seebeck calorimeter is based on the concept behind Eq. (2). There, the energy deposited within the calorimeter in some unit of time, that is, the net input power, is the difference between the total power entering the calorimeter and the thermal power leaving the calorimeter. As already noted, the increase in energy within the instrument in the time increment is the sum of the products of the interior masses and specific heats, times the rate of temperature change. Unlike most mass flow or isoperibolic calorimeters, there is a substantial volume of air within a Seebeck calorimeter. If both the Seebeck calorimeter and the interior experiment are taken to be cubic,

and it is assumed that the length of the side of the experiment is 10% of the length of a side of the calorimeter, the heat capacity of the air is about 3% of the heat capacity of the experiment, assumed to be all water.

The input power to Seebeck calorimeter with a fan to homogenize the internal air temperature can be written as:

$$P_{\text{in}} = I(V_c - V_h) + I_f V_f + P_{\text{LENR}} \quad (5)$$

The first term is the power needed for electrolysis of the light or heavy water in the LENR experiment, as above for isoperibolic calorimeters. The fan power is the product of the fan current I_f and voltage V_f , and P_{LENR} is the LENR power. The power exiting the calorimeter consists of (a) that passing by conduction through the TE modules, if they are used, (b) that passing through the parts of surfaces not covered with TE modules, also by conduction, and (c) power that is conducted through any other path, such as electrical or fluidic feedthroughs. If thermocouples, rather than TE modules, are used in a Seebeck calorimeter, the power exits by conduction through the four walls, top and bottom of the calorimeter. In either case, the overall Seebeck Calorimeter equation is:

$$\Sigma M_i C_{p_i} = I(V_c - V_h) + I_f V_f + P_{\text{LENR}} - \Sigma K_i (T_{\text{int}} - T_R), \quad (6)$$

where the K_i are constants related to the thermal conductivity and geometry of the walls and the temperature difference is between the interior of the calorimeter (T_{int}) and the reference temperature (T_R) of the walls or the exterior of the calorimeter.

2.2.3. Characteristics of calorimeters

Before reviewing the major specifications of calorimeters, in general, we note that it is possible to use some calorimeters in a differential mode. This involves having two identical calorimeters, one of which has the active LENR cell while the other contains an inactive (unpowered) cell with the same configuration. If they are near each other, both cells are subject to the same fluctuations in the temperature of the surroundings. Hence, comparison of the active and inactive cells enables computational removal of the effects of unwanted exterior fluctuations. Isoperibolic calorimeters can be configured as differential calorimeters if they are placed near each other in the same water bath. Seebeck calorimeters can be used similarly if they have a cylindrical shape, where the sides of the cylinder are heavily insulated. The bottom of the cylinder can be capped and placed on a single TE element. A colder constant temperature heat sink has to be on the other side of the TE element. It can be clamped at a constant temperature by use of TE elements, or by flow of water that has a well-controlled temperature. Then, heat flow from the calorimeter containing the LENR experiment to the heat sink will produce a voltage, which is measured. Similarly, heat will flow from another similar calorimeter and dead experiment to the same heat sink. Again, comparison of the two voltage signals permits cancellation of the effects of room temperature fluctuations. Loss of heat out of the top of the LENR experiment and calorimeter is an issue for cylindrical Seebeck calorimeters used in any configurations, either singly or in a differential mode.

Calorimeters for LENR experiments are scientific instruments, and like most instruments, they have a few key performance characteristics. They include:

- **Sensitivity:** Output value per internal Watt, usually Temperature (dT/dW) for Isoperibolic calorimeters or voltage (dV/dW) for Seebeck calorimeters. This is the slope of the calibration curve, which plots output values (T or V) versus input power (W).
- **Minimum Detectable Limit (MDL):** The lowest LENR power that can be measured. The MDL is determined by the noise on the output measurement.

- **Power range:** The lowest and highest powers, electrical and LENR, which can be handled by the calorimeter. The lowest powers are set by the MDL. The highest are due to temperature or voltage limitations of components of the LENR cell or calorimeter, or the sensors.
- **Time constants:** These limit the fastest temperature excursions in an experiment, which can be resolved. Ultimately are set by heat capacity and thermal conductivity of the experiment and calorimeter. They include the times it takes to heat up or cool down components of the cell and calorimeter, or the times it takes for heat to be transported to flowing coolant (for Mass Flow system) or to exterior temperature baths (for Heat Flow calorimeters).

3. Thermoelectric Devices and Thermocouples

Thermoelectric materials and devices are reciprocal, when they are configured properly. If they are powered electrically, they can pump heat from one side of a device to the other side (the Peltier effect). If they have different temperatures on two sides, a voltage will appear across the output leads (the Seebeck effect). Thermoelectric devices have a few chemical and geometrical characteristics, and one dominant performance parameter. Materials that exhibit thermoelectric effects are commonly doped semiconductors [15]. In the most common configurations, the thermoelectric materials are sandwiched between two ceramic plates, and connected in series. Figure 3 shows both the Peltier and Seebeck modes of operation, and the general design of a thermoelectric device [16].

The main performance parameter for thermoelectric materials and devices is denoted ZT , the TE Figure of Merit. It is determined by the material's electrical conductivity, thermal conductivity, and Seebeck coefficient (the ratio of generated volts to temperature difference) [17]. Values for ZT have increased over the decades due to the high interest

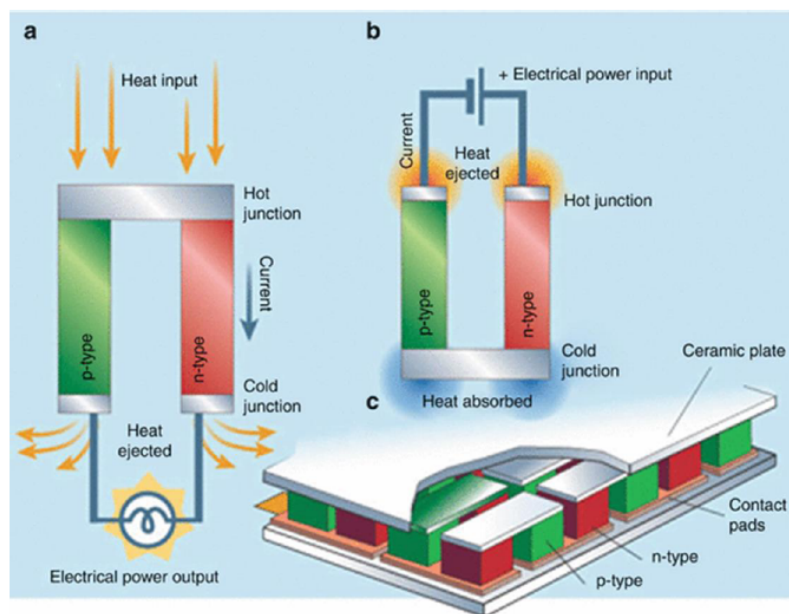


Figure 3. Schematic diagrams of thermoelectric elements (a) in the Peltier heat pump mode, (b) as Seebeck sensors of temperature differences, and (c) arrayed within a thermoelectric device.

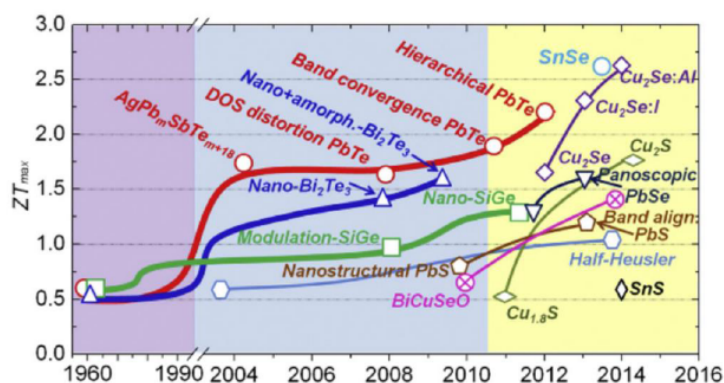


Figure 4. History of the primary performance specification (ZT) of thermoelectric materials for diverse thermoelectric materials.

in both use of thermoelectric materials, generation of electricity from waste heat and solid-state refrigeration free of compressor systems. Figure 4 shows the history of the evolution [18]. It also exhibits the compositions of diverse thermoelectric materials. In the recent past, there has been a great deal of interest and progress in thermoelectric materials with micro- and nano-structures. However, current performance remains short of the ZT value of about 4, which is needed for massive uses of thermoelectric devices in solid-state refrigerators and other applications.

As will be seen, thermocouples have also been used in Seebeck calorimeters for LENR experiments. They are intimate contacts between two metals with dissimilar electronic structures, usually produced by melting or welding together wires of the two materials. Like semiconductor thermoelectric materials, thermocouples produce voltages due to temperature differences. The voltage vs. temperature characteristics, and the compositions, of common thermocouples are available [19]. Figure 5 shows how thermocouples are used for practical temperature measurements [20]. Thermocouples have the important advantage of being small (less than 1 mm), so they can be inserted into systems to measure temperatures at specific points.

4. LENR Papers about Seebeck Calorimeters

Seebeck calorimeters were used for LENR experiments, and described in papers from 1990 to 2019. Table 1 contains a list of the papers, the references to which are in Appendix B. It is evident that Storms was one of the primary practitioners of Seebeck calorimetry. Figure 6 contains images of his Seebeck systems. The cylindrical 2003 system used thermocouples to develop a temperature-sensitive voltage. The other rectangular systems employed thermoelectric devices. Zhang was also a leader in the development and use of Seebeck calorimeters for LENR experiments. Plots in his papers show that the calorimeter is only one part of a system that supplies proper electrical voltages to and from the instrument and records data from it. The system also provides a stable temperature reference for the Seebeck calorimeters. Figure 7 contains examples of the published calibration curves for LENR Seebeck calorimeters.

5. Tabulation of Characteristics and Performance of Published Seebeck Calorimeters

The geometrical, physical and performance characteristics of the described calorimeters varied widely. A spread sheet of these factors was produced from the papers. Plots of the quantitative features of the reviewed calorimeters have been produced. Tables 2 and 3 summarize the physical and other characteristics, and the performance of published Seebeck calorimeters that were used in LENR experiments.

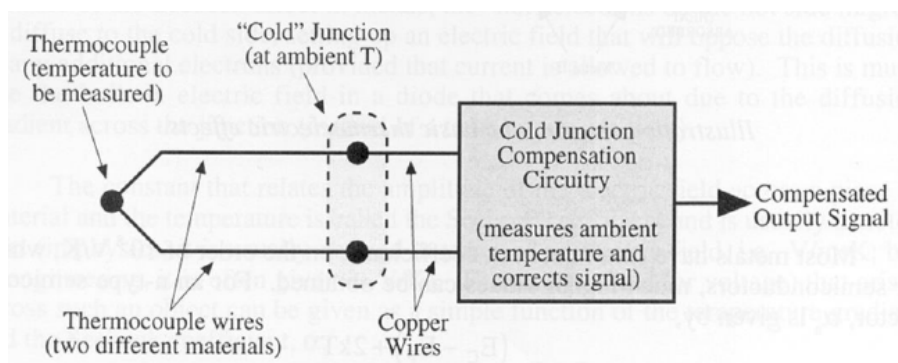


Figure 5. Schematic of a thermocouple with compensating circuitry for having the “cold junction” at temperatures above absolute zero.

The relationships between characteristics and performance of calorimeters are important, as they are for most scientific instruments. The Tables 2 and 3 provide quantitative information for making plots of such relationships. Four such graphs are shown in Fig. 8. Two data with the values of (4056, 190) and (4056, 160) were omitted from the plot of the inverse of the calibration constant (mV/W) vs. surface area (cm²) in order to make the lower such values more visible.

Table 1. Summary of the papers on LENR Seebeck calorimeters examined in this review.

Authors	Year	Paper
Oriani, Nelson, Lee, Broadhurst	1990	Calorimetric Measurements of Excess Power Output During the Cathodic Charging of Deuterium into Palladium
Oriani	1996	An Investigation of Anomalous Thermal Power Generation from a Proton Conducting Oxide
Bush, Lagowski	1998	Methods of Generating Excess Heat With the Pons and Fleischmann Effect: Rigorous and Cost-Effective Calorimetry, Nuclear Products Analysis of the Cathode and Helium Analysis
Zhang, Zhang Zhang	2001	Primary Calorimetric Results on Closed Pd/D ₂ O Electrolysis Systems by Calvet Calorimetry
Storms	2003	Maw to Make a Cheap and Effective Seebeck Calorimeter
Storms	2003	Use of a Very Sensitive Seebeck Calorimeter to Study the Pons–Fleischmann and Letts Effects
Storms	2005	Description of a Sensitive Seebeck Calorimeter Used for Cold Fusion Studies
Zhang, Dash, Wang	2005	Seebeck Envelope Calorimetry with a Pd/D ₂ O + H ₂ SO ₄ Electrolytic Cell
Zhang, Dash	2007	Excess Heat Reproducibility and Evidence of Anomalous Elements After Electrolysis in Pd in D ₂ O + H ₂ SO ₄
Storms	2008	The Method and Results Using Seebeck Calorimetry
Zhang, Dash, Zhang	2008	Construction of a Seebeck Envelope Calorimeter and Reproducibility of Excess Heat
Zhang	2009	Construction, Calibration and Testing of a Decimeter-Size Heat-Flow Calorimeter
Macleod, Fork, Lam, Berlinguette	2018	Electronic Supplementary Material for System Identification Calorimetry
Letts, Cravens	2019	Building and Testing a High Temperature Seebeck Calorimeter








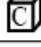




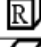

Authors	Dimensions	Shape	Frame	TEs or TCs	Insulation
Oriani, Nelson, Lee, Broadhurst (1990)	25cm (D) x 81 cm (H)		Cylinder	1961 TCs	Thermal & electrical insulation
Oriani (1996)			Box	335 x 2 TCs	Insulated jacket
Bush, Lagowski (1998)	3 cm x 3cm x 9 cm		Box	~100 TCs	Thermal insulation
Zhang, Zhang, Zhang (2002)	15 mm (D) x 80 mm (H)		Cylinder	496 TCs	Asbestos
Storms (2003)	12.7 cm (inner D)		PVC Pipes	~1000 TCs	Cooling water
Storms (2003)	17.78 cm x 17.78 cm x 17.78 cm		Box		Wooden enclosure
Storms (2005)	13.9 cm x 6.9 cm x 14.8 cm		Box		Waterproof Epoxy Paint
Zhang, Dash, Wang (2005)	18.3 cm x 18.3 cm x 18.3 cm		Box		Styrofoam
Zhang, Dash (2007)	18.3 cm x 18.3 cm x 18.3 cm		Box		Styrofoam
Storms (2008)	17.78 cm x 17.78 cm x 17.78 cm		Box		Waterproof paint
Zhang, Dash, Zhang (2008)	26 cm x 26 cm x 26 cm		Box	18796 TCs	Styrofoam
Zhang (2009)	26 cm x 26 cm x 26 cm		Box	18796 TCs	Styrofoam
Macleod, Fork, Lam, Berlinguette	25.9 cm x 25.9 cm x 23.4 cm		Box	6 Heat Flow Sensors	Aluminum isothermal enclosure
Letts, Cravens (2019)	7.62 cm x 7.62 cm x 38.1 cm		Rectangular Block	16 TCs + TE devices	A layer of high temperature insulation

Table 2. Compilation of the characteristics in LENR reports on Seebeck calorimeters. D is the diameter, H the height, R the rectangular prism, and C is the cube.

Another plot relates the maximum power that can be dissipated within the published LENR Seebeck calorimeters to their volume. It is shown in Fig. 9. The data in Tables 2 and 3, and the plots in Figs. 8 and 9 are discussed in Section 6.

6. Discussion of Published LENR Seebeck Calorimeters

The data in Figs. 7–9 show that Seebeck calorimeters used for LENR experiments have some commonalities and differences. Their shapes are cylindrical, or prismatic in most cases cubic (C) or rectangular (R). But, the volumes of the calorimeters varied widely from 81 to 39 760 cm³. The number of TE elements was also highly variable from less than 10 to about 1000 thermocouples. The type of exterior insulations was also quite variable.

The performance of the published Seebeck calorimeters was also quite different. The power handling capacities ranged from 0 to 80 W. Most of the instruments were limited in their maximum input power to about 10–25 W. Two instruments were designed for powers of only less than 1 W. The output signals ranged from a few mV to 9 V. The uncertainty related to the Minimum Detectable Limit (MDL) of input power was in the range of 10–87 mW. The

Authors	Power Range	Voltage Range	Minimum milliWatts	Temp. Range	mV/ W	Fan & Power	Calibration Method
Oriani, Nelson, Lee, Broadhurst (1990)	0 – 18 W	0 – 0.009 V	+/- 20 mW		0.5		Electric current through coil of nichrome wire set
Oriani (1996)	63 – 80 W	0.072 – 0.083 V		400 – 410 °C	1.1	1	Electric power
Bush, Lagowski (1998)	0 – 0.1 W		+/- 10 mW	450 °C			Controller
Zhang, Zhang, Zhang (2002)	0 – 0.5 W						Pd electrode acting as heater
Storms (2003)	0 – 10 W	0 – 0.06 V	+/- 35 mW		5.2	2	
Storms (2003)	5 – 20 W	0.02 – 0.09 V		47 °C	5	3 (5.3W)	Resistor made from platinum
Storms (2005)	2 – 16 W	0.02 – 0.21 V	+/- 60 mW		13.2	1	Resistor heat
Zhang, Dash, Wang (2005)	0 – 20 W	0 – 0.1 V		10 – 90 °C	5.5	1 (2.08W)	Pt/H ₂ O + H ₂ SO ₄ electrolytic cell
Zhang, Dash (2007)	9.3 – 11.1 W		+/- 87 mW	79 – 90 °C	5.7		Calibration resistor
Storms (2008)	0 – 12 W	0 – 0.14 V	+/- 35 mW	20 – 70 °C	12	1 (0.75W)	Dual calibration with Joule & electrolytic power
Zhang, Dash, Zhang (2008)	0 – 22.3 W	0 – 4 V	+/- 40 mW		190	1 (2.5W)	Electrical heater
Zhang (2009)	0.1 – 50 W	0 – 9 V			160	1 (2.5W)	Electrical heater
Macleod, Fork, Lam, Berlinguette (2018)	0 – 5 W	0 – 5 V					
Letts, Cravens (2019)	0 – 75 W	2.5 – 3.9 V		200 – 300°C	15.8		Resistive heating power

Table 3. Compilation of the performance of LENR Seebeck calorimeters.

temperature ranges that the published data showed were as low as 20°C and as high as 450°C. Powers required for the internal air circulation fans ranged from 0.75 W to a rather high value of 5.3 W. Electrical (resistive) heating was most commonly used for calibration, although electrolysis power was employed in three cases.

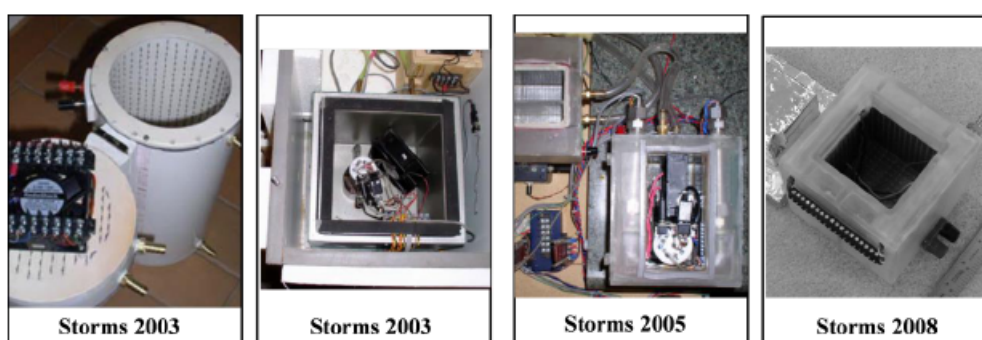


Figure 6. Images of Seebeck LENR calorimeters designed, constructed, calibrated and used by Storms.

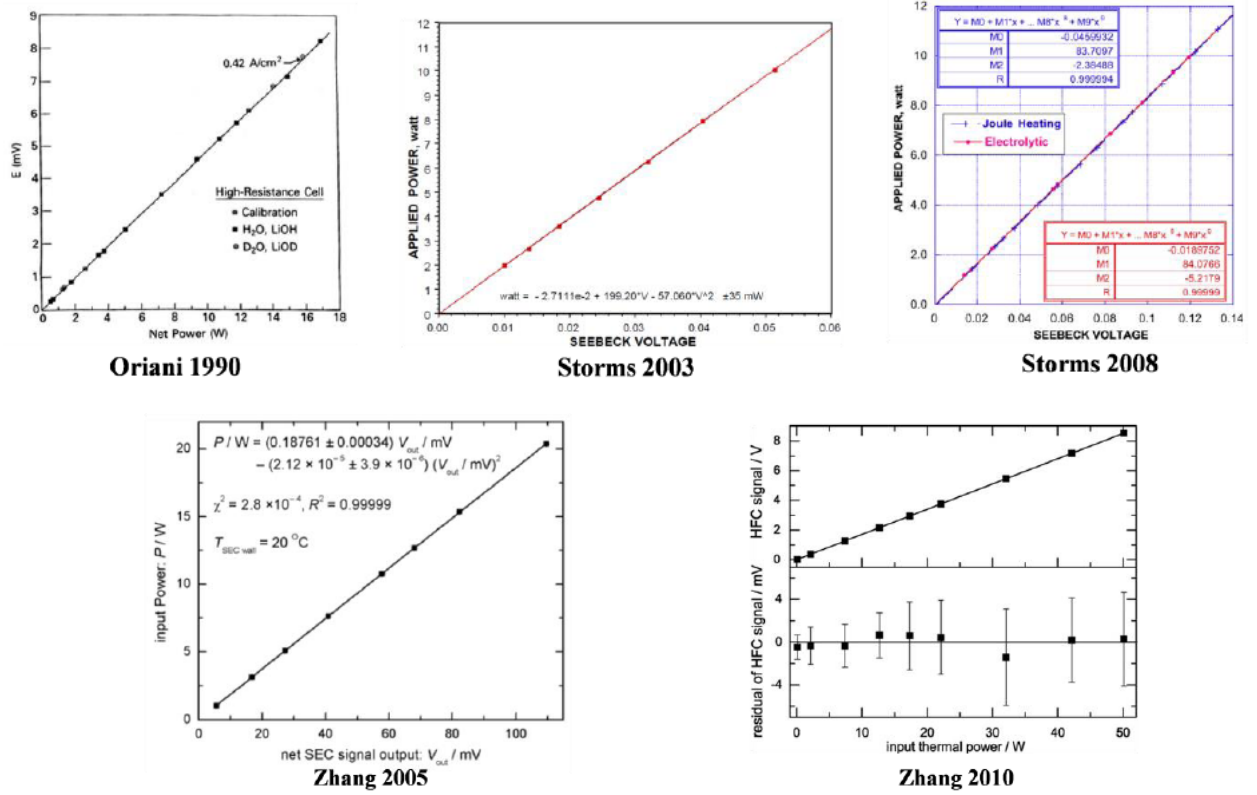


Figure 7. Example calibration curves of Seebeck calorimeters for LENR experiments.

It is important to relate the static descriptive characteristics of LENR calorimeters to their dynamic performance. Such correlations might provide significant information for designing new Seebeck calorimeters. The relationships between two characteristics (area and volume) and two performance parameters (MDL and inverse of the calibration constant), shown in Fig. 8 are not helpful. There is no clear trend in any of the four plots. We also plotted the maximum power that would be handled by the calorimeters against their volume. The result is in Fig. 9. It might be expected that the larger the calorimeter, the more power it could handle. The red curve is a linear fit to the (0,0) point and tabulated data. The correlation is poor. The lack of clear trends in performance with the calorimeter characteristics motivated us to consider ways to estimate such relationships, which are the subject of Section 7.

7. Scaling of the Size and Performance of Seebeck Calorimeters

It is possible to write a simple equation for how the performance (output) of a Seebeck calorimeter scales with its size. Assume that the calorimeter is a cube with edge length of D , that the thermoelectric units covering all interior walls have area A , and that the TE calibration factor is K_{TE} , so that the voltage output of each TE elements is $K_{TE} \Delta T$, where the temperature difference is that between the inside of the calorimeter and the thermally stabilized walls. Hence, the voltage output of the calorimeter is the number of TE elements times their individual output voltages, assuming the usual serial connection:

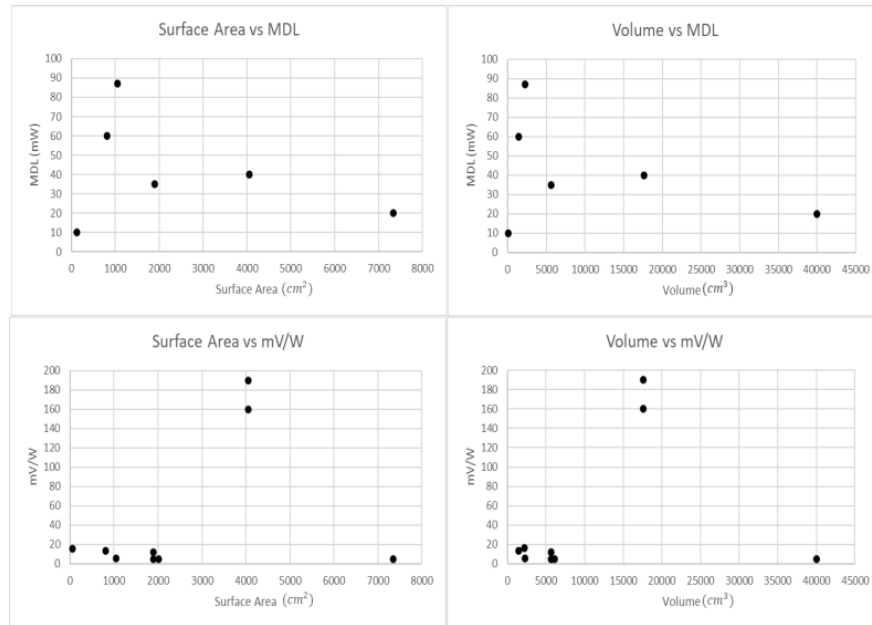


Figure 8. Relationships of the Minimum Detectable Power (MDL) (*top*) and inverse of the calibration constant (mV/W) (*bottom*) to the calorimeter area (*left*) and calorimeter volume (*right*).

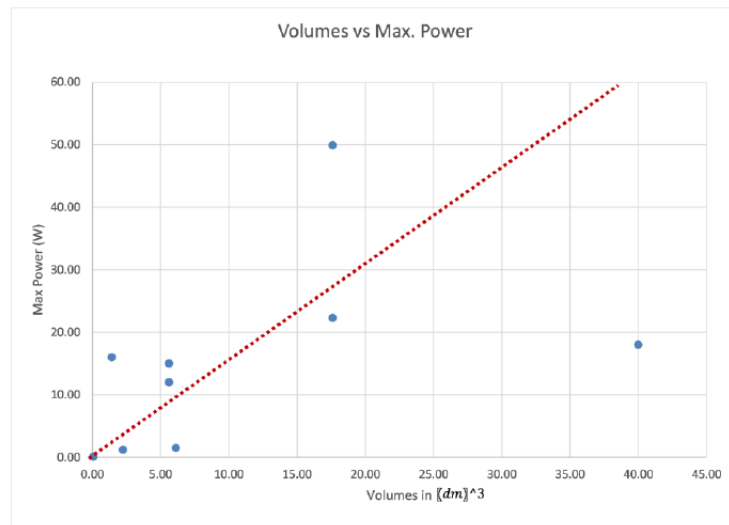


Figure 9. Plot of the maximum power of LENR Seebeck calorimeters as a function of their volume. The red line is a fit to the scattered data.

$$V = (6D^2/A) K_{TE} \Delta T. \quad (7)$$

This equation shows that the output performance varies with the square of the calorimeter linear size for fixed TE elements (K_{TE} and A).

Another relationship of interest is the maximum steady state power P_M of a Seebeck calorimeter as a function of volume D^3 [3]. Assume that the highest air temperature that the TE elements can tolerate is T_M . The power balance between the air inside of the calorimeter, heated by the combination of electrolysis, the fan and LENR, and the conduction of thermal power through the six walls, can be written as $P = [K_W (T_M - T_R)/W] 6D^2$, where K_W is the thermal conductivity of the walls of thickness W . Hence, the ratio of maximum total input power (not only i_{LENR}) to the calorimeter volume is

$$P_M/\text{Volume} = [K_W(T_M - T_R)/W] 6/D. \quad (8)$$

8. Conclusion

The review of Seebeck calorimeters in this paper raises the question about similar reviews of calorimeter characteristics and performance for other types of calorimeters. We do not know of related reviews for either LENR mass flow calorimeters, of which there are few, or LENR heat flow isoperibolic calorimeters, of which there are many. It is unclear now if there is any one best type of calorimeter, or if there is a best design for any type of calorimeter for LENR experiments. It ought to be possible to rank the minimum detectable LENR power levels for all published designs, but that is not particularly useful. The goal of LENR research is to produce LENR powers that are much larger than such minimum detectable limits. And, there are several other important factors, such as the maximum power that can be handled and the size of the experiments that a calorimeter can accommodate.

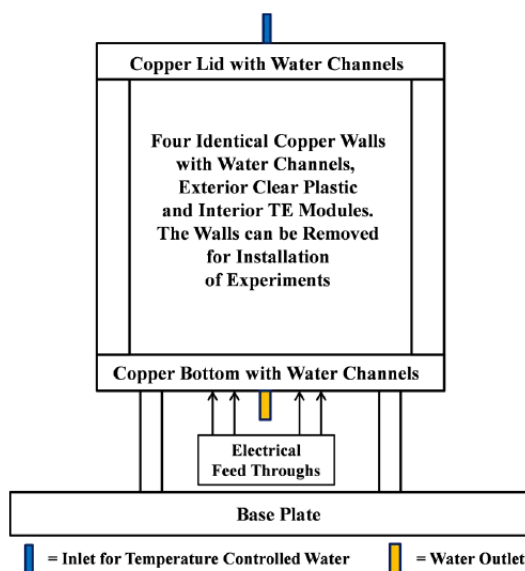


Figure 10. Schematic diagram of the calorimeter being made for the LENR Energy and Spectroscopy Laboratory of The George Washington University. Insulation, which will cover all sides, is not shown. A fan will be mounted on the interior of the calorimeter lid.

The results of this review might be useful to scientists considering the use of Seebeck calorimeters for LENR experiments. They also form the basis for the design of a new Seebeck calorimeter being made for our laboratory. The conceptual design for that instrument is shown in Fig. 10. There are two major design goals for this Seebeck calorimeter. One is performance, with a sensitivity and noise level that will enable detection of LENR powers as low as a few tens of milliwatts. The other goal is ease of use. The base plate, legs and calorimeter bottom will form a unit, with walls and calorimeter top that are removable for set up of experiments.

References

- [1] https://en.wikipedia.org/wiki/List_of_chemical_analysis_methods.
- [2] M. Fleischmann and S. Pons, Electrochemically induced nuclear fusion of deuterium, *J. Electroanal. Chem.* **261** (1989) 301–308 and Errata in Vol. 263.
- [3] D.J. Nagel and M.E. Melich (Eds.), Calorimetry, *Proc. of ICCF-14*, 2008, pp. 1–16.
- [4] E. Storms, *The Science of Low Energy Nuclear Reactions*, World Scientific, 2007, pp. 53–61.
- [5] E. Storms, *The Explanation of Low Energy Nuclear Reaction*, Infinite Energy Press, 2014, pp. 106–109.
- [6] M.C.H. McKubre and F. Tanzella, Mass flow calorimetry, *Proc of ICCF-14*, D.J. Nagel and M.E. Melich (Eds.), 2008, pp. 32–46.
- [7] A. Kitamura, A. Takahashi, R. Seto, Y. Fujita, A. Taniike and Y. Furuyama, Brief summary of latest experimental results with a mass-flow calorimetry system for anomalous heat effect of nano-composite metals under D(H)-gas charging, *Current Science* **108** (4) (2015) 589–593.
- [8] M. Fleischmann and S. Pons, Calorimetry of the Pd–D₂O systems from simplicity via complications to simplicity, *Phys. Lett. A* **176** (1993) 118–129.
- [9] W.-S. Zhang, Construction, calibration and testing of a decimeter-size heat-flow calorimeter, *Thermochimica Acta* **499** (2010) 128–132.
- [10] E. Storms, The method and results using Seebeck calorimetry, in *Proc of ICCF-14*, 2008.
- [11] <http://www.ling.fju.edu.tw/hearing/historical%20review1821.htm>.
- [12] M.H. Miles, Fundamentals of isoperibolic calorimetric measurements in cold fusion experiments, to be published.
- [13] M.H. Miles, Private communication.
- [14] E. Storms, Use of a very sensitive Seebeck calorimeter to study the Pons–Fleischmann and Letts effects, *Proc. of the Tenth Int. Conf. on Cold Fusion*, P.L. Hagelstein and S.R. Chubb (Eds.), World Scientific, New York, 2006, pp. 183–197.
- [15] https://en.wikipedia.org/wiki/Thermoelectric_materials.
- [16] M. Zhou and J. He, Nanostructured thermoelectric materials, in *Encyclopedia of Nanotechnology* B. Bhushan (Ed.), Springer, Dordrecht, 2012.
- [17] https://en.wikipedia.org/wiki/Thermoelectric_materials#device_efficiency.
- [18] X. Zhang and L.-D. Zhao, Thermoelectric materials: Energy conversion between heat and electricity, *J. Materiomics* **1** (2015) 92–105, <http://dx.doi.org/10.1016/j.jmat.2015.01.001>.
- [19] https://www.engineeringtoolbox.com/thermocouples-d_496.html.
- [20] <https://www.sciencedirect.com/topics/engineering/cold-junction>.

Appendix A. Qualitative Comparison of the Major Types of LENR Calorimeters

The varied types and designs of calorimeters, which have been used in LENR research, are the result of the preferences of experimenters, the tools available to them, and the characteristics and performance of particular calorimeters. A qualitative comparison of the three major types of calorimeters used to date for LENR experiments follows.

Appendix A.1. Volume

LENR calorimeters can be made for diverse internal shapes and sizes. Simple geometrical forms, such as cylinders or rectangular prisms are commonly used. The volumes for most mass flow and isoperibolic heat flow calorimeters

have commonly been relatively small. For Seebeck calorimeters, one can place the temperature sensing devices, the TE elements, in electrical series surrounding the internal volume. Doing this allows studying heat production in larger volumes compared to mass flow and isoperibolic calorimeters.

Appendix A.2. Sensors

For mass flow calorimeters, temperature sensors for measuring inlet and outlet temperature of the surrounding fluid, and flow rate sensors for measuring the surrounding fluid flow rate, are required. For heat flow isoperibolic calorimeters, temperature sensors are sufficient. Either thermoelectric devices or thermocouples can be used for heat flow Seebeck calorimeters, with TE devices being the most common.

Table A1. Comparison of types of calorimeters.

Characteristics	Mass flow calorimeters	Heat flow calorimeters	
		Isoperibolic	Seebeck
Internal volumes	Medium	Small to medium	Medium to large
Sensors	T and flow rate	Temperature	TE devices
Heat Paths	Cathode to electrolyte to solids and to: Water or oil	Water bath	Constant T walls
Time constant due to:	Thermal conductivity and thermal capacity of: Water or oil	Thermal barrier	Air in calorimeter
MDL limited by:	Cathode area changes due to bubbles and: Flow fluctuations	Bath T variations	Reference T variations

T is the Temperature, TE the thermoelectric and MDL is the minimum detectable power level.

Appendix A.3. Heat paths

For mass flow calorimeters, the temperature difference between inlet and outlet of the surrounding liquid occurs due to the heat production inside the container. Thus, the heat path for this type of calorimeter is through the walls of the experiment to the surrounding fluid. For isoperibolic calorimeters, heat flow is from heat source to a constant temperature surrounding water bath. For Seebeck calorimeters heat path is from the heat source through the internal air to the constant temperature walls. Insulation is commonly used for heat flow calorimeters to help maintain the constancy of the surrounding temperature.

Appendix A.4. Time constants

The response times of all of the LENR calorimeter types are limited to the medium into or through which the heat flows. For mass flow calorimeter, this is surrounding liquid. For isoperibolic calorimeters, the path is through the thermal barrier between the heat source and the surroundings. For Seebeck calorimeters, the generated heat must warm the air inside calorimeter.

Appendix A.5. Minimum detectable powers

For all electrochemical LENR experiments, variations in the cathode area due to transient coverage by bubbles can influence or limit the minimum detectable LENR power level. For mass flow calorimeters, fluctuations in the flow

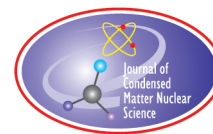
rate determine the minimum detectable power of the calorimeter. Therefore, using mass flow controllers, or weighing and timing, is usually done to obtain precision in the flow measurement. Both of the heat flow calorimeters require a reference temperature. Therefore, their minimum detectable LENR power levels are limited to the precision and stability of the measured reference temperature.

The following table shows the bibliography of papers on use of Seebeck calorimeters for LENR experiments.

Appendix B. The bibliography of papers on use of Seebeck calorimeters for LENR experiments.

Authors	Title	Reference
R.A. Oriani, John C. Nelson, Sung-Kyu Lee, J. H. Broadhurst	Calorimetric measurements of excess power output during the cathodic charging of deuterium into palladium	<i>Fusion Technol.</i> 18 (1990) 652
R.A. Oriani	An investigation of anomalous thermal power generation from a proton conducting oxide	<i>Fusion Technol.</i> 30 (1996) 281
Ben Bush and J. J. Lagowski	Methods of generating excess heat with Pons and Fleischmann effect: rigorous and cost-effective calorimetry, nuclear products analysis of the cathode and helium analysis	<i>Proc. of 7th Int.. Conf. on Cold Fusion</i> , 1998, p. 98
Wu-Shou Zhang, Zhao-Fu Zhang, Zhong-Lianf Zhang	Primary calorimetric results on closed Pd/D ₂ O electrolysis systems by calvet calorimetry	<i>Proc. of 9th Int.. Conf. on Cold Fusion</i> , 2002, p. 431
Edmund Storms	How To make a cheap and effective Seebeck calorimeter	<i>Proc. of 10th Int.. Conf. on Cold Fusion</i> , 2003, pp. 269–272
Edmund Storms	Use of a very sensitive Seebeck calorimeter to study the Pons–Fleischmann and Letts effects	<i>Proc. of 10th Int.. Conf. on Cold Fusion</i> , 2003, pp. 183–197
Edmund Storms	Description of a sensitive Seebeck calorimeter used for cold fusion studies	<i>Proc. of 10th Int.. Conf. on Cold Fusion</i> , 2005, pp. 108–116
Wu-Shou Zhang, John Dash, Qiongshu Wang	Seebeck envelope calorimetry with A Pd–D ₂ O + H ₂ (SO) ₄ electrolytic cell	<i>J. Condensed Matter Nucl. Sci.</i> 2005, pp. 86–96
Wu-Shou Zhang and John Dash	Excess heat reproducibility and evidence of anomalous elements after electrolysis in Pd in D ₂ O + H ₂ SO ₄	<i>Proc. of 10th Int.. Conf. on Condensed Matter Nucl. Sci.</i> , 2007, pp. 202–216
Edmund Storms	The method and results using Seebeck calorimetry	<i>Proc. of 14th Int.. Conf. on Condensed Matter Nucl. Sci.</i> , 2008, pp. 11–25
Wu-Shou Zhang, John Dash, Zhong-Liang Zhang	Construction of a Seebeck envelope calorimeter and reproducibility of excess heat	<i>Proc. of 14th Int.. Conf. on Condensed Matter Nucl. Sci.</i> , 2008, pp. 26–31
Wu-Shou Zhang	Construction, calibration and testing of a decimeter-size heat-flow calorimeter	<i>Thermochimica Acta</i> 499 (1–2) (2009) 128–132

Macleod, Fork, Lam, Berlinguette Letts and Cravens	Electronic supplementary material for system identification calorimetry Building and testing a high temperature Seebeck calorimeter	https://arxiv.org/ftp/arxiv/papers/ 1808/1808.04518.pdf , 2018 <i>J. Condensed Matter Nucl. Sci.</i> 29 (2019) 334–347
--	--	--



Research Article

Basics of Air-Flow Calorimetry

Jacques Ruer*

SFSNMC, France

Abstract

In the Mass Flow Calorimetry method, the heat released by an LENR reactor under test is measured by monitoring the temperature increase of a known flow of fluid passing over it. In the Air Flow Calorimetry method (AFC), the fluid is air. AFC appears to be a relatively simple method to measure the amount of heat produced by an LENR reactor. It is well suited when the LENR reactor surface temperature is high. It is easier to build than mass flow calorimeters using water-cooled or oil-cooled systems. Basically, the calorimeter is designed such that all the heat produced by the device under test is transferred to a known mass flow of cooling air. The accuracy of the method is governed by the control of the heat losses, the mass flow-rate of cooling air, the air heat capacity, the measure of the average air temperatures at inlet and outlet. Transpiration cooling is an efficient design to minimize the heat losses. The AFC method can be applied to reactors of any size and surface temperature. Its use is restricted to the testing of reactors that work continuously, because thermal equilibrium must be reached to make valid measurements. A thorough calibration procedure is essential to minimize the influence of errors on mass flows and temperature differences.

© 2020 ISCMNS. All rights reserved. ISSN 2227-3123

Keywords: Air flow calorimetry, Air heat capacity, Calibration, Flow meters, Heat measurement, High temperature, Transpiration cooling

1. Introduction

In the Mass Flow Calorimetry method, the heat released by a hot object is measured by monitoring the temperature increase of a known flow of fluid passing over it [1].

In the Air Flow Calorimetry method (AFC) the fluid is air. AFC appears to be a relatively simple method to measure the amount of heat produced by an LENR reactor. A recent example of the method was presented by Mizuno [2]. It is well suited when the LENR reactor surface temperature is high. It is easier to build than mass flow calorimeters using water-cooled or oil-cooled systems [1–3]

Basically, the calorimeter is designed such that all the heat produced by the device under test is transferred to a known mass flow of cooling air. According to the first principle of thermodynamics the rise of temperature of the air flow between the inlet and the outlet of the calorimeter is linked to the heat input by Eq. (1).

$$Q = C_{p\ m} (T_{out} - T_{in}) + Losses, \quad (1)$$

*E-mail: jsr.ruer@orange.fr.

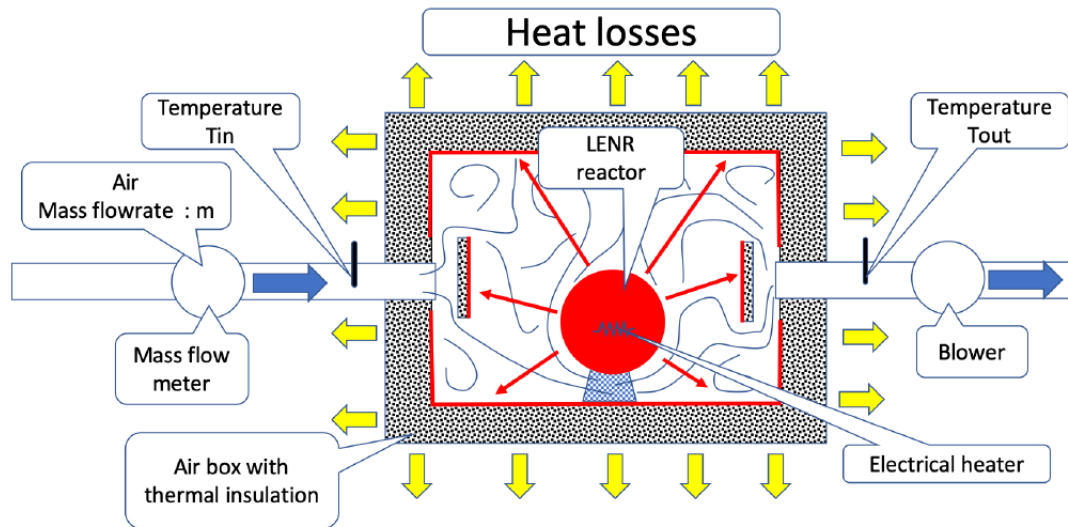


Figure 1. Sketch showing the main AFC features. The reactor tested is placed in an enclosed insulated box. A flow of air exports the heat released. Some heat is lost through the walls because the insulation is not perfect.

Q is the heat power (W), C_p the air heat capacity ($\text{J kg}^{-1} \text{K}^{-1}$), m the air mass flow rate (kg s^{-1}).

The AFC box that contains the reactor cannot be perfectly insulated. The losses must be taken into account. The method is well suited for stable continuous processes operated during periods much longer than the transient temperature evolution during the start-up phase. By nature, AFC is not applicable for the study of short-lived phenomena. For a discussion of this see also [1].

Transients may be analyzed by the technique developed by Higgins and Letts [4], but this is beyond the scope of this paper. In the following it is supposed that the heat flow is constant and that all measurements are taken when equilibrium conditions are reached.

Although the basic principle is simple, the accuracy of the method is influenced by many factors. We will show that AFC is able to deliver meaningful results with a careful calibration. This paper is an overview of the main parameters involved in air flow calorimetry, the possible problems that may affect the accuracy and the potential solutions to solve these problems.

2. Review of AFC Parameters

Figure 1 is a schematic view of an AFC system. AFC is governed by the following parameters:

- Air mass inlet and outlet – influence of enclosure leaks.
- Air heat capacity.
- Air temperatures at inlet and outlet.
- Heat losses: the insulation of the enclosure is not perfect.

These different factors are detailed later. But it is first necessary to examine how the heat released by the reactor is

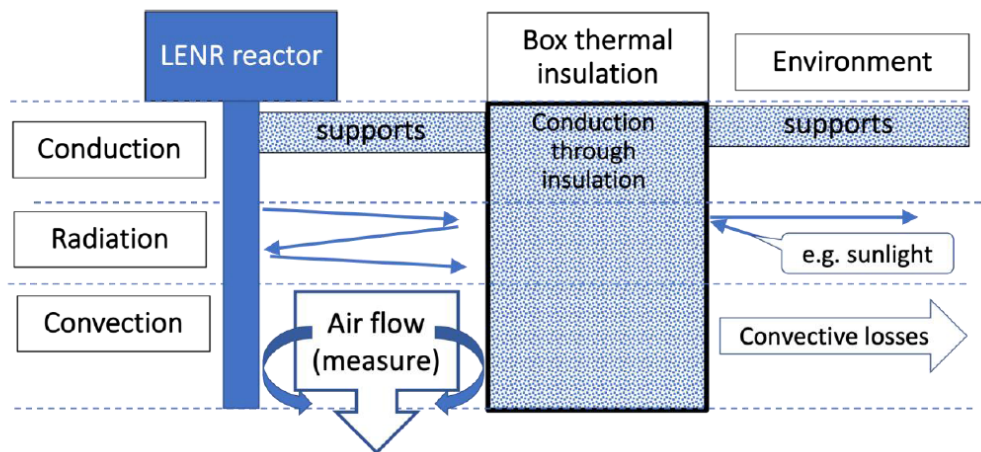


Figure 2. Heat transfer phenomena in AFC.

transferred to the flow of cooling air.

2.1. Transfer of heat between the hot device and air in AFC

How the heat is transferred from the hot LENR device to the air must be considered in detail. The different heat transfer mechanisms are summarized in Fig. 2. Conduction, radiation and convection must be taken into account.

- **Conduction:** Heat is conducted through the wall insulation and the mechanical supports that hold the LENR device in place. Insulation and supports must be designed to minimize the heat lost by conduction to the environment.
- **Radiation:** Air is transparent to infrared, at least if the dimensions of the enclosure are small enough to neglect the absorption by the tiny amounts of H_2O and CO_2 in the atmosphere. All the heat radiated by the reactor hits the walls. If the walls are coated by a reflective surface the infrared photons bounce several times between the solid surfaces contained in the box. Finally, all photons are absorbed by the solids. Heat is then transferred to the air by convection, unless it escapes to the environment via conduction through the box thermal insulation.
- Because the surface area of the walls is much larger than the reactor surface area the largest share of the infrared heat is exchanged to the air by the walls. The heat lost across the thermal insulation is evacuated to the environment by convection in free air and also by radiation. The room environment influences these exchanges. If a stream of air or if sunlight hit the box the thermal behavior is altered. Precautions should be taken to avoid a direct exposure of the box to uncontrolled air flows or the sun at any time of the day
- Radiation from the reactor can affect the sensors that monitor the air flow temperature if they are in direct view of the reactor, especially if the LENR reactor is very hot. To avoid this disturbance a screen should be arranged to block the direct view.
- **Convection:** Inside the box convection is the only useful heat transfer mechanism as far as AFC is considered. The surface area and the heat exchange coefficients between the reactor and the cooling air and between the walls and the air have an influence on the equilibrium surface temperature of the reactor and of the walls.

3. Influence of AFC size on Reactor Temperature

From this analysis we can conclude that the design of the AFC box has an influence on the relationship between the reactor power and its surface temperature.

Figure 3 shows an example. A simplified model calculates the behavior of an LENR reactor installed inside two different boxes with different wall areas. For a given heat power the reactor is hotter if it is located in the small box. Many authors report a correlation between the reactor temperature and its power. Therefore great care must be devoted to the analysis of measurements made by use of an AFC.

4. Influence of Heat Losses

Any heat that is not carried away by the cooling air flow is not measured directly. The calorimeter enclosure must be leak-free and a good thermal insulation is required to minimize the heat losses. The energy input of the air blower must be taken into account. An experimental discussion is provided in [2].

The heat lost through the walls depends on the insulation quality but also on the external conditions. The heat loss is governed by the surface area of the box walls and by the temperature difference between the inner face of the wall insulation and the environment. We have seen that the smaller the box, the higher the wall equilibrium temperature. The trade-off is not easy to find. We present a solution to this problem in the next section.

Other features of the calorimeter may have some impact on accuracy. For example, if the air inlet and air outlet are installed at different locations on the calorimeter enclosure the temperature distribution inside the air box is affected and heat losses are modified [56].

The hottest air tends to gather under the roof of the enclosure. It is therefore advisable to locate the air exit at the top in order to minimize the quantity of hot air accumulated in the box.

5. Transpiration Cooled Screen (TCS)

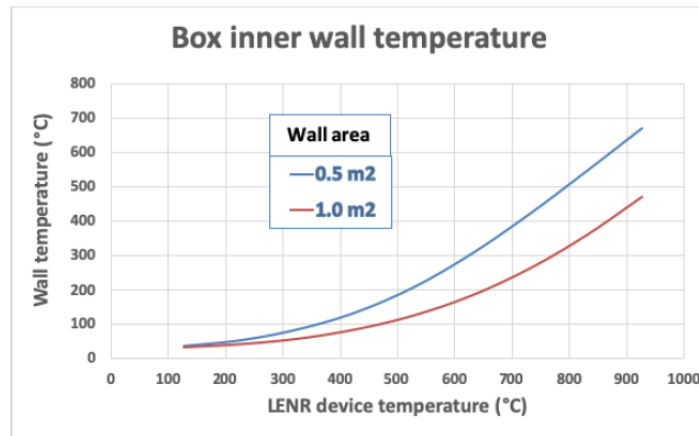
Transpiration cooling of a hot surface is caused by a flow of cool gas across the porous surface. Figure 4 shows for example the conceptual view of a gas turbine blade designed with transpiration cooling. Figure 5 shows a schematic view of an AFC system where the reactor is confined in an internal box made of Transpiration Cooled Screens (TCS). The cooling air percolates through the screens from the outside of the box to the internal volume. The air is pumped by a blower. With a proper design, all the heat received by the screens is transferred to the airflow.

Let us consider the heat flow on one of these screens (Fig. 6). On the inner face a given heating power is received (by example via radiation). The air flows through the screen with a space velocity V (assuming no solid in the screen). The screen thickness is L and the thermal conductivity of the screen material is λ . The screen material is ideally made of a porous material such as a layer of ceramic fibers. A numerical model has been written to simulate this. It uses an iterative method to calculate the temperature distribution of the solid and the air within the TCS. The calculation requires the introduction of the heat capacity of the solid to solve the transient evolution of the temperatures. However, the heat capacity has no influence on the temperature distribution at equilibrium.

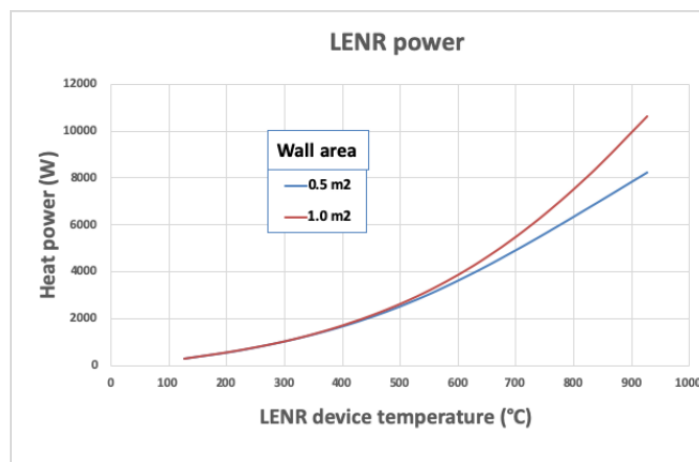
The model shows that the behavior of the TCS depends on the value of the ratio F :

$$F = \frac{\lambda}{L\rho C_p V} \quad (2)$$

F represents the ratio of the heat transported by the conduction in the solid and the heat transported in the reverse direction by the air flowing through the screen. Figures 7 and 8 present typical results. In Fig 7, the screen is made of a heat conductive metal (steel wool). The F factor is larger than 1. There is a large temperature gradient on the outer face of the screen, indicating that heat is lost to the environment. Such a TCS is inefficient.



(a)



(b)

Figure 3. Example of the interaction between the reactor and airflow calorimeters of different sizes. Model hypotheses: The insulation of the box is perfect. All the heat radiated by the reactor is absorbed by the box wall and exchanged to the cooling air. Convection exchange coefficient: $20 \text{ W m}^{-2} \text{ K}^{-1}$ on all surfaces, emissivity is 0.8, LENR reactor surface area 0.1 m^2 , blue curves, box surface area 0.5 m^2 , red curves, box surface area 1.0 m^2 the size of the box has an effect on the reactor surface temperature at a given power level. (a) Relationship between the temperature on the reactor surface and the box inner wall temperature. (b) Relationship between the reactor power and its surface temperature.

On the other hand, Fig. 8 shows the temperature distribution calculated in a screen made of an insulating fiber mat. The temperature gradient on the outer face is negligible. All the heat is recovered by the cooling air. There is basically no heat loss to the environment.

Transpiration cooling is therefore a very efficient arrangement to eliminate the heat losses in AFC. It eliminates the interference between the AFC size and the reactor temperature because the TCS inner surface is kept at a moderate

temperature level, close to the air outlet temperature.

6. Testing High Temperature Reactors

Some reactors are operated at a high temperature, well in excess of 300°C. AFC can be applied with the setup configuration shown in Fig. 9. The reactor is wrapped with an insulation mantle that creates a temperature drop between the reactor itself and the external surface of the mantle. The insulation thickness must be selected in order to obtain the desired operational characteristics. The mantle temperature governs the heat transfer while its thickness dictates the reactor temperature. Test of several mantles with increasing thicknesses may be required to find the correct balance of temperatures. The advantage of AFC is the absence of water or flammable oil that may cause some problems in case of leakage. Again, such an AFC experiment is only feasible if the reactor generates heat in a reproducible continuous and stable fashion.

7. AFC Measurements

7.1. AFC parameters

As mentioned earlier AFC requires the measurements of the following parameters:

- Air mass inlet and outlet.
- Air heat capacity.
- Air temperatures at inlet and outlet.
- Heat losses: the insulation of the enclosure is not perfect.

Any error on these parameters has an influence on the AFC accuracy. The influence of the different sources of error is discussed below.

7.2. Air mass flow rate and heat capacity

The cooling capacity of the air flow depends on the product mC_p

The mass flow is measured by appropriate sensors located in the air inlet or outlet pipe. If the pipe section area is S

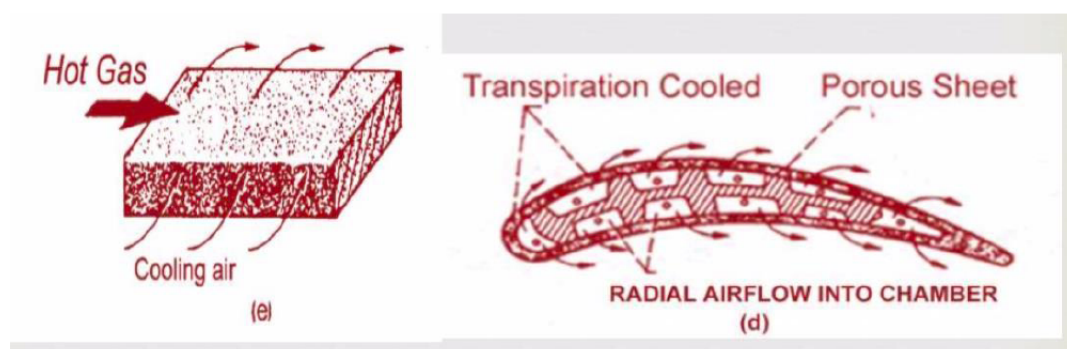


Figure 4. Conceptual view of transpiration cooling applied to gas turbine blades [7].

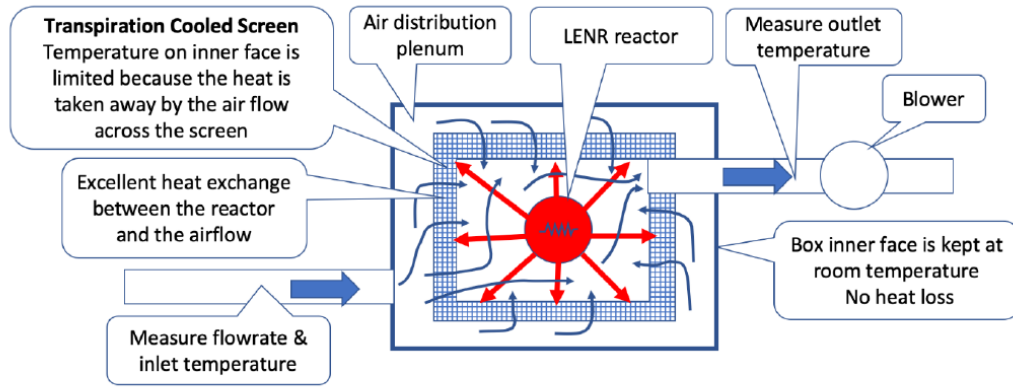


Figure 5. Schematic view of an AFC equipped with a transpiration cooled enclosure.

the mass flow is

$$mC_p = \rho S V C_p. \quad (3)$$

- ρ (kg m^{-3}) is the air density that depends on the local atmospheric pressure, room temperature and relative humidity.
- V (m s^{-1}) is the average velocity in the pipe. Most sensors give the air velocity at one point (e.g. on pipe

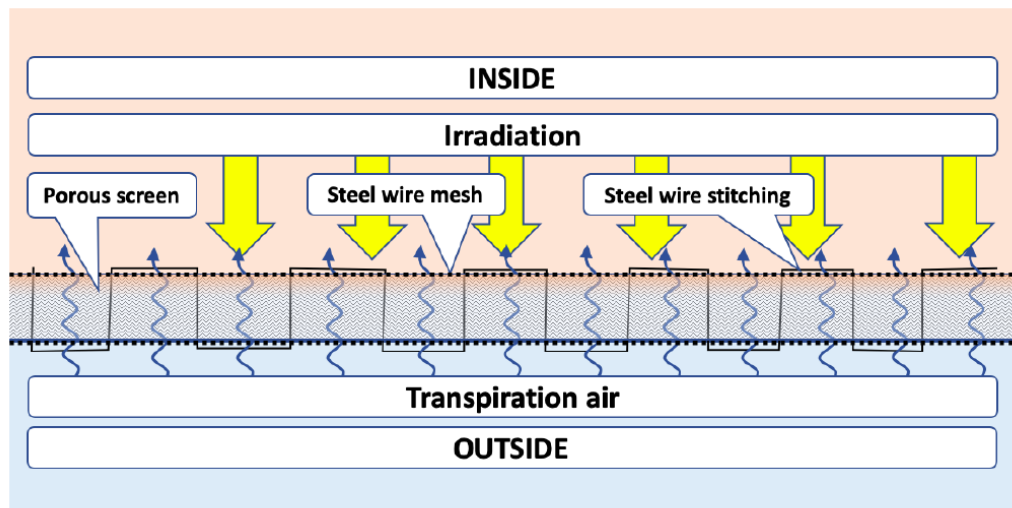


Figure 6. Sketch of a transpiration cooled screen.

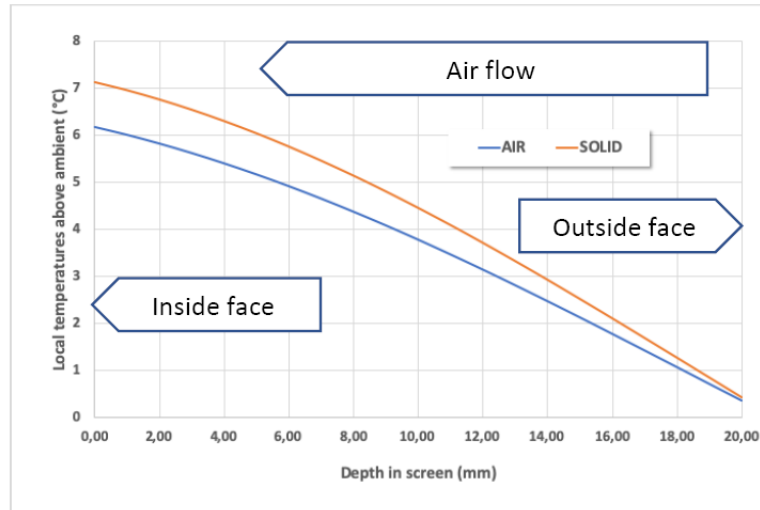


Figure 7. Temperature distribution in a TCS made of steel wool. Irradiation: 1000 W m^{-2} , $\lambda = 6.7 \text{ W m}^{-1} \text{ K}^{-1}$, $V = 0.05 \text{ m s}^{-1}$, and $F = 5.3$, note the temperature gradient on the outer face.

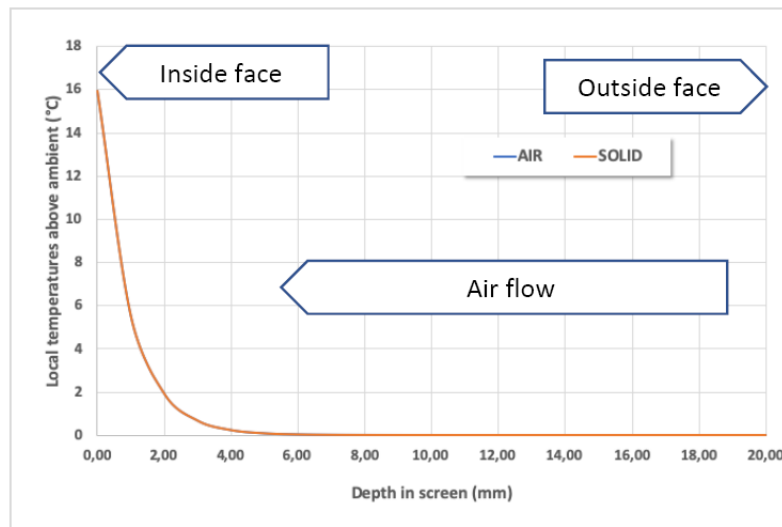


Figure 8. Temperature distribution in a TCS made of ceramic fibers. Irradiation: 1000 W m^{-2} , $\lambda = 0.03 \text{ W m}^{-1} \text{ K}^{-1}$, $V = 0.05 \text{ m s}^{-1}$ and $F = 0.024$. The air temperature is very close to the temperature of the solid so that the two curves are superposed. The temperature is close to ambient through most of the screen thickness.

centerline). The relationship between this local velocity and the average velocity may be affected by many geometrical factors like turbulence, friction on pipe wall, presence of straight lines and bends along the pipe length or other obstacles.

- C_p ($\text{J kg}^{-1} \text{K}^{-1}$) is the air heat capacity. The heat capacity varies with the relative humidity.

Appendix A gives a method of calculating the heat capacity as a function of the actual air conditions. The quantity of air that flows through the AFC box per second can be evaluated via different methods:

- Measurement of the air velocity in the inlet pipe connected to the box.
- Direct measurement of the air mass by a mass flow meter.

Different types of flow meters are available. An abundant literature describes the operation of the various sensors [8–16]. Table 1 summarizes some information on the main types of flow sensors.

Table 1. Main types of flow sensors.

Sensor type	Principle	Physical measure	Other parameters for mass flow knowledge	Remarks
Hot wire	Cooling of a heated wire	$k_1 \lambda + k_2 \sqrt{\lambda \rho V}$	$\lambda = f(T-H)$	Local point measure
Ultrasonic	Time of flight of US pulses or Doppler effect	V	$\rho = f(P-T-H)$	Average V
Orifice plate	Pressure drop through a restriction	$1/2 \rho V^2$	$\rho = f(P-T-H)$	Average V
Venturi	Bernoulli effect	$1/2 \rho V^2$	$\rho = f(P-T-H)$	Average V
Pitot tube	Bernoulli effect	$1/2 \rho V^2$	$\rho = f(P-T-H)$	Local point measure
Turbine	Freewheeling propeller	V	$\rho = f(P-T-H)$	Average V must exceed a minimum value to overcome propeller bearings friction

V is the air velocity (m s^{-1}), ρ the air density (kg m^{-3}), λ the air conductivity ($\text{W m}^{-1} \text{K}^{-1}$), P the air pressure (Pa), T the temperature (K), and H is the relative humidity (%).

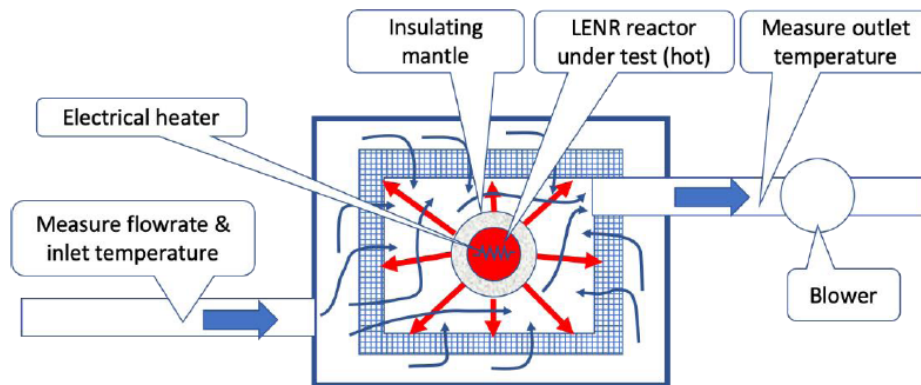


Figure 9. Schematic AFC setup to test a high temperature reactor (with TCS).

Some sensors give the velocity of the gas. The measurement of the mass flow requires the separate determination of the gas density. It depends on the local pressure temperature and humidity. Some sensors directly deliver the average velocity in the pipe. Others measure the velocity at a particular position in the pipe. Groups of sensors are sometimes arranged across the pipe section (e.g. arrays of Pitot tubes).

Mass flow sensors are generally calibrated for a specific range of environmental conditions. If high accuracy is desired the calibration may have to be revisited [17]. The relationship between the velocity measured on a single point and the average flow is influenced by many factors such as gas velocity, level of turbulence, geometrical configuration of the piping arrangement, etc. It is generally specified that long straight pipes must be installed upstream of a flow meter [18,19]. This requirement can be relaxed if flow straighteners are incorporated in the piping design [20–22].

The sensor must be selected for the specific range of expected air velocity. This is particularly true for the types sensitive to the product ρV^2 . Venturis or calibrated orifice plates are normally used for the calibration of other flow meter types [11]. In industry the hot wire type is frequently used, for example to control the air/fuel ratio in combustion engines [15].

7.3. Air inlet and outlet temperatures

The other important parameter for the measurement of heat generation is the air temperature difference between the inlet and the outlet. Different temperature sensors are available (thermocouples, thermistors, resistive temperature detectors (RTD)) [23–25]. In the inlet and outlet pipes the airspeed may be important depending on the design. The air temperature sensors must be arranged to measure the stagnation temperature [26].

The air inlet temperature must be as constant as possible. This depends on the laboratory room heating ventilation or air conditioning system performance. In the inlet and outlet pipes the air flow can be made turbulent, but the air velocity is rather low inside the calorimeter box. The presence of the hot reactor creates a plume of hot air that accumulates at the top. The temperature stratification may still be detectable in the air outlet pipe where the outlet temperature is measured, which would introduce incorrect readings. In order to have a valid measurement of the average temperature it is advisable to locate a static mixer in the outlet pipe upstream of the temperature sensor [27,28].

7.4. Evaluation of errors

Any fluctuation of the inlet temperature results in an error in the heat flow measurement. The heat storage capacity of the whole system introduces a time lag on the readings. For a given heat power there is an optimum combination of flow rate and temperature rise in order to maximize accuracy. The theoretical accuracy of air flow calorimetry is discussed based on the fractions of heat carried away by the air flow and heat losses. Any sensor is characterized by a relative error level on the value reading plus a systematic error given as a percentage of the full scale of the measurement.

Let us assume that the average air velocity V is subjected to a systematic error dv and that the temperature difference ΔT is similarly affected by an error dt . The heat flow value W can be written as

$$W = \rho C_p S V \Delta T = k V \Delta T, \quad (4)$$

W is measured within the error margin

$$[S(V - dv)] [\rho C_p (\Delta T - dt)] < W < [S(V + dv)] [\rho C_p (\Delta T + dt)]. \quad (5)$$

A first order approximation gives

$$S \rho C_p V \Delta T \left[1 - \left(\frac{dv}{V} + \frac{dt}{\Delta T} \right) \right] < W < S \rho C_p V \Delta T \left[1 + \left(\frac{dv}{V} + \frac{dt}{\Delta T} \right) \right]. \quad (6)$$

The relative error is the sum of the relative errors in the different parameters.

The following equations show there is an optimum choice of V to minimize the error. For a given heat flow value W the product $V\Delta T$ is theoretically constant. For a given value of V we have

$$\Delta T = \frac{W}{S\rho C_p V} = \frac{W}{kV}, \quad (7)$$

The relative error dt on ΔT can be written:

$$\frac{dt}{\Delta T} = \frac{kVdt}{W}. \quad (8)$$

The overall relative error is then

$$\text{relativeerror} = \frac{dv}{V} + \frac{dt}{\Delta T} = \frac{dv}{V} + \frac{kVdt}{W}. \quad (9)$$

Figure 10 shows schematically the relative error as a function of V . There is an optimum value of V that depends on W/k , dt and dv .

7.5. Other sources of errors

Any experimental installation must be thoroughly analyzed to identify all possible secondary sources of errors. An example is given by the presence of the electrical leads connecting the LENR device to the power supply and to the measurement equipment. On one hand Joule heating losses introduce a parasitic source of heat. On the other hand, the metallic wires can extract heat from the calorimeter by conduction. The resultant effect depends on the overall configuration. Another example is the design of the mechanical support of the device inside the enclosure.

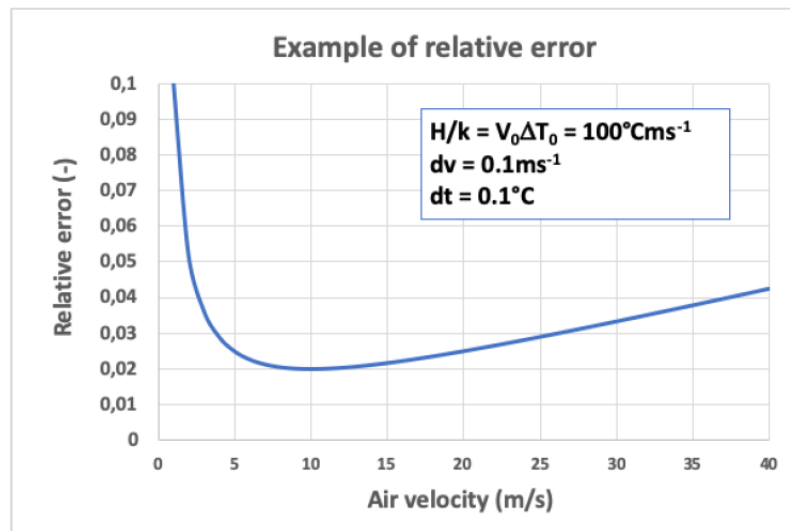


Figure 10. Example of relative error calculated for flow and temperature sensors affected by systematic errors. There is an optimum air velocity that minimizes the error.

8. Calibration

Because so many parameters can affect AFC it may seem difficult to do reliable experiments with this method. In fact, it is fortunately possible to minimize most of the uncertainties with a careful calibration. Calibration is done by monitoring the data obtained during the operation of a known heating power. The power dissipated by an electrical heater can be controlled with great accuracy.

If all AFC parameters are kept unchanged between the calibration run and the LENR test the heat generated by the LENR reactor can be obtained via a relative comparison of the power measures. The relative measurement method is able to deliver accurate results provided the following precautions are taken.

- Heat losses must be known. It is best to minimize the heat losses. The lower the heat losses the lower the sensitivity to external conditions. The TCS configuration that basically eliminates all heat losses is recommended.
- A run takes a long time, typically several hours because equilibrium must be reached before any measurement. During this time the air pressure and humidity may have changed. No calibration can prevent a modification of the air heat capacity. This value must be frequently checked during all experiments.

9. Conclusion

The AFC method can be utilized to measure the generation of heat of an LENR reactor. It is relatively cheap to set up and can be applied to reactors of any size and surface temperature. Its use is restricted to the testing of reactors that work continuously because thermal equilibrium must be reached to make valid measurements.

The AFC system must be designed to minimize the heat losses. The TCS configuration introduced here is an interesting solution. A thorough calibration procedure is essential to minimize the influence of errors on mass flows and temperature differences. The heat capacity of the air must be calculated separately.

Appendix A. Heat Capacity of Humid Air

AFC requires the knowledge of the heat capacity of the air that cools the sample. Any error on this parameter has a direct influence on the heat power measured. It is therefore necessary to introduce in the calculation of the results a precise value of the heat capacity.

The specific heat capacity of air for constant pressure C_p depends on several parameters. This appendix provides a method of determination of C_p for conditions that correspond to AFC needs, at ambient pressure and temperatures encountered in laboratories.

Calculation utilizes the C_p of dry air and the theoretical influence of humidity, as explained below (Table 2).

These data make it possible to write Eqs. (A.1) and (A.2):

$$\text{Dry air: } C_{pa}(\text{kJ kg}^{-1} \text{K}^{-1}) = 1.0037 + 3 \times 10^{-5} t + 3 \times 10^{-7} t^2, \quad (\text{A.1})$$

Table 2. Specific heat capacities of dry air and water vapor (sources: [29,30]).

T (K)	t (°C)	C_{pa} dry air (kJ kg ⁻¹ K ⁻¹)	C_{pw} vapor (kJ kg ⁻¹ K ⁻¹)
250	−23	1.0031	1.855
275	2	1.0038	1.859
300	27	1.0049	1.864
325	52	1.0063	1.871
350	77	1.0082	1.88

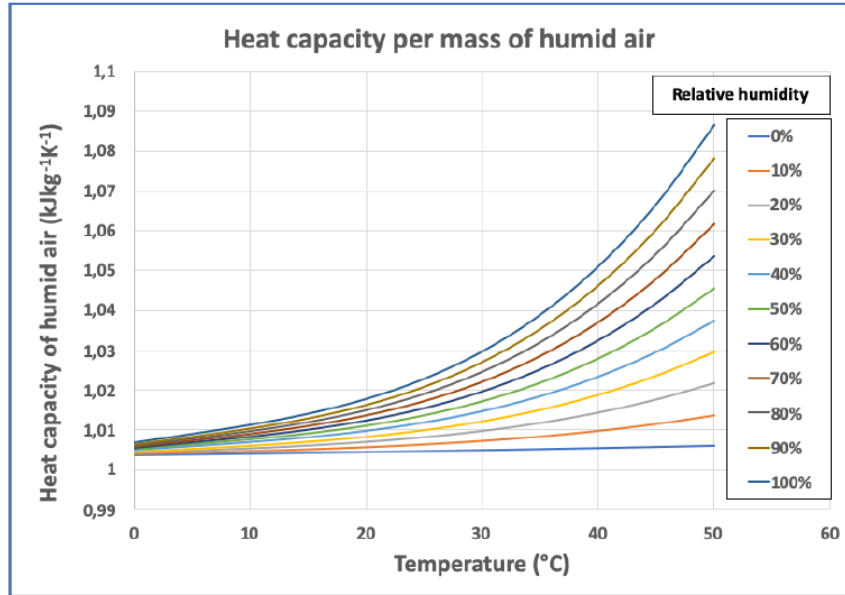


Figure 11. Specific heat capacity for a mass of humid air.

$$\text{Water vapor: } C_{pw}(\text{kJ kg}^{-1} \text{K}^{-1}) = 1.8584 + 2 \times 10^{-4} t + 10^{-6} t^2. \quad (\text{A.2})$$

The coefficients of determination R^2 of the above equations are respectively 0.9999 and 0.9997. The C_p of dry air varies slightly with the temperature. The pressure has no influence under our conditions. The heat capacity of water vapor is larger than dry air. The air humidity must be taken into account.

Let us assume the following air conditions:

- laboratory pressure: P (Pa),
- inlet temperature: t (°C),
- relative humidity: H (%).

Table 3. Vapor pressure at saturation in humid air (source: [31]).

t (°C)	Vapor saturation pressure P_s (Pa)
0	603
10	1212
20	2310
30	4195
40	7297
50	12210
60	19724

The vapor pressure at saturation ($H = 100\%$) is linked to the temperature as shown in Table 3. The saturation pressure P_s can be described by Eq. (A.3):

$$P_s = 568.62 + 75.215t - 1.1693t^2 + 0.0871t^3. \quad (\text{A.3})$$

The coefficient of determination R^2 of this formula is 0.9999. For a humidity H the actual partial pressure of the vapor is

$$P_w = P_s H / 100. \quad (\text{A.4})$$

The partial pressure of dry air P_a is then

$$P_a = P - P_w. \quad (\text{A.5})$$

For a volume of air of 1 m^3 under the conditions used for the calculation the masses of air M_a and water vapor M_w are:

$$M_a = 1.294(P_a/101325)273/(t + 273), \quad (\text{A.6})$$

$$M_w = 0.803(P_w/101325)273/(t + 273). \quad (\text{A.7})$$

The volumetric heat capacity is

$$C_p = M_a C_{pa} + M_w C_{pw} (\text{kJ m}^{-3} \text{K}^{-1}). \quad (\text{A.8})$$

The mass of the gases is $M_a + M_w$. The specific heat per mass of humid air is

$$C_p = \frac{M_a C_{pa} + M_w C_{pw}}{M_a + M_w} (\text{kJ kg}^{-1} \text{K}^{-1}). \quad (\text{A.9})$$

Figure 11 shows the specific heat capacity as a function of the temperature and humidity. Figure 12 shows the volumetric heat capacity as a function of the temperature and humidity.

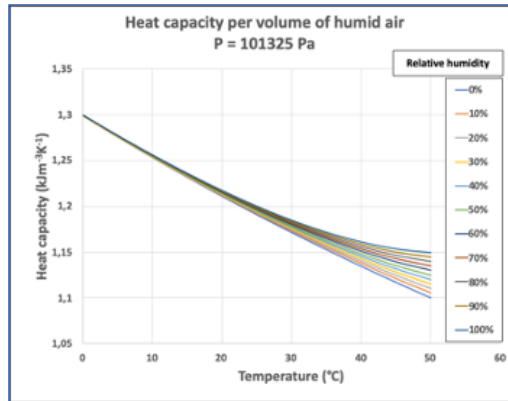
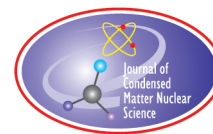


Figure 12. Volumetric heat capacity of humid air for a pressure of 101325 Pa.

References

- [1] M.C.H. McKubre and F. Tanzella. Mass flow calorimetry. in *ICCF-14 Int. Conf. on Condensed Matter Nuclear Science*, 2008, Washington, DC.
- [2] T. Mizuno and J. Rothwell, Excess heat from palladium deposited on nickel, *J. Condensed Matter Nucl. Sci.* **29** (2019) 2–33.
- [3] A. Kitamura, A. Takahashi, R. Seto, Y. Fujita, A. Taniike and Y. Furuyama, Mass-flow-calorimetry system for scaled-up experiments on anomalous heat evolution at elevated temperatures, *J. Condensed Matter Nucl. Sci.* **15** (2015) 231–239.
- [4] B. Higgins and D.G. Letts, Modeling and simulation of a gas discharge LENR prototype, *J. Condensed Matter Nucl. Sci.* **30** (2019) 309, 333.
- [5] M.R. Swartz, Time course of thermal stratification and its relevance to flow calorimeters, *J. New Energy* **4** (4) (2000) 120–125
- [6] M. Swartz, Buoyant heat transport in flow calorimetry, *ICCF22* (2019)
- [7] Ventaka Pavan Dharma, Gas turbine blades cooling technology,
<https://www.slideshare.net/VenkataPavanDharma/gas-turbine-blades-cooling-technology>
- [8] Wikipedia – Flow measurement
https://en.wikipedia.org/wiki/Flow_measurement
- [9] Gauthier – Cours sur les débits mètres
<https://www.slideserve.com/moriah/mesure-de-d-bit>
- [10] Engineering Toolbox – Types of fluid flow meters
https://www.engineeringtoolbox.com/flow-meters-d_493.html
- [11] Wikipedia – Venturi effect
https://en.wikipedia.org/wiki/Venturi_effect
- [12] Wikipedia – Pitot tube
https://en.wikipedia.org/wiki/Pitot_tube
- [13] Wikipedia – Orifice plate
https://en.wikipedia.org/wiki/Orifice_plate
- [14] Thermal mass flow meters
<https://www.omega.com/en-us/resources/thermal-mass-flow-meters>
- [15] Stefan Carstens - Thermal anemometer air flow sensors
https://dieselnet.com/tech/sensors_air-mass-flow.php#gen3
- [16] A.B. Raine, N. Aslam, C.P. Underwood and S. Danaher, Development of an ultrasonic airflow measurement device for ducted air, *Sensors* **15** (2015) 10705–10722.
- [17] G.B. Schubauer, Effect of humidity in hot wire anemometry, research paper RP850, *J. Res. National Bureau of Standards* **15** (December 1935).
- [18] Instrumentation and control Orifice plate installation guidelines
<https://instrumentationandcontrol.net/orifice-plate-installation-guidelines/>
- [19] J.X. Zhang, Analysis on the effect of venturi tube structural parameters on fluid flow - AIP Advances **7**, 065315 (2017),
<https://aip.scitation.org/doi/10.1063/1.499144>
- [20] Wikipedia Flow Straightener
https://en.wikipedia.org/wiki/Flow_straightener
- [21] Instrumentation Toolbox How a flow conditioner works
<https://www.instrumentationtoolbox.com/2016/01/how-flow-conditioner-works-flow.html>
- [22] Flow conditioning
<https://www.vortab.com/flow-conditioning/>
- [23] Wikipedia Resistance thermometer, https://en.wikipedia.org/wiki/Resistance_thermometer
- [24] Wikipedia Thermistor <https://en.wikipedia.org/wiki/Thermistor>
- [25] Wikipedia Thermocouple <https://en.wikipedia.org/wiki/Thermocouple>
- [26] Wikipedia – Stagnation temperature https://en.wikipedia.org/wiki/Stagnation_temperature
- [27] Wikipedia Static mixer
https://en.wikipedia.org/wiki/Static_mixer

- [28] Sulzer documentation
https://www.sulzer.com/-/media/files/products/static-mixers/mixing_and_reaction_technology_e_23270640.ashx?la=en
- [29] Engineering Tool Dry air properties
https://www.engineeringtoolbox.com/dry-air-properties-d_973.html
- [30] Engineering Tool Water vapor specific heat
https://www.engineeringtoolbox.com/water-vapor-d_979.html
- [31] Engineering Tool Water vapor saturation pressure in humid air
https://www.engineeringtoolbox.com/water-vapor-saturation-pressure-air-d_689.html



Research Article

Buoyant Heat Transport in Flow Calorimetry

Mitchell R. Swartz*

JET Energy Inc., Wellesley Hills, MA 02481, USA

Abstract

Reported 'excess heat' by flow calorimetric systems may be false positive or inflated, if the information was collected with temperature probes at two different heights or in the absence of confirmatory thermal Joule calibrations and η_B correction. This is especially true at higher temperatures. The non-dimensional number (η_B), which is the ratio of heat transported by the buoyant forces caused by any inhomogeneous temperature distribution to the heat transported by the expected solution convection, can yield an improved semiquantitative estimate of the actual gain: $\text{Power Gain}_{(\text{corrected})} = \text{Power Gain}_{(\text{indicated})} * (1 - \eta_B)$.

© 2020 ISCMNS. All rights reserved. ISSN 2227-3123

Keywords: Benard instability, Buoyancy correction, Buoyancy heat transport, Flow calorimetry, Flow calorimetry correction

1. Introduction – Overview of the Impact of the Buoyancy Effect

Although flow calorimetric systems are increasingly used to detect enthalpic changes (excess heat) secondary to putative CF/LANR/solid state nuclear reactions [1–6], there are serious potential problems when used with volumes passing unconstrained flow (that is, outside of simple pipes or arteries where there is no significant volume to enable buoyant heat flow). Flow calorimetry is simply not semiquantitative absent joule (ohmic) calibration and buoyancy correction. The equation(s) cannot be trusted to accurately derive the power output or putative excess heat if there are errors in the measured fluid flow, or the specific heat of the water, or absent buoyancy correction. Figure 1 shows this and the utterly huge amount of potential error.

Specifically, problems arise if uncalibrated outputs are taken from temperature probes at two different elevations (levels, heights), or with heat transported by buoyant forces between them. In those cases, the indicated values provide an inaccurate value. Figure 1 demonstrates that the indicated uncalibrated outputs are shown as a function of real, actual output power (from loss, through breakeven to circa 300%) and the non-dimensional number η_B which is the ratio of heat transported by the buoyant forces to the heat transported by the applied solution convection. Figure 1 saliently demonstrates that the temperature differential is only truly accurate and usable for a flow calorimetric equation IF the temperatures are taken at the same elevation. Simply put, even if all variables are correct, and although the equation may be dimensionally correct, it is not valid for low flow rates or where there is buoyancy instability of

*Mitchell R. Swartz ScD, MD, EE, E-mail: drswartz@nanortech.com.

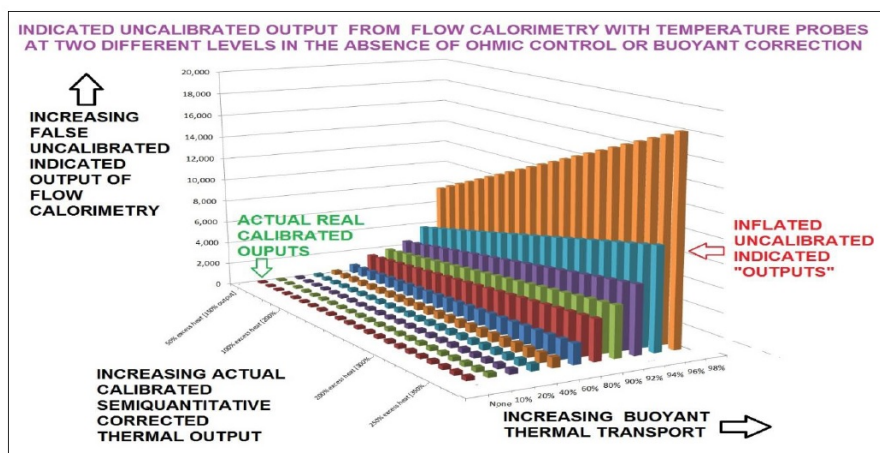


Figure 1. The indicated uncalibrated outputs from flow calorimetry with temperature probes at two different elevations (levels, heights) in the absence of ohmic controls or buoyant correction.

water (Benard instability). Instead, semiquantitative calibrated information is needed and it is achievable, as shown here using the non-dimensional number ($= \eta_B$) which is the ratio of heat transported by the buoyant forces to the heat transported by the applied solution convection.

2. Background

2.1. The buoyancy effect is quite real and observable

Many aspects of calorimeters have been discussed, including issues of potential problems with the thermometry, electrical grounding and crosstalk, thermal mixing, sensor positioning problems, and recombination. Yet, the potential impact of the buoyancy error is usually not considered despite its demonstrated significance and relevance to heat and mass flow and Benard instability (Fig. 2). The amplification can be quite significant, making this an important potential false positive. Worse, these errors do not average out over successive measurements.

2.2. Heat driven flow interferes with accurate calorimetry

We first demonstrated the significance of this effect in a series of papers [7–12], beginning with Potential for Positional Variation in Flow Calorimetric Systems which discussed a theoretical examination of heat and mass flow [13] with inclusion of the Benard instability [14]. Therefore, as can be seen even in this early model of the impact of buoyancy movement in flow calorimetry, the indicated results are not semiquantitative without calibration and correction. The effect can yield the appearance of excess heat when there is none, and it can also magnify the real excess heat far beyond what is actually obtained in the absence of buoyancy instability of water. Such indicated values can deceive the experimenter and can be misused, or used by crafty individuals, in the absence of timely synchronous ohmic/joule controls. In either case, this can give everyone the wrong impression based on an indicated number rather than semiquantitative calibrated data.

2.3. Error increases with additional heat

The impact of buoyant velocity interfering with flow calorimetric indicated measurements increases and is especially true at higher temperatures. Figures 1 and 3 show typical examples of this. Large volumes of fluids, moving or not, can yield temperature differentials which are not excess heat, and must be accounted for, and corrected in all semiquantitative flow calorimetric calculations.

3. Results

3.1. Understanding the buoyancy effect

This error can be semiquantitatively corrected by continuum electromechanical/flow principles [13] and the Navier–Stokes equation. That equation is essentially an equation of energy flow, but to understand this continuum equation requires a closer look at heat capacity of a volume of mass and how heat can flow from that volume through a surface encompassing that volume (Fig. 6). Together the local heat increase ($\Delta T * \text{Heat capacity}$) and heat flux and the power input. Here, with electrical or other input (such as $V * I$) the local power and the other variables define Incremental Power Gain. Integrated over time this becomes the excess heat.

4. Methods

4.1. Derivation of Navier–Stokes equation, Benard instability

The Navier–Stokes equation is derived from $F = ma$, which is conservation of momentum and from the equations for conservation of mass and energy. Conservation of mass requires the continuity equation.

- Conservation of momentum

$$m\vec{a} = \sum \vec{F}. \quad (1)$$

where m is the mass, \vec{a} the acceleration, and \vec{F} is the sum of all forces acting on fluid.

- Conservation of mass (continuity equation)

$$\nabla \cdot \vec{u} = 0. \quad (2)$$

- Conservation of energy

$$\rho c \frac{\partial T}{\partial t} = k \nabla^2 T + \dot{q}. \quad (3)$$

The term on the left-hand side represents rate of change of local heat energy stored, the first term on the right-hand side represents heat conducted out and \dot{q} is the heat generated.

The desired equations, therefore, add the forces on the right-hand side of Eq. (4), which here have forces which here arise from a pressure gradient, from gravity, and diffusion. Finally, because this is a Euler equation (a flow through a volume) rather than a Lagrangian (such as where is the ball as a $f(x, y, z)$) the convective derivative is needed and used on the left-hand side of Eq. (4).

- Navier–Stokes equation

$$\rho \left[\frac{\partial \vec{V}}{\partial t} + (\vec{V} \cdot \nabla) \vec{V} \right] = \rho \frac{D\vec{V}}{Dt} = -\nabla p + \rho \vec{g} + \mu \nabla^2 \vec{V}. \quad (4)$$

where $\partial \vec{V} / \partial t$ and $D\vec{V} / Dt$ represent convective derivatives, p the pressure, g the gravity, and ∇ is the diffusion.

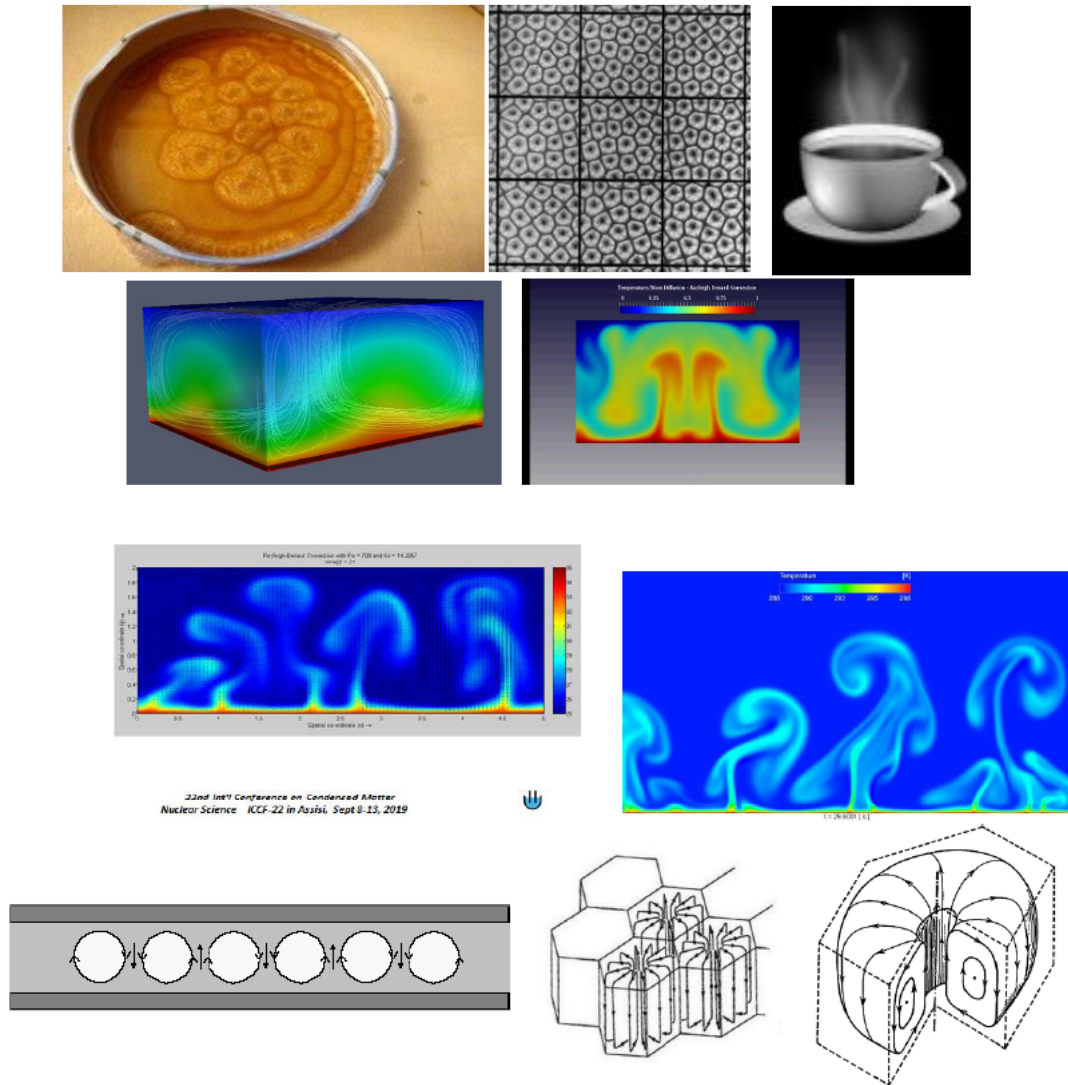


Figure 2. Examples of Benard–Rayleigh instability range from both the aqueous and gaseous regions in/near a cup of coffee, to the circulation cells which result from the uplift of fluid (and heat) arising from the difference of density. Shown are cells such as observed by Benard, and computer simulations and thermography and a cartoon schematic further showing the buoyancy effect and the induced circulations.

5. Results

5.1. Thermal expansion, Boussinesq approximation

In these cases, the thermal expansion must next be addressed. The key problem is that water and air and other fluids used in flow calorimetry suffer from thermal expansion. Their density is a function of temperature. Thus, water when

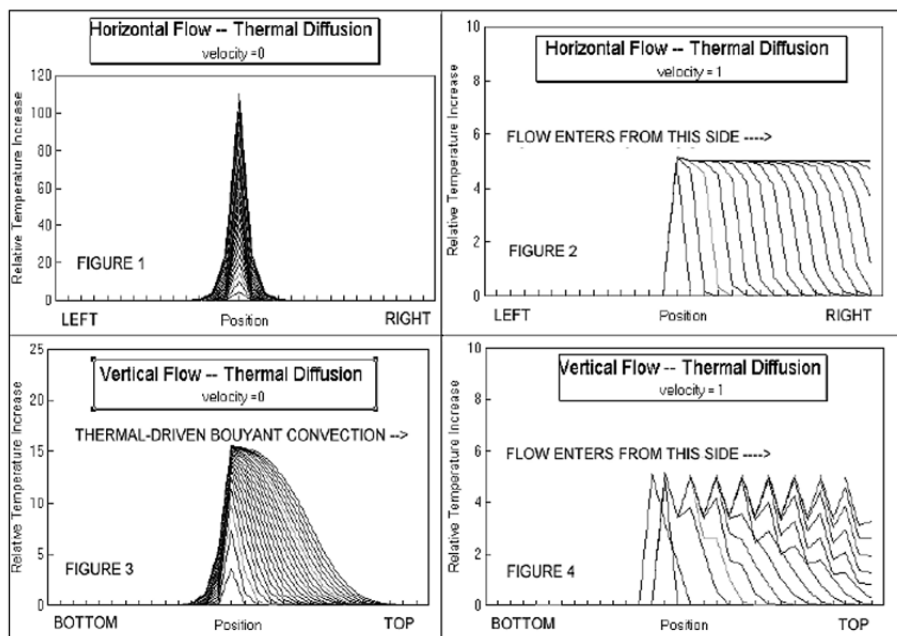


Figure 3. Impact of the direction of fluid velocity in flow calorimetry. Figure 3 from the Potential for Positional Variation in Flow Calorimetric Systems first discussed these theoretical issues/errors of heat and mass flow. The direction of the flow (horizontal with the input and output being measured at the same height) are shown on the top. The bottom shows vertical flow, although the curve itself remains horizontal for easy comparison.

it freezes floats on top, as one example, thereby fortunately saving all of the life below in the pond during the Winter.

For simplicity, the Boussinesq approximation is used, which only considers the thermal expansion in any term of Eq. (4) involving gravity (such as on the right hand side). Solution leads to Benard instability, the Rayleigh Taylor wavelength, and what is universally observed (Fig. 2). This equation is generally ignored in simplistic flow calorimetric systems/calculations.

5.2. η_B evaluates impact of buoyancy effect

We derived a non-dimensional number ($= \eta_B$) which can determine if flow calorimetry is defective when it is significantly greater than zero, and can be used to correct the flow calorimetry to the first order [7–10]. η_B is the ratio of heat transported by the buoyant forces to the heat transported by the applied solution convection.

η_B is also derivable from other non-dimensional factors including the Archimedes non-dimensional number (which is the ratio of the buoyant force to the viscous force), and the Rayleigh non-dimensional number (which is the ratio of gravity to thermal conductivity).

Swartz, M. "BUOYANT HEAT TRANSPORT", ICCF-22 (September 13, 2019 Assisi, Italy) 5

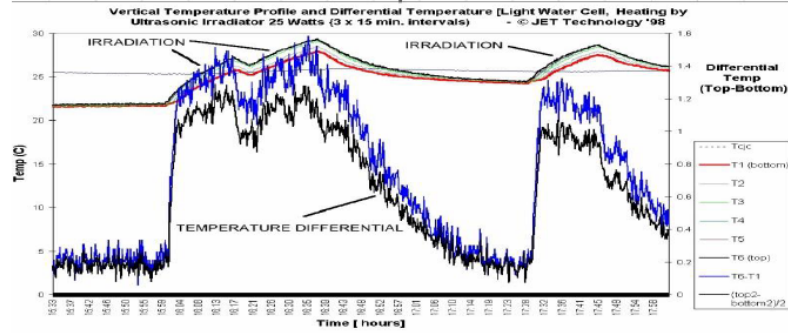


Figure 4. False indicated differential masquerading as excess heat. Examples of higher temperature Benard instability effect are seen during ultrasonic irradiation of palladium loaded cathode located in a simple tank (aquarium) of ordinary water. There is an initial ΔT between the top and the bottom (left hand y -axis) of several degrees. THIS IS NOT EXCESS HEAT prior to the irradiation, and that proves the entire issue. This temperature differential increases markedly to 20°C, and more, after initiation of the ultrasonic irradiation. Note that the time for fall off is significant.

5.3. First order correction using buoyancy factor

To zeroth order one can write using the specific heat capacity, the temperature differential, and the rate of mass transfer caused by both the expected convection and the buoyancy movement secondary to the temperature inhomogeneity.

$$P_{\text{observed}} = P_{\text{out}} + P_{\text{error}} = C_p * \Delta T * V_{\text{total}} = C_p * \Delta T * (V_{\text{convection}} + V_{\text{buoyancy}}) \quad (5)$$

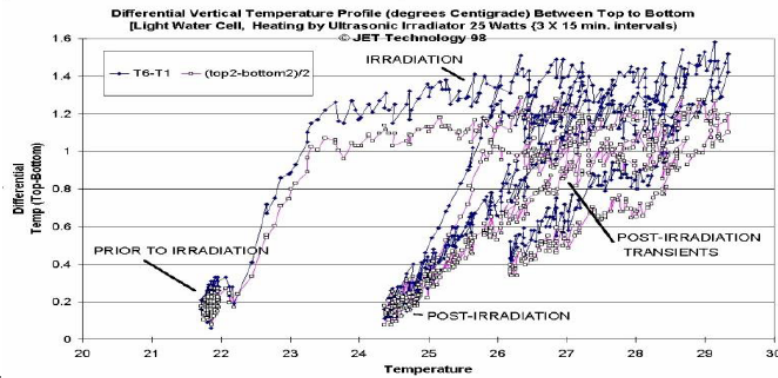


Figure 5. Second false indicated differential masquerading as excess heat. A second example of higher temperature Benard instability effects which were seen during ultrasonic irradiation of a cathode in a simple tank of ordinary water. The x -axis shows the temperatures recorded, and the y -axis is the differential (ΔT) between top and bottom. Notice a clear differential of 0.2°C, before and after the experimental run. There is an initial Δt between the top and the bottom (left hand y -axis). This increases markedly to 20°C differential and more after initiation of the ultrasonic irradiation.



Figure 6. Scientific heroes of buoyant heat flow. The concept of specific heat originated with Dr. Joseph Black (1728–1799; left top), a Scottish physician and chemist who reported on the latent heat and heat capacity of ice and water. In 1761, Black reported of these findings in melting ice and boiling water, and realized that different materials have different specific heats. The heat flow issues were developed by Jean Baptiste Joseph Fourier (1768–1830; mid top), French mathematician and physicist, while with Napoleon Bonaparte on his 1798 Egyptian expedition, became governor of Lower Egypt and secretary of the Institut d'Égypte. It focused his attention to heat propagation. After the British victories, in 1822, he presented his equation on heat flow now used [15,16]. George Gabriel Stokes (1819–1903; top right), a mathematician and physicist, put the continuum flow equation together incorporating both heat conduction {from his research of crystals (1851) and incompressible fluid flow (1843)}. Henri Claude Bénard (1874–1939; bottom left), a French physicist, became known for his experiments on convection in liquid including the buoyancy circulations, which were analyzed by John William Strutt, the third Baron Rayleigh (1842–1919; bottom right).

The chain rule in calculus and consideration of coolant redistribution reveal the higher order terms from the impact of the buoyant flow.

$$\frac{\partial P_{\text{error}}}{\partial \eta_B} = (C_p * \Delta T * V_{\text{convection}}) + (C_p * V_{\text{convection}}) * \eta_B * \frac{\partial \Delta T}{\partial \eta_B} \quad (6)$$

The term containing $\partial \Delta T / \partial \eta_B$ depends upon many factors including the total tank volume just outside the reactor (or thermal control) and the actual input temperature boundary condition. However, that term appears to be higher order, and so the linear correction to the observed power becomes

$$P_{\text{corrected}} = P_{\text{observed}} - (C_p * \Delta T * V_{\text{convection}} * \eta_B). \quad (7)$$

An improved estimate of the purported gain (or over-unity gain) then becomes, corrected to first order,

$$P_{\text{corrected}} = P_{\text{observed}} - (C_p * \Delta T * V_{\text{convection}} * \eta_B) \quad P_{\text{corrected}} = P_{\text{observed}} * (1 - \eta_B) \quad (8a)$$

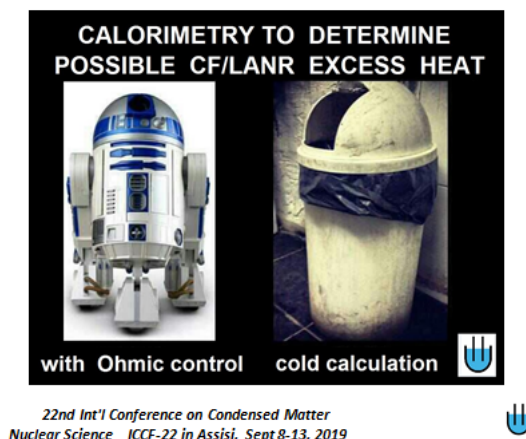


Figure 7. *Sine qua non* for good calorimetry. Good calorimetry absolutely requires an ohmic control at the same location as the heat source being examined. This and correction for buoyancy error will markedly improve the accuracy and reliability of flow calorimetry.

$$\text{Incremental Power Gain}_{\text{corrected}} = \text{Incremental Power Gain}_{\text{indicated}} * (1 - \eta_B). \quad (8b)$$

6. Conclusion

Buoyancy error exists, as does the means to correct it.

- (1) In summary, reported excess heat by flow calorimetric system may be false positive or inflated, if the information was indeed collected with temperature probes at two different heights, in the absence of confirmatory thermal Joule calibrations, and especially under low to moderate flow conditions where the non-dimensional number (η_B) is not trivial.
- (2) Flow calorimetry is not semiquantitative absent calibration and buoyant correction. Uncalibrated outputs from flow calorimetry with temperature probes at two different elevations (levels, heights), or with heat transported buoyant forces, may be inaccurate in the absence of ohmic controls and buoyant correction. This was corroborated at ICCF-22 by Dr. Jacques Ruer [18]. It is important to consider that alternative methods of calorimetry are not sensitive to this type of error, including multiring systems [19,20].
- (3) The effect can yield the appearance of excess heat when there is none, and it can also magnify the real excess heat far beyond what is actually obtained in the absence of buoyancy instability of water. Such would provide the wrong impression based on the indicated numbers rather than semiquantitative calibrated information.
- (4) This is especially true at higher temperatures.
- (5) The non-dimensional number (η_B) is important. For more accurate measurements, semiquantitative correction can be made even in the presence of buoyant flow by use of the linear correction based on the indicated values of data and the measured, or estimated, values of η_B .
- (6) The buoyancy effect can be misused, or misunderstood, in the absence of timely synchronous iso-located ohmic/joule controls and correction for buoyancy. By failing to use ohmic/joule controls and then succumbing to the siren of buoyant heat's contribution to obtain an elevated, uncalibrated number is not accurate, is wrong, is risky and should not be repeated.

6.1. Failure to correct buoyancy error has risk

There is a substantial risk to the reputation of the entire field, if individuals within it take advantage of the error of thermal-induced buoyancy instability of water, and if it is for the wrong reason, such as without correction, without ohmic controls, and perhaps not even indicating by figure where the temperature measurements for the flow calorimetry are made. Are they made at the same level?

The science and engineering of cold fusion/LANR are still under unwarranted scrutiny and attack by outside powers that ignore discoveries, achievements, and the entire literature of the field. In that light, we must as scientists and engineers continue our research unabated for as was said at Waterloo: “*La Garde meurt, elle ne se rend pas*”! (“*The Guard dies, it does not surrender*”!). The loss in that battle, as might happen in this field which has worked uphill for 30 years, resulted from failure to admit huge mistakes, sheer recklessness, and, above all, overreaching ambition that exceeded all realistic possibilities [17].

By failing to use ohmic/joule controls and then succumbing to the siren of buoyant heat’s contribution to obtain an elevated, uncalibrated number is wrong and should not be repeated.

Acknowledgements

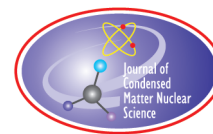
The author thanks Gayle Verner and Isidor Straus for editorial help and suggestions for this manuscript.

References

- [1] D. Cravens, Flowing electrolyte calorimetry, *Proc. of 5th Int. Conf. on Cold Fusion*, 1995, pp. 79–86.
- [2] H. Fox, Dramatic cold fusion demonstration seen by hot fusion scientists, *Fusion Facts* **7** (4) (1995) 1–4.
- [3] M. Jones, Some Simple Calculations Assuming 42 Cubic Feet per Minute, posted on sci.physics. fusion; excerpts in *Cold Fusion Times* **4**(1) (1996) 6–8.
- [4] M.R. Swartz, Elementary survey of CETI microsphere demo, *Cold Fusion Times* **4**(10) (1996) 7–9.
- [5] M.C.H McKubre, S. Crouch-Baker, R.C. Rocha-Filho, S.I. Smedley, F.L. Tanzella, T.O. Passell and J. Santucci, Isothermal flow calorimetric investigations of the D/Pd and H/Pd systems, *J. Electroanal. Chem.* **368** (1994) 55.
- [6] T. Mizuno and J. Rothwell, Increased excess heat from palladium deposited on nickel for 22nd Int. Conf. for Condensed Matter Nuclear Science, ICCF-22, 2019, preprint.
- [7] M.R. Swartz, Potential for positional variation in flow calorimetric systems, *J. New Energy* **1**(1) (1996) 126–129. [http://world.std.com/~mica/Swartz_Calib-ErrorsbyVerticalFlow\(1996\).pdf](http://world.std.com/~mica/Swartz_Calib-ErrorsbyVerticalFlow(1996).pdf).
- [8] M.R. Swartz, heat transported by buoyant force may augment solution convection in flow calorimetric systems, *Sixth Int. Conf. on Cold Fusion*, October 1996, Toya, Hokkaido, Japan, 1996. http://world.std.com/~mica/Swartz_Calib-HeatBouyantForce.pdf.
- [9] M.R. Swartz, Linear correction for heat transport secondary to buoyant forces in flow calorimetric calculations, 1996. [http://world.std.com/~mica/Swartz-Calib-LinearCorrxn\(1996\).pdf](http://world.std.com/~mica/Swartz-Calib-LinearCorrxn(1996).pdf).
- [10] M.R. Swartz, Improved calculations involving energy release using a buoyancy transport correction, *J. New Energy* **1** (3) (1996) 219–221. [http://world.std.com/~mica/Swartz-Calib-ImprovCalc\(1996\).pdf](http://world.std.com/~mica/Swartz-Calib-ImprovCalc(1996).pdf).
- [11] M.R. Swartz, Letter to Editor, The relative impact of thermal stratification of the air surrounding a calorimeter, *J. New Energy* **1** (2) (1996) 141, 219–221, www.iscmns.org/FIC/J/JNE1N2.pdf. [http://world.std.com/~mica/Swartz_Calib-RelImpactAirandStratification\(JNE1N2,1996\).pdf](http://world.std.com/~mica/Swartz_Calib-RelImpactAirandStratification(JNE1N2,1996).pdf).
- [12] M.R. Swartz, Time course of thermal stratification and its relevance to flow calorimeters, *J. New Energy* **4** (4) (2000) 120–125. [http://world.std.com/~mica/Swartz_Calib-ThermalTimeStratific\(2000\).pdf](http://world.std.com/~mica/Swartz_Calib-ThermalTimeStratific(2000).pdf).
- [13] J. Melcher, *Continuum Electromechanics*, MIT Press, Cambridge, 10. 13–10. 18 (1981), <https://www.google.com/url?sa=t&rct=j&q=&esrc=s&source>

=web&cd=4&cad=rja&uact=8&ved=2ahUKEwj8pc7XrIjjAhVorlKHfQjBI4QFjADegQIBhAC&url
F=https%3A%2F%2Focw.mit.edu%2Focw.mit.edu%2Fresources%2Fmelcher%2Fresized%2Fcem_811.pdf&usg
=AOvVaw1ityC4BWIPTM792pP5DX7.

- [14] S. Chandrasekhar, *Hydrodynamic and Hydromagnetic Stability*, Clarendon Press. Oxford, 1961, pp. 9–75.
- [15] J. Fourier, *Théorie analytique de la chaleur*, Paris: Firmin Didot Père et Fils, 1822.
- [16] J. Fourier, *Annales de chimie et de physique*, 27, Paris, *Annals of Chemistry and Physics*, 1824, pp. 236–281.
- [17] von Clausewitz and Carl - confer Daniel Moran, Clausewitz on Waterloo: Napoleon at Bay, in Carl von Clausewitz and Arthur Wellesley, 1st Duke of Wellington, *On Waterloo: Clausewitz, Wellington, and the Campaign of 1815*, ed./trans. Christopher Bassford, Daniel Moran, and Gregory W. Pedlow (Clausewitz.com, 2010), p.242, n.11.
- [18] J. Ruer, Basics of air flow calorimetry, paper n58, *22nd Int. Conf. for Condensed Matter Nuclear Science*, ICCF-22, 2019.
- [19] M. Swartz, Consistency of the biphasic nature of excess enthalpy in solid state anomalous phenomena with the quasi-1-dimensional model of isotope loading into a material, *Fusion Technol.* **31** (1997) 63–74.
- [20] M. Swartz and G. Verner, Excess heat from low electrical conductivity heavy water spiral-wound Pd/D₂O/Pt and Pd/D₂O-PdCl₂/Pt devices, *Condensed Matter Nuclear Science, Proc. ICCF-10*, Peter L. Hagelstein and R. Scott Chubb (Eds.), World Scientific, NJ, 2006, pp. 29–44. ISBN 981-256-564-6.



Research Article

Highly Relativistic Deep Electrons and the Dirac Equation

Jean-Luc Paillet*

University of Aix-Marseille, France

Andrew Meulenberg

Science for Humanity Trust Inc., Tucker, GA, USA

Abstract

After analyzing, in the literature, deep orbit results of relativistic quantum equations, we studied them in a semi-classical way, by looking for a local minimum of total energy of an electron near the nucleus, while respecting the Heisenberg Uncertainty Relation (HUR). Now, while using new information thanks to semi-classical computations, we come back to deep electrons as solutions of the Dirac equation, to solve several important and subtle outstanding issues, such as the continuity of derivatives of wave functions, a spectral problem about the energy levels associated with the wave functions to compute, as well as essential relativistic and energy parameters of the solutions. We thus obtain a better completeness of the solutions. Finally, we give some approaches on the probability of the presence of Electron Deep Orbit (EDO) states in H atom.

© 2020 ISCMNS. All rights reserved. ISSN 2227-3123

Keywords: Deep electron levels, Dirac equation, Heisenberg Uncertainty Relation, LENR, Relativistic effects

1. Introduction

Our works on the Electron Deep Orbits (EDOs) are motivated by the need to develop and complete a theoretical model to explain some of the outstanding questions about low-energy nuclear reaction (LENR) results. These results, such as the quasi-absence of high-energy radiation and ejection of particles, require an understanding of the nuclear processes involved [1,2] as well as the means of influencing them from a lattice. Moreover, a better understanding of EDOs and their interaction with nuclear fields will hopefully lead to a practical means of populating these deep levels in a nuclear region from which they can alter nuclear properties (e.g., transmutation and nuclear-decay processes [3]) and facilitate electron capture into the nucleus.

Over the last three years, we have analyzed results based on the use of relativistic quantum equations, because it was to be expected that an electron required to mediate fusion of two nuclei must maintain its high-probability of being between them and therefore must be relativistically or otherwise confined. That is why we particularly analyzed and extended [4] the results of [5] and validated [2] the need for relativity.

*Corresponding author. E-mail: jean-luc.paillet@club-internet.fr.

In our more recent works, we took the question of the EDO from a different angle, by studying in a semi-classical way, the possibility of a local minimum of total energy for an electron in the vicinity of the nucleus. For this, we consider combinations of attractive and repulsive potentials [6], as well as the action of radiative corrections, such as the Lamb shift, while satisfying both the Heisenberg Uncertainty relation (HUR) [7,8] and the Virial theorem. Facing for the first time the thorny question of the HUR for electrons confined in deep orbits, we were able, not only to evaluate the coefficient γ of these highly relativistic electrons, but also to show that a strong relativistic correction to the Coulomb potential leads to an effective potential capable of confining such energetic electrons.

In the present work, being equipped with these new insights and methods, we come back to a important and subtle theoretical question encountered during initial EDO calculations with the Dirac equation, which showed a significant overlap of the electron wave function with the physical nucleus: Should the energy levels, usually obtained with the Dirac equation solved while considering a point-like nucleus, be modified and how? In fact, computation of the energy of a deep-orbit electron from its probability-density distribution, allows us to adjust its initial energy level by applying a fixed-point method. Moreover, we improve the semi-analytical solutions of the radial equations, to obtain wave functions having continuous derivatives on the femto-meter scale, including the surface delimiting the inside and outside of the nucleus. Doing this, we study how to preserve the initial coupling between the two components of Dirac solutions for EDOs. Finally, we give some approaches on the question of populating EDO states

2. Initial EDO Results, as Solutions of Dirac Equation for Atom H

2.1. The anomalous solutions of the Dirac equation

We had analyzed specific works of Maly and Vávra on deep orbits as solutions of the Dirac equation. These orbits were named by those authors Deep Dirac Levels (DDLs). They present the most complete solution and development available, including an infinite family of EDO solutions [9] for hydrogen-like atoms.

The Dirac equation for an electron in the central external Coulomb field of a nucleus, can take the following form:

$$(i\hbar\partial_t + i\hbar c \boldsymbol{\alpha} \cdot \boldsymbol{\nabla} - \beta mc^2 - V) \Psi(t, \mathbf{x}) = 0, \quad (1)$$

where $\boldsymbol{\alpha}$ and β represent the Dirac matrices, $\boldsymbol{\alpha}$ is a 3-vector of 4×4 matrices built from the well-known Pauli matrices, and V is the Coulomb potential, defined by $-e^2/r$. During the solution process with an ansatz, the following condition must be satisfied by a parameter occurring in the ansatz: $s = \pm(k^2 - \alpha^2)^{1/2}$. The scalar α represents the coupling constant (not to be confused with the vector of Dirac matrices $\boldsymbol{\alpha}$ occurring in the above Dirac equation). If taking the positive sign for s , one has the usual regular solutions for energy levels, whereas with the negative sign, one has the so-called anomalous solutions. The general expression obtained for the energy levels of atom H is the following:

$$E = mc^2 \left[1 + \frac{\alpha^2}{(n' + s)^2} \right]^{-1/2} \quad (2)$$

So, while considering the anomalous solution, with negative s , the expression of E reads

$$E = mc^2 \left[1 + \frac{\alpha^2}{(n' - \sqrt{k^2 - \alpha^2})^2} \right]^{-1/2}, \quad (3)$$

where n' is the radial quantum number while k is the specific Dirac angular quantum number, which can take any integer value $\neq 0$. In fact, all solutions expressed by E do not correspond to deep orbits, but only those satisfying the relation $n' = |k|$ (note that k can be < 0). Indeed, we can see that if $|k| = n'$, the sub-expression D occurring at the

denominator of the expression E , $D = n' - (k^2 - \alpha^2)^{1/2}$, becomes $D = n' - (n'^2 - \alpha^2)^{1/2}$, which is very small since $D \sim \alpha^2/2n'$, and so $E \sim mc^2\alpha/2n'$. Then $|\text{BE}| \sim mc^2(1 - \alpha/2n')$ and $|\text{BE}|$ is close to the rest mass energy of the electron, 511 keV. Note, that since k cannot equal 0, then neither can n' .

Here, we summarize some features of the anomalous solutions of the Dirac equation [6]

- If $|k| > n'$, the solutions correspond to negative-energy states.
- If $|k| = n'$, these special solutions correspond to positive-energy states, and they are the only ones providing EDOs. Moreover, we can observe, in the energy tables in [9], the following property: the binding energy in absolute value, $|\text{BE}|$, increases when n' increases. This is a behavior opposite to that of the regular states. Note that one can also directly deduce this property from the algebraic expression of $|\text{BE}| \sim mc^2(1 - \alpha/2n')$.
- If $|k| < n'$, each solution corresponds to a positive energy state, but E is very close to the energy of a *regular level* corresponding to a value of the principal quantum number N taken equal to $n' - |k|$.

2.2. The deep orbits, as solutions of the Dirac equation with a corrected potential for a nucleus of finite size

In a second work [5], the authors determined the wave functions of EDOs for hydrogen-like atom solutions of the Dirac equation. But this time, they consider the nucleus not to be point-like, and thus the potential inside the nucleus is finite at the origin $r = 0$. We have seen, in the previous works on criticisms [10,11], that this allows eliminating the problems related to the singularity of the classical Coulomb potential in $1/r$.

To solve the Dirac equation, the authors use results from Fluegge [12]. As usual, the process includes separate angular and radial variables and leads to a system of coupled first order differential equations on both radial functions $f(r)$ and $g(r)$. In the method used by Fluegge, the equation system is transformed into a second order differential equation, a Kummer's equation, and the general solutions of this equation take the following form, with confluent hyper-geometrical series requiring suitable convergence conditions:

$$\begin{aligned} g &= \frac{1}{2}Cr^{s-1}e^{-r/a} \left\{ {}_1F_1\left(s+p, 2s+1; 2\frac{r}{a}\right) - \frac{s+p}{k+q} {}_1F_1\left(s+p+1, 2s+1; 2\frac{r}{a}\right) \right\}, \\ f &= \frac{-i}{2\mu}Cr^{s-1}e^{-r/a} \left\{ {}_1F_1\left(s+p, 2s+1; 2\frac{r}{a}\right) + \frac{s+p}{k+q} {}_1F_1\left(s+p+1, 2s+1; 2\frac{r}{a}\right) \right\}. \end{aligned} \quad (4)$$

Note: The parameters a and μ include the energy E defined by expression (2). For example, we have $\mu = [(mc^2 - E)/(mc^2 + E)]^{1/2}$; likewise, p and q are defined by means of μ , so they depend on E too.

To solve the equation with a nucleus of finite size $\neq 0$, the authors carry out the following steps:

- To choose a radius R , the so-called “matching radius”, delimiting two spatial domains: an outside one, where the potential is correctly expressed by the usual $1/r$ Coulomb potential, and an inside one, where the potential cannot be expressed by the Coulomb potential. Of course, this choice may seem arbitrary, but it takes physical meaning if one chooses a value R close to the charge radius R_c of the nucleus.
- To choose a suitable expression for the inside potential. It is again an arbitrary point, but we observed [4] this choice has weak influence on the numerical results that interested us, especially the value of mean radius as function of the radial number n' .
- To satisfy continuity conditions at the matching radius R for connecting the inside and outside potentials. The potential chosen by the authors is derived from the Smith–Johnson potential, corresponding to a uniformly distributed spherical charge, whose expression is the following:

$$V(r) = - \left[\frac{3}{2} - \frac{1}{2} \left(\frac{r^2}{R^2} \right) \right] \frac{Ze^2}{R}, \quad (5)$$

where $Z = 1$ for atom H, and e is the electron charge.

- To solve the system of radial equations for the outside potential, i.e. Coulomb potential, that gives the outside solution composed of two components: functions f_o and g_o . Here, the outside functions f_o and g_o are, respectively, the functions f and g expressed above while choosing $s < 0$, i.e. $s = -(k^2 - \alpha^2)^{1/2}$, to have anomalous solutions and by putting $|k| = n'$ to discriminate the special solutions corresponding to EDOs.

2.2.1. Ansatz used for finding the inside solutions and continuity conditions

The choice of ansatz is a very important element for finding f_i and g_i , solutions inside the nucleus, of the system of radial equations. Moreover, its expression is determinant to satisfy the continuity condition. A complete analysis of this question is given in [4].

In their paper [5], the authors put the ansatz in the following form:

$$g_i = Ar^{S_i-1}G_i(r),$$

$$f_i = iBr^{S_i-1}F_i(r),$$

where $G_i(r)$ and $F_i(r)$ are in principle power series, i.e.

$$G_i(r) = a_1r + a_2r^2 + a_3r^3 + \dots \quad \text{and} \quad F_i(r) = b_1r + b_2r^2 + b_3r^3 + \dots$$

But one may consider approximations of these series by polynomials by taking into account the following facts:

- f_i and g_i must be defined for $r < R$.
- For $r < R$, very small, the higher-power terms vanish as the degree increases.

The classical method used, after inserting the ansatz into the equations, allows one to determine the exponent s_i and the polynomial coefficients, in order to obtain the solutions. This requires solving a couple of interdependent recurrent formulas for computing the coefficients of both power series $G_i(r)$ and $F_i(r)$. Nevertheless, it seems the information given in the paper is incomplete, or more precisely, the chosen ansatz is not complete and it does not contain enough free parameters to satisfy the continuity condition for both couples of functions (f_i, g_i) and (f_o, g_o) in R . In fact useful information was included in another paper by the same authors, referenced as to be published, but never published.

To resolve this problem, we looked for a more complex ansatz including an additional free real parameter λ , necessary to connect in a suitable manner the inside and outside functions, where the series/polynomials have the following form:

$$G_i(r) = a_1(\lambda r) + a_2(\lambda r)^2 + a_3(\lambda r)^3 + \dots \quad \text{and} \quad F_i(r) = b_1(\lambda r) + b_2(\lambda r)^2 + b_3(\lambda r)^3 + \dots$$

The continuity conditions $\{g_i(R) = g_o(R), f_i(R) = f_o(R)\}$ lead to a system of two algebraic equations. We showed in [4] that, for any degree n of the polynomials, the maximum power of λ in this system of equation remains constant and equals 2, and so this system provides suitable solutions.

2.2.2. Computing the orbital mean radii

Summarily, the computation process for mean orbit radius for a given value of n' includes the following steps:

- To determine both couples (f_o, g_o) and (f_i, g_i) of respective outside and inside solutions. At this step, the four functions f_o, g_o, f_i , and g_i include parameters still to be determined.

- To connect them in a suitable manner, e.g., by satisfying the continuity conditions, in order to obtain a couple of global wave function solutions (F, G) . During this step, the unknown parameters included in the initial functions $f_o, g_o, f_i,$ and g_i are fixed. The functions, thereby completely defined, can be denoted by $F_o, G_o, F_i,$ and G_i
- To compute the normalization constant N by using the following formula:

$$1/N = \int_0^{R_0} \text{ElDi} \, dr + \int_{R_0}^{+\infty} \text{ElDo} \, dr,$$

where ElDi represents the electron probability density corresponding to the couple of inside functions (F_i, G_i) :

$$\text{ElDi} = 4\pi r^2 (|F_i|^2 + |G_i|^2).$$

- Finally, to compute the mean radius $\langle r \rangle$ by using the following formula:

$$\langle r \rangle = N \left[\int_0^R r \, \text{ElDi} \, dr + \int_R^{+\infty} r \, \text{ElDo} \, dr \right].$$

2.2.3. Obtained results and discussion on imperfections

We give some examples of wave function solutions computed for the hydrogen atom H, while using the following choices

- $R = 1.2 \, \text{F}$,
- A nuclear potential defined by expression (4) given previously, where the proton is approximated by a uniformly charged solid sphere,
- The polynomials of our ansatz have degree 6.

In Fig. 1, we plot the *normalized electron probability density functions* (NEPD) for $n' = 1, 2,$ and 3 . The peak values for NEPD correspond to $r \sim R$.

Values of mean radius $\langle r \rangle$ and total energy E for $n' = 1, 2,$ and 3 . Note that in these computations, E is deduced from Eq. (3), which gives $E \sim mc^2 \alpha / 2n'$.

- $n' = 1, \langle r \rangle \sim 6.6 \, \text{F}, E \sim 1.86 \, \text{keV},$
- $n' = 2, \langle r \rangle \sim 1.7 \, \text{F}, E \sim 0.93 \, \text{keV},$
- $n' = 3, \langle r \rangle \sim 1.4 \, \text{F}, E \sim 0.62 \, \text{keV}.$

Now, we can make the following remark: to find out how to populate deep levels, an essential and concrete question about utility of EDOs for LENR, we need to know more information and to correct some imperfections. These are listed here in the form of three problems, in an order that has no significance of importance.

- Problem #1. The ansatz we had used does not allow us to have continuous derivatives at the connection radius R . This problem is more serious than it appears at first sight. The initial Dirac equation and the resulting system of two radial equations, after separating the variables, are 1st order equations. Nevertheless, the radial equations are not independent (see e.g. [13]) but interdependent, as both components f and g occur in each equation. In fact the system is equivalent to a differential equation of second order, and it is completely

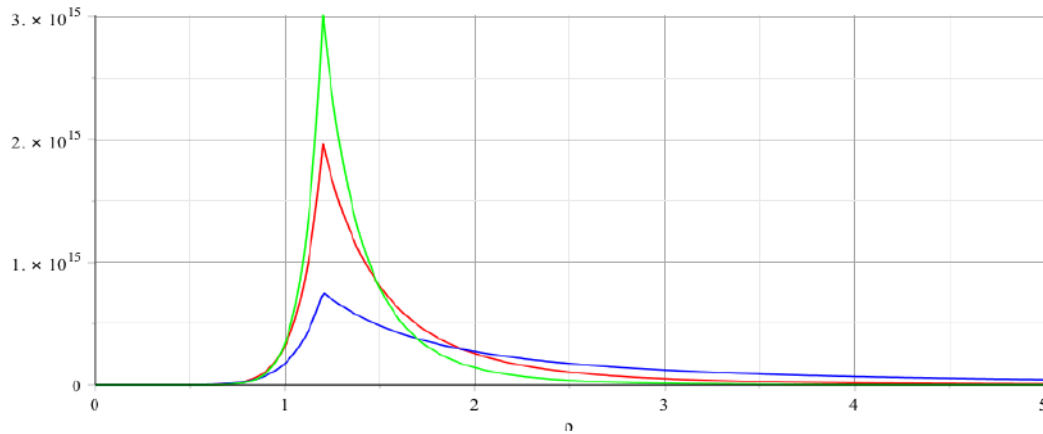


Figure 1. NEPD, for $n' = 1$ (blue), $n' = 2$ (red), $n' = 3$ (green), with $n' = |k|$. The radius ρ is in F.

solved by using effectively a second order equation, e.g. a Kummer's equation [14] or a Whittaker's [15] equation. Under these conditions, it is mathematically necessary for the global solution function to be not only continuous, but also to have a continuous derivative everywhere in the domain of real numbers. In [16], we have obtained this result for the large component, but it is an approximation, and it should be extended to both components to have better information on the wave functions.

- Problem #2. Expression (4), used to compute the wave function (in fact the part outside the nucleus), depends on an energy parameter E occurring in its parameters a, μ, p , and q . But the value of the energy E is the energy of solution for a point-like nucleus case. This is not really suitable in the case of the solution for a nucleus of finite size with a corrected potential.
- Problem #3. It is difficult to correctly evaluate the relativistic coefficient γ and the energy parameters, such as the kinetic energy, required for a better understanding of EDOs and possible interaction of deep-orbit electrons with nuclear fields.

Finally, it should be noted that there was a rather serious problem, in our early work on EDO solutions of the Dirac equation, about the HUR, apparently unsolved also in similar works existing in the literature: how can electrons confined in EDOs, very close to the nucleus, respect the HUR? This issue has been solved in an unexpected way, through the use of relativity, and a change in strategy towards HUR. Therefore, it is not indicated in the previous list and the solution, explained in detail in recent works [7], is briefly recalled in Section 3.

3. Semi-classical Computations/Simulations

To better know the energy parameters of EDOs and their possible existence, we made semi-classical studies [6–8] with many computations, by applying the following principles:

- We consider a radial potential energy PE built as a sum of inverse power terms, including the Coulomb potential, magnetic interactions, and possibly radiative corrections.
- We look for a local minimum of energy (LME) for an electron near the nucleus, while we consider its total energy TE including the potential energy PE. TE is specified below.
- But, most important for stable orbits, the HUR must be respected.

3.1. Special relativity and the HUR

3.1.1. Respecting the HUR

We decided to take HUR as a starting point, while considering an electron confined near the nucleus. We previously showed [2] that Special Relativity is necessary to have deep orbit solutions of quantum equations. Nevertheless, while starting from HUR [6,7], we find that the relativistic coefficient γ expected for EDOs had been greatly underestimated. In fact, electrons confined in deep orbits (EDO), with mean radius of order a few F, are highly relativistic (γ can be > 200). Here we summarily give some elements and results, specified in detail in the quoted references.

For an electron confined in a sphere of radius r , from momentum $|\mathbf{p}| \sim \hbar / r$ (to respect the HUR), and from its relativistic expression $p = \gamma mv$, we can deduce the following results:

$$\gamma = (1 - v^2/c^2)^{-1/2} \sim [1 + (\lambda_c)^2/r^2]^{1/2} \quad (6)$$

where λ_c denotes the “reduced” Compton wavelength, i.e. $\lambda_c = \hbar/mc$. For electrons, one has $\lambda_c \sim 386$ F. For EDOs, as it seems that $r \ll \lambda_c$, γ can be simplified into $\gamma \sim \lambda_c/r$. We gave examples [8] showing expression (6) gives realistic and rather precise values.

3.1.2. Relativistic correction of the Coulomb potential energy and confinement of electron in deep orbit

Because of the high level of the relativistic coefficient γ , it is interesting to consider the effects of the relativistic correction to the static Coulomb potential, as indicated in [17,18], under the resulting form of an effective dynamical potential noted V_{eff} , and already considered in [2,16]. The general form (3) of V_{eff} comes from the development of relativistic quantum equations (Dirac, Klein–Gordon) with the expression of the relativistic energy of a particle in a central field for a Coulomb potential energy V :

$$V_{\text{eff}} = V(E/mc^2) - V^2/2mc^2. \quad (7)$$

On the other hand, by replacing E by an approximate value γmc^2 in (7), we obtain the following form (8) including the coefficient γ :

$$V_{\text{eff}} = \gamma V - V^2/2mc^2. \quad (8)$$

While putting the full expression (6) of γ into (8), we obtain V_{eff} as a function of r , where α is the coupling constant:

$$V_{\text{eff}} = -(\alpha\hbar/r)([1 + (\lambda_c)^2/r^2]^{1/2} + \alpha\lambda_c/2r). \quad (9)$$

Finally, if r is of order a few F, one can obtain the following approximate form:

$$V_{\text{eff}} \sim \gamma V. \quad (10)$$

So, we have the two following results:

- (1) V_{eff} is always attractive
- (2) $|V_{\text{eff}}| \geq |V|$, i.e. V_{eff} is always a strengthening over the static Coulomb potential energy.

Moreover, and most importantly for the EDO's, we showed in previous works [7,8] that V_{eff} can easily confine an electron near the electron. Indeed, for r very small, the kinetic energy $\text{KE} = (\gamma - 1)mc^2$ has behavior in $1/r$, whereas V_{eff} has behavior in $1/r^2$. More precisely ([8], Fig. 1) we showed that for $r < 2.8$ F, one has $|V_{\text{eff}}| > \text{KE}$.

In fact, Relativity involvement, as defined by the HUR constraint on KE, is the solution for EDO confinement.

3.2. Semi-classical computations of EDOs

In order to find EDOs, we look for a Local Minimum of Energy (LME) of electron in a central potential PE, obtained by a balanced combination of electro-magnetic (EM) potentials near the nucleus. The total energy is equal to $TE = E_H + PE$, where E_H is defined by the following expression:

$$E_H = \sqrt{\frac{\hbar^2 c^2}{r^2} + m^2 c^4} \quad (11)$$

It is obtained from the relativistic expression of energy of a free electron, $(\mathbf{p}^2 c^2 + m^2 c^4)^{1/2}$, by putting $|\mathbf{p}| \sim \hbar/r$ for respecting the HUR. Note that $KE = E_H - mc^2$.

In previous work [7], we built a combination of EM potential energies, inspired by a study [6] of the Vigier–Barut model [19–24] and related works, then we took radiative corrections into account, i.e. essentially the Lamb shift (LS) [25–29], including two phenomena: electron Self-Energy (SE) and Vacuum Polarization (VP). In fact, the LS supplies a specific extra energy, corresponding to a *decrease of the binding energy*. So it has a global repulsive effect on the bound electron.

We made numerous computations of LME with variants on the combinations of EM potentials. Here, we give only a variant of example from [8], where the LS is expressed as a repulsive quasi-potential energy by means of extrapolations from known data tables on QED effects on orbital parameters. In fact, we put $V_{LS} = 0.623 \times 10^{-10}/\rho^3$ in J/F³. In Fig. 2, we plot an example curve of the binding energy $BE = KE + PE = TE - mc^2$, where the LME corresponds to $\rho \sim 1.4$ F.

In this example, the main parameters of the electron at the LME (at $\rho \sim 1.4$ F) have the following values:

- $\gamma \sim 275$,
- $BE \sim -509$ keV,
- $PE \sim -140.5$ MeV,

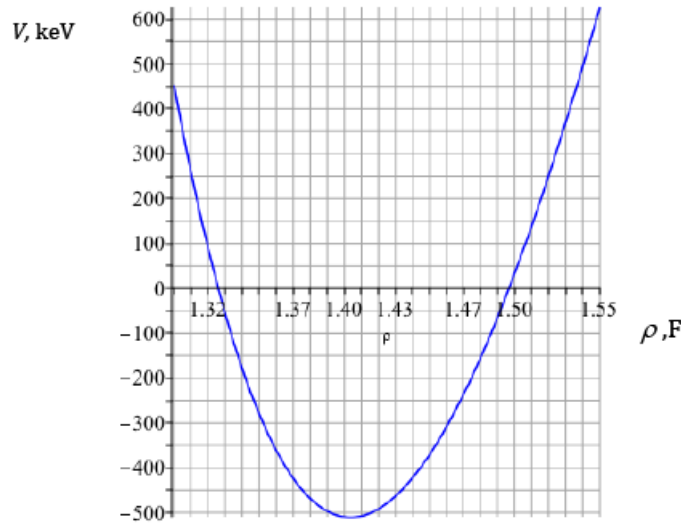


Figure 2. Plot of electron BE, for $1.3 \text{ F} < \rho < 1.55 \text{ F}$.

- $KE \sim 140 \text{ MeV}$.

3.3. Key information from semi-classical calculations

Semi-classical studies provided a lot of useful information for correcting the imperfections of the initial Dirac EDO's for finite nucleus case. Not only we can evaluate the relativistic coefficient γ , but also all the energy parameters. Moreover we found that the relativistic *Virial theorem* [30] was respected by ultra-relativist EDOs, in a very simple form and for various combinations of potentials. So, we can see that

- Electrons confined near the nucleus are ultra-relativistic.
- The relativistic Virial theorem is respected at the LME, in the following form: $KE/|PE| \sim \gamma/(\gamma + 1)$.

This allows us to deduce all the main parameters of the Dirac EDOs, computed at the mean radius of the probability density distribution, and to check their coherence: With a corresponding LME radius \rightarrow mean radius $\langle r \rangle$ of Dirac EDO solutions with finite nucleus, we can evaluate γ , TE, KE, and BE at $\langle r \rangle$. For example, one can show $TE \sim m_e c^2 / \gamma \sim m_e c^2 \langle r \rangle / \lambda_c$.

So, we can correctly adjust the energy levels of Dirac EDO's solution (see Problem #2), and know all the energy parameters (see Problem #3).

4. How to Apply the New Information Provided by Semi-Classical Computations, to Dirac EDOs?

4.1. A brief reminder of what the solution of a quantum equation for wave function consists of

Such a quantum equation generally has the following form: $H\psi = E\psi$. Summarily, we have two concomitant mathematical issues.

- (1) H is a “Hamiltonian”, representing the total energy of the considered system. It is generally a Hermitian operator including differential operators. For example, the momentum \mathbf{p} is expressed by the expression $-i\hbar \frac{\partial}{\partial \mathbf{X}}$, including a vector of partial derivatives on spatial coordinates, $\frac{\partial}{\partial \mathbf{X}}$.
Note a Hamiltonian can be multidimensional (e.g. in the Dirac equation). *So, we have to solve a differential equation.*
- (2) We look for ψ , an unknown wave function, and for E , unknown eigenvalues, which are *energy values* associated with eigenvectors ψ corresponding to wave function solutions. These can be characterized by integers, quantum numbers, if the set of eigenvalues is a discrete set, *composing energy levels*.

So, we have *to solve a spectra problem* [31] for H atom: to find eigenvalues associated with solutions of the differential equation.

4.2. Solving the Dirac equation for hydrogen atom with finite nucleus

4.2.1. Solving the system of radial differential equations

After separation of the angular and radial variables, one ends up with a system of two radial equations.

As we consider a H atom with non-point-like nucleus of radius $\sim R$, we have to solve radial differential equations, where the radius belongs to two separate domains of the real numbers, associated with the inside and the outside of the nucleus respectively. And the central potentials are very different in these domains.

- (i) Outside the nucleus, the static potential energy corresponds to the classical Coulomb potential, and is expressed by means of the formula $V_O = -e^2/r$, where e is the charge of the electron (expressed in suitable units).

- (ii) Inside the nucleus, the potential energy V_I is expressed by the chosen formula (4), with $Z = 1$, equivalent to $V_I = -(e^2/2R)(3 - r^2/R^2)$.

So the whole potential energy is described by a *piecewise* expression:

$$\text{Pot}(r) = V_I \quad \text{if } 0 \leq r \leq R \quad \text{and} \quad = V_O \quad \text{if } r > R.$$

As a consequence, the differential equation $\text{Eq}(r)$, using $\text{Pot}(r)$, will have a piecewise form:

$$\text{Eq}(r, \text{Pot}(r)) = \text{Eq}_I(V_I) \quad \text{if } 0 \leq r \leq R \quad \text{and} \quad = \text{Eq}_O(V_O) \quad \text{if } r > R.$$

The software used for differential equations, Maple, can solve any differential equation on a limited domain. For the system of Dirac radial equations, we can observe the following:

- (1) First, the formal solutions are very different in the two domains. As complex expressions including very different special functions (defined by series), they are very difficult to unify.
- (2) A solution on the limited domain considered (here the domain outside the nucleus) is formally the same as on the whole domain of real numbers.

Note we apply this reasoning only on the limited domain outside the nucleus: for the very small domain inside the nucleus, it is sufficient to solve the differential equations approximated by polynomials.

From the point #2, we deduce *the general solution for point-like nucleus case*, i.e. the solution on the whole domain of real numbers, *can be used for the domain associated with the nucleus outside*. So, for this domain, we can use, in principle, the solution indicated in Section 2.2, i.e. expression (4) of the pairs of functions (f, g) . Nevertheless, as noted in Problem #2, Section 2.2.3, expression (4) used to compute the wave functions solutions of the radial equations, depends on an energy parameter E occurring in the expressions of several parameters, a, μ, p, q . But the only value of E that we know is the one given by formula (3), corresponding to the energy levels of Dirac solutions for point-like nucleus case. Of course this is not really suitable in the case of solution for a nucleus of finite size with a corrected potential. When applying the *general solution* to *limited domain* $r > R$, for solutions *outside the nucleus*, the eigenvalue E' associated with the wave functions (f_O, g_O) must be different from the energy E of general solutions for point-like nucleus. So, *we have to solve a spectral problem*.

To address this issue, we use a kind of perturbative method, in the form of iterative computation until we reach a fixed point. It is explained in Section 4.2.3.

4.2.2. Connecting inside and outside solutions (Problem #1)

Before the fixed-point process, we consider the question of connecting the couples of inside and outside solutions at the nucleus surface, with continuity of the total functions and their derivatives.

More precisely, the couples of inside (f_I, g_I) and outside (f_O, g_O) solutions have to be *connected* at the surface of the nucleus, under the following conditions (Problem #1, Section 2.2.3):

- (1) We must satisfy the *continuity* at $r = R$, i.e. $f_I(R) = f_O(R)$ and $g_I(R) = g_O(R)$.
- (2) We must satisfy the *continuity of respective derivatives*

$$f'_I|_R = f'_O|_R \quad \text{and} \quad g'_I|_R = g'_O|_R.$$

Here we indicate, in a rather brief and simplified way, the successive steps that allow us to satisfy these conditions.

The functions f_O and g_O determined by expression (4), include the same multiplicative constant C , because of the coupling of the radial equations: i.e. we have $f_O = C \text{Exp}f$, $g_O = C \text{Exp}g$, where $\text{Exp}f$ and $\text{Exp}g$ are the expressions deduced from the computation of (4) and represent two functions of the radius r .

- I As a first step, we decouple these two functions, while writing $f_O = C1 \text{Exp}f$ and $g_O = C2 \text{Exp}g$.
- II (a) While using an ansatz as in Section 2.2.1, we compute a polynomial P_f as an approximation of f_I . So f_I is expressed in powers of the radius r and includes the free parameter λ_f .
We compute also the derivative f'_I in r of f_I ; f'_I also includes the free parameter λ_f .
(b) Then, we compute the derivative $f'_{O'}$ in r of the function f_O . Of course, the function f'_O includes the multiplicative parameter $C1$.
(c) Finally, we calculate $f_I(R)$, $f_O(R)$, $f'_I(R)$ and $f'_O(R)$, where R is the “junction” radius between the inside and outside of the nucleus. Then we solve the system of equations $\{f_I(R) = f_O(R), f'_I(R) = f'_O(R)\}$. The solution of this equation gives a result in the form $\{C1 = a, \lambda_f = b\}$, where a and b are two real numbers, and we replace $C1$ and λ_f by their values in the expressions for f_I , f_O , f'_I , and f'_O .
- III A similar process is applied to the second component, represented by the couple of functions (g_I, g_O) , which leads, after solving a system of equation at the junction radius R , to a result having the form $\{C2 = c, \lambda_g = d\}$, with two real numbers c and d .
- IV In order to restore the initial coupling of components f and g , we put $F_I = cf_I$, $F_O = cf_O$ and similarly for their derivatives (just for checking the condition (ii) above).

For the g components, we multiply by a , i.e. $G_I = ag_I$, $G_O = a g_O, \dots$

Finally, we denote, by $F = f_I U f_O$, the total function obtained by connecting f_I with f_O at $r = R$, and similarly $G = g_I U g_O$.

4.2.3. Fixed point method for solving the spectral problem (Problem #2)

We indicate in very simplified form, the iterative process used. Starting point: for a given value of radial quantum number n' , expression (3) of energy for solution in the point-like nucleus case, gives a value noted E_0 .

- Step 0: we take E_0 to determine the total wave function $\Psi_0 = (F, G)$, as explained in the prior sub-section, and we compute the electron probability density. Then we deduce the average orbital radius r_0 and we can directly calculate the total energy E_1 of electron at r_0 , as explained in Section 4.3. Next we will go to Step 1, where a new value r_1 of orbital radius is computed.
- Step 1: Normally we have $E_1 \neq E_0$. Then, as in Step 0, E_1 determines a new wave function Ψ_1 and we compute the mean orbital radius r_1 from the new electron probability density distribution. From this, we calculate the new energy E_2 at the radius r_1
 - If $E_2 \sim E_1$ (up to three digits), we consider that we reached a fixed point.
 - If $E_2 \neq E_1$, we go to a Step 2 similar to Step 1.

In fact, many computations, for different values of the radial number n' and even by varying the “initial” value of energy E_0 , lead to the following observations:

- The mean radius corresponding to wave function Ψ varies very slowly as a function of the energy E injected in expression (4) to calculate Ψ .
- At Step 1, r_1 is already close to r_0 .
- We can stop the process at Step 1 to check that the fixed point is practically reached and, if so, take Ψ_1 as a wave function solution of the problem and E_1 as total energy of this solution.

4.2.4. EDO solutions of Dirac equation for H atom with finite nucleus

In Fig. 3, we plot the curves of normalized probability density corresponding to $n' = 1$ and $n' = 2$, while considering a junction radius $R = 1$ F, and for $0.4 \text{ F} < \rho < 3 \text{ F}$, where ρ denotes the radius in F.

We give the mean radius $\langle \rho \rangle$, and the values of the relativistic coefficient γ and the kinetic energy KE, which were not obtained with the initial results indicated in Section 2. Moreover, we compare the values for the total energy, denoted by TE, and the binding energy BE obtained with our new method, with those obtained in the initial solutions, corresponding to the point-like nucleus case (PLN), written in italic.

- $n' = 1$, $\langle \rho \rangle \sim 4.5 \text{ F}$, $\gamma \sim 84$,
KE $\sim 42.5 \text{ Mev}$, TE $\sim 6 \text{ kev}$ (1.8 kev, PLN), BE $\sim -505 \text{ kev}$ ($\sim -509 \text{ kev}$, PLN).
- $n' = 2$, $\langle \rho \rangle \sim 1.13 \text{ F}$, $\gamma \sim 405$,
KE $\sim 206 \text{ Mev}$, TE $\sim 1.5 \text{ kev}$ (1 kev, PLN), BE $\sim -509.5 \text{ kev}$ ($\sim -510 \text{ kev}$, PLN).

Moreover, one can verify the mean radius $\langle \rho \rangle$ and the total energy TE satisfy the following relationship: $\langle \rho \rangle \sim \lambda_c \text{TE}/mc^2$, where λ_c is the reduced Compton wavelength ($\sim 386 \text{ F}$) and m is the electron mass.

5. Can EDO States be Populated?

5.1. Heisenberg barrier

Here is a first attempt to evaluate a possible population of EDO states by tunneling from the atomic-electron ground state, in the form of superposition of quantum states. To simplify the situation, we consider only two antagonistic interactions, one due to the attractive relativistic effective potential energy V_{eff} , and the other to the HUR, increasing the kinetic energy to prevent the containment of electron: we call it Heisenberg barrier ([8], p. 478).

These are not static fields, but *dynamic effects* associated with a possible increasing confinement of the electron.

- On one hand, we consider the kinetic energy $\text{KE} = (\gamma - 1)mc^2$.

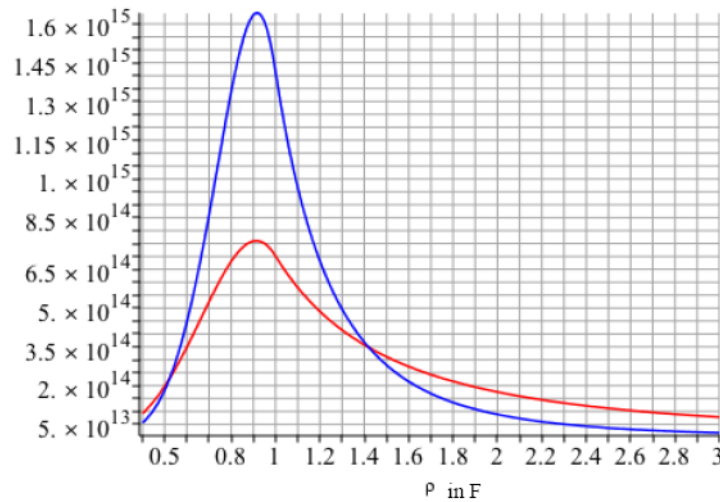


Figure 3. Plot of the normalized probability density, for $n' = 1$ (red) and $n' = 2$ (blue).

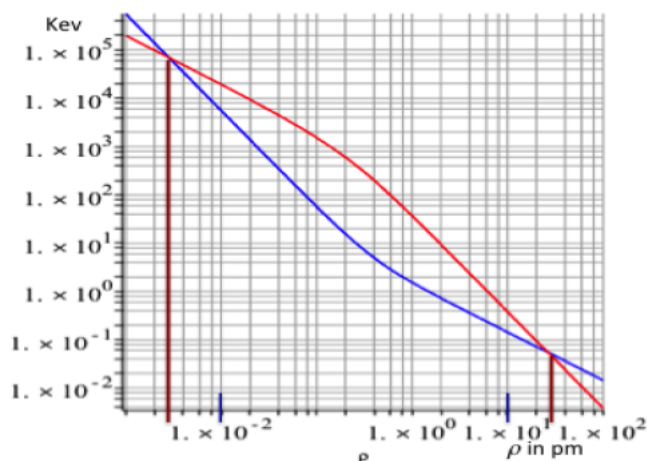


Figure 4. Loglogplot of KE and $|V_{\text{eff}}|$ for $1 F < \rho < 100$ pm.

- On the other hand, the relativistic effective potential energy $V_{\text{eff}} = \gamma V - V^2/2mc^2$, where the relativistic coefficient γ for an electron confined at a radius $\leq \rho$ is given by $\gamma \sim [1 + (\lambda_c/r)^2]^{1/2}$.

In Fig. 4, we plot KE and $|V_{\text{eff}}|$, for $1 F < \rho < 100$ pm, to clearly show the existence of three zones: for $1 F < \rho < 100$ pm.

- (1) For $26.5 \text{ pm} < \rho$, the atomic zone, where $\text{KE} < |V_{\text{eff}}|$.
- (2) For $2.8 F < \rho \leq 26.5 \text{ pm}$, a zone where $\text{KE} > |V_{\text{eff}}|$.
- (3) For $1 F < \rho \leq 2.8 F$, an EDO zone, where $\text{KE} < |V_{\text{eff}}|$.

Remark. In fact, the presence of EDO electrons is not limited to the zone #3, since we found an EDO wave function having a probability density with mean radius at $4.5 F$, because of the very large tail extending far beyond the range displayed in Fig. 3. But here, we only considered the strongly attractive potential V_{eff} , in a simplified semi-classical analysis.

We make the assumption that an increasing containment of electron wave packet is possible.

The start of this increasing containment is possible, because in the atomic zone #1, we have $\text{KE} < |V_{\text{eff}}|$, which can push a (tiny) fraction of the electron wave packet, whose maximum probability of presence is at the Bohr radius, i.e. at $53 \text{ pm} \sim 2 \times 26.5 \text{ pm}$, to move towards the nucleus until 26.5 pm .

But, arrived at 26.5 pm and for reaching the zone #3, the wave packet should have to go through the zone #2, where the repulsive effect of kinetic agitation required to satisfy the HUR is greater than the attractive effect of the potential V_{eff} .

We say the zone #2 forms a *Heisenberg barrier* between the zone #1 and the zone #3. Of course, this Heisenberg barrier is a virtual dynamic barrier, unlike the usual potential barriers. In addition, there is a reversal of roles between potential energy and kinetic energy: in the usual cases, the kinetic energy KE pushes an electron to cross a barrier, while the potential energy Pr is repulsive and prevents the electron from crossing the potential barrier, and if $Pr > \text{KE}$, a pure classical mechanical reasoning prohibits the crossing. Then only a quantum process of tunneling allows a fraction of the amplitude of the wave associated with the electron to cross the barrier.

Here, it is the attractive dynamic potential of V_{eff} that tends to push the electron to cross the barrier for having an increasing containment, whereas the increasing kinetic energy KE due to the containment, a reactive agitation implied by the HUR, tends to push the electron back. And in pure classical mechanical reasoning, if $|V_{\text{eff}}| < \text{KE}$, the containment of the electron should not increase. But we consider an *extension of the quantum tunneling process* to this specific situation, allowing a fraction of the amplitude of the electron wave to cross the Heisenberg barrier to reach zone #3.

If considering $\Delta E = \text{KE} - |V_{\text{eff}}|$, we can find a maximum of ΔE , equal to ~ 17 MeV, at $\rho \sim 5.6$ F. This is the point at which the barrier to orbital stability is greatest. We plot the curve of ΔE in Fig. 5 for $2.8 \text{ F} < \rho < 27 \text{ pm}$.

5.2. Tunneling through the Heisenberg barrier

To compute a possible tunneling, we use the WKB (*Wenzel–Kramers–Brillouin*) approximation [32,33] in one dimension, similar to the calculation of the Gamow astrophysical factor [34].

We put $K(\rho) = (2m\Delta E)^{1/2}$, where $\Delta E = \text{KE} - |V_{\text{eff}}|$. Note that $K(\rho)$ has physical dimension of momentum. We plot the curve of $K(\rho) \times 10^{21}$, for $2.8 \text{ F} < \rho < 27 \text{ pm}$ in Fig. 6 (the multiplicative factor 10^{21} is only used to simplify the writing of values on the vertical axis). We can remark the similarity of the shape of curves in Figs. 5 and 6.

Then, we compute $Q = \int_{\rho_0}^{\rho_1} K(\rho) d\rho$, where $\rho_0 \sim 2.8 \text{ F}$, $\rho_1 \sim 27 \text{ pm}$, and we put $w_{\text{exp}} = Q/\hbar = 5.65$ which is a dimensionless number. Note that the integral Q of $K(\rho)$ corresponds to the blue area (divided by 10^{21}) below the curve of $K(\rho)$.

The weakening factor of the electron wave amplitude is given by $w \sim e^{-w_{\text{exp}}} \sim 0.003$. So, the electron presence probability is $P = w^2 \sim 9 \times 10^{-6}$. We interpret this result by saying that the general wave function of an 1S electron orbital could be a *linear combination* of EDO state and atomic ground state, with amplitude coefficient $\lambda_{\text{EDO}} \sim 0.003$.

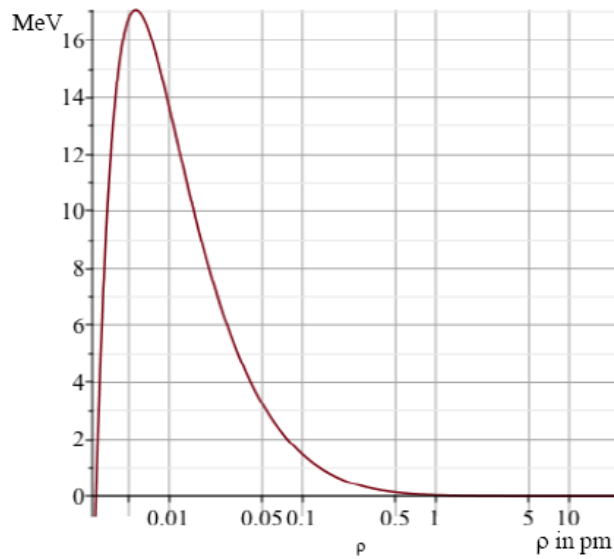


Figure 5. Semilogplot of ΔE , the energy of the Heisenberg barrier, for $2.8 \text{ F} < \rho < 27 \text{ pm}$.

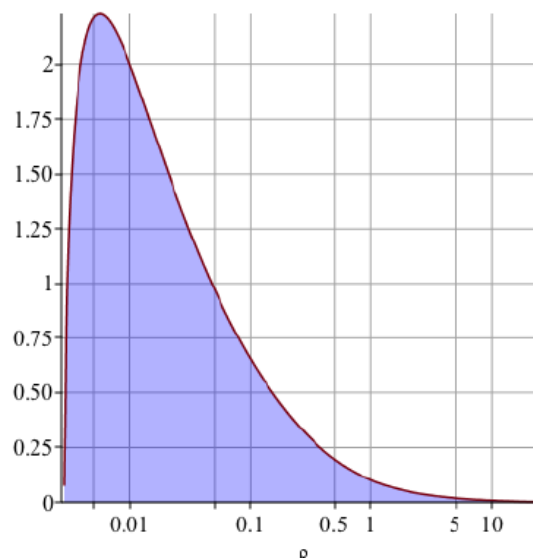


Figure 6. Semilogplot of $K(\rho) \times 10^{21}$ for $2.8 \text{ F} < \rho < 27 \text{ pm}$.

Remark. In [35], the authors also consider that a general solution of the Dirac equation for an electron (or a muon) bound in an atom is a linear combination of the regular (usual) solution and an extra solution, usually neglected; Indeed, this latter solution is eliminated when considering a point-like nucleus; but, it becomes acceptable when taking into account the size of the nucleus, which eliminates the singularity at the origin. Nevertheless, in their numerical results on many atoms, they do not provide the coefficients of linear combinations but the energy shifts due to the size of the nucleus, which is the purpose of their work.

6. Conclusion and Prospect

- (1) Semi-classical simulations carried out in our previous works allow us to solve questions about EDOs as solutions of the Dirac equation with finite nucleus. Indeed, while making semi-classical analysis and computation, we showed the following results:
 - (a) For an electron confined near the nucleus, the HUR requires a strong containment energy but allows us to determine a value for the relativistic γ .
 - (b) We know that the *EDO solutions are highly relativistic*, which is an *important result for LENR*, and as a consequence, the *magnitude order of KE* can be in the 100 MeV range
 - (c) The effective potential, V_{eff} , a relativistic correction of the Coulomb potential deduced from relativistic quantum equations (Dirac or Klein–Gordon equations), can confine deep-orbit electrons within the nuclear region.
 - (d) For a deep electron having an LME and respecting the HUR, we can compute the relativistic coefficient γ , the total energy TE, the kinetic energy KE and the binding energy BE, at the radius r of the LME.

While going back to EDO solutions of Dirac equation for atomic H, by considering a finite nucleus:

- (i) We can recalculate the radial wave functions of Dirac EDO solutions and determine the correct energy level E associated with the radial quantum number n' , and moreover we can compute the coefficient γ , and BE for electron at the mean radius $\langle r \rangle$ of the probability density distribution. So, we solve Problems #2 and #3 (Section 2.2.3, *Obtained results and discussion on imperfections*)
 - (ii) Moreover, we obtain wave functions with smooth continuous shapes and having continuous derivatives everywhere i.e., we solve Problem #1.
- (2) (a) Nevertheless, the Dirac equation seems to provide an EDO solution for each value n' of the radial quantum number, whereas semi-classical computations that do not include resonances between electron-orbital and emitted-photon frequencies as described in [36], give only a single EDO solution. On the one hand, this behavior difference between the quantum equation and semi-classical results also happens for regular solutions: semi-classical computation of electron LME in H atom, carried out while considering only the total energy, provides only the ground (Bohr) state, while a quantum equation, e.g. the Schrödinger equation provides all the excited states, corresponding to increasing values of the main quantum number n (involving the angular quantum number l , as $n = n' + l + 1$). On the other hand, unlike the regular solutions while considering Dirac EDO wave functions, the mean $\langle r \rangle$ radius of the probability radial density distribution decreases when the radial number n' increases. As a consequence, and since $\langle r \rangle$ decreases on a bounded interval, the sequence $\langle r \rangle (n')$ of the values of $\langle r \rangle$ as function of n' , has an accumulation point when n' tends towards infinity. In other words, it means that for high values of n' , the wave function solutions are practically and physically indistinguishable. The meaning of this situation would require further physical interpretation. Can we say that because of quantum fluctuations, from a certain integer N to be defined, all the solutions for $n' > N$ are confounded, and that finally there is only a finite number N of solutions?
- (b) Another question about the Dirac solutions arises, when comparing the characteristic energy parameters of these solutions and those of the semi-classical computations: it seems that semi-classical solution, with LME at radius $r \sim 1.4 F$, is closer to the Dirac solutions for $n' = 2$, where $\langle r \rangle \sim 1.13 F$ than the one for $n' = 1$, where $\langle r \rangle \sim 4.5 F$. Of course, we know the Dirac results are dependent on a somewhat arbitrary choice of the junction radius R between inside and outside the nucleus. But even with reasonable decrease of R , we still have a significant gap between the semi-classical solution and the Dirac solution for $n' = 1$: for example, by putting $R = 0.84 F$, i.e. $< 0.87 F$, which is at the present time the official value of charge radius of the proton, we obtain a mean radius $\langle r \rangle \sim 3.95 F$ for $n' = 1$. And on another hand, despite many semi-classical calculations with various combinations of potentials, we never found an LME at a radius $r > 2 F$. The question therefore arises as to *what the solution for $n' = 1$ physically represents, if it is not the basic EDO state?*
- (3) In Section 5, we only began to address the issue of EDO population, by using the WKB approximation for tunneling from atomic state to EDO state. On one hand, the WKB method has been applied in dimension one, when it would make more sense to do it in dim 3. For the time being, various attempts in this direction have not led to realistic results, and the question remains to be addressed.

On another hand, a possible lead would be to look for physical parameters in condensed matter, likely to increase the tunneling toward EDO states. Finally, it should be noted that the analysis carried out in Section 5.1 allows us to give an answer to a legitimate question posed by the referee: why all hydrogen atoms in the Universe (and this is about 74% of all atoms in the Universe) do not spontaneously transfer from standard states to these super-deep levels?

Indeed, we can reasonably expect that the existence of the Heisenberg barrier prevents the electron from *spontaneously* transferring from standard states to super-deep levels. This also answers the naïve question

encountered in forums: *why the electron does not fall into the nucleus?*

- (4) Finally, LENR features such as energy transfer with neither gamma radiation nor energetic particles, requires *enhanced internal conversion*. So, we study possible connections between highly energetic deep electrons and nuclei, hadrons and quarks.

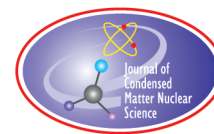
Acknowledgement

This work is supported in part by HiPi Consulting, Windsor, VA, USA; and by the Science for Humanity Trust Inc., Tucker, GA, USA. The authors would like to thank the reviewer for his judicious advice and recommendations allowing us to improve the comprehension of our work

References

- [1] A. Meulenberg and K.P. Sinha, Deep-electron orbits in cold fusion, *17th Int. Conf. on Condensed Matter Nuclear Science*, Daejeon, South Korea, 12–17 August, 2012, *J. Condensed Matter Nucl. Sci.* **13** (2014) 368–377, http://coldfusioncommunity.net/pdf/jcmns/v13/368_JCMNS-Vol13.pdf.
- [2] J.L. Paillet and A. Meulenberg, Special relativity: the source of the electron deep orbits, *Found. Phys.* **47**(2) (2017) 256–264.
- [3] A. Meulenberg and J.L. Paillet, Nuclear-waste remediation with femto-atoms and femto-molecules, ICCF-21, *21st Int. Conf. for Condensed Matter Nuclear Science*, 3–8 June 2018, Fort Collins, CO, USA, *J. Condensed Matter Nucl. Sci.* **29** (2019) 353–371, http://coldfusioncommunity.net/pdf/jcmns/v29/353_JCMNS-Vol29.pdf, <https://www.youtube.com/watch?v=J6zQXb-L7L8&t=136s>.
- [4] J.L. Paillet and A. Meulenberg, Electron deep orbits of the hydrogen atom, *Proc. 11th Int. Workshop on Hydrogen Loaded Metals*, Airbus Toulouse, 15–16 Oct. 2015, *J. Condensed Matter Nucl. Sci.* **23** (2017) 62–84, http://coldfusioncommunity.net/pdf/jcmns/v23/62_JCMNS-Vol23.pdf.
- [5] J.A., Maly and J. Va'vra, Electron transitions on deep Dirac levels II, *Fusion Sci.Technol.* **27**(1) (1995) 59–70, http://www.ans.org/pubs/journals/fst/a_30350.
- [6] J.L. Paillet and A. Meulenberg, Advance on electron deep orbits of the hydrogen atom, Proc. of ICCF20, *20th Conf. on Cond. Matter Nuclear Science*, Sendai, Japan, 2–7 October 2016, *J. Condensed Matter Nucl. Sci.* **24** (2017) 258–277, http://coldfusioncommunity.net/pdf/jcmns/v24/258_JCMNS-Vol24.pdf.
- [7] J.L. Paillet and A. Meulenberg, deepening questions about electron deep orbits of the hydrogen atom, *Proc. 12th Int. Workshop on Hydrogen Loaded Metals*, Asti (Italy), 5–9 June 2017, *J. Condensed Matter Nucl. Sci.* **26** (2018) 56–68, http://coldfusioncommunity.net/pdf/jcmns/v26/56_JCMNS-Vol26.pdf, <http://vixra.org/abs/1707.0284>.
- [8] J.L. Paillet and A. Meulenberg, On highly relativistic deep electrons, Proc. of ICCF21, *21th Conf. on Cond. Matter Nuclear Sci.* Fort Collins, CO, USA, 3–8 June 2018, *J. Condensed Matter Nucl. Sci.* **29** (2019) 472–492, http://coldfusioncommunity.net/pdf/jcmns/v29/472_JCMNS-Vol29.pdf.
- [9] J.A. Maly and J. Va'vra, Electron transitions on deep Dirac levels I, *Fusion Sci.Technol.* **24** (3) (1993) 307–318, http://www.ans.org/pubs/journals/fst/a_30206.
- [10] J.L. Paillet and A. Meulenberg, Basis for electron deep orbits of the hydrogen atom, Proc. of ICCF19, *19th Int. Conf. on Cond. Matter Nuclear Science*, Padua, Italy, 13–17 April 2015, *J. Condensed Matter Nucl. Sci.* **19** (2016) 230–243, 2016, http://coldfusioncommunity.net/pdf/jcmns/v19/230_JCMNS-Vol19.pdf.
- [11] J.L. Paillet and A. Meulenberg, Arguments for the Anomalous Solutions of the Dirac equations, *J. Condensed Matter Nucl. Sci.* **18** (2016) 50–75, http://coldfusioncommunity.net/pdf/jcmns/v18/50_JCMNS-Vol18.pdf.
- [12] S. Fluegge, *Practical Quantum Mechanics*, Vol. 2, Springer, Berlin, 1974.
- [13] L.I. Schiff, *Quantum Mechanics*, 3rd Edn., McGraw-Hill, New-York, 1968.
- [14] http://en.wikipedia.org/wiki/Confluent_hypergeometric_function.
- [15] E.T. Whittaker and G.N. Watson, *Modern Analysis*. 4th Edn., Chapter XVI, Cambridge Univ. Press, 1940.
- [16] J.L. Paillet and A. Meulenberg, Relativity and electron deep orbits of the hydrogen atom, *Proc. of the 1st French Symp. RNBE-2016 on Cond. Matter Nucl. Sc.*, Avignon, 18–20 March 16, *J. Condensed Matter Nucl. Sci.* **21** (2016) 40–58, http://coldfusioncommunity.net/pdf/jcmns/v21/40_JCMNS-Vol21.pdf.

- [17] S.V. Adamenko and V.I. Vysotskii, Mechanism of synthesis of superheavy nuclei via the process of controlled electron–nuclear collapse, *Found. Phys. Lett.* **17**(3) (2004) 203–233.
- [18] S.V. Adamenko and V.I. Vysotskii, Evolution of annular self-controlled electron–nucleus collapse in condensed targets, *Found. Phys.* **34** (??) (2004) 1801–1831.
- [19] J.P. Vigier, New hydrogen (deuterium) Bohr orbits in quantum chemistry and cold fusion processes, *Proc. of ICCF 4*, 3–6 Dec. 1993, Lahaina, Maui, Hawaii. TR-104188-V4, Section 7, 1994, pp. 1–25.
- [20] A.O. Barut Prediction of new tightly-bound states of H_2^+ (D_2^+) and cold fusion experiments, *Int. J. Hydrogen Energy* **15** (12) (1990) 907–909.
- [21] A. Dragic, Z. Maric and J.P. Vigier, *Phys. Lett. A* **237** (1998) 349–353.
- [22] N.V. Samsonenko, D.V. Tahti and F. Ndahayo, On the Barut–Vigier model of the hydrogen atom physics, *Phys. Lett. A* **220** (1996) 297–301.
- [23] S. Ozelik and M. Simsek, *Phys. Lett. A* **152** (1991) 145–149.
- [24] R.L. Amoroso and J.P.(Posth) Vigier, Evidency ‘Tight Bound States’ in the hydrogen atom, *Unified Field Mechanics, 9th Int. Symp. Honoring Math. Physicist J.-P. Vigier*, Dec. 2014.
- [25] H.A. Bethe, The electromagnetic shift of energy levels, *Phys. Rev.* **72** (1947) 337.
- [26] W. Lamb and R. Retherford, Fine structure of the hydrogen atom by a microwave method, *Phys. Rev.* **72**(3) (1947) 241–243.
- [27] J.M. Jauch and F. Rohrlich, *The Theory of Photons and Electrons*, Addison–Wesley, Reading, USA, 2nd Printing, June 59.
- [28] F.J. Dyson, *Advanced Quantum Mechanics*, 2nd Edn., arXiv:quant-ph/0608140v1 18 Aug. 2006.
- [29] F.Mandl and G. Shaw, *Quantum Field Theory*, 2nd Edn., Wiley, Chichester, UK, 2010.
- [30] *Virial Theorem*, https://en.wikipedia.org/wiki/Virial_theorem, 3 Nov. 2019.
- [31] *Spectral Theory*, https://en.wikipedia.org/wiki/Spectral_theory, 26 Sept. 2019.
- [32] W. Göss, Hole trapping and the negative bias temperature instability, Ph.D. thesis, Technische Universität Wien, 2011, *Physical Basis A2: Wenzel-Kramers-Brillouin Method*, <http://www.iue.tuwien.ac.at/phd/goes/>.
- [33] *WKB approximation*, Wikipedia, https://en.wikipedia.org/wiki/WKB_approximation, 17/11/2019.
- [34] *Gamow Factor*, Wikipedia, https://en.wikipedia.org/wiki/Gamow_factor, 14/10/2019.
- [35] R.T. Deck, Jacques G. Amar and Gustave Fralick, Nuclear size corrections to the energy levels of single- electron and -muon atoms, *J. Phys. B: At. Mol. Opt. Phys.* **38** (2005) 2173–2186.
- [36] A. Meulenberg, Creation and fusion of photons, Paper 8121-29, presented at SPIE Optics + Photonics 2011, Conference 8121 The Nature of Light: What are Photons? IV, 21–25 August 2011, San Diego, CA USA in Appendix B: Conditions for Radiation and A. Meulenberg, “The Photon-Quantized Atom”, https://www.researchgate.net/publication/337155472_The_Photon-Quantized_Atom.



Research Article

Distant Behind-screen Action of Undamped Temperature Waves (Long-distance Propagation, X-ray Generation, LENR Stimulation)

V.I. Vysotskii* and M.V. Vysotsky

Taras Shevchenko National University of Kyiv, Ukraine

A.A. Kornilova, T.B. Krit and S.N. Gaydamaka

Moscow State University, Moscow, Russia

P.L. Hagelstein

Massachusetts Institute of Technology, USA

Abstract

The physical mechanism of the generation, features of propagation and the possible use of undamped temperature waves are considered. The process of generation of these waves is related to the possibility of reversibility of local relaxation thermodynamic processes of heat transfer. In the course of experiments, it was shown that such waves can exist only at certain frequencies, depending on the relaxation time. The possibility of energy transfer using these waves over a long distance has been investigated. It is shown that using of these waves X-ray generation is possible, and effective stimulation of nuclear fusion in a TiD target located behind a thick metal screen which is remote from the wave source. In this work is also considered a possible physical mechanism for the realization of LENR reactions connected with the formation of coherent correlated states of interacting particles under the action of these temperature waves.

© 2020 ISCMNS. All rights reserved. ISSN 2227-3123

Keywords: Alpha particle generation, Coherent correlated states, LENR, Undamped temperature waves, X-ray generation

1. Introduction

The problem of the realization and use of LENR, which began with simple electrolytic experiments of Fleishman and Pons, is currently being implemented in different material media and based on fundamentally different physical phenomena. One of the interesting and promising methods is the possibility of stimulation of such nuclear processes in remote objects. Previously, such problems were investigated and partially resolved only through the use of ultrashort

*Corresponding author. E-mail: vivysotskii@gmail.com.

and superpower laser pulses, on the basis of which attempts were made to realize inertial hot nuclear fusion. Years of research have shown that this is an incredibly expensive and very inefficient system.

In contrast to this practically dead-end system, we have proposed a fundamentally new concept for implementing remote LENR using previously unknown undamped temperature waves. Detailed analysis has shown that the base (“standard”) equations of thermodynamics are incorrect in the analysis of very fast thermal processes [1–3], due to the fact that these equations do not take into account local the thermal relaxation time in the material propagation medium. Taking into account this very important circumstance has led to the possibility of the existence of undamped heat waves, which can exist only at certain high frequencies [1–3]. After conducting a series of basic studies [4–8] we created and successfully demonstrated a remote LENR system that works on the basis of these waves and this concept [9].

2. Paradox and Realization of Undamped Temperature (Thermal) Waves

Let us look at the typical logic of constructing the thermal diffusivity equation. The standard method for obtaining the thermal diffusivity equation is based on the use of two heat conduction equations. In these “standard” equations, the process of heat transfer is considered as a transition between infinitely small cells, each of which is always in equilibrium state. One of the basic equations for heat transfer is the well known Fourier law, which determines the temperature dependence of the heat flux $\vec{q}(\vec{r}, t)$ and has the following form

$$\vec{q}(\vec{r}, t) = -\lambda \cdot \text{grad}(T(\vec{r}, t)) \quad (1)$$

in any material medium with a constant heat-conduction coefficient λ .

Another basic relationship is the continuity equation

$$\rho c_v \frac{\partial T(\vec{r}, t)}{\partial t} = \text{div } \vec{q}(\vec{r}, t), \quad (2)$$

which causally relates a spatial change in the energy flux to a temperature change in a medium with volume (mass) density ρ and the heat capacity c_v . From these two equations follows the equation of thermal diffusion in a material medium without heat sources

$$\rho c_v \frac{\partial T(\vec{r}, t)}{\partial t} = \lambda \text{div } \{\text{grad}[T(\vec{r}, t)]\} \quad (3)$$

The general and well known solution of this equation corresponds to two counter-propagating plane waves

$$T = A e^{-\kappa x} e^{i(\omega t - \kappa x)} + B e^{\kappa x} e^{i(\omega t + \kappa x)}. \quad (4)$$

Here $\kappa = \sqrt{\omega/2G}$ is the spatial attenuation coefficient of these waves, $G = \lambda/\rho c_v$ is the coefficient of thermal-diffusivity.

A very important feature of this solution is the equality of the attenuation coefficient κ and the wave number. It means that the temperature wave attenuates over a spatial interval equal to several wavelengths.

It was shown in our works (e.g. [1–3]) that the “standard” heat conduction equations (1)–(3) of classical thermodynamics are incorrect at the analysis of very fast thermal processes. This is due to the fact that these equations do not take into account the final (non-zero) local thermal relaxation time τ in the material propagation medium.

Let us consider in more detail the two initial equations. The first of them is quite logical and determines the energy flow based on the spatial distribution of the temperature of the medium. In this ratio, a non-uniform temperature distribution produces an instantaneous value of the heat flux. In contrast, the second equation (continuity equation) contains an internal contradiction, since it follows that the temperature change is determined by the magnitude of the heat flux at the same time t . In the general case, this is an incorrect assumption, since the very concept of “temperature” corresponds to a locally equilibrium state of the system, the implementation of which requires a certain time – the time of thermal relaxation.

Obviously, if we consider processes with a slow change in temperature, then the relaxation process is insignificant. But if the temperature changes rapidly, then such an assumption (ignoring the final relaxation time) can lead to very significant errors.

The thermal relaxation time depends completely on the type of material medium and the nature of the interaction of particles in it. The shortest relaxation time corresponds to metals in which it does not exceed $\tau \approx 10 - 100$ fs. In water, it is determined by the quantity $\tau \approx 1 - 10$ ps, and in gas it can be calculated by the simple formula $\tau \approx 10/n\langle\sigma(\nu)v\rangle$, in which $\sigma(\nu)$ is a scattering cross section of the molecules, n is the concentration of molecules, v is the speed of molecules. In air under normal conditions (atmospheric pressure and room temperature), the relaxation time is equal to $\tau \approx 10$ ns and may change with changes in humidity and impurities of other gases.

The simplest (but rather effective) way of this relaxation accounting is to modify the continuity equation with the time shift and taking into account which part of this equation is the result of thermal action: a change in temperature $T(\vec{r}, t + \tau)$ over time

$$\rho c_v \frac{\partial T(\vec{r}, t + \tau)}{\partial t} = -\text{div } \vec{q}(\vec{r}, t), \quad (5a)$$

or a change in the flow of thermal energy $\vec{q}(\vec{r}, t + \tau)$ in space

$$\text{div } \vec{q}(\vec{r}, t + \tau) = -\rho c_v \frac{\partial T(\vec{r}, t)}{\partial t}. \quad (5b)$$

In the process of propagation of a heat wave, these processes are always connected and for this reason it is necessary to take into account both variants of this equation.

As a result, a joint analysis of Eqs. (1) and (5) leads to a modified equation of thermal conductivity

$$\frac{\partial T(\vec{r}, t \pm \tau)}{\partial t} = G \nabla^2 T(\vec{r}, t), \quad (6)$$

which takes into account the time delay (for thermal relaxation) between the local thermal energy flux and the change in the local temperature.

If we use the general form of the wave solution of this equation

$$T(\vec{r}, t) = A e^{i(\omega t + \vec{g}\vec{r})} + B e^{i(\omega t - \vec{g}\vec{r})},$$

then in 1D case we arrive at the system of dispersion equations for the real and imaginary parts of wave number $g = g' + i g'' \equiv k + i \delta$

$$g^2 = -i(\omega/G) e^{\pm i \omega \tau}, \quad (7)$$

$$(g')^2 - (g'')^2 = \pm(\omega/G) \sin \omega \tau, \quad g' g'' = -(\omega/2G) \cos \omega \tau.$$

From these equations follow expressions for the actual wave number k and coefficient of attenuation δ of the temperature wave

$$k = \kappa |\cos(\omega\tau/2) \pm \sin(\omega\tau/2)|, \quad (8a)$$

$$\delta = \kappa |\cos(\omega\tau/2) \mp \sin(\omega\tau/2)|, \quad \kappa = \sqrt{\omega/2G}. \quad (8b)$$

The final solution of the modified equation of thermal conductivity (6) corresponds to two oncoming plane waves and takes the form

$$\begin{aligned} T(\omega, x, t) &= A_\omega e^{-\delta x} e^{i(\omega t - k'x)} + B_\omega e^{\delta x} e^{i(\omega t + kx)} \\ &\equiv A_\omega \exp\left(-\kappa \left|\cos \frac{\omega\tau}{2} \pm \sin \frac{\omega\tau}{2}\right| x\right) \exp\left\{i\left(\omega t - \kappa \left|\cos \frac{\omega\tau}{2} \mp \sin \frac{\omega\tau}{2}\right| x\right)\right\} \\ &+ B_\omega \exp\left(\kappa \left|\cos \frac{\omega\tau}{2} \pm \sin \frac{\omega\tau}{2}\right| x\right) \exp\left\{i\left(\omega t + \kappa \left|\cos \frac{\omega\tau}{2} \mp \sin \frac{\omega\tau}{2}\right| x\right)\right\}. \end{aligned} \quad (9)$$

In the case of instant thermal relaxation (at $\tau = 0$), the resulting Eq. (9) corresponds to the “standard” solution (4) of the classical equation of thermal diffusivity (3) with a very strong spatial attenuation of the temperature waves.

From expressions (8) and (9) it follows that the coefficient of attenuation and actual wave number of the temperature wave in the considered arbitrary material medium depend on the frequency of this wave and thermodynamic relaxation time. The most important conclusion from these results is the following – when the condition $\omega_n = (n + 1/2)\pi/\tau$, $n = 0, 1, 2, \dots$ is satisfied, the attenuation coefficient δ becomes equal to zero, which corresponds to non-dissipative propagation of the temperature wave. For air, the minimum frequency of such wave ω_0 depends on pressure, humidity and average equilibrium temperature and lies in the interval $\omega_0 \approx 75 - 85$ MHz. This fundamental result was first predicted in the works [1–3], and was experimentally observed in [4–7].

The physical mechanism for this unique regime of dissipation-free propagation of a temperature (thermal) wave is the mutual co-phasing and reversibility of two alternative processes - variation of energy flow $\vec{q}(\vec{r}, t)$ (1) due to the variation of temperature $T(\vec{r}, t)$ and non-stationary change of temperature (5) due to the influx (outflow) of energy flow $\vec{q}(\vec{r}, t)$ into a given microvolume.

The generation of such waves can be associated with different processes. The first of them occurs when using a modulated heating source (for example, a laser beam with a modulation frequency equal to one of the frequencies $\omega_n = (2n + 1/2)\pi/\tau$ of possible undamped waves). Another, simpler method involves the use of pulsed heat sources, if the duration Δt of each of these pulses should be quite short and $\Delta t \leq \tau = (2n + 1/2)\pi/\omega_n$. In this case, undamped temperature waves will be present in the Fourier spectrum of the thermal pulse.

In our studies, we used short acoustic pulses as sources of pulsed heating. These pulses were generated in the volume of the cavitation chamber by the cavitation of water jet. The pulses generated during cavitation formed very short shock waves in the volume of the outlet wall of the cavitation chamber, which generated very short thermal pulses at the outer boundary of this wall. The action of these pulses leads to at least two important processes.

The first one is associated with the ionization and excitation of atoms on the outer surface, which leads to generation of X-ray radiation in the space near this surface [5]. The other process is associated with the generation of the undamped temperature waves discussed above that propagate in air.

Earlier we investigated the process of the excitation of undamped temperature waves and their detection at a long distance without an additional screen [5–8]. The fragment of the spectrum of these waves generated by cavitation of water jet and registered at $L = 20$ cm from the area of its excitation (the outer wall of the cavitation chamber) is presented in Fig. 1.

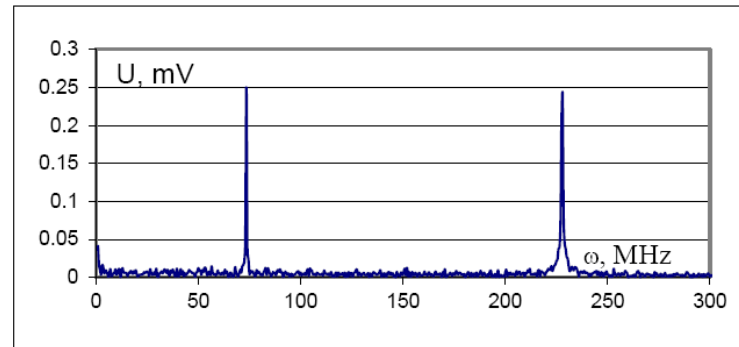


Figure 1. The low-frequency part of the spectrum of temperature waves recorded at a distance of 20 cm from the outer surface of cavitation chamber wall.

The maximum frequency of these waves at such a distance corresponded to about 2000 MHz. The specific values of these frequencies corresponded very well with the formula $\omega_n = (2n + 1/2)\pi/\tau$.

3. Effective Behind Screen X-ray Generation and Nuclear Fusion in Remote Targets

The current paper presents the results of experiments with undamped temperature waves in the presence of an additional thick screen located between the region of wave formation and a distant TiD target. These experiments were carried out with the active participation of Hagelstein. The experimental setup is shown in Fig. 2.

It should be noted that the presence of an additional thick screen significantly affects the propagation of these waves. The process of reflection of these waves from any boundary (e.g., air–metal) was theoretically considered in [7,8]. It was shown that the transmission coefficient depends on thermophysical parameters of both media, as well as on the quality of the input surface (small for a polished surface and large for inhomogeneous (unpolished) surface). The reflection coefficient of the temperature wave from the sharp air–metal boundary is determined by the formula

$$R_\omega = 1 - \frac{\lambda_{\text{air}}}{\lambda_{\text{metal}}} \sqrt{\frac{2G_{\text{metal}}}{G_{\text{air}}}} = 1 - \sqrt{\frac{2(\lambda\rho cV)_{\text{air}}}{(\lambda\rho cV)_{\text{metal}}}} \approx 1. \quad (10)$$

In contrast, in the case of a boundary with smoothly changing thermodynamic parameters, an enlightenment effect and an increase in the transmission coefficient $1 - R_\omega$ takes place. For an unpolished surface, the reflection coefficient decreases due to the presence of a pass-through (enlightening) layer, the thickness of which should be comparable with the length of this heat wave in air (1–2 μm). This effect is similar to quasiclassical enlightenment of the boundary in quantum mechanics. It is obvious that an increase in the coefficient of transmission of the initial temperature wave into the volume of the remote screen leads to the formation of a more intense acoustic wave in this screen and, as a result, to a higher amplitude of both the secondary temperature wave and the X-ray radiation in the area behind the screen.

At the beginning of the experiments, we investigated the features of X-ray generation in this area. Figure 3 shows two possible orientations of the remote steel screen relative to the cavitation chamber, as well as X-ray images and the type of the recorded signal (temperature wave with frequency about 83 MHz) at these orientations.

The wave was recorded by a piezoelectric acoustic detector. The process of such registration is due to the fact that when a wave hits the surface of a piezocrystal, it periodically heats and cools, which causes elastic vibrations in

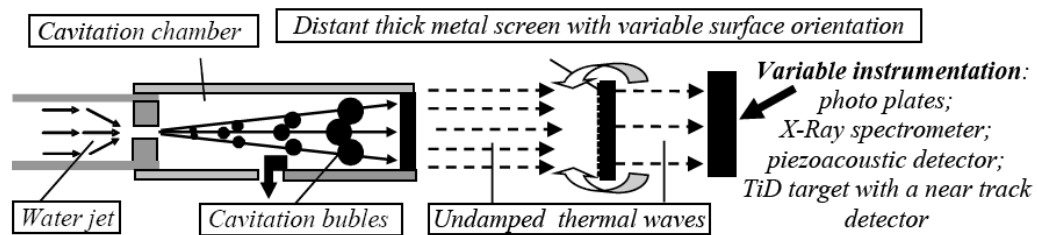


Figure 2. Scheme of experiments on the measurement of undamped temperature waves, the study of X-ray radiation, as well as the stimulation of nuclear fusion at a great distance from the source of the waves in the region behind a thick steel screen.

the detector. A slight difference between this frequency and the frequency of 75 MHz of a similar wave shown in Fig. 1 is due to the fact that these experiments were carried out at different times and the frequencies are different due to different air conditions (humidity, pressure P and equilibrium temperature T), which significantly affects the relaxation time $\tau \sim 1/P\sqrt{T}$. The frequency of this X-ray radiation corresponded to 1.5 keV. The X-ray spectrum was completely similar to our previous results for targets made of Fe (Fig. 4) [5–8].

From these data, it can be seen that the results of theoretical analysis coincide with the experimental data – the X-ray radiation and the temperature wave behind the screen with an input matted (unpolished) surface (the results presented in the left column in Fig. 3) are more intense than with the opposite screen orientation (right column for polished input surface).

The last (main) part of the research relates to the stimulation of nuclear fusion in a remote (off-screen) target by stimulation with temperature waves. In this case instead of X-ray and piezoacoustic detectors, a TiD target (length, 10 mm, diameter, 7 mm, saturation ~150%) was installed at a distance about 5–7 mm together with a nearby track detector.

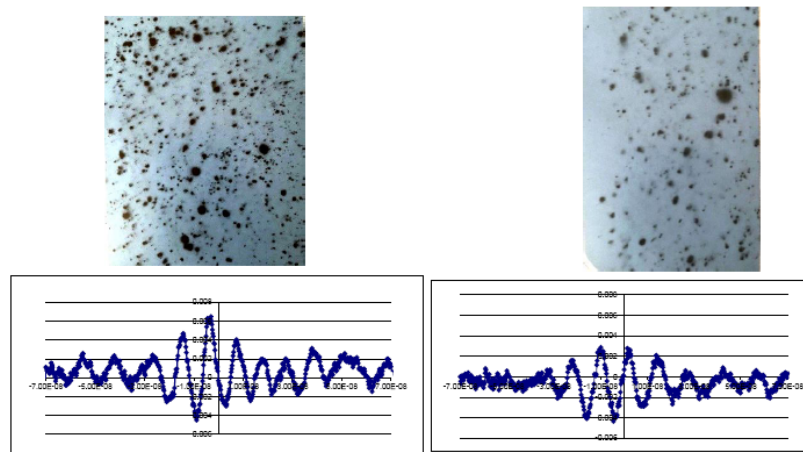


Figure 3. Registration of undamped temperature waves and X-ray behind thick steel screen at different screen surface orientation: the left column – the unpolished surface is directed to the source of temperature waves (cavitation chamber), the right column – the polished surface of the screen is directed to the source.

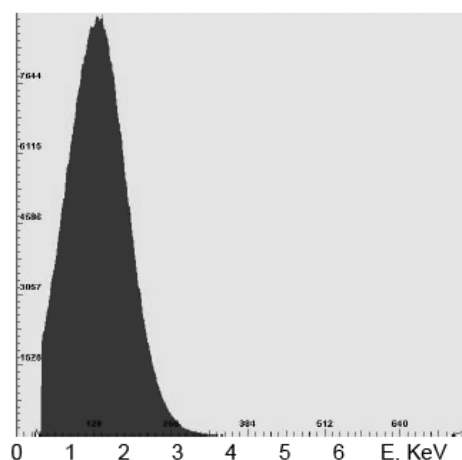


Figure 4. Spectrum of X-ray radiation recorded behind the back of a screen (plate) made of Fe.

For carrying out the alpha-track analysis, a plastic detector made of polycarbonate of the CR-39 type with a density of 1.3 g / cm^3 was used. The thickness of the “TASTRAK[®]” detector was 1 mm thick. The typical setting of the experiments corresponded to the location of the detector at a distance of 5 mm from the surface of the target, which was affected by the thermal wave for a certain time (about 1 h).

Figure 5 shows the general view of the track detector, on which the areas of track analysis are highlighted, as well as the location of tracks in some of these areas. It is seen that during the process of irradiating the target with a temperature wave, very significant nuclear reactions took place in it, the products of which are alpha particles. Effective registration of alpha tracks in the target under the influence of temperature waves indicates the possibility of stimulation of nuclear fusion reactions



in the target located behind a thick steel screen. The mechanism of stimulation of these LENR by action of temperate waves is may be connected with different processes. According to our analysis these LENR are associated with the influence of temperature waves on the dynamic structure of TiD target and, possible, on formation of coherent correlated states [10–21] of interacting particles during such structural and topological processes in the target lattice.

Such influence can take place in several stages. Initially, during the interaction of a temperature wave with a distant target, a shock waves is excited in the target volume, and then this shock wave affects the state of deuterium localized in the volume of nanocracks in the target or in the space between titanium atoms in the lattice. The modulation of the parameters of these potential wells at the nanoscale, as shown by a direct analysis, conducted in our works [12–21], leads to the formation of a coherent correlated state of deuterons. This process can be greatly enhanced. if we take into account the additional influence of high-frequency phonons that can form during such reactions on the base of phonon-nuclear coupling mechanism of LENR (e.g. [22,23]).

When the deuteron is localized in an interatomic space typical for any condensed media with a period $a \approx 2A$, the energy fluctuation in the coherent correlated state exceeds the value

$$\delta E = G^2 \hbar^2 / 8M(\delta x)^2 \approx 30 - 50 \text{ keV}, \quad (12)$$

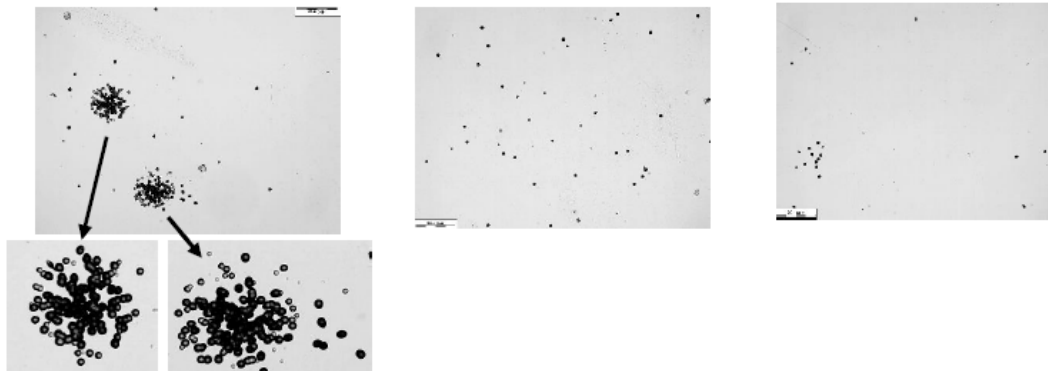


Figure 5. The general view of track detector and tracks at the areas 5, 9, 4 (from left to right).

that is much more than the temperature in a “standard” TOKAMAK.

Here

$$\delta x \approx a/2 \approx 1A, \quad G \equiv 1/\sqrt{1-r^2} \approx 10^4$$

is the realistic coefficient of correlation efficiency, r – coefficient of correlation [12–20].

Such a very large increase in particle energy fluctuation δE during the formation of a coherent correlated state is directly related to the Schrödinger–Robertson uncertainty relation [10,11] and is connected with the further development of the method of such states as applied to problems of quantum mechanics and nuclear physics [12–21].

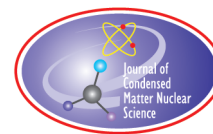
It is very important that in the coherent correlated state formed by such a modulation of the potential well, not only energy fluctuations δE will increase very significantly (by many orders of magnitude), but very significantly increase the duration δt of these fluctuations as compared to the “usual” Heisenberg uncertainty relation [19]. It is obvious that without such increase of δt , no reaction would be possible.

It should also be noted, that if all the conditions for LENR realization related to the formation of correlated deuteron states in the lattice are fulfilled, the probability of a neutron-free reaction $d + d = \text{He}^4$ (11), which is very small for “hot” fusion, can very significantly increase and such reaction can become the main one for LENR.

References

- [1] V.I. Vysotskii, V.B. Vassilenko and A.O. Vasylenko, Heat transfer equation with delay for media with thermal memory, *Int. J. Sci.: Basic and App. Res. (IJSBAR)* **12** (2013) 160.
- [2] V.I. Vysotskii, V.B. Vassilenko and A.O. Vasylenko, Generation and propagation of undamped temperature waves under pulse action on a target surface, *J. Surface Investigation: X-ray, Synchrotron and Neutron Techniques* **8** (2014) 367–373.
- [3] V.I. Vysotskii and V.B. Vassilenko and A.O. Vasylenko, Nonequilibrium thermal effects during pulsed action on conducting medium, *Inorganic Materials: Appl. Res.* **6** (2015) 199–204.
- [4] V.I. Vysotskii, A.A. Kornilova, A.O. Vasylenko and V.I. Tomak, Detection and investigation of undamped temperature waves excitation under water jet cavitation, *J. Surface Investigation: X-ray, Synchrotron and Neutron Techniques* **b** (2014) 1186–1192.
- [5] V.I. Vysotskii, A.A. Kornilova, A.O. Vasylenko. Observation and investigation of X-ray and thermal effects at cavitation. *Current Science*, 108 (2015) 114–119.
- [6] V.I. Vysotskii, A.A. Kornilova, A.O. Vasylenko and M.V. Vysotskyy, The prediction, observation and study of long-distant undamped thermal waves generated in pulse radiative processes, *Nucl. Instrum. Methods Phys. Res. B* **402** (2017) 251–255.

- [7] V.I. Vysotskii, A.A. Kornilova, A.O. Vasylenko, T.B. Krit and M.V. Vysotskyy, On the long-range detection and study of undamped directed temperature waves generated during the interaction between a cavitating water jet and targets. *J. Surface Investigation: X-Ray, Synchrotron and Neutron Techniques* **11** (2017) 749–755.
- [8] V.I. Vysotskii, A.A. Kornilova, T. Krit and S. Gaydamaka, Generation and detection of undamped temperature waves at large distance in LENR related experiments, *J. Condensed Matter Nucl. Sci.* **29** (2019) 368–375.
- [9] A.A. Kornilova, V.I. Vysotskii et al., The problem and realization of the stable generation of alpha particles by deuterated titanium located in the field of a heat wave, *Eng. Phys.* **5** (2018) 13–22 (in Russian).
- [10] E. Schrodinger, *Sitzungsber. Kgl. Akad. Wiss. Berlin* **24** (1930) 296.
- [11] H.P. Robertson, *Phys. Rev. A: At. Mol. Opt. Phys.* **35** (1930) 667.
- [12] V.I. Vysotskii and M.V. Vysotskyy, Coherent correlated states and low-energy nuclear reactions in non-stationary systems, *Eur. Phys. J. A* **49** (8: 99) (2013) 1–12.
- [13] V.I. Vysotskii, S.V. Adamenko and M.V. Vysotskyy, Acceleration of low energy nuclear reactions by formation of correlated states of interacting particles in dynamical systems, *Ann. Nucl. Energy* **62** (2013) 618–625.
- [14] V.I. Vysotskii and M.V. Vysotskyy, Correlated states and transparency of a barrier for low-energy particles at monotonic deformation of a potential well with dissipation and a stochastic force, *J. Exp. Theoret. Phys. (JETP)* **118** (2014) 534–549.
- [15] V.I. Vysotskii and M.V. Vysotskyy, Formation of correlated states and optimization of nuclear reactions for low-energy particles at nonresonant low-frequency modulation of a potential well, *J. Exp. Theoret. Phys. (JETP)* **120** (2015) 246–256.
- [16] V.I. Vysotskii and M.V. Vysotskyy, The formation of correlated states and optimization of the tunnel effect for low-energy particles under nonmonochromatic and pulsed action on a potential barrier, *J. Exp. Theoret. Phys. (JETP)* **121** (2015) 559–571.
- [17] V.I. Vysotskii and M.V. Vysotskyy, Coherent correlated states of interacting particles – the possible key to paradoxes and features of LENR. *Current Science*, 108 (2015) 30–36.
- [18] V.I. Vysotskii and M.V. Vysotskyy, The formation of correlated states and tunneling at low energy at controlled pulse action on particles, *J. Exp. Theoret. Phys. (JETP)* **125** (2017) 195–209.
- [19] V.I. Vysotskii and M.V. Vysotskyy, Features of correlated states and a mechanism of self-similar selection of nuclear reaction channels involving low-energy charged particles, *J. Exp. Theoret. Phys. (JETP)* **128** (2019) 856–864.
- [20] V.I. Vysotskii, M.V. Vysotskyy and S. Bartalucci, Features of the formation of correlated coherent states and nuclear fusion induced by the interaction of slow particles with crystals and free molecules, *J. Exp. Theoret. Phys. (JETP)* **127** (2018) 479–490.
- [21] Sergio Bartalucci, V.I. Vysotskii and M.V. Vysotskyy, Correlated states and nuclear reactions: An experimental test with low energy beams. *Phys. Rev. Accelerators and Beams* **22** (2019) 054503.
- [22] F. Metzler, P.L. Hagelstein and S. Lu, Developing phonon–nuclear coupling experiments with vibrating plates and radiation detectors, *J. Condensed Matter Nucl. Sci.* **24** (2017) 98–113.
- [23] P.L. Hagelstein and I.U. Chaudhary, Coupling between the center of mass and relative degrees of freedom in a relativistic quantum composite and applications, *J. Condensed Matter Nucl. Sci.* **24** (2017) 114–122.



Research Article

Application of Correlated wave Packets for Stimulation of LENR in Remote Targets

V.I. Vysotskii* and M.V. Vysotsky

*Taras Shevchenko National University of Kyiv, Ukraine***Abstract**

The paper discusses the features of the formation, evolution and propagation of coherent wave packets and their energy characteristics. Such packages can be created with a certain effect on a slow moving particles. A feature of such packets is a self-controlled remote collapse, in the zone of which there is a very strong self-compression of the packet and a giant increase in the fluctuation of its kinetic energy. Such correlated states can be used to carry out LENR reactions in remote targets.

© 2020 ISCMNS. All rights reserved. ISSN 2227-3123

Keywords: Coherent correlated states, Collapse of wave function, Correlated wave packet, LENR in remote targets

1. Introduction

The traditional method for generating LENR involves fulfilling the appropriate conditions (optimal screening, local micro-acceleration, local compression, “proton-electron to neutron” conversion etc.) for fixed interacting particles in a specific material medium. The situation remains approximately the same in the case of particles with low energy of motion (e.g. injection or diffusion of low energy protons into the material medium). In any of these methods, the properties of particles (except for a change in their energy) remain almost unchanged as they approach the target.

The typical example of such a system is the interaction of moving particle with target nuclei. We can describe the state of this particle in the form of a normalized Gaussian wave packet with the wave function

$$\Psi(x, t) = \left\{ \left(u + \frac{i\hbar t}{mu} \right) \sqrt{\pi} \right\}^{-1/2} \exp \left\{ - \left[\frac{(x - v_0 t)^2}{2(u^2 + t^2 \hbar^2 / m^2 u^2)} \right] + ip_0 x / \hbar \right\} \quad (1)$$

and initial structure

$$|\Psi(x, 0)|^2 = (\pi u^2)^{-1/2} e^{-x^2 / u^2}. \quad (2)$$

*Corresponding author. E-mail: vivysotskii@gmail.com.

Here $\Delta x(0) = u$ is the initial (at $t = 0$) “size” of wave packet, $v_0 = p_0/m$ is the average speed of the packet, m is the mass of the particle.

Such a packet is synthesized from a continuous continuum of spectral components $c(p)$, the specific form of which

$$c(p) = \int_{-\infty}^{\infty} \Psi(x, 0) \Psi_p^*(x) dx = \sqrt{u/\sqrt{\pi}\hbar} \exp \left\{ -\frac{(p_0 - p)^2 u^2}{2\hbar^2} \right\} \quad (3)$$

can be determined from the standard expansion of the total nonstationary wave function

$$\Psi(x, t) = \int c(p) \Psi_p(x) \exp \{ -iE_p t/\hbar \} dp, \quad E_p = p^2/2m \quad (4)$$

in plane waves

$$\Psi_p(x) = (2\pi\hbar)^{-1/2} e^{ipx/\hbar} \quad (5)$$

in free space. It is traditionally believed that the description of a realistic particle using a Gaussian wave packet is more adequate than using a plane wave, which is typical for quantum mechanics. Such Gaussian wave packets correspond to uncorrelated states of a moving particle with a minimal initial dispersion of the coordinate

$$\sigma_x(0) = \langle (x - \langle x \rangle)^2 \rangle = u^2/2 \quad (6a)$$

and momentum

$$\sigma_p(0) = \langle (p - \langle p \rangle)^2 \rangle = \hbar^2/2u^2 \quad (6b)$$

of the particle, which corresponds to the minimum of Heisenberg uncertainty relation

$$\sigma_x(0)\sigma_p(0) = \hbar^2/4. \quad (7)$$

These features of the spatial evolution of the Gaussian wave packet are connected with phase relations between different spectral (Fourier) components. These components correspond to the wave function of the same packet in momentum space.

The presence of spatially localization of a moving wave packet allows us to describe the dynamics of its interaction with a specific target in more detail. The possibility of such localization of the particle wave function favorably distinguishes this description from the traditionally used particle wave function in the form of a fully delocalized plane wave.

On the other hand, such a package is characterized by a very strong dispersion and spatial “spreading”, which corresponds to the variance of the coordinate

$$\begin{aligned} \sigma_x &= \langle x^2 \rangle - (\langle x \rangle)^2 = \int_{-\infty}^{\infty} \Psi^*(x, t) x^2 \Psi(x, t) dx - \left\{ \int_{-\infty}^{\infty} \Psi^*(x, t) x \Psi(x, t) dx \right\}^2 \\ &= u^2 \{ 1 + (t\hbar/mu^2)^2 \} / 2, \quad \langle x \rangle = v_0 t. \end{aligned} \quad (8)$$

The similar results follow from a direct analysis of the wave function (4). In particular, it can be seen from the structure of the packet

$$|\Psi(x, t)|^2 = \left\{ \pi \left[u^2 + \left(\frac{t\hbar}{mu} \right)^2 \right] \right\}^{-1/2} \exp \left\{ - \left[\frac{(x - v_0 t)^2}{(u^2 + t^2 \hbar^2 / m^2 u^2)} \right] \right\}, \quad (9)$$

that its width

$$\Delta x \approx \sqrt{u^2 + (t\hbar/mu)^2} \quad (10)$$

and the area of space localization during spatial propagation continuously increases, while the packet amplitude

$$|\Psi(x, t)|_{\max}^2 = 1 / \sqrt{u^2 + (t\hbar/mu)^2} \quad (11)$$

continuously decreases.

These well known features of the packet structure are presented in Fig. 1. These features do not allow the effective (localized) distant action of such packages (e.g., stimulation of nuclear reactions in the remote targets).

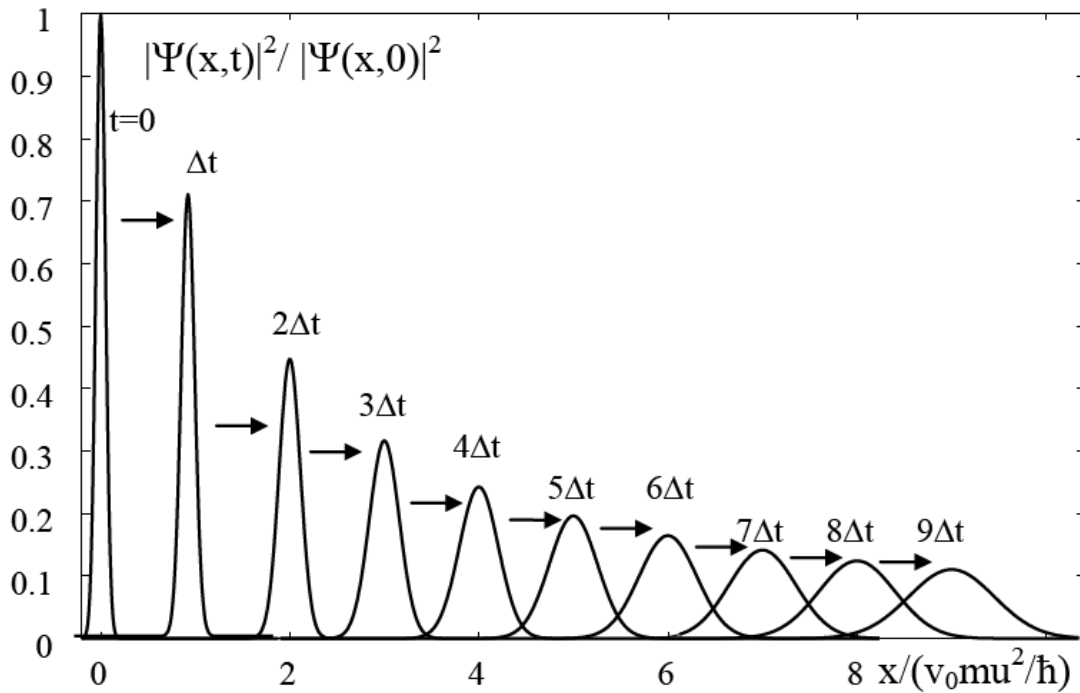


Figure 1. Spatial evolution of Gaussian uncorrelated wave packet. Here $\Delta t = mu^2/\hbar$.

2. Features of Space Structure, Energy Fluctuations and Space Evolution of the Correlated Wave Packet

As noted above, fundamental drawbacks (spatial spreading and amplitude reduction immediately after the creation) of a standard Gaussian wave packet can be completely eliminated and even inverted using a correlated wave packet.

In the initial state (at $t = 0$), the wave function of the correlated wave packet, which describes the motion of the same particle with velocity $v_0 = p_0/m$, has the form [1]

$$\Psi(x, 0) = \frac{1}{\sqrt[4]{\pi u^2}} \exp \left\{ -\frac{x^2 g}{2u^2} + ip_0 x / \hbar \right\}. \quad (12)$$

At the initial moment of time, the structure of the correlated wave packet

$$|\Psi(x, 0)|^2 = (\pi u^2)^{-1/2} e^{-x^2/u^2} \quad (13)$$

completely coincides with the initial structure of the “ordinary” Gaussian uncorrelated packet.

Here $g = 1 + i\rho$ and $\rho = r/\sqrt{1 - r^2}$ is a parameter that can change in the interval $-\infty < \rho < \infty$. The parameter r is the coefficient of correlation. For a pair of dynamic variables A and B this coefficient r is introduced by the expressions

$$r = \frac{\sigma_{AB}}{\sqrt{\sigma_A \sigma_B}}, \quad \sigma_{AB} = \frac{(\langle \widehat{AB} + \widehat{BA} \rangle)}{2} - \langle A \rangle \langle B \rangle, \quad \sigma_C = \langle (\widehat{C} - \langle C \rangle)^2 \rangle, \quad |r| \leq 1. \quad (14)$$

For correlated states, the product of the variances of the variables A and is limited by the Schrödinger–Robertson uncertainty relation [2–16]

$$\sigma_A \sigma_B \geq \frac{|\langle [\widehat{AB}] \rangle|^2}{4(1 - r^2)} \equiv G^2 \frac{|\langle [\widehat{AB}] \rangle|^2}{4}, \quad G = 1/\sqrt{1 - r^2}, \quad (15)$$

which is the generalization of the Heisenberg uncertainty relation and coincides with it under the condition $r = 0$. In the case under consideration $A = x$, $B = p$ this relation (15) takes the following form

$$\sigma_p \sigma_x \geq \frac{\hbar^2}{4(1 - r^2)} \equiv \frac{(\hbar^*)^2}{4}, \quad \delta p \delta x \geq \frac{\hbar}{2\sqrt{1 - r^2}} \equiv \frac{\hbar^*}{2}, \quad \hbar^* = G\hbar. \quad (16)$$

Here $G \equiv \hbar^*/\hbar = 1/\sqrt{1 - r^2}$ is the correlation efficiency coefficient, which can vary in the unlimited interval $1 \leq G < \infty$.

The wave function of the correlated packet can be found on the basis on the general presentation of packet wave function in the form of a spectral expansion (4) in plane waves (5) and formula (3) for determining the coefficients $c(p)$

$$\begin{aligned} c(p) &= \int_{-\infty}^{+\infty} \Psi(x, 0) \Psi_p^*(x) dx \\ &= \frac{1}{\sqrt[4]{4\pi^3 \hbar^2 u^2}} \int_{-\infty}^{+\infty} \exp \left\{ -\frac{x^2 g}{2u^2} + i(p_0 - p)x/\hbar \right\} dx = \sqrt{\frac{u}{g\hbar\sqrt{\pi}}} \exp \left\{ -\frac{(p_0 - p)^2 u^2}{2\hbar^2 g} \right\}. \end{aligned} \quad (17)$$

This is the standard method of calculating the weighting factors (weighting coefficients) in any superposition state in the equations of quantum mechanics.

The combination (complete set) of these coefficients, supplemented by the time evolution operator

$$\hat{K} = \exp\{-i(p^2/2m)t/\hbar\}$$

is the full wave function of the same particle in p -representation.

After substituting this coefficient into Eq. (4), we can obtain the wave function of the correlated wave packet

$$\begin{aligned} \Psi(x, t) &= \int_{-\infty}^{\infty} c(p) \Psi_p(x) \exp\{-iE_p t/\hbar\} dp \\ &= \left(1/\sqrt{[(1 - \rho t\hbar/mu^2) + it\hbar/mu^2]u\sqrt{\pi}}\right) \exp\left\{-\frac{x^2(1 + i\rho) - 2iu^2k_0x + it\hbar k_0^2u^2/m}{2u^2[(1 - \rho t\hbar/mu^2) + it\hbar/mu^2]}\right\} \end{aligned} \quad (18)$$

and the expression for the probability density of localization of a moving correlated packet

$$|\Psi(x, t)|^2 = \left\{u\sqrt{\pi}\sqrt{\left\{1 - \rho\frac{t\hbar}{mu^2}\right\}^2 + \left\{\frac{t\hbar}{mu^2}\right\}^2}\right\}^{-1} \exp\left\{-\frac{[x - v_0t]^2}{u^2[(1 - \rho t\hbar/mu^2)^2 + (t\hbar/mu^2)^2]}\right\}. \quad (19)$$

The spatial evolution of Gaussian uncorrelated wave packet for different consecutive moments of time is presented in Fig. 2.

Using this wave function, one can calculate the variances of the coordinate of a moving particle corresponding to the correlated wave packet

$$\sigma_x = \frac{u^2}{2} \left\{ \left(1 - \rho\frac{t\hbar}{mu^2}\right)^2 + \left(\frac{t\hbar}{mu^2}\right)^2 \right\}. \quad (20)$$

From the analysis of formulas (18)–(20) it follows that the spatial width of the correlated packet

$$u(t) = u(0)\sqrt{\left\{1 - \rho\frac{t\hbar}{mu^2}\right\}^2 + \left\{\frac{t\hbar}{mu^2}\right\}^2} \quad (21)$$

over the time

$$t_{\text{collapse}} = \frac{\rho mu^2}{(1 + \rho^2)\hbar} \quad (22)$$

decreases from the initial value $u(0)$ to the minimum value (state of collapse of the wave packet)

$$u_{\min} = u(0)/\sqrt{1 + \rho^2} = u(0)/G \quad (23)$$

and then monotonically increases. It is very important to note that the spatial spreading rate of the correlated packet immediately after its collapse

$$u(t > t_{\text{collapse}}) \approx u(0)\hbar t G/mu^2 \quad (24)$$

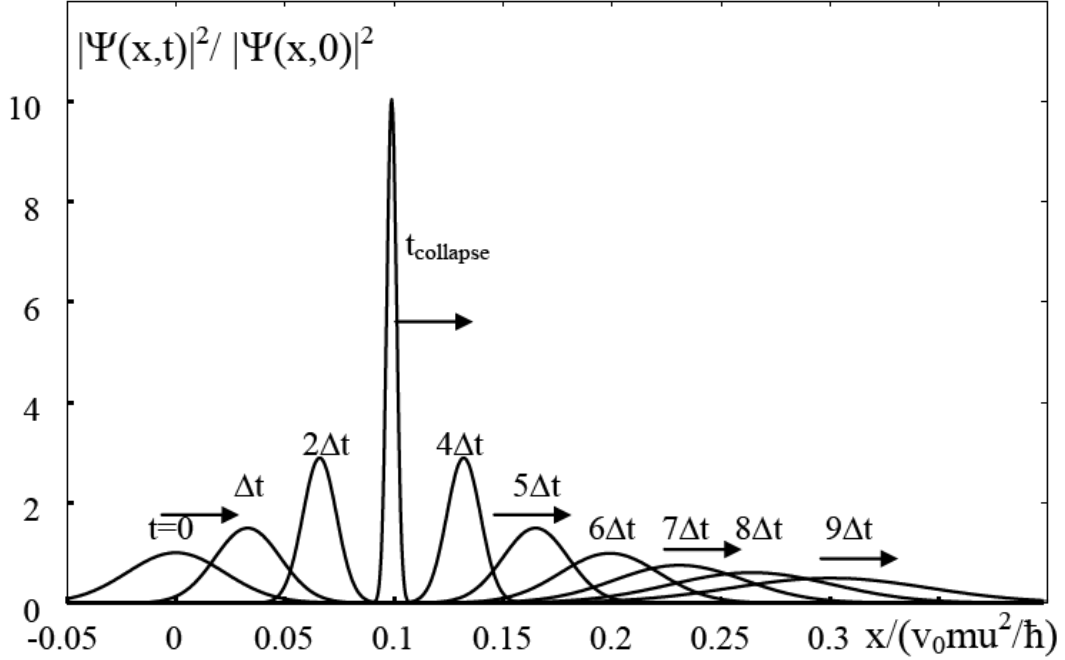


Figure 2. Spatial evolution and controlled remote collapse of a correlated wave packet at $G=10$. Here $\Delta t = mu^2/30\hbar$.

at $G \gg 1$ significantly exceeds the rate of similar spreading of the uncorrelated packet

$$u(t) \approx u(0)\hbar t/mu^2 \quad (25)$$

for the same time interval.

The coordinate of the spatial collapse of the correlated packet corresponds to the distance

$$x_{\text{collapse}} = v_0 t_{\text{collapse}} = \frac{v_0 \rho mu^2}{(1 + \rho^2)\hbar} \approx v_0 mu^2/G\hbar. \quad (26)$$

Synchronously with the compression of the packet to the state of collapse, its amplitude increases sharply by $\sqrt{1 + \rho^2} \approx G$ times from the initial value $|\Psi(x, 0)|_{\text{max}}^2 \approx 1/u\sqrt{\pi}$ to the maximum value

$$|\Psi(x_{\text{collapse}}, t_{\text{collapse}})|_{\text{max}}^2 = \sqrt{1 + \rho^2}/u\sqrt{\pi} \approx G/u\sqrt{\pi}. \quad (27)$$

It is important to note that after moving through the collapse region, the amplitude of the packet very quickly decreases (much faster than in the case of uncorrelated packet). It can be described by the asymptotic law determined by the formula

$$|\Psi(x > x_{\text{collapse}}, t > t_{\text{collapse}})|_{\text{max}}^2 \approx \frac{mu}{t\hbar\sqrt{\pi}(1 + \rho^2)} \approx \frac{mu}{Gt\hbar\sqrt{\pi}}. \quad (28)$$

These features of the evolution of the package are presented in Fig. 2.

The most important transformations correspond to the energy characteristics of a moving packet. The dispersion of a particle momentum in a correlated state can be determined using the explicit form (18) of the wave function $\Psi(x, t)$

$$\begin{aligned}\sigma_p &= \langle p^2 \rangle - (\langle p \rangle)^2 = \int_{-\infty}^{\infty} |\hat{p}\Psi(x, t)|^2 dx - \left\{ \int_{-\infty}^{\infty} \Psi^*(x, t) \hat{p} \Psi(x, t) dx \right\}^2 \\ &= \frac{\hbar^2(1 + \rho^2)}{2u^2} \left\{ \left(1 - \rho \frac{t\hbar}{mu^2} \right)^2 + \left(\frac{t\hbar}{mu^2} \right)^2 \right\}^{-1}.\end{aligned}\quad (29)$$

This dispersion corresponds to a very large (under conditions $|\rho| \gg 1, G \gg 1$) fluctuations of the kinetic energy of the particle

$$\begin{aligned}\delta T &= \frac{\sigma_p}{2m} = \frac{\hbar^2(1 + \rho^2)}{4mu^2} \left\{ \left(1 - \rho \frac{t\hbar}{mu^2} \right)^2 + \left(\frac{t\hbar}{mu^2} \right)^2 \right\}^{-1} \\ &\approx \frac{\hbar^2(1 + G^2)}{4mu^2} \left\{ \left(1 - G \frac{t\hbar}{mu^2} \right)^2 + \left(\frac{t\hbar}{mu^2} \right)^2 \right\}^{-1}.\end{aligned}\quad (30)$$

The dependences of the variances of coordinate, momentum and kinetic energy of such correlated packet for different values of the correlation efficiency coefficient G are shown in Fig. 3. The maximum fluctuation of the kinetic energy of a particle

$$\delta T_{\max} = \delta T(x_{\text{collapse}}, t_{\text{collapse}}) \approx \frac{\hbar^2(1 + G^2)^2}{4mu^2} \quad (31)$$

is generated in the region of the collapse $x_{\text{collapse}} = v_0 t_{\text{collapse}}$ (23) of wave function of correlated wave packet (18).

3. Possible Applications of the Correlated Wave Packet in LENR Experiments

Basing on such coherent correlated states, it is possible to generate targeted nuclear reactions using particles of relatively low energy. The analysis above has shown that the correlated wave packet can be used to implement LENR experiments in remote targets. It is easy to verify that in the region of the collapse, the fluctuation of the kinetic energy of a particle can significantly exceed its average kinetic energy.

For example, if a moving proton is represented in the form of a “usual” uncorrelated Gaussian wave packet with a longitudinal size $u = 0.2$ nm, then in the uncorrelated state the energy fluctuation of such a packet is limited to a small value

$$\delta T_{\text{uncorr}} = \frac{\sigma_p}{2m} = \frac{\hbar^2}{4mu^2} \approx 2 \times 10^{-4} \text{ eV}. \quad (32)$$

A completely different situation corresponds to a correlated state. With a real (and very far from record values $G \approx 10^3$ – 10^4 [8–16]) correlation efficiency coefficient $G = 100$ – 200 , this fluctuation increases to a value that can

$$\delta T_{\text{corr}} \approx \hbar^2 G^4 / 4mu^2 \approx 25 \text{ to } 100 \text{ keV} \quad (33)$$

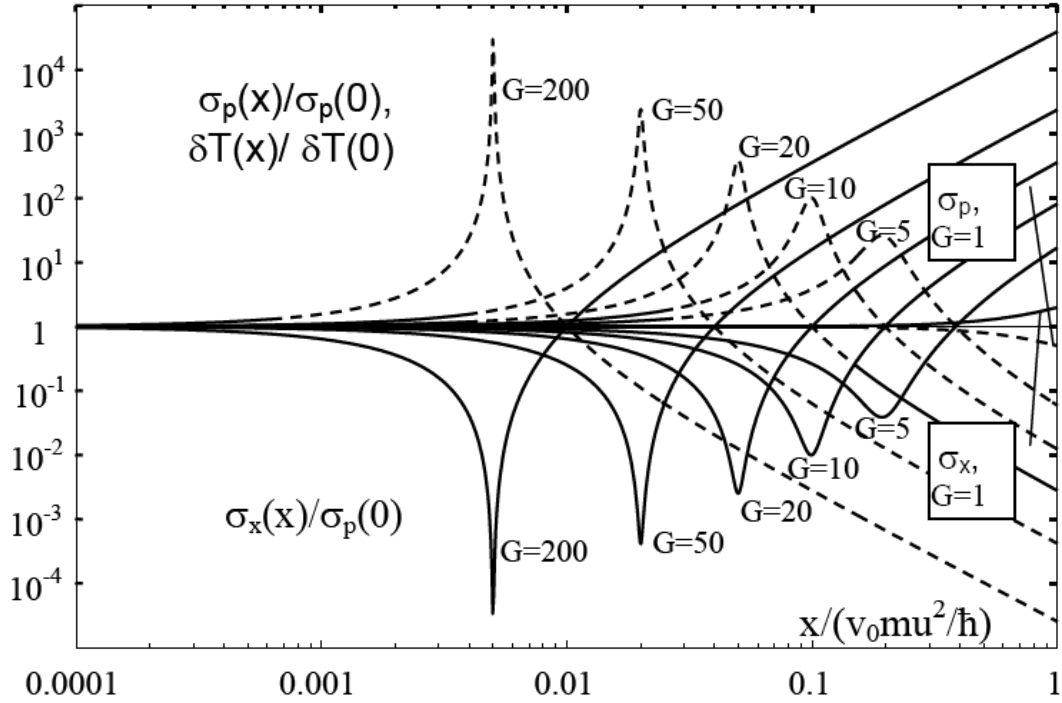


Figure 3. Variances of coordinate, momentum and kinetic energy of a particle in the form of correlated packet for different values of the coefficient G of correlation efficiency.

significantly exceed the average energy of the longitudinal motion, which can be equal, for example, $\langle T \rangle \approx p_0^2/2m \approx 100\text{--}200$ eV.

For such a system, the distance from the formation region of such a packet to the zone of its collapse is equal to

$$x_{\text{collapse}} \approx v_0 m u^2 / G \hbar \approx 250 / G \text{ cm} \approx 1 \text{ to } 2 \text{ cm}, \quad (34)$$

which makes it possible to implement such experiments in the conditions of the simplest laboratory.

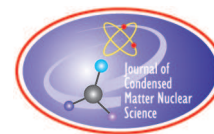
In works [6–17] various methods for the formation of such a correlated state are considered. Such correlated states can be formed, for example, when particles pass through a local region of existence of a periodic or monotonically changing electric or magnetic field, at crossing of laser beams, at passing through a crystal etc. Apparently, one of the simplest methods is to pass a beam of weakly accelerated protons through a thin magnetic crystal or above the surface of a periodic magnetic domain structure.

It is interesting to note that although some features of the evolution of the “standard” Gaussian packet in free space were investigated almost a hundred years ago [18], only recently there have been proposed new interesting methods for optimizing the use of such a package (including methods directly related to the LENR systems and models).

These problems will be discussed in another article.

References

- [1] V.V. Dodonov and A.V. Dodonov, Transmission of correlated Gaussian packets through a delta-potential, *J. Russ. Laser Res.* **35** (1) (2014) 39–46.
- [2] E. Schrödinger, Zum Heisenbergschen Unschärfeprinzip, *Ber. Kgl. Akad. Wiss.* **24** (1930) 296.
- [3] H.P. Robertson, A general formulation of the uncertainty principle and its classical interpretation, *Phys. Rev. A* **35** (1930) 667.
- [4] V. Dodonov, E. Kurmishev and V. Manko, Generalized uncertainty relation and correlated coherent states, *Phys. Lett. A* **79** (1980) 150–152.
- [5] V.V. Dodonov and V.I. Maňko, *Proceed. P. N. Lebedev Phys. Inst.* **183** (1987), 71.
- [6] V.V. Dodonov, A. V. Klimov, V. I. Maňko, *Proceed. P. N. Lebedev Phys. Inst.* **200** (1991) 56–; V.I. Vysotskii and S.V. Adamenko, Correlated states of interacting particles and problems of the coulomb barrier transparency at low energies in nonstationary systems, *J. Tech. Phys.* **55** (5) (2010) 613–621.
- [7] V.I. Vysotskii, M.V. Vysotskyy and S.V. Adamenko, Formation and application of correlated states in non-stationary systems at low energy of interacting particles, *J. Exp. Theoret. Phys.* **114** (2) (2012) 243–352.
- [8] V.I. Vysotskii and M.V. Vysotskyy, Coherent correlated states and low-energy nuclear reactions in non stationary systems, *Euro. Phys. J. A* **49** (8:99) (2013) 1–13.
- [9] V.I. Vysotskii, S.V. Adamenko and M.V. Vysotskyy, Acceleration of low energy nuclear reactions by formation of correlated states of interacting particles in dynamical systems, *Ann. Nucl. Energy* **62** (2013) 618–625.
- [10] V.I. Vysotskii and M.V. Vysotskyy, Formation of correlated states and optimization of nuclear reactions for low-energy particles at nonresonant low-frequency modulation of a potential well, *J. Exp. Theoret. Phys.* **120** (2) (2015) 246–256.
- [11] V.I. Vysotskii and M.V. Vysotskyy, The formation of correlated states and optimization of the tunnel effect for low-energy particles under nonmonochromatic and pulsed action on a potential barrier, *J. Exp. Theoret. Phys.* **121**(4) (2015) 559–571.
- [12] V.I. Vysotskii and M.V. Vysotskyy, Coherent correlated states of interacting particles – the possible key to paradoxes and features of LENR, *Current Sci.* **108** (4) (2015) 524–530.
- [13] V.I. Vysotskii and M.V. Vysotskyy, The formation of correlated states and tunneling at low energy at controlled pulse action on particles, *J. Exp. Theoret. Phys.* **125** (2) (2017) 195–209.
- [14] V.I. Vysotskii, M.V. Vysotskyy and S. Bartalucci, Features of the formation of correlated coherent states and nuclear fusion induced by the interaction of slow particles with crystals and free molecules, *J. Exp. Theoret. Phys.* **127** (3) (2018) 479–490.
- [15] V.I. Vysotskii, M.V. Vysotskyy and S. Bartalucci, Correlated states and nuclear reactions: An experimental test with low energy beams, *Phys. Rev. Accel. Beams* **22** (5) (2019) 054503.
- [16] V.I. Vysotskii and M.V. Vysotskyy, Features of correlated states and a mechanism of self-similar selection of nuclear reaction channels involving low-energy charged particles, *J. Exp. Theoret. Phys.* **128** (6) (2019) 856–864.
- [17] V.I. Vysotskii and M.V. Vysotskyy, *J. Surf. Invest.: X-Ray Synchrotron Neutron Tech.* **13** (2019) 1116.
- [18] C.G. Darwin, Free motion in the wave mechanics. *Proc. Roy. Soc. London Series A* **117** (1927) 258–293.



Research Article

Could LENR Change the World?

Jacques Ruer*

SFSNMC, France

Abstract

World energy consumption is equivalent to 13865 million tons of oil (2018). Eighty one percent of energy is provided by fossil fuels. Energy generation releases 34 Gt of CO₂ into the environment annually, which produces climate change. This paper considers the potential scenario with LENR sources of clean energy. It is based on the supposition that the new energy is generated by Metal Hydrogen Energy (MHE) stationary reactors that deliver heat at different temperature levels (100–200–350°C) as the technology evolves along the years. The potential penetration of LENR energy is analyzed taking into account the different conversion routes between the primary energy sources and the final industrial and domestic users. It is assumed that MHE replaces all conventional sources operated at a similar temperature level.

- 100°C-class sources can be used for heating. The corresponding market is 700 Mtoe,
- 200°C-class sources can supply all industrial processes using steam. Market: 500 Mtoe,
- 350°C-class reactors can generate electricity in renewed power stations. Market: 5200 Mtoe.

If cheap electricity is generated by such MHE reactors, there will be no need to increase the temperature of operation further. Hydrogen can be produced via water electrolysis. Future mobile equipment will be fueled by hydrogen. Extraction of CO₂ from the atmosphere combined with hydrogen makes it possible to manufacture synthetic fuels to supply the fleet of vehicles and aircrafts using present technology. According to this scenario LENR combined with renewable energies may ultimately eliminate the need for fossil fuels.

© 2020 ISCMNS. All rights reserved. ISSN 2227-3123

Keywords: Climate change, Final energy, Fossil fuels, Global energy consumption, Greenhouse gases, Hydrogen, MHE, Nuclear, Oil, Primary energy, Renewables, Toe

1. Introduction

Humanity consumes huge amounts of energy and 81% of the total is provided by fossil fuels coal, oil and natural gas [1]. These sources emit CO₂ during combustion.

Figure 1 shows the global emissions between 1870 and 2017 [2]. Energy generation released 34 Gt of CO₂ or 83% of the total of 41 Gt emitted that year. This figure also shows that global emissions increased rapidly over the years.

*E-mail: jsr.ruer@orange.fr.

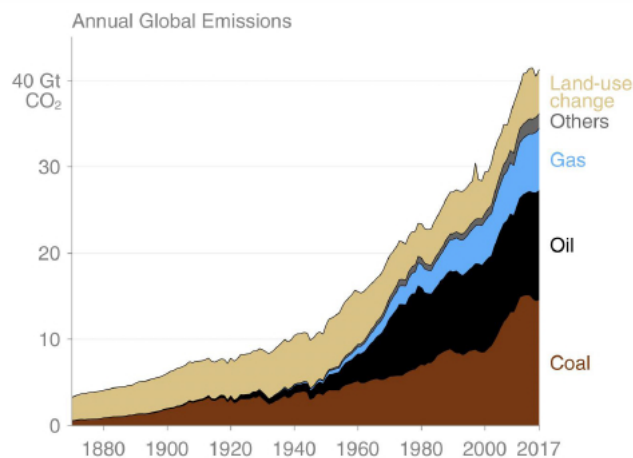


Figure 1. Annual global CO₂ emissions – Others: cement and gas flaring – emissions caused by energy production amounts to 34 Gt CO₂ or 83% of the total – Source [2].

The influence of the greenhouse gases on climate change is now well established [3,4]. Carbon-free energy like wind and solar are presently developed in many countries. Unfortunately, to harness these energies large infrastructures must be deployed in the environment. The resources vary along the day and the year. An electrical grid relying largely on renewable energies must include facilities for energy storage and policies to manage demand by the customers. This is a major change compared to the present situation where the customers can consume in a non-restricted manner with the production following at best it can.

Nuclear energy is also carbon-free but the technology is only accessible to a limited number of countries because of the high safety standards, the management of wastes and the fear of proliferation.

A general problem is that the countries that consume large quantities of energy are different from the countries rich in energy resources. This is true today for oil and gas, but the situation will be similar tomorrow if solar PV becomes a major energy supplier worldwide. This problem generates a large disparity between the different regions and leads to geopolitical tensions and uncertainties [5].

Our modern civilization could not exist without easy access to energy. Any event that affects the cost of energy is a factor toward a recession of the global economy. Our societies are highly dependent on mobility and sensitive on transportation costs (marine, land and air transport). The absence of flexibility in energy costs makes it very difficult to introduce political incentives to control consumption.

On the other hand, 850 million people around the world have no access to electricity [5]. In the future the developing countries will sharply increase their energy consumption.

The overall result is that it will be very difficult to limit the emissions of greenhouse gases if the world energy system does not undergo a profound mutation.

LENR may help modify the situation in a very positive way [6,7]. The purpose of this paper is to discuss how the development of the breakthrough sources of LENR energy could influence the global energy production, conversion and use.

Table 1. CO₂ emissions of various combustibles [12].

Combustible	Emissions of CO ₂ (kg CO ₂ / toe)
Lignite (Rhineland)	4773
Wood	4589
Coal	3950
Oil	3069
Gas	2349

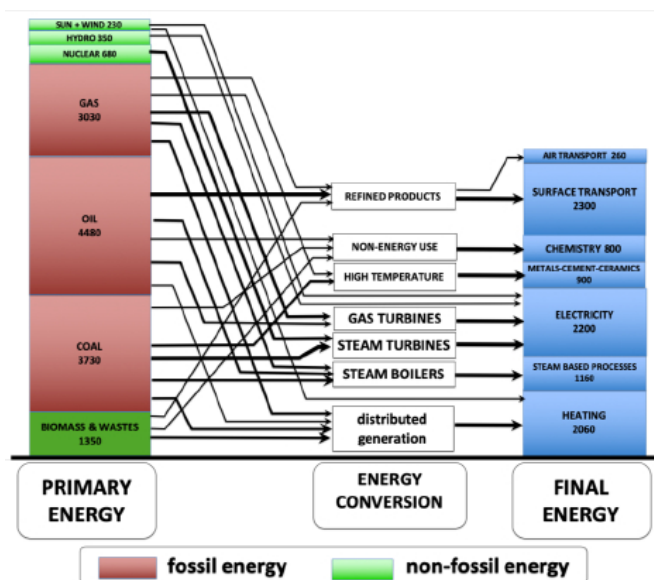
2. World Energy Consumption Today

The global consumption of energy in 2018 was 580×10^{18} J [1]. It is difficult to apprehend such a large number. Therefore, it is a custom to account for the energy as the quantity of oil that would be required to obtain the same amount of energy by combustion. This quantity is measured in metric tons of oil equivalent (1 toe = 41.87 GJ). This practical unit is used in this paper. The 2018 world consumption corresponds to $13\,865 \times 10^6$ toe or 13 865 Mtoe. Because all of this energy is extracted from the Nature in diverse forms (from oil and coal, to uranium fission, to wind and sun light) this is designated primary energy [11].

The different fuels release different quantities of CO₂ as shown in Table 1 [12].

In general, the primary energies cannot be used directly. It must be transformed into secondary energy types, which are easier to handle. For example, coal is processed in power plants to generate electricity. After transportation and distribution to the final consumers, the usable forms of energy are called final energies. The conversion introduces some losses, so that the quantity of final energy available for consumers is less than primary energy. Figure 2 exhibits the situation in 2018. The global final energy consumption was 9700 Mtoe.

For the purpose of this paper this figure introduces the conversion processes that allow the transformation of the primary energies into secondary ones. For example, coal is used to produce electricity via steam turbines, and refineries

**Figure 2.** Present global energy flowchart showing main conversion routes between primary and secondary energies.

transform crude oil into fuels suitable for cars or aircraft. The arrows indicate the main process routes to transform primary energies into specific usable forms.

3. Introduction of LENR (MHE) as a Commercial Energy Source

3.1. LENR energy sources

LENR offers the theoretical possibility to provide unprecedented energy sources:

- Sources can be built in any size including small devices,
- large power units can be obtained by clustering many independent reactors,
- the consumables are very small, so a reactor can run for a long time with a single load of active materials,
- no radiation is emitted, so the reactors are inherently safe,
- no green-house gases are produced,
- scrapped units can be easily recycled because they do not contain radioactive wastes.

For the moment, LENR energy sources cannot be put on the market because it is still not possible to initiate the reaction in a controlled manner. The precise features required to make the materials active are not yet understood and mastered. Recent progress has been made, which indicates that complete success is reachable [8]. Therefore, it is now time to start to think about the possible applications of these new energy sources.

In the following we consider a particular type of LENR reactor that is activated by simple heating. The corresponding reactors are called MHE for Metal–Hydrogen Energy [8]. The reaction occurs with specially prepared nanoparticles containing several metals (e.g., Ni + Cu or Ni + Pd) exposed to an atmosphere of hydrogen isotopes at high temperature. Once the reactor is hot, it starts to generate heat, and is able to do so continuously for several weeks or months. An earlier paper describes how to operate and control such reactors [9].

3.2. Analysis hypotheses

Any prospective study must rely on some assumptions. In this paper, we consider the following set of hypotheses:

- (1) The MHE reactors produce only heat,
- (2) the heat quality is characterized by its temperature level (temperature class),
- (3) MHE production is only made in stationary installations,
- (4) the deployment is progressive as the technology evolves,
- (5) when the technology is improved the temperature of the heat production increases,
- (6) three progressive levels are taken as hypotheses:
 - (a) 100°C,
 - (b) 200°C,
 - (c) 350°C.

This last level is sufficient to convert MHE heat into electricity with acceptable Carnot efficiency. By way of comparison, nuclear reactors also operate at 350°C [10].

Other hypotheses could have been considered, involving, for example, mobile energy sources or reactors able to operate at much higher temperatures. These would have resulted in other scenarios quite different from the one discussed here.

It is further assumed that the cost of MHE energy will be cheaper than conventional energy so that all market segments technically accessible by a given class will adopt the new type of energy. However, an exception is made

for renewable energy sources that will continue to grow. In some specific cases renewable energy will be the easiest and cheapest solution (e.g., solar water heating in regions with a high solar insolation). Renewable energy will also continue to receive some support for political reasons.

The advent of MHE energy may have a profound impact on the global energy market. The revolution will evolve progressively. It is supposed that the applications will come stepwise, following the temperature class of the heat delivered by the MHE reactors.

An analysis of the conversion processes to transform primary energy into final energy shows which domains of the industry will be progressively impacted as the MHE reactors reach the supposed temperature levels.

To simplify the analysis, it is supposed that the total energy consumption remains unchanged in the different scenarios. This is a static analysis. It is an oversimplification, because the introduction of MHE in the industry will take several years and during this time the global consumption will continue to increase.

It must be emphasized that this study does not pretend to be exhaustive, and that all quantities mentioned in the following only have an indicative value. Our objective is to demonstrate the boldness of the change.

3.3. Direct utilization of MHE heat source in the industry

In a first intermediate scenario, MHE is introduced as a heat source only in the processes that make a direct use of heat. Further utilization of MHE energy, for instance via the electricity produced, is not considered here, but is discussed below.

3.3.1. 100°C Class MHE

This temperature is relatively low. It can be used for space heating and some process heat. Small MHE heaters can be installed in houses and buildings, with large ones for district heating. Presently, such heating systems rely heavily on the combustion of coal, oil, gas, and to a limited extent wood. Incineration of wastes supplies district heating facilities and will remain, and solar systems will expand.

It is assumed that the overall heat produced by MHE will be 700 Mtoe, displacing 300 Mtoe coal, 300 Mtoe gas and 100 Mtoe oil.

3.3.2. 200°C Class MHE

This temperature level is sufficient to power the boilers that produce steam for many process industries like paper mills, food processing, chemical industries, and other process heat, also for steam turbines for mechanical power in some industries. It is assumed that 1200 Mtoe MHE will be introduced for steam generation displacing 500 Mtoe coal, 500 Mtoe gas and 200 Mtoe oil.

3.3.3. 350°C Class MHE

We make the optimistic assumption that all electricity that is produced by fossil-fuels power stations will be generated by MHE steam turbines. If this hypothesis comes true, all fission-nuclear power stations and gas turbines are phased out. Generation of electricity represents a large share of the global energy consumption. It is assumed that 5200 Mtoe MHE will be introduced displacing 2030 Mtoe coal, 1370 Mtoe gas and 780 Mtoe oil.

Table 2 summarizes the results these predicted scenarios. The reductions of CO₂ are higher than the energy reductions because coal is the first fuel removed from the energy mix.

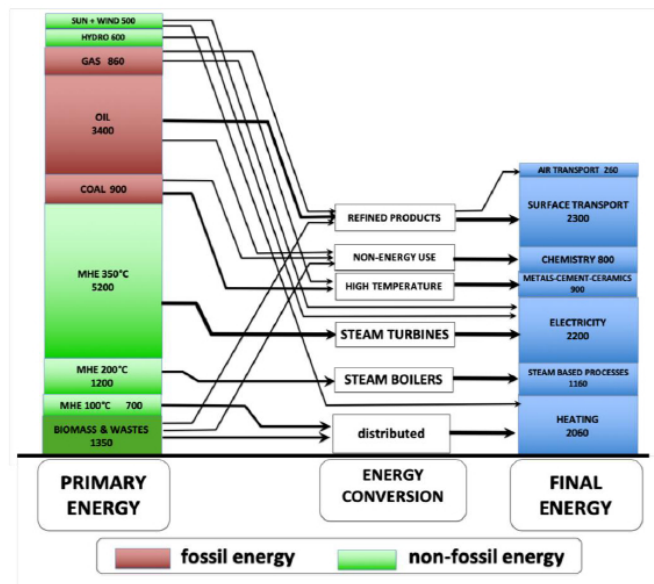


Figure 3. Intermediate scenario with introduction of 7100 Mtoe of MHE as heat source.

Figure 3 shows the global energy flowchart after the introduction of 7100 Mtoe MHE. Fossil fuels share of primary energy falls to 6750 Mtoe or 35% of the Global consumption. Their use is limited to high temperature combustion processes, chemistry, surface and air transport.

Besides combustion, some oil, as well as some biomass, are used as feedstock in chemical plants for the manufacture of plastics, pharmaceutical and food products, etc. We assumed that these uses will not be affected by MHE.

We suppose that renewables will also progress as a result of the trend to foster carbon-free energies.

3.4. Use of MHE for a complete conversion of the global energy flowchart

If we follow the hypothesis of low cost of MHE, a further development is possible with electricity used to generate hydrogen via water electrolysis. Hydrogen can be used as an energy vector for transportation and for long-term storage

Table 2. Introduction of MHE as heat source in the industry.

MHE heat class (°C)	Main market segments	Cumulative MHE primary energy (Mtoe)	Fossil fuels primary energy (Mtoe)	Energy CO ₂ emissions (Gt)
Reference	–	0	13 865	34
100	Building heating	700	13 150	31.9
	District heating		(–5%)	(–6%)
200	Boilers,	1900	11 950	28.3
	steam driven processes, paper mills, food processing, etc.		(–13%)	(–16.8%)
350	Electricity generation	7100	6750	15.2
			(–51%)	(–55.3%)

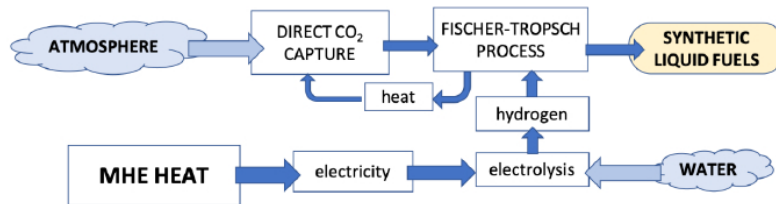


Figure 4. Schematic process of fuel synthesis from water and atmospheric CO₂.

of energy [13].

Synthetic fuels can be manufactured by reacting H₂ with CO₂ extracted from the atmosphere as shown in Fig. 4. These gases are transformed into liquid or gaseous fuels via a series of chemical reaction and the Fischer–Tropsch process [14]. Although this technology is not justified under the prevailing economic conditions today, it is already been studied and developed in niche applications [15,16].

It is then theoretically possible to describe a final scenario without any need of fossil fuels.

The synthetic fuels can be directly used by the existing vehicles and aircraft engines without any new technology. The distribution infrastructure of the fuels would also be kept. This is a distinct advantage compared to hydrogen, which is difficult to store onboard vehicles.

Figure 5 shows the flowchart corresponding to the final scenario. The manufacture of hydrogen and synthetic fuels is only possible with a loss of energy. The amount of MHE primary energy must cover the losses, so that the global primary energy consumption is increased to 23 250 Mtoe, including 19 900 Mtoe of MHE plus 2000 Mtoe of solar and wind.

The energy transition will involve direct use of electricity for vehicles and electricity-driven industrial processes.

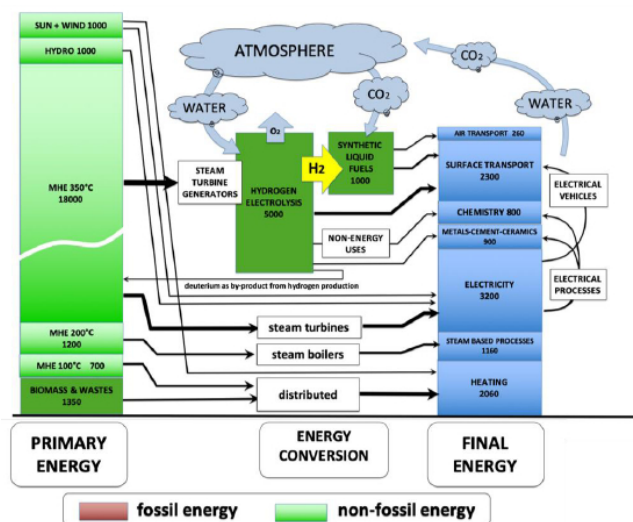


Figure 5. Final scenario global energy flowchart with 100% MHE and renewable energies.

Some hydrogen will be used directly for chemical and metallurgical processes, as well as fuel for a fraction of the fleet of vehicles.

4. Conclusions

The potential benefits of MHE energy are unsurpassable. It would be a compact source of energy available anywhere, at any time, with a positive influence on climate change.

Assuming MHE reaction involves the transmutation of hydrogen into helium, the annual theoretical consumption of hydrogen to cover all the primary energy consumed by humanity would be about 100 tons obtained via the electrolysis of 900 tons of water if normal hydrogen is the feedstock. If deuterium is required, it could be extracted as a by-product of hydrogen production by water electrolysis. The resource has virtually no limit.

The penetration of this new energy in the industrial sector will take some time, the limiting factor being the manufacture of the reactors and modification of infrastructures. The likely development route will probably be similar to all breakthrough technologies:

- First applications will take place in prime market segments, where the new energy will bring a distinct added value.
- The technology will improve as the overall installed power increases. New reactors will be engineered.
- The operation temperature will increase giving access to new markets.

In the power business, experience shows that each time you double the cumulative installed power of a given technology, the cost new installation is reduced by 20%. Figure 6 shows the learning curves for several types of energy [17]. It is likely that the development of MHE sources will obey a similar law.

References

- [1] BP Statistical Review of World Energy, 68th Edition (2019).

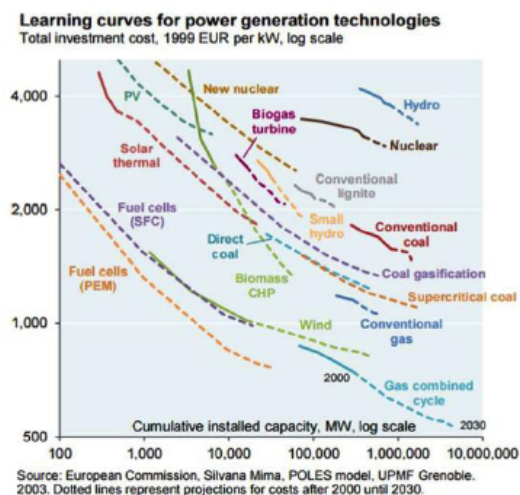
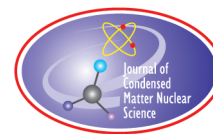


Figure 6. The learning curves for several types of energy generation technologies.

- [2] Le Quéré, Global Carbon Budget (2018), www.globalcarbonproject.org.
- [3] IPCC Climate Change 2014, Synthesis Report Summary for Policymakers, https://www.ipcc.ch/site/assets/uploads/2018/02/AR5_SYR_FINAL_SPM.pdf.
- [4] J. Butler, The NOAA Annual Greenhouse Gas Index (AGGI), Earth System Research Laboratory, Global Monitoring Division Website, 2019.
- [5] IEA, World Energy Outlook, 2019.
- [6] Carl Page, Anthropocene Institute, PageC_NuclearSolution_2019ColloquiumMIT.pdf.
- [7] Poponi, Daniele and Come Carpentier de Gourdon, Breakthrough energy technologies in the twenty-first century: economic and geopolitical implications, *World Affairs: J. Int. Issues* **17**(2) (2013) 142–173.
- [8] A. Kitamura, Excess heat evolution from nanocomposite samples under exposure to hydrogen isotope gases, *Int. J. Hydrogen Energy* **43** (2018) 16187–16200.
- [9] J. Ruer, Basic design considerations for industrial LENR reactors, *J. Condensed Matter Nucl. Sci.* **22** (2017) 7–26.
- [10] Pressurized Water Reactor, Wikipedia, https://en.wikipedia.org/wiki/Pressurized_water_reactor.
- [11] Primary and secondary energy, Wikipedia, https://en.wikipedia.org/wiki/Primary_energy.
- [12] Erneuerbare Energien und Klimaschutz, <https://www.volker-quaschnig.de>.
- [13] Shell hydrogen study, Energy of the future? (2017) , www.shell.com.
- [14] Fisher, Tropsch Process, Wikipedia, https://en.wikipedia.org/wiki/Fischer-Tropsch_process.
- [15] Carbon Engineering, <https://carbonengineering.com>.
- [16] Climeworks, <https://www.climeworks.com/our-customers/energy-fuels-and-materials/>.
- [17] Silvana Mima, European Commission, POLES model, 2003.



Research Article

Creation of Fe Isotopes in Natural Geology Crusts as the Result of Self-controlled Global Biostimulated LENR in Oceans and Seas

V.I. Vysotskii* and M.V. Vysotskyy

Taras Shevchenko National University of Kyiv, Kyiv, Ukraine

A.A. Kornilova, S.N. Gaydamaka, A.A. Novakova, D.S. Novikov and V.V. Avdonin

Moscow Lomonosov State University, Moscow, Russia

Abstract

The paper considers the mechanism of formation of natural iron–manganese crusts, which are located at the bottom of all seas and oceans. These crusts are characterized by a periodic structure and an anomalous ratio of iron isotopes. These anomalies are similar in all seas and oceans and consist in excess of Fe^{54} and Fe^{56} isotope concentration and, accordingly, decrease of Fe^{57} isotope concentration compared to their standard values. It is shown that these anomalies are completely explained by the process of LENR (nuclear transmutation) in the bottom region of the seas and oceans, leading to nuclear fusion with the participation of manganese, sodium, and phosphorus and stimulated by the processes of natural metabolism of microbiological communities.

© 2020 ISCMNS. All rights reserved. ISSN 2227-3123

Keywords: Anomalies in the structure and isotopic ratio of iron–manganese crusts, Coherent correlated states and LENR, Isotope transmutation in seas and oceans

1. Introduction

It is traditionally believed that LENR processes can be generated only in specially designed laboratory experiments. Among these processes is the problem of transmutation of isotopes in biological systems, which, in the general opinion, is quite difficult to implement and analyze.

A more detailed analysis has shown that such processes can occur in nature, and their results can directly compete with global geological processes.

The typical example of such global competition can be related to the isotopic anomalies of natural geological Fe–Mn crusts, which are present on most of the coastal areas of all seas and oceans.

It is well known that Fe–Mn crusts are among the most mysterious geological objects. Usually, they occur in sediments of the Eocene-Quaternary age and continue to accumulate at present at depths of 2–5 km, although they

*Corresponding author. E-mail: vivysotskii@gmail.com.

are also present at substantially lower depths. Their size is from 1 mm to 1 m in diameter, nodules 3–7 cm in size predominate. The total mass of such structures is about 300 billion of tons.

A typical concentrations of metals in these crusts and nodules are the following:

$$\eta_{\text{Mn}} \approx 20 \%, \eta_{\text{Fe}} \approx 15 \%, \eta_{\text{Ni}} \approx 0,5 \%, \eta_{\text{Co}} \approx 0,5 \%, \eta_{\text{Cu}} \approx 0,5 \%.$$

The internal structure of crusts is characterized by a periodical alternation of thin layers of Fe and Mn. The traditional description of such anomalous structures is connected with the possible action of volcanoes. However, such a hypothesis has some problems. First of all, such crusts are found in different places of the Earth and majority of these places are not connected with the volcanic activity. In addition, the strictly periodic structure of such crusts and the approximate constancy of the period, regardless of their location, also confirm that they are not connected with the random activity of volcanoes. It should be noted that there are no consistent data on the age of these structures (there are assumptions about both many millions of years and about an age that is thousands of times less).

Even more mysterious is the violation of the “standard” isotope ratios in all samples of these structures (regardless of their location in all oceans and near the coasts of all continents). In all cases the relative concentration of the Fe^{57} isotope $\eta(\text{Fe}^{57})$ decreases in comparison with concentrations of Fe^{54} and Fe^{56} isotopes $\eta(\text{Fe}^{54})$ and $\eta(\text{Fe}^{56})$ [1].

It is also very important that these objects are always connected with water. It should be noted that usually the standard ratios of main Fe isotopes, determined by their relative concentrations

$$\text{Fe}^{54}(\eta = 5.845\%), \text{Fe}^{56}(\eta = 91.754\%) \text{ and } \text{Fe}^{57}(\eta = 2.119\%) \quad (1)$$

are nearly the same with very high accuracy on Earth and in space (analysis based on meteorites and lunar samples).

Data of ferromanganese crusts samples location and change of normalized $\text{Fe}^{57}/\text{Fe}^{54}$ isotope ratio

$$\delta\text{Fe}^{57}(0/00) \equiv 1000 \left\{ \frac{\{\eta(\text{Fe}^{57})/\eta(\text{Fe}^{54})\}_{\text{object}}}{\{\eta(\text{Fe}^{57})/\eta(\text{Fe}^{54})\}_{\text{reference}}} - 1 \right\} \quad (2)$$

are presented in Fig.1. Part of these data are presented in Table 1.

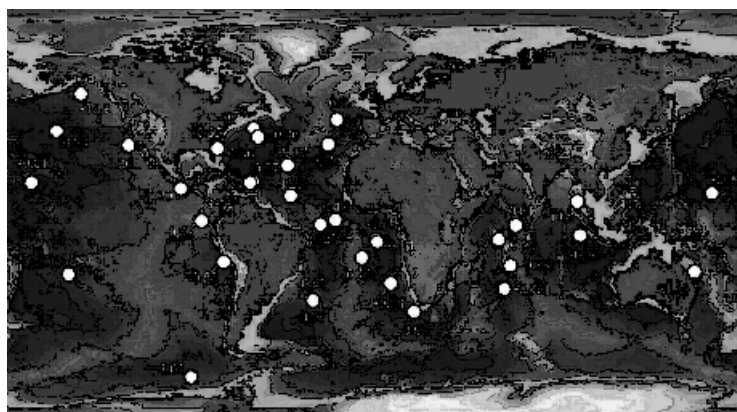


Figure 1. Map of Fe–Mn crust sample location and normalized $\text{Fe}^{57}/\text{Fe}^{54}$ isotope ratio values from each crust [1].

Table 1. Typical isotopic composition of crusts in different oceans [1].

Location	Latitude	Longitude	Water deep (m)	$\delta \text{Fe}^{57} (0/00)$	$\delta \text{Fe}^{57*} (0/00)$
Northwest Atlantic	31° 38' N	78° 40' W	512	−0.85	−0.34
Northwest Atlantic	16° 55' N	61° 10' W	2000	−0.27	−0.10
Northeast Atlantic	32° 36' N	24° 25' W	5347	−0.42	−0.15
Southeast Atlantic	16° 9' S	8° 21' W	1990	−0.27	−0.18
Southwest Atlantic	32° 11,55' S	32° 43' W	3210	−0.95	−0.39
South Atlantic	26° 03' S	5° 42' E	1800	−0.90	−0.26
Indian	7° 20' S	57° 36' E	2421	−0.90	−0.34
Indian	8° 37' N	36° 15' E	449	−1.08	−0.34
Northeast Pacific	32° 15' N	121° 16' W	2267	−1.06	−0.29
Pacific	17° 09' S	75° 15' W	4218	−0.82	−0.28

These data demonstrate a unique and inexplicable result: the ratio of concentrations of $\text{Fe}^{57}/\text{Fe}^{54}$ isotopes in all (without any exception!) geological crusts is significantly less than the same standard ratio. Full data on Fe isotope analysis for all research points in the oceans (Fig. 1) are presented in the work [1].

A similar regularity corresponds to a ratio of Fe^{57} to another Fe^{56} isotope, and in all samples without exceptions a decrease of the normalized $\text{Fe}^{57}/\text{Fe}^{56}$ isotope ratio

$$\delta \text{Fe}^{57*} (0/00) \equiv 1000 \left\{ \frac{\{\eta(\text{Fe}^{57})/(\eta(\text{Fe}^{56}))\}_{\text{object}}}{\{\eta(\text{Fe}^{57})/\eta(\text{Fe}^{56})\}_{\text{reference}}} - 1 \right\} \quad (3)$$

takes place (see Table 1).

These data have shown that the changes in the corresponding isotopic ratios $\text{Fe}^{57}/\text{Fe}^{54}$ and $\text{Fe}^{57}/\text{Fe}^{56}$ have the same tendency, but in all cases the changes for the ratio $\text{Fe}^{57}/\text{Fe}^{54}$ are more significant than for the ratio $\text{Fe}^{57}/\text{Fe}^{56}$.

If we present the relative $\Delta(\text{Fe}^A)$ and absolute $\Delta\eta(\text{Fe}^A)$ change of the concentration $\eta(\text{Fe}^A)_{\text{object}}$ of considered isotopes in the form of the ratio

$$\eta(\text{Fe}^A)_{\text{object}} = \eta(\text{Fe}^A)_{\text{reference}} (1 + \Delta(\text{Fe}^A)) \equiv \eta(\text{Fe}^A)_{\text{reference}} + \Delta\eta(\text{Fe}^A), \quad (4)$$

then the initial formulas (2) and (3) take the form

$$\delta \text{Fe}^{57} (0/00) \equiv 1000 \left\{ \frac{1 + \Delta(\text{Fe}^{57})}{1 + \Delta(\text{Fe}^{54})} - 1 \right\} \approx 1000 \{ \Delta(\text{Fe}^{57}) - \Delta(\text{Fe}^{54}) \}, \quad (5)$$

$$\delta \text{Fe}^{57*} (0/00) \equiv 1000 \left\{ \frac{1 + \Delta(\text{Fe}^{57})}{1 + \Delta(\text{Fe}^{56})} - 1 \right\} \approx 1000 \{ \Delta(\text{Fe}^{57}) - \Delta(\text{Fe}^{56}) \}.$$

In these formulas $\Delta(\text{Fe}^{57}) \leq 0$, $\Delta(\text{Fe}^{54}) \geq 0$, $\Delta(\text{Fe}^{56}) \geq 0$ in accordance with the data of Table 1.

There are no reasonable explanations of these anomalies in the literature using the “standard” physical mechanisms (diffusion, the influence of volcanoes and geysers, gravitational deposition and fractionation, sea currents, etc.).

2. LENR-Mechanism and Biological Stimulation of the Formation of Iron–Manganese Isotopic Anomalies in Marine Geology

There are two possible ways to solve this isotope problem.

The first one (non-realistic) is connected with the assumption of a real decrease of the absolute concentration and absolute mass of the Mössbauer Fe^{57} isotope. However, this hypothesis immediately leads to the questions of the mechanism and causes of the disappearance of this isotope. These questions have no answers.

The second way, according to which the increase of the concentrations (mass density) of Fe^{54} and Fe^{56} isotopes is greater than the increase of Fe^{57} , is much more realistic.

The explanation of the origin of such anomalous structures and abnormal isotope ratios is connected with natural LENR reactions



of nuclear transmutation of Mn^{55} , Na^{23} and P^{31} isotopes dissolved in water into the considered iron isotopes.

The probability of such reactions is negligible if we consider them on the basis of the theory of hot nuclear fusion, for which the probability of a tunnel effect at a typical ocean temperature does not exceed $10^{-200} - 10^{-1000}$. The situation fundamentally changes if we take into account influences on such processes of growing microbiological cultures, which successfully grow in the bottom region of all seas and oceans.

This “fusion pathway” is in a good agreement with the results of our experiments on the efficient fusion of the same iron isotopes at the presence of growing microbiological cultures and chemical elements which are necessary for the growth of microbes and corresponding transmutation of isotopes.

The high probability of reactions (6) in growing microbiological systems is connected, according to our calculations and the results of our experiments [2–5], with the formation of coherent correlated states (CCS) of interacting nuclei [6–16]. It was shown that CCS formation leads to the generation of extremely great fluctuations of kinetic energy of these nuclei. When one of these particles with mass M is localized in non-stationary potential wells of nanoscale with the size a , the energy fluctuation in CCS exceeds the value [8–16]

$$\delta E^{(\min)} \approx G_{pq}^2 \hbar^2 / 2Ma^2 \approx 10 - 100 \text{ keV}. \quad (7)$$

It is very important that such giant fluctuations can exist an anomalously large (compared to the characteristic value

$$\delta t \geq \hbar / 2\delta E \quad (8a)$$

determined from the standard Heisenberg uncertainty relation) time

$$\delta t \geq G_{Et} \hbar / 2\delta E, \quad (8b)$$

that is sufficient for realization of all fusion reactions (6) in the case $G_{Et} \gg 1$ [15].

These results are based on the Schrödinger–Robertson uncertainty relations [17–19] for energy and time

$$\delta E \delta t \geq \frac{\hbar^*}{2}, \quad \hbar^* = \frac{\hbar^*}{\sqrt{1 - r_{Et}^2}} \equiv G_{Et} \hbar, \quad r_{Et} = \frac{\langle \widehat{Et} + \widehat{tE} \rangle / 2 - \langle \widehat{E} \rangle \langle \widehat{t} \rangle}{\sqrt{\langle E^2 \rangle \langle t^2 \rangle}}, \quad 0 \leq |r_{Et}| \leq 1 \quad (9a)$$

and relations

$$\delta q \delta p \geq \frac{\hbar^*}{2}, \quad \hbar^* = \frac{\hbar^*}{\sqrt{1 - r_{pq}^2}} \equiv G_{pq} \hbar, \quad r_{pq} = \frac{\langle \widehat{qp} + \widehat{pq} \rangle / 2 - \langle \widehat{q} \rangle \langle \widehat{p} \rangle}{\sqrt{\langle q^2 \rangle \langle p^2 \rangle}}, \quad 0 \leq |r_{pq}| \leq 1 \quad (9b)$$

for momentum p and coordinate q .

Here r_{Et} and r_{pq} are correlation coefficients for corresponding dynamic variables (E , t and q , p) and

$$G_{Et} = 1 / \sqrt{1 - r_{Et}^2} \approx 10^3 - 10^4, \quad G_{pq} = 1 / \sqrt{1 - r_{pq}^2} \approx 10^3 - 10^4$$

are the achievable coefficients of correlation efficiency for the pairs of these variables [8–14]. The method of calculation of the coefficient G_{Et} for the first time was considered in [16].

The process of the formation of such states, as it is shown in the works [6–14], can be realized in any non-stationary potential well on the nanoscale, which correspond to many typical biophysical processes (e.g. cell division region, DNA replication, processes on the surface of plasma biomembranes, etc.).

Due to the constant and very small ($0.014 \pm 0.002\%$) natural ratio of D to H concentrations in water, changes of concentration of created Fe^{56} and Fe^{57} isotopes is always synchronized, but the total probability of transmutation differs greatly. Obviously, the total mass of the synthesized Fe^{57} isotope is nearly in the same time lower than the mass of the synthesized Fe^{56} isotope.

This tendency can explain the decrease of the relative concentration of Fe^{57} isotope ($\Delta(\text{Fe}^{57}) < 0$), which accompanies a simultaneous slight increase of its mass in comparison with a much more significant increase of the mass and concentration of Fe^{56} isotope $\Delta(\text{Fe}^{56}) > 0$.

From the other hand, the effectiveness of such reactions depends on the mass and concentration of manganese, for which the natural concentration in ocean water equals $\eta(\text{Mn}) \approx 4.39 - 274.7 \text{ ng/kg}$ (average values is $\langle \eta(\text{Mn}) \rangle \approx 207.98 \text{ ng/kg} \approx 0.0002 \text{ ppm}$) [20]. By the way, the natural concentration of iron in ocean water is much less and equal to

$$\eta(\text{Fe}) \approx 1.12 \text{ to } 111.7 \text{ ng/kg and } \langle \eta(\text{Fe}) \rangle \approx 27.9 \text{ ng/kg} \approx 0.000028 \text{ ppm [20].}$$

There are several fundamental circumstances that significantly change this situation. It is well known that different types of microorganisms (e.g. *Oscillatoria terebriformis*) play important role in the natural self-concentration (biological extraction) of certain metals (mainly manganese) from sea water [21–23]. There are a lot of different types of such microbial metallophages. A typical example of such microbes that assimilate the metal and include them in the metabolic process can be seen on the legendary Titanic (Fig. 2), which is located at a depth of 3750 m.

The additional method of increase of the manganese concentration in the area of ??crust formation can be connected with a well-known effect of the biological extraction of manganese from sea water with the help of *Foraminifera* — single-celled shell organisms. After the natural death of these microorganisms, they dissolve in the water column without reaching the bottom. Nowadays, these silts cover at least a quarter of the bottom of the oceans and consist mainly of foraminifera shells of the genus *Globigerina*. In this case, a natural effective accumulation of manganese in the layer of this sludge takes place.



Figure 2. The growth of colonies of microorganisms on the metal parts of the Titanic [24,25].

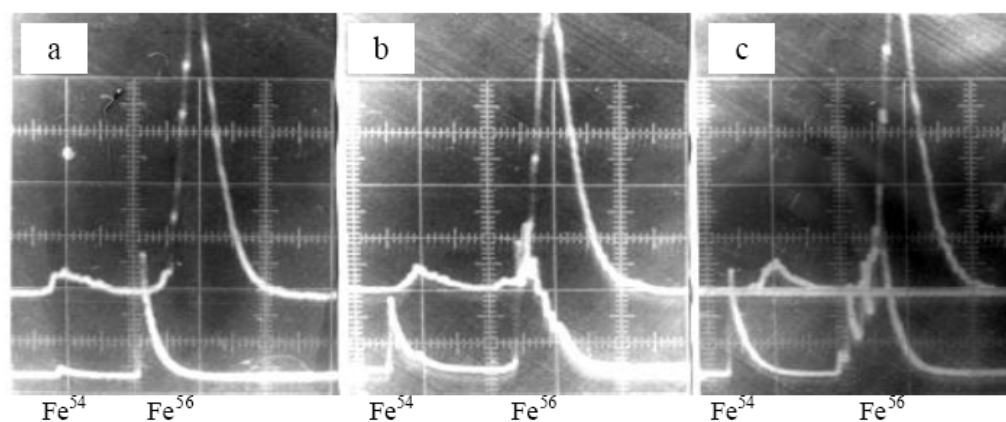


Figure 3. Time-of-flight mass-spectrometric analysis of the results of experiments on isotope Fe^{54} creation in laboratory reaction $\text{Na}^{23} + \text{P}^{31} = \text{Fe}^{54}$; fragments of the mass spectrum of the same bacterial culture *Bacillus subtilis*, grown in a nutrient medium based on H_2O in the presence of Na^{23} and P^{31} , (b), (c) and the absence of P^{31} . (a) The upper graphs on each of the photos correspond to the control spectrum of the natural iron masses obtained in the same series as the corresponding lower graphs. These results were obtained using a time-of-flight mass spectrometer and were displayed on the screen of an oscilloscope with memory.

In contrast to such complicated prehistory of Mn localization and concentration, the efficiency of Fe^{54} fusion (6) depends on the concentration of sodium Na^{23} ($\eta(\text{Na}^{23}) \approx 10.8$ ppm) and phosphorus P^{31} ($\eta(\text{P}^{31}) \approx 0.09$ ppm), which are presented in seawater in significant quantity (much more than Mn^{55}).

The above-listed circumstances show that there are all the necessary prerequisites for the effective transmutation of isotopes in growing microorganisms. The possibility of such transmutations (Na^{23} and P^{31} to Fe^{54} and Mn^{55} to Fe^{37}) has been reliably confirmed in our experiments (see Figs.3 and 4) [2–5].

The effectiveness of such a transmutation processes depends on many circumstances and in the case of a balanced composition of the necessary macro and microelements are the following:

$$\lambda = \frac{\Delta N(\text{Fe}^A)}{N(\text{Mn}^{55})\Delta t} \approx 10^{-8} \text{ synthesized Fe}^A \text{ nuclei per s and per single Mn}^{55} \text{ isotope,} \quad (10)$$

$$\lambda = \frac{\Delta N(\text{Fe}^{54})}{N(\text{Na}^{23})\Delta t} = \frac{\Delta N(\text{Fe}^{54})}{N(\text{P}^{31})\Delta t} \approx 10^{-8} \text{ synthesized Fe}^{54} \text{ nuclei per s and per (Na}^{23}, \text{P}^{31}) \text{ isotopes}$$

for the case of transmutation with a participation of pure microbiological cultures (similar *E.Coli*) and

$$\lambda = \frac{\Delta N(\text{Fe}^A)}{N(\text{Mn}^{55})\Delta t} \approx \frac{\Delta N(\text{Fe}^{54})}{N(\text{Na}^{23})\Delta t} \approx \frac{\Delta N(\text{Fe}^{54})}{N(\text{P}^{31})\Delta t} 10^{-6} \text{ per s and per Mn}^{55}, \text{Na}^{23}, \text{P}^{31} \text{ isotopes} \quad (11)$$

using of microbiological syntrophic associations [2–5].

The characteristic feature of such a transmutation is self-limiting and self-control: the process begins to be inhibited when a great amount of toxins (as the result of metabolic processes) are released and when the local environment is depleted with the necessary isotopic components.

Under laboratory conditions, these factors can be controlled and corrected by periodical adding of appropriate chemical components into the liquid “working” environment.

Under natural conditions, a sufficiently long time is needed to re-launch the transmutation process, during which a natural self-purification of the nearest environment from toxins takes place and the necessary isotopic composition is restored.

This process of self-healing of the local environment can be quite lengthy. In nature, it is carried out using reducers – heterotrophic organisms that return the necessary micro and macro elements from dead organisms to inanimate nature. They implement such a process, decomposing organic residues into simple inorganic chemical compounds in the process of their natural activity. The most effective reducers are bacteria.

After restoration of the necessary composition of micro and macronutrients, the process of transmutation of isotopes begins a new cycle.

Such a self-similar process justifies the periodicity of iron synthesis in crust volume and the formation of thin layers of Fe and Mn.

3. Summary

The scenario considered above fully substantiates all the quantitative and qualitative features of the formation of iron–manganese crusts.

If we use the “standard” estimate for the total mass of iron–manganese crusts and nodules on the ocean bottom ($M_{\text{total}} \approx 300$ billions of tons) and take into account the average experimental values for normalized isotope ratios ($\langle \delta\text{Fe}^{57}(0/00) \rangle \approx 0.8$, $\langle \delta\text{Fe}^{57*}(0/00) \rangle \approx 0.25$) and the relative concentration of iron in these structures ($\eta_{\text{Fe}} \approx 15\%$), then the masses of created isotopes that are connected with such a transmutation are very large and are equal to

$$\Delta M(\text{Fe}^{54}) \approx M_{\text{total}} \eta_{\text{Fe}} \eta(\text{Fe}^{54})_{\text{reference}} \langle \Delta(\text{Fe}^{54}) \rangle \approx 4 \times 10^6 \text{ tons of Fe}^{54} \text{ isotope ,} \quad (12)$$

$$\Delta M(\text{Fe}^{56}) \approx M_{\text{total}} \eta_{\text{Fe}} \eta(\text{Fe}^{56})_{\text{reference}} \langle \Delta(\text{Fe}^{56}) \rangle \approx 2 \times 10^7 \text{ tons of Fe}^{56} \text{ isotope .}$$

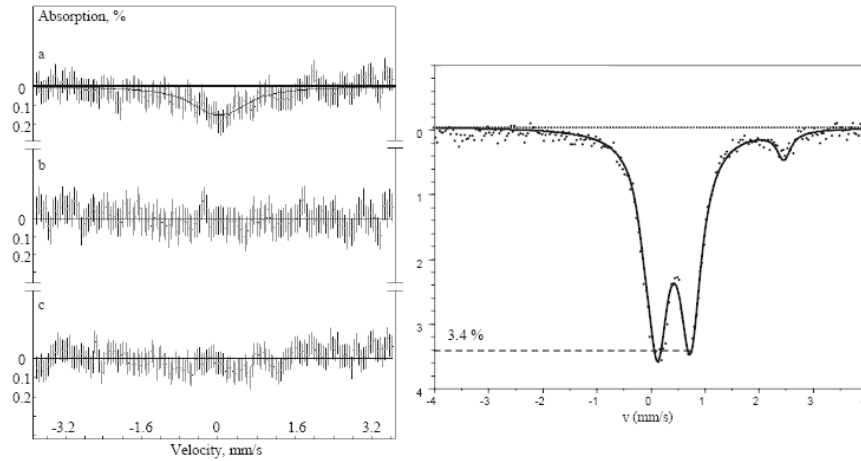


Figure 4. Left: Mössbauer spectrum of the dried microbiological culture of *Saccharomyces cerevisiae* T-8, grown in a liquid nutrient medium based on: (a) heavy water D₂O in the presence of the Mn⁵⁵ isotope; (b) light water H₂O in the presence of Mn⁵⁵; (c) heavy water D₂O in the absence of the Mn⁵⁵ isotope. Right: Mössbauer spectrum of dried microbiological association grown in the volume with presence of D₂O and Mn⁵⁵ isotope.

If we accept that the maximal rate of transmutation of Mn to Fe in natural conditions is close to the values (10) corresponding to transmutation in the laboratory, then the maximal rate of global transmutation in ocean bottom is

$$\Lambda \approx \lambda \frac{M_{\text{total}}}{m(\text{Mn}^{56})} \eta_{\text{Mn}} m(\text{Fe}^{56}) \approx 600 \text{ tons of synthesized Fe}^{56} \text{ isotope per second} \quad (13a)$$

for pure culture and

$$\Lambda \approx \lambda \frac{M_{\text{total}}}{m(\text{Mn}^{56})} \eta_{\text{Mn}} m(\text{Fe}^{56}) \approx 60\,000 \text{ tons of synthesized Fe}^{56} \text{ isotope per second} \quad (13b)$$

for microbiological association.

It is also necessary to take into account that laboratory conditions as a rule are better than natural conditions. On the other hand, it is obvious that the biological substance at the bottom of the oceans roughly corresponds to the microbiological association. Based on these circumstances, we can conclude that a reasonable estimate for the maximal total rate of transmutation is close to the value

$$\Lambda \approx 6000 \text{ tons of synthesized Fe}^{56} \text{ isotope per second.} \quad (13c)$$

This maximal total rate is 100 times higher than the average steel smelting rate worldwide which is equal to 60 tons per second or about 1.8 billions tons per year. Of course, the average rate of transmutation will be several orders of magnitude smaller than this value.

From these results follows that the LENR process based on the transmutation of isotopes in grown biological systems is not limited to the framework of a precision laboratory experiment, but is a significant factor in the geological evolution of the Earth.

In conclusion, one more remark can be made regarding the fundamental problems of the geochemical evolution of the Earth.

It is easy to show that processes, which are close to the results discussed in this paper, can be connected with pulsed stimulation of nuclear reactions due to the action of strong shock waves caused by earthquakes. Such processes, which are connected with cracking of brittle rocks and generation of THz pressure waves, can lead to fission or fusion reactions with formation of new elements and (in selected cases) concomitant neutron emission. These processes have been actively discussed in numerous works (e.g., [26–31]).

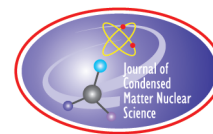
In our opinion, the specific physical mechanism of such a stimulation can be connected with traditional piezonuclear reactions [31] and with the discussed process of formation of coherent correlated states of particles located in the region of unsteady deformation [11,13]. Of course, it is impossible to explain the mechanism of formation of iron and manganese periodic layers in the crust volume using such a pulsed random process connected with earthquakes, but in other cases this scenario is quite real. It is very interesting that similar mechanism for stimulation of nuclear fusion has been predicted and implemented in recent experiments on the effects of high-frequency temperature waves on a distant TiD target [32].

References

- [1] S. Levasseura, M. Franka, J.R. Heinb and A.N. Halliday, *Earth and Planetary Sci. Lett.* **224** (2004) 91–105.
- [2] V.I. Vysotskii and A.A. Kornilova, Nuclear fusion and transmutation of isotopes in biological systems, “Mir” Publ. House, Moscow, 2003, 302 p.
- [3] V.I. Vysotskii and A.A. Kornilova, *Nuclear Transmutation of Stable and Radioactive Isotopes in Biological Systems*, Pentagon Press, India, 2010, 187 p.

- [4] V.I. Vysotskii and A.A. Kornilova, Transmutation of stable isotopes and deactivation of radioactive waste in growing biological systems, *Ann. Nucl. Energy* **62** (2013) 626–633.
- [5] V.I. Vysotskii and A.A. Kornilova, Microbial transmutation of Cs-137 and LENR in growing biological systems *Current Science* **108** (2015) 636–640.
- [6] V.I. Vysotskii and A.A. Kornilova, Correlated states of interacting particles and problems of the coulomb barrier transparency at low energies in nonstationary systems. *J. Technical Phys.* **55** (5), (2010), 613–621.
- [7] V.I. Vysotskii, M.V. Vysotskyy, S.V. Adamenko, Formation and application of correlated states in non-stationary systems at low energy of interacting particles, *J. Exp. Theoret. Phys.* **114** (2) (2012) 243–352.
- [8] V.I. Vysotskii and A.A. Kornilova, Coherent correlated states and low-energy nuclear reactions in non stationary systems. *Euro. Phys. J. A*, **49** (8) (2013) 1–13.
- [9] V.I. Vysotskii, S.V. Adamenko, M.V. Vysotskyy, Acceleration of low energy nuclear reactions by formation of correlated states of interacting particles in dynamical systems, *Ann. Nucl. Energy* **62** (2013) 618–625.
- [10] V.I. Vysotskii and A.A. Kornilova, Formation of correlated states and optimization of nuclear reactions for low-energy particles at nonresonant low-frequency modulation of a potential well, *J. Exp. Theoret. Phys.* **120**(2) (2015) 246–256.
- [11] V.I. Vysotskii and A.A. Kornilova, The formation of correlated states and optimization of the tunnel effect for low-energy particles under nonmonochromatic and pulsed action on a potential barrier. *J. Exp. Theoret. Phys.* **121**(4) (2015) 559–571.
- [12] V.I. Vysotskii and A.A. Kornilova, Coherent correlated states of interacting particles – the possible key to paradoxes and features of LENR. *Current Science*, **108**(4) (2015) 524–530.
- [13] V.I. Vysotskii and A.A. Kornilova, The formation of correlated states and tunneling at low energy at controlled pulse action on particles, *J. Exp. Theoret. Phys.* **125** (2) (2017) 195–209.
- [14] V.I. Vysotskii, A.A. Kornilova and S. Bartalucci, Features of the formation of correlated coherent states and nuclear fusion induced by the interaction of slow particles with crystals and free molecules, *J. Exp. Theoret. Phys.* **127**(3) (2018) 479–490.
- [15] S. Bartalucci, V.I. Vysotskii, M.V. Vysotskyy, Correlated states and nuclear reactions: An experimental test with low energy beams, *Phys. Rev. Accel. Beams* **22**(5) (2019) 054503.
- [16] V.I. Vysotskii and M.V. Vysotskyy, Features of correlated states and a mechanism of self-similar selection of nuclear reaction channels involving low-energy charged particles, *J. Exp. Theoret. Phys.* **128** (6) (2019) 856–864.
- [17] E. Schrodinger, *Ber. Kgl. Akad. Wiss. Berlin S* **24** (1930) 296.
- [18] H.P. Robertson, *Phys. Rev. A* **35** (1930) 667.
- [19] V.V. Dodonov, E.V. Kurmishev and V.I. Manko, *Phys. Lett. A* **79** (1980) 150.
- [20] K.W. Bruland and M.C. Lohan, Controls of trace metals in seawater, in H. Elderfield (Ed.), *Treatise on geochemistry. Vol. 6, The Ocean and Marine Geochemistry*, Elsevier, Amsterdam, 2004, pp. 23–47.
- [21] B.M. Tebo, H.A. Johnson, J.K. McCarthy and A.C. Templeton, Geomicrobiology of manganese oxidation, *Trends Microbiol.* **13** (2005) 421–428.
- [22] G.N. Lysyuk, Silified organisms in manganese forming processes, *Proc. Int. Sem. “Kvarts. Kremnezem”(Quartz. Silica)*, Syktyvkar, 2004, pp. 273–274.
- [23] L.M. Gerasimenko, V. K. Orleanskii and L.V. Zaitseva, Accumulation and precipitation of Mn^{2+} by the Cells of *oscillatoria terebriformis* and transformation, *Microbiology* **82**(3)(2013) 609–617.
- [24] <https://encrypted-tbn0.gstatic.com/images?q=tbn:ANd9GcS1JAik17G3XbCq41GySXuY54T7NXbVf7umybZODCK84fa1Enu-&s>.
- [25] https://ichef.bbci.co.uk/news/976/cpsprodpb/128C4/production/_103727957_tit2.jpg].
- [26] A. Carpinteri and O. Borla, Nano-scale fracture phenomena and teraHertz pressure waves as the fundamental reasons for geochemical evolution, *Strength, Fracture and Complexity* **11** (2018) 149–168.
- [27] A. Carpinteri, G. Lacidogna and A. Manuello (Eds.), *Acoustic, Electromagnetic, Neutron Emissions from Fracture and Earthquakes*, Springer, Switzerland, 2015, VIII + 264.
- [28] A. Carpinteri, G. Lacidogna, O. Borla, A. Manuello and G. Niccolini, Electromagnetic and neutron emissions from brittle rocks failure: Experimental evidence and geological implications, *Sadhana* **37** (2012) 59–78.
- [29] A. Carpinteri, G. Lacidogna, A. Manuello and O. Borla, Piezonuclear fission reactions in rocks: Evidences from microchemical analysis, neutron emission, and geological transformation, *Rock Mechanics and Rock Engineering* **45** (2012) 445–459.
- [30] A. Carpinteri and A. Manuello, Geomechanical and geochemical evidence of piezonuclear fission reactions in the Earth's

- Crust, *Strain* **47** (Suppl. 2) (2011) 267–281.
- [31] A. Carpinteri, G. Lacidogna, A. Manuello and O. Borla: Energy emissions from brittle fracture: Neutron measurements and geological evidences of piezonuclear reactions, *Strength, Fracture and Complexity* **7** (2011) 13–31.
- [32] A. A. Kornilova, V.I. Vysotskii, T. Krit, M.V. Vysotsky and S.N. Gaydamaka, Study of the influence of remote undamped temperature waves on nuclear fusion, *J. Surface Investigation: X-ray, Synchrotron and Neutron Techniques*, **14** (1) (2020) 117–123.



Research Article

The Possible Role of LENR in Dentistry (Reasons, Effects and Prevention)

A.A. Kornilova, S.N. Gaydamaka and A.I. Panchishin

Lomonosov Moscow State University, Russia

V.I. Vysotskii* and M.V. Vysotskyy

Taras Shevchenko National University of Kyiv, Ukraine

A.A. Bolotokov

LLC "Amtertek", Moscow, Russia

Abstract

The possibility of the influence of nuclear effects on the destruction of the tooth surface using dental implants made of titanium is considered. It has been shown for the first time that this process is associated with LENR occurring between selective titanium and calcium isotopes and leading to the formation of a molybdenum isotope. This reaction is stimulated by the growth of natural microbiological cultures located in the oral cavity. The mechanism of such reactions is associated with the formation of coherent correlated states, which are formed due to the topological features of growing microcultures.

© 2020 ISCMNS. All rights reserved. ISSN 2227-3123

Keywords: Coherent correlated states of particles, LENR in medicine, Nuclear reaction in microbiological systems

1. Introduction

The traditional areas of research and application of LENR related effects are limited, as a rule, by a simple model of physical systems. A more detailed analysis has shown that such effects can successfully occur in microbiological systems [1–4]. The next obvious step is to search for LENR effects in a human body. This is a completely new field of research.

In this article we present only the preliminary results related to dentistry studies. In the practice of dentistry, it is well known that dental implants made of titanium often have a negative effect on teeth. This is manifested in the form of "leaching" of calcium from the composition of teeth and leads to their destruction. This very unpleasant effect is

*Corresponding author. E-mail: vivysotskii@gmail.com.

well known, but it does not have a clear biophysical explanation, and its specific reason is still incomprehensible to medical experts. In the following analysis, we have shown for the first time that these critical processes connected with the installation of dental implants can be directly related to LENR effects in the human oral cavity.

2. Microbiological and Biophysical Aspects of Dentistry-related Processes

It is well known that the installation of dental implants is an effective method of tooth restoration. The main element of any implant is a metal base with a thread that is twisted into the bone tissue. The effectiveness of implant ingrowth depends on a number of factors:

- the state of the bone,
- the requirements for mechanical stabilization,
- the structure and properties of implant material.

The basic requirements are, as a rule, hardness, chemical inertness and non-toxicity of the implant material. It should not enter into different chemical reactions, taking into account the fact that among the products may be those that contain a large amount of sodium chloride NaCl, have a high acidity or alkalinity, and also a high alcohol content. Based on these parameters, the most popular material at present is titanium (Ti).

It can be seen that all these requirements apply only to chemical processes and chemical reactions. The practice of experimental dentistry shows that, despite the fulfillment of these conditions, processes leading to catastrophic destruction of the area of the installed implant, embrittlement of a tooth adjacent to the implant, and other local tooth destruction are often observed. On the other hand, the oral cavity is a complex object that contains not only the listed objects, but also many microbiological cultures and their associations.

In fact, this system is very similar to those working cells in which we have conducted experiments on isotope transmutation using stimulating action of growing microbiological systems [1–4]. Similar nuclear effects could be expected in such a system. It is obvious that these experiments should include such main “objects” of operative dentistry as titanium and calcium (the first is the “standard” strength element of all implants, and the second is the basis of the tooth material).

No one has discussed these important problems before and no one has analyzed the possible consequences of such processes. The human oral cavity is a unique ecological system for a wide variety of microorganisms that form a constant microflora. The richness of food resources, constant humidity, optimal pH and temperature create favorable conditions for adhesion, colonization and reproduction of various microbial species. The microflora of the oral cavity takes part in the primary processes of digesting food, assimilation of nutrients and the synthesis of vitamins. It is also necessary to maintain the proper functioning of the immune system, to protect the body from fungal, viral and bacterial infections.

- (a) About 50% of all bacteria in the mouth are streptococci of the *Streptococcaceae* family. *Streptococcus mutans* bacteria form a film on the surface of teeth and can corrode tooth enamel and dentin, which leads to caries and gum infections,
- (b) Bacteria *Solobacterium moorei* and *Lactobacillus casei* are responsible for bad breath
- (c) The bacteria *Porphyromonas gingivalis* is the cause of periodontal disease, and is also “responsible” for the body’s resistance to antibiotics.

This list can be supplemented by many other microbiological cultures and their associations. It should also be noted that all these microorganisms are not mutual antagonists, but form a syntrophic community, which, according to our previous studies [3–6], is one of the prerequisites for effective nuclear transmutation.



Figure 1. From Left to right. Photo of an implants made of pure titanium (*left*) and titanium with Zr protective coating (*right*) before the experiment; the appearance of tubes with implants, nutrient medium and biomass at the beginning and at the end of the experiment (in 12 days).

3. Experiments and Results

We have conducted experiments to study the effect of standard titanium implants on the state of calcium in the laboratory liquid medium, representing a solution of natural saliva, which fully corresponds to the human oral cavity. For the experiment, we have used the anaerobic syntrophic association (anSA) of bacteria inhabiting the human oral cavity and digestive tract. The composition of the association includes more than 500 strains. As a nutrient medium, human saliva with the addition of an iron salt ($\text{FeSO}_4 \cdot 7\text{H}_2\text{O}$) was used, which simulates the possible presence of trace amounts of blood from the gums on the dental implant, as well as the consumption of iron-containing products.

The volume of the nutrient medium was 8 ml, the weight of the moist concentrated biomass of anSA was about 0.5 g. As a substrate for anSA, glucose was added to the bioreactors (0.1 g / l per day). At the end of the experiment implants were removed from the bioreactor tubes, washed and dried in a desiccator.

The photos of both types of implants (made of pure Ti and Ti with Zr protective coating) are shown in Fig. 1. The appearance of the implants after the experiment remained unchanged.

Figure 1 also shows photos of test tubes with the studied objects before the start of the experiment and after its completion (in 12 days).

The study of the nutrient medium, microcultures and the surface of the implants after the end of the experiment has shown that the total calcium content in these components in the presence of Ti implant decreased. At the same time, the results of X-ray fluorescence analysis have shown the presence of molybdenum on the surface of titanium implants after the experiments (see Fig. 2). Before the experiment, molybdenum was absent in the volume and on the surface of the implants and in the composition of the nutrient medium.

In an alternative experiment it was found that during the cultivation of anSA in the presence of a Ti implant with a Zr coating, the situation was fundamentally different – the calcium concentration did not change and molybdenum was not detected on the implant surface!

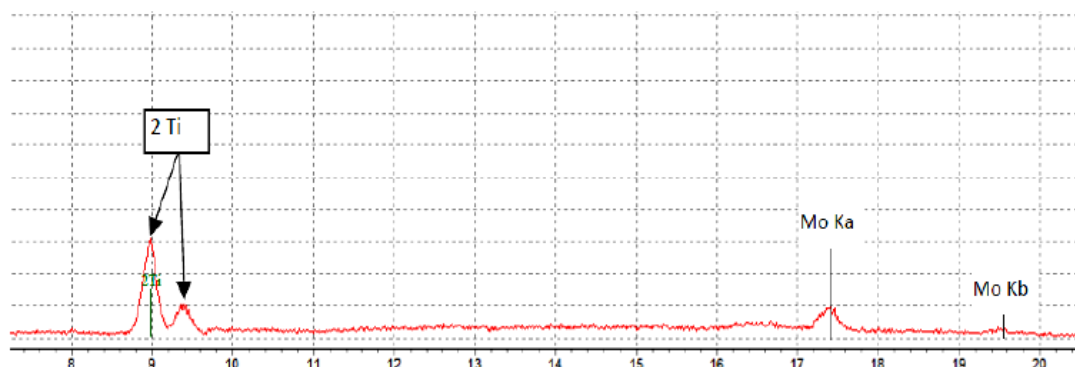
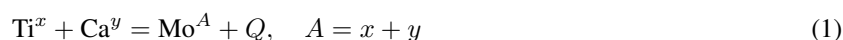


Figure 2. X-ray fluorescence analysis of Ti implant after a 12-day experiment.

4. Analysis and Conclusions

It is well known that calcium is the main chemical element (~36%) in the structure of the tooth. It is the important part of the tooth in the form of a crystal of hydroxy apatite $\text{Ca}_{10}(\text{PO}_4)_6(\text{OH})_2$. The process of creating a foreign element molybdenum (foreign to original system), is connected with possible transmutation reactions:



stimulated by active microbiological associations, which are present in laboratory test tubes and are similar in composition to those microorganisms that are present in saliva and are located on the surface of teeth. Two basic requirements are necessary to produce these reactions at low energy:

- these reactions must be exoenergetic with positive energy $Q > 0$ of reactions,
- the reaction should lead to the formation of stable (non-radioactive) Mo isotopes [7].

The first condition is obvious for any exoenergetic reaction.

The second condition relates to LENR specifics. It has been proved on the basis of the laws of quantum mechanics and nuclear physics [7] that such a feature (the absence of radioactive daughter isotopes) is an obligatory feature of LENR, and it is due to the fact that these reactions are based on the use of fluctuations of energy

$$\delta E_{G \gg 1} \geq \hbar^2 G^2 / 8ma^2 \quad (2)$$

repeatedly amplified (by G^2 times) compared with fluctuations determined by expression

$$\delta E_{G=1} \geq (\delta p)^2 / 2m \approx \hbar^2 / 8ma^2 \quad (3)$$

immediately following from the “standard” Heisenberg uncertainty relations

$$\delta E \delta t \geq \hbar/2, \quad \delta p \delta q \geq \hbar/2 \quad (4)$$

for, respectively, energy, time, momentum and coordinate.

Here

$$G \equiv 1/\sqrt{1-r^2} \geq 10^3 - 10^4$$

is the coefficient of correlation efficiency [8–18], which corresponds to the Schrödinger–Robertson uncertainty relation

$$\delta p \delta q \geq \hbar/2\sqrt{1-r^2} \quad (5)$$

with a correlation coefficient $|r| \leq 1$.

Generation of these giant fluctuations $\delta E_{G \gg 1}$ takes place during the formation of coherent correlated states of interacting particles in a natural non-stationary potential nanowells with a size about $a \approx 0.2 - 1$ nm, which continuously appear and disappear in areas of microculture growth (during cell division, at DNA replication, etc.).

An important feature of these states is a very significant (by many orders of magnitude) increase of the duration δt of these fluctuations to values sufficient to stimulate nuclear reactions [7].

On the other hand, even such increased duration of the existence of these fluctuations is a small value at the level of several picoseconds or femtoseconds, limiting the duration of the corresponding fusion reactions. It is easy to see that reactions with a longer duration (including reactions that form radioactive daughter isotopes) cannot be generated due to these very short fluctuations [7].

In fact, this rule forbids the generation of nuclear reactions that are stimulated by virtual energy in any reaction channels that are characterized by a large duration of the first stage of nuclear transformations after the formation of the initial compound nucleus.

This conclusion explains the absence of radioactive daughter isotopes in any experiments that are stimulated by the virtual energy (including LENR experiments in biological systems).

A direct calculation has shown that among all possible nuclear reactions of molybdenum fusion (1) with participation of all stable isotopes of titanium, calcium and molybdenum (Ti^{46} , Ti^{47} , Ti^{48} , Ti^{49} , Ti^{50} , Na^{40} , Ca^{42} , Ca^{43} , Ca^{44} , Ca^{46} , Ca^{48} , Mo^{92} , Mo^{94} , Mo^{95} , Mo^{96} , Mo^{97} , Mo^{98} , Mo^{100}), only one fusion reaction



involving three “key” isotopes (Ti^{46} (natural abundance is 8.25%), Ca^{48} (0.187%), Mo^{94} (9.15%)) satisfies the both necessary requirements!

Other potentially possible reactions (1) result in the formation of daughter radioactive Mo^{A*} isotopes or are endoenergetic reactions with negative energies of reactions ($Q < 0$) and for their realization, a sufficiently large additional energies $\Delta E \geq |Q|$ (in the interval 0.2–7 MeV) are necessary. The sources of such real (not virtual) and very great energy ΔE are absent in any realistic biological system and such reactions are fundamentally impossible!

There are many biophysical reasons for the synthesis of molybdenum in growing biological systems. Molybdenum significantly increases the effectiveness of antioxidants, including vitamin C. It is also an important component of the tissue respiration system. Molybdenum enhances the synthesis of amino acids, improves the accumulation of nitrogen. Molybdenum also is a part of a number of enzymes (aldehyde oxidase, sulfite oxidase, xanthine oxidase, etc.) that perform important physiological functions, in particular, the regulation of uric acid metabolism. Molybdenum and its chemical compounds play an important role in certain biochemical processes (including effective biochemical replacement). It should be noted that although the natural abundance of the “key” calcium isotope Ca^{48} (0.187%) is small, the consequences of reaction (6) with its participation can be very significant. There are several important factors for the possible effect of this reaction on the condition of teeth and implants, including three most likely:

- violation of the monolithic structure of a small tooth due to a local replacement of calcium with molybdenum,
- possible influence of the positive reaction energy $Q > 0$ on the structure of the bone tissue of the tooth,
- development of microbiological infections in nano-regions adjacent to the site of the destructive local nuclear reaction.

These processes can be connected, e.g., with the phonon mechanism of LENR energy transfer proposed by Hagelstein [19,20]. The THz frequency of such high-frequency phonons is close to the Debye frequency (about 10^{13} Hz). These phonons are characterized by a short mean free path and transfer their energy to the nearest atoms. In this case, there is a small-sized zone around each nucleus of the synthesized molybdenum, inside which the atoms receive energy of about 10–20 eV, which leads to the destruction of the crystal structure of the tooth. Based on these (not yet completed) studies, many useful recommendations can be made.

One of the main ones is to use titanium as the basis for the implant, from which the “key” and most “potentially dangerous” Ti^{46} isotope must be removed. In this case, we can completely eliminate the nuclear reaction between titanium and calcium and prevent possible catastrophic tooth destruction after implantation!

References

- [1] V.I. Vysotskii and A.A. Kornilova, Nuclear fusion and transmutation of isotopes in biological systems, Monograph, Mir, Moscow, 2003, p. 302.
- [2] V.I. Vysotskii and A.A. Kornilova, *Nuclear Transmutation of Stable and Radioactive Isotopes in Biological Systems*, Pentagon Press, India, 2010, p. 187.
- [3] V.I. Vysotskii and A.A. Kornilova, Transmutation of stable isotopes and deactivation of radioactive waste in growing biological systems, *Ann. Nucl. Energ.* **62** (2013) 626–633.
- [4] V.I. Vysotskii and A.A. Kornilova, Microbial transmutation of Cs-137 and LENR in growing biological systems, *Current Science* **108** (2015) 636–640.
- [5] A.A. Kornilova, V.I. Vysotskii, S.N. Gaydamaka and M.A. Gladchenko, *Nuclear Reactions in Living Nature: The Possibility of Biological Processing and Deactivation of Liquid Radioactive Waste. Springer Proceedings in Earth and Environmental Sciences*, Springer, (SPEES), 25 March 2019, pp. 213–230.
- [6] V.I. Vysotskii and A.A. Kornilova, “Biological Transmutation” of stable and radioactive isotopes in growing biological systems. *J. Condensed Matter Nucl. Sci.* **28** (2019) 7–20.
- [7] V.I. Vysotskii and M.V. Vysotskyy, Features of correlated states and a mechanism of self-similar selection of nuclear reaction channels involving low-energy charged particles, *J. Exp. Theoret. Phys. (JETP)* **128** (6) (2019) 856–864.
- [8] V.I. Vysotskii and M.V. Vysotskyy, Coherent correlated states and low-energy nuclear reactions in non-stationary systems, *Eur. Phys. J. A* **49** (2013) 99.
- [9] V.I. Vysotskii, M.V. Vysotskyy and S.V. Adamenko, Formation and application of correlated states in non-stationary systems at low energy of interacting particles, *J. Exp. Theoret. Phys. (JETP)* **114** (2) (2012) 243–352.
- [10] V.I. Vysotskii and M.V. Vysotskyy, Coherent correlated states and low-energy nuclear reactions in non stationary systems, *Eur. Phys. J. A* **49** (8) (2013) 1–13.
- [11] V.I. Vysotskii, S.V. Adamenko and M.V. Vysotskyy, Acceleration of low energy nuclear reactions by formation of correlated states of interacting particles in dynamical systems, *Ann. Nucl. Energy* **62** (2013) 618–625.
- [12] V.I. Vysotskii and M.V. Vysotskyy, Coherent correlated states of interacting particles – the possible key to paradoxes and features of LENR, *Current Science* **108**(4) (2015) 30–36.
- [13] V.I. Vysotskii and M.V. Vysotskyy, Formation of correlated states and optimization of nuclear reactions for low-energy particles at nonresonant low-frequency modulation of a potential well, *J. Exp. Theoret. Phys. (JETP)* **120**(2) (2015) 246–256.
- [14] V.I. Vysotskii and M.V. Vysotskyy, The formation of correlated states and optimization of the tunnel effect for low-energy particles under nonmonochromatic and pulsed action on a potential barrier, *J. Exp. Theoret. Phys. (JETP)* **121**(4) (2015) 559–571.
- [15] V.I. Vysotskii and M.V. Vysotskyy, Coherent correlated states of interacting particles – the possible key to paradoxes and features of LENR. *Current Science* **108**(4) (2015) 524–530.
- [16] V.I. Vysotskii and M.V. Vysotskyy, The formation of correlated states and tunneling at low energy at controlled pulse action on particles *J. Exp. Theoret. Phys. (JETP)* **125** (2) (2017) 195–209.

- [17] V.I. Vysotskii, M.V. Vysotskyy and S. Bartalucci, Features of the formation of correlated coherent states and nuclear fusion induced by the interaction of slow particles with crystals and free molecules, *J. Exp. Theoret. Phys. (JETP)* **127**(3) (2018) 479–490.
- [18] S. Bartalucci, V.I. Vysotskii and M.V. Vysotskyy, Correlated states and nuclear reactions: An experimental test with low energy beams, *Phys. Rev. Accel. Beams* **22**(5) (2019) 054503.
- [19] P.L. Hagelstein and I.U. Chaudhary, Phonon–nuclear coupling for anomalies in condensed matter nuclear science, *J. Condensed Matter Nucl. Sci.* **12**, (2013) 105.
- [20] P.L. Hagelstein, Quantum composites: a review, and new results for models for condensed matter nuclear science, *J. Condensed Matter Nucl. Sci.* **20** (2016) 139.